Computational Mechanics in Structural Engineering

Recent Developments

Edited by Franklin Y. Cheng and Yuanxian Gu

ELSEVIER

COMPUTATIONAL MECHANICS IN STRUCTURAL ENGINEERING

Recent Developments

Elsevier Science Internet Homepage

http://www.elsevier.nl (Europe)
http://www.elsevier.com (America)
http://www.elsevier.co.jp (Asia)

Consult the Elsevier homepage for full catalogue information on all books, journals and electronic products and services.

Elsevier Titles of Related Interest

CHENG & SHEU
Urban Disaster Mitigation – The Role of Engineering and Technology
ISBN: 008-041920-8

CHENG & WANG
Post-Earthquake Rehabilitation and Reconstruction
ISBN: 008-042825-8

SRIVASTAVA
Structural Engineering World Wide 1998 (CD-ROM Proceedings with Printed Abstracts Volume, 702 papers)
ISBN: 008-042845-2

OWENS
Steel in Construction (CD-ROM Proceedings with Printed Abstracts Volume, 268 papers)
ISBN: 008-042997-1

GODOY
Thin-Walled Structures with Structural Imperfections: Analysis and Behavior
ISBN: 008-042266-7

FUKUMOTO
Structural Stability Design
ISBN: 008-042263-2

USAMI & ITOH
Stability and Ductility of Steel Structures
ISBN: 008-043320-0

GUEDES-SOARES
Advances in Safety and Reliability (3 Volume Set)
ISBN: 008-042835-5

FRANGOPOL, COROTIS & RACKWITZ
Reliability and Optimization of Structural Systems
ISBN: 008-042826-6

Related Journals

Free specimen copy gladly sent on request: Elsevier Science Ltd, The Boulevard, Langford Lane, Kidlington, Oxford, OX5 1GB, U.K.

- Advances in Engineering Software
- Composite Structures
- Computers and Structures
- Construction and Building Materials
- Computer Methods in Applied Mechanics and Engineering
- Engineering Analysis with Boundary Elements
- Engineering Failure Analysis
- Engineering Structures
- Journal of Constructional Steel Research
- Probabilistic Engineering Mechanics
- Reliability Engineering and System Safety
- Structural Safety
- Thin-Walled Structures

COMPUTATIONAL MECHANICS IN STRUCTURAL ENGINEERING

Recent Developments

Edited by

Franklin Y. Cheng
University of Missouri-Rolla, USA

and

Yuanxian Gu
Dalian University of Technology, China

1999

ELSEVIER

An Imprint of Elsevier Science
Amsterdam • Lausanne • New York • Oxford • Shannon • Singapore • Tokyo

ELSEVIER SCIENCE Ltd
The Boulevard, Langford Lane
Kidlington, Oxford OX5 1GB, UK

First edition 1999

Library of Congress Cataloging in Publication Data

Computational mechanics in structural engineering : recent developments / edited by Franklin Y. Cheng and Yuanxian Gu. -- 1st ed.
p. cm.
ISBN 0-08-043008-2 (hc.)
1. Structural analysis (Engineering)--Data processing. 2. Computer-aided engineering. I. Cheng, Franklin Y. II. Gu, Yuanxian.
TA647.C64 1999
624.1'7--dc21 98-51822
CIP

ISBN: 0-08-043008-2

∞ The paper used in this publication meets the requirements of ANSI/NISO Z39.48-1992 (Permanence of Paper).
Printed in The Netherlands.

CONTENTS

This Page Intentionally Left Blank

PREFACE

Since the First Sino-US Joint Symposium/Workshop on Recent Developments and Future Trends of Computational Mechanics in Structural Engineering was held September 24-28, 1991, in Beijing, both countries have been actively engaged in cooperative research benefitting both countries and the research communities at large. Researchers from the US and China have a strong desire and commitment to exchange state-of-the-art information and to advance scientific progress.

The Second Sino-US Symposium Workshop on Recent Advancement of Computational Mechanics in Structural Engineering was held May 25-28, 1998, in Dalian, China. The objectives were:

- to share the insights and experiences gained from recent developments in theory and practice
- to assess the current state of knowledge in various topic areas of mechanics and computational methods and to identify joint research opportunities
- to stimulate future cooperative research and to develop joint efforts in subjects of common needs and interests
- to build and to strengthen the long-term bilateral scientific relationship between academic and professional practicing communities

Topic areas discussed cover the entire field of computational structural mechanics. These topics have advanced broad applications in the engineering practice of modern structural analysis, design and construction of buildings and other structures, and in natural hazard mitigation.

Speakers were invited through steering committees in both countries. The Chinese steering committee consisted of:

Professor Wanxie Zhong (chair)
Department of Engineering Mechanics, Dalian University of Technology

Professor Junzhi Cui
Institute of Computational Mathematics and Science-Engineering Computation, Academia Sinica

Professor Yuanxian Gu
Department of Engineering Mechanics, Dalian University of Technology

Professor Jianjing Jiang
Department of Engineering Mechanics, Tsinghua University

The US steering committee consisted of:

Dr. Jann N. Yang (chair)
Professor of Civil Engineering, University of California at Irvine

Dr. Franklin Y. Cheng
Curators' Professor of Civil Engineering, University of Missouri-Rolla

Dr. Zhen Chen
Assistant Professor of Civil Engineering, University of Missouri-Columbia

Chinese delegates included:

Professor Pu Chen, ... *Beijing University*
Professor Yingjun Chen, ... *Northern Jiaotong University*
Professor Gengdong Cheng, ... *Dalian University of Technology*
Professor Junzhi Cui, ... *Chinese Academy of Sciences*
Professor Baoyan Duan, ... *Xian University of Electronic Science & Technology*
Professor Yuanxian Gu, ... *Dalian University of Technology*
Professor Zhichao Hou, ... *Tsinghua University*
Professor Haiyan Hu, ... *Nanjing University of Aeronautics & Astronautics*
Professor Yi Huang, *Xian University of Architectural Science & Technology*
Professor Jianjing Jiang, ... *Tsinghua University*
Professor Xikui Li, ... *Dalian University of Technology*
Professor Jiahoa Lin, ... *Dalian University of Technology*
Professor J.G. Teng, ... *Hong Kong Polytechnic University*
Professor Changchun Wu, ... *University of Science & Technology of China*
Professor Youlin Xu, ... *Hong Kong Polytechnic University*
Professor Zhenhan Yao, ... *Tsinghua University*
Professor Si Yuan, ... *Tsinghua University*
Professor Wanxie Zhong, ... *Dalian University of Technology*

US delegates included:

Professor Lawrence A. Bergman, .. *University of Illinois at Urbana-Champaign*
Professor Zhen Chen, ... *University of Missouri-Columbia*
Professor Franklin Y. Cheng, ... *University of Missouri-Rolla*
Professor Carlos A. Felippa, ... *University of Colorado at Boulder*
Professor Henri P. Gavin, ... *Duke University*
Professor Le-Wu Lu, ... *Lehigh University*
Professor Arif Masud, ... *University of Illinois at Chicago*
Professor Kevin Z. Truman, ... *Washington University*
Professor Sara Wadia-Fascetti, ... *Northeastern University*
Professor Ming L. Wang, ... *University of Illinois at Chicago*
Professor Jann N. Yang, ... *University of California at Irvine*

All technical papers were carefully reviewed by the steering committees. Professor Franklin Y. Cheng completed the final editing of the papers in the proceeding's volume for publication. Their contributions are specially acknowledged.

S.C. LIU, Program Director
K.P. CHONG, Program Director
Civil & Mechanical Systems
National Science Foundation

ACKNOWLEDGMENTS

The Second Sino-US Symposium/Workshop on Recent Advancement of Computational Mechanics in Structural Engineering was jointly sponsored by the US National Science Foundation and the Chinese National Natural Science Foundation and Ministry of Education.

As Editors of the proceedings, we gratefully acknowledge Drs. S.C. Liu and K.P. Chong of the National Science Foundation and Professors L.X. Qian and W.X. Zhong of Dalian University of Technology for their encouragement and advice.

Papers were reviewed by both steering committees as well as Professors Lawrence Bergman, Zhen Chen, Carlos Felippa, Henri Gavin, Arif Masud, Kevin Truman, Sara Wadia-Fascetti, and Ming Wang. Workshop resolutions were integrated by Professor Bergman. We thank them all for their cooperation and assistance.

Our gratitude goes to Dr. James Milne, Senior Publishing Editor, Engineering and Technology, Elsevier Science Ltd, Oxford, England for his guidance and to Ms. Elizabeth Farrell at the University of Missouri-Rolla for her technical support.

Papers assembled in the proceedings volume are intended to serve as a reference tool and as supplementary course material for educators, researchers and practitioners in the international engineering community.

FRANKLIN Y. CHENG
Curators' Professor of Civil Engineering, University of Missouri-Rolla, USA
Honorary Professor, Harbin University of Architecture & Engineering, China
Honorary Professor, Xian University of Architecture & Technology, China
Honorary Professor, Yunnan Polytechnic University, China

YUANXIAN GU
Professor and Head, Department of Engineering Mechanics
Research Institute of Engineering Mechanics
Dalian University of Technology, China

This Page Intentionally Left Blank

Second Sino-US Joint Symposium on Recent Advancement of Computational Mechanics in Structural Engineering
25-28 May 1998, Dalian, China

Front row: K. Fu, J.H. Lin, X.S. Xu, M.L. Wang, P. Chen, Z.C. Hou, Y.X. Gu, J.G. Teng, Y.L. Xu
Back row: R.F. Wu, Q.G. Meng, C.C. Wu, Y.J. Chen, H.Y. Hu, G.D. Cheng, W.M. Dong, A. Masud, Z.H. Yao, X.K. Li, W.X. Zhong, K.Z. Truman, C.A. Felippa, S.C. Liu, L.W. Lu, F.Y. Cheng, L.A. Bergman, J.Z. Cui, L.X. Qian, S. Wadia-Fascetti, J.J. Jiang, H. Gavin, J.N. Yang, Z. Chen, B.Y. Duan, S. Yuan

Opening remarks by G.D. Cheng, President, Dalian University of Technology, with speakers (left to right) L.X. Qian, W.X. Zhong, S.C. Liu, F.Y. Cheng, J.N. Yang, C.A. Felippa, Q.G. Meng

Conference Room

Welcoming remarks by Junwen Liu, Deputy Mayor of Dalian
(left to right) L.X. Qian (partially hidden), W.X. Zhong, S.C. Liu,
Mayor Liu, F.Y. Cheng, J.N. Yang, C.A. Felippa, Q.G. Meng

G.D. Cheng and F.Y. Cheng outside conference building

US delegates (left to right) S. Wadia-Fascetti, M.L. Wang, L.W. Lu, J.N. Yang, L.A. Bergman, H.P. Gavin, K.Z. Truman, C.A. Felippa, F.Y. Cheng, Z. Chen, A. Masud

Delegates at reception

Luncheon for delegates (clockwise) K.Z. Truman, L.A. Bergman, S. Wadia-Fascetti, J.Z. Cui, W.H. Zhong, M.L. Wang, F.Y. Cheng, A. Masud, C.A. Felippa

Longtime friends
(seated) X.S. Li, F.Y. Cheng, W.X. Zhong, (standing) J.H. Lin

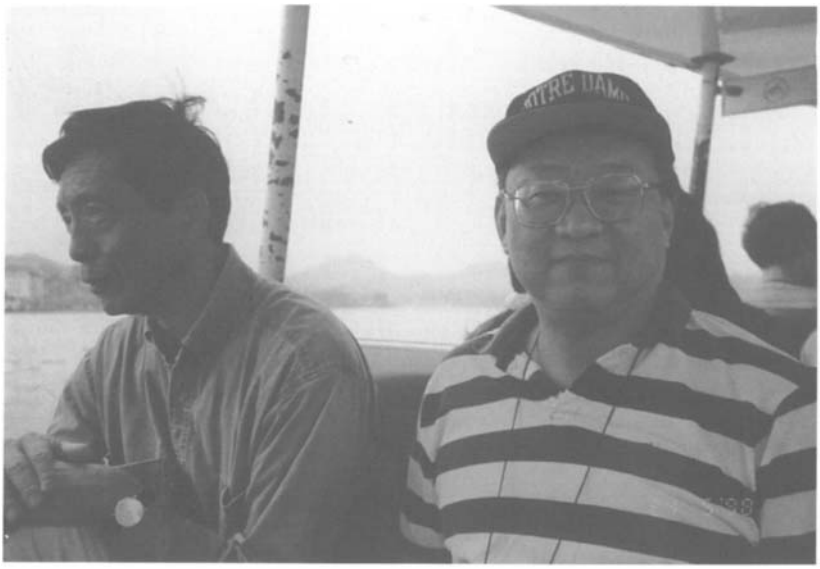

W.M. Dong and S.C. Liu en route to site visit

W.A. Anderson, NSF Senior Advisor, and F.Y. Cheng
in front of hotel

RESOLUTIONS OF SECOND SINO-US JOINT SYMPOSIUM / WORKSHOP ON RECENT ADVANCEMENT OF COMPUTATIONAL MECHANICS IN STRURCTURAL ENGINEERING

The second Sino-US Joint Symposium/Workshop on Recent Advancement of Computational Mechanics in Structural Engineering, jointly chaired by Professor Wanxie Zhong of the Dalian University of Technology and Professor Jann N. Yang of the University of California at Irvine, was held May 25-28, 1998, in Dalian, China. Presentations and discussions during the symposium mainly focused on the areas of structural optimization, stochastic structural dynamics, structural control and system identification, linear and nonlinear finite element analysis, large-scale and parallel computing, and structural design.

At the conclusion of the workshop, which followed the symposium, the participants unanimously passed the following resolutions:

- Encourage collaborative research projects between Chinese and US individual investigators and groups of investigators, through short-term exchange of science and engineers;

- Seek NSF (US) and NNSF (China) joint research support to promote and facilitate the evaluation of joint research proposals;

- Establish future Sino-US joint symposia/workshops on a biennial basis, with venues alternating between the US and China;

- Propose that the Third Sino-US Joint Symposium/Workshop be scheduled for the year 2000 and that the theme of the symposium be "Methods and Applications of Optimization in Design" with St. Louis, Missouri as a possible location. Professor Kevin Truman of Washington University in St. Louis will investigate such possibilities and will coordinate his efforts with Professor Yuanxian Gu of the Dalian University of Technology.

Resolutions thanking the co-chairs for their efforts and the local organizing committee for their outstanding arrangements and hospitality also passed unanimously.

Topics of mutual interest that were recommended for further investigation as potential joint research activities by the three working groups are as follows.

Working Group 1: Optimization of Civil Infrastructure Systems

Structural Design Using Optimization Theory

Performance-Based Design - application of optimization theory to performance-based design including objectives and constraints that reflect reliability, serviceability, and strength.

Life-Cycle Costs - development of optimization-based system (integrated) design including

elements such as multiple objectives, damage costs, strength degradation, and environmental loads.

Upgrade, Repair and Retrofit - development of advanced optimization theory to assess structural enhancements (designs) for improved safety, risk mitigation, and potential loss reduction.

Nonlinear Systems - development of advanced optimization theory for application to nonlinear systems due to conditions such as material nonlinearity, large deformations, environmental loads, dynamic loads, optimal control, deterioration or fracture.

Socio-Economic Impact - integration of socio-economic factors into the optimal structural design theory based on a given structure's impact on elements such as commerce, transportation networks, and community living.

US/China Joint Meeting - exchange of practical applications of structural optimization through a joint meeting between the ASCE committee on Optimal Design, other qualified US researchers, and their Chinese counterparts.

High-Performance Computing - application of high-performance computing for the optimal design of large-scale systems.

Working Group II: New Technologies in Structural Engineering

High-Performance Structures - objective-based issues include durability, damage control, and survival.

Random Vibration-Based Design - development of computational methods for random vibration analysis, statistical identification of loading, and development of probability-based design criteria.

Advanced Monitoring Systems for Large Structures - new sensor technologies, algorithm development, damage identification, and prediction models for life-cycle design.

Advanced Materials - homogenization for composite materials, engineering-based design of advanced materials, and design of structural components (i.e., connections).

Passive/Hybrid/Active/Semi-Active Technologies for Structural Control - practical implementation, theoretical developments, and device development.

Working Group III: Mathematical and Computational Aspects of Design and Optimization

Long-Span Bridges - advanced methods for analysis and design under multiple loadings (earthquake, wind, traffic).

Integrated Structural and Material Design - development of unified approaches.

High-Performance Computing - application of high-performance computing and communication, and virtual reality modeling and visualization, to the analysis and engineering design of large-scale structures.

Multiphysics - development of a computational testbed for multiphysics, multiscale, material modeling and testing.

Symbolic Computation - integration of symbolic computation into large-scale multidisciplinary problems in infrastructural engineering.

MULTIOBJECTIVE OPTIMUM DESIGN OF STRUCTURES WITH GENETIC ALGORITHM AND GAME THEORY: APPLICATION TO LIFE-CYCLE COST DESIGN

Franklin Y. Cheng

Curators' Professor, Department of Civil Engineering
Senior Investigator, Intelligent Systems Center
University of Missouri-Rolla
Rolla, MO 65409-0030 USA

ABSTRACT

Loss of life and property from possible future earthquakes as well as the expense and difficulty of post-earthquake rehabilitation and reconstruction strongly suggest the need for proper structural design with damage control. Design criteria should balance initial cost of the structure with expected losses from potential earthquake-induced structural damage. Life-cycle cost design addresses these issues. Such a design methodology can be developed using multiobjective and multilevel optimization techniques. Presentation here focuses on genetic algorithm and game theory as well as a life-cycle cost model for this innovative design methodology.

Genetic algorithms (GAs) have the characteristic of maintaining a population of solutions, and can search in a parallel manner for many nondominated solutions. These features coincide with the requirement of seeking a Pareto optimal set in a multiobjective optimization problem. The rationale for multiobjective optimization via GAs is that at each generation, the fitness of each individual is defined according to its nondominated property. Since nondominated individuals are assigned the highest fitness values, the convergence of a population will go to the nondominated zone - the Pareto optimal set. Based on this concept, a Pareto GA whose goal is to locate the Pareto optimal set of a multiobjective optimization problem is developed. In this GA, to avoid missing Pareto optimal points during evolutionary processes, a new concept called Pareto-set filter is adopted. At each

generation, the points of rank 1 are put into the filter and undergo a nondominated check. In addition, a niche technique is provided to prevent genetic drift in population evolution. This technique sets a replacement rule for reproduction procedures. For a constrained optimization problem, a revised penalty function method is introduced to transfer a constrained problem into a nonconstrained one. The transferred function of a point contains information on a point's status (feasible or infeasible), position in a search region, and distance to the Pareto optimal set. Three numerical examples are provided: 1) optimum design of a seismic-resistant structure with/without control, 2) optimum design for a final structural system selected from steel frame, reinforced concrete, or composite system, and 3) sensitivity analysis of the effect of cost function on structural probability failure. It is concluded that multiobjective and multilevel optimization is essential to determine target reliability and seismic building code performance.

KEYWORDS

Genetic algorithm, game theory, life-cycle cost, multiobjective and multilevel optimization, earthquake, probability failure, fuzzy logic, Pareto set filter, niche technique, control.

INTRODUCTION

In the current engineering design community, major design efforts are based on a conventional trial and error approach for which the relative stiffness of a structure's constituent members must be assumed. If preliminary stiffness is misjudged, then repeat analysis, even with a sophisticated computer program, will usually not yield an improved design. The optimum design concept is recognized as being more rational and reliable than the conventional design approach. Considerable literature has been published on the subject of optimal structural design for single-objective function (Cheng and Truman, 1985; Cheng [ed.], 1986; Cheng and Juang, 1988; Frangopol and Cheng [eds.], 1996)

Most real-world design optimization problems in structures are multimodal. There often exist several objectives to be considered by the designer. Usually these objectives are conflicting rather than complementary. A single-objective optimization formulation does well with respect to an optimal objective, but the design may not always be a "good" design. Consider a hypothetical example. If a structure is optimized for minimum weight subject to constraints such as stress, displacement, buckling and vibration period, a structure is then obtained with minimum constructed materials. However, the structure may have a poor performance of dynamic response under the action of seismic loadings. If the minimum earthquake input energy is also included as objective, a more rational, compromise design will be produced (Cheng and Li, 1996; Cheng and Li, X.S., 1998)). This combined formulation is a multiobjective optimization problem (MOP). Multiobjective optimization offers the possibility to consider effectively all the different, mutually conflicting requirements inherent in a design problem.

In game theory, if players agree to cooperate, a Pareto optimum will be an ideal solution because it has the property that if any other solution is used, at least one player's performance index is worse, or all the players do the same. This study demonstrates how game theory as a design tool applies to an MOP, and describes the relationship between cooperative game theory and Pareto optimal solution. Three genetic algorithms for multiobjective optimization are proposed based on game theory. In the Pareto GA, whose goal is to find a representative sampling of solutions along with the Pareto optimal set, two new techniques are investigated: a new operator called Pareto-set filter is introduced to prevent the loss of Pareto optimum points in evolutionary progress; and niche technique is created by putting limitations on reproduction operators. Pareto GA for a constrained MOP is further studied tc include fuzzy-logic scheme. Life-cycle cost model is introduced along with multilevel optimization concept. The proposed multiobjective optimization techniques are applied to the optimum design of a seismic structure with/without control and applied to evaluate a structural system as wether it should be steel frame, reinforced concrete frame, or composite steel-and-reinforced-concrete frame. Numerical results show that multiobjective optimization is essential to produce a good seismic structural design.

MULTIOBJECTIVE OPTIMIZATION AND PARETO OPTIMUM

Multiobjective optimization can be defined as determining a vector of design variables that are within the feasible region to minimize (maximize) a vector of objective functions and can be mathematically expressed as follows

$$\begin{aligned} &\textit{Minimize} && F(x) = \left\{f_1(x),\ f_2(x),\ldots,\ f_m(x)\right\} \\ &\textit{Subject to} && g(x) \le 0 \end{aligned} \tag{1}$$

where $\mathbf{x}$ is the vector of design variables, $f_i(\mathbf{x})$ is the ith objective function, and $g(\mathbf{x})$ is the constraint vector.

One feature of multiobjective optimization involves possible conflicting objectives. Therefore there exists a trade-off among objectives, i.e., an improvement gained for one objective is only achieved by making concessions to another objective. There is no optimum solution for all m objective functions simultaneously. There only exists a "compromise solution" rather than an optimum solution (see Fig. 1). Thus the solution of a multiobjective optimization problem can be defined so that if vector $\mathbf{x}^*$ is a solution to Eq. (1), there exists no feasible vector $\mathbf{x}$ which would decrease an objective function without causing a simultaneous increase in at least one other objective function. The solution by the above definition is also called a Pareto optimum or nondominated solution. A feasible vector $\mathbf{x}^*$ is a Pareto optimum for Eq. (1), if and only if there exists no feasible vector $\mathbf{x}$ such that $f_i(\boldsymbol{x}) \le f_i(\boldsymbol{x}*)$, $i \in \{1,2,\ldots,m\}$ and $f_i(\boldsymbol{x}) < f_i(\boldsymbol{x}*)$, for at least one $i \in \{1,2,\ldots,m\}$. For a multiobjective optimization problem, the solution procedure is composed as generating its Pareto optimal set and deciding the final selection from the set.

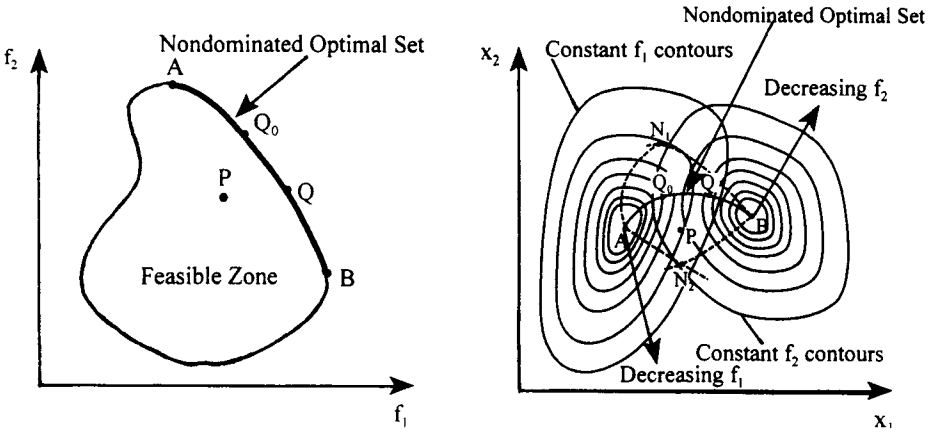

a. Objective Function Space b. Conflicting Objectives

Figure 1: Two-Objective Maximization Problem

GAME THEORY ALGORITHMS

Game theory has been developed for both cooperative and non-cooperative games (Neumann *et al.*, 1947). In the latter each player acts independently in an effort to maximize his own payoff, which produces an outcome (Nash equilibrium solution) that may be favorable for one player, but not for another. The concept of player cooperation therefore becomes important when considering compromise game outcomes. A cooperative game means that the players agree to form coalitions under the expectation that, by working together, a mutually beneficial outcome can be obtained. The measure of success of a cooperative play is embodied in the concept of Pareto optimum since it has the property of a nondominated (Pareto optimum) solution. A cooperative game theory consists of analyzing conflicts existing in objectives or interest groups (players), providing an unemotional form for discussion and negotiations among players, and then suggesting a "compromise solution" which can be accepted by all players.

A multiobjective optimization problem can be cast as a cooperative game problem in which it is assumed that one player is associated with an objective. The objective function f_i can be regarded as the payoff of the *i*th player. With cooperative multiobjective optimization, the "compromise solution" should make sure that each objective obtains its maximum possible value even though each objective cannot arrive at its own best value. Optimal trade-off among the objectives is sought by using the concept of game theory as follows (Cheng *et al.*, 1996). First, the m individual objective functions are minimized respectively subject to given constraints.

$$\begin{aligned} &\textit{Minimize} && F_i(x) \\ &\textit{Subject to} && g(x) \le 0 \end{aligned} \qquad (2)$$

For each objective function f_i, an optimal solution x^*_i is obtained; then a pay-off matrix is

constructed. The best and worst values in the Pareto set can be obtained from the pay-off matrix as

$$\begin{aligned} f_{i,\min} &= f_i(x_i^*) \qquad j=1,\ldots,m \\ f_{i,\max} &= Max\left[f_1(x_j^*)\right] \quad j=1,\ldots,m \quad i=1,\ldots,m \end{aligned} \tag{3}$$

Consequently the ith objective function should not expect a value better than $f_{i,min}$, but not worse than $f_{i,max}$. Thus a substitute objective function can be constructed as

$$S = \prod_{i=1}^{m} \frac{\left[f_{i,\max} - f_1(x)\right]}{\left[f_{i,\max} - f_{i,\min}\right]} = \prod_{i=1}^{m} \bar{f}_i(x) \tag{4}$$

Maximizing the function S produces a solution that results in optimal compliance with multiple objectives subject to given constraints. The solution is a Pareto optimum (Cheng *et al.*, 1996) and stands for the "rational compromise" of the conflicting objectives.

MULTIOBJECTIVE OPTIMIZATION WITH GENETIC ALGORITHMS

GAs can be used directly for unconstrained single-objective optimization problems. A fitness function connects with the objective function in a linear or nonlinear formulation. For constrained optimization problems, one approach is to transform them to unconstrained ones by penalty function methods (Richardson *et al.*, 1989). There are usually two categories of algorithms to solve multiobjective optimization problems. One is directly seeking the rational compromise solution; the other is generating the Pareto optimal set of a problem. Then the decision maker's preference should be determined from the set on the basis of trade-off analysis of objectives. For an MOP, the analysis procedure for the proposed Pareto GA is composed as follows: (1) obtain an evenly distributed subset of Pareto optimal set, and (2) choose a reasonable solution from the set. The decision procedure to choose a compromise solution from a Pareto optimal set is constructed by the Pareto-set filter with the cooperative game theory. At each generation, the maximum and minimum values of each objective are found from the filter. Then the substitute function S (Eq. 4) is constructed. Checking each group of functions in the filter, the group which makes S the maximum value produces the optimum solution for the current generation. If maximum S keeps constant, continuing for more generations, it can be considered the convergence of the evolutionary processes and the analysis ends. The points in the Pareto-set filter are on or close to the Pareto optimal set -- trade-offs among objectives.

PARETO GA WITH CONSTRAINED MULTIOBJECTIVE OPTIMIZATION

GAs cannot be directly applied to a constrained optimization problem. One way to solve such a problem via GAs is to transform a constrained into an unconstrained optimization

problem through penalty function methods. A Pareto GA has the unique ability to seek a set of solutions by means of rank rather than function values of a point. To determine rank of a point, it is necessary to know the point's status (feasible or infeasible), distance from Pareto optimal set, and position in an infeasible zone. Three rules should be followed to construct the input function of a point for a Pareto GA to implement ranking. (A) The point's status as feasible or infeasible should be indicated by the function. (B) The closer a point is to the feasible zone, the higher its fitness evaluation is. (C) The closer a point is to the Pareto optimal set, the higher its fitness evaluation is. Rule B supersedes rule C because an infeasible point is an unacceptable solution in a constrained optimization problem. A fuzzy-logic penalty function method is developed for GA MOP problems (Cheng and Li, 1997).

LIFE-CYCLE COST AND MULTILEVEL OPTIMIZATION

Recent studies have focused on loss estimation for earthquakes and other natural hazards (FEMA, 1994). Jones and Chang (1995) provide an overview of current work on the economic impact of natural disasters. Nigg (1995) presents community-level disaster preparedness planning and response as well as mitigation actions. These studies are generally conducted to determine the after-effects of an event, or to estimate gross regional losses expected in a future event, and were intended primarily for post-earthquake recovery and response planning (Cheng and Wang [eds.], 1996).

From a theoretical standpoint, the first definitive mathematical model for aseismic design optimization on the basis of minimum life-cycle cost was presented by Liu *et al.* (1972) in which the objective was the determination of a "design earthquake" for structures including buildings (Liu *et al.*, 1976; Decapna and Liu, 1976). Other studies have addressed particular aspects of the same issue: e.g., the present worth of future damage cost, assuming that extreme hazards occur as a random process (Rosenblueth, 1976), and the importance of a trade-off between risk and cost (Kupfer and Freudenthal, 1977).

The platform for the systematic integration of seismic reliability engineering and socioeconomic is the expected life-cycle cost function which can be summarized as follows

$$C_T = C_I + C_D \tag{5}$$

where C_I is the initial cost of a structure, and C_D is the damage cost over the life of the structure composed of the following (for buildings)

$$C_D = C_r + C_c + C_e + C_s + C_f \tag{6}$$

in which C_r = repair or replacement cost of the structure; C_c = loss of contents; C_e = economic impact of structural damage; C_s = cost of injuries caused by structural damage; and C_f = cost of fatalities from structural damage or collapse. Items in Eq. (6) comprising the total damage cost are functions of structural damage level, x; for example, item C_r has an expected repair cost of

$$C_r = \int_0^\infty C_r(x) fx(x) dx \tag{7}$$

where x = damage level, and fx(x) = probability density function (PDF) of X. Structural damage, x, and its PDF fx(x) are calculated for a given earthquake, from which the particular damage costs, $C_r(x)$, can be determined as a function of the damage level, x.

Direct losses caused by an earthquake include human fatality and injury, as well as physical damage to structures and their contents. Concerning human fatality, Wiggins (1979) correlated the number of fatalities to building damage; Shiono and Krimgold (1989) reported fatality data for a hospital that collapsed during the 1985 Mexico City earthquake; and Coburn *et al.* (1992) suggested a simulation model to estimate the number of fatalities in buildings of a given structural type. Besides immediate or direct losses from an earthquake, there is also secondary or indirect impact: e.g., economic loss associated with the disruption of business due to structural damage (Nigg, 1996).

Ang and De Leon (1996) examined the minimum expected life-cycle cost vis-a-vis structural damage, and the reliability analysis of an RC frame building based on actual cost data from Mexico City buildings damaged in the 1985 earthquake. Ang *et al.* (1998) investigated a class of Japanese RC frame-wall structures and designed a five-story model building based on the conventional approach and Japan's building code. Cost of damage repair and loss of contents was obtained from six Japanese RC buildings (two to six stories) after previous

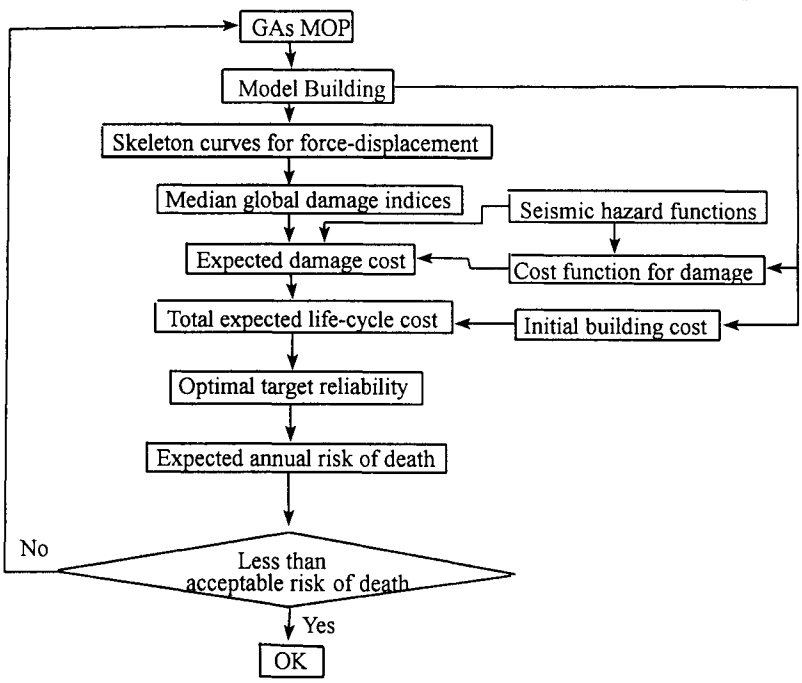

Figure 2: Multiobjective and Multilevel Optimization Scheme

earthquakes. Cheng *et al.* (1994) studied reliability-based design of structures subjected to seismic loading from UBC-94 and Newmark's nondeterministic seismic response spectra considering initial and expected damage costs. The difference in approach between the work of Ang and Cheng is that Ang's structure is based on conventional design without optimization; the structure is then studied with sophisticated damage model derived from casualties. In Cheng's study, the structure results from optimization for which the sensitivity of each structural member changes is in function of structural system cost and external seismic input, while the cost function is based on a mathematical modal. These two approaches are being merged by interweaving the GAs of MOP with target reliability and minimum expected life-cycle cost as multilevel optimization as shown in Fig. 2.

NUMERICAL EXAMPLES

Optimum Design of Seismic Structure with/without Control

Consider a three-story steel shear frame with an active control system located on the top floor (Cheng *et al.* 1996) shown in Fig. 3. Floor diaphragms are rigid and axial deformations are neglected. Thus the system has only one degree of freedom (in the lateral direction) at each floor. The total of live and dead loads at each story is 56kN/m, which does not include the weight of the columns. Lateral forces as well as weight density ρ and elastic module E of the structure are also presented in Fig. 3.

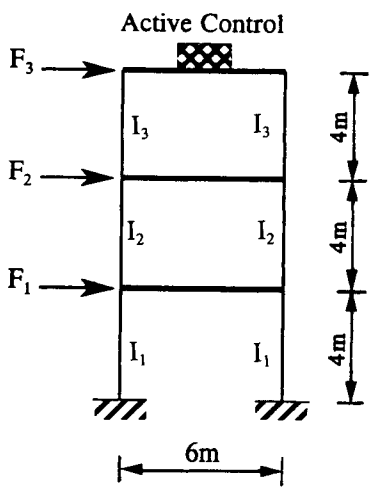

Figure 3: Three-Story Shear Frame

Optimum design of the system takes place under two cases. The first case is optimizes the system without control. Optimization criteria are structural weight W to better utilize materials and reduce structural cost, and earthquake input energy E_i to reduce dynamic

response and damage to the structure under the action of seismic loadings. Input energy E_i represents the work done by the structure's base shear as the structure moves through ground displacements. The second case optimizes the system with an active control system. Optimization criteria are weight W and performance index PI to optimize control energy input. The two multiobjective optimization problems are formed as

$$\textit{Case I: Min. } (W, E_i); \qquad \textit{Case II: Min. } (W, PI) \tag{8}$$

Both cases are subject to the same constraints as

$$|\sigma_i| \le 165{,}000 \ kN/m^2; \quad T_1 \ge 0.3; \quad 0.00001 \le I_i \le 0.002 m^4$$
$$|\delta_i| \le \frac{1}{400} h_i; \quad 0.5 \le \frac{K_{i+1}}{K_i} \le 1 \tag{9}$$

where σ_i, δ_i and K_i are column stress, relative story stiffness of the ith story, respectively, and i=1,2,3. T_1 is the fundamental natural period of the structure. Details of the integrated structural/control optimization design are given previously (Cheng and Tian, 1993). The proposed genetic algorithms have been applied to optimum design. Due to space limitation, only the results from the Pareto GA are presented and discussed. GA parameters are that uniform crossover (Davis, 1991) and stochastic remainder selection (Goldberg, 1989) are used in crossover and selection operating procedures.

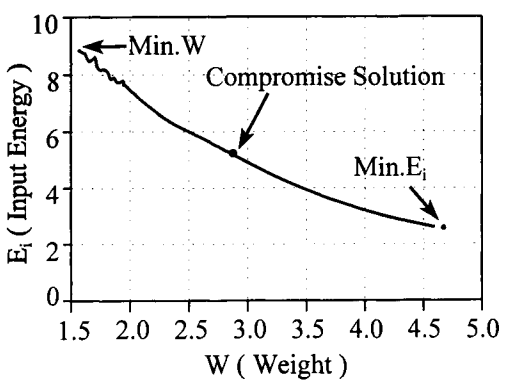

Figure 4: Points in Pareto-Set Filter

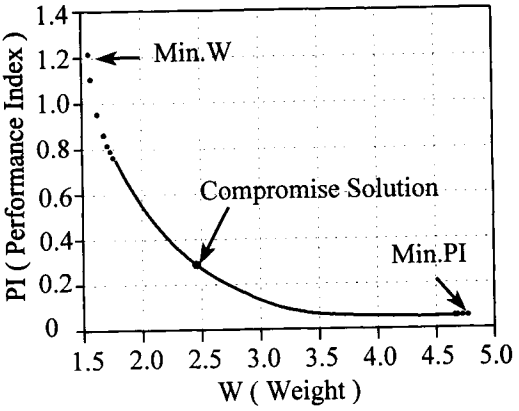

Figure 5: Points in Pareto-Set Filter

Figures 4 and 5 illustrate part of the solution. Figure 4 shows the points in the Pareto-set filter which gives the trade-offs between the two conflicting objectives. The two points (Min. W and Min. E_i), determined by using a traditional optimal method, are drawn as reference points because they are the two end-points of the Pareto optimal set for this problem. Note that the points in the filter are on or very close to the Pareto optimal set. The compromise solution point (W=2.8110, E_i=5.1635) is the decision-making result. Results of case II are given in Fig. 5.

Optimum Design for Selection of a Structural System

For a ten-story building shown in Fig. 6, MOP is applied to evaluate three choices: steel frame, reinforced concrete frame, and composite system of reinforced concrete (1st - 4th floor) and steel (5th - 10th floor). The structural weight and construction cost are obtained from Cox and Horsley handbook (1983). Design variables are defined as follows. At each story, cross-sectional areas of all the beams are identical. Cross-sectional areas of the internal columns are the same, and the two outside columns are identical. Structural members and member locations of first and second stories are the same as those of the third and fourth, fifth through seventh, and eighth through tenth stories.

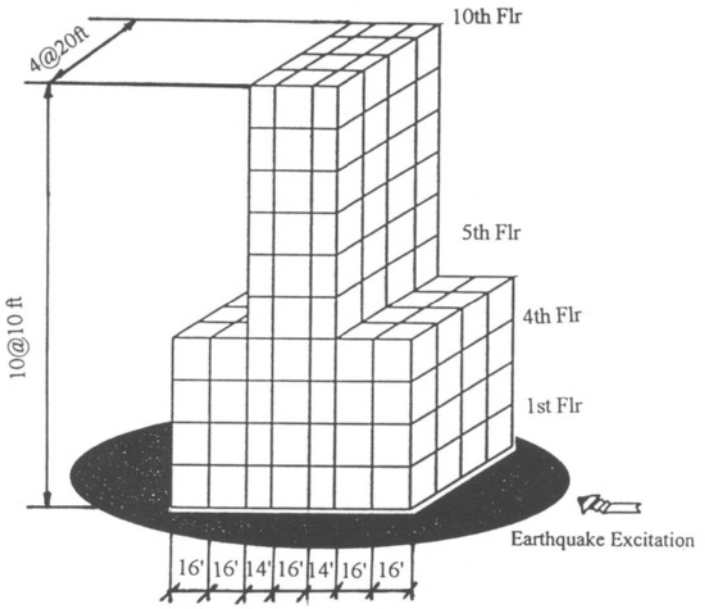

Figure 6: Ten-Story Building (1 ft = 0.3048 m)

For seismic design, calculation of the earthquake force is based on UBC requirements (UBC, 1994), and the following assumptions are made. The building is located in seismic zone 2B with factor Z=0.20; site coefficient S=1.2, and importance factor I=1.0. The building is a moment-resisting frame type with factor R_w=6 for the steel frame, and R_w=5 for the RC and the composite frame. The building is in the occupancy category of seismic zone 2, static lateral force procedure in UBC can be used. Objective functions comprise construction cost and potential energy for steel, reinforced concrete, and composite frames. Constraints include allowable stress and allowable drift as well as upper and lower bound of member cross section (Cheng and Li, D. 1998).

The optimum design results are shown in Fig. 7, where the curves reveal a tradeoff between structural cost and structural potential energy: minimum cost vs max. potential energy. A compromise solution could be selected at any point along the prospective curve.

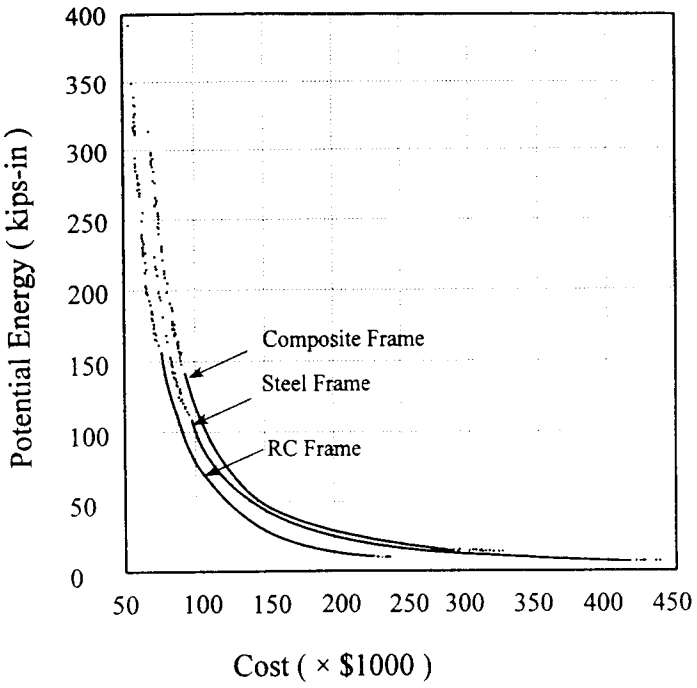

Figure 7: Pareto Optimal Solutions for Steel, RC and Composite Frames (1 kip-in=0.113 kN-m)

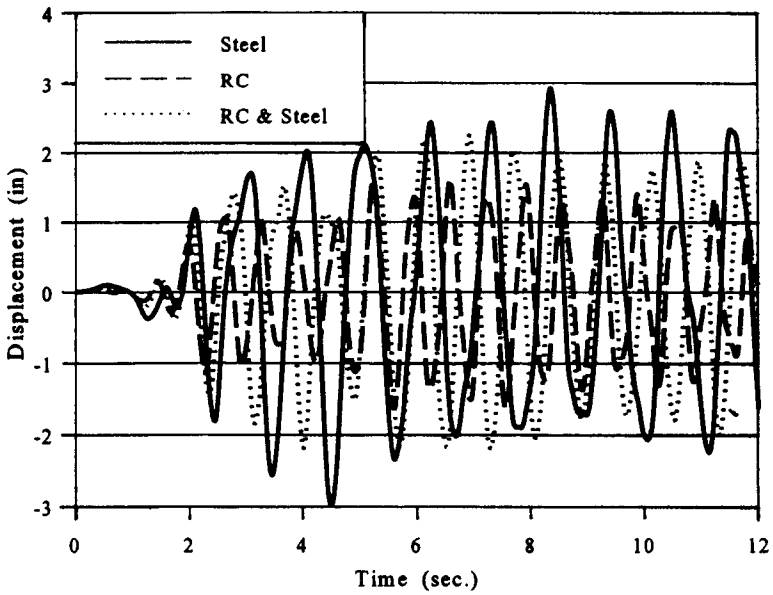

Figure 8: Comparison between Top-Story Displacements (1 in = 2.54 cm)

Response performance of these three structures is studied. The structures are selected at the same cost of $118,000; each of them undergoes time-history analysis with N-S El Centro May 18, 1940 earthquake. One of the essential response parameters is top-story displacement which is compared in Fig. 8. The RC frame has the smallest displacement response, and the steel frame has the largest.

Sensitivity of Cost Function on Structural Probability Failure and Optimum Solution

This example shows the influence of cost function on structural probability failure (or safety). The sensitivity observation is studied using mathematical programming with single objective function (Cheng *et al.*, 1994). A ten-story one-bay steel shear-building is optimized with probability failure at $P_{fo}=10^{-1}$, 10^{-3}, 10^{-5}, and 10^{-7}, where P_{fo} is based on normal distribution. The structure is optimized with the earthquake load of equivalent lateral force recommended in UBC. The cost function comprises three components: initial construction cost (C_I), future failure cost (L_f), and system probability of failure (p_{f_T}). They are expressed as

$$C_T = C_I + L_f P_{f_T} \tag{10}$$

in which $C_I = C_u \Sigma L_i A_i + C_n$; C_u = a unit steel volume cost; C_n = nonstructural members cost; $L_f = C_V C_I + C_L$; C_V = coefficient to describe the ratio of repair cost to initial cost; C_L = business and human losses; and P_{f_T} = system probability of failure.

Although initial construction cost and future failure cost can be classified into many items, these quantities are difficult to estimate. Therefore two coefficients of the ratio of initial cost to members cost (C_{in}) and the ratio of future failure cost to initial cost (C_{VL}) are used to represent the various magnitudes of initial construction cost and future failure cost which may now be expressed as:

$$C_I = C_{in} C_u \sum_i l_i A_i; \qquad L_f = C_{VL} C_I \tag{11}$$

The influences of nonstructural cost and future failure on the optimum cost design are shown in Fig. 9. Note that the initial cost affects the total cost more at higher probability of failure and the influence depends on the ratio of future cost to initial cost. C_{VL} is assumed to be 1 for this example. Therefore the life-cycle cost model based on actual building damages earthquake casualties is essential for determining target reliability along with minimum seismic force level as presented in Fig. 2.

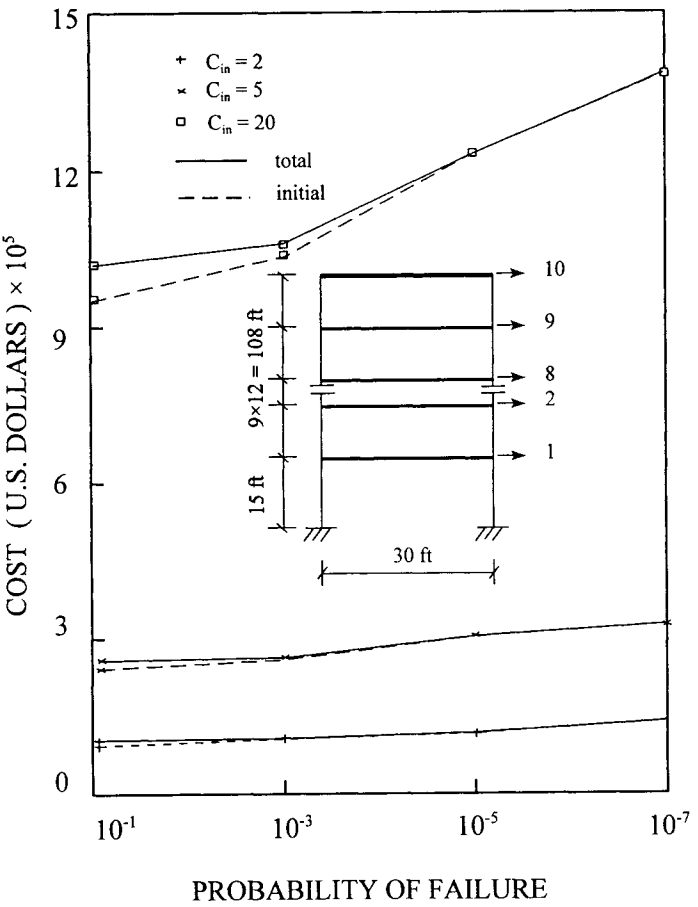

Figure 9: Total Cost Based on Various Initial Cost (C_T vs C_{in}) (1 ft = 0.3048 m)

CONCLUSIONS

In this paper, the concepts of genetic algorithms, game theory, Pareto optimal set with/without constraints, and life-cycle cost are discussed. For constrained Pareto GA and life-cycle cost, fuzzy logic and multilevel concepts are respectively introduced. Based on them, new algorithms for multiobjective optimization are developed. The Pareto GA is demonstrated on a seismic structure with/without control. Seismic structures are designed for selected construction materials: steel frame, reinforced concrete frame, or a frame comprised of steel and reinforced concrete members. With cost kept uniform, these three systems are further investigated for their performance such as displacement response subjected the same earthquake input.

Multiobjective optimization provides a designer with a systematic method for considering all the conflicting requirements inherent in an application. Game theory offers a decision method for guiding an optimum process and as such, results in optimal compliance with

multiple objectives. Comparing traditional multiobjective optimization methods, Pareto GA is an effective numerical algorithm for generating Pareto optima. The Pareto-set filter enables the Pareto GA to be more robust, stable and computationally feasible for even extremely difficult problems. The niche technique effectively prevents genetic drift. It involves no new parameters, and the computational cost for niche operating is negligible. The sensitivity of cost function on structural probability failure and optimum solution indicates multiobjective and multilevel optimization along with life-cycle cost model based on actual earthquake casualties and building damages are essential to determine target reliability and seismic building code performance.

ACKNOWLEDGMENTS

This paper is a portion of research results from the projects partially supported by the National Science Foundation under grants NSF CMS-9703725 and CMS-9520804 as well as Intelligent Systems Center at UMR. The financial support is gratefully acknowledged.

REFERENCES

Ang, A.H-S and DeLeon, D. (1996). "Basis for Cost-Effective Decision on Upgrading Existing Structures for Earthquake Protection," *Post-Earthquake Rehabilitation and Reconstruction* (eds. F.Y. Cheng and Y.Y. Wang), Elsevier Science Ltd.

Ang, A.H-S, Lee, J.C. and Pires, J.A. (1998). "Cost-Effectiveness Evaluation of Design Criteria," *Optimal Performance of Civil Infrastructure systems* (ed. D.M. Frangopol), ASCE, Reston, Va.

Cheng, F.Y. and Tian, P. (1993). "Generalized Optimal Active Control algorithm with Weighting Matrix Configuration, Stability and Time-Delay," *Structural Engineering and Mechanics: An International Journal*, **1: 1**, 119-135.

Cheng, F.Y. and Li, D. (1996). "Multiobjective Optimization of Structures with and without Control," *Journal of Guidance Control and Dynamics*, **19: 2**, 392-397.

Cheng, F.Y. and Li, D. (1997). "Multiobjective Optimization Design with Pareto Genetic Algorithm," *Journal of Structural Engineering*, ASCE, **123: 9**, 1252-1261.

Cheng, F.Y. and Li, D. (1998). "Multiobjective Design of Seismic-Resistant Structures with Game Theory and Genetic algorithm," *Proc. Structural Engineers World Congress*, San Francisco.

Cheng, F.Y. (ed.). (1986). *Recent Developments in Structural Optimization*, ASCE, 1986.

Cheng, F.Y., Ger, J.F. and Chang, C.C. (1994). "Reliability-Based Optimum Design for

UBC and Nondeterministic Seismic Spectra," *Journal of Structural Engineering*, **120: 1**, 139-160.

Cheng, F.Y. and Li, X.S. (1998). "Generalized Center Method for Multiobjective Engineering Optimization," to appear in *Journal of Engineering Optimization*.

Cheng, F.Y. and Truman, K.Z. (1985). *Optimum Design of RC and Steel 3-D Static and Seismic Building systems with Assessment of ATC-03*, NSF Report, U.S. Department of Commerce, National Technical Information Service, Virginia, NTIS PB 87-168564/AS (414 pages).

Cheng, F.Y. and Juang, D.S. (1988). "Assessment of Various Code Provisions Based on Optimum Design of Steel Structures," *International Journal of Earthquake Engineering and Structural Dynamics*, **16**, 45-61.

Cheng, F.Y. and Wang, Y.Y. (eds.). (1996). *Post-Earthquake Rehabilitation and Reconstruction*, Elsevier Science Ltd.

Coburn, A.W., Spence, R.J.S. and Pomonis, A. (1992). "Factors Determining Human Casualty Levels in Earthquakes: Mortality Prediction in Building Collapse," *Proc. 10th World Conference on Earthquake Engineering,* Madrid, 5989-5994.

Cox, B.J. and Horsley, F.W. (1983). *Square Foot Estimating*, Robert Snow Means Co., Inc.

Davis, L. (ed.). (1991). *Handbook of Genetic Algorithms*. Van Nostrand Reinhold, New York.

Decapna, N.J. and Liu, S.C. (1976). "Protection of Communications Facilities in Earthquake Areas," *Proc. of International Symposium on Earthquake Structural Engineering* (ed. F.Y. Cheng), **I**, 253-268.

FEMA-2149 (1994). "Assessment of the State-of-the-Art Earthquake Loss Estimation Methodologies," Washington, D.C.

Frangopol, D. And Cheng, F.Y. (eds.). (1996). *Advances in Structural Optimization*, ASCE.

Goldberg, D.E. (1989). *Genetic Algorithms in Search, Optimization, and Machine Learning*, Addison-Wesley, Reading, Mass.

Jones, B.G. and Chang, S.E. (1995). "Economic Aspects of Urban Vulnerability and Disaster Mitigation," *Urban Disaster Mitigation: The Role of Engineering and Technology*, (eds. F.Y. Cheng and M.S. Sheu), Elsevier Science Ltd., 311-320.

Kupfer, H. and Freudenthal, A.M. (1977). "Structural Optimization and Risk Control," Proceedings of 2nd International Conference on Structural Safety and Reliability, Munich,

627-639.

Liu, S.C. and Neghabat, F. (1972). A Cost-Optimization Model for Seismic Design of Structures," *The Bell System Technical Journal*, **51**.

Liu, S.C., Dougherty, M.R. and Neghabat, F. (1976). Optimal Aseismic Design of Buildings and Equipment," *Journal of Engineering Mechanics*, ASCE, **102**, 395-414.

Neumann, V. and Morgenstern O. (1947). *Theory of Games and Economic Behavior*, Princeton University Press, Princeton, N.J.

Nigg, J.M. (1995). "Social Science approaches in Disaster Research: Selected Research Issues and Findings on Mitigating Natural Hazards in the Urban Environment," *Urban Disaster Mitigation: The Role of Engineering and Technology*, (eds. F.Y. Cheng and M.S. Sheu), Elsevier Science Ltd., 303-310.

Nigg, J.M. (1996). Anticipated Business Disruption Effects due to Earthquake-Induced Lifeline Interruptions," *Post-Earthquake Rehabilitation and Reconstruction*, (eds. F.Y. Cheng and Y.Y. Wang), Elsevier Science Ltd., 47-58.

Richardson, J.T., M.R. Palmer, G. Liepins and M. Hilliard (1989). Some Guidelines for Genetic Algorithms with Penalty Functions, *Proc. 3rd International Conference on Genetic Algorithms*, San Mateo, Calif. 191-197.

Rosenblueth, E. (1976). "Optimum Design for Infrequent Disturbances," *Journal of Structural Engineering*, ASCE, **102**.

Shiono, K. and Kirmgold, F. (1989). "A Computer Model for the Recovery of Trapped People in a Collapsed Building: Development of a Theoretical Framework and Direction for Future Data Collection," *International Workshop on Earthquake Injury Epidemiology for Mitigation and Response.*

UBC, *Uniform Building Code* (1994). International Conference of Building Officials, Whittier, Calif.

Wiggins, J.H. (1979). "Estimated Building Losses from U.S. Earthquakes," *Proc. 2nd National Conference on Earthquake Engineering*, 253-262.

NEW SOLUTION SYSTEM FOR PLATE BENDING

W. X. Zhong and W. A. Yao

Department of Engineering Mechanics, Dalian University of Technology,
Dalian, 116024, P.R. China

ABSTRACT

Instead of the biharmonic type equation, a set of new governing equations and solution methodology for plate bending classical theory is presented in this paper, which is based on the analogy between plate bending and plane elasticity, so Hamiltonian system formulation can also be applied to plate bending problems. The new methodology presents the analytical solutions in rectangular plate via the methods of separation of variables and eigenfunction-vector expansion; it breaks through the limitation of traditional semi-inverse solution. The results show that the new methodology will have vast application vistas.

KEYWORDS

Plate bending, Plane elasticity, Hamiltonian system, Bending moment function vector

ANALOGY BETWEEN PLATE BENDING AND PLANE ELASTICITY PROBLEMS

It is well-known that the governing equation for plate bending is biharmonic equation (Timoshenko, *et al.*1959). It fixed in last century, but the critical problem is how to solve it. The traditional solution methodology is the semi-inverse one that causes limitations. The Airy stress function is usually applied traditionally for plane elasticity problems; it also satisfies biharmonic equation (Timoshenko and Goodier 1970, Muschelishvili 1953). The analogy between plate bending and plane elasticity problems had been noticed long before (Hu 1981), but their solution systems are different each other, and the analogy relationship had not been used systematically. FEM was developed firstly in plane elasticity. The formulation of elements is based on displacement method, and the Airy stress function is given up. It is noticed that giving up biharmonic equation in plane elasticity was successful for FEM.

The deflection w for plate bending corresponds to the Airy stress function in plane elasticity; conversely, the displacements in plane elasticity correspond to two bending moment functions ϕ_x, ϕ_y in plate bending, but their theory and solution system have not been set up yet. Particularly, a new systematic methodology for plane elasticity has been developed (Zhong 1995); therefore new methodology for plate bending can also be developed along the same way. New solution system for plate bending is presented in this paper.

BENDING MOMENT FUNCTION VECTOR

For plate bending, the variables corresponding to displacements u, v in plane elasticity are bending moment function vector ϕ_x, ϕ_y. Let the positive internal force be defined as in Fig.1,

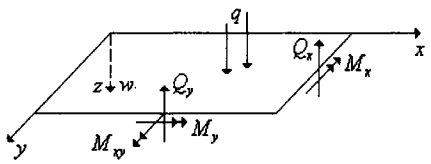

Figure 1: Internal force positive sign

so traditional equilibrium equation can be written as

$$\partial^2 M_x / \partial x^2 - 2\partial^2 M_{xy} / \partial x \partial y + \partial^2 M_y / \partial y^2 = q \tag{1}$$

The load q can be handled via a special solution beforehand, so the homogeneous equation of $q = 0$ are considered first. Let the relation for bending moments and bending moment function vector be given below, and it is easily seen that Eqn. 1 is automatically satisfied.

$$M_y = \partial \phi_x / \partial x, \qquad M_x = \partial \phi_y / \partial y, \qquad 2M_{xy} = \partial \phi_x / \partial y + \partial \phi_y / \partial x \tag{2}$$

Curvature-deflection relations can be described as

$$\kappa_x = \partial^2 w / \partial x^2, \qquad \kappa_y = \partial^2 w / \partial y^2, \qquad \kappa_{xy} = -\partial^2 w / \partial x \partial y \tag{3}$$

The constitutive relation for bending moments and curvatures is given as

$$\boldsymbol{m} = \boldsymbol{C}^{-1}\boldsymbol{\kappa}, \text{ i.e. } \begin{Bmatrix} M_y \\ M_x \\ 2M_{xy} \end{Bmatrix} = D \begin{bmatrix} 1 & \nu & 0 \\ \nu & 1 & 0 \\ 0 & 0 & 2(1-\nu) \end{bmatrix} \begin{Bmatrix} \kappa_y \\ \kappa_x \\ \kappa_{xy} \end{Bmatrix}, \text{ where } D = \frac{Eh^3}{12(1-\nu^2)} \tag{4}$$

Firstly, we notice that functions $\phi_x = a_0 + a_2 y, \phi_y = a_1 - a_2 x$ are similar to rigid body translation in plane elasticity, which generate no bending moments, where a_0, a_1, a_2 are any constants. We call them the null moment functions. Let (x', y') rotate an angle α from (x, y); the moment should be transformed as

$$\begin{aligned} M'_x &= M_x \cos^2\alpha + M_y \sin^2\alpha - M_{xy}\sin 2\alpha \\ M'_y &= M_x \sin^2\alpha + M_y \cos^2\alpha + M_{xy}\sin 2\alpha \\ M'_{xy} &= M_{xy}\cos 2\alpha + (M_x - M_y)\sin\alpha\cos\alpha \end{aligned} \tag{5}$$

The ϕ_x, ϕ_y should also be transformed so that Eqn.2 still valid in the rotated coordinate .

$$\phi'_x = \phi_x \cos\alpha + \phi_y \sin\alpha\,, \qquad \phi'_y = -\phi_x \sin\alpha + \phi_y \cos\alpha \tag{6}$$

i.e. ϕ_x, ϕ_y transformed just as a vector, so we call it the bending moment function vector. ϕ_x, ϕ_y correspond to the displacement vector u, v in plane elasticity.

The boundary condition is considered next. For convenience, we regard the boundary as a straight line. Let external normal and tangent directions be n and s, respectively, that composes right-handed coordinate system, and the bending moment functions are (ϕ_n, ϕ_s), so

$$Q_n = \partial M_n / \partial n - \partial M_{ns} / \partial s = \left(\partial^2 \phi_s / \partial n \partial s - \partial^2 \phi_n / \partial s^2\right)/2 \tag{7}$$

The given force and displacement boundaries are denoted as s_m and s_w respectively. In theory of plate bending, there are given normal bending moment and equivalent shearing force

$$(M_n =)\partial\phi_s / \partial s = \overline{M}_n\,, \quad (V_n = Q_n - \partial M_{ns}/\partial s =) - \partial^2 \phi_n / \partial s^2 = \overline{V}_n \quad \text{on } s_m \tag{8}$$

Only differentials along s exist in Eqn.8, so the equations can be integrated as

$$\phi_s = \overline{\phi}_s = \int_{s_0}^{s} \overline{M}_n \mathrm{d}s' + a_1\,, \quad \phi_n = \overline{\phi}_n = \int_{s_0}^{s} (s' - s)\overline{V}_n \mathrm{d}s' + a_0 + a_2 s \tag{9}$$

where a_0, a_1, a_2 are constants to be determined. There may be several segments of given force boundary s_m, but only for one of the boundary segment its a_0, a_1, a_2 can be brought to zero via applying null bending moment functions. The ϕ_n, ϕ_s correspond to normal and tangent displacements u_n, u_s in plane elasticity.

In terms of bending moment functions, the complementary strain energy is

$$U^* = \iint_\Omega \frac{6}{Eh^3}\left[\left(\frac{\partial\phi_x}{\partial x}\right)^2 + \left(\frac{\partial\phi_y}{\partial y}\right)^2 - 2\nu\frac{\partial\phi_x}{\partial x}\frac{\partial\phi_y}{\partial y} + \frac{1+\nu}{2}\left(\frac{\partial\phi_y}{\partial x} + \frac{\partial\phi_x}{\partial y}\right)^2\right]\mathrm{d}x\mathrm{d}y \tag{10}$$

The strain energy density can be expressed with bending moments

$$U_0^*(\boldsymbol{m}) = \frac{1}{2}\boldsymbol{m}^{\mathrm{T}}\boldsymbol{C}\boldsymbol{m} = \frac{6}{Eh^3}[M_x^2 + M_y^2 - 2\nu M_x M_y + 2(1+\nu)M_{xy}^2] \tag{11}$$

Besides, complementary support displacement energy is expressed as

$$U_e^* = -\int_{s_w} \left(M_n \bar{\theta}_n - V_n \bar{w}\right) ds = -\int_{s_w} \left(\bar{\theta}_n \partial \phi_s / \partial s + \bar{w} \partial^2 \phi_n / \partial s^2\right) ds \tag{12}$$

where, $\bar{w}$ and $\bar{\theta}_n$ are given deflection and normal rotation which are functions of s. Via integration by parts, Eqn.12 can be rewritten as

$$U_e^* = \int_{s_w} \left(\phi_s \partial \bar{\theta}_n / \partial s - \phi_n \partial^2 \bar{w} / \partial s^2\right) ds - \left[\phi_s \bar{\theta}_n + \bar{w} \partial \phi_n / \partial s - \phi_n \partial \bar{w} / \partial s\right]_{s_0}^{s_1} \tag{13}$$

where s_0, s_1 are two ends of straight line s_w. The principle of minimum complementary energy can be written as

$$\Pi^* = U^* + U_e^*, \qquad \min_{\phi_x, \phi_y} \Pi^* \tag{14}$$

Carrying out the variation, the following equations are derived

$$\frac{\partial^2 \phi_x}{\partial x^2} + \frac{1+\nu}{2} \frac{\partial^2 \phi_x}{\partial y^2} + \frac{1-\nu}{2} \frac{\partial^2 \phi_y}{\partial x \partial y} = 0, \qquad \frac{\partial^2 \phi_y}{\partial y^2} + \frac{1+\nu}{2} \frac{\partial^2 \phi_y}{\partial x^2} + \frac{1-\nu}{2} \frac{\partial^2 \phi_x}{\partial x \partial y} = 0 \tag{15}$$

Their physical meaning is strain compatibility. In fact, they can also be derived from

$$\partial \kappa_y / \partial x + \partial \kappa_{xy} / \partial y = 0, \qquad \partial \kappa_x / \partial y + \partial \kappa_{xy} / \partial x = 0 \tag{16}$$

The Eqn.15 is almost the same as plane stress besides changing the sign of Poisson ratio ν. Via variational principle, the boundary conditions on s_w are given as (in case of the given displacement being zero)

$$\begin{aligned} &\frac{12}{Eh^3}\left[\left(\frac{\partial \phi_y}{\partial y} - \nu \frac{\partial \phi_x}{\partial x}\right)\sin\alpha + \frac{1+\nu}{2}\left(\frac{\partial \phi_y}{\partial x} + \frac{\partial \phi_x}{\partial y}\right)\cos\alpha\right] = 0, \text{ i.e. } \kappa_x \sin\alpha + \kappa_{xy}\cos\alpha = 0 \\ &\frac{12}{Eh^3}\left[\left(\frac{\partial \phi_x}{\partial x} - \nu \frac{\partial \phi_y}{\partial y}\right)\cos\alpha + \frac{1+\nu}{2}\left(\frac{\partial \phi_y}{\partial x} + \frac{\partial \phi_x}{\partial y}\right)\sin\alpha\right] = 0, \text{ i.e. } \kappa_y \cos\alpha + \kappa_{xy}\sin\alpha = 0 \end{aligned} \tag{17}$$

The formulations are the same as given force boundary condition in plane elasticity, where α is the angle between x axes and normal direction n. They can also be expressed with coordinates (n,s)

$$\kappa_{ns} = -\partial^2 w / \partial n \partial s = \bar{\kappa}_{ns}, \qquad \kappa_s = \partial^2 w / \partial s^2 = \bar{\kappa}_s \qquad \text{on } s_w \tag{18}$$

Integrating Eqn.18 for s, the given displacement conditions can be written as $\theta_n = known$, $w = known$ on s_w.

For force method, displacements aren't the basic variables; therefore boundary conditions must be expressed with ϕ_x, ϕ_y. These are the natural boundary conditions for the principle of

minimum complementary energy.

$$\partial\phi_s / \partial n + \partial\phi_n / \partial s = known, \qquad \partial\phi_n / \partial n - \nu\partial\phi_s / \partial s = known \qquad \text{on } s_w \tag{19}$$

Corresponding to the Hellinger-Reissner variational principle for plane elasticity, the new variational principle called the Pro-H-R one for plate bending can be proposed as

$$\begin{aligned}\delta\Pi_{PHR} = \delta\Bigg\{ & \iint_\Omega \left[\kappa_x \frac{\partial\phi_y}{\partial y} + \kappa_y \frac{\partial\phi_x}{\partial x} + \kappa_{xy}\left(\frac{\partial\phi_y}{\partial x} + \frac{\partial\phi_x}{\partial y} \right) - U_0(\kappa_y, \kappa_x, \kappa_{xy}) \right] dxdy \\ & - \oint_{s_m} [\kappa_{ns}(\phi_s - \bar{\phi}_s) + \kappa_s(\phi_n - \bar{\phi}_n)]ds - \oint_{s_w} (\phi_s \bar{\kappa}_{ns} + \phi_n \bar{\kappa}_s) ds \Bigg\} = 0 \end{aligned} \tag{20}$$

where $\bar{\phi}_s, \bar{\phi}_n, \bar{\kappa}_{ns}, \bar{\kappa}_s$ are given functions, and the strain energy density is

$$U_0(\kappa) = \frac{1}{2}\kappa^{\mathrm{T}} \boldsymbol{C}^{-1} \kappa = \frac{1}{2} D[\kappa_x^2 + \kappa_y^2 + 2\nu\kappa_x\kappa_y + 2(1-\nu)\kappa_{xy}^2] \tag{21}$$

Carrying out the variations of Eqn.20 for $\kappa_y, \kappa_x, \kappa_{xy}, \phi_x, \phi_y$ gives the relation between bending moment and curvatures,

$$\partial\phi_y / \partial y = \partial U_0 / \partial\kappa_x, \ \partial\phi_x / \partial x = \partial U_0 / \partial\kappa_y, \ \partial\phi_y / \partial x + \partial\phi_x / \partial y = \partial U_0 / \partial\kappa_{xy} \tag{22}$$

the equation of curvature compatibility Eqn. 16, and boundary conditions Eqn. 9, 18. In the Pro-H-R variational principle Eqn. 20, deflection w doesn't appear, and it must be solved after $\kappa_x, \kappa_y, \kappa_{xy}$ are solved. Table 1 gives the analogy relationship between plate bending and plane elasticity problems.

THE FUNDAMENTAL EQUATIONS FOR RECTANGULAR PLATE

Analogy between plate bending and plane elasticity problems can be applied to FEM formulation. Elements developed so far for plane elasticity are better than those for plate bending; based on the analogy relationship these elements can be transplanted to plate bending problem (Zhong and Yao, 1998). In this paper, we consider only analytic solution. A new systematic methodology for plane elasticity has been set up via introducing the Hamiltonian system theory (Zhong 1995), so a new systematic methodology for plate bending can also be developed according to the analogy. Let us initiate to derive from the Pro-H-R variational principle Eqn. 20.

The new systematic methodology can be applied to rectangular and sectorial domain as those in plane elasticity. In this paper, we consider only solutions for rectangular plate. Let y denote the lateral coordinate; $b_1 \le y \le b_2$, boundary conditions of both sides are considered free, simply supported or clamped. The first step is to introduce the Hamiltonian system theory into the fundamental equations, and the longitudinal coordinate x is treated analogous to the time coordinates (Zhong and Yang, 1991); thus $(\dot{\ })$ represents $\partial(\ ) / \partial x$. Minimization

TABLE 1
ANALOGY RELATIONSHIP BETWEEN PLANE ELASTICITY AND PLATE BENDING

Plane elasticity	**Plate bending**
Airy stress function φ	Deflection $w(x,y)$
Displacement vector u,v	Bending moment function vector ϕ_x,ϕ_y
Strain $\varepsilon_x,\varepsilon_y,\gamma_{xy}$; $\varepsilon_x=\frac{\partial u}{\partial x},\ \varepsilon_y=\frac{\partial v}{\partial y},\ \gamma_{xy}=\frac{\partial u}{\partial y}+\frac{\partial v}{\partial x}$	Bending moment $M_y, M_x, 2M_{xy}$; $M_y=\frac{\partial \phi_x}{\partial x}, M_x=\frac{\partial \phi_y}{\partial y}, 2M_{xy}=\frac{\partial \phi_x}{\partial y}+\frac{\partial \phi_y}{\partial x}$
Stress function-stress relation $\sigma_x=\frac{\partial^2\varphi}{\partial y^2},\sigma_y=\frac{\partial^2\varphi}{\partial x^2},\tau_{xy}=-\frac{\partial^2\varphi}{\partial x\partial y}$	Deflection-curvature relation $\kappa_y=\frac{\partial^2 w}{\partial y^2},\kappa_x=\frac{\partial^2 w}{\partial x^2},\kappa_{xy}=-\frac{\partial^2 w}{\partial x\partial y}$
Stress-strain relation, $\varepsilon_x=(\sigma_x-\nu\sigma_y)/E,\varepsilon_y=(\sigma_y-\nu\sigma_x)/E,$ $\gamma_{xy}=\tau_{xy}2(1+\nu)/E$	Bending moment-curvature relation $M_y=D(\kappa_y+\nu\kappa_x),\ M_x=D(\kappa_x+\nu\kappa_y),$ $2M_{xy}=2(1-\nu)D\kappa_{xy}$
The principle of minimum potential energy	The principle of minimum complementary energy
Determined displacement boundary s_u, $u=\bar{u},\ v=\bar{v}$	Given force boundary s_m, $\phi_s=\bar{\phi}_s,\ \phi_n=\bar{\phi}_n$
Determined force boundary s_σ, $\sigma_x\cos\alpha+\tau_{xy}\sin\alpha=0$ $\tau_{xy}\cos\alpha+\sigma_y\sin\alpha=0$	Given displacement boundary s_w, $\kappa_y\cos\alpha+\kappa_{xy}\sin\alpha=0$ $\kappa_{xy}\cos\alpha+\kappa_x\sin\alpha=0$
H-R variational principle	Pro-H-R variational principle
Pro-H-R variational principle	H-R variational principle
Rigid body translation	Null moment functions

of Eqn. 20 for κ_x and rewritten Eqn.20 can give, respectively

$$\kappa_x=\partial\phi_y/D\partial y-\nu\kappa_y \tag{23}$$

$$\delta\{\int_{x_0}^{x_f}\int_{y_1}^{y_2}[\kappa_y\dot{\phi}_x+\kappa_{xy}\dot{\phi}_y-\nu\kappa_y(\partial\phi_y/\partial y)+\kappa_{xy}(\partial\phi_x/\partial y) +(\partial\phi_y/\partial y)^2/2D-D(1-\nu)\kappa_{xy}^2-D(1-\nu^2)\kappa_y^2/2]dydx\}=0 \tag{24}$$

Carrying out the variation of Eqn.24 for $\phi_x,\phi_y,\kappa_y,\kappa_{xy}$ gives

$$\dot{\boldsymbol{v}}=\boldsymbol{H}\boldsymbol{v},\ \text{where}\ \boldsymbol{v}=\begin{Bmatrix}\phi_x\\ \phi_y\\ \kappa_y\\ \kappa_{xy}\end{Bmatrix},\ \boldsymbol{H}=\begin{bmatrix}0 & \nu\partial/\partial y & D(1-\nu^2) & 0\\ -\partial/\partial y & 0 & 0 & 2D(1-\nu)\\ 0 & 0 & 0 & -\partial/\partial y\\ 0 & -\partial^2/D\partial y^2 & \nu\partial/\partial y & 0\end{bmatrix} \tag{25}$$

It is natural to apply the method of separation of variables to Eqn.25. Let

$$\boldsymbol{v}(x,y)=\xi(x)\cdot\boldsymbol{\Psi}(y),\quad \text{and}\qquad \boldsymbol{H}\boldsymbol{\Psi}(y)=\mu\boldsymbol{\Psi}(y)\ ,\quad \xi(x)=\exp(\mu x) \tag{26}$$

where μ is the eigenvalue, and $\boldsymbol{\Psi}$ is the eigenfunction-vector which must satisfy both side edge boundary conditions. Let us define the operation

$$<\boldsymbol{v}_1^{\mathrm{T}},\boldsymbol{P},\boldsymbol{v}_2>=\int_{\phi_1}^{\phi_2}\boldsymbol{v}_1^{\mathrm{T}}\boldsymbol{P}\boldsymbol{v}_2\mathrm{d}y \tag{27}$$

It can be verified that the following equation is valid when $\boldsymbol{v}_1,\boldsymbol{v}_2$ satisfy the homogeneous boundary conditions being free, simply supported or clamped.

$$<\boldsymbol{v}_1^{\mathrm{T}},\boldsymbol{J}\boldsymbol{H},\boldsymbol{v}_2>\equiv<\boldsymbol{v}_2^{\mathrm{T}},\boldsymbol{J}\boldsymbol{H},\boldsymbol{v}_1>\qquad \text{where}\quad \boldsymbol{J}=\begin{bmatrix}\boldsymbol{0} & \boldsymbol{I}\\ -\boldsymbol{I} & \boldsymbol{0}\end{bmatrix} \tag{28}$$

so $\boldsymbol{J}\boldsymbol{H}$ is a symmetric operator, i.e., $\boldsymbol{H}$ is a Hamilton symplectically self-adjoint operator. Let $\boldsymbol{\Psi}_i,\boldsymbol{\Psi}_j$ be eigenfunction-vector corresponding to eigenvalues μ_i,μ_j, respectively,

$$\boldsymbol{H}\boldsymbol{\Psi}_i=\mu_i\boldsymbol{\Psi}_i\ ,\quad \boldsymbol{H}\boldsymbol{\Psi}_j=\mu_j\boldsymbol{\Psi}_j \tag{29}$$

so
$$<\boldsymbol{\Psi}_i^{\mathrm{T}},\boldsymbol{J}\boldsymbol{H},\boldsymbol{\Psi}_j>=\mu_j<\boldsymbol{\Psi}_i^{\mathrm{T}},\boldsymbol{J},\boldsymbol{\Psi}_j> \tag{30}$$

also
$$<\boldsymbol{\Psi}_j^{\mathrm{T}},\boldsymbol{J}\boldsymbol{H},\boldsymbol{\Psi}_i>=\mu_i<\boldsymbol{\Psi}_j^{\mathrm{T}},\boldsymbol{J},\boldsymbol{\Psi}_i>=-\mu_i<\boldsymbol{\Psi}_i^{\mathrm{T}},\boldsymbol{J},\boldsymbol{\Psi}_j> \tag{31}$$

According to Eqn. 28,30,31, adjoint symplectic orthogonality relationship for eigenfunction-vectors can be proved

$$<\boldsymbol{\Psi}_i^{\mathrm{T}},\boldsymbol{J},\boldsymbol{\Psi}_j>=0\ ,\qquad \text{when}\quad \mu_i+\mu_j\neq 0 \tag{32}$$

Any state function-vector $\boldsymbol{v}$ can be expanded with the eigenfunction-vectors,

$$\boldsymbol{v}=\sum_{i=1}^{\infty}(c_i\boldsymbol{\Psi}_i+d_i\boldsymbol{\Psi}_{-i}) \tag{33}$$

where c_i and d_i are constants to be determined.

In cases of some lateral boundary conditions, there are solutions corresponding to zero eigenvalue, which can be solved analytically. For solutions corresponding to non-zero eigenvalue, the eigensolution of Eqn. 26 can be given the general form

$$\begin{aligned}
\phi_x &= A_1\cos(\mu y)+B_1\sin(\mu y)+C_1 y\sin(\mu y)+D_1 y\cos(\mu y)\\
\phi_y &= A_2\sin(\mu y)+B_2\cos(\mu y)+C_2 y\cos(\mu y)+D_2 y\sin(\mu y)\\
\kappa_y &= A_3\cos(\mu y)+B_3\sin(\mu y)+C_3 y\sin(\mu y)+D_3 y\cos(\mu y)\\
\kappa_{xy} &= A_4\sin(\mu y)+B_4\cos(\mu y)+C_4 y\cos(\mu y)+D_4 y\sin(\mu y)
\end{aligned} \tag{34}$$

in which the constants aren't independent each other. According to Eqn.26, the relations are

solved as

$$\left.\begin{array}{ll} A_1 = -A_2 - C_2(3+\nu)/[\mu(1-\nu)] & C_1 = C_2 \\ DA_3 = -A_2\mu/(1-\nu) - C_2(3-\nu)/(1-\nu)^2 & DC_3 = C_2\mu/(1-\nu) \\ DA_4 = A_2\mu/(1-\nu) + 2C_2/(1-\nu)^2 & DC_4 = C_2\mu/(1-\nu) \end{array}\right\} \tag{35}$$

$$\left.\begin{array}{ll} B_1 = B_2 - D_2(3+\nu)/[\mu(1-\nu)] & D_1 = -D_2 \\ DB_3 = B_2\mu/(1-\nu) - D_2(3-\nu)/(1-\nu)^2 & DD_3 = -D_2\mu/(1-\nu) \\ DB_4 = B_2\mu/(1-\nu) - 2D_2/(1-\nu)^2 & DD_4 = D_2\mu/(1-\nu) \end{array}\right\} \tag{36}$$

there are only four independent constants selected as A_2, C_2 and B_2, D_2 above. It should be mentioned that relations Eqn.35,36 can only be applied to basic eigenfunction-vectors of eigenvalue μ. Substituting Eqn. 34,35,36 into the boundary conditions, equations for non-zero eigenvalue μ and their eigenfunction-vector are determined. In case of duplicate eigenvalue, the equation for Jordan normal form is

$$H\Psi^k = \mu\Psi^k + \Psi^{k-1} \qquad k = 1,2,\cdots,m \tag{37}$$

The Jordan vectors depend on their lower order eigenfunction-vector.

PLATE SIMPLY SIMPLY SUPPORTED ON BOTH SIDES

This problem is classical but typical, because it has Jordan form solution. Assuming two edges $y = 0,\ b$ are simply support, the lateral boundary conditions can be written as

$$\phi_x(y=0) = 0,\ \ \phi_x(y=b) = a_1, \qquad \partial\phi_y / D\partial y - \nu\kappa_y(y = 0 \text{ or } b) = 0 \tag{38}$$

Due to the given force conditions, there is an indeterminate constant a_1 according to Eqn.9. Because eigensolution can only be applied to the homogeneous equation and lateral boundary conditions, the non-homogeneous factor, i.e. the indeterminant constant a_1, is considered first. The related governing equations are ($a_1 = 1$)

$$H\Psi_0 = 0;\ \ \phi_x(0) = 0, \phi_x(b) = 1;\ \ \partial\phi_y / D\partial y - \nu\kappa_y = 0 \quad \text{when } y = 0 \text{ or } b \tag{39}$$

Via some integration procedures its solution is given as

$$\begin{aligned} &\Psi_0 = \left\{\phi_x = y/b,\ \phi_y = 0,\ \kappa_y = 0,\ \kappa_{xy} = 1/[2bD(1-\nu)]\right\}^{\mathrm{T}} \\ &v_0 = \Psi_0, \quad w = -xy/[2bD(1-\nu)] + \text{rigid body motions} \end{aligned} \tag{40}$$

It is a superfluous solution of the original problem due to substituting the boundary condition $w = 0$ with $\kappa_x = 0$, and should be discarded. So we consider only homogeneous boundary conditions for both sides simply support plate.

$$\phi_x = 0\,, \qquad \partial\phi_y / D\partial y - \nu\kappa_y = 0 \qquad \text{when } y = 0 \text{ or } b \tag{41}$$

It can be proved that solution corresponding to zero eigenvalue doesn't exist. Substituting Eqn. 34,35,36 into Eqn.41, the transcendental equation for non-zero eigenvalue can be derived as

$$\sin^2(\mu b) = 0\,, \quad \text{that is, } \mu_n = n\pi / b \quad (n = \pm 1, \pm 2, \cdots) \quad \text{double root} \tag{42}$$

the basic eigenfunction-vector is

$$\boldsymbol{\Psi}_n^0 = \left\{ \frac{D(1-\nu)}{\mu_n}\sin(\mu_n y);\ \ \frac{D(1-\nu)}{\mu_n}\cos(\mu_n y);\ \ \sin(\mu_n y);\ \ \cos(\mu_n y) \right\}^{\mathrm{T}} \tag{43}$$

The solution of the original Eqn.25 is

$$\boldsymbol{v}_n^0 = \exp(\mu_n x)\boldsymbol{\Psi}_n^0\,; \qquad w_n^0 = -\exp(\mu_n x)\sin(\mu_n y) / \mu_n^2 \tag{44}$$

Due to the eigenvalue μ_n is double root, the first order solution of Jordan normal form exists. According to Eqn.37 with $k = 1$, the solution can be solved as

$$\boldsymbol{\Psi}_n^1 = \left\{ -\frac{3+\nu}{2\mu_n^2} D\sin(\mu_n y);\ \ \frac{3+\nu}{2\mu_n^2} D\cos(\mu_n y);\ \ -\frac{1}{2\mu_n}\sin(\mu_n y);\ \ \frac{1}{2\mu_n}\cos(\mu_n y) \right\}^{\mathrm{T}} \tag{45}$$

The solution of the original Eqn.25 is

$$\boldsymbol{v}_n^1 = \exp(\mu_n x)(\boldsymbol{\Psi}_n^1 + x\boldsymbol{\Psi}_n^0)\,; \qquad w_n^1 = (1 - 2\mu_n x)\exp(\mu_n x)\sin(\mu_n y) / (2\mu_n^3) \tag{46}$$

It is easy to verify that

$$< \boldsymbol{\Psi}_n^{1\mathrm{T}}, \boldsymbol{J}, \boldsymbol{\Psi}_{-n}^0 >= 2Db / \mu_n^2 \tag{47}$$

and relationships among the eigenfunctions of different eigenvalues are all symplectic orthogonal each other.

According to adjoint symplectic orthogonality and the expansion theorem, the general solutions for both sides simply support plate can be expanded as

$$\boldsymbol{v} = \sum_{n=1}^{\infty}(f_n^0\boldsymbol{v}_n^0 + f_n^1\boldsymbol{v}_n^1 + f_{-n}^0\boldsymbol{v}_{-n}^0 + f_{-n}^1\boldsymbol{v}_{-n}^1)\,; \quad w^* = \overline{w} + \sum_{n=1}^{\infty}(f_n^0 w_n^0 + f_n^1 w_n^1 + f_{-n}^0 w_{-n}^0 + f_{-n}^1 w_{-n}^1) \tag{48}$$

where $\overline{w}$ is a special solution of the original problem. Eqn.48 satisfy exactly the differential equation in domain and two lateral boundary conditions; the $f_i^k (k = 0,1; i = \pm 1, \pm 2, \cdots)$ are constants, which should be determined from the two end boundary conditions.

In case of four edges simply supported rectangular plate ($-a/2 \le x \le a/2$, $0 \le y \le b$) under

uniform load $q = q_0$, the special solution is given as

$$\begin{aligned} &\overline{w} = q_0(y^4 - 2by^3 + b^3y)/24D; \quad \overline{\kappa}_y = q_0 y(y-b)/2D; \quad \overline{\kappa}_x = \overline{\kappa}_{xy} = 0 \\ &\overline{M}_x = \nu q_0 y(y-b)/2; \qquad \overline{M}_y = q_0 y(y-b)/2; \qquad \overline{M}_{xy} = 0 \end{aligned} \tag{49}$$

Substituting Eqn. 48 into two end simply support boundary conditions

$$M_x^* = \overline{M}_x + M_x = 0, \quad \kappa_y^* = \overline{\kappa}_y + \kappa_y = 0 \qquad \text{when} \quad x = \pm a/2 \tag{50}$$

After some algebraic derivations, the solution is given as

$$f_n^0 = -f_{-n}^0 = f_n^1 = -f_{-n}^1 = 0 \Big\} \qquad (n = 2,4,6,\cdots) \tag{51}$$

$$\left.\begin{aligned} f_n^0 &= -f_{-n}^0 = \frac{q_0[\alpha_n \mathrm{th}(\alpha_n) + 1.5]}{Db\mu_n^3 \mathrm{ch}(\alpha_n)} \\ f_n^1 &= f_{-n}^1 = -\frac{q_0}{Db\mu_n^2 \mathrm{ch}(\alpha_n)} \end{aligned}\right\}; \quad \text{where} \quad \alpha_n = \frac{an\pi}{2b} \quad (n = 1,3,5,\cdots) \tag{52}$$

This solution is the same as the classical solution. In fact, Eqn. 48 is equivalent to the Levy single trigonometrical series expansion method, so all analytic solutions for both sides simply supported plate can be solved via the new method; the detail is neglected. The new method is not the same as the classical semi-inverse method; the new method is derived rationally and analytically, and therefore it can easily be applied to other lateral boundary conditions.

BOTH SIDES FREE PLATE

The two lateral edges $y = \pm b$ are free; the boundary conditions can be written as

$$\phi_x(y=-b) = 0, \quad \phi_x(y=b) = a_1 - a_2 b; \qquad \phi_y(y=-b) = 0, \quad \phi_y(y=b) = a_0 + a_2 x \tag{53}$$

The indeterminant constants a_0, a_1, a_2 are non-homogeneous terms, and are considered first. For a_0, the governing equations are ($a_0 = 1$)

$$\boldsymbol{H}\boldsymbol{\Psi}_0^0 = 0; \ \phi_x(-b) = \phi_x(b) = \phi_y(-b) = 0, \ \phi_y(b) = 1 \tag{54}$$

Its solution is

$$\boldsymbol{\Psi}_0^0 = \{0, \ (y+b)/(2b) \ ; \ -\nu/[2bD(1-\nu^2)], \ 0\}^{\mathrm{T}}; \tag{55}$$

that is, $$\boldsymbol{v}_0^0 = \boldsymbol{\Psi}_0^0, \qquad w_0^0 = (x^2 - \nu y^2)/[4bD(1-\nu^2)] + \text{rigid body motions} \tag{56}$$

For a_2, because of the multiplier x, this solution is similar to Jordan normal form. The governing equations are ($a_2 = 1$)

$$\boldsymbol{H}\boldsymbol{\Psi}_0^2 = \boldsymbol{\Psi}_0^0;\quad \phi_x(-b) = \phi_y(-b) = \phi_y(b) = 0,\qquad \phi_x(b) = -b \tag{57}$$

Its solution is

$$\boldsymbol{\Psi}_0^2 = \left\{-(1-\nu)(y^2-b^2)/[4b(1+\nu)] - (y+b)/2,\, 0,\, 0,\, \nu y/[2bD(1-\nu^2)]\right\}^{\mathrm{T}} \tag{58}$$

that is, $$\boldsymbol{v}_0^2 = \boldsymbol{\Psi}_0^2 + x\boldsymbol{\Psi}_0^0,\quad w_0^2 = (x^3 - 3\nu x y^2)/[12bD(1-\nu^2)] + \text{rigid body motions} \tag{59}$$

For a_1, the governing equations are ($a_1 = 1$)

$$\boldsymbol{H}\boldsymbol{\Psi}_0^1 = 0;\quad \phi_x(b) = 1,\ \phi_x(-b) = \phi_y(-b) = \phi_y(b) = 0 \tag{60}$$

Its solution is

$$\boldsymbol{\Psi}_0^1 = \left\{\phi_x = (y+b)/[2b],\ \phi_y = 0,\ \kappa_y = 0,\ \kappa_{xy} = 1/[4bD(1-\nu)]\right\}^{\mathrm{T}} \tag{61}$$

that is, $$\boldsymbol{v}_0^1 = \boldsymbol{\Psi}_0^1,\qquad w_0^1 = -xy/[4bD(1-\nu)] + \text{rigid body motions} \tag{62}$$

The physical interpretation of $\boldsymbol{v}_0^0$ is the pure bending solution, $\boldsymbol{v}_0^1$ is the pure torsion, and $\boldsymbol{v}_0^2$ is the bending solution with constant shearing force. In fact, displacement Hamiltonian system can also be introduced into plate bending (Zhong and Yang, 1991); then there are six eigensolutions corresponding to eigenvalue zero, that is, three rigid body motions and other three solutions corresponding to the present solutions $\boldsymbol{v}_0^0, \boldsymbol{v}_0^1, \boldsymbol{v}_0^2$ respectively. Due to substituting deflection with curvature boundary conditions, three rigid body motions don't appear presently, so their dual solution appear as the special solutions for non-homogeneous boundary conditions. The remaining solutions are all with homogeneous boundary conditions.

The homogeneous boundary conditions are

$$\phi_x = \phi_y = 0 \qquad \text{when} \quad y = \pm b \tag{63}$$

It is easy to show that only solutions with non-zero eigenvalue for Eqn.26, 63 exist, which can be divided into two groups (1) symmetric eigensolutions. (2) anti-symmetric eigensolutions.

Choosing group A, C of Eqn.34, the symmetric eigenvalue equation is given as

$$2(1-\nu)\mu b = (3+\nu)\sin(2\mu b) \tag{64}$$

the related eigenfunction-vector is

$$\boldsymbol{\Psi}_n = \begin{cases} -(3+\nu)\sin^2(\mu_n b)\cos(\mu_n y)/(1-\nu) + \mu_n y\sin(\mu_n y) \\ -(3+\nu)\cos^2(\mu_n b)\sin(\mu_n y)/(1-\nu) + \mu_n y\cos(\mu_n y) \\ \mu_n\{[(3+\nu)\cos^2(\mu_n b) - 3 + \nu]\cos(\mu_n y) + (1-\nu)\mu_n y\sin(\mu_n y)\}/[D(1-\nu)^2] \\ \mu_n\{[2-(3+\nu)\cos^2(\mu_n b)]\sin(\mu_n y) + (1-\nu)\mu_n y\cos(\mu_n y)\}/[D(1-\nu)^2] \end{cases} \tag{65}$$

$$\text{that is, } v_n = \exp(\mu_n x)\Psi_n;\ w_n = \exp(\mu_n x)\left\{\frac{1+\nu-(3+\nu)\cos^2(\mu_n b)}{D(1-\nu)^2\mu_n}\cos(\mu_n y) - \frac{y\sin(\mu_n y)}{D(1-\nu)}\right\} \tag{66}$$

The Newton iteration method is used to solve Eqn.64; the first several non-zero eigenvalues are solved for $\nu = 0.3$ (see Table 2).

TABLE 2
SYMMETRIC NON-ZERO EIGENVALUES ($\nu = 0.3$)

n=	1	2	3	4	5	6
$\mathrm{Re}(\mu_n b)$ =	1.2830	π +0.6973	2π +0.7191	3π +0.7313	4π +0.7393	5π +0.7450
$\mathrm{Im}(\mu_n b)$ =	0.0	0.5446	0.8808	1.0730	1.2101	1.3172

where each eigenvalue $\mu_n (n > 1)$ contains also its symplectic adjoint $-\mu_n$ and their complex conjugate $\pm\overline{\mu}_n$. The eigenvalue μ_1 is a real number, there is symplectic adjoint $-\mu_1$. All these eigenvalues are single roots.

Choosing group B, D of Eqn.34, the anti-symmetric eigenvalue equation is

$$2(1-\nu)\mu b + (3+\nu)\sin(2\mu b) = 0 \tag{67}$$

and the related eigenfunction-vector is

$$\hat{\Psi}_n = \begin{cases} -(3+\nu)\cos^2(\hat{\mu}_n b)\sin(\hat{\mu}_n y)/(1-\nu) - \hat{\mu}_n y\cos(\hat{\mu}_n y) \\ (3+\nu)\sin^2(\hat{\mu}_n b)\cos(\hat{\mu}_n y)/(1-\nu) + \hat{\mu}_n y\sin(\hat{\mu}_n y) \\ \hat{\mu}_n\{[(3+\nu)\sin^2(\hat{\mu}_n b) - 3 + \nu]\sin(\hat{\mu}_n y) - (1-\nu)\hat{\mu}_n y\cos(\hat{\mu}_n y)\}/[D(1-\nu)^2] \\ \hat{\mu}_n\{[(3+\nu)\sin^2(\hat{\mu}_n b) - 2]\cos(\hat{\mu}_n y) + (1-\nu)\hat{\mu}_n y\sin(\hat{\mu}_n y)\}/[D(1-\nu)^2] \end{cases} \tag{68}$$

$$\text{that is, } \hat{v}_n = \exp(\hat{\mu}_n x)\hat{\Psi}_n;\ \hat{w}_n = \exp(\hat{\mu}_n x)\left\{\frac{1+\nu-(3+\nu)\sin^2(\hat{\mu}_n b)}{D(1-\nu)^2\hat{\mu}_n}\sin(\hat{\mu}_n y) + \frac{y\cos(\hat{\mu}_n y)}{D(1-\nu)}\right\} \tag{69}$$

The Newton iteration method is used to solve Eqn.67; the first several non-zero eigenvalues are solved for $\nu = 0.3$ (see Table 3)

TABLE 3
ANTI-SYMMETRIC NON-ZERO EIGENVALUES ($\nu = 0.3$)

n=	1	2	3	4	5
$\mathrm{Re}(\hat{\mu}_n b)$ =	0.5π +0.5690	0.5π +0.7863	1.5π +0.7100	2.5π +0.7259	3.5π +0.7357
$\mathrm{Im}(\hat{\mu}_n b)$ =	0.0	0.0	0.7439	0.9865	1.1464

where each eigenvalue $\hat{\mu}_n (n > 2)$ contains also its symplectic adjoint $-\hat{\mu}_n$ and their complex conjugate $\pm\overline{\hat{\mu}}_n$. Because of the eigenvalue $\hat{\mu}_1$ and $\hat{\mu}_2$ are real numbers; there are

only symplectic adjoint $-\hat{\mu}_1$ and $-\hat{\mu}_2$ respectively. All eigenvalues are single roots.

As an example, the pure bending of semi-infinitely long free strip plate ($b = 1$) is solved. The condition for $x = 0$ end is clamped, and the end condition for $x \to \infty$ is a unit bending moment acted upon. Because this problem is symmetric for x-axis and only bending moment exist when $x \to \infty$, its expansion is composed of Eqn.55 and the symmetric solutions Eqn.65 with non-zero eigenvalues with negative real parts $\mathrm{Re}(\mu_n) < 0$.

$$v = 2v_0^0 + \sum_{n=1} f_n \exp(\mu_n x)\Psi_n \tag{70}$$

the Eqn.70 satisfy the differential Eqn. 25 the two lateral boundary condition at $y = \pm b$ and the $x \to \infty$ end boundary conditions. Now the end boundary condition of $x = 0$ is applied to determine the constants f_n, $(n = 1,2,\cdots)$. Only the first k terms of Eqn. 70 are selected to solve, the variational equation of $x = 0$ end boundary reads

$$\int_{-1}^{1}\left[\kappa_y \delta\phi_x + \kappa_{xy}\delta\phi_y\right]_{x=0} \mathrm{d}y = 0 \tag{71}$$

Due to some of eigenvalues are complex numbers, the real valued canonical equation of Eqn.70~71 (Zhong, 1995) is applied.

As an example, let $\nu = 0.3$, $k = 11$ and $k = 21$ respectively. The distributions of bending moment at the clamped end are shown in Figure 2. It is clear that the corner has stress singularity ($M_x \to -\infty$). The wavy form of bending moment appears due to choosing only finite number of terms in expansion solution.

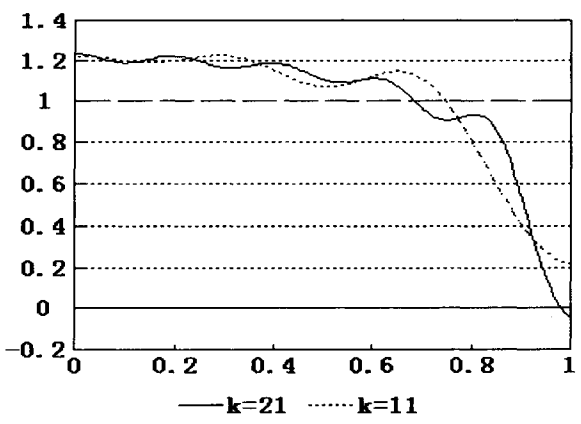

Figure 2: Distribution of bending moment at clamped end ($x = 0$)

The method proposed in this paper can also be applied to other boundary conditions. A series of analytic solution can be derived.

CONCLUDING REMARKS

In this paper, a new formulation of fundamental equations and the respective solution methodology for classical theory of plate bending is presented, which contrasts with the traditional methodology (Timoshenko and Woinowsky-Krieger,1959). The traditional solution uses displacement method and biharmonic equation; the new methodology applies bending moment function vector and differential Eqn.15. The traditional method is semi-inverse solution; thus only a few of solutions available. For example, only solution for both lateral simply support plate have been given for rectangle plate, and it is difficult to solve for other lateral boundary conditions. However, the new methodology presents a direct solution via introducing Hamiltonian system. Therefore the efficient mathematical methods, for example separation of variables and eigenfunction expansion etc., can be applied. The new methodology breaks the limitation of traditional semi-inverse solution. The solution for both sides free plate given in this paper can't be solved by the traditional method.

The analogy between plate bending and plane elasticity can be applied to not only analytical solutions but also to plate bending finite element; therefore the plate bending finite element can be improved to the same level as plane elasticity (Zhong and Yao, 1998).

Generally speaking, the new advances in plate bending mathematical theory present many opportunities. More research is anticipated.

ACKNOWLEDGMENTS

This work was supported by the National Natural Science Foundation of China.

REFERENCES

Hu H.C. (1981). *Variational Principle of Elasticity and Its Application*, Science Press, Beijing, P.R. China (in Chinese)

Muschelishvili N.I. (1953). *Some Basic Problems of the Mathematical Theory of Elasticity*. P. Noordhoff, Groningen, Netherlands

Timoshenko S.P. and Woinowsky-Krieger S. (1959). *Theory of Plates and Shells*, McGraw-Hill, New York, USA

Timoshenko S.P. and Goodier J.N. (1970). *Theory of Elasticity*, 3rd Ed. McGraw-Hill, New York, USA

Zhong W.X. (1995). *A New Systematic Methodology for Theory of Elasticity,* Dalian University of Technology Press. Dalian , P.R. China (in Chinese)

Zhong W.X. and Yang Z.S.(1992). Partial Differential Equations and Hamiltonian System, *Computational Mechanics in Structural Engineering*, Elsevier. SINO/US Joint Symposium on Computational Mechanics in Structural Engineering, Sept. 1991, Beijing.

Zhong W.X. and Yao W.A. (1998). Similarity Between Finite Element in Plane Elasticity and Plate Bending, *Chinese J. of Computational Mechanics*, 15(1): 1~13 (in Chinese)

FINITE ELEMENT ALGORITHM BASED ON TWO-SCALE ANALYSIS METHOD[1]

J.Z. CUI

Institute of Computational Mathematical & Science/Engineering Computing, Academia Sinica, Beijing, 100080, P.R.China

ABSTRACT

The FE algorithm based on two-scale analysis method for the structural problems of composite materials and the structures with small period in 2-dimension case is briefly presented in this paper, and some numerical results are shown. It is an effective method in computational mechanics to be developing.

KEYWORDS

Two-Scale Analysis Method, Composite Material, Structure with Small Period, Finite Element Algorithm.

INTRODUCTION

The structures shown in Fig. 1 are often encountered in structural engineering and in the design of new industrial products. They are made from woven composite materials or composed of numbers of same basic configurations.

The analysis problems for this kind of structure have some common properties as follows: The material parameters vary sharply and periodically, and the period ε of material change is very

[1] Project supported by National Natural Science Foundation of China

small; it means that, in mathematics and in mechanics, the coefficient of materials satisfy

$$a^{\varepsilon}_{ijhk}(x+\varepsilon) = a^{\varepsilon}_{ijhk}(x) \ , \quad \varepsilon/L \ << \ 1 \qquad (1)$$

where L is the size of considered structures.

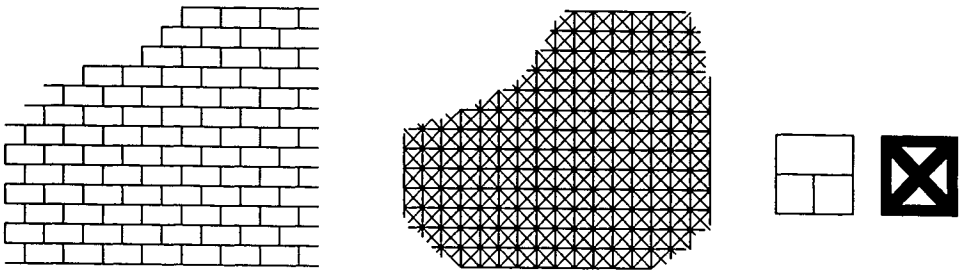

Fig. 1 Composite materials and structure with periodicity

The mechanical behaviour of this kind of structure depends not only on the macroscopic conditions, such as the geometry of the structure, the effective constants of the materials, the loadings and the constraints, but also on the detailed configurations. Since the stresses within a basic cell vary sharply in locale and the size of a cell is very small, either macroscopic analysis or microscopic analysis cannot obtain an accurate evaluation of stresses.

A Two-Scale Analysis (TSA) for this kind of structure, which combines the macroscopic behaviour of the structure with its detailed configurations, is proposed by author in Ref.[1].

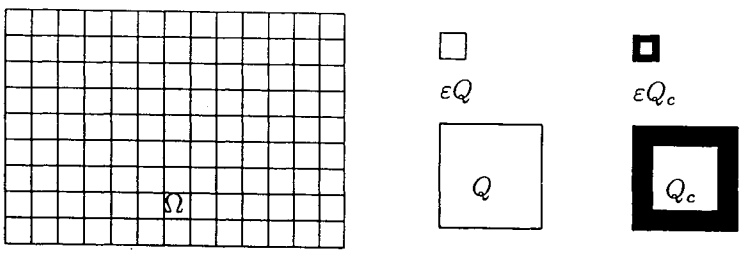

Fig. 2 Structure only including entirely basic configurations

From Eqn.1 for the analysis problem of the structure shown in Fig. 2 in 2-dimension case the displacements can be asymptotically expressed in two-scale variables x, ξ as follows

$$u(x) = u_0(x) + \sum_{l=1}^{\infty} \varepsilon^l \sum_{\alpha_l=1,2} N_{\alpha_1\cdots\alpha_l}(\xi) \frac{\partial^l u_0}{\partial x_{\alpha_1}\cdots\partial x_{\alpha_l}} \qquad (2)$$

$$N_{\alpha_1\cdots\alpha_l}(\xi) = \begin{bmatrix} N_{\alpha_1\cdots\alpha_l 11}(\xi), & N_{\alpha_1\cdots\alpha_l 12}(\xi) \\ N_{\alpha_1\cdots\alpha_l 21}(\xi), & N_{\alpha_1\cdots\alpha_l 22}(\xi) \end{bmatrix}$$

$$N_{\alpha_1\cdots\alpha_l m}(\xi)=\begin{pmatrix} N_{\alpha_1\cdots\alpha_l 1m}(\xi) \\ N_{\alpha_1\cdots\alpha_l 2m}(\xi) \end{pmatrix},\quad \mathrm{m}=1,2 \tag{3}$$

where $\boldsymbol{x}$ denotes the global coordinates of structure, and $\xi=\dfrac{\boldsymbol{x}}{\xi}$ the local coordinates, and all $N_{\alpha_1\cdots\alpha_l}(\xi)$ $(1=1,2,\cdots,\ \alpha_i=1,2)$ are the periodical functions defined on space R^2 with period 1; they can be determined on I- square Q, and $\boldsymbol{u}_0(\boldsymbol{x})$ is the solution of homogenized problem defined on whole Ω.

1. The m-th column $N_{\alpha_l m}(\xi)$ $(\alpha_1,m=1,2)$ of $N_{\alpha_l}(\xi)$ is the solution of the following virtual work equation

$$\int_Q \varepsilon_{ij}(\boldsymbol{v})a_{ijhk}(\xi)\varepsilon_{hk}\left(N_{\alpha_l m}\right)\mathrm{d}\xi=\int_Q \varepsilon_{ij}(\boldsymbol{v})a_{ij\alpha_l m}(\xi)\mathrm{d}\xi\quad \forall \boldsymbol{v}\in H_0^1(Q) \tag{4}$$

where $\mathrm{d}\xi=\mathrm{d}\xi_1\mathrm{d}\xi_2$, $H_0^1(Q)$ is the set of the functions fixed on the boundary of the unit square.

2. The m-th column $N_{\alpha_1\alpha_2 m}(\xi)$ $(\alpha_1,\alpha_2,m=1,2)$ of $N_{\alpha_l\alpha_2}(\xi)$ is the solution of the following virtual work equation

$$\begin{aligned}\int_Q \varepsilon_{ij}(\boldsymbol{v})a_{ijhk}(\xi)\varepsilon_{hk}\left(N_{\alpha_1\alpha_2 m}\right)\mathrm{d}\xi=&-\int_Q\left[\hat{a}_{i\alpha_2\alpha_1 m}-a_{i\alpha_2\alpha_1 m}(\xi)-a_{i\alpha_2 hk}(\xi)\varepsilon_{hk}\left(N_{\alpha_1 m}\right)\right]v_i\mathrm{d}\xi\\&+\int_Q a_{ij\alpha_1 h}(\xi)N_{\alpha_2 hm}(\xi)\varepsilon_{ij}(\boldsymbol{v})\mathrm{d}\xi\qquad \forall \boldsymbol{v}\in H_0(Q)\end{aligned} \tag{5}$$

where $\hat{a}_{ijhk}$ are the homogenized coefficients of materials computed from $N_{\alpha_l m}(\xi)$ $(\alpha_1,m=1,2)$ in following formulation

$$\hat{a}_{ijhk}=\int_Q\left[a_{ijhk}(\xi)+a_{ijpq}\varepsilon_{pq}\left(N_{hk}(\xi)\right)\right]\mathrm{d}\xi \tag{6}$$

$$\varepsilon_{pq}\left(N_{hk}(\xi)\right)=\frac{1}{2}\left(\frac{\partial N_{hpk}}{\partial\xi_q}+\frac{\partial N_{hqk}}{\partial\xi_p}\right) \tag{7}$$

3. The m-th column $N_{\alpha_l\cdots\alpha_l m}(\xi)$ $(\alpha_1,\cdots,\alpha_l,m=1,2)$ of $N_{\alpha_1\cdots\alpha_l}(\xi)$ $(l=3,4,\cdots)$ is the solution of the following virtual work equation

$$\begin{aligned}&\int_Q \varepsilon_{ij}(\boldsymbol{v})a_{ijhk}(\xi)\varepsilon_{hk}\left(N_{\alpha_1\cdots\alpha_l m}\right)\mathrm{d}\xi=\\&-\int_Q\left[a_{i\alpha_l\alpha_{l-1}m}(\xi)N_{\alpha_1\cdots\alpha_{l-2}hm}(\xi)+a_{i\alpha_l hk}(\xi)\varepsilon_{hk}\left(N_{\alpha_1\cdots\alpha_{l-1}m}\right)\right]v_i\mathrm{d}\xi\\&+\int_Q a_{ij\alpha_{l-1}h}(\xi)N_{\alpha_1\cdots\alpha_{l-1}hm}\varepsilon_{ij}(\boldsymbol{v})\mathrm{d}\xi,\qquad \forall \boldsymbol{v}\in H_0(Q)\end{aligned} \tag{8}$$

4. $\boldsymbol{u}_0(\boldsymbol{x})$ is the solution of the homogenized problem defined on global Ω

$$\int_\Omega \varepsilon_{ij}(\boldsymbol{v})\hat{a}_{ijhk}\varepsilon_{hk}(\boldsymbol{u}_0)\mathrm{d}x-\int_{\Gamma_\sigma}p_i(\boldsymbol{x})v_i\mathrm{d}s-\int_{\Gamma_u}\bar{u}_i\hat{a}_{ijhk}\varepsilon_{hk}(\boldsymbol{u}_0)n_j\mathrm{d}s$$

$$= \int_{\Omega} f_i v_i \mathrm{d}x \qquad \forall \boldsymbol{v} \in H_u(\Omega) \tag{9}$$

Since the asymptotic expression can not be strictly evaluated in practical computation, the sum of fore terms $(l \le M)$ in Eqn. 2 is evaluated as the approximation of $\boldsymbol{u}(\boldsymbol{x})$; let

$$\boldsymbol{u}^M(\boldsymbol{x}) = u_0(\boldsymbol{x}) + \sum_{l=1}^{M} \varepsilon^l \sum_{\alpha_i=1,2} N_{\alpha_1 \cdots \alpha_l}(\xi) \frac{\partial^l \boldsymbol{u}_0}{\partial x_{\alpha_1} \cdots \partial x_{\alpha_l}} \tag{10}$$

We have proved that Eqn.9 if Ω is convex domain with piecewise smooth boundaries and $f(\boldsymbol{x})$ satisfies the conditions so that the homogenization solution $\boldsymbol{u}_0(\boldsymbol{x}) \in \mathrm{C}^{M+2}(\Omega)$, then

$$\| \boldsymbol{u}^M(\boldsymbol{x}) - \boldsymbol{u}(\boldsymbol{x}) \|_{H_0^1(\Omega)} \le (\mathrm{A}\varepsilon)^{M-1} C \tag{11}$$

where A and C are constants independent of ε . Therefore $\boldsymbol{u}^M(\boldsymbol{x})$ is a proper approximation of $\boldsymbol{u}(\boldsymbol{x})$.

FE SOLUTION BASED ON TSA

From previous description it is not difficult to see that the FE displacements can be approximately expressed in two-scale variables $\boldsymbol{x}, \xi = \dfrac{\boldsymbol{x}}{\varepsilon}$ as follows

$$\mathbf{u}^{Mh}(\mathbf{x}) = u_0^{h_0}(x) + \sum_{l=1}^{M} \varepsilon^l \sum_{\alpha_i=1,2} \mathbf{N}^h_{\alpha_1 \cdots \alpha_l}\left(\frac{\mathbf{x}}{\varepsilon}\right) \frac{\partial^l \mathbf{u}_0^{h_0}}{\partial x_{\alpha_1} \cdots \partial x_{\alpha_l}} \tag{12}$$

where $N^h_{\alpha_1 \cdots \alpha_l m}(\xi)$, m = 1, 2, l = 1,$\cdots$, M, and $\boldsymbol{u}_0^h(\boldsymbol{x})$ are the FE solutions of the following problems respectively :

1. $N^h_{\alpha_l m}(\xi)$ (α_1 , m = 1, 2) is the solution of the following virtual work equation on FE space $S_0^h(Q) = \left\{ \mathbf{v} \in S^h(Q) / \ \mathbf{v}(\partial Q) = \mathbf{0} \right\}$

$$\sum_{e \in S^h} \int_e \varepsilon_{ij}(v) a_{ijhk}(\xi) \varepsilon_{hk}\left(N^h_{\alpha_l m}(\xi)\right) \mathrm{d}\xi = \sum_{e \in S^h} \int_e \varepsilon_{ij}(v) a_{ij\alpha_l m}(\xi) \mathrm{d}\xi \quad \forall \boldsymbol{v} \in S_0^h(Q) \tag{13}$$

where $\mathrm{d}\xi = \mathrm{d}\xi_1 d\xi_2$, and S^h denotes the FE partition on 1-square Q.

Then $\hat{a}^h_{ijhk}$ approximate to homogenized material constants $\hat{a}_{ijhk}$ can be computed in the following formulation from $N^h_{\alpha_l m}(\xi)$ $(\alpha_1,$ m = 1,2)

$$\varepsilon^e_{pq}\left(N^h_{hk}(\xi)\right) = \frac{1}{2}\left(\frac{\partial N^h_{hpk}}{\partial \xi_q} + \frac{\partial N^h_{hqk}}{\partial \xi_p} \right) \tag{14}$$

$$\hat{a}^h_{ijhk} = \sum_{e \in S^h} \int_e \left[a_{ijhk}(\xi) + a_{ijpq}(\xi) \varepsilon^e_{pq}\left(N^h_{hk}(\xi)\right) \right] \mathrm{d}\xi \tag{15}$$

2. From virtual work Eqn. 5 its FE solution $N^h_{\alpha_l \alpha_2 m}(\xi)$ $(\alpha_1, \alpha_2, m = 1,2)$ should be the solution of the following FE virtual work equation

$$\sum_{e\in S^h}\int_e \varepsilon_{ij}(\boldsymbol{v})a_{ijhk}(\xi)\varepsilon_{hk}\left(\boldsymbol{N}^h_{\alpha_1\alpha_2 m}\right)\mathrm{d}\xi$$
$$=-\sum_{e\in S^h}\int_e\left[\hat{a}_{i\alpha_2\alpha_1 m}-a_{i\alpha_2\alpha_1 m}(\xi)-a_{i\alpha_2 hk}(\xi)\varepsilon_{hk}\left(\boldsymbol{N}_{\alpha_1 m}(\xi)\right)\right]v_i\,\mathrm{d}\xi$$
$$+\sum_{e\in S^h}\int_e a_{ij\alpha_1 h}(\xi)N_{\alpha_1 hm}(\xi)\varepsilon_{ij}(\boldsymbol{v})\mathrm{d}\xi \qquad \forall \boldsymbol{v}\in S_0^h(Q) \tag{16}$$

It is well-known that the true solution $\boldsymbol{N}_{\alpha_1 m}(\xi)\ (\alpha_1, m=1,2)$ of Eqn. 4 cannot be obtained as well as the accurate values of homogenization coefficients $\hat{a}_{ijhk}$. So $\boldsymbol{N}^h_{\alpha_1\alpha_2 m}(\xi)\ (\alpha_1,\alpha_2,m=1,2)$ are corrected as the FE solutions of the following virtual work equation

$$\sum_{e\in S^h}\int_e \varepsilon_{ij}(\boldsymbol{v})a_{ijhk}(\xi)\varepsilon_{hk}\left(\boldsymbol{N}^h_{\alpha_1\alpha_2 m}\right)\mathrm{d}\xi$$
$$=-\sum_{e\in S^h}\int_e\left[\hat{a}^h_{i\alpha_2\alpha_1 m}-a_{i\alpha_2\alpha_1 m}(\xi)-a_{i\alpha_2 hk}(\xi)\varepsilon_{hk}\left(\boldsymbol{N}^h_{\alpha_1 m}(\xi)\right)\right]v_i\,\mathrm{d}\xi$$
$$+\sum_{e\in S^h}\int_e a_{ij\alpha_1 h}(\xi)N^h_{\alpha_1 hm}(\xi)\varepsilon_{ij}(\boldsymbol{v})\mathrm{d}\xi \qquad \forall \boldsymbol{v}\in S_0^h(Q) \tag{17}$$

3. In the same way $\boldsymbol{N}^h_{\alpha_1\cdots\alpha_l m}(\xi)\ (\alpha_1,\cdots\alpha_l, m=1,2,\ l=1,\cdots,\mathrm{M})$ is considered as the FE solution of the following virtual work equation

$$\sum_{e\in S^h}\int_e \varepsilon_{ij}(\boldsymbol{v})a_{ijhk}(\xi)\varepsilon_{hk}\left(\boldsymbol{N}^h_{\alpha_1\cdots\alpha_l m}\right)\mathrm{d}\xi$$
$$=-\sum_{e\in S^h}\int_e\left[a_{i\alpha_l\alpha_{l-1}m}(\xi)N^h_{\alpha_1\cdots\alpha_{l-2}hm}(\xi)+a_{i\alpha_l hk}(\xi)\varepsilon_{hk}\left(\boldsymbol{N}^h_{\alpha_1\cdots\alpha_{l-1}m}\right)\right]v_i\,\mathrm{d}\xi$$
$$+\sum_{e\in S^h}\int_e a_{ij\alpha_{l-1}h}(\xi)\boldsymbol{N}^h_{\alpha_1\cdots\alpha_{l-1}hm}\varepsilon_{ij}(\boldsymbol{v})\mathrm{d}\xi\ , \qquad \forall \boldsymbol{v}\in S_0^h(Q) \tag{18}$$

4. From virtual work Eqn. 9 its FE solution $\boldsymbol{u}_0^h(\boldsymbol{x})$ should be the solution of the following homogenized FE problem defined on global Ω

$$\int_\Omega \varepsilon_{ij}(\boldsymbol{v})\hat{a}_{ijhk}\varepsilon_{hk}\left(\boldsymbol{u}_o^{h_0}\right)\mathrm{d}x-\int_{\Gamma_\sigma}p_i(\boldsymbol{x})v_i\mathrm{d}s-\int_{\Gamma_u}\overline{u}_i\hat{a}_{ijhk}\varepsilon_{hk}\left(\boldsymbol{u}_0^{h_0}\right)n_j\mathrm{d}s$$
$$=\int_\Omega f_i v_i\mathrm{d}x \quad \forall \boldsymbol{v}\in S_u^{h_0}(\Omega) \tag{19}$$

where $S_u^{h_0}(\Omega)$ denotes the FE space defined on global structure Ω. Since the exact $\{\hat{a}_{ijhk}\}$ cannot be obtained they are substituted by their approximate values $\{\hat{a}^h_{ijhk}\}$. So here we consider $\boldsymbol{u}_0^{h_0}(\boldsymbol{x})$ to be the FE solution of the following approximate problem from Eqn. 9

$$\int_\Omega \varepsilon_{ij}(\boldsymbol{v})\hat{a}^h_{ijhk}\varepsilon_{hk}\left(\boldsymbol{u}_o^{h_0}\right)\mathrm{d}x-\int_{\Gamma_\sigma}p_i(\boldsymbol{x})v_i\mathrm{d}s-\int_{\Gamma_u}\overline{u}_i\hat{a}^h_{ijhk}\varepsilon_{hk}\left(\boldsymbol{u}_0^{h_0}\right)n_j\mathrm{d}s$$
$$=\int_\Omega f_i v_i\mathrm{d}x \qquad \forall \boldsymbol{v}\in H_{\dot{u}}(\Omega) \tag{20}$$

FE COMPUTATION OF $N^h_{\alpha_1\cdots\alpha_l m}(\xi)$

FE Computation of $N^h_{\alpha_1 m}(\xi)$ *and* $\hat{a}^h_{ijhk}$

$N^h_{\alpha_1 m}(\xi)$ can be obtained by solving FE virtual work Eqn.13 defined on 1-square Q. Partition Q into the set S^h of consistently triangular or/and quadrangular elements according to material distribution $a_{ijhk}(\xi)$ of the basic configuration shown in Fig. 3, where h denotes the maximum size of the elements. Let

$$S_0^h(Q)=\left\{\boldsymbol{v}=(v_1,v_2)^{\mathrm{T}}\,\middle|\, v_i\in P_{\mathrm{k}}(e),\ e\in S^h \text{ and } v_i=0 \text{ on } \partial Q\right\} \tag{21}$$

where $P_k(e)$ denotes the set of $k-$order polynomials defined on element e. Since the basic configuration is so complex and the material coefficients $a_{ijhk}(\xi)$ vary so sharply, the true solutions $N_{\alpha_1 m}(\xi)$ (α_1 , m = 1, 2) have not more than 2-order smoothness only linear or/and bilinear elements are chosen to solve FE virtual work Eqn.13. By making use of FE program based on linear or/and bilinear elements, $N^h_{\alpha_1 m}(\xi)$ (α_1 , m = 1, 2) can be evaluated. In this case, from finite element analysis, it follows that

$$\left\| \nabla\left(N_{\alpha_1 m}-N^h_{\alpha_1 m}\right)\right\|_{L^2(Q)}\le Ch\left\| D^2 N_{\alpha_1 m}\right\|_{L^2(Q)} \tag{22}$$

$$\left\| N_{\alpha_1 m}-N^h_{\alpha_1 m}\right\|_{L^2(Q)}\le Ch^2\left\| D^2 N_{\alpha_1 m}\right\|_{L^2(Q)} \tag{23}$$

where C is independent of h.

Making use of Eqns. 14 and 15, one can evaluate $\hat{a}^h_{ijhk}$ from $N^h_{\alpha_1 m}(\xi)$ (α_1 , m = 1, 2). Using Eqns. 6 and 15, one can prove that the approximate homogenization coefficients $\left\{\hat{a}^h_{ijhk}\right\}$ converge the true $\left\{\hat{a}_{ijhk}\right\}$ as $h\to 0$, and they satisfy the following inequality

$$\left|\hat{a}_{ijhk}-\hat{a}^h_{ijhk}\right|\le CAh \tag{24}$$

where C and A is independent of h.

In order to verify the effectiveness of previous computational formulations on homogenization coefficients using the following two kinds of original materials, the first is much stiffer than the second

$$\begin{pmatrix} 3\,125\,000 & 625\,000 & 0 \\ 625\,000 & 3\,125\,000 & 0 \\ 0 & 0 & 1\,250\,000 \end{pmatrix},\quad \begin{pmatrix} 178\,571.43 & 71\,428.57 & 0 \\ 71\,428.57 & 178\,571.43 & 0 \\ 0 & 0 & 53\,571.43 \end{pmatrix} \tag{25}$$

We constructed three basic configurations as shown in Fig.3. The numerical results on homogenization coefficients evaluated by 40×40 meshes are shown in Fig. 3.

FE Computation of $N^h_{\alpha_1\cdots\alpha_l m}(\xi)$ $(2\le l\le \mathrm{M})$

From the formulations of the previous section, it is noticed that all FE virtual work equations

satisfied by $N^h_{\alpha_1\cdots\alpha_l m}(\xi)$ are defined on 1-square Q. The left sides are the same , and the right sides are different, but they can be recursively evaluated from the material coefficients $a_{ijhk}(\xi)$, $N^h_{\alpha_1\cdots\alpha_{l-2}}(\xi)$ and $N^h_{\alpha_1\cdots\alpha_{l-1}}(\xi)$. In this case, the finite element meshes for evaluating $N^h_{\alpha_1\cdots\alpha_l m}(\xi)$ $(2 \le l \le \mathrm{M})$ are chosen the same as for evaluating $N^h_{\alpha_1 m}(\xi)$ (α_1 , m = 1, 2). So the global stiffness matrix $\boldsymbol{K}$ is computed, decomposed as $\boldsymbol{K} = \boldsymbol{LDL}^{\mathrm{T}}$ and saved only one time, in the stage of evaluating $N^h_{11}(\xi)$. When evaluating $N^h_{\alpha_1\cdots\alpha_l m}(\xi)$, we only need to evaluate the right side of FE equation, forward substitution and backward substitution in succession.

Through complicated finite element analysis, see [3,9], we can obtain the following results: the

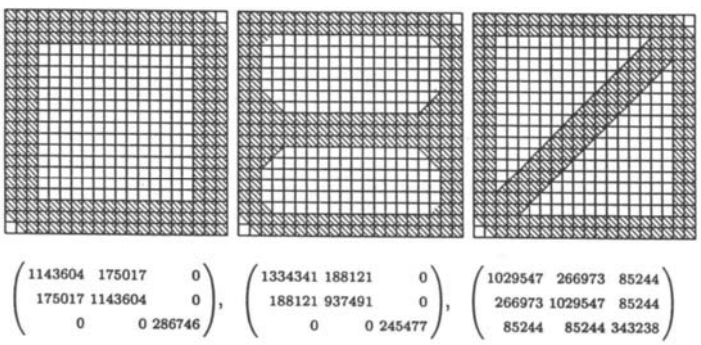

Fig. 3 Basic configurations and their homogenization constants

true $N_{\alpha_1\cdots\alpha_l m}(\xi)$ and its FE approximation $N^h_{\alpha_1\cdots\alpha_l m}(\xi)$ satisfy these inequalities

$$\left\| \nabla\left(N_{\alpha_1\cdots\alpha_l m} - N^h_{\alpha_1\cdots\alpha_l m}\right)\right\|_{L^2(\Omega)} \le C(\varepsilon h)A \tag{26}$$

$$\left\| N_{\alpha_1\cdots\alpha_l m} - N^h_{\alpha_1\cdots\alpha_l m}\right\|_{L^2(\Omega)} \le C\varepsilon(\varepsilon h)A \tag{27}$$

where C and A are constants independent of h, ε and Ω, and

$$A = \mathrm{Max}\left\{\left\|D^2 N_{\alpha_1 m}\right\|_{L^2(\Omega)}, \left\|D^2 N_{\alpha_1\alpha_2 m}\right\|_{L^2(\Omega)}, \cdots, \left\|D^2 N_{\alpha_1\cdots\alpha_l m}\right\|_{L^2(\Omega)}\right\}. \tag{28}$$

FE COMPUTATION OF $u^{Mh}(x)$

FE Computation of $u_0^{h_0}(x)$

According to Eqn. 12, the next step of computing $u^{Mh}(x)$ is to solve the homogenized FE vitual work equation (19) to obtain $u_0^{h_0}(x)$. Since $\{\hat{a}^h_{ijhk}\}$ are constant for global Ω, the true solution $\bar{u}_0(x)$ of Eqn.19 must be sufficiently smooth inside Ω according to the regularity theorem of PDE problems. So high-order elements can be chosen to evaluate $u_0^{h_0}(x)$. Using

high-order elements with mesh size h_0 partition Ω into FE set S^{h_0}. Let

$$S_u^{h_0}(\Omega)=\left\{\boldsymbol{v}=(v_1,v_2)^{\mathrm{T}}\,|\,v_i\in P_k(e),\ e\in S^{h_0}\text{ and }\boldsymbol{u}(\boldsymbol{x})=\bar{\boldsymbol{u}}\text{ on }\Gamma_u\subset\partial\Omega\right\} \tag{29}$$

where k is the order of the interpolation polynomials within elements. Taking advantage of FE program we obtain $\boldsymbol{u}_0^{h_0}(\boldsymbol{x})$.

Through detailed FE calculus, see [3,9], we can prove that

$$\left\|\boldsymbol{u}_0(\boldsymbol{x})-\boldsymbol{u}_0^{h_0}(\boldsymbol{x})\right\|_{H^1(\Omega)}\le C\left(h\|f\|_{L^2(\Omega)}+h_0^k\left\|D^{k-1}f\right\|_{L^2(\Omega)}\right) \tag{30}$$

where $\boldsymbol{u}_0(\boldsymbol{x})$ is the true solution of the homogenized Eqn. 9 and $\boldsymbol{u}_0^{h_0}(\boldsymbol{x})$ is the FE solution of Eqn. 19 obtained by previous procedure , and h is the mesh size for evaluating $N^h_{\alpha_1 m}(\xi)$ (α_1 , m = 1, 2).

Evaluation of $\dfrac{\partial^l \boldsymbol{u}_0^{h_0}(\boldsymbol{x})}{\partial x_{\alpha_1}\cdots\partial x_{\alpha_l}}$

Below the formulations for evaluating high-order partial derivatives of scale function $u^{h_0}(\boldsymbol{x})$ are shown. Let

$$\delta_{x_i}u^{h_0}(M)=\frac{1}{\tau(M)}\sum_{e\in S^h(M)}\left[\frac{\partial u^{h_0}}{\partial x_i}\right]_e \tag{31}$$

where M is a node of FE set S^{h_0}, $S^h(M)$ denotes the set of the elements with node M and $\tau(M)$ is the number of the elements in $S^h(M)$. For $l=1,2,\cdots$ and $\boldsymbol{x}\in e$, let

$$\delta^{l+1}_{x_{\alpha_1}\cdots x_{\alpha_l}x_{\alpha_{l+1}}}u^h(\boldsymbol{x})=\sum_{M\in S^h(e)}\delta^l_{x_{\alpha_1}\cdots x_{\alpha_l}}(M)\frac{\partial\lambda^e_M(\boldsymbol{x})}{\partial x_{\alpha_{l+1}}} \tag{32}$$

where $S^h(e)$ is the set of the nodes located on element e, and $\lambda^e_M(\boldsymbol{x})$ is the shape function corresponding to node M on element e. If $\boldsymbol{x}$ coincides with node M, let

$$\delta^{l+1}_{x_{\alpha_1}\cdots x_{\alpha_{l+1}}}u^{h_0}(M)=\frac{1}{\tau(M)}\sum_{e\in S^h(M)}\delta^{l+1}_{x_{\alpha_1}\cdots x_{\alpha_{l+1}}}u^{h_0}(e) \tag{33}$$

and if $\boldsymbol{x}\in e_1\cap e_2$, let

$$\delta^l_{x_{\alpha_1}\cdots x_{\alpha_l}}u^{h_0}(\boldsymbol{x})=\frac{1}{2}\left(\delta^l_{x_{\alpha_1}\cdots x_{\alpha_l}}u^{h_0}(e_1)+\delta^l_{x_{\alpha_1}\cdots x_{\alpha_l}}u^{h_0}(e_2)\right) \tag{34}$$

In the approximate computation of $\boldsymbol{u}^{Mh}(\boldsymbol{x})$, let

$$\frac{\partial^l u^{h_0}(\boldsymbol{x})}{\partial x_{\alpha_1}\cdots\partial x_{\alpha_l}}\approx\delta^l_{x_{\alpha_2}\cdots x_{\alpha_l}}u^{h_0}(\boldsymbol{x}) \tag{35}$$

From $\boldsymbol{u}^{Mh}(\boldsymbol{x})$ the approximate strains can be evaluated in the following formulation

$$\varepsilon^M_{hk}(\boldsymbol{x})=\varepsilon_{hk}\left(\boldsymbol{u}_0^{h_0}(\boldsymbol{x})\right)+\sum_{l=1}^{M}\varepsilon^{l-1}\sum_{\alpha_l=1,2}\varepsilon_{hk}\left(N^h_{\alpha_1\cdots\alpha_l m}\left(\frac{\boldsymbol{x}}{\varepsilon}\right)\right)\frac{\partial^l u^{h_0}_{0m}}{\partial x_{\alpha_1}\cdots\partial x_{\alpha_l}}$$

$$+\sum_{l=1}^{M}\varepsilon^{l}\sum_{\alpha_l=1,2}\left[N^{h}_{\alpha_1\cdots\alpha_l hm}\left(\frac{\boldsymbol{x}}{\varepsilon}\right)\frac{\partial^{l+1}u^{h_0}_{0m}}{\partial x_{\alpha_1}\cdots\partial x_{\alpha_l}\partial x_k}+N^{h}_{\alpha_1\cdots\alpha_l km}\left(\frac{\boldsymbol{x}}{\varepsilon}\right)\frac{\partial^{l+1}u^{h_0}_{0m}}{\partial x_{\alpha_1}\cdots\partial x_{\alpha_l}\partial x_h}\right] \quad (36)$$

and then the approximate stresses

$$\sigma^{M}_{ij}(\boldsymbol{x})=a_{ijhk}\left(\frac{\boldsymbol{x}}{\varepsilon}\right)\varepsilon^{M}_{hk}(\boldsymbol{x}) \quad (37)$$

NUMERICAL EXPERIMENTS

Procedure of FE Algorithms

Summing up the procedure of FE algorithms:

1. Set up the mechanical model :

* Form and verify the geometry of the structure, the loading conditions and constraints.

* Form and verify the composition of the basic configurations for every component with periodicity, the matrix, reinforcement and their interfaces.

2. Partition Q into set S^h of triangular or/and quadrangular elements in mesh length h according to the distribution of $a_{ijhk}(\xi)$, and Ω into S^{h_0} in h_0.

3. Solve FE Eqn.13 to obtain $N^{h}_{\alpha_1 m}(\xi)$ (α_1 , m = 1, 2) .

4. Evaluate $\hat{a}^{h}_{ijhk}$ in Eqns.14 and 15 from $N^{h}_{\alpha_1 m}(\xi)$ (α_1 , m = 1, 2).

5. Solve FE Eqn.17 to obtain $N^{h}_{\alpha_1\alpha_2 m}(\xi)$ $(\alpha_1,\alpha_2,m=1,2)$, and solve Eqn. 18 to obtain $N^{h}_{\alpha_1\cdots\alpha_l m}(\xi)$ $(\alpha_i,m=1,2)$ for $3\le l\le M$.

6. Solve FE Eqn. 20 to obtain $\boldsymbol{u}^{h_0}_0(\boldsymbol{x})$.

7. Evaluate $\dfrac{\partial^{l}\boldsymbol{u}^{h_0}_0(\boldsymbol{x})}{\partial x_{\alpha_1}\cdots\partial x_{\alpha_l}}$ in the formulations (31)—(35).

8. Evaluate the approximate displacements $\boldsymbol{u}^{Mh}(\boldsymbol{x})$ in formulation (12) , the strains $\varepsilon^{M}_{hk}(\boldsymbol{x})$ in formulation (36) , and the stresses $\sigma^{M}_{ij}(\boldsymbol{x})$ in formulation (37).

Numerical Results

We have coded the computing program of the FE method based on TSA for 2-dimension case , and made some numerical experiments to verify its effectiveness. Here are some numerical results.

The structure is a cantilever investigated by us; the macroscopic model is shown in Fig. 4 and three types of basic configurations are shown in Fig. 3. The basic configuration is partitioned into 40×40 meshes, and the structure into 38×94 meshes. The stress states for three typical cells are shown in Fig.5. By using the classical FE method to obtain such detailed results, 190×470 rectangle meshes might be needed.

The FE method based on TSA is thus very effective for solving problems raised by woven

composite materials and structures with small periodicity.

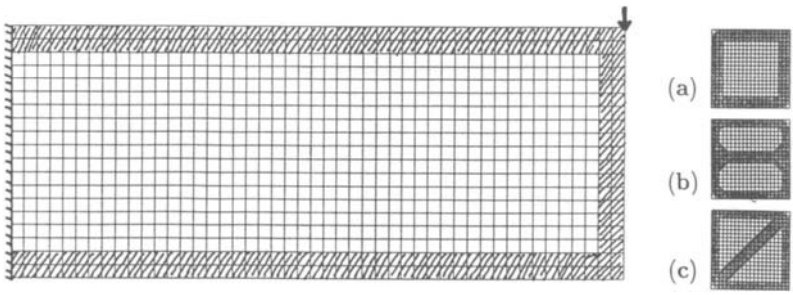

Fig. 4 Cantilever with periodic configurations

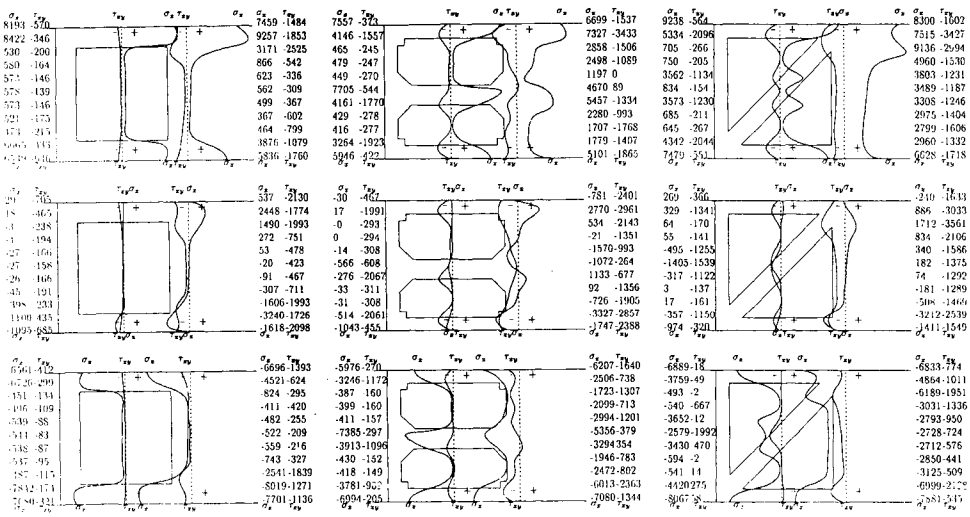

Fig.5 The stress distribution for 3-typical basic configurations

REFERENCES

1. Cui J.Z., Shih T.M. and Wang Y.L.(1997), Two-Scale Analysis Method for Bodies with Small Periodic Configuration. Invited Paper in CASCM-97, Sydney, Australia, *Proc. of CASCM-97.*

2. Cui J.Z. and Yang H.Y.(1996), A Dual Coupled Method of Boundary Value Problems of PDE with Coefficients of Small Period. *Intern. J. Comp. Math.*, 14: 159-174.

3. Cao L.Q. and Cui J.Z.(1998), Finite Element Computation For Elastic Structures of

Composite Materials Formed by Entirely Basic Configurations, to be published on *Math. Numer. Sinica*, Vol. 20, No. 3.

4. Bensoussan A., Lions J. L. and Papanicolaou G.(1978), *Asymptotic Analysis for Periodic Structures,* Amsterdam; North-Holland.

5. Aboudi J.(1991), *Mechanics of Composite Materials - A Unified Micromechanical Approach*, Elsevier, Amsterdam - Oxford- New York -Tokyo.

6. Oleinik O.A., Shamaev A.S. and Yosifian G.A.(1992), *Mathematical Problems in Elasticity and Homogenization,* Amsterdam, North-Holland.

7. Cui J.Z., Shih T.M., Shin F.G. and Wang Y.L.(1997), Finite Element Methods Based on Two-Scale Analysis. presented in WSC97-HK, *Proc. of WSC97-HK.*

8. Cui J.Z.(1996), The Two-Scale Analysis Methods for Woven Composite Materials and The Structure With Small Period, in *The Advances in Computational Mechanics,* edited by Zhong W.X. et al, International Academic Publishers.

9. Cui J.Z., Shih T.M., Shin F.G. and Wang Y.L.(1997), The Two-Scale Analysis Method for Composite Materials and Structures with Period Configurations, *ICM-97 Report.*

This Page Intentionally Left Blank

Control of Lateral-Torsional Motion of Nanjing TV Transmission Tower

J. C. Wu [1] and J. N. Yang [2]

[1] Department of Civil Engineering, Tamkang University, Taipei, Taiwan, R.O.C.
[2] Dept. of Civil and Environ. Engrg., University of California, Irvine, CA 92697, U. S. A.

ABSTRACT

The 310 m Nanjing TV transmission tower in China will be installed with an active mass driver on the upper observation deck in order to reduce the acceleration responses under strong winds. This paper presents the Linear Quadratic Gaussian (*LQG*) control strategy using acceleration feedback to reduce the tower response. Emphasis is placed on the practical applications, such as the limitations on actuator peak force and stroke, limited number of sensors, etc. The along-wind and across-wind components of the wind velocity are defined by the Davenport cross-power spectra. The power spectral density and *rms* of acceleration responses of the TV transmission tower equipped with an active mass driver have been computed. Simulation results demonstrate that the performance of the *LQG* control strategy is remarkable in reducing the coupled lateral-torsional motions of the tower and it is suitable for the full-scale implementation of active mass driver on Nanjing Tower.

Keywords: structural control, active mass driver, Linear Quadratic Gaussian (*LQG*) control, dynamic output feedback, coupled lateral-torsional motion, wind response.

INTRODUCTION

The newly constructed 310-meter Nanjing Tower in China consists of three prestressed concrete legs with hollow rectangular sections, as shown in Fig. 1(a) and (b). It has two observation decks at the heights of 180-meter and 240-meter, respectively. Preliminary investigations indicate that the acceleration response of the upper observation deck is too high and that a passive mass damper is not capable of reducing the acceleration response to an acceptable level for human comfort [Cao et al (1998)]. Consequently, an active mass driver system, in the form of a ring mass driven by three actuators as shown in Fig. 2, was designed [Cao et al (1998)] to

be installed on the upper observation deck to reduce the acceleration response. Active control of wind-excited tall buildings has been investigated in the literature [e. g., Samali et al (1985), Ankireddi et al (1996), etc.], including the applications of advanced control theories, such as H_2 control [Suhardjo et al (1992)], *LQR* and $H\infty$ static output feedback control [Wu et al (1998)], sliding mode control [Yang et al (1997)], etc. Today, full-scale active tuned mass dampers have been installed on many high-rise buildings in Japan [e. g., Spencer & Sain (1997)].

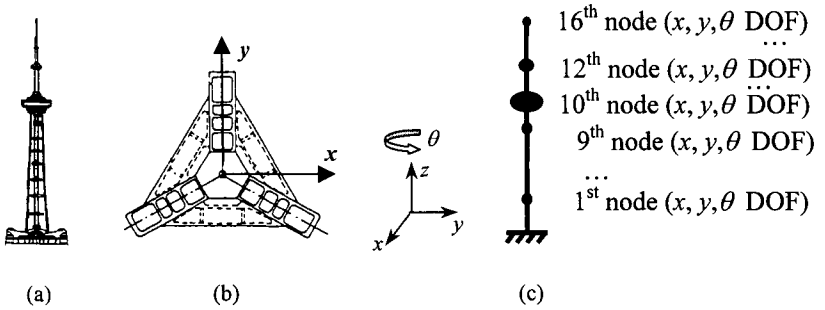

Fig. 1: (a) Configuration of Nanjing Tower; (b) cross-section of concrete leg; (c) Discrete Structural Model

The structural properties of the Nanjing Tower in the along-wind direction, as modeled by a discrete 16-degree-of-freedom system shown in Fig. 1(c), have been described in Cao et al (1998). Previous investigations [Wu et al (1997a,b), Cao et al (1998)] assumed that the tower is completely symmetric and the axes of mass centers, elastic centers, and aerodynamic centers coincide with each other. Based on this premise, the along-wind motion and the across-wind motion of the tower can be analyzed and computed independently. In reality, the elastic center and mass center may not coincide, for instance, the mass centers of the observation decks may not locate at the elastic center of the cross-section due to the arrangement of indoor furnitures and equipments. As such, coupled lateral-torsional motion is introduced when the tower is subjected to wind gusts. Since the tower is not symmetric in one of the principal axes, the aerodynamic center may be different from the elastic center and mass center. Hence, the wind forces acting on the aerodynamic center will introduce an eccentricity, resulting in an external torque to the tower.

In this paper, we present the Linear Quadratic Gaussian (*LQG*) control strategy for the acceleration reduction of the tower equipped with an active mass driver, taking into account the coupled lateral-torsional motion. Emphasis is placed on practical considerations of full-scale implementations, including limited number of sensors, limitations on actuator peak force and stroke, noise pollution, acceleration feedback, etc. Since civil engineering structures involve too many degrees of freedom, a state reduced-order system [Wu et al (1998)], that can capture the significant modes of acceleration response, is established for the controller design. The size of the reduced-order system is reasonable for the on-line computation of the dynamic output controller.

The performance of LQG controller is measured by the acceleration reduction criterion. The spatial correlation of wind loads is accounted for in the LQG observer designs. The Davenport spectrum is used for the fluctuating wind velocity in the along-wind (x) direction and across-

wind (y) direction. Both deterministic and stochastic analyses have been used to demonstrate the performance of the controller. For the deterministic approach, a set of sample functions of wind loads on every degree-of-freedom is simulated from the wind velocity spectrum and the peak responses are computed. For the stochastic approach, the root-mean-square and the power spectral densities of the response quantities are obtained using random vibration analyses. It is demonstrated that the LQG controller is quite suitable for practical implementations and its performance is remarkable.

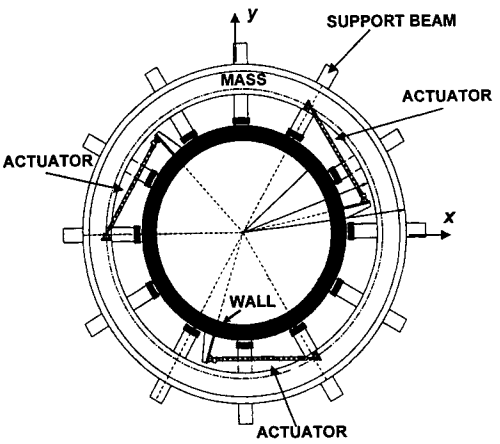

Fig. 2 : Configuration of Active Mass Driver System with Three Actuators on the Upper Observation Deck [from Cao et al (1998)].

FORMULATION

Equations of Motion of Tower Structure with Lateral-Torsional Motion

To compute the stroke of the actuator, the active mass driver is modeled as an active tuned mass damper in the following formulation and numerical simulation. Then, the forces in the springs and dashpots of the active tuned mass damper are added to the control forces for the active mass driver system. Finally, the required actuator forces and strokes will be determined through the transformation later.

Full-Order System (FOS) : The Nanjing TV transmission tower has been modeled by a 16-node linear system, as shown in Fig. 1(c). With an active mass damper to be installed on the upper observation deck (12^{th} node), the total number of nodes is 17. We consider the elastic center of the cross-section of the tower as the geometric center while the mass center of the designated *i*-th node is shifted by a distance (x_{ci}, y_{ci}) from the elastic center. The vector equation of motion is expressed as

$$M_s\ddot{X}(t) + C_s\dot{X}(t) + K_s X(t) = H_1\, U(t) + W(t) \qquad (1)$$

in which $X(t) = [x_1, x_2, ..., x_n, y_1, y_2, ..., y_n, \theta_1, \theta_2, ..., \theta_n]'$ is a $3n$ vector (n = 17) with $x_i(t)$, $y_i(t)$, $\theta_i(t)$, i = 1, 2,..., 16, being the displacement of the elastic center of the designated *i*-th node in x (along-wind), y (across-wind) and θ directions w.r.t. the ground, as shown in Fig. 1(c); x_{17}, y_{17} and θ_{17} are the relative displacements of the center of the mass damper with respect to the upper observation deck; $U(t) = [u_1(t), u_2(t), ..., u_r(t)]'$ is a *r* control force vector (*r* = 3) in x, y and θ directions generated by three actuators; $W(t) = [w_{1x}(t), w_{2x}(t), ..., w_{16x}(t), 0, w_{1y}(t), w_{2y}(t), ..., w_{16y}(t), 0, w_{1\theta}(t), w_{2\theta}(t), ..., w_{16\theta}(t), 0]'$ is a $3p$ vector (p = 17) denoting the wind loads on the tower in x, y and θ directions, respectively; and a prime denotes the transpose of a vector or a matrix. In Eqn.1 M_s, C_s and K_s are ($3n$x$3n$) mass, damping and

stiffness matrices, respectively, in which the mass in the equations of torsion is the mass moment of inertia and the stiffness is the torsional stiffness. H_1 is a ($3nxr$) matrix denoting the location of controllers. The inertial force term for the equation of motion of the i-th node in x, y and θ directions are expressed as $m_i\ddot{x}_i - m_i y_{ci}\ddot{\theta}_i$, $m_i\ddot{y}_i + m_i x_{ci}\ddot{\theta}_i$, and $-m_i y_{ci}\ddot{x}_i + m_i x_{ci}\ddot{y}_i + [J_i + m_i (x_{ci}^2 + y_{ci}^2)]\ddot{\theta}_i$, respectively, where J_i is the mass moment of inertia of the i-th node w.r.t. the mass center.

In the state space, Eqn. 1 becomes

$$\dot{Z} = A\,Z + B\,U + E\,W \tag{2}$$

where $Z(t)$ is a $6n$ state vector; A is a ($6n \times 6n$) system matrix; B is a ($6n \times r$) control location matrix; and E is a ($6n \times 3p$) excitation influence matrix given, respectively, by

$$Z = \begin{bmatrix} X(t) \\ \dot{X}(t) \end{bmatrix}; A = \begin{bmatrix} 0 & I \\ -M_s^{-1}K_s & -M_s^{-1}C_s \end{bmatrix}; B = \begin{bmatrix} 0 \\ M_s^{-1}H_1 \end{bmatrix}; E = \begin{bmatrix} 0 \\ M_s^{-1} \end{bmatrix} \tag{3}$$

Since Eqn. 2 represents the dynamics of the entire structure, it is referred to as the full-order system (FOS). In general, a l-dimensional controlled output vector z and a m-dimensional measured output vector y can be expressed, respectively, by

$$z = C_z Z + D_z U + F_z W \tag{4}$$

$$y = C_y Z + D_y U + F_y W + v \tag{5}$$

in which C_z , D_z , F_z , C_y , D_y and F_y are matrices with appropriate dimensions, v is a m-dimensional measurement noise vector. If only the state variables (displacement and velocity) are measured, then $D_y = F_y = 0$. In civil engineering applications, since acceleration measurements are easier to obtain, Eqn. 5 is the general expression including acceleration measurements. The same remark applies to the controlled output in Eqn. 4.

Reduced-Order System (ROS): Under wind excitations, the acceleration response of civil engineering structures is dominated by the first few modes. Hence, the controller can be designed based on the reduced-order system (ROS), referred to as reduced-order control (ROC). There are many system reduction methods available in the literature, which can be used to obtain the reduced-order system. The method of state reduced-order system [Davison (1966)] that retains the same eigen properties of selected modes has been demonstrated to be very useful for civil engineering applications [Wu et al (1998)]. Such a method will be used in this paper. Then, a k-dimensional state equation of the state reduced-order system (SROS) can be derived as

$$\dot{Z}_r = A_r Z_r + B_r U + E_r W \tag{6}$$

in which the eigenvalues and the eigenvector matrix of A_r are equal to the first k eigenvalues and eigenvectors of A. Since the eigenvalues of A are complex conjugates in pairs, it is necessary to choose even number for k so that A_r, B_r and E_r are real. The controlled output vector and the measured output vector of the SROS, z_r and y_r, can be obtained accordingly

[Wu et al (1998)],

$$z_r = C_{zr} Z_r + D_{zr} U + F_{zr} W \tag{7}$$

$$y_r = C_{yr} Z_r + D_{yr} U + F_{yr} W \tag{8}$$

in which C_{zr} , D_{zr} , F_{zr} , C_{yr} , D_{yr} and F_{yr} are matrices with appropriate dimensions.

Wind Model

The along-wind velocity is usually decomposed into an average wind velocity and a wind fluctuation, that is a stationary random process in time. The average wind velocity varies along the structure, and hence the wind load is nonhomogeneous in space. In the across-wind direction, the wind velocity is also modeled by a set of fluctuation random processes, which could be different from the along-wind fluctuation. The wind-structure interaction effect is neglected herein, and therefore the wind load can be computed from the wind velocity. Consequently, the wind load consists of a set of static loads due to the average wind velocity and a set of dynamic loads due to wind fluctuations in both along-wind and across-wind directions. For the reduction of acceleration responses in structural control, only the fluctuating wind loads should be considered. It has been assumed in the literature that the along-wind and across-wind velocity fluctuations are mutually uncorrelated random processes with zero mean. The well-known Davenport wind velocity spectrum will be used to simulate the along-wind and across-wind velocities. The (*i*, *j*) element of the two-sided Davenport cross-power spectral density matrix S_{VV} of fluctuating wind velocity can be expressed as

$$S_{v_i v_j}(\omega) = \frac{2 K_0 V_r^2}{|\omega|} \left(\frac{600\omega}{\pi V_r} \right)^2 \left[1 + \left(\frac{600\omega}{\pi V_r} \right)^2 \right]^{-4/3} \exp\left(-\frac{c_1 |\omega| |h_i - h_j|}{2\pi} \frac{}{V_r} \right) \tag{9}$$

where ω is in radian per second; V_r is the reference mean wind velocity in meters per second at 10 m above the ground; c_1 is a constant; h_i is the height of the *i*-th node; and K_0 is a constant depending on the surface roughness of the ground [Simiu et al (1986)].

The location that wind forces apply, i. e. aerodynamic center, is determined by the geometry of the cross section of the structure. Due to the eccentricity between the elastic center and the aerodynamic center, an external torsional moment will be generated to the structure. Yang et al (1981) has derived a set of wind loads in the along-wind, across-wind and torsional directions in which the aerodynamic damping effect is neglected and small deformation is assumed. The static wind loads $\overline{w}_{ix}$, $\overline{w}_{iy}$ and $\overline{w}_{i\theta}$ on the *i*-th node in x, y and θ directions are given by $\overline{w}_{ix} = 0.5 \rho A_i \overline{V}_i^2 C_{xi}$; $C_{xi} = C_{Di} \cos\beta - C_{Li} \sin\beta$; $\overline{w}_{iy} = 0.5 \rho A_i \overline{V}_i^2 C_{yi}$; $C_{yi} = C_{Di} \sin\beta + C_{Li} \cos\beta$; $\overline{w}_{i\theta} = 0.5 \rho A_i \overline{V}_i^2 g_{li}$; $g_{li} = x_{Ai} C_{yi} - y_{Ai} C_{xi}$, respectively, where $\overline{V}_i$ is the mean wind velocity, ρ is the air density, C_{Di} and C_{Li} are the drag and lift coefficients for the *i*-th node, A_i is the tributary area for the *i*-th node, β is the angle of attack, x_{Ai} and y_{Ai} are the coordinates of aerodynamic center w.r.t. the elastic center at the *i*-th node. The dynamic loads due to fluctuating part on the *i*-th node in x, y and θ directions are [Yang et al (1981)]

$$w_{ix} = 0.5\rho A_i \overline{V}_i \ (2C_{xi} v_{ix} - C_{yi} v_{iy}) \tag{10}$$

$$w_{iy} = 0.5\rho A_i \overline{V}_i \ (2C_{yi} v_{ix} + C_{yi} v_{iy}) \tag{11}$$

$$w_{i\theta} = 0.5\rho A_i \overline{V}_i \ (2g_{1i} v_{ix} + g_{2i} v_{iy}) \ ; \quad g_{2i} = x_{Ai} C_{xi} + y_{Ai} C_{yi} \tag{12}$$

, respectively. In Eqns. 10-12, v_{ix} and v_{iy} are the fluctuating wind velocities in x and y directions, respectively, and both of them follow the spectrum in Eqn. 9. The mean wind velocity $\overline{V}_i$ is assumed to follow a power law

$$\overline{V}_i = V_g (h_i / h_g)^{\alpha} \tag{13}$$

in which h_g is the gradient height; V_g is the average wind velocity at the gradient height; and α is a constant between 0.15 and 0.5. The values for the parameters h_g and α can be found in [Simiu et al (1986)], which are characterized by the ground condition, such as the roughness. Note that, in Eqns. 10-12, C_{xi}, C_{yi}, g_{1i}, g_{2i} are functions of the angle of attack β. Consequently, the power spectral density matrix of the wind loads on the structure can be written as

$$S_{WW} = \begin{bmatrix} S_{w_x w_x} & S_{w_x w_y} & S_{w_x w_\theta} \\ S_{w_y w_x} & S_{w_y w_y} & S_{w_y w_\theta} \\ S_{w_\theta w_x} & S_{w_\theta w_y} & S_{w_\theta w_\theta} \end{bmatrix} \tag{14}$$

where $S_{w_y w_x}(i,j) = \overline{S}_{w_x w_y}(j,i)$; $S_{w_\theta w_x}(i,j) = \overline{S}_{w_x w_\theta}(j,i)$; $S_{w_\theta w_y}(i,j) = \overline{S}_{w_y w_\theta}(j,i)$ and $\overline{S}$ indicates the complex conjugate of S. The (i, j) element in each block matrix can easily be obtained from Eqns. 10-13 knowing that V_{ix} and V_{iy} are uncorrelated, for instance

$$\begin{aligned} S_{w_x w_x}(i,j) &= 0.25\rho^2 A_i A_j \overline{V}_i \overline{V}_j (4C_{xi} C_{xj} S_{v_{ix} v_{jx}} + C_{yi} C_{yj} S_{v_{iy} v_{jy}}) \\ S_{w_x w_y}(i,j) &= 0.25\rho^2 A_i A_j \overline{V}_i \overline{V}_j (4C_{xi} C_{yj} S_{v_{ix} v_{jx}} - C_{yi} C_{xj} S_{v_{iy} v_{jy}}) \\ S_{w_\theta w_\theta}(i,j) &= 0.25\rho^2 A_i A_j \overline{V}_i \overline{V}_j (4g_{1i} g_{1j} S_{v_{ix} v_{jx}} + g_{2i} g_{2j} S_{v_{iy} v_{jy}}) \end{aligned} \tag{15}$$

Linear Quadratic Gaussian (LQG) Control Method

The Linear Quadratic Gaussian (*LQG*) control method is presented to demonstrate the control effectiveness for the Nanjing tower equipped with an active mass driver. The *LQG* theory is derived based on the assumption that the excitation W and the measurement noise v are uncorrelated Gaussian white noise processes. However, different components within W or v can be correlated as indicated by the wind load spectrum in Eqns. 9 and 14. Based on the separation theorem [Skelton (1988)], the design procedures for the *LQG* method are divided into two parts; namely, the design of controller and the design of observer.

Design of Controller : The state feedback control gain is obtained by minimizing the quadratic objective function

$$J = \lim_{\tau \to \infty} (1/\tau) E \{ \int_0^\tau (\bar{z}' Q \bar{z} + U' R U) \, dt \} \tag{16}$$

in which $\bar{z} = z_r - F_{zr} W = C_{zr} Z_r + D_{zr} U$ (see Eqn. 7), and Q and R are weighting matrices. The optimal controller is obtained as [Skelton (1988)]

$$U = K_b Z_r \; ; \; K_b = -\bar{R}^{-1} (B_r' P_c + \bar{S}') \tag{17}$$

where P_c is the solution of the Riccati matrix equation

$$P_c \bar{A} + \bar{A}' P_c - P_c B_r \bar{R}^{-1} B_r' P_c + \bar{Q} - \bar{S} \bar{R}^{-1} \bar{S}' = 0 \tag{18}$$

$$\bar{Q} = C_{zr}' Q C_{zr} \; ; \; \bar{R} = D_{zr}' Q D_{zr} + R \; ; \; \bar{S} = C_{zr}' Q D_{zr} \; ; \; \bar{A} = A_r - B_r \bar{R}^{-1} \bar{S}' \tag{19}$$

Design of Observer : The optimal controller obtained in Eqn. 17 requires the state feedback Z_r, which will be estimated from an observer based on the measurements from a limited number of acceleration sensors installed at strategic locations. Such an observer should be designed appropriately. With the assumption that the wind gust W and the measurement noise v are uncorrelated Gaussian white noise processes, the Kalman-Bucy filter can be used to estimate the state Z_r ;

$$\dot{\hat{Z}}_r = A_r \hat{Z}_r + B_r U + L_o (y_r - C_{yr} \hat{Z}_r - D_{yr} U) \tag{20}$$

in which $\hat{Z}_r$ is the estimate of the state Z_r, and y_r is the measured output. The procedures for determining appropriate observer gain matrix L_o in Eqn. 20 are well-known [e.g., Skelton (1988), Wu & Yang (1997b)]. It is mentioned that the observer gain matrix L_o is a function of $\bar{S}_{WW}$ and $\bar{S}_{vv}$ which are the power spectral density matrices of the white noises W and v, respectively, for the design purpose. For the observer design, $\bar{S}_{WW}$ and $\bar{S}_{vv}$ can be scaled appropriately for convenience of numerical computations.

Thus, the control vector U follows from Eqns. 17 and 20 as

$$U = K_b \hat{Z}_r \tag{21}$$

Substituting Eqn. 21 into Eqn. 20, the estimate $\hat{Z}_r$ is computed on-line from the following dynamic output feedback equation

$$\dot{\hat{Z}}_r = [A_r + B_r K_b - L_o C_{yr} - L_o D_{yr} K_b] \hat{Z}_r + L_0 y_r \tag{22}$$

In practical implementation, y_r in Eqn. 22 should be replaced by the real measured output y.

Actuator Forces and Strokes

The required control forces $U = [u_1, u_2, u_3]$ computed above represent the control forces

in x-direction, y-direction and torsional moment in θ direction. u1, u2 and u3 should be modified for the active mass driver system by adding the corresponding forces in springs and dashpots in x, y and θ directions of the active tuned mass damper. These modified control forces are denoted by $\bar{u}_1, \bar{u}_2$ and $\bar{u}_3$, for instance $\bar{u}_1 = u_1 - k_{dx}x_{17} - c_{dx}\dot{x}_{17}$ where k_{dx} and c_{dx} are the spring constant and damping coefficient of the tuned mass damper in x-direction. Based on the actuator configuration shown in Fig. 2, the control forces from three actuators are denoted by F_1, F_2 and F_3 as shown in Fig. 3. The required actuator forces F_1, F_2 and F_3 as well as the strokes can be obtained through the transformation of $\bar{u}_1, \bar{u}_2$ and $\bar{u}_3$ as well as the geometric configuration in the following. The actuators are connected between the 12-th node and the mass damper (17-th node). The points of attachment on the 12-th node are denoted by $A_i (i = 1, 2, 3)$ and that on the mass damper are denoted by $B_i (i = 1, 2, 3)$ in Fig. 3. In motion, the coordinates (positions) of A_i and B_i (e. g., A_{1x} is the x coordinate and A_{1y} is the y coordinate of A_1) are tabulated in Table 1, in which $l = 368$ cm, $r = 405$ cm.

The directions of F_1, F_2 and F_3 are defined by the angles α_1, α_2 and α_3, respectively, which are measured counterclockwising from the x-axis as follows

$$\alpha_1 = \tan^{-1}\left(\frac{B_{1y} - A_{1y}}{B_{1x} - A_{1x}}\right),\ \alpha_2 = \tan^{-1}\left(\frac{B_{2y} - A_{2y}}{B_{2x} - A_{2x}}\right),\ \alpha_3 = \tan^{-1}\left(\frac{B_{3y} - A_{3y}}{B_{3x} - A_{3x}}\right) \tag{23}$$

, in which the quadrant should be considered in computing angles α_i, $i = 1, 2, 3$. Hence, the actuator forces F_1, F_2 and F_3 are related to the computed control forces $\bar{u}_1$, $\bar{u}_2$ and $\bar{u}_3$ as follows

$$\begin{aligned} &F_1\cos\alpha_1 + F_2\cos\alpha_2 + F_3\cos\alpha_3 = \bar{u}_1 \\ &F_1\sin\alpha_1 + F_2\sin\alpha_2 + F_3\sin\alpha_3 = \bar{u}_2 \\ &F_1\left[(B_{1x} - x_{12} - x_{17})\sin\alpha_1 - (B_{1y} - y_{12} - y_{17})\cos\alpha_1\right] \\ &+ F_2\left[(B_{2x} - x_{12} - x_{17})\sin\alpha_2 - (B_{2y} - y_{12} - y_{17})\cos\alpha_2\right] \\ &+ F_3\left[(B_{3x} - x_{12} - x_{17})\sin\alpha_3 - (B_{3y} - y_{12} - y_{17})\cos\alpha_3\right] = \bar{u}_3 \end{aligned} \tag{24}$$

TABLE 1
COORDINATES OF A_i AND B_i IN MOTION

A_1	$A_{1x} = x_{12} + l\cos(-107.6° + \theta_{12})$ $A_{1y} = y_{12} + l\sin(-107.6° + \theta_{12})$	B_1	$B_{1x} = x_{12} + x_{17} + r\cos(-60° + \theta_{12} + \theta_{17})$ $B_{1y} = y_{12} + y_{17} + r\sin(-60° + \theta_{12} + \theta_{17})$
A_2	$A_{2x} = x_{12} + l\cos(12.4° + \theta_{12})$ $A_{2y} = y_{12} + l\sin(12.4° + \theta_{12})$	B_2	$B_{2x} = x_{12} + x_{17} + r\cos(60° + \theta_{12} + \theta_{17})$ $B_{2y} = y_{12} + y_{17} + r\sin(60° + \theta_{12} + \theta_{17})$
A_3	$A_{3x} = x_{12} + l\cos(132.4° + \theta_{12})$ $A_{3y} = y_{12} + l\sin(132.4° + \theta_{12})$	B_3	$B_{3x} = x_{12} + x_{17} + r\cos(180° + \theta_{12} + \theta_{17})$ $B_{3y} = y_{12} + y_{17} + r\sin(180° + \theta_{12} + \theta_{17})$

The length of the actuators without motion as arranged in Fig. 2 is 313.8 cm. The actuator strokes can be determined by computing the difference in the length between A_iB_i (i = 1, 2, 3) and 313.8 cm for each actuator, see Fig. 3, i.e.,

$$\text{Stroke of the ith Actuator} = |A_iB_i| - 313.8 \text{ cm for } i = 1, 2, 3 \tag{25}$$

in which $|A_iB_i|$ can be computed using Table 1.

SIMULATION RESULTS

The control performance of the *LQG* controller in reducing the coupled lateral-torsional response of the Nanjing tower will be demonstrated through numerical simulations. The mass and stiffness matrices modeled by a 16-node system (Fig. 1 (c)) in x direction are given in Cao et al (1998). The stiffness in the y direction is assumed to be 20% higher than that in the x direction. In this preliminary study, the structural parameters for the torsional motion are obtained by estimation, whereas the actual data will be available in the future. The mass moment of inertia J_i (i = 1, 2, ..., 16) w.r.t. the mass centers are 2.5e5, 1.8e5, 8.4e4, 5.5e4, 3.6e4, 2.1e4, 1.5e4, 1.2e4, 8.4e4, 1.6e5, 6e4, 4e4, 3e3, 2e2, 1.5e2, 50 Ton-m^2, respectively. The torsional stiffness vector (between adjacent nodes) is 1/5 x [6.0e9, 3.5e9, 2.1e9, 1.5e9, 1.0e9, 6.7e8, 3.3e8, 4.3e8, 6.4e8, 4.0e8, 5.7e7, 5.3e7, 2.5e7, 1.2e7, 8e6, 5e5] KN-m/rad. The natural frequencies of the first five modes in x, y and θ directions are 1.529, 3.980, 7.926, 11.749, 15.768 rad/sec, 1.675, 4.360, 8.682, 12.870, 17.273 rad/sec, and 6.038, 12.079, 22.836, 28.180, 37.459 rad/sec, respectively. The dampings in each direction are assumed to be a combination of the mass and stiffness matrices in each direction such that the resultant damping ratios for each mode are 2%, 3%, 5.4%, 8%, 10%, 19%, 21%, 37%, 39%, 40%, 40%, 40%, 40%, 40%, 40%, 40%. The mass centers are different from the elastic centers only for both observation decks, i.e., x_{c10} = 2 m, y_{c10} = 2 m, x_{c12} = 1 m, y_{c12} = 1 m. A 60 metric tons active mass driver (mass ratio of 0.194%) shown in Fig. 2 will be installed on the upper deck (12-th node). We modify the active mass driver system into an active tuned mass damper in the numerical simulation for computing the relative displacements of the damper and required control forces u_1, u_2 and u_3 in x, y and θ directions. A tuned mass damper with a damping ratio of 7% in each direction and the frequency tuned to the first mode in each direction will be used in the simulation. For the actuator capacity, the peak force is 150 kN and the peak stroke is 75 cm.

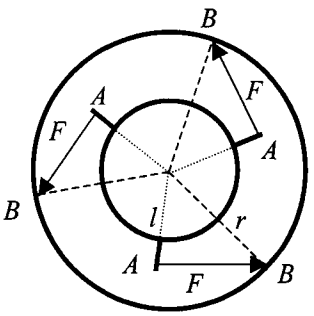

Fig. 3 : Actuator forces applied to the mass driver

The fluctuating wind velocities in the along-wind and across-wind directions are uncorrelated random processes with zero mean, and their cross-power spectra are considered identical in the simulation for simplicity. The parameters used in the Davenport wind velocity spectrum, Eqn. 9, have been adjusted to match the Chinese design specifications for wind velocity in the Nanjing area. The resulting parameters are as follows: K_0 = 0.008, c_1 = 7.7, α = 0.16, air density ρ = 1.25 kg/m^3, gradient height h_g = 300 m, and V_r = 20.7 m/sec. The angle of attack of wind velocity is assumed to be zero, and consequently, the drag coefficient C_D is 1.39 for 1st-8th node;

1.2 for 9^{th}-12^{th} node; 1.3 for 13^{th}-16^{th}, the lift coefficient C_L is 0.3 for each node. The tributary areas for each node are 413.24, 536.02, 469.5, 387.18, 323.73, 271.35, 277.38, 233.65, 182.51, 183.85, 213.51, 175.58, 66.38, 21.55, 11.28, and 4.13 m^2. The heights of each node are 10.1, 32.2, 58.6, 80.2, 101.8, 119.8, 137.8, 158.6, 171.8, 185.8, 199.2, 240.4, 270.1, 286.1, 299.1, and 310.1 m. Since the external torsional moment is also induced by the off-set between elastic centers and aerodynamic centers, a set of aerodynamic centers is assumed in the simulation to investigate the structural response and the performance of active control as follows: x_{Ai} (i = 1, 2, ..., 16) are all zero and y_{Ai} (i = 1, 2, ..., 16) are 15/4, 12/4, 10/4, 9/4, 8/4, 7/4, 6/4, 5/4, 4/4, 0, 0, 0, 0, 0, 0 and 0 m, respectively.

Both the stochastic and deterministic analyses were used to compute the response quantities of the tower. For the deterministic analysis, one set of sample functions of wind velocities in along-wind and across-wind directions, v_{ix} and v_{iy}, on every node is simulated using the cross-power spectral density matrix in Eqn. 9 for a duration of 300 seconds. The method of simulation is described in Wu & Yang (1997a,b) and Wu et al (1998). Then, the sample functions of wind loads on every node, w_{ix}, w_{iy} and $w_{i\theta}$ are computed from Eqn.10-12, and these sample excitations are used to compute the response quantities. For the stochastic approach, the random vibration analysis in the frequency domain, based on the transfer function of the closed-loop system, has been conducted to compute response power spectral densities and the rms values. Such an approach is described in Wu & Yang (1997a,b) and Wu et al (1998).

Without the mass damper, the response quantities of both observation decks (10-th and 12-th nodes) are shown in columns (2)-(13) of Table 2, denoted by "No Control". The results for the tower equipped with the passive tuned mass damper (without actuators) are presented in columns (15)-(26) of Table 2, denoted by "Passive Control". In Table 2, $x_i, \ddot{x}_{ai}, y_i, \ddot{y}_{ai}, \theta_i$ and $\ddot{\theta}_{ai}$ represent the peak displacements and peak absolute accelerations of each node in x, y and θ directions, respectively, based on the deterministic analysis. Likewise, $\sigma_{x_i}, \sigma_{\ddot{x}_{ai}}, \sigma_{y_i}, \sigma_{\ddot{y}_{ai}}, \sigma_{\theta_i}$ and $\sigma_{\ddot{\theta}_{ai}}$ denote the standard deviations of the displacements and the rms values of the absolute accelerations for each node in x, y and θ directions, respectively, based on the stochastic analysis. Note that x_{17}, $\sigma_{x_{17}}$, $y_{17}, \sigma_{y_{17}}$, θ_{17} and $\sigma_{\theta_{17}}$ represent the peak values and standard deviations of the relative displacements of the mass damper w.r.t. the 12-th node (upper observation deck) in x, y and θ directions, respectively. The values in the parentheses are the reduction percentages with respect to the "No Control" case. Based on the stochastic analysis, the acceleration power spectral densities of the upper observation deck $\ddot{x}_{12}$, $\ddot{y}_{12}$, $\ddot{\theta}_{12}$ for "No Control" and "Passive Control" cases are denoted by the dotted curve and solid curve , respectively, in Fig. 4. In Fig. 4, the passive tuned mass damper is capable of reducing the response of the first mode only. As observed from the "No Control" case in Table 2, the accelerations of two observation decks due to torsional motion are in the same order of magnitude as the lateral accelerations in x and y directions. This indicates the importance of considering the coupled lateral-torsional motion. With a passive tuned mass damper, the acceleration response is not reduced to the design requirements. Therefore, an active mass driver system is used.

TABLE 2

RESPONSE QUANTITIES OF THE TV TOWER

	No Control											
Node No. (1)	x_i cm (2)	$\ddot{x}_{ai}$ cm/s^2 (3)	σ_{x_i} cm (4)	$\sigma_{\ddot{x}_{ai}}$ cm/s^2 (5)	y_i cm (6)	$\ddot{y}_{ai}$ cm/s^2 (7)	σ_{y_i} cm (8)	$\sigma_{\ddot{y}_{ai}}$ cm/s^2 (9)	θ_i 10^{-5} rad (10)	$\ddot{\theta}_{ai}$ 10^{-5} rad/s^2 (11)	σ_{θ_i} 10^{-5} rad (12)	$\sigma_{\ddot{\theta}_{ai}}$ 10^{-5} rad/s^2 (13)
10	3.155	5.549	1.063	2.073	1.353	3.033	0.469	1.083	9.098	151.41	2.590	63.64
12	5.466	14.119	1.850	4.198	2.275	6.595	0.817	2.202	13.364	325.43	3.609	119.71
	Passive Control											
Node No. (14)	x_i cm (15)	$\ddot{x}_{ai}$ cm/s^2 (16)	σ_{x_i} cm (17)	$\sigma_{\ddot{x}_{ai}}$ cm/s^2 (18)	y_i cm (19)	$\ddot{y}_{ai}$ cm/s^2 (20)	σ_{y_i} cm (21)	$\sigma_{\ddot{y}_{ai}}$ cm/s^2 (22)	θ_i 10^{-5} rad (23)	$\ddot{\theta}_{ai}$ 10^{-5} rad/s^2 (24)	σ_{θ_i} 10^{-5} rad (25)	$\sigma_{\ddot{\theta}_{ai}}$ 10^{-5} rad/s^2 (26)
10	2.766 (12.3)	4.725 (14.9)	0.888 (16.5)	1.560 (24.7)	1.174 (13.3)	2.647 (12.7)	0.397 (15.4)	0.818 (24.5)	6.784 (25.4)	147.41 (2.7)	2.010 (22.4)	60.88 (4.3)
12	4.823 (11.8)	12.234 (13.4)	1.551 (16.2)	3.460 (17.6)	1.937 (14.9)	5.394 (18.2)	0.694 (15.1)	1.825 (17.1)	9.701 (27.4)	321.83 (1.1)	2.692 (25.4)	115.31 (3.7)
17	13.666	32.156	5.480	12.898	6.180	17.504	2.391	6.774	16.443	605.58	5.464	201.28
	***LQG* Control**											
Node No. (27)	x_i cm (28)	$\ddot{x}_{ai}$ cm/s^2 (29)	σ_{x_i} cm (30)	$\sigma_{\ddot{x}_{ai}}$ cm/s^2 (31)	y_i cm (32)	$\ddot{y}_{ai}$ cm/s^2 (33)	σ_{y_i} cm (34)	$\sigma_{\ddot{y}_{ai}}$ cm/s^2 (35)	θ_i 10^{-5} rad (36)	$\ddot{\theta}_{ai}$ 10^{-5} rad/s^2 (37)	σ_{θ_i} 10^{-5} rad (38)	$\sigma_{\ddot{\theta}_{ai}}$ 10^{-5} rad/s^2 (39)
10	2.653 (15.9)	4.313 (22.2)	0.809 (23.9)	1.199 (42.2)	1.145 (15.4)	2.695 (11.1)	0.368 (21.5)	0.679 (37.3)	5.436 (40.3)	111.15 (26.6)	1.644 (36.5)	43.93 (31.0)
12	4.508 (17.5)	7.481 (47.0)	1.424 (23.0)	2.359 (43.8)	2.093 (8.0)	3.731 (43.4)	0.647 (20.8)	1.273 (42.2)	7.481 (44.0)	151.80 (53.4)	2.101 (41.8)	52.31 (56.3)
17	56.136	147.99	18.798	42.873	33.798	94.791	9.629	29.722	99.813	5140.8	29.604	1632.0
u_i	$u_{1\max} = 57.1$ kN, $u_{2\max} = 51.8$ kN, $u_{3\max} = 44.3$ kN-m						$\sigma_{u_1} = 18.2$ kN, $\sigma_{u_2} = 14.2$ kN, $\sigma_{u_3} = 14.4$ kN-m					

To design the controller and observer for active control, a state reduced-order system, Eqn. 6, has been constructed which retains the first 24 complex modes ($k = 24$) of the entire structure, i. e., the first twelve pairs of complex conjugate eigenvalues and eigenvectors. The reduced-order state vector is $Z_r = [x_{10}, x_{12}, x_{14}, x_{17}, y_{10}, y_{12}, y_{14}, y_{17}, \theta_{10}, \theta_{12}, \theta_{14}, \theta_{17}, \dot{x}_{14}, \dot{x}_{17}, \dot{x}_{14}, \dot{x}_{17}, \dot{y}_{10}, \dot{y}_{12}, \dot{y}_{14}, \dot{y}_{17}, \dot{\theta}_{10}, \dot{\theta}_{12}, \dot{\theta}_{14}, \dot{\theta}_{17}]'$. The main objective of control is to reduce the accelerations $\ddot{x}_{12}$, $\ddot{y}_{12}$ and $\ddot{\theta}_{12}$ of the upper observation deck. Likewise, the actuator constraints, including the peak stroke of 75 cm and the peak force of 150 kN should not be exceeded. Although other measurements can be made, we only install three acceleration sensors

to measure the accelerations at the upper observation decks, i. e., $\ddot{x}_{12}$, $\ddot{y}_{12}$, and $\ddot{\theta}_{12}$. Therefore, the measured output feedback vector is $y_r = [\ddot{x}_{12}, \ddot{y}_{12}, \ddot{\theta}_{12}]'$ in Eqn. 8. The noises associated with the 3 measurements are uncorrelated white noise processes with power spectral densities of $7.7\text{x}10^{-13}/2\pi$ $m^2/sec^3/rad$, $2.1\text{x}10^{-13}/2\pi$ $m^2/sec^3/rad$ and $1.0\text{x}10^{-9}/2\pi$ $rad^2/sec^3/rad$ for $\ddot{x}_{12}$, $\ddot{y}_{12}$, and $\ddot{\theta}_{12}$, respectively. These noises are introduced in the simulation of the structural response at a sampling rate of 10^{-4} sec (Nyquist frequency = 5000 Hz). These *rms* values are about 0.25 % of $\sigma_{\ddot{x}_{12}}$, $\sigma_{\ddot{y}_{12}}$ and $\sigma_{\ddot{\theta}_{12}}$ of the controlled structure.

LQG Controller : The control parameters used for the LQG controller are as follows : controlled output $z_r = [\ \ddot{x}_{10}, \ddot{x}_{12}, \ddot{x}_{17a}, \ddot{y}_{10}, \ddot{y}_{12}, \ddot{y}_{17a}, \ddot{\theta}_{10}, \ddot{\theta}_{12}, \ddot{\theta}_{17a},]'$, $Q = \text{diag}\ [\ 10^5, 10^5, 0, 10^5, 10^5, 0, 10^2, 10^2, 0]$, $R = \text{diag}\ [\ 8\text{x}10^{-3}, 8\text{x}10^{-3}, 5\text{x}10^{-2}\ ]$, $\bar{S}_{vv} = \text{diag}\ [7.7\text{x}10^{-13}, 2.1\text{x}10^{-13}, 1.0\text{x}10^{-9}]$, and $\bar{S}_{WW} = 10 \bullet S_{WW}(\omega)$ at $\omega = 1.6$ rad/sec, where $S_{WW}(\omega)$ is the cross-power spectral density of the wind load given by Eqn. 9 and 14. It is important to emphasize that in designing the observer, although the wind loads are assumed to be Gaussian white noise processes, their spatial correlations should be taken into account. Consequently, the cross- power spectral density matrix $\bar{S}_{WW}$ chosen above retains the spatial correlations $S_{WW}(\omega)$, Eqn. 14, at the dominant frequency $\omega = 1.6$ rad/sec (first mode in x direction). The response quantities of the structure with the LQG controller are presented in columns (28)-(39) of Table 2. The peak value u_{imax} (i = 1, 2, 3) and the *rms* value σ_{u_i} (i = 1, 2, 3) of the computed control forces in x, y and θ directions are shown in the last row of Table 2. For the stochastic analysis, the acceleration power spectral densities of the upper observation deck $\ddot{x}_{12}$, $\ddot{y}_{12}$ and $\ddot{\theta}_{12}$ are plotted in Fig. 4, denoted by the long-dashed-short-dashed curve. As observed from Table 2 and Fig. 4, the percentages of acceleration reductions for the peak and *rms* responses of the upper observation deck are remarkable, in particular the torsional acceleration.

The actuator forces F_1, F_2 and F_3 and strokes computed from Eqn. 24 and 25 based on the deterministic analysis are listed in Table 3, in which the rms value are obtained by taking temporal averages over a duration of 300 seconds. As shown in Table 3, the actuator forces and strokes do not exceed the actuator capacity and stroke limitations.

TABLE 3

ACTUATOR FORCES AND STROKES

Actuator No. (1)	F_i (KN)		*Strokes* (cm)	
	Peak value	*Temporal rms*	*Peak value*	*Temporal rms*
1	64.6	17.9	56.53	19.35
2	34.8	9.4	25.05	8.14
3	51.9	16.0	49.48	16.16

CONCLUSION

The *LQG* control strategy using dynamic output feedback controller has been applied to the 310 meters Nanjing TV transmission tower equipped with an active mass driver. The coupled lateral-torsional motion due to noncoincidence of the mass center, elastic center and aerodynamic center has been considered. The along-wind and across-wind velocities are both modeled as random processes defined by the Davenport cross-power spectra. The main objective of active control is to reduce the acceleration response of two observation decks under the design wind gusts. Emphasis has been placed on the control performance and practical applications of the *LQG* controller, such as acceleration feedback, limitations on peak control force and stroke for the actuator. The statistical response quantities of the tower with and without active control, including the power spectral densities and the *rms* of the acceleration response, have been computed. The deterministic analyses based on simulated sample functions of wind loads have been conducted for comparison. Simulation results demonstrate that the performance of passive mass damper is not acceptable. Based on the stochastic and deterministic analyses, the *LQG* control strategy is suitable for full-scale implementations of the active mass driver system and its control performance is quite remarkable.

ACKNOWLEDGMENTS

This research is supported by the National Science Foundation through Grant No. CMS-96-25616. Valuable discussion and advice by Professor A.M. Reinhorn of SUNY, Buffalo and Dr. Anil K. Agrawal are gratefully acknowledged.

REFERENCES

1. Ankireddi, S. and Yang, H. T. Y.(1996). Simple ATMD Control Methodology for Tall Buildings Subject to Wind Loadd. *ASCE J. of Struct. Engrg.* 122(1), 83-91.
2. Cao, H., Reinhorn, A. M. and Soong, T. T.(1998). Design of an Active Mass Damper for Wind Response of Nanjing TV Tower. Journal of Engineering Structures. 20(3), 134-143.
3. Davison, E. J. (1966). A Method for Simplifying Linear Dynamic Systems. IEEE Transactions on Automatic Control, Vol. AC-11 (1), 93-101.
4. Kareem, A. (1981). Wind-Excited Response of Buildings in Higher Modes. ASCE J. of Structural Division, 107 (ST4), 701-706.
5. Samali, B., Yang, J. N. and Yeh, C. T.(1985). Control of Lateral-Torsional Motion of Wind-Excited Buildings. ASCE J. of Engrg. Mech., 111 (6), 777-796.
6. Simiu, E. and Scanlan, R. H. (1986). Wind Effects on Structures, John Wiley, NY.
7. Skelton, R. E. (1988). Dynamic Systems Control : Linear Systems Analysis and Synthesis, John Wiley & Sons, NY.
8. Spencer, B.F. and Sain, M.K.(1997). Controlling Buildings: A New Frontier in Feedback. Journal of Control System. IEEE, 17 (6), 19-35.
9. Spencer, B. F, Dyke, S. J. and Deoskar, H. S. (1998). Benchmark Problems in Structural Control Part I: Active Mass Driver System; Part II : Active Tendon System. to appear in Journal of Earthquake Engineering and Structural Dynamics.
10. Suhardjo, J., Spencer, B. F. and Kareem, A.(1992). Frequency Domain Optimal Control of Wind Excited buildings. ASCE J. of Engrg Mech., 118 (12), 2463-2481.
11. Wu, J. C. and Yang, J. N.(1997a). Continuous Sliding Mode Control of a TV Transmission Tower under Stochastic Wind. Proc. 16th American Control Conference, 2, 883-887.

12. Wu, J. C. and Yang, J. N.(1997b). *LQG* and H_∞ Control of a TV Transmission Tower under Stochastic Wind. 7th Int. Conf. on Structural Safety and Reliability, Kyoto, Japan.
13. Wu, J. C., Yang, J. N. and Schmitendorf, W.(1998). Reduced-order H∞ and LQR Control for Wind-Excited Tall Buildings. Journal of Engineering Structures, 20 (3), 222-236.
14. Yang, J. N., Lin, Y. K., and Samli, B. (1981). Coupled Motion of Wind-Loaded Multi-Story Building. ASCE Journal of Engineering Mechanics Division, 107 (EM6), 1209-1226.
15. Yang, J.N., Wu, J.C., Agrawal, A.K. and Hsu, S.Y.(1997). Sliding Mode Control With Compensators for Wind and Seismic Response Control. Journal of Earthquake Engineering and Structural Dynamics. 26, 1137-1156.

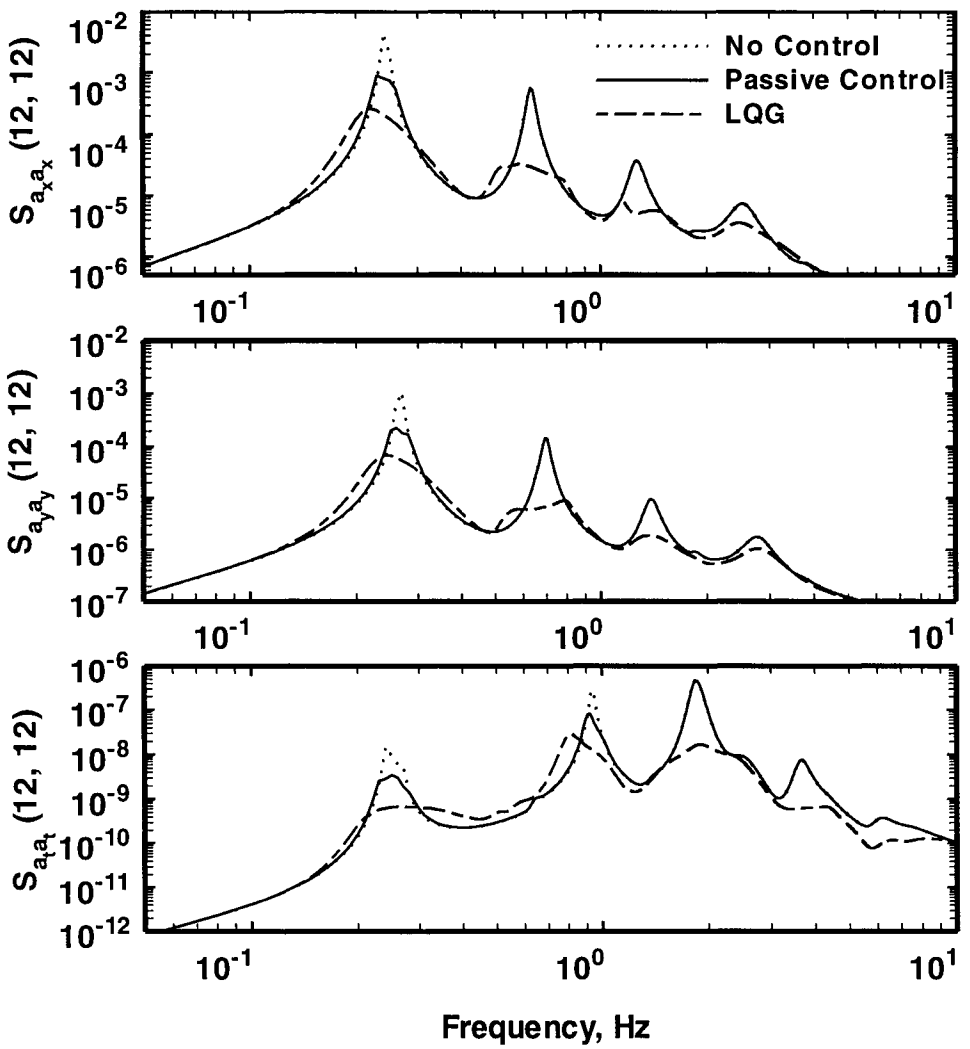

Fig. 4 : Acceleration Power Spectral Densities of Upper Observation Deck in $m^2/sec^3/rad$: (a) x direction; (b) y direction; and (c) rotation.

FAST COMPUTATION OF STATIONARY/NON-STATIONARY RANDOM RESPONSES OF COMPLEX STRUCTURES

J.H. Lin and W.X. Zhong

State Key Laboratory of Structural Analysis of Industrial Equipment,
Dalian University of Technology,116023,P.R.China

ABSTRACT

The PEM (Pseudo Excitation Method) for analyzing structural stationary/non-stationary random responses is outlined. Because any stationary random response analysis is converted into harmonic response analyses, while any evolutionary non-stationary random response analysis is converted into step-by-step integration computations, this method is very simple to use. It is accurate because both the cross-modal and cross-excitation terms are included. Its efficiency is much higher than the traditional methods; therefore complex engineering structures with thousands of degrees of freedom subjected to dozens of fully or partially coherent stationary/non-stationary excitations can be computed easily on ordinary personal computers.

KEYWORDS

random, structure, response, power, spectrum, stationary, non-stationary, coherency

INTRODUCTION

It is known that the basic framework of linear random vibration theory has been well established. However, its applications to practical engineering have been seriously restricted. This is mainly because of the huge amount of computational efforts required for complex

engineering problems, particularly for multiple excitation problems or non-stationary problems. Der Kiureghian and Neuenhofer (1992) pointed out that : *While the random vibration approach is appealing for its statistical nature, it is not yet accepted as a method of analysis by practising engineers.* Ernesto and Vanmarcke(1994) further pointed out that: *The theoretical framework of a methodology for stochastic-response analysis to random-excitation fields is already available; however, its use by the earthquake-engineering community is viewed as impractical except for simple structures with a small number of degrees of freedom and supports.* It is quite natural that they hold a pessimistic viewpoint since they both base their computations on the traditional, inefficient random response algorithms. As a result, when they dealt with the equations derived from the random vibration theory, they both selected the approximate response spectrum methods. Their point of view is quite representative, and is now out of date because this problem has been solved, using the PEM, exactly and efficiently (Lin 1985, Lin 1992, Lin, et al. 1992-1997). By using it, structures with thousands of DOFs and dozens of supports, subjected to stationary or non-stationary multiple random seismic excitations, can be computed on ordinary personal computers quite easily.

The PEM is not only efficient, but also easy to implement on computers because stationary random response analyses are replaced by harmonic response analyses, while evolutionary non-stationary random response analyses are replaced by step-by-step integration computations. Therefore, the computation processes are very simple. Various complex engineering structures can be modeled delicately and be computed very quickly. These advantages are particularly useful for some traditionally difficult problems, such as the stationary or non-stationary 3D random seismic analysis of long-span structures(Lin and Li, et al. 1995, Lin and Li, et al. 1997a,b); 3D buffeting analysis of aero-elastic structures; the propagation of stationary or non-stationary random waves along infinitely long structure chains (Lin and Fan, et al. 1995a ,b).

STRUCTURAL RESPONSES TO STATIONARY SINGLE EXCITATION

Traditional Algorithm

Firstly, consider the equations of motion of an elastic structure subjected to a zero-mean-valued stationary random excitation $x(t)$, with its PSD $S_{xx}(\omega)$ given,

$$[M]\{\ddot{y}\}+[C]\{\dot{y}\}+[K]\{y\}=\{p\}x(t) \tag{1}$$

in which $\{p\}$ is an n dimensional constant vector. For complex structures, n is very large, and so the mode superposition scheme is usually used to reduce the equations, i.e. let

$$\{y\}=\sum_{j=1}^{q}\{\phi_j\}u_j = [\Phi]\{u\} \tag{2}$$

where $[\Phi]$ consists of the lowest q M-normalized modes of the structure. When [C] is proportionally damped, Eqn.1 can be reduced and uncoupled into the q SDOF equations

$$\ddot{u}_j + 2\zeta_j\omega_j\dot{u}_j + \omega_j^2 u_j = \gamma_j x(t) \tag{3}$$

in which ζ_j, ω_j are the j-th modal damping ratio and angular frequency, while γ_j is the j-th modal participation factor

$$\gamma_j = \{\phi_j\}^T \{p\} \tag{4}$$

The solution of Eqn.3 is

$$u_j(t) = \int_{-\infty}^{\infty} \gamma_j h(\tau) x(t-\tau) d\tau \tag{5}$$

in which $h(\tau)$ is the pulse response function, and so

$$\{y(t)\} = \sum_{j=1}^{q} \{\phi_j\} \int_{-\infty}^{\infty} \gamma_j h(\tau) x(t-\tau) d\tau \tag{6}$$

Its correlation matrix is

$$\begin{aligned}[R_{yy}(\tau)] &= E\left[\{y(t)\}\{y(t+\tau)\}^T\right] \\ &= \sum_{j=1}^{q}\sum_{k=1}^{q} \gamma_j\gamma_k \{\phi_j\}\{\phi_k\}^T \int_{-\infty}^{\infty}\int_{-\infty}^{\infty} [R_{xx}(\tau+\tau_1-\tau_2)] h(\tau_1) h(\tau_2) d\tau_1 d\tau_2 \end{aligned} \tag{7}$$

Transform it into the frequency domain to give

$$[S_{yy}(\omega)] = \sum_{j=1}^{q}\sum_{k=1}^{q} \gamma_j\gamma_k H_j^* H_k \{\phi_j\}\{\phi_k\}^T S_{xx}(\omega) \tag{8}$$

This is the traditional CQC (complete quadratic combination) formula for computing the PSD matrix of structural displacement responses. It is exact because all the cross-modal terms have been included. When both n and q are big, the computational efforts are very significant because Eqn. (8) involves double summation operations. For example, when q=30, the operation after the summation symbols must be repeated 900 times, in other words 900 n-dimensional vector multiplication operations are required. Therefore, for engineering computations, the following SRSS (squareroot of the sum of squares) approximation equation, by neglecting the cross-modal terms, was widely suggested

$$[S_{yy}(\omega)] \approx \sum_{j=1}^{q} \gamma_j^2 |H_j|^2 \{\phi_j\}\{\phi_j\}^T S_{xx}(\omega) \tag{9}$$

Equation (9) approximately applies only for lightly damped structures with sparsely spaced participant frequencies. For most complex structures, there always exist some participant frequencies which are closely spaced. Therefore Eqn.9 is, in fact, not applicable; only Eqn.8 is applicable. Thus the remarkable efforts caused the viewpoint "the random vibration approach is impractical except for very simple structures".

Pseudo Excitation Method

For stationary single excitation problems, the PEM can be described as: A linear system is subjected to a zero-mean-valued stationary random excitation with its PSD (power spectral density) $S_{xx}(\omega)$ specified. If $\{y(t)\}$ and $\{z(t)\}$ are two arbitrary stationary response vectors due to the pseudo harmonic excitation $x(t)=\sqrt{S_{xx}(\omega)}\,e^{i\omega t}$, then $\{y\}^*\{y\}^T=[S_{yy}(\omega)]$ must be the PSD matrix of the corresponding random response vector $\{y(t)\}$, and $\{y\}^*\{z\}^T=[S_{yz}(\omega)]$ must be the cross-PSD matrix between the corresponding random response vectors $\{y(t)\}$ and $\{z(t)\}$.

As an example, let the random excitation $x(t)$ on the right-hand side of Eqn.1 be replaced by the following pseudo sinusoidal excitation

$$x(t)=\sqrt{S_{xx}(\omega)}\,e^{i\omega t} \tag{10}$$

and so Eqn.1 gives the pseudo harmonic solution

$$\{y(t)\}=\{Y(\omega)\}\,e^{i\omega t} \tag{11}$$

in which

$$\{Y(\omega)\}=\sum_{j=1}^{q}\gamma_j H_j\{\phi_j\}\sqrt{S_{xx}(\omega)} \tag{12}$$

Therefore the PSD of $\{y(t)\}$, according to the PEM, would be

$$[S_{yy}(\omega)]=\{y\}^*\{y\}^T=\{Y(\omega)\}^*\{Y(\omega)\}^T \tag{13}$$

The computational formula of PEM, i.e. Eqns.12 and 13, can also be written as

$$[S_{yy}(\omega)]=\left(\sum_{j=1}^{q}\gamma_j H_j\{\phi_j\}\right)^* S_{xx}(\omega)\left(\sum\gamma_k H_k\{\phi_k\}\right)^T \tag{14}$$

or in the matrix form

$$\begin{aligned}[S_{yy}(\omega)] &= \left([\Phi][H]\{\gamma\}\right)^* S_{xx}(\omega)\left([\Phi][H]\{\gamma\}\right)^T \\ &= [\Phi][H]^*\{\gamma\}\,S_{xx}(\omega)\,\{\gamma\}^T[H]\,[\Phi]^T\end{aligned} \tag{15}$$

where $[H]$ is a diagonal matrix.

Equation 8 can be obtained by substituting Eqn.12 into Eqn.13 and expanding it. It shows that the PEM also produces the exact CQC solution. However, in order to produce exact $[S_{yy}(\omega)]$, the PEM formula only needs one n-dimensional vector multiplication operation. And it is still so for q=300 or even bigger. It can be seen that the computational efforts required by the PEM are only about $1/q^2$ of that required by the traditional CQC method, i.e. Eqn.8.

An important character of the PEM is its exactness, because it is impossible for the PEM to neglect the cross-modal terms; in other words,the PEM always gives the exact CQC results even though the required computational efforts are only about $1/q$ of that required by the

SRSS approximation formula, Eqn.9. Compared with the PEM, the SRSS equation is neither exact nor efficient. Unfortunately, this sort of approximation has been widely recommended, e.g. by Ellishakoff, Lin & Zhu(1994), Simiu & Scanlan(1978), Dowell, Curtiss, Scanlan & Sisto(1978), Nigam(1983), Clough & Penzien(1975), Warburton(1976), and many other well-known scholars. None of the references ever pointed out the above disadvantages of the SRSS approximation. Computational methodologies are very important for the applications of various theories. Because of the limitations of the traditional CQC and SRSS methods, the theoretical development and engineering applications of the random vibration theory have long been subjected to insurmountable obstacle. The PEM just provides a new way to solve this difficulty.

Because this is a very important problem, we use the following very simple algebraic equations to further clarify the main points. Let

$$\Omega = \left(a_1 + a_2 + \cdots + a_{30}\right) \times \left(b_1 + b_2 + \cdots + b_{30}\right) \tag{a}$$

and

$$\Omega = a_1b_1 + a_1b_2 + \cdots + a_1b_{30} + a_2b_1 + a_2b_2 + \cdots + a_2b_{30} + \cdots\cdots + a_{30}b_1 + a_{30}b_2 + \cdots + a_{30}b_{30}$$

(b)

Clearly, the above two equations are mathematically identical to each other. However, nobody would use the form of Eqn.b because it needs 900 multiplication and 899 summation operations, while Eqn.a needs only 1 multiplication and 58 summation operations. The difference is remarkable. It amounts to one day and three years of computational time . Traditional CQC method corresponds to Eqn.b, and its SRSS form is

$$\Omega \approx a_1b_1 + a_2b_2 + \cdots\cdots + a_{30}b_{30} \tag{c}$$

It still needs 30 multiplication and 29 summation operations; the computation remains very inefficient while losing precision.

For simplicity, we did not distinguish between real or complex operations in the above; however it does not affect the essence of the efficiency comparison.

STRUCTURAL RESPONSES TO STATIONARY MULTIPLE EXCITATIONS

The equations of motion of a structure subjected to stationary multiple excitations are

$$[M]\{\ddot{y}\} + [C]\{\dot{y}\} + [K]\{y\} = [R]\{x(t)\} \tag{16}$$

in which $[R]$ is a $n \times m$ matrix consisting of 0 and 1only, which expands the m dimensional vector $\{x(t)\}$ into an n dimensional vector. Similar to the derivation in the last section, the traditional CQC algorithm has the form

$$\left[S_{yy}(\omega)\right] = \sum_{j=1}^{q} \sum_{k=1}^{q} H_j^* H_k \left\{\phi_j\right\}\left\{\phi_j\right\}^T [R][S_{xx}][R]^T \left\{\phi_k\right\}^T \left\{\phi_k\right\} \tag{17}$$

It can be expressed as

$$\left[S_{yy}(\omega)\right]=\sum_{j=1}^{q}\sum_{k=1}^{q} H_j^* H_k \left\{\phi_j\right\}^T \left\{\phi_k\right\} S_{F_jF_k} \tag{18}$$

in which

$$S_{F_jF_k}= \left\{\phi_j\right\}^T [R]\left[S_{xx}\right][R]^T \left\{\phi_k\right\}^T \tag{19}$$

The computation based on Eqns.18-19 is very time-consuming; therefore its SRSS approximation was also widely suggested

$$\left[S_{yy}(\omega)\right] \approx \sum_{j=1}^{q} \left|H_j\right|^2 \left\{\phi_j\right\}\left\{\phi\right\}^T S_{F_jF_j} \tag{20}$$

The above problem can be dealt with by the use of PEM. The first step is to decompose $\left[S_{xx}\right]$ into the sum of $r\ (r \le m)$ matrices; each corresponds to a pseudo excitation $\left\{x_p\right\} e^{i\omega t}$

$$\left[S_{xx}\right] =\sum_{p=1}^{r}\left[S_{xx}\right]_p = \sum_{p=1}^{r}\left\{x_p\right\}^* \left\{x_p\right\}^T \tag{21}$$

where r is the rank of matrix $\left[S_{xx}\right]$. The generation of $\left\{x_p\right\}$ was originally in terms of the eigenpairs of $\left[S_{xx}\right]$ (Lin, Zhang and Li 1994); and was then further simplified by taking the Cholesky decomposition of $\left[S_{xx}\right]$ (Lin and Sun 1995). The response corresponding to $\left\{x_p\right\}$ is

$$\left\{y_p\right\}= \sum_{j=1}^{q} H_j \left\{\phi_j\right\}\left\{\phi_j\right\}^T [R] \left\{x_p\right\} \tag{22}$$

and the total PSD matrix of the displacement vector $\left\{y\right\}$ is

$$\left[S_{yy}(\omega)\right]= \sum_{p=1}^{r} \left\{y_p\right\}^* \left\{y_p\right\}^T \tag{23}$$

Analogous to the previous section, substituting Eqn.22 into Eqn.23 gives

$$\left[S_{yy}(\omega)\right]= \left(\sum_{j=1}^{q} H_j \left\{\phi_j\right\}\left\{\phi_j\right\}^T [R]\right)^* \sum_{p=1}^{r} \left\{x_p\right\} \left\{x_p\right\}^T \left(\sum_{j=1}^{q} H_j \left\{\phi_j\right\}\left\{\phi_j\right\}^T [R]\right)^T \tag{24}$$

or its matrix form

$$\left[S_{yy}(\omega)\right] = [\Phi][H]^*[\Phi]^T[R]\left[S_{xx}\right][R]^T[\Phi][H][\Phi]^T \tag{25}$$

It is not difficult to establish the traditional CQC algorithm Eqn.17, or Eqns.18-19 from Eqns.22-23, 24 or 25. Because of the unacceptable computation cost of the traditional CQC Eqns. 17-19, the SRSS approximation which neglects the cross-modal terms was suggested in many areas, e.g. in the analysis of wind-excited random vibration (Simiu and Scanlan 1978,Dowell, et al. 1978), or multi-support random seismic responses in which the argument

between Der Kiureghian and Vanmarcke is very typical. Der Kiureghian and Neuenhofer (1992) put forward the PSD formulas for such multiple excitation aseismic problems, whose essence is the use of Eqn.17. Thus their algorithm involves the operations of a four-fold summation($\sum_{j=1}^{q}\sum_{k=1}^{q}\sum_{p=1}^{r}\sum_{s=1}^{r}$).In order to reduce this enormous effort , Ernesto and Vanmarcke (1994) proposed an algorithm which involves only the three-fold summation ($\sum_{j=1}^{q}\sum_{p=1}^{r}\sum_{s=1}^{r}$) by neglecting the cross-modal terms, whereas they added some extra computations for reducing the errors due to this neglect. In fact, this is a revised version of the SRSS algorithm. Der Kiureghian and Neuenhofer(1995) commented it as "*This reduction is seemingly advantageous, since it eliminates the need to compute cross-modal terms……etc. However, this reduction comes at the cost of extra calculations for each modal response and possibly a gross error.*" Ernesto and Vanmarcke (1995) defended themselves by "(their method) *is advantageous not only in the eliminates the need to compute cross-modal terms, but also because the analysis of the modal oscillators can be performed a priori ……*" In fact, none of them has got rid of the frame of the traditional CQC or SRSS methods. This problem has also been computed using the PEM (Li 1994, Lin and Li, et al. 1997), which is accurate, simple and very efficient. Moreover, the much more difficult non-stationary version of this problem has also be solved using the PEM.

It should be noted that when implementing Eqns.22 and 23 by PEM, the following operations should be executed first

$$\gamma_{jp}=\{\phi_j\}^T[R]\{x_p\} \tag{26}$$

where the function of $[R]\{x_p\}$ is to expand $\{x_p\}$ into an n dimensional vector, i.e. to put the m elements of $\{x_p\}$ into the appropriate positions of an n dimensional vector , and the required effort is negligible. γ_{jp} is the project of $\{x_p\}$ on the j-th mode, only n real multiplication operations are required to produce it . Thus, the computation of $\{y_p\}$ according to Eqn.22 requires about $3qn$ real multiplication operations in all. If it is done on an available program for structural harmonic analysis, the displacement vector $\{y_p\}$ can be computed by taking $[R]\{x_p\}$ as the vector of the harmonic force amplitudes. That makes the implementation of Eqn.22 very simple. The implementation of Eqn.23 needs about $4rn^2$ real multiplication operations. In addition, to execute the Cholesky (LDLT) decomposition of $[S_{xx}]$ needs about $m^3/6$ or $8m^3/6$ real multiplication operations (when $[S_{xx}]$ is a real symmetric or Hermitian matrix) . The sum of the above three terms is much smaller than that required by the traditional CQC method, i.e. Eqn.17 or Eqns.18-19. It should also be noted that if using the matrix multiplication form Eqn.25, the computational efficiency is also much higher than using Eqn.17. In case the rank r of matrix $[S_{xx}]$ is very large, the direct use of Eqn.25 to

compute the whole matrix $[S_{yy}]$ may need less effort than using Eqns.22-23(Lin, et al. 1995). But, for most practical engineering problems, it is not necessary to compute the whole matrix $[S_{yy}]$. Usually only $n'(n' << n)$ of its diagonal elements are of interest. So that only the following computation should be implemented

$$\{S_{yy}(\omega)\} = \sum_{p=1}^{r} \{|y_p'|\}^2 \tag{27}$$

in which $\{|y_p'|\}^2$ means to square the norms of the n' elements in the pseudo response vector $\{y_p\}$. Thus, the computational effort reduces from $4rn^2$ multiplication operations to only $4rn'$ multiplication operations. The storage requirement is also reduced considerably.

If the PSDs of some internal forces (or stresses) are required, using the PEM is particularly efficient. Traditionally, the displacement PSD matrix, the strain PSD matrix, the transfer matrices between the displacements and strains and between the strains and stresses need be produced before the stress PSD matrix is computed. If the PEM is used, none of such matrices is required. Instead, it only need compute the harmonic strains from the pseudo sinusoidal displacement, and then the harmonic stresses (or internal forces). The interested stress PSDs can be directly obtained by squaring the norms of the corresponding stress components. The computation of various cross-PSDs is equally convenient. Because of this advantage, the period for developing corresponding computation software is short, and so the cost is low.

For non-proportionally damped problems, the conventional means is to reduce and uncouple Eqns.1 or 16 in terms of the complex modes, so as to lead to the traditional CQC Eqns.8 or 17, and their SRSS forms. For complicated structures, however, a great amount of complex operations may cause a considerable increase of the computational cost. In order to avoid such complex operations, Connor (1979) used the classical real modes to reduce the equations of motion in the computations of random wave responses of offshore platforms. For the resulting non-diagonal damping matrix $[C]^* = [\Phi]^T[C][\Phi]$, he diagonalized it by means of some approximate means in order to adopt the traditional CQC or SRSS formulae. Clearly, this processing is neither exact nor efficient. This problem can be dealt with by means of the PEM very easily since all pseudo excitations are sinusoidal; therefore even though the reduced damping matrix $[C]^*$ is non-diagonal, the responses of various displacements, internal forces, etc. can be computed analytically. To square the norms of such pseudo responses gives the required PSDs accurately.

STRUCTURAL RESPONSES TO NON-STATIONARY SINGLE OR MULTIPLE EXCITATIONS

The pseudo excitation method for non-stationary single excitation problem can be described as follows: A linear system initially at rest is subjected to an evolutionary random excitation $f(t) = g(t)\, x(t)$, in which $g(t)$ is a given slowly varying modulation function while

$x(t)$ is a zero-mean-valued stationary random process whose PSD $S_{xx}(\omega)$ has also been specified. If $\{y(t)\}$ and $\{z(t)\}$ are two arbitrary transient response vectors due to the pseudo excitation $x(t) = g(t)\sqrt{S_{xx}(\omega)}\, e^{i\omega t}$, then $\{y\}^*\{y\}^T = [S_{yy}(\omega,t)]$ must be the time-dependant PSD matrix of the random response vector $\{y(t)\}$, and $\{y\}^*\{z\}^T = [S_{yz}(\omega,t)]$ must be the time-dependent cross-PSD matrix between the random response vectors $\{y(t)\}$ and $\{z(t)\}$.

Take Eqn.1 as the example. It is now necessary to replace $x(t)$ on its right-hand side by the following pseudo excitation before it is integrated numerically for a series of selected frequency points.

$$x(t) = g(t)\sqrt{S_{xx}(\omega)}\, e^{i\omega t} \tag{28}$$

In general, this can be done by means of the Duhamel integration formula, Wilson-θ or Newmark scheme, etc. However, when the precise integration method is instead used (Zhong 1995, Zhong & Williams 1995) the efficiency has been proved to be extremely high(Lin, Shen and Williams 1995a,b, Lin,Shen and Williams 1997). That means rather complex structures with thousands of DOFs subjected to non-stationary random excitations can be computed on personal computers easily.

The time-dependant PSD matrix $[S_{xx}(\omega,t)]$ of zero-mean-valued evolutionary multiple random excitations can be decomposed into the sum of a limited number of PSD matrices. Each of such matrices corresponds to a single pseudo excitation (Li 1994, Lin and Li, et al. 1997). Therefore, $[S_{xx}(\omega,t)]$ can be decomposed into the form

$$[S_{xx}(\omega,t)] = g^2(t)\sum_{p=1}^{r}[S_{xx}(\omega,t)]_p = g^2(t)\sum_{p=1}^{r}\{x_p\}^*\{x_p\}^T \tag{29}$$

and $g(t)\{x_p\}e^{i\omega t}$ is one of the pseudo excitations, which is deterministic. Superposing all the responses due to these r pseudo excitations gives the total response PSD matrix; which is entirely similar to Eqn.23.

This algorithm also applies to the analysis of non-stationary random responses of structures subjected to non-uniformly modulated evolutionary single or multiple random excitations(Lin and Sun, et al. 1997).

EXAMPLES

Three examples on multi-excitation stationary/non-stationary random seismic analysis were computed and are given below. The following 6 cases were computed using PEM:

Case 1. Stationary uniform ground excitations, i.e. all ground nodes move synchronously.

Case 2. Stationary fully coherent ground excitations, i.e. the phase-lags between all ground node excitations were taken into account.

Case 3. Stationary partially coherent ground excitations, i.e. the phase-lags and a partial loss of

the coherency between all ground node excitations were taken into account.

Case 4. Non-stationary uniform ground excitations, all ground nodes move synchronously.

Case 5. Non-stationary fully coherent ground excitations, i.e. the phase-lags between all ground node excitations were taken into account.

Case 6. Non-stationary partially coherent ground excitations, i.e. the phase-lags and a partial loss of the coherency between all ground node excitations were taken into account.

We are interested in the scale of the structures and the computational efficiency. Therefore the physical and geometrical parameters of the structures are not given in detail here.

Example 1 25-column platform

The platform of Figure 1 was modeled as a space frame. Its finite element model has 239 nodes of which 25 are ground nodes, 318 3D beam elements, 1284 degrees of freedom. Its lowest 20 modes were taken for mode-superposition. The apparent speed of the horizontally traveling SH waves is 500 m/s; they travel at a 30° angle with the longitudinal axis of the platform. The variances of selected 1434 displacements and 300 internal stresses were computed. In order to compute these variances, 122 frequency points within the frequency band $\omega \in [0.5, 9.5] 1/s$ were used. In the non-stationary analysis, 161 time steps were computed. The computations were executed on an IBM/486 personal computer (main frequency 66 mHZ). The computing time for the six cases is listed in Table 1.

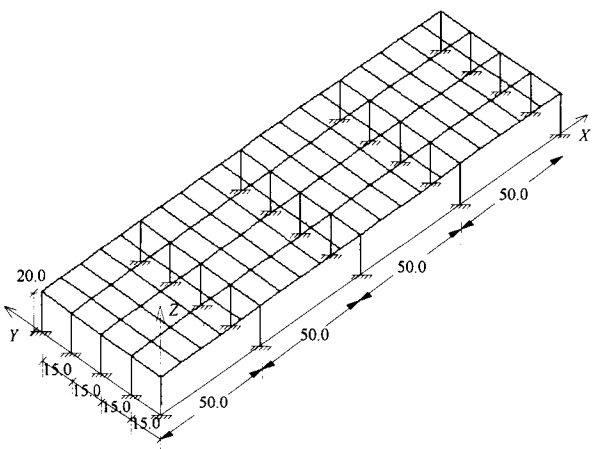

Figure 1: 25-column platform

TABLE 1

COMPUTING TIME FOR THE 25-COLUMN PLATFORM

	STATIONARY			NON-STATIONARY		
COMPUTING 20 MODES	CASE1	CASE2	CASE3	CASE4	CASE5	CASE6*
2'15"	2'40"	5'23"	49'10"	32'39"	2°15'25'	6°36'25"

*CASE6 was computed on a Pentium-2 Personal Computer (main frequency 233 MHZ)

Example 2 Concrete Dam

The concrete dam of Figure 2 is located in Jilin Province, China, as part of a power station. Its finite element model has 1020 nodes of which 27 are ground nodes, 720 8-node iso-parametric elements, 2979 degrees of freedom. Its lowest 32 modes were taken for mode-superposition. The apparent speed of the horizontally traveling P waves is 500 m/s; they travel at a 30° angle

with the longitudinal axis of the dam. The variances of selected 1800 displacements and 480 internal stresses were computed. In order to compute these variances, 127 frequency points within the frequency band $\omega \in [10.0,85.0] s^{-1}$ were used. In the non-stationary analysis, 161 time steps were computed. The computations were executed on a Pentium-2 personal computer with main frequency 233 mHZ. The computing time for the six cases is listed in Table 2.

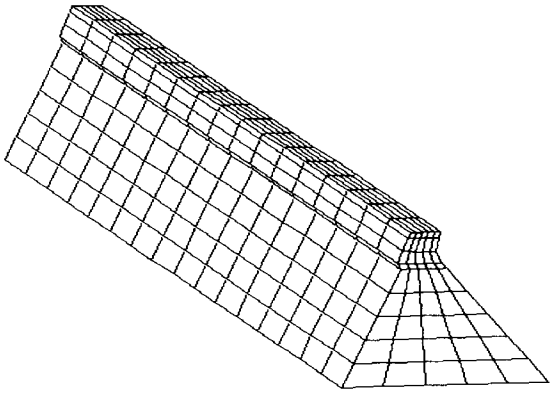

Figure 2: Concrete dam

TABLE 2

COMPUTING TIME FOR THE CONCRETE DAM

	STATIONARY			NON-STATIONARY		
COMPUTING 32 MODES	CASE1	CASE2	CASE3	CASE4	CASE5	CASE6
7'5"	7'25"	10'31'	39'10'	21'17"	1°12'5"	24°48'12"

Example 3 Complex Frame

The frame of Figure 3 has 1789 nodes of which 45 are ground nodes, 3540 3D beam elements, 10536 degrees of freedom. Its lowest 30 modes were taken for mode-superposition. The apparent speed of the horizontally traveling SH waves is 500 m/s; they travel at a 30° angle with the longitudinal axis of the frame. The variances of selected 1800 displacements and 300 internal stresses were computed. 122 frequency points within the frequency band $\omega \in [0.1, 3.7] 1/s$ and 161 time steps were computed. The computations were executed on a Pentium-2 personal computer with main frequency 233 mHZ. The computing time for the six cases is listed in Table 3.

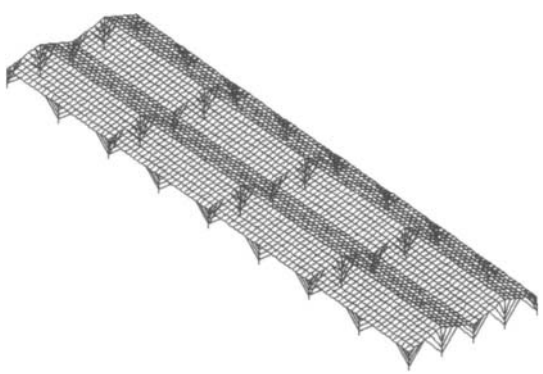

Figure 3: Complex frame

TABLE 3

COMPUTING TIME FOR THE COMPLEX FRAME

	STATIONARY			NON-STATIONARY		
COMPUTING 30 MODES	CASE1	CASE2	CASE3	CASE4	CASE5	CASE6
16'10"	17'9"	26'5"	2°4'56"	52'28"	1°43'3"	43°34'19"

It is seen that even for this complex structure, the CASE 3 that Der Kiureghian and Neuenhofer(1992), Ernesto and Vanmarcke (1994) tried to compute by means of the approximate response spectrum method, needs only about 2 hours on a personal computer.

CONCLUSIONS

The PEM is an exact and efficient method series. For stationary excitations, the random analyses are transformed into harmonic analyses; for evolutionary non-stationary excitations, the random analyses are referred to deterministic step-by-step integration. Hence it is very easy to use because such deterministic harmonic analysis or direct integration analysis is quite ordinary for general engineering major undergraduates.

For non-stationary random response analysis, the traditional time-dependant PSD computations are very cumbersome and inefficient , e.g. see To(1986). However, it is quite simple and efficient for the PEM to do it. In particular, if the precise integration scheme is combined with the PEM(Zhong 1995, Zhong and Williams 1995, Lin, et al. 1997), the computation efficiency can be further raised remarkably.

It is concluded that the PEM is computationally much better than the traditional CQC method and its SRSS approximation, which have been used for many years.

ACKNOWLEDGMENTS

In the past ten years, the PEM algorithm series has been developed under the support of the Natural Science Foundation of China and the Doctoral Research Foundation of China. The British Royal Society and the Hong Kong Research Grants Council also partly supported its development. Mr. Zhang Yahui completed the major part of the programming and computing work for this article, as part of his Ph.D. thesis.

REFERENCES

Clough R.W. and Penzien J.(1975), *Dynamics of Structures.* McGraw-Hill Inc.,New York, USA

Connor J.(1979), *Wave, Current and Wind Loads, Department of Civil Engineering*, Massachusetts Institute of Technology, Cambridge, Massachusetts, USA

Der Kiureghian A. and Neuenhofer A.(1992). Response Spectrum Method for Multi-Support Seismic Excitations. *Earthquake Engineering and Structural Dynamics* **21,** 713-740.

Der Kiureghian A. and Neuenhofer,A.(1995). A discussion on above [2], *ASCE, Journal of*

Engineering Mechanics. **121:9,** 1037.
Dowell E.H., Curtiss H.C., Scanlan R.H. and Sisto,F.(1978), *A Modern Course in Aeroelasticity*. Sijthoff & Noordhoff Int. Publisher, The Netherlands

Elishakoff I., Lin Y.K. and Zhu L.P.(1994). *Probabilistic and Convex Modelling of Acoustically Excited Structures*, Elsevier, Amsterdam, The Netherlands

Ernesto H.Z. and Vanmarcke(1994).E.H., Seismic Random-Vibration Analysis of Multi-support Structural Systems. *ASCE, Journal of Engineering Mechanics* **120:5,** 1107-1128.

Ernesto H.Z. and Vanmarcke E.H.(1995). Closure on the discussion, *ASCE, Journal of Engineering Mechanics* **121:9,** 1038.

Li J.J.(1994), *Pseudo Excitation Method of Random Seismic Response Analysis*. Ph.D. Thesis, Research Institute of Engineering Mechanics, Dalian University of Technology.

Lin J.H.(1985). A deterministic Method for the Computation of Stochastic Earthquake Response *Earthquake Engineering and Engineering Vibration (in Chinese)* **5:1**,89-94.

Lin J.H. (1992). A fast CQC algorithm of PSD matrices for random seismic responses, *Computers & Structures,* **44:3,** 683-687.

Lin J.H., Zhang W.S. and Li J.J.(1994). Structural Response to Arbitrarily Coherent Stationary Random Excitations. *Computers & Structures* **50:5**, 629-634.

Lin J.H., Zhang W.S. and Williams F.W.(1994). Pseudo-Excitation Algorithm for Nonstationary Random Seismic Responses. *Engineering Structures* **16,**270-276.

Lin J.H., Fan Y. and Williams F.W.(1995). Propagation of non-stationary waves along substructural chains, *Journal of Sound and Vibration*,**187:4**,585-593

Lin J.H., Fan Y., Bennett P.N. and Williams F.W.(1995). Propagation of stationary random waves along substructural chains, *Jnl of Sound and Vibration*. **180:5**,757-767

Lin J.H. and Sun D.K.(1995). Wind-excited Random Vibration of Irregular Structures. *Proc.Int.Conf.EPMESC-V*, Macao, 839-845.

Lin J.H., Shen W.P. and Williams F.W.(1995a). A High Precision Direct Integration Scheme for Non-Stationary Random Seismic Responses of Non-Classically Damped Structures. *Structural Engineering and Mechanics*,**3:3**,215-228.

Lin J.H., Shen W.P. and Williams F.W.(1995b). A High Precision Direct Integration Scheme

for Structures Subjected to Transient Dynamic Loading. *Computers Struct.* **56:1**,113-120.

Lin J.H., Li J.J. and Zheng H.Z.(1995). Structural Random Responses to Arbitrarily Coherent Excitations. *Chinese Journal of Applied Mechanics,* **12:4**, 97-103.

Lin J.H., Li J.J., Zhang W.S. and Williams F.W.(1997a). Non-stationary Random Seismic Responses of Multi-Support Structures in Evolutionary Inhomogeneous Random Fields. *Earthquake Engineering & Structural Dynamics*,**26**,135-145.

Lin J.H., Li J.J., Zhang W.S. and Williams F.W.(1997b). Structural Seismic Response to Inhomogeneous Random Field. *Engineering Computations*,**14:7**,718-734.

Lin J.H., Shen W.P. and Williams F.W.(1997). Accurate High-Speed Computation of Non-Stationary Random Structural Response. *Engineering Structures*, **19:7**,586-593.

Lin J.H., Sun D.K., Sun Y. and Williams F.W.(1997). Structural Responses to Non-uniformly Modulated Evolutionary Random Seismic Excitations. *Communications in Numerical Methods in Engineering*, **13**,605-616.

Nigam N.C.(1983), *Introduction to Random Vibrations.* The MIT Press, Cambridge, Massachussetts, USA

Simiu E. and Scanlan R.H.(1978), *Wing Effects on Structures: an Introduction to Wind Engineering.* John Wiley & Sons, New York, USA

To C.W.S.(1986). Response Statics of Discretized Structures to Non-Stationary Random Excitation. J. Sound Vib. **105:2**,217-231.

Warburton G.B.(1976), *The Dynamical Behavior of Structures.* Pergamon, Oxford, UK

Zhong W.X. and Williams,F.W.(1995). A Precise Time Step Integration Method. *Proc. Inst. Mech. Engrs* **208C**,427-430.

Zhong W.X.(1995), *A New Systematic Methodology for Theory of Elasticity.* Press of Dalian University of Technology. Dalian, China

Zhong W.X.(1996).Review of a High-Efficiency Algorithm Series for Structural Random Responses. *Progress in Natural Science* **6:3,** 257-268.

RESPONSE OF DYNAMICAL SYSTEMS DRIVEN BY ADDITIVE GAUSSIAN AND POISSON WHITE NOISES

L. A. Bergman[1], S.F. Wojtkiewicz[1] and M. Grigoriu[2]

[1]Department of Aeronautical and Astronautical Engineering
University of Illinois at Urbana-Champaign
Urbana, IL 61801 USA

[2]Department of Civil Engineering
Cornell University
Ithaca, NY 14853 USA

ABSTRACT

A numerical method previously developed by the authors for the solution of stochastic systems excited by Poisson white noise will be applied to several dynamical systems. The stationary probability density function of the response process for the single degree-of-freedom Duffing oscillator will be obtained by solving the Fourier-transformed forward generalized Kolmogorov equation directly for the characteristic function, followed by numerical Fourier inversion to recover the probability density function. The excitation process will modeled as a sum of Gaussian and Poisson white noises. Resulting second and fourth order moments of response will be examined in order to assess relative effects of the two inputs.

KEYWORDS

Poisson white noise, stochastic dynamical system, generalized Kolmogorov equation, finite difference method, Fourier transform, characteristic function, probability density function.

INTRODUCTION

A number of analytical and computational methods have evolved over the past forty years to determine the response of linear and nonlinear dynamical systems subjected to additive and/or multiplicative Gaussian white noise excitations. While Gaussian white noise and the more general filtered Gaussian white noise provide useful models of environmental loads such as earthquakes and wind, a broader class of random processes, filtered Poisson processes, have been shown to be more realistic in modeling disturbances that originate from impact-type loads. These representations have been used, for example, by Tung (1972) to examine the response of bridges to moving loads, by Lin (1963) and Cornell (1964) to model seismic loads acting on structures, and by Roberts (1972) to analyze the effects of wave action on ships. In a recent monograph, Grigoriu (1995) assessed the efficacy of combinations of Gaussian and Poisson white noises as models for a wide range of loadings, including the aforementioned earthquake, wave and traffic, as well as wind and a number of others, and showed its superiority to purely Gaussian white noise in many situations.

Several methods for characterizing the response of nonlinear dynamical systems to combinations of Gaussian and Poisson white noises have been developed. Some of these techniques include Monte Carlo simulation, moment closure techniques, path integral methods, and numerical methods including those based on the characteristic function of the response process. A more thorough review of these methods can be found in Wojtkiewicz, *et al.* (1998) and the references therein.

The method used here falls into the group utilizing the characteristic function, $\Phi_{\mathbf{X}}(\mathbf{u}, t)$, to describe the response. Tylikowski and Marowski (1986) used a partial differential equation for the characteristic function, obtained by taking the Fourier transform of the forward generalized Kolmogorov equation, to study the response of a single degree of freedom nonlinear oscillator to Poisson impulses. Grigoriu (1996) showed that the characteristic function satisfies a boundary value problem which can be derived directly from the state equations of the system using a generalized version of Itô's rule. In that paper, he investigated two scalar examples by solving the boundary value problem for the characteristic function using a standard finite difference procedure. Recently, the method introduced by Grigoriu was extended in Wojtkiewicz, *et al.* (1998) to the case of multi-state dynamical systems, and the stationary probability density function of the response process for several one- and two-state dynamical systems was found by numerically solving the Fourier-transformed forward generalized Kolmogorov equation (the TFGK equation, for convenience) for the characteristic function, followed by numerical Fourier inversion to recover the density function.

In this paper, the response of a particular nonlinear system to a combination of Gaussian and

Poisson white noises will be further examined in order to assess the sensitivity of the solution and subsequent moment calculations to the relative weight of each.

PROBLEM FORMULATION

Consider the stochastic differential equation describing a time-independent discrete dynamical system subject to Gaussian and Poisson white noises, given by

$$\dot{\mathbf{X}}(t) = \mathbf{a}(\mathbf{X}(t), t) + \mathbf{G}\mathbf{W}(t) + \mathbf{c}Y(t) \tag{1}$$

$$\mathbf{X}(t_0) = \mathbf{X}_0 \tag{2}$$

where $\mathbf{X}$ and $\mathbf{a}(\mathbf{X}, t) \in \mathfrak{R}^n$, $\mathbf{W}(t) \in \mathfrak{R}^m$ is a unit intensity Gaussian vector white noise process, $\mathbf{G}$ is an $n \times m$-dimensional matrix, and $\mathbf{c}$ is an $n \times 1$ constant vector. The statistics of the Gaussian white noise are given by

$$E[\mathbf{W}(t)] = 0, \quad E[\mathbf{W}(t)\mathbf{W}(t+t')] = \mathbf{I}\delta(t') \tag{3}$$

where $\delta(\cdot)$ is the Dirac delta function and $\mathbf{I}$ is the $m \times m$ identity matrix. $Y(t)$ in Eqn. 1 is a scalar Poisson white noise excitation (*i.e.*, $Y(t) = \Sigma_{i=1}^{N(t)} Z_i \delta(t - t_i)$, a sequence of Dirac impulses with Poisson arrivals) characterized by the intensity, λ, of the underlying Poisson counting process, $N(t)$, and $\mathbf{Z}$ is a sequence of random variables representing independent random amplitudes identically distributed with density function $p_Z(z)$.

It has been established in Gikhman and Skorohod (1972) that Eqns. 1-3 define a vector Markov process, the behavior of which is completely characterized by its transition probability density function $p(\mathbf{x}, t|\mathbf{x}_0, t_0)$, where $\mathbf{x}_0 = \mathbf{X}(0)$. The density function satisfies both the forward

$$\frac{\partial p}{\partial t} + L_{\mathbf{x}} p = 0 \quad \text{on } \mathbf{\Omega}, \tag{4}$$

and backward generalized Kolmogorov equations

$$-\frac{\partial p}{\partial t_0} + L^*_{\mathbf{x}_0} p = 0 \quad \text{on } \mathbf{\Omega}, \tag{5}$$

subject to the initial, boundary, and normalization conditions, respectively,

$$p(\mathbf{x}, t_0|\mathbf{x}_0, t_0) = \delta(\mathbf{x} - \mathbf{x}_0), \lim_{\|\mathbf{x}\| \to \infty} p(\mathbf{x}, t) \to 0, \text{ and } \int_{\mathfrak{R}^n} p(\mathbf{x}, t|\mathbf{x}_0, t_0) d\mathbf{x} = 1. \tag{6}$$

The operators $L_{\mathbf{x}}$ and $L^*_{\mathbf{x}_0}$ are, respectively,

$$L_{\mathbf{x}}p = \lambda p + \sum_{k=1}^{n} \frac{\partial}{\partial x_k}[a_k(\mathbf{x}, t)p] - \frac{1}{2}\sum_{k=1}^{n}\sum_{j=1}^{n} \frac{\partial^2}{\partial x_k \partial x_j}[\sigma_{kj}p] - \lambda \int_{-\infty}^{\infty} p(\mathbf{x} - \mathbf{c}z, t|\mathbf{x}_0, t_0)p_Z(z)dz \quad (7)$$

and

$$L^*_{\mathbf{x}_0}p = \lambda p - \sum_{k=1}^{n} a_k(\mathbf{x}_0, t_0)\frac{\partial p}{\partial x_{0_k}} - \frac{1}{2}\sum_{k=1}^{n}\sum_{j=1}^{n} \sigma_{kj}\frac{\partial^2 p}{\partial x_{0_k}\partial x_{0_j}} - \lambda \int_{-\infty}^{\infty} p(\mathbf{x}, t|\mathbf{x}_0 + \mathbf{c}z, t_0)p_Z(z)dz \quad (8)$$

where λ is the average arrival rate of the Poisson impulses and $\mathbf{\Sigma} = \mathbf{G}\mathbf{G}^T = [\sigma_{ij}]$.

While exact solutions have been found for several special scalar systems by Vasta (1995), the generalized Kolmogorov equations for dynamical systems with two or more states and arbitrary nonlinearity currently defy analytical solution, leaving computational approaches such as path integral, finite element and finite difference methods, as well as Monte Carlo simulation, to fill the void.

A boundary value problem for the response characteristic function can be derived by exploiting the fact that the response probability density function and characteristic function form a Fourier transform pair. Consequently, the TFGK equation can be found by applying an n-dimensional Fourier transform to the FGK equation. An equivalent method, where the boundary value problem is obtained directly from the state equations of the system, Eqn. 1, is outlined in Grigoriu (1996). The response characteristic function of the system given by, Eqn. 1, is governed by

$$\frac{\partial}{\partial t}\Phi_{\mathbf{X}}(\mathbf{u}, t) = i\mathbf{u}^{\mathrm{T}}E[\mathbf{a}(\mathbf{X}, t)\exp i\mathbf{u}^{\mathrm{T}}\mathbf{X}] - \left[\frac{1}{2}\sum_{k=1}^{n}\sum_{l=1}^{n} u_k u_l \sigma_{kl} - \lambda\{\Phi_Z(\mathbf{c}^{\mathrm{T}}\mathbf{u}) - 1\}\right]\Phi_{\mathbf{X}}(\mathbf{u}, t) \quad (9)$$

subject to the boundary conditions

$$\lim_{\|\mathbf{u}\| \to \infty} \Phi_{\mathbf{X}}(\mathbf{u}, t) \to 0, \qquad \Phi_{\mathbf{X}}(\mathbf{0}, t) = 1, \quad (10)$$

and to an initial condition satisfying the boundary conditions at $t = t_0$. In Eqn. 9, $\Phi_Z(z)$ is the characteristic function of the amplitudes of the pulse train, $\mathbf{u}$ is the n x 1 vector of transform variables, and $\mathbf{a}$, λ, Σ, $\Phi_{\mathbf{X}}(\mathbf{u}, t)$ are as previously defined. The precise nature of Eqn. 9 is not clear at this point; *i.e.*, whether it is a partial differential or an integro-differential equation. However, if analysis is restricted to systems in which the drift coefficient, $\mathbf{a}(\mathbf{x}, t)$, is polynomial in the states, the situation clarifies. The boundary value problem becomes, for $n = 1$ and 2,

respectively,

Case 1: $n = 1$

$$a(x, t) = \sum_{r=1}^{d} a_r(t)x^r \tag{11}$$

$$\frac{\partial}{\partial t}\Phi_X(u, t) = u\sum_{r=1}^{d} a_r(t)i^{1-r}\frac{\partial^r}{\partial u^r}\Phi_X(u, t) - \left[\frac{1}{2}u^2\sigma - \lambda\{\Phi_Z(cu) - 1\}\right]\Phi_X(u, t) \tag{12}$$

Case 2: $n = 2$

$$a_1(\mathbf{x}, t) = \sum_{r=1}^{d}\sum_{s=1}^{d} d_{rs}(t)x_1^r x_2^s, \qquad a_2(\mathbf{x}, t) = \sum_{r=1}^{d}\sum_{s=1}^{d} e_{rs}(t)x_1^r x_2^s \tag{13}$$

$$\begin{aligned}\frac{\partial}{\partial t}\Phi_{\mathbf{X}}(\mathbf{u}, t) = {} & u_1\sum_{r=1}^{d}\sum_{s=1}^{d} i^{1-r-s}d_{rs}(t)\frac{\partial^{r+s}}{\partial u_1^r \partial u_2^s}\Phi_{\mathbf{X}}(\mathbf{u}, t) \\ & + u_2\sum_{r=1}^{d}\sum_{s=1}^{d} i^{1-r-s}e_{rs}(t)\frac{\partial^{r+s}}{\partial u_1^r \partial u_2^s}\Phi_{\mathbf{X}}(\mathbf{u}, t) \\ & - \left[\frac{1}{2}\sum_{k=1}^{n}\sum_{l=1}^{n} u_k u_l \sigma_{kl} - \lambda\{\Phi_Z(\mathbf{c}^{\mathrm{T}}\mathbf{u}) - 1\}\right]\end{aligned} \tag{14}$$

since

$$E[X^r \exp i\mathbf{u}^{\mathrm{T}}X] = \frac{1}{i^r}\frac{\partial^r}{\partial u^r}\Phi_X(u, t), \qquad E[(X_1^r X_2^s)\exp i\mathbf{u}^{\mathrm{T}}\mathbf{X}] = \frac{1}{i^{r+s}}\frac{\partial^{r+s}}{\partial u_1^r \partial u_2^s}\Phi_{\mathbf{X}}(\mathbf{u}, t) \tag{15}$$

by definition of the characteristic function. Similar equations can be derived for cases in which $n > 2$.

Note that, for this class of system, the boundary value problem (TFGK) for the characteristic function, $\Phi_{\mathbf{X}}(\mathbf{u}, t)$, is an n-dimensional partial differential rather than integro-differential equation. Note, also, that the TFGK equations can be complex valued, although here only systems with odd nonlinearities will be studied; consequently, the equations will be purely real. Finally, it is interesting to further note that the highest order derivative appearing in the TFGK equation is equivalent to the highest order nonlinearity appearing in the drift vector $\mathbf{a}(\mathbf{X}, t)$ of the system, as has been observed by Grigoriu (1996). Eqn. 14 is the boundary value problem that will be the

focus of our study.

SOLUTION OF THE TWO-DIMENSIONAL TFGK EQUATION

The numerical solution of Eqn. 14 can be divided into four parts: (1) spatial discretization, (2) temporal discretization, (3) solution of the system of linear equations governing the nodal values of the characteristic function, and (4) postprocessing of results.

Spatial Discretization

The authors have previously applied standard Bubnov-Galerkin finite element techniques to the solution of Fokker-Planck equations in two and three dimensions in Spencer and Bergman (1993) and Wojtkiewicz, *et al.* (1995). Here, though, it was decided to use finite difference methods in order to avoid shape functions of high order necessitated by the higher order derivative terms in the TFGK equation.

Recently, high order finite difference schemes to solve Fokker-Planck equations have been developed by Wojtkiewicz, Bergman and Spencer (1998), and similar methods will be employed herein. Through the use of Taylor expansions of the characteristic function about prudently selected points on a uniform mesh, difference stencils of arbitrary orders of accuracy can be developed. By including more of the neighboring nodal points, schemes with smaller discretization error are obtainable. Derivative approximations corresponding to a tenth order accurate scheme were determined and can be found in Wojtkiewicz, *et al.* (1998).

Boundary conditions must be imposed as part of the spatial discretization process. The formal conditions for the TFGK equation are Dirichlet, located at infinity as implied in Eqn. 10, along with the constraint at the origin. The former are not readily implementable within a finite difference framework. Rather, one prescribes Dirichlet conditions at the edges of a finite, computational mesh of sufficient extent such that the characteristic function is essentially (*i.e.*, within roundoff) zero everywhere outside the mesh.

Spatial discretization of the TFGK equation using the tenth order finite difference scheme results in a system of first order differential equations given by

$$\dot{\Phi}_{m,n} + \mathbf{K}\Phi_{m,n} = \mathbf{0} \tag{16}$$

where $\Phi_{m,n} = \Phi(m\Delta u_1, n\Delta u_2)$ and $\mathbf{K}$ is a matrix of dimension $max(m)$ x $max(n)$.

Temporal Discretization

The system of differential equations for the nodal characteristic values, Eqn. 16, is further discretized in time using the second order accurate (in time) Crank-Nicholson method,

$$\left(\mathbf{I}+\frac{\mathbf{K}\Delta t}{2}\right)\Phi_{m,n}^{k+1} = \left(\mathbf{I}-\frac{\mathbf{K}\Delta t}{2}\right)\Phi_{m,n}^{k}. \tag{17}$$

By solving this system of algebraic equations at each time step, the evolution of the nodal characteristic function values can be computed from a given initial condition. An initial multivariate Gaussian characteristic function with origin at $\mathbf{x}_0$ is prescribed which satisfies the boundary conditions of the problem and which is sufficiently smooth to make the evolution computation tractable.

Solution of the Linear System of Evolution Equations

The efficient solution of the linear system, Eqn. 17, is a formidable computational task as the coefficient matrix $\left(\mathbf{I}+\frac{\mathbf{K}\Delta t}{2}\right)$ is, in general, nonsymmetric and sign indefinite. Sparse matrix techniques were used to assemble and store the coefficient matrices to conserve memory. The iterative solver GMRES (Generalized Minimum Residual) (*cf.* Saad (1996)) was used in concert with an incomplete LU preconditioner to solve Eqn. 17 at each time step. Further details can be found in Wojtkiewicz, et al. (1998).

Postprocessing of Numerical Results

Once the characteristic function is determined at all times of interest, various response statistics such as moments and upcrossing rate can be computed from it directly. For instance, when $n = 2$, the response moments are given by

$$E[X_1^p(t)X_2^q(t)] = \frac{\partial^{p+q}}{\partial u_1^p \partial u_2^q}\Phi_{\mathbf{X}}(\mathbf{u},t)\bigg|_{\mathbf{u}=\mathbf{0}} \tag{18}$$

and the mean upcrossing rate of level a, ν_a^+, by

$$\nu_a^+(a,t) = -\frac{1}{(2\pi)^2}\int_{-\infty}^{\infty}\int_{-\infty}^{\infty}\frac{1}{u_2}\frac{\partial}{\partial u_2}\Phi_{\mathbf{X}}(\mathbf{u},t)\exp(-iu_1 a)d\mathbf{u}. \tag{19}$$

The probability density function, no longer conditional due to application of the theorem of total probability, can be recovered by taking an inverse Fourier transform of the unconditional characteristic function; *i.e.*,

$$p_{\mathbf{X}}(\mathbf{x}, t) = \int_{-\infty}^{\infty} \cdots \int_{-\infty}^{\infty} \exp(-i\mathbf{u}^{\mathrm{T}}\mathbf{x})\Phi_{\mathbf{X}}(\mathbf{u}, t)d\mathbf{u}. \tag{20}$$

Though the response moments and upcrossing rate can be computed directly from the characteristic function, their determination can sometimes be made more tractable by determining them from the computed density function obtained from the characteristic function by numerical Fourier inversion. For the present case, the response moments are given by

$$E[X_1^p(t)X_2^q(t)] = \int_{-\infty}^{\infty}\int_{-\infty}^{\infty} x_1^p x_2^q p_{\mathbf{X}}(\mathbf{x}, t)d\mathbf{x} = \alpha(p, q) \tag{21}$$

and the mean upcrossing rate, ν_a^+, by

$$\nu_a^+(a, t) = \int_0^{\infty} x_2 p_{\mathbf{X}}(a, x_2, t)dx_2. \tag{22}$$

The solution process is general and can be applied to any memoryless system possessing polynomial nonlinearities. A single degree-of-freedom Duffing oscillator subjected to a combination of additive Gaussian and Poisson white noise excitations will be examined to assess the sensitivity of the response to each.

SINGLE DEGREE-OF-FREEDOM DUFFING OSCILLATOR

The Duffing oscillator models the stiffness nonlinearity encountered in many mechanical and structural systems. Here, the response of two Duffing systems to the sum of additive Gaussian and Poisson white noises will be analyzed using the previously described method. The system of stochastic differential equations is given by

$$\dot{X}_1 = X_2, \qquad \dot{X}_2 = -\varepsilon\omega^2 X_1^3 - 2\zeta\omega X_2 - \gamma\omega^2 X_1 + Y(t) + \sqrt{2D}W(t) \tag{23}$$

where $W(t)$ is a unit intensity Gaussian white noise process, and $Y(t)$ is Poisson white noise, defined previously. The FGK equation for this system is given by

$$\frac{\partial}{\partial t}p_{\mathbf{X}}(\mathbf{x}, t) + \frac{\partial}{\partial x_1}(x_2 p_{\mathbf{X}}(\mathbf{x}, t)) - \frac{\partial}{\partial x_2}[(2\zeta\omega_n x_2 + \gamma\omega^2 x_1 + \varepsilon\omega^2 x_1^3)p_{\mathbf{X}}(\mathbf{x}, t)] - D\frac{\partial^2}{\partial x_2^2}p_{\mathbf{X}}(\mathbf{x}, t)$$

$$+\lambda p_{\mathbf{X}}(\mathbf{x}, t) - \lambda \int_{-\infty}^{\infty} p_{\mathbf{X}}(x_1, x_2 - z, t) p_Z(z) dz = 0 \tag{24}$$

where $p_{\mathbf{X}}(\mathbf{x}, t) = p_{X_1 X_2}(x_1, x_2, t)$. Taking the Fourier transform of Eqn. 24 with respect to the spatial variables x_1 and x_2 results in the TFGK equation for the characteristic function, $\Phi_{\mathbf{X}}(\mathbf{u}, t) = \Phi_{X_1 X_2}(u_1, u_2, t)$,

$$\begin{aligned}
&\frac{\partial}{\partial t}\Phi_{\mathbf{X}}(\mathbf{u}, t) + (2\zeta\omega u_2 - u_1)\frac{\partial}{\partial u_2}\Phi_{\mathbf{X}}(\mathbf{u}, t) \\
&+ \gamma\omega^2 u_2 \frac{\partial}{\partial u_1}\Phi_{\mathbf{X}}(\mathbf{u}, t) - \varepsilon\omega^2 u_2 \frac{\partial^3}{\partial u_1^3}\Phi_{\mathbf{X}}(\mathbf{u}, t) \\
&+ \lambda\Phi_{\mathbf{X}}(\mathbf{u}, t)[1 - \Phi_Z(u_2)] + D u_2^2 \Phi_{\mathbf{X}}(\mathbf{u}, t) = 0
\end{aligned} \tag{25}$$

boundary conditions $\Phi_{\mathbf{X}}(\mathbf{0}, t) = 1$ and $\Phi_{\mathbf{X}}(\mathbf{u}, t) = 0 \ \forall \ \mathbf{u} \notin [-20, 20] \times [-20, 20]$, and initial condition $\Phi_{\mathbf{X}}(\mathbf{u}, 0) = e^{-(u_1^2 + u_2^2)/2}$ corresponding to a zero-mean, bivariate Gaussian process with unit variances.

The nonstationary problem was solved by the finite difference method for system parameters $\varepsilon = 1$, $\zeta = 0.2$, and $\omega = 1$ on the computational domain $[-20,20] \times [-20,20]$. Six systems were considered: the first three examined a system with positive linear stiffness $\gamma = 1$ exhibiting a single stable equilibrium at the origin, while the second three examined a system with negative linear stiffness $\gamma = -1$ possessing two stable equilibria at $x = \pm\sqrt{1/\varepsilon}$, respectively, and one unstable equilibrium at the origin. For each group, three different excitations were studied. These consisted of the pure Poisson white noise case with bilateral exponential pulses (*i.e.*, $\Phi_Z(z) = \alpha^2/(\alpha^2 + z^2)$), the combination noise, and the pure Gaussian white noise case. In each case, parameters of the Gaussian and Poisson white noises were chosen to maintain equivalent second moment characteristics (*i.e.*, $2D + 2\frac{\lambda}{\alpha^2} = \text{constant}$).

TABLE 1: SYSTEM PARAMETERS

System #	γ	α	λ	D
1	1.0	5.0	10.0	0.0
2	1.0	4.0	4.0	0.15
3	1.0	4.0	0.0	0.40
4	-1.0	10.0	5.0	0.0
5	-1.0	4.0	4.0	0.15
6	-1.0	4.0	0.0	0.40

The system parameters are summarized in Table 1. While the excitation parameters were chosen so that, in all cases, the inputs were second order equivalent, no such property is guaranteed of the higher order moments of the input. The effects of the non-Gaussian input are of interest. The stationary response characteristic function for the first three systems is shown in Fig. 1, and the corresponding stationary probability density function is shown in Fig. 2. The stationary response characteristic function for the second three systems is shown in Fig. 3, and the corresponding stationary probability density function in Fig. 4. For both systems, the characteristic functions and probability density functions were indistinguishable for the three load combinations. The effects of the non-Gaussian components of the input can, however, be seen by examining the higher order moments of response. This analysis was performed, and the results summarized in Table 2.

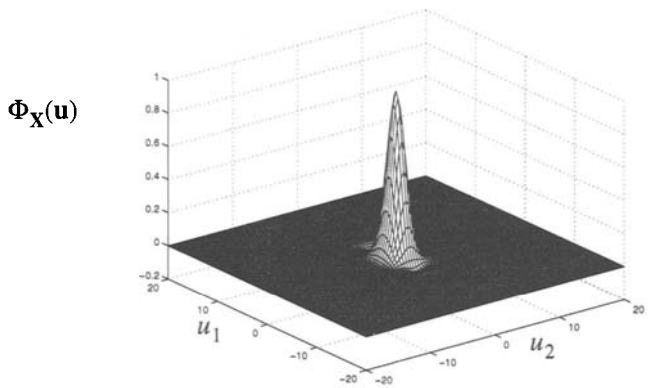

Fig. 1: Stationary characteristic function, $\Phi_{\mathbf{X}}(\mathbf{u})$, for the SDOF Duffing example; $\gamma = 1$.

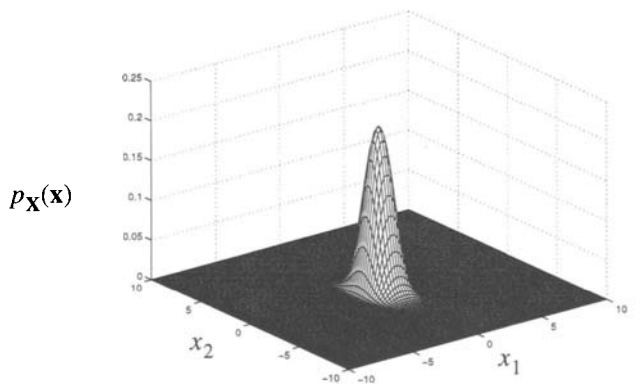

Fig. 2: Stationary probability density function, $p_{\mathbf{X}}(\mathbf{x})$, for the SDOF Duffing example; $\gamma = 1$.

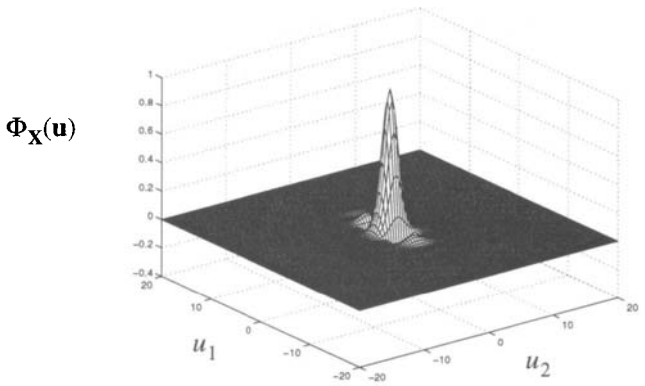

Fig. 4: Stationary characteristic function, $\Phi_{\mathbf{X}}(\mathbf{u})$, for the SDOF Duffing example; $\gamma = -1$.

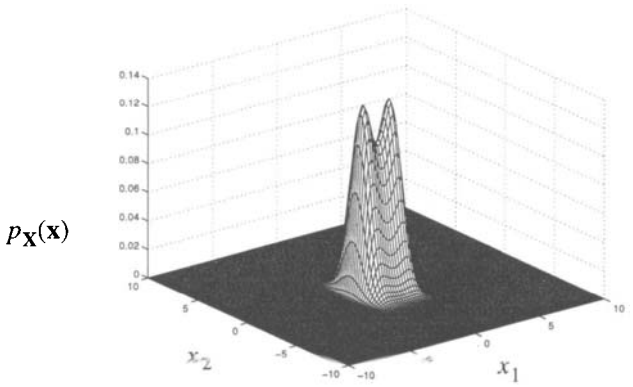

Fig. 5: Stationary probability density function, $p_{\mathbf{X}}(\mathbf{x})$, for the SDOF Duffing example; $\gamma = -1$

It can be seen in Table 2 that the effects of the non-Gaussianaity of the input on second order response moments is very small. However, the effects are quite apparent in the fourth order moments, especially that of the velocity process, $\alpha(0, 4)$, where deviations ranging up to eight percent are observed.

TABLE 2: SECOND AND FOURTH MOMENTS OF RESPONSE

	$\alpha(2, 0)$	$\alpha(0, 2)$	$\alpha(4, 0)$	$\alpha(2, 2)$	$\alpha(0, 4)$
$\gamma = 1 \quad D = 0 \; \lambda = 10 \quad \alpha = 5$	0.4638	1.0003	0.53626	0.4832	3.198
$\gamma = 1 \quad D = 0.15 \; \lambda = 4 \quad \alpha = 4$	0.4640	1.0003	0.53604	0.4828	3.193
$\gamma = 1 \quad D = 0.4 \; \lambda = 0 \quad \alpha = 5$	0.4679	1.0002	0.53210	0.4680	2.999
Exact Solution: $\gamma = 1 \quad D = 0.4$	0.4679	1	0.53208	.04679	3
$\gamma = -1 \quad D = 0 \; \lambda = 10 \quad \alpha = 5$	1.0396	1.0020	2.0409	1.0612	3.224
$\gamma = -1 \quad D = 0.15 \; \lambda = 4 \; \alpha = 4$	1.0394	1.0003	2.0397	1.0584	3.210
$\gamma = -1 \quad D = 0.4 \; \lambda = 0 \; \alpha = 5$	1.0419	1.0002	2.0420	1.0420	2.999
Exact Solution: $\gamma = 1 \quad D = 0.4$	1.0418	1	2.0418	1.0418	3

CONCLUSIONS

The ability to formulate and solve a broad class of boundary value problems describing the nonstationary response of both linear and nonlinear systems subjected to excitations modeled as combinations of Gaussian and Poisson white noise has been demonstrated. The proposed method can accommodate a wide variety of pulse distributions and intensities. These input processes provide a more realistic way to model natural phenomena, more so than prior models employing only Gaussian white noise. The formulation allows the simultaneous application of Gaussian and Poisson input processes as well as the computation of nonstationary response probability and statistics. The boundary value problem, which we have called the TFGK equation, is obtained through Fourier transformation of the integro-differential forward generalized Kolmogorov equation and is solved here by a high order finite difference method. Recovery of the joint probability density function of the response process is accomplished through inverse numerical Fourier transformation. The computation has been shown to be efficacious for the two-dimensional problem presented herein and is able to identify important non-normal characteristics of the response, most apparent in higher order moments.

REFERENCES

Cornell, C.A. (1964). *Stochastic Process Models in Structural Engineering.* Technical Report 34. Department of Civil Engineering, Stanford University, Stanford, CA.

Gikhman, I.I. and Skorohod, A.W. (1972). *Stochastic Differential Equations.* Berlin: Springer-Verlag.

Grigoriu, M. (1995). *Applied Non-Gaussian Processes.* New Jersey: Prentice-Hall.

Grigoriu, M. (1996). A partial differential equation for the characteristic function of the response of non-linear systems to additive Poisson white noise. *Journal of Sound and Vibration*, **198**, 193-202.

Lin, Y.K., (1963). Application of non-stationary shot noise in the study of system response to non-stationary excitations. *Journal of Applied Mechanics, ASME* **30,** 555-558.

Roberts, J.B. (1972). System response to random impulses. *Journal of Sound and Vibration* **24**:1, 23-34.

Saad, Y. (1996). *Iterative Methods for Sparse Linear Systems*. PWS:Boston.

Spencer, B.F. Jr. and Bergman, L.A. (1993). On the numerical solution of the Fokker–Planck equation for nonlinear stochastic systems. *Nonlinear Dynamics* **4,** 357-372.

Tung, C.C., (1972). Random response of highway bridges to vehicle loads. *Journal of Engineering Mechanics, ASCE* **93,** 79-94.

Tylikowski, A. and Marowski, W. (1986). Vibration of a non-linear single degree of freedom system due to Poissonian impulse excitation. *International Journal of Nonlinear Mechanics* **21**, 229-238.

Vasta, M. (1995). Exact stationary solution for a class of non-linear systems driven by non-normal delta-correlated processes. *International Journal of Non-linear Mechanics* **30**, 407-418.

Wojtkiewicz, S.F., Bergman, L.A., and Spencer, B.F. Jr., (1995). Numerical solution of some three state random vibration problems. *Proceedings of the 15th Biennial Conference on Mechanical Vibration and Noise*, New York:ASME, 939-947.

Wojtkiewicz, S.F., Bergman, L.A. and Spencer, B.F. Jr. (1998). High fidelity numerical solutions of the Fokker-Planck equation. *Proceedings of the 7th International Conference on Structural Safety and Reliability,* Kyoto:IASSAR, in press.

Wojtkiewicz, S.F., Johnson, E.A., Bergman, L.A., Grigoriu, M. and Spencer, B.F. Jr. (1998). Response of stochastic dynamical systems driven by additive Gaussian and Poisson white noises: solution of a forward generalized Kolmogorov equation by a spectral finite difference method. *Computer Methods in Applied Mechanics and Engineering*, in press.

This Page Intentionally Left Blank

SOLVING LARGE SYSTEMS OF EQUATIONS ON INTEL-PARAGON

P. Chen[1] P. Tong[2] T.Y.P. Chang[2] S.L. Sun[1]

[1]Peking University, 100871 Beijing, China
[2]The Hong Kong University of Science & Technology, Hong Kong

ABSTRACT

In the area of high-performance computation, direct methods for solving large systems of equations on distributed memory machines is one very important issue. In general, there are two ways to improve the computational efficiency of the solution procedure. One is to increase the sequential efficiency by maximizing vector operations and/or using other techniques, such as unrolling. The other is to decrease the communication cost across processors. Conventionally, the pure JIK form of $\mathbf{LDL}^T$ factorization algorithms based on the column skyline storage scheme lead to natural synchronization, i.e., starting a step, all but one processor waits for the result of a particular processor for the j-th column or j-th block. Carefully rearranging the communication order, this paper proposes a mixed JIK form with one-step overshoot for sending and receiving. Associated with asynchronous communication, the mixed asynchronous approach can greatly reduce the processor idling time and enhance therefore the performance of parallel computation. Several practical examples show the efficiency of this approach.

KEYWORDS: linear equation, parallel computation, finite element method

INTRODUCTION

General purpose finite element codes have been widely used for both linear and non-linear structural problems. Many of the real-world problems in science and engineering applications are large in size, and require extensive computational efforts. A prevailing trend in industry is that products must meet more stringent design requirements and in turn require more detailed analysis. Therefore, even more computational efforts for solving large-scale problems will be needed. The computing power of current sequential machines is generally inadequate. Recent

development in parallel computers provides an opportunity for significant gains in computing capability and also in broadening the range of structural problems that can be solved. The key to success is in the effective implementation of suitable parallel algorithms that can exploit the concurrent features of such machines. In this connection, we shall study a very important stage of finite element analysis – solving large system of equations. Originally the code runs on sequential machines; we shall convert the code using parallel constructions for Intel-Paragon and study their performance.

In computation, the finite element discretization of elliptical differential equations usually results in a large linear system of equations in the form $\mathbf{Ax} = \mathbf{f}$ with positive stiffness matrix $\mathbf{A}^T=\mathbf{A}$. In this paper, we consider the direct method of solution for solving a large sparse system of linear equations with symmetric matrix. The focus of the study is to design an efficient computational algorithm that exploits the multiple-processing and vector capabilities of today's high-performance computer architecture of distributed memory.

Conventionally, the pure JIK form of $\mathbf{LDL}^T$ factorization algorithm based on the skyline or half-bandwidth storage scheme has been widely implemented in parallel computation on machines with distributed memory. At each step of the extraneous loop, the JIK form lead to a sending and receiving synchronization due to message passing for the j-th column or j-th block. This is obviously the bottleneck of solving scheme. In order to enlarge the bottleneck, this paper proposes a mixed JIK form with one-step overshoot for asynchronous sending and receiving. This mixed approach can greatly reduce the processor idling time and enhance therefore the performance of parallel computation. Several practical examples show the efficiency of this approach.

REVIEW OF FACTORIZATION

Solving the following equation

$$\mathbf{Ax} = \mathbf{f} \quad \text{with} \quad \mathbf{A}^T = \mathbf{A}, \tag{1}$$

involves three major steps:

1. Factorization:

$$\mathbf{A} = \mathbf{LU} = \mathbf{LDL}^T; \tag{2}$$

2. Forward reduction:

$$\mathbf{LD\,y} = \mathbf{f}; \tag{3}$$

3. Back substitution:

$$\mathbf{L}^T\mathbf{x} = \mathbf{y}. \tag{4}$$

Here $\mathbf{L}$ denotes a lower triangular matrix with its diagonal elements equal to 1, and $\mathbf{D}$ a diagonal matrix. Among the three steps, factorization takes much more computing time as

compared to the other two steps. Therefore, we shall focus on the solution efficiency of factorization.

Following the notation in [2,3], there are two basic operations in $\mathbf{LDL}^T$ factorization, which are designated by Task(i,j,k) and Div(i,j). The operation Task(i,j,k), k<j<=i, uses L(j,k) and U(k,i) to modify A(j,i), i.e. A(i,j). The operation Div(i,k) converts U(k,i) to L(i,k); i.e.

Task(i,j,k):

$$A(j,i) = A(j,i) - L(j,k)*U(k,i)$$

Div(i,k):

$$L(i,k) = U(k,i) / D(k)$$

Since the stiffness matrix **A** is symmetric, only the upper (or lower) triangle of the matrix is loaded into memory , and **L** as well as **U** will occupy the same memory location as **A**. One may notice that Task(i,j,k) can be done in various orders Operation Task(i,j,k) uses L(j,k) and U(k,i), which are results of Task(i,j,:), Div(j,k) and Task(i,k,*), respectively, to modify A(j,i). Once Task(i,j,k) is done for all k, A(j,i) becomes U(i,j) and then one is ready to modify the next A(j,i). Circling the indices i, j and k, we can obtain different factorization schemes. Their performance is strongly related to the storage scheme used and the vector processing implementation[3].

Denoting neq as the number of equations, the factorization of JIK form can be outlined for a full sparse symmetric matrix as:

```
do j = 1, neq
   CTask(j,j)
   do i = j+1, ie
      CTask(i,j)
   end do
end do
```

JIK Algorithm

```
do bj = 1, nblk
   BCTask(bj,bj)
   do bi = bj+1, bie
      BCTask(bi,bj)
   end do
end do
```

Blocked JIK Algorithm

Where ie specifies the last column that has a common part with column j. The CTask(i,j)= Task(i,j,*) denotes *reduction of column j by column i*, and it produces the matrix element U(i,j) in the j-th column. The operation is a dot-product of two vectors over the index k in Task(i,j,k). The task CTask(j,j)=Task(j,j,*)+Div(j,*) is known as *reduction of column j by itself*; it converts U(i,j) to L(j,i) and produces the matrix element D(j). The operation involves both dot-product and vector division[1,4,6,7].

Since the matrix **A** arising from FEM is usually a sparse matrix, there are several ways to exploit its sparsity. In finite element analysis the column-oriented *skyline storage scheme* has been known as to be particularly effective[1]. In this scheme, only those terms of the upper triangle of matrix under the skyline of the highest non-zero term in each column are stored in

a one-dimensional pattern. It is well-known that only the terms under the skyline can be non-zero in the factorization procedure. Because the height of each column varies, it is also called as *active column scheme*. Associated with this storage scheme, the JIK form for parallel computation and the IJK form for sequential computation can easily arrange the arithmetic operations in the dot-product dominated procedure[3].

In implementation, all columns are linked into a one-dimensional real array, while an integer array points the beginning of each column, and only those terms of the upper triangle of global stiffness matrix under the skyline of the highest non-zero term in each column are handled. It is well-known that only the terms under the skyline can be non-zero in the factorization procedure. Some equation numbering technique such as reverse Cuthill-Mckee (RCM) algorithm can be employed to minimize the total number of terms under skyline.

In parallel computation, a *block* concept has been introduced to reduce the communication overhead by sending or receiving a number of columns simultaneously[4,5]. Replacing column operations CTask(i,j) by block operations BCTask(bi,bj), and the number of equations neq by the number of blocks nblk, we obtain the *Blocked JIK Algorithm*, in which BCTask(bi,bj) consists of several CTask(i,j)'s.

3 INTEL-PARAGON MACHINE AND ITS PERFORMANCE

The Intel-Paragon is a particular form of parallel machines which makes concurrent computation available at relatively low cost. The hardware consists of a number of nodes, disk systems, communications networks all mounted together in one or several cabinets with power supply for the whole system. Each node is a separate board, rather like a separate computer. It has memory, network interface, expansion port, cache and so on. The nodes are linked together through a back plane which provides communication between them[10].

The Paragon is a multiple instruction multiple data stream (MIMD) type machine. Each single node works like a sequential machine; data communication between nodes is realized in message passing style. The Paragon node is based on the 64 bit i860XP™ microprocessor produced by Intel, whose theoretical speed is 100 MFLOPS in 32 bit floating point and 75 MFLOPS for 64 bit in floating point operations.

A single node of the Paragon XP/S consists of two i860XP™ microprocessors: one for computation and the other for communication. The compute processor is for computation and the communication processor handles all message-protocol processing, thus freeing the computation processor to perform computations. Each compute processor has 32 MB of local memory but only about 24 MB is available for applications, the rest being used for the micro kernel, OSF (Operating System Foundation) server and system buffers.

The Paragon at the Hong Kong University of Science & Technology (HKUST) has 140 compute nodes. Mostly, 128 nodes can be used for one application under control of the *Network Queuing System* (NQS). In this study we utilized maximum 64 nodes.

The Paragon Operating System *Open Software Foundation* (OSF/1) used in this study is version R1.3.3. The software platform in the study consists of Paragon FORTRAN version 4.1 and the native message passing library NX.

As a benchmark, the dot-product of the simple form:

```
do 100 i=1,nn
   ss = ss + a(i)*b(i)
end do
```

is tested on the Intel-Paragon machine, because the dot-product is the key operation of factorization in the skyline storage scheme. Utilizing different compiler switches, dynamic allocated common block and various vector lengths, we obtained the wall-clock time scaled to 10^6 multiplications as shown in Table 1.

TABLE 1
WALL-CLOCK TIME FOR DOT-PRODUCT (SEC.)

vector length	case 1	case 2
10^3	0.7031	0.1178
10^4	0.7891	0.0938
10^5	0.7785	0.0836
10^6	0.7781	0.0822

Compiling case 1: no optimization
Compiling case 2: -O4 -Mvect optimization

Besides the dot-product, the average wall-clock time scaled to 10^6 operations of more tests on vector operations resulted in Table 2.

TABLE 2
AVERAGE WALL-CLOCK TIME OF VECTOR OPERATION (SEC.)

dot-product ss=a(i)*b(i)	addition a(i)=a(i)+b(i)	multiplication a(i)=a(i)*b(i)	division a(i)=a(i)/b(i)
0.0920	0.1250	0.1289	4.0927

Compiling: -O4 -Mvect optimization

Reading from Table 2, division needs much more time than other operations. In our tests the factor is about 35 in comparison with vector multiplication and about 45 in comparison with dot-product. Our tests show that on SUN Sparc 30, HP 9000/730, SGI Power Indigo 2 the wall-clock time ratios of vector division and vector multiplication are in the same order.

These test results show that in vector operation the practical running speed of Paragon is about 10 MFLOPS, which is unfortunately much lower than the announced theoretical speed of 75 MFLOPS. Although some delicate techniques, such as unrolling, can greatly improve the vector performance[8,9], they are not installed in our code.

Due to the huge time difference between multiplication and division, the inverse of diagonal matrix **D** is suggested by authors to be stored in the calculation, so that a large amount of divisions in CTask(j,j)can be replaced by corresponding multiplications. This improvement makes the sequential code more efficient.

BASIC PARALLELIZATION

Consider the case that there are Np processors labeled from 1 to Np. The columns and/or blocks are *scattered* to different processors for the skyline solver in a wrapping manner where block bi is held by its owner processor mod(bi-1,Np)+1=iam as shown in Figure 1 for 4 nodes[5,6,7,8,9].

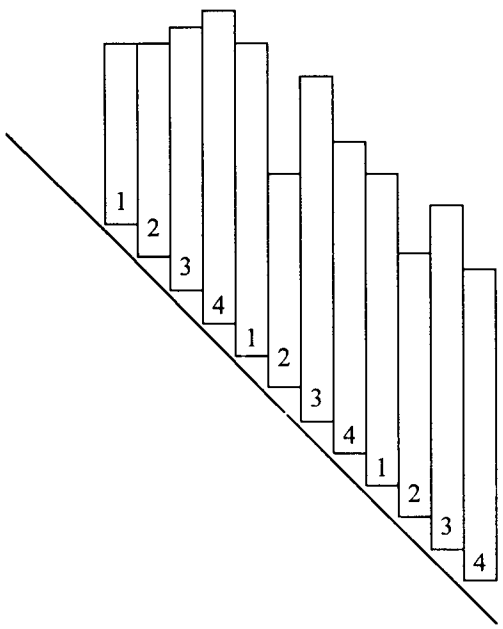

Figure 1: Wrapping Distribution of Blocks (4 nodes)

In programming, all blocks stored in an individual processor iam, that are of an identical label in Figure 1,are linked into a one-dimensional real array. Any block of other labels does not reside permanently in this processor iam, and it is passed to this processor iam only when it is the master block bj of extraneous loop in Algorithm 1. This distributed data structure allows the data locality to be independent of that of the target processor. The corresponding algorithm is outlined as:

```
do bj = 1, nblk
   ! sequential computation for master block bj
   if it is owner of block bj
     BCTask (bj,bj)
   end if
   ! sending and receiving synchronization
   if it is owner of block bj
```

```
    send bj to others
  else
    receive bj
  end if
  ! parallel computation
  do bi = bjb, bje, Np
    BCTask (bi,bj)
  end do
end do
```

Algorithm 1: Basic Parallel Block JIK Algorithm

in which blocks bjb and bje (bje>=bjb>bj) are, respectively, the first and last blocks that couple block bj. They are determined by the profile of matrix **A** and the processor labeling.

PARALLELIZATION WITH ONE-STEP OVERSHOOT

We shall analyze the algorithm given above. For simplification, we assume that there is enough core memory to hold the matrix **A** across all the nodes of the computer. The computation can be classified into the sequential part BCTask(bj,bj) and the parallel part BCTask(bi,bj), bi>bj, where bi's are distributed across all nodes. The key to get higher speedup is to reduce the sequential part (including computing and waiting). We found that the bottleneck occurred in communication. At each loop of bj, all processors except the master processor iam [=mod(bj-1,Np)+1] of block bj waited for the factored master block bj. In other words, all processors are *synchronized* by the sending and receiving activities.

In practice, the idle time due to communication and working load could be much longer than the computation time for most of the processors. This limits the extent of possible speedup improvement. We must reduce the idle time in order to improve the parallel performance.

As an example, we consider an execution with 4 nodes, that are labeled from 1 to 4. Assume that the extraneous loop for bj=5, processor 1 is clearly the owner of block bj=5. While doing self-reduction BCTask(5,5), processors labeled 2,3 and 4 wait for receiving block 5 sent by processor 1. Once processor 2 receives block bj=5, it starts its own works BCTask(6,5), BCTask(10,5), BCTask(14,5) and so on. Assume the height of each column takes a constant value; processor 2 will have the heaviest working load in the parallel part of tasks. So the sequential part of step bj=6 will start when all other processors have finished their own tasks and have been waiting for the next master block 6.

Clearly, the sending and receiving *synchronization* of the master block is a bottleneck of parallel computation on distributed memory machines. For this reason, the parallel computation efficiency of $\mathbf{LDL}^T$ in the JIK form on distributed memory machines is much lower than expected.

The prerequisite to start BCTask (bj+1,bj+1) (A in Figure 2) depends only upon the complement of BCTask (bj+1, bj) (α in Figure 2) and not upon the complement of BCTask

(bj+1,bj+Np), BCTask (bj+1,bj+2Np) .. (β,χ in Figure 2). In conclusion, the blocked JIK form is not the only way to arrange the $\mathbf{LDL}^T$ factorization.

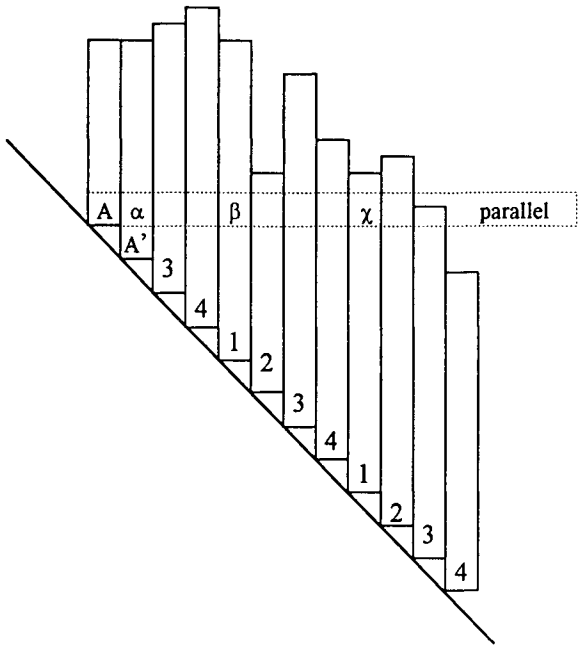

Figure 2: One-step Overshoot Concept (4 nodes)

Using the asynchronous communication model for receiving, we adopt an algorithm with overshoot to minimize the idle time as shown in Fig. 1. In the design, the task order by the processor 2 follows the route A-A'-α-β-χ... rather than the route A-α-β-χ...-A' in the algorithm of Table 1. Clearly, the A' corresponding task BCTask (bj+1=6,bj+1=6) has been overshot into the parallel part of the step bj=5. Once the block bj+1=6 is factored, the master processor for block bj+1 will immediately send the block to the others that may still work on the parallel part for step bj=5. This leads to the one-step overshoot scheme. Please note that in this algorithm synchronous communication model cannot be used.

NUMERICAL RESULTS AND REMARKS

In order to evaluate the computational time and parallelism of the one-step overshot algorithm, we consider the flex joint of a tension-leg of an offshore platform. We discretize the flex joint using finite elements of different mesh sizes. Because of symmetry in geometry, material and loading, only half of the flex joint is considered in the analysis. Table 3 summarizes the parameters of the analysis, where *numnp* denotes the number of nodes, *neq* denotes number of equations, and *m* is the average half-bandwidth.

TABLE 3
FINITE ELEMENT MODELS OF A FLEX JOINT

model	n_r	n_θ	n_z	*numnp*	*neq*	*m*
1	8	20	23	4536	12764	554
2	1	35	24	8100	23155	667
3	10	35	32	13068	37557	1071

In Table 4, the average wall-clock time, *Tp*, required for one-step overshoot $\mathbf{LDL}^T$ factorization with *p* processors running at HKUST is listed in Table 4. The corresponding results of the parallel speedup, $Sp=T_1/Tp$, and the parallel efficiency, $Ep=Tp/p$, calculated on *Tp* are shown in the same table. The wall-clock time reflects the parallel computation performance. In order to test the speedup and the efficiency equitably, all cases were executed four times for each given number of processors. In the table, BC and RS represent broadcasting and ring-sending models of communication[6,8,9]. All communications are asynchronous. We have to mention that the recorded wall-clock times are very discretized. In some cases of small number of processors, the standard deviation were as high as 30%, so the performance measurement was a difficult job.

TABLE 4
PERFORMANCE OF ONE-STEP OVERSHOOT ALGORITHM

performance			number of processors						
model	sending	term	1	2	4	8	16	32	64
1	BC	*Tp*	278.3	153.5	89.1	70.1	59.7	41.7	33.1
		Sp	1.000	1.812	3.124	3.969	5.086	6.675	8.400
		Ep	1.000	0.906	0.781	0.496	0.424	0.209	0.131
	RS	*Tp*		138	85.6	65.2	64.6	51.6	53.6
		Sp		2.014	3.251	4.268	4.308	5.393	5.192
		Ep		1.007	0.813	0.534	0.269	0.169	0.081
2	BC	*Tp*	674.5	344.8	224.5	151.9	132	103	85.7
		Sp	1.000	1.956	3.004	4.439	5.109	6.547	7.871
		Ep	1.000	0.978	0.751	0.555	0.319	0.205	0.123
	RS	*Tp*		344.8	210.1	125.5	215.1	137	123.1
		Sp		1.956	3.21	5.375	3.136	4.923	5.479
		Ep		0.978	0.803	0.672	0.196	0.154	0.086
3	BC	*Tp*	2300.8	1188.1	632.9	479.4	326.3	187.4	112.3
		Sp	1.000	1.937	3.636	4.800	7.051	12.28	20.48
		Ep	1.000	0.968	0.909	0.600	0.441	0.380	0.320
	RS	*Tp*		1191.7	680.1	388.6	700.1	524.4	289.9
		Sp		1.930	3.383	5.921	3.286	4.387	7.936
		Ep		0.965	0.846	0.740	0.205	0.274	0.124

As a reference, the wall-clock time, *Tp*, required by the basic parallel algorithm is listed. We can observe great difference.

TABLE 4
WALL-CLOCK TIME FOR BASIC PARALLEL ALGORITHM

wall-clock time		number of processors						
model	sending	1	2	4	8	16	32	64
1	BC	278.3	171.5					78.5
	RS		161.0	115.6				65.6
2	BC	674.5	370.1	265.5				199.0
	RS		369.8	231.1				144.4
3	BC	2300.8	1308.4	681.9	506.3	467.7	433.1	389.2
	RS		1295.1	681.1	497.4	450.4	358.4	308.8

Because of the size of problems, unavoidable I/O has influence on the performance, although the asynchronous read and write control are used in the coding. Research on quantitative influence of I/O has not been reported in the literature for MIMD machine.

We obtained the maximum computation rate of 382.65 MFLOPS (multiplication and addition) for FE model 3 using 64 processors, which corresponds to 7.99% of the theoretical peak performance of 64×75 MFLOPS. This is 24.66% of the peak performance of dot-product of Intel Paragon processor measured in the same machine. The best single node computation rate takes 18.7 MFLOPS for FE model 3, that is, 12.5% of the theoretical peak performance and 77.7% of the measured dot-product performance. From this view, the influence of I/O cannot be over 22.3% of the wall-clock time.

We have the following observations:

- Unlike the basic parallel algorithm reported in [6,8,9], broadcasting communication is in general better than the ring-node sending for the proposed algorithm. The exception is for the small-scale problem using only a small number of processors.
- The upper limit on the number of processors is 64, beyond which there is no additional speedup for the $\mathbf{LDL}^T$ decomposition.
- The wall-clock time is dominated by inter-processor communication when larger number of processors are used.

In summary, we have implemented the $\mathbf{LDL}^T$ parallel factorization on a distributed memory machine such as the Intel-Paragon. Compared with conventional approaches, two improvements have been made to increase sequential and parallel calculation, respectively. Since inter-processor communication across network dominates the efficiency of parallel calculation, using an asynchronous communication algorithm with one-step overshoot can greatly reduce the processor idling time and enhance the performance of parallel computation.

ACKNOWLEDGMENTS

The authors wish to acknowledge the support of this research effort by UPGC research funding. The first author wishes to thank Professor Duc T. Nguyen at Old Dominion University, Norfolk, Virginia, for his kind discussion.

REFERENCES

[1] E.L. Wilson and H. Dovey. (1978). Solution or Reduction of Equilibrium Equations for Large Complex Structural Systems, Adv. Engrg. Software **1**, 19-25

[2] D. Zheng and T.Y.P Chang. (1995). Parallel Cholesky Method on MIMD with Shared Memory, Computers & Structures, **56:1**, 25-38

[3] J. Ortega (1978). Introduction to Parallel and Vector Solution of Linear Systems, Plenum Press, USA

[4] O.C. Zienkiwicz and R.L. Taylor. (1990) The Finite Element Method, McGraw-Hill

[5] P. Chen, T.Y.P. Chang and P. Tong, Implementation of a General Purpose FE code NFAP on Intel Paragon Platform, to be published

[6] C. Farhat and F.-X. Roux (1994). Implicit Parallel Processing in Structural Mechanics, Comp. Mech. Adv. **2**, 1-124

[7] C. Farhat and E.L. Wilson (1988) A Parallel Active Column Equation Solver, Computers & Structures, **28**, 289-304

[8] J. Qin and D.T. Nguyen. (1994). A Parallel-Vector Equation Solver for Distributed Memory Computers, Computing System in Engineering Journal, **5:1**

[9] Qin and D.T. Nguyen. (1993). A New Parallel-Vector Finite Element Analysis Software on Distributed Memory Computers Proceedings of the AIAA/ASME/ASCE/AHS 34th Conference, La Jolla, CA

[10]Intel Paragon™ User's Guide, Intel Corporation (1994)

[11]Intel Paragon™ FORTRAN Compiler User's Guide, Intel Corporation (1994)

This Page Intentionally Left Blank

DYNAMIC BEHAVIOR OF RAILWAY BRIDGES UNDER RANDOM LOADING AND ASSESSMENT OF VEHICLE-RUNNING SAFETY

Ying-Jun Chen, He Xia and Daqing Wang

Civil Engineering Department, Northern Jiaotong University, Beijing 100044, China

ABSTRACT

The dynamic model of a train-bridge system consists of the train model and the bridge model. Self-excitations of the system are the track irregularity and the vehicle hunting movement. As the main external excitations, there are wind load and earthquake action. This paper studies this problem of different cases for the purpose of assessment of vehicle-running safety and serviceabiliy; three methods are used and the theoretical characteristics of them are studied from the viewpoint of engineering application.

KEYWORDS

railway bridge, dynamic behavior, wind loading, earthquake, computer simulation, dynamic interaction, vehicle-running safety, stochastic process, dynamic serviceability

ASSESSMENT BY EXPERIMENT AND SIMULATION

The "snake-hunting" movement by vehicle tracking is a principal self-excitation source. It can be expressed as follows

$$Y_s = A_s \sin\left(\frac{2\pi V}{L_s} t + \zeta_i\right) \tag{1}$$

where A_s and L_s are the amplitude and wave length respectively, and ζ_i is the phase angle of ith wheelset; it is a random variable. $A_s = 3.0$mm, $L_s = 20.0$m.

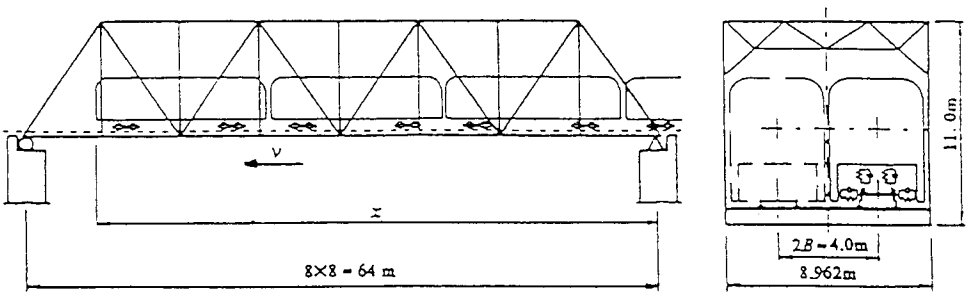

Figure 1: Train-bridge system model

In order to increase train speed, a truss bridge of 64m span is studied; the dynamic interaction model is shown in Fig. 1. Degrees-of-freedom for movement are 23 and 17 for 6—axle diesel locomotive and 4—axle passenger-freight cars respectively.

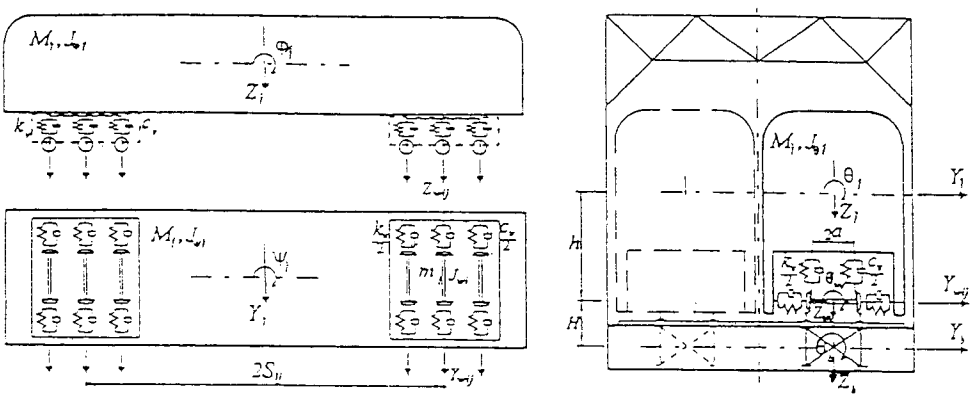

Figure 2: Model of diesel locomotive

The vehicle model is shown in Fig. 2[1]. Horizontal torsional vibration is coupled with vertical vibration for it is a two-track bridge, so a spatial model should be used. In order to simplify the calculation, the modal analysis method is used.

The train on the bridge is directly concerned with the stringer. Suppose that there is no relative displacement between the stringers and the track. When the vibration

modes of the bridge are normalized as $\varphi_n^T m\varphi_n = 1$, the nth order modal equation is expressed as follows

$$\ddot{q}_n + 2\omega\xi\dot{q}_n + \omega^2 q_n = \sum_i \sum_j [\varphi_{uij}^n F_{uij} + \varphi_{vij}^n F_{vij} + \varphi_{\theta ij}^n F_{\theta ij}] \tag{2}$$

in which F_{uij}, F_{vij} and $F_{\theta ij}$ are horizontal, vertical and torsional force components when the j th wheel of the i th car acts on the bridge position, ω and ξ are natural frequency and damping ratio respectively, φ_{uij}^n, φ_{vij}^n and $\varphi_{\theta ij}^n$ are horizontal, vertical and torsional displacement components at the stringer of nth mode at the position of ith car and jth wheel, respectively. When a train is moving on the bridge, lateral displacement Y_{wij}, torsional angle θ_{wij}, vertical displacement Z_{wij} of the wheelset, displacements of the girder $Y_b(x_{ij})$, $\theta_b(x_{ij})$ and $Z_b(x_{ij})$, hunting movements and irregularities of rails $Y_s(x_{ij})$, $\theta_s(x_{ij})$ and $Z_s(x_{ij})$ should satisfy the following relations

$$\begin{Bmatrix} Y_{wij} \\ \theta_{wij} \\ Z_{wij} \end{Bmatrix} = \begin{Bmatrix} Y_b(x_{ij}) + H_i\theta_b(x_{ij}) + Y_s(x_{ij}) \\ \theta_b(x_{ij}) + \theta_s(x_{ij}) \\ Z_b(x_{ij}) + B\theta_b(x_{ij}) + Z_s(x_{ij}) \end{Bmatrix} = \sum_{n=1}^{N_q} \begin{Bmatrix} q_n(\varphi_{uij}^n + H_i\varphi_{\theta ij}^n) + Y_s(x_{ij}) \\ q_n\varphi_{\theta ij}^n + \theta_s(x_{ij}) \\ q_n(\varphi_{vij}^n + B\varphi_{\theta ij}^n) + Z_s(x_{ij}) \end{Bmatrix} \tag{3}$$

in which distances H and B are shown in Figs. 1 and 2.

Dynamic spatial equilibrium equations can be obtained by combining the vehicle models and the bridge modes with the wheel-rail relations (3):

$$\boldsymbol{M}\ddot{\boldsymbol{A}} + \boldsymbol{C}\dot{\boldsymbol{A}} + \boldsymbol{K}\boldsymbol{A} = \boldsymbol{F} \tag{4}$$

Matrices of mass $\boldsymbol{M}$, damping $\boldsymbol{C}$ and stiffness $\boldsymbol{K}$, generalized displacement $\boldsymbol{A}$ and generalized force $\boldsymbol{F}$ in Eqns. 4 and 2 can be written in detailed form[2]. A similar problem is also studied in this paper for Fig. 10. The equations are solved by Newmark β method, $\beta = 1/4$. In this example (Fig. 1), the train consists of two locomotives and eight passenger-freight cars. In order to investigate the effect of phase angle ζ in Eqn. 1 which is a random number of uniform distribution in $0 \sim 2\pi$, the Monte Carlo simulation method is used; 30 sets are calculated for each train speed. Dynamic deflexions of the bridge are analyzed statistically.

Figs. 3 and 4 show the dynamic factor and horizontal amplitude (maximum, mean and standard deviation σ) at the midspan lower chord panel point respectively. But values higher than 200km/h are only reference values. They are also compared with the field

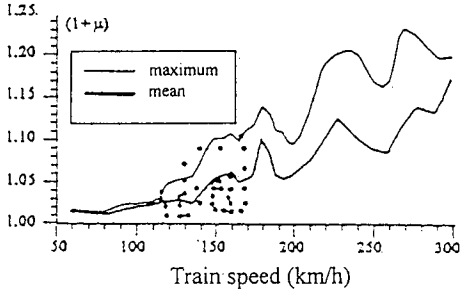

Figure 3: Dynamic factor $(1+\mu)$

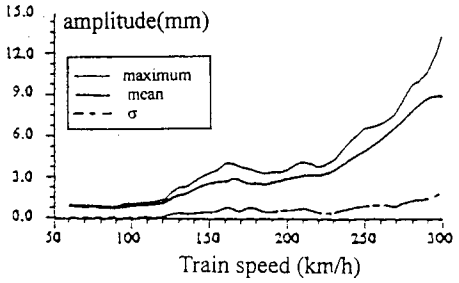

Figure 4: Horizontal amplitude of bridge lower chord

experiments. From the Chinese code, it is known that vehicle-running safety is assured when maximum train speed is 160km/h.

ASSESSMENT OF VEHICLE-RUNNING SAFETY UNDER EARTHQUAKE BY USING THE WHEEL-RAIL INTERACTION MECHANISM

Due to lack of data, the method by Wakui H. [3]is used. But in our case, maximum train speed is 300km/h, degrees-of-freedom of movement of the vehicle are 17 in order to study lateral responses, and earthquake acceleration record during the Tangshan earthquake is used. Vehicle-running safety is controlled by horizontal bent angle θ_y of the track; track deformation y_R can be expressed as follows(Fig. 5)

$$\begin{aligned} y_R &= 0, && x < -\frac{x_c}{2} \\ y_R &= \frac{\theta_y}{2x_c}\left(x + \frac{x_c}{2}\right)^2, && |x| = \frac{x_c}{2} \\ y_R &= \theta_y x, && x > \frac{x_c}{2} \end{aligned} \tag{5}$$

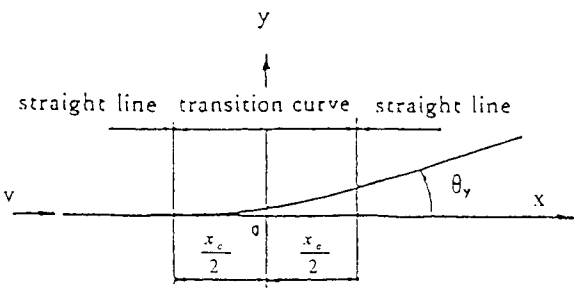

Figure 5: Track shape of bent angle portion

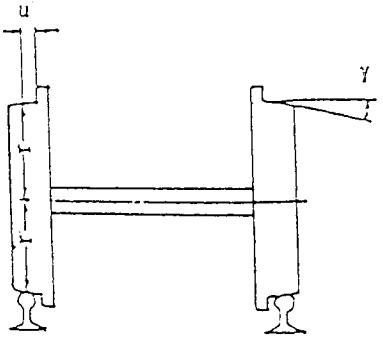

Figure 6: Tread surface slope of wheel

When the train passes through this portion, a relative displacement between the wheel

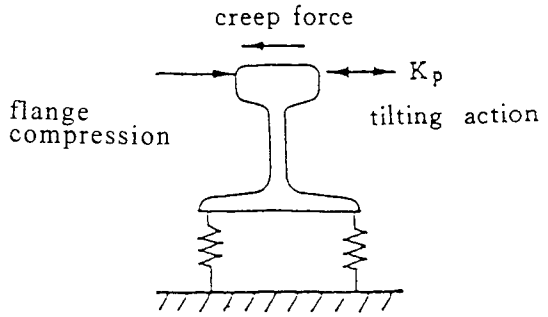

Figure 7: Cause of horizontal compressions[3]

axle and the track may happen from the inertial force of the train; if this displacement is greater than clearance u, the flange may accept a shock; the wheel radius also varies owing to the tread surface slope γ(Fig. 6); then the wheel axle may accept an action in the direction of the bent angle. This is the mechanism of the "snake hunting" movement. Fig. 7 shows the action of horizontal forces; creep forces also play an essential role in determining the lateral dynamic performance of rail vehicles[4].

Fig. 8 shows a mechanical model of vehicle; it consists of one car body, two bogies and four wheelsets connected with various springs; all data of the Japanese Shinkansen car [3] are used in this study. The total degrees-of-freedom of movement are 17 for one car, for car body: lateral moving (y_B), rolling (Φ_B), yawing (Ψ_B); for bogies ($i = 1,2$): lateral moving (y_{Ti}), rolling (Φ_{Ti}), yawing (Ψ_{Ti}); for wheelsets ($i = 1,2, j = 1,2$): lateral moving (y_{wij}), yawing (Ψ_{wij}), where $i = 1,2$ represents front and rear bogie respectively, $j = 1,2$ represents former and latter axle respectively; the effects of rolling Φ_{wij} and vertical motion z_{wij} can be neglected; it is different from [3] for earthquake acceleration a_g is considered in this case. The springs are divided into two kinds (Fig. 8): one is the nonlinear spring with damping; it consists of vertical support spring K_2, horizontal spring K_3, axle box spring K_1; the other is linear spring without damping. For the bolster anchor spring K_0, suppose the relation between the relative yawing angle and the moment has bilinear hysteresis characteristic. The resultant F from spring stiffness K and damping C can be obtained from spring displacement q and its velocity; q has a limited value q_s by a stopper, for example

$$q_{3i^{\Lambda}_{B}} = \mp y_B \pm (-1)^i L\Psi_B \mp h_2\Phi_B \pm y_{Ti} \mp h_1\Phi_{Ti}$$

$$|q_{3i^{\Lambda}_{B}}| \leqslant q_{3s}, \qquad F_{3i^{\Lambda}_{B}} = K_3 q_{3i^{\Lambda}_{B}} + C_3 \dot{q}_{3i^{\Lambda}_{B}}$$

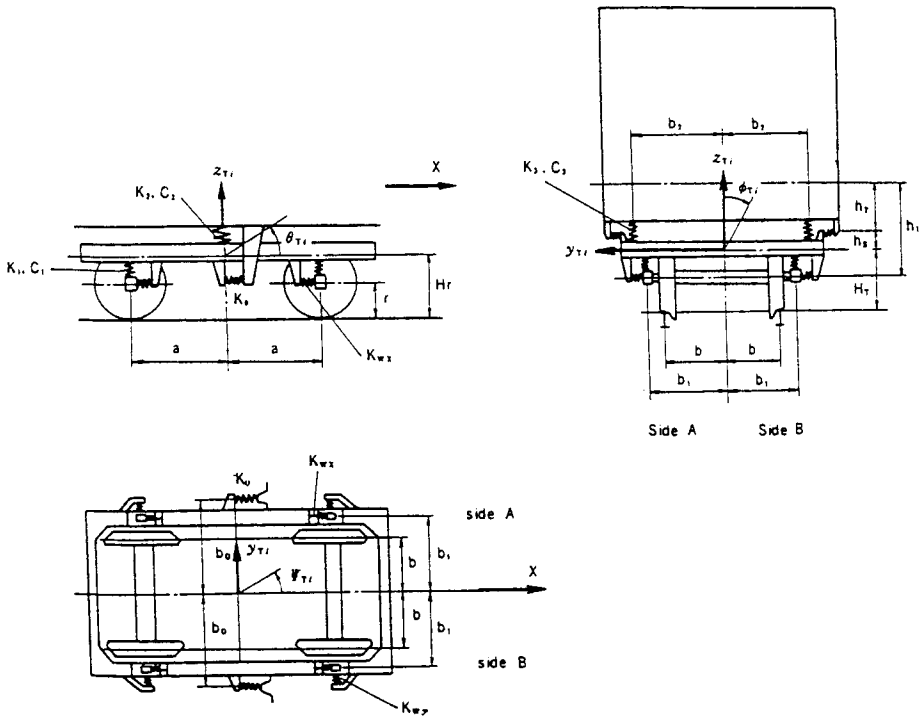

Figure 8: Mechanical model of vehicle[3]

$$|q_{3i_B^A}| > q_{3s}, \qquad F_{3i_B^A} = \frac{q_{3i_B^A}}{|q_{3i_B^A}|}\{K_3 q_{3s} + K_{3s}(|q_{3i_B^A}| - q_{3s})\} + C_3 \dot{q}_{3i_B^A} \tag{6}$$

The other notations are $2m_B$: mass of car body, $2I_{Bx}$ and $2I_{Bz}$: moment of inertia of the car about x axis and that about z axis, m_T : mass of bogie frame, I_{Tx} and I_{Tz} : moment of inertia of bogie about x axis and that about z axis, m_w : mass of wheel axle, I_w : moment of inertia of wheel axle about its center of gravity, 2L: distance of two bogies, center to center. Thus the dynamic equilibrium equations of the car are as follows:

$$\text{car body}\begin{cases} 2m_B\ddot{y}_B = F_{3.1A} - F_{3.1B} + F_{3.2A} - F_{3.2B} + 2m_B\bar{a}_g \\ 2I_{BZ}\ddot{\Psi}_B = (F_{3.1A} - F_{3.1B} - F_{3.2A} + F_{3.2B})L - (M_1 + M_2) \\ 2I_{Bx}\ddot{\Phi}_B = (F_{2.1A} - F_{2.1B} + F_{2.2A} - F_{2.2B})b_2 + (F_{3.1A} - F_{3.1B} + F_{3.2A} - F_{3.2B})h_2 \end{cases} \tag{7}$$

$$\text{bogie}\begin{cases} m_T\ddot{y}_{Ti} = -F_{3.1A} + F_{3.1B} + F_{Wy.i_1A} + F_{Wy.i_2A} - F_{Wy.i_1B} - F_{Wy.i_2B} + m_T\bar{a}_g \\ I_{TZ}\ddot{\Psi}_{Ti} = M_i + (F_{Wx.i_1A} - F_{Wxi_1B} - F_{Wx.i_2A} + F_{Wx.i_2B})b_1 + \\ \qquad (F_{Wy.i_1A} - F_{Wy.i_1B} - F_{Wy.i_2A} + F_{Wy.i_2B})a \\ I_{Tx}\ddot{\Phi}_{Ti} = (-F_{2.iA} + F_{2.iB})b_2 + (F_{3.iA} - F_{3.iB})h_s + (F_{1.i_1A} - F_{1.i_1B} + F_{1.i_2A} - F_{1.i_2B})b_1 + \\ \qquad (F_{Wy.i_1A} - F_{Wy.i_1B} + F_{Wy.i_2A} - F_{Wy.i_2B})(H_T - r) \end{cases} \tag{8}$$

$$\text{wheelset}\begin{cases} m_W \ddot{y}_{wij} = -F_{Wy,ijA} + F_{Wy,ijB} - Q_{ijA} + Q_{ijB} + m_w \ddot{a}_g \\ I_W \ddot{\Psi}_{wij} = (-1)^j (F_{Wx,ijA} - F_{Wx,ijB}) b_1 - T_{\Psi ij} \end{cases} \tag{9}$$

in which horizontal compression $Q_{ij_B^A} = Q_{cij_B^A} + Q_{fij_B^A}$, $Q_{cij_B^A}$ is horizontal creep force, $Q_{fij_B^A}$ is the flange compression (Fig. 7), $Q_{fij_B^A} = K_p \cdot y_{tij_B^A}$, where K_p is the spring constant from tilting action of the rail, $y_{tij_B^A}$ is the rail-tilting displacement when the flange collides against the rail. Restoring moment M of the bolster anchor spring is $M = 2K_0 b_0^2 \psi_E$, relative yawing angle $\Psi = \Psi_B - \Psi_T$, and Ψ_E is a value of Ψ within the elastic limit, when $\Psi > \Psi_{E\max}$, M has a bilinear relation [3]. $T_{\Psi ij}$ is yawing moment from the creep action. Equilibrium equations (7)～(9) are a time-dependent system; on the basis of the above idea, simulation analysis is used.

The initial condition is that the train passes in uniform speed at the position of the beginning point of the bent angle portion when $t = 0$, and the earthquake acts at the same time.

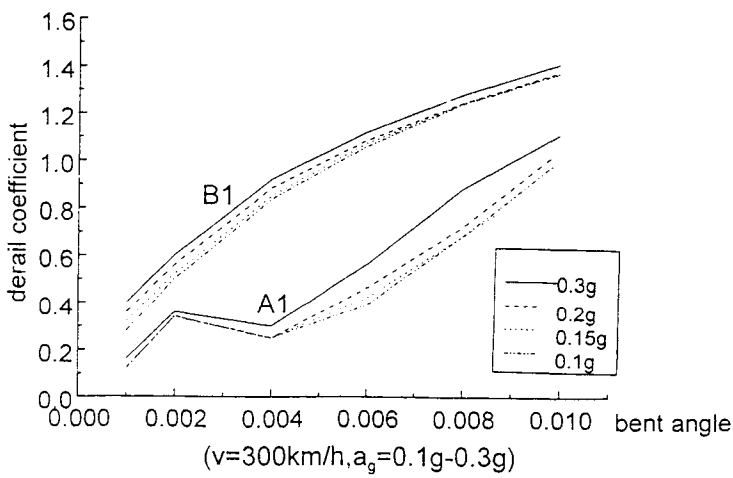

Figure 9: Horizontal bent angle versus derail coefficient

Fig. 9 shows the relation between the horizontal bent angle (in radian) and the derail coefficient when train speed $v = 300$km/h and earthquake acceleration $a_g = 0.1g \sim 0.3g$; in the figure, A indicates inner rail, B indicates outer rail. In the same manner, this angle can be calculated for various parameters (derail coefficient, side compression of wheel flange, horizontal vibration acceleration of car) and for other vehicle models (TGV, ICE) and other design earthquake actions. Then the allowable bent angle value can be decided in order to satisfy vehicle-running safety. In our case, the calculated

results are shown in Table 1; earthquake acceleration is $a_g = 0.2g$, it approximately corresponding to Richter Magnitude $M = 6$, Modified Mercalli Intensity $I = 7 \sim 8$.

TABLE 1
ALLOWABLE BENT ANGLE

Train Speed km/h	Horizontal Bent Angle θ (1/1000)			
	Horizontal Moving (1)		Folding (2)	
	$L < 30$m	$L \geqslant 30$m	$L < 30$m	$L \geqslant 30$m
300	3.5	3.0	4.5	3.5
350	2.5	2.0	3.0	2.5

Note: L represents girder length or block length of rigid frame viaduct.

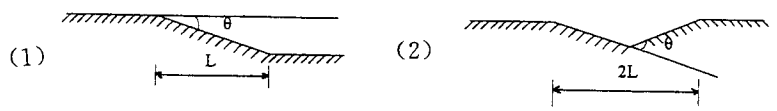

ASSESSMENT BY STOCHASTIC PROCESS EXTREME ANALYSIS FOR SERVICEABILITY OF TRAIN-BRIDGE SYSTEM UNDER RANDOM WIND LOAD

For the dynamic interaction of a train-bridge system under wind action, the random responses become a complex nonlinear problem owing to the continuous movement of the train, which cannot be generally treated as a stationary process. The proposed method [5] is to analyze serviceability by studying the peak distribution of structural responses, and transforming their first-passage probability distribution into the extreme distribution which is more convenient for engineering purposes. The calculation process is explaind by an example. Fig. 10 shows a truss bridge stiffened by a flexible arch. The dynamic behavior of the train-bridge system under random wind loading is studied. According to the Chinese bridge code [6], the transverse wind load per unit area exposed to the wind ($A = 1$) is calculated by the following expression

$$W_t = K_1 K_2 K_3 W_0 \qquad \text{(in Pa)} \tag{10}$$

where basic wind pressure $W_0 = \dfrac{V^2}{1.6}$, V is wind speed (m/sec), K_1 is drag coefficient,

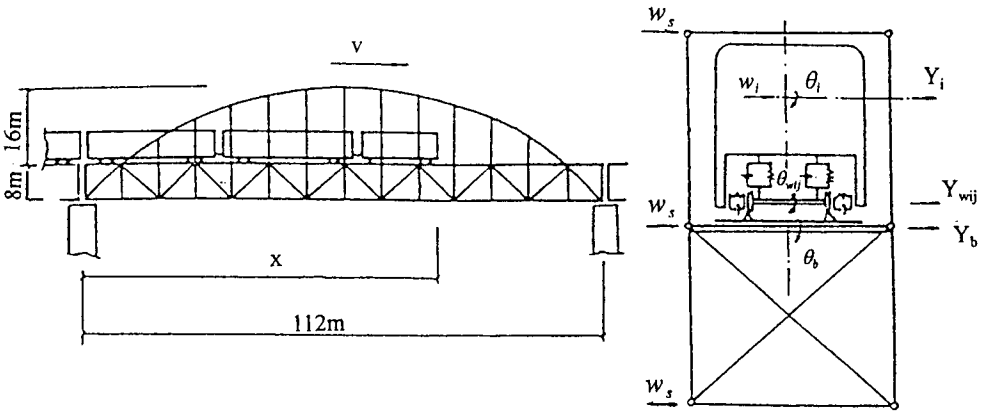

Figure 10: Train-bridge system model

K_2 is gust distribution coefficient, K_3 is a coefficient referring to the topography and terrain condition. For dynamic analysis, the power spectrum $S_n(f)$ of horizontal wind speed proposed by Davenport is used

$$S_n(f) = \frac{4K_r\overline{V}_{10}^2}{f}\frac{X_1^2}{(1+X_1^2)^{4/3}} \tag{11}$$

where $X_1 = 1200f/\overline{V}_{10}$; $\overline{V}_{10}$ —average wind speed at 10m's height; f —frequency; K_r — ground roughness factor (0.003—0.03). The random wind speed samples can be obtained by the trigonometric series[7]. Considering the effect of wind-structure interaction, the response velocity should be considered together with the wind speed; then aerodynamic damping $C^a = 1.25K_1\mu_z K_3 A \cdot V$ and wind force $W_t = \frac{1}{1.6}K_1\mu_z K_3 A V^2$, where μ_z is a coefficient referring to the altitude z of the structure above ground level; since the wind gust consists of mean and turbulent components, μ_z is used instead of K_2; here the wind tunnel test for C^a is avoided.

The vehicle model is the same as Fig. 2, and with the same notations, basically in the same manner, the dynamic equations of the train-bridge system acted on by wind composed of vehicle model and bridge model are [7][8]:

$$\begin{bmatrix} M_i & 0 & 0 \\ 0 & J_{\theta i} & 0 \\ 0 & 0 & J_{\Psi i} \end{bmatrix}\begin{Bmatrix} \ddot{Y}_i \\ \ddot{\theta}_i \\ \ddot{\Psi}_i \end{Bmatrix} + \begin{bmatrix} C_i + C_i^a & -h_i C_i & 0 \\ -h_i C_i & C_{\theta i} & 0 \\ 0 & 0 & C_{\Psi i} \end{bmatrix}\begin{Bmatrix} \dot{Y}_i \\ \dot{\theta}_i \\ \dot{\Psi}_i \end{Bmatrix} + \begin{bmatrix} K_i & -h_i K_i & 0 \\ -h_i K_i & K_{\theta i} & 0 \\ 0 & 0 & K_{\Psi i} \end{bmatrix}\begin{Bmatrix} Y_i \\ \theta_i \\ \Psi_i \end{Bmatrix}$$

$$= \sum_{j=1}^{2N_{wi}} \sum_{n=1}^{N_q} \frac{1}{2N_{wi}} \begin{Bmatrix} G_{ij}^n(K_i q_n + C_i \dot{q}_n) \\ 2g_{ij}^n(K_{\theta wi} q_n + C_{\theta wi} \dot{q}_n) - H_i G_{ij}^n(K_i q_n + C_i \dot{q}_n) \\ 0.5\hat{\xi}_j S_{ij} G_{ij}^n(K_i q_n + C_i \dot{q}_n) \end{Bmatrix} + \begin{Bmatrix} W_i \\ 0 \\ 0 \end{Bmatrix}$$

$$+ \sum_{j=1}^{2N_{wi}} \frac{1}{2N_{wi}} \begin{Bmatrix} K_i Y_s(x_{ij}) + C_i \dot{Y}_s(x_{ij}) \\ -h_i[K_i Y_s(x_{ij}) + C_i \dot{Y}_s(x_{ij})] + 2[K_{\theta wi}\theta_s(x_{ij}) + C_{\theta wi}\dot{\theta}_s(x_{ij})] \\ 0.5\hat{\xi}_j S_{ij}[K_i Y_s(x_{ij}) + C_i \dot{Y}_s(x_{ij})] \end{Bmatrix}$$

$$M^n \ddot{q}_n + (C_n + C_n^a)\dot{q}_n + K_n q_n = \sum_{i=1}^{N_v} \sum_{j=1}^{N_{bi}} \sum_{m=1}^{N_q} - \{(G_{ij}^{nm} M_{wij} + g_{ij}^{nm} J_{wij})\ddot{q}_m$$

$$+ \frac{1}{2N_{wi}}[(\frac{1}{2} G_{ij}^{nm} C_i + g_{ij}^{nm} C_{\theta wi})\dot{q}_m + (\frac{1}{2} G_{ij}^{nm} K_i + g_{ij}^{nm} K_{\theta wi}) q_m]\}$$

$$+ \sum_{i=1}^{N_v} \sum_{j=1}^{N_{bi}} \{\frac{1}{2} G_{ij}^n(K_i Y_i + C_i \dot{Y}_i) + [(g_{ij}^n K_{\theta wi} - \frac{1}{2} h_i K_i)\theta_i + (g_{ij}^n C_{\theta wi} - \frac{1}{2} h_i C_i)\dot{\theta}_i]$$

$$+ \frac{1}{4}\hat{\xi}_j S_{ij}(K_i \Psi_i + C_i \dot{\Psi}_i)\} + \sum_{i=1}^{N_q} \sum_{j=1}^{N_{bi}} \{-[G_{ij}^n M_{wij} \ddot{Y}_s(x_{ij}) + g_{ij}^n J_{wij} + \ddot{\theta}_s(x_{ij})]$$

$$+ \frac{1}{2N_{wi}} G_{ij}^n[C_i \dot{Y}_s(x_{ij}) + K_i Y_s(x_{ij})] + \frac{1}{N_{wi}}[C_{\theta wi}\dot{\theta}_s(x_{ij}) + K_{\theta wi}\theta_s(x_{ij})]\} + W_n$$

$$(i = 1, 2 \cdots, N_v, n = 1, 2, \cdots, N_q) \tag{12}$$

in which C_n^a and W_n are respectively the general damping coefficient and the general wind force acting on the nth bridge mode. Suppose there are N_s joints, and the modal value of the nth mode at the sth joint is $\Phi_n(s)$; we have

$$C_n^a = 1.25 K_1 K_3 V \sum_{s=1}^{N_s} \Phi_n^2(s)\Big[\frac{1}{2}\sum_{l=1}^{L_s} \mu_z A_l\Big]; W_n = \frac{1}{1.6} K_1 K_3 \sum_{s=1}^{N_s} \Phi_n(s)\Big[\frac{1}{2}\sum_{l=1}^{L_s} \mu_z A_l\Big] V^2 \tag{13}$$

In Eqn. 12, $G_{ij}^n = \Phi_n'(x_{ij}) + h_3 \Phi_n''(x_{ij}); g_{ij}^n = \Phi_n''(x_{ij}); G_{ij}^{nm} = G_{ij}^n \cdot G_{ij}^m; g_{ij}^{nm} = g_{ij}^n \cdot g_{ij}^m$; where $\Phi_n'(x_{ij})$ and $\Phi_n''(x_{ij})$ are respectively the horizontal displacement and the torsional angle components, (x_{ij}) means the position of jth wheel of ith car on the bridge.

In this example, the joint number of the bridge equals 82, the train consists of two locomotives and six passenger cars, the total degrees of freedom are 96. Calculation results show that the displacement at midspan under random wind load is 15 ~ 20% greater than that by statical analysis based on the code.

To avoid the difficulty of directly determining the joint probability distributions of extremes of the responses and wind speeds, the extreme value distributions of system responses under certain wind speeds are firstly studied with a large amount of simulation calculations. The joint distributions of system responses and wind speeds are finally

obtained by combining extreme value distributions of the wind itself.

Supposing $\{x(t_i)\}$ $(i = 0,1,\cdots,N)$ is the simple sample series of the stochastic process, the sample set composed of their extremes $X = \{\max|x(t_i)|;t \in (0,t_0)\}$ are also random variables. Where t_0 is the lasting time of the structural vibration, it is approximately equal to the entire time of the train passing through the bridge each time; $x(t_i)$ is the response series. When the original distribution of the random variable is unknown, as in the usual case, the asymptotic distribution of $N \to \infty$ is considered. It is proved that the extreme value distributions of system responses are close to the first asymptotic distribution[7], the PDF and the CDF of which are

$$F(x) = \exp[-e^{-a_n(x-u_n)}]; \quad f(x) = a_n\exp[-a_n(x-u_n) - e^{-a_n(x-u_n)}] \tag{14}$$

where a_n is the extreme intensity function, u_n is the character extreme.

For continuous random variables X (here a dynamic response) and V (mean wind speed), the joint cummulative distribution function when $V < v$ and $X > x$ is

$$\begin{aligned} P(X > x, V < v) &= \int_x^{\infty}\int_{-\infty}^{v} f(x,v)\mathrm{d}v\mathrm{d}x \\ &= \int_x^{\infty}\int_{-\infty}^{v} f(x|v)f(v)\mathrm{d}v\mathrm{d}x = \int_0^{v}[1 - F(x|v)]f(v)\mathrm{d}v \end{aligned} \tag{15}$$

where $f(x|v)$ is the conditional probability density function of the extreme responses, $f(x,v)$ is the joint probability density function.

Structural serviceability is defined as the probability of which structural response extreme X does not surpass its threshold within service period T. This probability is an evaluation index for the bridge-train system reliability and can be called dynamic serviceability. Since $F_{XT}(X < x|t < T) = 1 - P_{X,T}(X > x, t < T)$, we have

$$\begin{aligned} F_{XT}(X < x|t < T) = 1 - \int_0^{v(T)} &\exp[-e^{-a_v(v-\mu_v)}]e^{-a_v(v-\mu_v)}a_v \\ \times \left\{1 - \exp\left[-\exp\left(-\frac{1}{a_0 + a_1v + a_2v^2}[x - (b_0 + b_1v + b_2v^2)]\right)\right]\right\}&\mathrm{d}v \end{aligned} \tag{16}$$

where the upper limit of the integration is the maximum expected mean wind speed de-

termined by the return period. Taking a bridge in south China for example, the local annual extreme parameters for wind speed are $\mu_v = 14.94$m/s and $\alpha_v = 0.417$. For a given return period $T = 100year$, the maximum mean wind speed is 26.0m/s.

The average passage time $T_n(x)$ is the inverse of the probability of which an event happens in one unit period

$$T_n(x) = \frac{1}{P_{X,T}} = \frac{1}{1 - F_{X,T}(x)} \tag{17}$$

The threshold for response X can be calculated from a given service period T_0.

TABLE 2
DYNAMIC SERVICEABILITY INDEXES AND THEIR REFERENCE THRESHOLDS

	Horizontal Deflexion(mm)		Amplitude(mm)		Bridge Accleration(g)	Vehicle Acceleration(g)
Threshold	56	28	7.8	24.8	0.2	0.50
	Japan	UIC	China	Japan	Japan	China
$T = 100$	0.9291	0.4262	0.2657	0.9024	0.9997	0.9999996
$V = 30.0$	0.9208	0.4178	0.2574	0.8947	0.9993	0.999993

The calculated dynamic serviceability indexes (DSI) are shown in Table 2 for $T = 100year$, $V = 26$ m/s and $V = 30$m/s; the latter is the maximum wind speed for an empty car. For such a complicated system as bridge-train interaction, since wind and train loads do not correlate with each other, all the DSIs are neither fully correlative nor independent. The system DSI can therefore be estimated by the following equation

$$\prod F_{X_i} \leqslant F_s \leqslant \min\{F_{X_i}\} \tag{18}$$

In this example, for $T = 100$ years and the threshold of Japanese code, the system DSI is between 0.8381 and 0.9024.

Figure 11 shows the distribution of the calculated DSI versus maximum mean wind

speed. Thresholds for lateral deflexion, amplitude and acceleration of this bridge for service period $T = 100y$, inversely calculated by Eqn. 17, can be 70mm, 45mm and 160gal respectively.

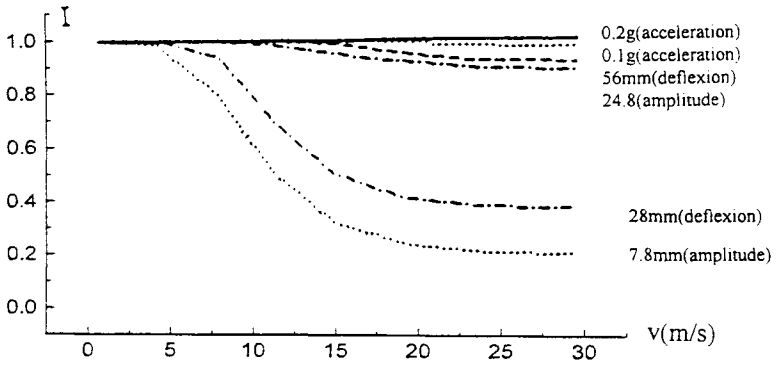

Figure 11: System DSI versus wind threshold

For this kind of bridge, methods for design and assessment aiming at assurance of bridge serviceability for train and wind interaction should be emphasized. In this example, the estimated DSIs for lateral bridge deflexion and amplitude are only 0.9 or so upon the local wind speed distribution and design period $T = 100year$, not suitable to the Chinese code.

CONCLUSION

Although the computer simulation can be used for the research of train-bridge system, some difficulties remain to be further studied, for instance, the power spectrum of rail irregularity, the vehicle hunting movement function and its amplitude, wave length and phase angle, unless it is a case study. It is more reasonable to use the mechanism of wheel-rail interaction, but the exact data of parameters are necessary. For the assessment of serviceability, vibration thresholds to ensure train-running stability and human comfort, deterioration of strength caused by external loading and environmental conditions, etc. are now further studied.

ACKNOWLEDGEMENT

This research is supported by National Natural Science Foundation and Ministry of Railways of China.

REFERENCES

1. Chen Y-J. , Wang D. (1992), Dynamic Behavior of Bridges Under Random Loading and Dynamic Reliability Problem, *Computational Mechanics in Structural engineering*, edited by Cheng F. Y. , Fu Z. , Elsevier Science Publishers, England, 398～411
2. Xia H. , Chen Y-J. , Zhang D. , Ke Z. (1996), Dynamic Analysis of Steel Truss Bridges Under Increased Train Speeds (in Chinese), *Journal of the China Railway Society* **18 : 5**, 75～82
3. Wakui H. (1978), Allowable Bent-Angle of Long-Spanned Suspension Bridges Determined by Running Property of Shinkansen Car (in Japanese), *Report of Railway Technical Research Institute*, No. 1087, 1～59
4. Shen Z. Y. , Hedrick J. K. , Elkins J. A. (1983), A Comparison of Alternative Creep Force Models for Rail Vehicle Dynamic Analysis, *Proc. 8th IAVSD Symposium*, Swets & Zeitlinger-Lisse, 591～605
5. Chen Y-J. (1992), Development in Dynamic Reliability of Bridge Structures (in Chinese), *Proc. 6th Symposium on Bridge Technology*, Wuhan, China, 76～81
6. Chen Y-J. et al. (1993), Development of Wind Load Standard for Chinese Bridge Code, *Proc. Third Asia-Pacific Symposium on Wind Engineering*, Hong Kong, 793～798
7. Xia H. , Chen Y-J. (1994), Dynamic Reliability of Train-Bridge System Under Wind Action (in Chinese), *Journal of China Civil Engineering Association* **27 : 2**, 14～21
8. Chen Y-J. , Xia H. , Gao R. (1991), Dynamic Analysis of Truss Bridge Stiffened by Flexible Arch Unter Train Loads, *Proc. EASEC — 3*, Shanghai, 1451～1456

A REVIEW ON THE NUMERICAL SOLUTION SCHEMES FOR LOCALIZATION PROBLEMS

Z. Chen, X. Xin and D. Qian
Department of Civil and Environmental Engineering, University of Missouri
Columbia, Missouri 65211, USA

ABSTRACT

An introduction is given on the current status of research on localization problems. Numerical solution schemes to simulate the evolution of localization are then reviewed in detail. First, material integration schemes are discussed for both plasticity and damage models for which a continuum tangent stiffness tensor can be formulated for bifurcation analysis. Second, structural integration schemes are reviewed for the post-limit responses including snap-back and snap-through. Finally, one of the "meshless" methods, the material point method (MPM) is introduced for localization problems. Sample problems are then considered to demonstrate the robustness and potential of a newly proposed procedure based on the moving jump forms of conservation laws. Conclusions and future work are given based on the review paper.

KEYWORDS

Softening with Localization, Plasticity and Damage, Post-limit Response, Jump Conditions, Transition between Governing Equations, Failure Wave

INTRODUCTION

For modern engineering design, the limit design methodology based on elastic or yield strength might not be suitable in many cases. In dynamic cases such as impact or seismic disturbances,

the loads are of very short duration so that collapse may not occur even if the limit point is reached. Engineering structures are often designed to be statically indeterminate which also helps to preclude collapse. In addition, the current interest in explosion-resistant design requires the understanding of the post-limit structural responses. Since a significant part of energy dissipation in the post-limit regime is associated with the evolution of localization, much research has been conducted to investigate the experimental, analytical and numerical aspects of localization problems, as reviewed by Chen [1996b], Chen and Schreyer [1994], and Xie et al. [1994].

Localization is manifested by softening or degradation of material properties, which is accompanied by localized large deformations in a finite zone. To predict the evolution of inhomogeneous interactions among material particles within the localization zone, several kinds of unconventional constitutive models have been proposed with the use of higher order terms in space and/or time, such as nonlocal (gradient or integral), Cosserat continuum and rate-dependent approaches. Although the advantages of these unconventional models over conventional (local) ones have been demonstrated for many academic problems, there still exist some pressing limitations that prohibit the routine prediction of localization phenomena in practical applications. In particular, it might not be feasible, with current computational facilities, to perform large-scale simulation of structural failure due to the use of higher order terms. Since the shift from a test-based to a simulation-based design environment requires an efficient numerical procedure for localization problems, an alternative approach is to catch the essential feature of localization phenomena without invoking higher order terms for constitutive modeling.

As can be found from the literature review [Chen and Schreyer, 1994; Chen and Sulsky, 1995], the key component of various higher order models is an attempt to predict the evolution of inhomogeneous interactions among material particles, with mesh-independent results. Before the initiation of localization, there is no need to use higher order terms. In a macro-mechanical sense, however, the evolution process might be equally well characterized by the formation and propagation of a moving material boundary that is associated with a local change in material properties. With the introduction of a moving material boundary, a partitioned-modeling approach has been proposed for localization problems [Chen, 1993a]. The basic idea of the approach is that different local constitutive models are used inside and outside the localization zone, with a moving boundary being introduced between different material domains, if localization occurs. As a result, the extrapolation of material properties beyond the limitations of current experimental techniques can be avoided in identifying the evolution of localization, and simplified governing differential equations can be formulated in the partitioned domains for given boundary and initial conditions.

To establish a sound mathematical foundation for the partitioned-modeling approach, an attempt has been made to investigate the use of the jump forms of conservation laws in defining the moving material boundary, with one-dimensional analytical illustrations for rate-independent local models [Chen and Sulsky, 1995]. By taking the initial point of localization

as that point where the type of the governing differential equations changes, i.e., a hyperbolic to an elliptic type for dynamic problems and an elliptic to another elliptic type for static problems, a moving material boundary can be defined through the jump forms of conservation laws across the boundary. Jumps in density, velocity, strain and stress can be accommodated on this moving surface of discontinuity between two material domains. Interestingly, the problems involving the change in the types of governing differential equations also occur in other areas such as fluid mechanics [Chen and Clark, 1995] and thermal shock wave propagation [Tzou, 1989]. It has been shown that the transition from continuum damage mechanics to fracture mechanics might be linked through the moving jump forms of conservation laws so that a complete failure evolution process might be simulated with the use of simple models [Chen, 1996a and b].

Based on the previous research results, numerical solution schemes for localization problems are reviewed in this paper. First, material integration schemes are discussed for both plasticity and damage models for which a continuum tangent stiffness tensor can be formulated for bifurcation analysis. Second, structural integration schemes are reviewed for the post-limit responses including snap-back and snap-through. Finally, one of the "meshless" methods, the material point method (MPM) [Sulsky et al., 1994; Zhou et al., 1998] is discussed for localization problems. To demonstrate the robustness and potential of a newly proposed procedure that is based on the moving jump forms of conservation laws, sample problems are considered for both quasi-static and dynamic cases. Conclusions and future work are then given based on the review paper. A direct notation is employed to describe the constitutive models, with bold-faced letters denoting tensors of first or higher orders.

EXISTING NUMERICAL PROCEDURES

Structural solution schemes consist of constitutive model solvers, spatial and temporal discretization methods. With a focus on the localization problems, the numerical solution schemes are reviewed as follows for nonlinear structural analyses including failure simulation.

Material Integration Schemes

To perform large-scale computer simulation, a simple stress-strain relation, that can predict the essential feature of nonlinear material responses, must be formulated for structural analyses. Nonlinear material behaviors arise from two distinct modes of microstructural changes: one is plastic flow and the other is the degradation of material properties. Plastic flow, which is reflected through permanent deformation, is the consequence of a dislocation process along preferred slip planes as in metals, or particle motion and rearrangement as in geologic materials. Because the number of bonds between material points is hardly altered during the flow process, the material stiffness remains insensitive to this mode of microstructural motion, and change of strength is reflected through plastic strain hardening

and apparent softening. On the other hand, the nucleation, crushing and coalescence of microcracks and microvoids result in debonding, which is reflected through the damaging of material stiffness and strength. In general, both modes are present and interacting although some mode might dominate at some stage of the evolution process. Final rupture occurs when macrocracks form and propagate from the cluster of microcracks.

A systematic procedure, which satisfies thermodynamic restrictions, has been used to formulate local plasticity and damage models [Chen and Schreyer, 1990b and 1994]. A family of incremental-iterative integration rules has also been given with or without the use of a tangent stiffness tensor. In general, both the generalized trapezoidal and midpoint rules can be employed for the integration of inelastic constitutive equations, depending on the feature of a specific model.

Structural Integration Schemes

There exist two major computational difficulties in simulating the post-critical structural response. One is the occurrence of an ill-conditioned tangent stiffness matrix around critical points, namely, limit and bifurcation points. The other is the selection of a suitable constraint on the solution path such that the post-critical response can be traced. Since a robust and efficient solution scheme is necessary to make failure simulation available in a routine manner, several procedures have been proposed to circumvent the difficulties associated with critical points [de Borst et al., 1993; Chen, 1993b and 1996b; Chen and Schreyer, 1990a and 1991; Pijaudier-Cabot and Bode, 1995]. The standard arc-length control is still commonly employed in geometrically nonlinear cases, and with some modifications in materially nonlinear cases. Because the material failure zone is localized into a small region, the arc-length constraint formulated in the global deformation field is insensitive to the evolution of the localized deformation mode. As a result, a suitable constraint should be constructed in terms of a localized kinematical field if localized failure needs to be simulated. Due to the fact that the localization zone is evolving and there is a sign change of the load increment at a critical point, the control point (element) should also vary in position with a suitable measure of failure, and the localized constraint parameter that reflects the extent of irreversible energy dissipation should be constrained to increase monotonically.

Preliminary results obtained for plasticity and damage problems indicate that the use of an evolving localized control is a reasonable choice for localization problems including snap-back or snap-through [Chen, 1993b; Chen and Schreyer, 1990a and 1991]. As a remedy to avoid the use of an ill-conditioned tangent stiffness matrix around critical points, a secant stiffness matrix based on continuum damage mechanics has been used with a dramatic increase in the rate of convergence with respect to the rate obtained using a tangent stiffness matrix. In order to incorporate both damage and plasticity models into one computer code, it has been proposed that an incremental-iterative solution scheme be constructed through the use of an initial elasticity stiffness matrix together with an evolving-localization constraint [Chen and Schreyer, 1994]. Thus, only one inverse calculation is required, and the amount of

computation involved in the iterative loop is dramatically reduced. It can be found that the numerical procedure for tracing the post-bifurcation path depends mainly on the choice of a suitable constraint instead of a stiffness matrix. Different constraints generally yield different solution paths. In other words, the constraint imposed on the solution path plays a crucial role whether or not the stiffness matrix is ill-conditioned. Thus, the dependence of the evolving-localization constraint on the location of initial imperfections and on the evolution history of localization detects the solution path following the critical point, while the use of a well-conditioned stiffness matrix guarantees that a numerical solution can be obtained.

The Material Point Method

As one of the innovative spatial discretization methods, the Material Point Method is an extension to solid mechanics problems of a hydrodynamics code called FLIP which, in turn, evolved from the Particle-in-Cell Method. The motivation of the development was to simulate those problems, such as penetration, perforation, metal forming and cutting, which involve large deformations, the transition from continuous to discontinuous failure modes and the creation of new material surfaces, with history-dependent internal state variables. The essential idea is to take advantages of both Eulerian and Lagrangian methods. And also, this MPM and other unconventional spatial discretization methods employ the concept of local moving interpolation so that local remeshing can be achieved without the cost of global remeshing. Although the MPM is still under development, sample calculations have demonstrated the robustness and potential of this method [Sulsky et al., 1994]. It is believed that the MPM can be developed into a robust spatial discretization method, combined with solid modeling and post-processors, for large-scale computer simulation of structural failure responses.

A DEVELOPING NUMERICAL PROCEDURE

Recently, efforts have been made to simulate the evolution of localization without invoking higher order terms, and to fill the gap between continuum damage mechanics and fracture mechanics. A developing numerical procedure is presented as follows.

Based on the previous study [Chen 1996a], a set of moving jump forms of the conservation laws is used here to define a material failure criterion that can predict the initiation and orientation of localized failure, and the transition between continuous and discontinuous failure modes. In a three-dimensional framework, the use of the jump forms of conservation of mass and linear momentum would result in

$$\boldsymbol{v}_b \cdot \boldsymbol{n} = \frac{\rho_1 \boldsymbol{v}_1 \cdot \boldsymbol{n} - \rho_2 \boldsymbol{v}_2 \cdot \boldsymbol{n}}{\rho_1 - \rho_2} \tag{1}$$

and

$$\left[-\frac{\rho_1\rho_2 \boldsymbol{n}\cdot(\boldsymbol{v}_1-\boldsymbol{v}_2)}{\rho_1-\rho_2}\right](\boldsymbol{v}_1-\boldsymbol{v}_2) = (\sigma_1 - \sigma_2)\cdot \boldsymbol{n} \tag{2}$$

if there is a jump in mass density ρ. In Eqs. (1) and (2), the subscripts 1 and 2 denote field variables on the two sides of a moving material surface that has a velocity $\boldsymbol{v}_b$ in the three-dimensional space, and $\boldsymbol{n}$ is the unit normal to the material surface. The other variables are $\boldsymbol{v}$ (particle velocity vector) and σ (stress tensor), with body forces being omitted. For purely mechanical problems where there exists no energy sources or sinks, the conservation of mass and linear momentum implies the conservation of energy. Since the evolution of localization involves jumps in certain field variables, a material failure criterion is defined based on the jump types of the kinematic field variables as follows:

Localized Failure := $\boldsymbol{v}_1 = \boldsymbol{v}_2$ and $\dot{\varepsilon}_1 \neq \dot{\varepsilon}_2$

Discrete Failure := $\boldsymbol{v}_1 \neq \boldsymbol{v}_2$ and $\dot{\varepsilon}_1 \neq \dot{\varepsilon}_2$

with $\dot{\varepsilon}$ being the strain rate tensor. In other words, the change in the jump type of the kinematic field variables identifies the initiation of different failure modes. As can be seen, the transition from continuous to discontinuous failure modes is characterized by the condition of localized failure. Because there is a jump in the strain rate for localized failure, it makes sense to claim that a corresponding jump must exist in the mass density due to a jump in the volumetric strain rate. The jump in the volumetric strain rate is manifested by micro-cracking in the localization zone. The use of Eqs. (1) and (2) then yields

$$\boldsymbol{v}_1 \cdot \boldsymbol{n} = \boldsymbol{v}_2 \cdot \boldsymbol{n} = \boldsymbol{v}_b \cdot \boldsymbol{n} \tag{3}$$

and the continuity of the traction across the moving material surface, namely

$$(\sigma_1 - \sigma_2)\cdot \boldsymbol{n} = \boldsymbol{0} \tag{4}$$

for localized failure. Thus, Eqs. (3) and (4) together with a jump in the mass density represent the essential feature of localization.

To examine how the jump in the strain rate is derivable from Eq. (4), assume that side 1 initiates localization from a weak material point. The stress tensor on side 1 is then related to that on side 2 by

$$\sigma_1 = \sigma_2 + \boldsymbol{T}_1 : \Delta\varepsilon_k \tag{5}$$

in which $\boldsymbol{T}_1$ denotes a fourth-order tangent stiffness tensor with minor symmetries, and $\Delta\varepsilon_k$ is the incremental strain within side 1 due to the evolution of localization. According to Maxwell's compatibility conditions, $\Delta\varepsilon_k$ must be a rank-one tensor of the form

$$\Delta\varepsilon_k = \frac{1}{2l}(\Delta \boldsymbol{m} \otimes \boldsymbol{n} + \boldsymbol{n} \otimes \Delta \boldsymbol{m}) \tag{6}$$

with l being the half-band width of the localization zone. The use of Eqs. (4) - (6) then yields the classical necessary condition for a discontinuous bifurcation or loss of ellipticity:

$$\boldsymbol{Q} \cdot \Delta \boldsymbol{m} = \boldsymbol{0} \tag{7}$$

with $\boldsymbol{Q}=\boldsymbol{n}\cdot\boldsymbol{T}_1\cdot\boldsymbol{n}$ being the acoustic tensor. An eigen analysis can be performed to find out the orientation of localization, $\Delta \boldsymbol{m}$, corresponding to a zero eigenvalue of the acoustic tensor. However, the magnitude of $\Delta \boldsymbol{m}$ depends on the evolution of localization. If $\Delta \boldsymbol{m}$ is determined from a constitutive model, then the jump in the strain rate can be found.

To determine the jump in mass density, an evolution equation for damage must be defined. It is assumed that the shear-induced cracking in a representative volume is governed by a strain-based damage surface [Chen and Xin, 1997],

$$f = \bar{e} - \bar{e}_0(1 + m_0 D) \tag{8}$$

where $\bar{e}$ is the second invariant of deviatoric strain tensor, $\bar{e}_0$ is the critical state parameter, D is damage, and m_0 is a model parameter. With the use of a standard procedure (Chen and Schreyer 1994), it can be shown that the damage surface satisfies the thermodynamic restrictions and the rate of damage is determined by

$$\dot{D} = \frac{\dot{\bar{e}}}{\bar{e}_0 m_0}. \tag{9}$$

To represent the overall effect of shear-induced local dilatation on the change in mass density, an integral average of damage over the representative volume, $\overline{D}$, is used to find ρ_1, namely,

$$\rho_1 = \rho_2 + (\rho_m - \rho_2)\left(1 - e^{-m_1 \overline{D}}\right) \tag{10}$$

with m_1 being a model parameter. As can be found from Eq. (10), $\rho_1 = \rho_2$ if there is no damage, and ρ_1 will approach the maximum value ρ_m with an increase in $\overline{D}$. If ρ_m is reached, phase transformation might occur, a further discussion on which is beyond the scope of this paper. Because of $\rho_1 > \rho_2$ with the evolution of damage, the localization zone will expand based on Eq. (1).

A partitioned-modeling approach is employed in the proposed numerical procedure with a total-strain-control scheme, as discussed next. Since the condition of $\boldsymbol{v}_1 \cdot \boldsymbol{n} = \boldsymbol{v}_2 \cdot \boldsymbol{n} = \boldsymbol{v}_b \cdot \boldsymbol{n}$

holds across the moving material surface between the damaging and unloading zone, the increase in the total strain inside the localization zone would expand the zone. A typical example is the formation and propagation of a shear band under uniaxial compression as shown in Fig. 1. As can be seen, local micro-cracking (dilation) would push the materials inside the band to the boundary of the band so that $\rho_1 > \rho_2$ across the moving boundary.

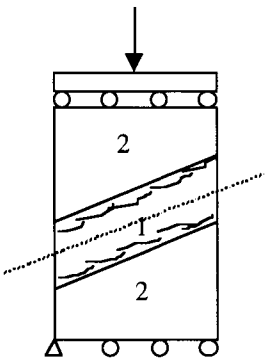

Figure 1: Evolution of shear band after failure occurs

To implement a moving material surface into the numerical procedure, a local remeshing process is proposed here [Chen et al., 1997]. If the eigen analysis on the acoustic tensor indicates that the material is still in the pre-limit stage, no change needs to be made to the original mesh. If material failure occurs, the moving speed of the material surface between the elastic unloading zone and the localization zone is determined based on the jump conditions. For the orientation of the localization zone given by the eigen analysis, a simple remeshing process can be demonstrated through a 2-D example as shown in Fig. 2. If the weak element is located in the center, a shear band will occur between the boldfaced lines. The unit normal obtained from the eigen analysis is given as $\mathbf{n} = (\cos\alpha, \sin\alpha)$ in the 2-D space. Due to the evolution of the failure process, a new material surface is shown by the dashed lines. Assuming the coordinate for a node along the top surface of the shear band is (x_1, y_1), and the magnitude of the moving speed for the current incremental step is v_{bi}, then the new coordinate of this node (x_1', y_1') is given by

$$x_1' = x_1 + v_{bi}\Delta t \cdot \cos\alpha \tag{11a}$$

$$y_1' = y_1 + v_{bi}\Delta t \cdot \sin\alpha \tag{11b}$$

in which Δt is the time interval. The same operations will be performed for the other nodes along this moving material surface. It should be noted that when a shear band forms, there are two moving material surfaces, both departing from the original shear band in the contrary direction. Hence, an upper and a lower surface with corresponding normals should be defined based on the location of the node.

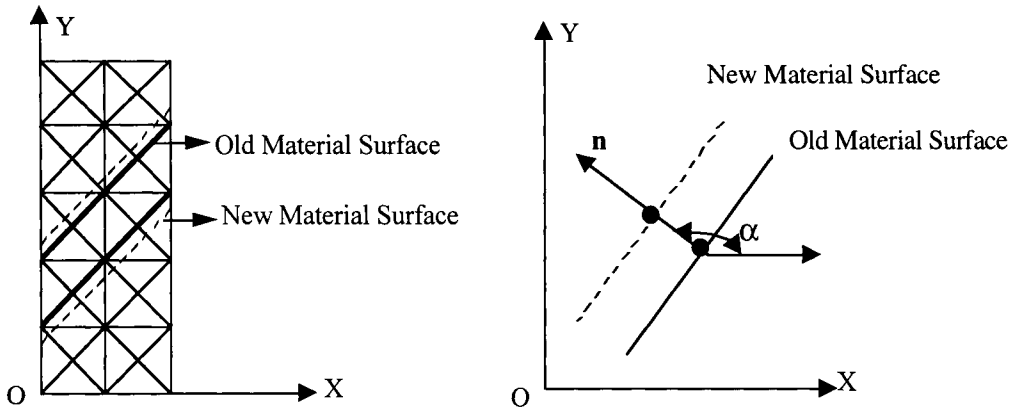

Figure 2 : A 2-D demonstration for the moving material surface and the remesh process at a specific node

In summary, the proposed solution scheme for simulating the evolution of localization consist of the following steps:

Step 1: At the beginning of a new incremental step, an eigen analysis is performed on the acoustic tensor for each element. If failure is detected, find the unit normal to the moving material surface and record the element number, then go to next step; If no failure is indicated, go to step 4.

Step 2: Based on the jump conditions, the moving speed of the material surface can be obtained.

Step 3: Starting a loop for the elements in which material failure occurs, and update the configuration for the nodes inside the localization zone by using Eq. (11). Attention should be paid to those nodes shared by two or more elements: only one update in the configuration can be made for each of these nodes in a single shear band case. For the nodes inside the elastic regime, no change needs to be made.

Step 4: Return to the main program which employs the total-strain-control algorithm.

In the proposed procedure, several assumptions have been made as a result of numerical approximation. First of all, in order to get the displacement of the node at the new location, certain interpolation is performed in the displacement field, depending on the assumption used for a specific type of elements. For example, linear interpolation is applied in the case of classical triangular element. In addition, since there is a change in the nodal position along the material surface, we can expect a change in the shapes of the corresponding elements both inside and outside the localization zone. In this case, we assume that the basic variables such as stress, strain and internal variables are the same as the values from the last step for these elements. For a small incremental step, this is reasonable and therefore the algorithm can be

greatly simplified. The remeshing process is designed so that the size of the localization zone is updated based on the moving jump conditions.

DEMONSTRATIONS

To demonstrate the robustness and potential of the proposed procedure that is based on the moving jump forms of conservation laws, sample results s are presented for both quasi-static and dynamic cases.

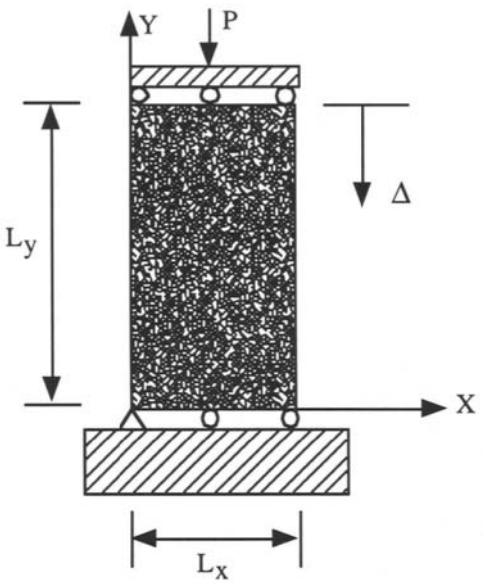

Figure 3: The geometry and notation for a plane problem

For the quasi-static loading case, the problem geometry is given in Fig. 3. The sizes of the specimen are L_x = 3m and L_y = 6m. Rectangular elements composed of four triangles are employed for the simulation. The load is applied such that all the points at the top surface will have the same vertical displacements. In addition, all the points at the bottom are constrained in the vertical direction and no horizontal displacement is allowed for the left most point. An associated von Mises model with bilinear hardening and softening function is used, with Young's Modulus E = 50GPa and Poisson's ratio ν = 0.2. An initial imperfection is introduced by assigning a weaker limit strength in the weak element. With the use of a fine mesh, the deformation pattern with the local von Mises model is shown in Fig. 4, and the corresponding deformation pattern with the proposed procedure is given in Fig. 5. As can be seen, the use of a moving material surface expands the localization zone. Figure 6 demonstrates the mesh-independence of numerical solutions with the proposed procedure.

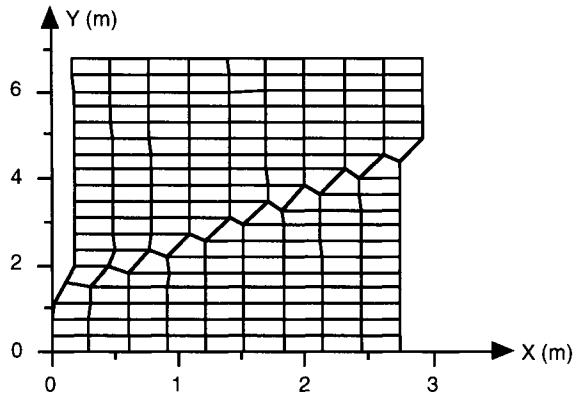

Figure 4: Deformation pattern with local von Mises model for mesh III

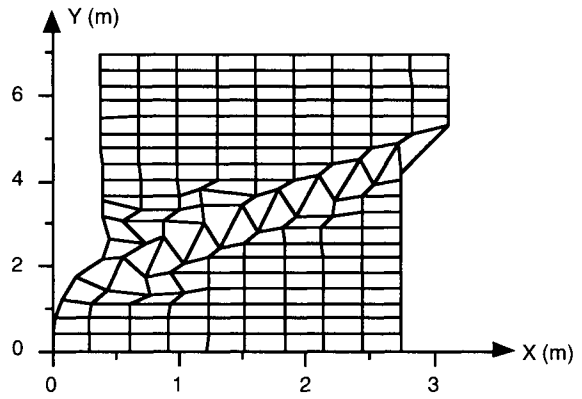

Figure 5: Deformation pattern with proposed procedure for mesh III

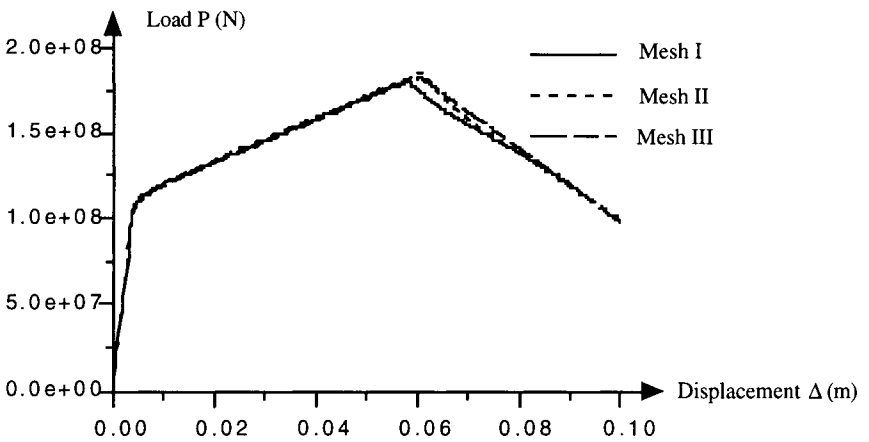

Figure 6: Mesh-independent solutions with the proposed procedure

For the dynamic case, a bar of length $L = 1m$ is considered here [Chen et al., 1997]. The bar is fixed at $x=0$ and loaded at $x=L$. A Newmark integrator is used in the time domain with the

time step satisfying the standard stability condition. After the limit state is reached at the fixed end, the evolution of localization is shown in Fig. 7, and the corresponding decrease of stress is given in Fig. 8. Figure 9 demonstrates the convergence of numerical solutions with different meshes at $t = 300\mu s$.

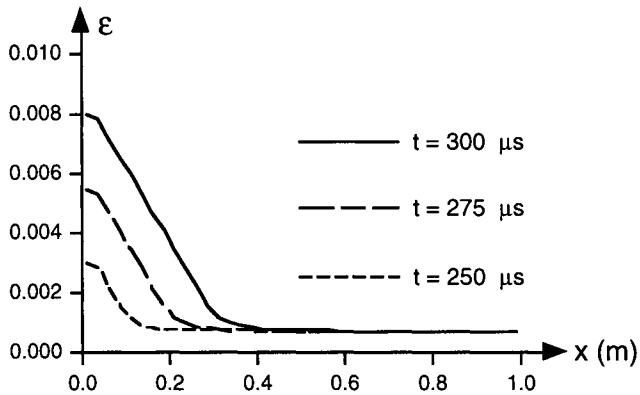

Figure 7: The evolution of localization after the limit state is reached

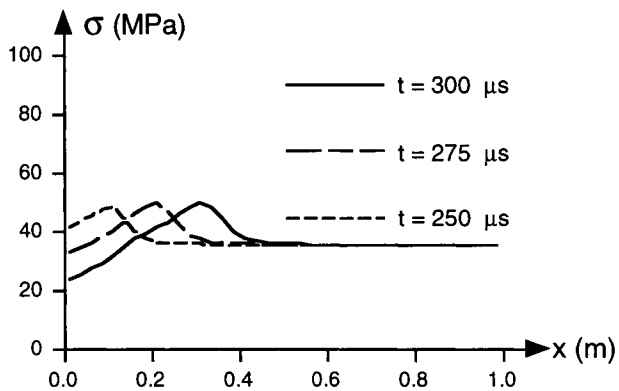

Figure 8: The decrease of stress corresponding to Fig.7

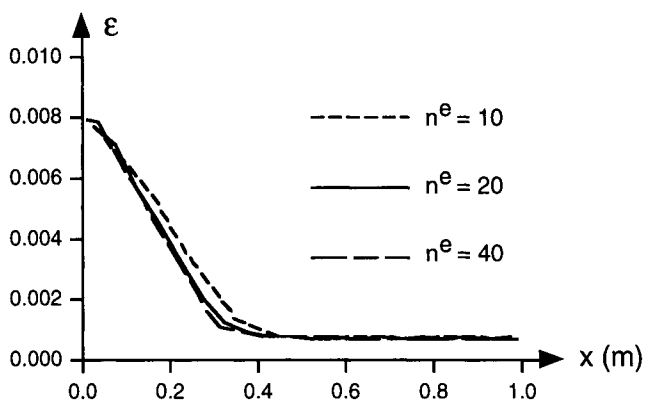

Figure 9: Convergence study with different meshes at t = 300 μs

CONCLUDING REMARKS

Existing numerical procedures for simulating the evolution of localization have been reviewed in this paper. To simulate the evolution of localization without invoking higher order terms, a developing numerical scheme has also been introduced. As a result, a simple solution procedure with the use of local models can be designed for localization problems, if localization is considered as a phase transition (diffusion) process. In this procedure, the initiation of localization is identified via monitoring the transition between different types of governing differential equations, and the evolution of localization is traced by using a moving material surface of discontinuity. The proposed procedure has been demonstrated through sample problems under dynamic (an elliptic equation inside the localization zone and a hyperbolic one outside the zone) and quasi-static (two different elliptic equations inside and outside the zone, respectively) loading conditions. The numerical results are consistent with the essential feature of localization phenomena.

Further study is required to apply the proposed procedure to a general case, which involve multi-dimensional effects, large deformations, discontinuity, anisotropy and phase transition. Although several promising approaches have been proposed for spatial discretization in localization problems, it is still a challenging task to tackle different types of governing equations in a single computational domain, because of different temporal and spatial scales. Since the design of advanced engineering structures needs the solutions for this kind of problems, it is hoped that more innovative ideas will come from the international research community in the near future.

ACKNOWLEDGMENTS

This work was sponsored (in part) by NSF and AFOSR.

REFERENCES

R. de Borst, L.J. Sluys, H.B. Muhlhaus and J. Pamin (1993). Fundamental Issues in Finite Element Analyses of Localization of Deformation. *Engineering Computation* **10**, 99-121.

Z. Chen (1993a). A Partitioned-Solution Method with Moving Boundaries for Nonlocal Plasticity. *Modern Approaches to Plasticity*, edited by D. Kolymbas, Elsevier, New York, 449-468.

Z. Chen (1993b). A Semi-Analytical Solution Procedure for Predicting Damage Evolution at Interfaces. *International Journal for Numerical and Analytical Methods in Geomechanics* **17**, 807-819.

Z. Chen (1996a). Continuous and Discontinuous Failure Modes. *Journal of Engineering Mechanics* **122**, 80-82.

Z. Chen (1996b). A Simple Procedure to Simulate the Failure Evolution. *International Journal of Structural Engineering and Mechanics* **4**, 601-612.

Z. Chen and H.L. Schreyer (1990a). A Numerical Solution Scheme for Softening Problems Involving Total Strain Control. *Computers and Structures* **37**, 1043-1050.

Z. Chen and Schreyer, H.L. (1990b). *Formulation and Computational Aspects of Plasticity and Damage Models with Application to Quasi-Brittle Materials*, SAND95-0329, Sandia National Laboratories, Albuquerque, NM.

Z. Chen and H.L. Schreyer (1991). Secant Structural Solution Strategies under Element Constraint for Incremental Damage. *Computer Methods in Applied Mechanics and Engineering* **90**, 869-884.

Z. Chen and H.L. Schreyer (1994). On Nonlocal Damage Models for Interface Problems. *International Journal of Solids and Structures* **31**, 1241-1261.

Z. Chen and D. Sulsky (1995). A Partitioned-Modeling Approach with Moving Jump Conditions for Localization. *International Journal of Solids and Structures* **32**, 1893-1905.

Z. Chen and T. Clark (1995). Some Remarks on Domain-Transition Problems. *Archives of Mechanics* **47**, 499-512.

Z. Chen and X. Xin (1997). An Analytical and Numerical Study of Failure Waves. To appear in *International Journal of Solids and Structures*.

Chen, Z., X. Xin and D. Qian (1997). A Study of Localization Problems Based on the Transition between Governing Equations. Submitted for publication in *International Journal of Mechanics of Cohesive-Frictional Materials*.

G. Pijaudier-Cabot and L. Bode (1995). Arbitrary Lagrangian-Eulerian Finite Element Analysis of Strain Localization in Transient Problems. *International Journal for Numerical Methods in Engineering* **38**, 4171-4191.

D. Sulsky, Z. Chen and H.L. Schreyer (1994). A Particle Method for History-Dependent Materials. *Computer Methods in Applied Mechanics and Engineering* **118**, 179-196.

D.Y. Tzou (1989). On the Thermal Shock Wave Induced by a Moving Heat Source. *ASME Journal of Heat Transfer* **111**, 232-238.

M. Xie, W. Gerstle and Z. Chen (1994). Finite Element Analysis of Combined Smeared and Discrete Mechanisms in Rock Salt. *Computer Methods and Advances in Geomechanics*, edited by H.J. Siriwardane and M.M. Zaman, A.A. Balkema Publishers, Brookfield, VT, pp. 1659-1664.

ε-CONTINUATION APPROACH FOR TRUSS TOPOLOGY OPTIMIZATION

Xu Guo and Gengdong Cheng

State Key Laboratory of Structural Analysis of Industrial Equipment
Dalian University of Technology
Dalian 116023, PR CHINA

ABSTRACT

A so-called ε-continuation approach is proposed for the solution of singular optima in truss topology optimization. In the approach, we start the optimization process from a relatively large value of ε, apply the ε-relaxed formulation and obtain an optimum design of this relaxed problem; then we decrease the value of ε by $\Delta\varepsilon$, and choose the design from the previous optimization as initial design to begin the next optimization, and continue the process until convergence. It is shown by numerical examples that this scheme alleviates the dependence of the final solution on the choice of the initial design and increases greatly the probability of finding the singular optima from rather arbitrary choice of the initial design.

KEYWORDS

structural topology optimization; numerical algorithm; singular optima; relaxed formulation;

INTRODUCTION

While many efforts have been made in solving topology optimization problems of truss structures, it is well-recognized that there are still serious difficulties in this field. One of them is the so-called singular optima phenomenon which prevents the iterative algorithms from

converging to the true optimal solution. Singular optima in structural topology optimization was first shown by Sved and Gions[1]. They found that in some cases, global optimal topology could not be obtained by employing the nonlinear programming techniques unless one deleted the unnecessary bars from the ground structure in advance. Since then, the phenomena of singular optima was studied intensively by many authors. Kirsch[2] investigated the singular optima in truss and grillage topology optimization problems. He suggested that singular optima corresponds to a singular point in the design space and it is very difficult or even impossible to arrive at it by numerical search algorithms. Cheng and Jiang[3] pointed out that singular optima appears mainly due to the nature of local behaviour constraint. Illustrating by truss topology optimization problems subjected to stress constraints, they demonstrated that the discontinuity of the bar's stress constraint function when its cross sectional area takes zero value is the essential cause of the existence of singular optima. The authors suggested to establish a rational formulation which unifies the sizing and topology optimization and enables one to apply the sizing optimization techniques for the solution of topology optimization problems. Rozvany[4] studied the singular optima in the light of exact optimal layout theory and proposed a precise definition of singular optima.

Since singular optima is a major obstacle to structural topology optimization, various methods have been suggested to overcome the difficulties. Kirsch[5] proposed a design procedure to find the optimum of singular topologies by neglecting the compatibility conditions and applying linear programming technique. His method is appropriate only when the optimal design is statically determined. Recently, Kirsch[6] has presented another two-stage topology optimization procedure consisting of reduction and expansion process in order to eliminate the problems of singular optima which may appear in the conventional approach. Rozvany[7] suggested that for truss topology optimization problems subjected to stress constraints ,smooth envelope functions should be used to make the feasible set nonsingular. Recently, a ε-relaxed approach for the solution of singular optima has been developed by Cheng and Guo[8]. In this approach, the problem is reformulated by relaxing the local behaviour constraint through the introduction of a relaxation parameter ε. Under this relaxed formulation, singular optima does not exist in the design space, so that one can now apply the sizing optimization technique to solve this reformulated problem. It is proved that the solution of the relaxed problem is a good approximation of the solution of the original problem as long as ε is sufficiently small. Although great successes have been achieved by applying this approach for the solutions of singular problems, however, it should be noted that this approach cannot locate the global optimal solution exactly unless the relaxation parameter ε is small enough and initial design is properly chosen. Hoback[9] proposed a percent method to find the global optimal design of singular problems and presented a number of numerical examples.

In the present paper, based on the aforementioned ε-relaxed approach, a so-called ε-continuation approach is developed for the solutions of truss topology optimization. By applying this approach, in most of the test cases, global optimal solution, even if a singular

one, can be obtained from rather arbitrary choice of the uniform initial design. The effectiveness of this approach is illustrated by several numerical examples.

ε-RELAXED APPROACH

For completeness, in this section, we will describe the ε-relaxed approach briefly. The problem of truss topology optimization subject to stress constraints can be given as follows.

P_0: to find $A_1, A_2, \ldots, A_N$

$$\text{Min } W = \sum_{i=1}^{N} \rho_i l_i A_i \tag{1a}$$

St
$$\mathbf{KU}_j = \mathbf{P}_j \qquad j = 1,\ldots,M \tag{1b}$$
$$\sigma_i^L - \sigma_{ij} \le 0 \qquad j = 1,\ldots,M; \quad i = 1,2,\ldots,N \tag{1c}$$
$$\sigma_{ij} - \sigma_i^U \le 0 \qquad j = 1,\ldots,M; \quad i = 1,2,\ldots,N \tag{1d}$$
$$A_i \ge 0 \qquad i = 1,2,\ldots,N \tag{1e}$$

As noted in [8], under ε-relaxed approach, the problem can be reformulated as follows:

P_ε: to find $A_1, A_2, \ldots, A_N$

$$\text{Min } W = \sum_{i=1}^{N} \rho_i l_i A_i \tag{2a}$$

St
$$\mathbf{KU}_j = \mathbf{P}_j \qquad j = 1,\ldots,M \tag{2b}$$
$$(\sigma_i^L - \sigma_{ij}) A_i \le \varepsilon \qquad j = 1,\ldots,M; \quad i = 1,2,\ldots,N \tag{2c}$$
$$(\sigma_{ij} - \sigma_i^U) A_i \le \varepsilon \qquad j = 1,\ldots;M; \quad i = 1,2,\ldots,N \tag{2d}$$
$$A_i \ge A_i^L \qquad i = 1,2,\ldots,N \tag{2e}$$

where N is the total number of bars in the ground structure, M denotes the number of loading cases. A_i, ρ_i, l_i are cross sectional area, mass density and the length of i-th bar. The superscript U and L refer to the upper and lower bounds of the relevant quantities, respectively.

Under this formulation, the stress constraints are relaxed by introducing a relaxation parameter ε. It can be seen that for any given $\varepsilon > 0$, the constraint (2c),(2d) can always be satisfied for sufficiently small A_i. Thus, in the vicinity of the degenerated subdomain corresponding to $A_i = 0$, the measure of the feasible design space is non-zero. Therefore, under this formulation, optima is not singular and one can apply the conventional numerical search algorithms to arrive at the optima of the relaxed problem. With the help of the theory of point to set mapping [10], it can be proved that the optimal solution of the relaxed problem will converge to the solution of the original problem as the relaxation parameter ε tends to zero. Thus the optimal solution of the relaxed problem provides a good approximation of the corresponding optima of the original problem, even if it is singular.

ε-CONTINUATION APPROACH

Although the ε-relaxed approach enables one to reach the singular optima by numerical optimization, it should be noted that just like most of the optimization techniques, this approach cannot locate the global optimal design unless the initial design is properly chosen. In fact, the global optimization is still a challenge in the field of structural optimization. From mathematical point of view, it is essentially unsolvable. In order to obtain the global optimal design, various methods have been proposed. But unfortunately, these methods are either computationally expensive or not suitable for the solution of large-scale problems. Thus for a practical problem, if global optima is needed, it seems that the best thing one can do is to extend the "attractive region" of the global optima if one is not willing to bear the enormous cost. The ε-continuation approach follows this idea. Its basic steps can be described as follows.

Step 1. Under ε-relaxed formulation, start the optimization process from a relatively large value of ε and an arbitrary chosen uniform initial design;

Step 2. Decrease ε by $\Delta\varepsilon$, and choose the optimal solution obtained from the previous optimization step as initial design to begin the next optimization step;

Step 3. Continue this until a small desired value of ε has been reached.

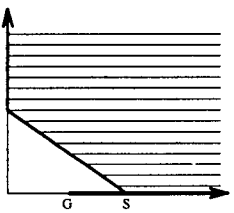

Figure 1: Feasible domain for singular problem

To explain the idea behind the approach, let us consider a typical geometric representation of singular topology optimization (see Fig. 1). There is a degenerated sub-domain in the design space and the global singular optima is located at point G in whose vicinity the measure of the feasible domain is zero. Under conventional formulation, numerical search algorithms terminate at non-optimal solution point S.

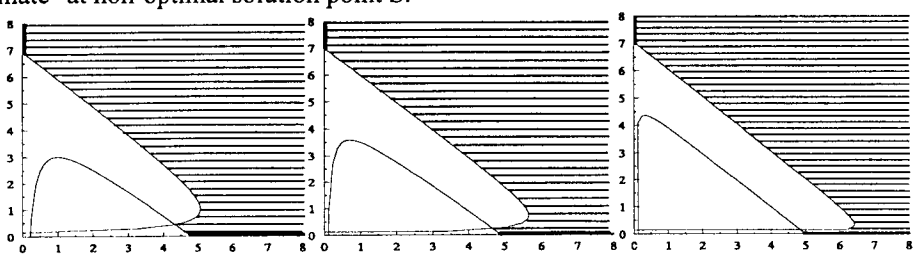

Figure 2: Feasible domain under different values of ε

Under ε-relaxed formulation, the design space for different values of ε can be shown in Fig.2. Observing these figures, it is clear that under ε-relaxed formulation, the shape of the feasible domain is rather regular for a large ε; with the decreasing of the value of ε, the feasible domain of the relaxed problem approaches more and more that of the original problem, but becomes irregular. Since the shape of the feasible domain is rather regular for a large ε , the attractive region of the global optima of the relaxed problem may also be relatively large; therefore the probability with which numerical search algorithms converge to the global optima from an arbitrary choice of the initial design is high. Moreover, based on the convergence analysis of ε-relaxed approach in [8] it has been concluded that the global optimal design of the relaxed problem is a continuous function of ε, so the optimal designs from two successive optimization steps may be very close if the degradation of ε is not too large. Thus the optimal solution obtained from previous optimization step is a good initial design for the next optimization step. In other words, by means of this continuation approach, we can choose a proper direction to converge to the global optimal solution of the original problem. Numerical examples show that in most of the cases, the global singular optima can be obtained by means of this approach without much extra computation effort.

CONVERGENCE ANALYSIS

In this section, proof of convergence for our ε-continuation approach will be given. It is established under the following assumptions.

Assumption 1 . The original optimization problem P_0 has a bounded optimal solution $W_0^{opt} < +\infty$.

Assumption 2. In every optimization step, we can get the global optimal solution W_ε^{opt} of the relaxed problem P_ε.

Denoting the feasible set of the design variable associated with problem P_0 and problem P_ε as U_0 and U_ε respectively, we have the following lemmas.

Lemma 1. $U_{\varepsilon_k} \subset U_{\varepsilon_l}$ for $\varepsilon_k < \varepsilon_l$, $\varepsilon_k \geq 0, \varepsilon_l \geq 0$.

The proof of this lemma is obvious.

Lemma 2. If $\varepsilon_k < \varepsilon_l$, $\varepsilon_k \geq 0, \varepsilon_l \geq 0$, then $W_{\varepsilon_k}^{opt} \geq W_{\varepsilon_l}^{opt}$.

Proof: Denoting the optimal design corresponding to problem P_ε as $\mathbf{A}_\varepsilon^{opt}$, then from lemma 1, we have $\mathbf{A}_{\varepsilon_k}^{opt} \subset U_{\varepsilon_k} \subset U_{\varepsilon_l}$, if $\varepsilon_k < \varepsilon_l$. Then $W_{\varepsilon_l}^{opt} = W(\mathbf{A}_{\varepsilon_l}^{opt}) = \inf_{\mathbf{A} \in U_{\varepsilon_l}} W(\mathbf{A}) \leq W(\mathbf{A}_{\varepsilon_k}^{opt}) = W_{\varepsilon_k}^{opt}$. In particular, we have $W_{\varepsilon_k}^{opt} \leq W_0^{opt} = W(\mathbf{A}_0^{opt})$ for all $\varepsilon_k \geq 0$.

From the above lemmas, we have the following theorem.

Theorem 1: For a positive sequence $\{\varepsilon_k\}, \varepsilon_k > \varepsilon_{k+1} > 0$ and $\lim_{k\to\infty} \varepsilon_k = 0$; then under assumptions 1-2, we have $\lim_{k\to\infty} W_{\varepsilon_k}^{opt} = W_0^{opt}$.

Proof: By lemma 2 and assumption 1, it is clear that $\{W_{\varepsilon_k}^{opt}\}$ is an above bounded monotontically increasing sequence. Therefore, from the theory of mathematical analysis, the sequence $\{W_{\varepsilon_k}^{opt}\}$ must have limit $\lim_{k\to\infty} W_{\varepsilon_k}^{opt} = \overline{W} \le W_0^{opt}$. For the completeness of the proof, it is only required to show that $\overline{W} < W_0^{opt}$ is impossible. Assuming that $\overline{W} < W_0^{opt}$, then we can find a real number $\delta > 0$ such that $\theta = W_0^{opt} - \overline{W} - \delta > 0$. Since $\lim_{k\to\infty} W_{\varepsilon_k}^{opt} = \overline{W}$, there exists an integer $K_0 > 0$, for all ε_k such that $k \ge K_0$, $\left|W_{\varepsilon_k}^{opt} - \overline{W}\right| < \theta$; then for all $k \ge K_0$,

$$W_{\varepsilon_k}^{opt} < \overline{W} + \theta = W_0^{opt} - \overline{W} - \delta + \overline{W} = W_0^{opt} - \delta \qquad (3)$$

On the other hand, based on the continuity result of $W^{opt}(\varepsilon)$ with respect to ε when $\varepsilon = 0$ which was established in [8], we have for $\delta > 0$; there exists an integer $K_1 > 0$, such that for all $k > K_1$, $\left|W_{\varepsilon_k}^{opt} - W_0^{opt}\right| < \delta$. So it readily follows that for all $k > K_1$, $W_{\varepsilon_k}^{opt} > W_0^{opt} - \delta$. This contradicts (4a) when k is sufficiently large. Thus the assumption of $\overline{W} < W_0^{opt}$ is invalid and $\overline{W} = W_0^{opt}$ holds. The proof is completed.

NUMERICAL EXAMPLES

In this section, several numerical examples will be presented to illustrate the effectiveness of our ε-continuation approach. A program which implements the Constraint Variable Metric optimization technique was used as optimizer and another structural analysis program has also been developed for the function calculations. All the design variables and constraints are scaled. Sensitivity analysis is carried out by means of backward finite difference approach. The difference step was T=0.005 for all examples.

Generally speaking, the starting value of ε may be chosen heuristically as long as ε_0 is larger than a critical value ε_{cr}. It is clear that this value is problem-dependent. Setting ε_{cr}=10.0 was found to be adequate for all examples shown below. The value of Δε also depends on the characteristics of the particular problem; setting $\varepsilon_{k+1}=\varepsilon_k$-0.5 often works well. The termination value ε_{ter} can be taken as 0.01-0.00001. If ε_{ter} is too small, machine error will predominate; thus the effect of relaxation can not be manifested. The symbol SF,IF,RF in the following text denotes the stress formulation (1), internal force formulation which impose constraints on bar internal force, i.e., set ε=0 in (2c) and (2d), and ε-relaxed formulation (2), respectively.

3-bar truss example

A three-bar truss subjected to three load cases (see Fig.3) is optimized. It is a classical example from [1]. E=1.0,h=1.0,ρ=1.0. The allowable stresses are $\sigma_{ia} = \pm 5.0, i = 1,3$; $\sigma_{2a} = \pm 20.0$. The three loading cases are (a) P=40,c=45°; (b) P=30, c=90° ; (c) P=20,c=135°, respectively.

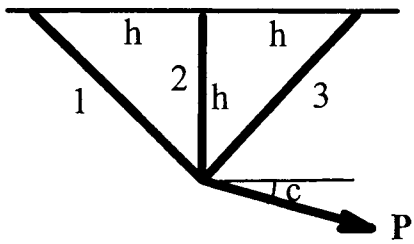

Figure 3: Sved and Gions' 3-bar truss example

As was shown[1], its global optimal design is a 2-bar truss, i.e.,
$A_1 = 8.00, A_2 = 1.50, A_3 = 0.00$. This is a singular optima because for this design

$$\lim \sigma_{23} = 20.00 > 5.00, \quad \lim \sigma_{33} = 21.36 > 5.00$$

The optimization results obtained under different problem formulations are listed in Table 1.

TABLE 1

OPTIMIZATION RESULTS UNDER DIFFERENT FORMULATIONS

Final results of different formulations from different initial designs							
Initial Design			Relaxed Formulation				Stress
A1	A2	A3	A1	A2	A3	W	Formulation
8.0	2.4	3.2	7.024	2.135	2.767	15.97	W=15.97
0.0	12.0	18.0	0.000	2.828	8.000	14.14	W=15.97
0.7	4.0	10.0	0.000	2.828	8.000	14.14	W=15.97
1.0	1.0	1.0	7.024	2.135	2.767	15.97	W=15.97
10.0	10.0	10.0	7.024	2.135	2.767	15.97	W=15.97
1.0	1.0	0.1	8.00	1.50	0.00	12.81	W=15.97
10.0	10.0	0.1	8.00	1.50	0.00	12.81	W=15.97
Gl.Opt			8.00	1.50	0.00	12.81	W=15.97

From Table 1, it can be seen that under conventional stress formulation, the singular global optimal solution cannot be obtained no matter how you choose the initial design. The numerical search algorithms always terminate at a local optima. But if the initial design is properly chosen, it is possible for ε-relaxed approach to arrive at the global optimal solution. It is worth noting , however, that if we start the optimization process from an arbitrary chosen initial design, ε-relaxed approach cannot always locate the global optima. For this example,

the global optima cannot be achieved unless the initial value of A_3 is less than 0.1. This unpleasant behavior can be attributed to the fact that when the value of the relaxation parameter ε is very small, the shape of the feasible domain may be rather irregular in the vicinity of the singular optima; thus the attractive region of the singular optima may be very small, so the global optima can be found only when the initial design is very close to it.

TABLE 2

OPTIMIZATION HISTORY AND CORRESPONDING ELEMENT STRESS

Continuation History (3*10.0)					Element Stress		
ε	A1	A2	A3	W	1	2	3
5.0	6.8409	0.8214	0.2406	10.684	5.735	1.680	-4.056
					0.891	26.087	25.197
					-2.028	23.756	25.783
4.0	7.0232	0.9554	0.2075	11.094	5.570	1.309	-4.261
					0.694	24.187	23.493
					-2.130	22.150	24.280
2.0	7.4931	1.2270	0.1149	11.937	5.267	0.616	-4.651
					0.327	21.630	21.303
					-2.326	20.085	22.410
1.0	7.7425	1.3635	0.0595	12.371	5.129	0.298	-4.831
					0.158	20.733	20.575
					-2.416	19.399	21.814
0.5	7.8703	1.4318	0.0317	12.592	5.062	0.154	-4.909
					0.082	20.319	20.237
					-2.454	19.080	21.534
0.1	7.9739	1.4864	0.0061	12.768	5.013	0.029	-4.983
					0.015	20.067	20.052
					-2.492	18.905	21.397
0.01	7.9974	1.4986	0.0006	12.808	5.001	0.003	-4.998
					0.002	20.007	20.005
					-2.499	18.860	21.360
0.001	8.0000	1.4999	0.0000	12.812	5.000	0.000	-5.000
					0.000	20.001	20.000
					-2.500	18.857	21.357
Gl.Opt	8.0000	1.5000	0.0000	12.812			

To illustrate the effectiveness of our ε-continuation approach, optimizations are performed by means of the propose method under different choice of the initial design. Since in practice, we have no idea about which bar will remain in the final optimal topology, it is natural to

start the optimization process from a uniform initial design. Taking the initial design as 3*1.0, 3*5.0, 3*10.0, 3*20.0, in all cases, ε-continuation approach gives the same optimal result. Table 2 gives the optimization results from initial design 3*1.0 with $\varepsilon_0 = 5.0$. With reference to Table 2, it may be seen clearly that the proposed approach could achieve result very close to the global optima of the original problem when ε is sufficiently small. It can also be observed that with the decreasing of ε, all of the constraints can be satisfied to a high accuracy. In this example, the termination value of ε is taken as 0.001; further iterations did not improve the result. Fig.4 shows the continuation history of the structural weight.

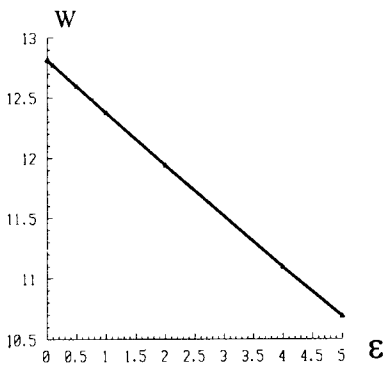

Figure 4: Continuation history of structural weight of 3-bar truss

5-bar truss example

Fig.5 shows the ground structure. Geometrical and material data are $E = 1.0, h = 1.0, \rho = 1.0$, allowable stresses are $\sigma_{ia} = \pm 5.0, i = 1,3,4,5$; $\sigma_{2a} = \pm 20.0$. Two loading cases are considered; they are (a) P_{ax}=0.0, P_{ay}=0.0, P_{bx}=-5.0, P_{by}=50.0; (b) P_{ax}=-5.0, P_{ay}=50.0, P_{bx}=0.0 P_{by}=0.0; the optimization results of this example are given in TABLE 3. The global optimal solution of this problem is a still a singular one because for the optimal design we have

$$|\lim \sigma_{14}| = 15.00 > 5.00, \quad |\lim \sigma_{24}| = 7.25 > 5.00$$

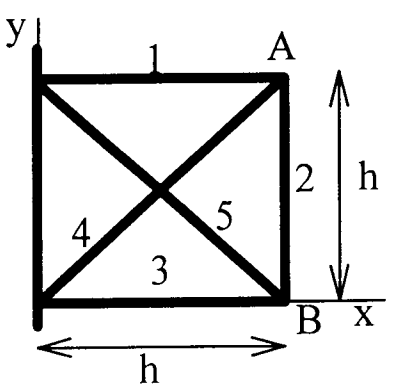

Figure 5: 5-bar truss example

Inspection of Table 3 reveals that the conventional formulation generates only non-optimal design no matter from what initial design the iteration starts. For ε-continuation approach, global optimum was obtained. Table 3 gives the optimization results with 5*10.0 and $\varepsilon_0 = 10.0$. Global optimal design is obtained after 7 continuation steps.

TABLE 3
OPTIMIZATION RESULTS FOR 5-BAR TRUSS

Continuation History(5*10.0)						
	A1	A2	A3	A4	A5	W
10.0	0.776	1.55	6.23	0.97	11.06	26.933
8.0	1.12	1.67	6.68	0.84	11.51	28.551
6.0	1.11	1.87	7.50	0.64	12.14	30.173
4.0	1.07	2.08	8.33	0.43	12.79	32.657
1.0	1.01	2.40	9.59	0.10	13.80	33.416
0.01	1.00	2.49	9.96	0.01	14.14	33.486
0.001	1.00	2.50	10.00	0.00	14.14	33.496
GL.Opt	1.00	2.50	10.00	0.00	14.14	33.500
SF	7.219	4.735	4.531	8.795	7.828	39.990

Hoback's 4-bar truss example

The 4-bar truss shown in Fig.6 was optimized. This example was discussed by Hoback for demonstrating the effectiveness of his percent method for the solution of singular problems. The structure is subjected to two load conditions, that is, P_1=10, P_2=0 for load case 1, P_1=0, P_2=10 for load case 2. The allowable stresses for all members are 20 and 5 in tension and compression respectively.

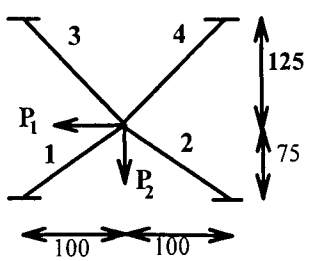

Figure 6: Hoback's 4-bar truss example

Its global optimal solution is $A_1 = 0.000, A_2 = 0.4286, A_3 = 0.4773$ and $A_4 = 0.3476$. This is a singular and static indeterminate design because for this design the limiting stress of bar 1 violates the constraint imposed on it. The results of ε-continuation approach are shown in

Table 4. Singular optima was obtained after 7 continuation steps from the uniform initial design 4*10.0 (see Table 4). Optimization from other uniform initial design gives the same results. Under conventional formulations, numerical algorithms iterate only to the local optimum. Compared with the percent method[9], ε-continuation approach can obtain the global optimal solution from arbitrary choice of the initial design without introducing extra design variables. And our result is lighter in weight than the one given by the percent method.

TABLE 4

CONTINUATION HISTORY, FINAL DESIGNS FROM HOBACK, SF AND IF FOR 4-BAR TRUSS

	A1	A2	A3	A4	W
2.0	0.0529	0.1451	0.1521	0.1592	79.39
1.5	0.0481	0.2083	0.2586	0.2021	105.79
1.0	0.0372	0.2757	0.3361	0.2483	132.66
0.5	0.0210	0.3480	0.4109	0.2969	159.42
0.1	0.0046	0.4115	0.4653	0.3373	180.48
0.01	0.0000	0.4274	0.4757	0.3471	185.15
0.001	0.0000	0.4286	0.4773	0.3476	185.62
Hoback	0.0000	0.5600	0.3980	0.3620	191.00
SF	1.0157	1.0115	0.4939	0.4886	410.69
IF	0.0000	1.2500	0.0000	2.1479	500.08

10-bar truss example

This example is a modified version of the well-known 10-bar truss problem(see Fig. 7). The truss is subjected to two load cases, that is, P_1=100, P_2=0 for load case 1, P_1=0, P_2=200 for load case 2. $E = 1.0E + 04, h = 360.0, \rho = 1.0$. The allowable stress for all members is 20 and 5 in tension and compression respectively.

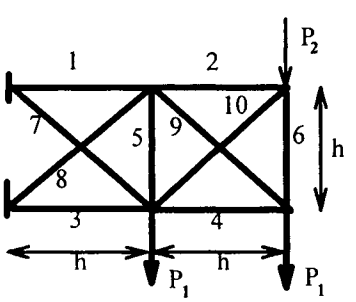

Figure 7: 10-bar truss example

To show the superiority of our ε-continuation approach to other methods; the example was optimized under different formulations. The results are listed in Table 5. From the uniform initial design 10*10.0, ε-continuation approach gives the global optimal solution denoted by GO whereas algorithms under stress formulations can only arrive at the solution which is non

optimal. In Table 6 we list the bar stresses under the two load cases for the two designs obtained by the ε-continuation approach and the stress formulation. It shows that the solution from stress formulation is not the optimum one because for this set of cross sectional area, the stress constraint imposed on bar 9 is active though this bar does not exist in the final structure.

TABLE 5
OPTIMIZATION RESULTS FOR 10-BAR TRUSS

Continuation History (initial design 10*10.0)								
	10.0	6.0	1.0	0.1	0.01	SF	IF	GO
A1	10.09	10.07	9.99	10.00	10.00	10.00	11.43	10.00
A2	8.91	9.33	9.90	9.99	10.00	10.59	8.65	10.00
A3	75.66	77.33	79.64	79.96	80.00	81.24	74.28	80.00
A4	1.04	0.67	0.08	0.01	0.00	0.02	6.06	0.00
A5	0.00	0.00	0.00	0.00	0.00	0.00	0.11	0.00
A6	3.74	4.23	4.90	4.99	5.00	11.30	5.40	5.00
A7	12.81	13.32	14.03	14.13	14.14	22.54	12.47	14.14
A8	2.29	1.44	0.09	0.02	0.00	0.04	9.18	0.00
A9	1.17	0.71	0.12	0.01	0.00	0.00	2.14	0.00
A10	51.25	53.29	56.14	56.52	56.56	96.62	48.94	56.56
W	7017	7160	7346	7376	7380	10142	7517	7380

TABLE 6
BAR STRESS FOR FINAL DESIGNS UNDER DIFFERENT FORMULATIONS

		Bar Stress									
	Bar	1	2	3	4	5	6	7	8	9	10
C-ε	Load 1	10.00	10.00	-3.75	-9.59	1.73	20.00	20.00	-16.01	13.57	-2.50
	Load 2	20.00	20.00	-5.00	-8.00	0.62	0.00	20.00	-12.19	11.31	-5.00
SF	Load 1	10.00	9.44	-3.69	0.00	18.78	8.85	12.55	0.00	20.00	-1.46
	Load 2	20.00	18.88	-4.92	0.00	10.02	0.00	12.55	0.00	17.38	-2.93

RANDOM TEST OF THE ε-CONTINUATION APPROACH

The present ε-continuation approach is a heuristic algorithm. It cannot guarantee the convergence to global optimal solution from any initial design. But as we know, a good heuristic algorithm should locate the global optimal solution with high probability. To study the practical performance of our ε-continuation approach for finding the singular global optimal solutions, in this section, a set of random tests are performed by applying the ε-

continuation approach together with Constraint Variable Metric optimization technique with different randomly generated initial designs and checking whether the global optimal solution of the problem is attainable.

3-bar truss example

Let us consider the above mentioned 3-bar truss example. Using the random number generator, the sample space SNU(non-uniform initial design) and SU(uniform initial design) of the test are generated respectively. Table 7 lists the optimization results obtained from different sets of non-uniform initial designs and optimization algorithms. With 20 randomly chosen initial uniform designs,algorithms all converge to the global optima.

Here symbol S denotes the fact that the singular global optima can be obtained starting from the corresponding set of initial design, whereas symbol F denotes that only local optima is achieved with this set of initial design.

TABLE 7

TESTS FOR 3-BAR TRUSS WITH NON-UNIFORM INITIAL DESIGN

	A_1^0	A_2^0	A_3^0	$C-\varepsilon$	ε
1	8.91	6.85	1.09	S	S
2	4.30	3.59	9.46	S	F
3	5.35	9.65	10.06	S	F
4	9.00	7.76	2.32	S	S
5	5.29	2.35	8.62	S	F
6	4.36	9.22	10.56	S	F
7	8.92	8.53	3.71	S	F
8	6.20	1.08	7.64	S	F
9	3.30	8.62	10.88	S	F
10	8.69	9.15	5.04	S	F
11	7.01	2.19	6.51	S	F
12	2.20	7.86	11.00	F	F
13	8.30	9.60	6.29	S	F
14	7.69	3.44	5.28	S	F
15	1.07	6.97	10.92	F	F
16	7.77	9.89	7.44	S	F
17	8.24	4.64	3.96	S	F
18	2.06	5.96	10.64	S	F
19	7.10	9.99	8.45	S	F
20	8.65	5.76	2.58	S	S

Hoback's 4-bar truss example

In this example, 20 non-uniform and 20 uniform random generated initial designs are used to perform the test. The optimization results corresponding to each of the non-uniform initial design are listed in Table 8. Again, with 20 randomly chosen initial designs, algorithms all converge to the global optima.

TABLE 8

RESULTS OF 4-BAR TRUSS WITH NON-UNIFORM INITIAL DESIGN

	A_1^0	A_2^0	A_3^0	A_4^0	$C-\varepsilon$	ε
1	12.00	11.04	6.25	3.22	F	F
2	6.90	1.10	8.17	13.83	S	F
3	5.62	11.15	14.00	12.64	S	F
4	11.90	11.87	7.88	1.25	F	F
5	8.15	2.59	6.57	12.91	S	F
6	4.17	10.15	13.89	13.63	S	F
7	11.58	12.48	9.37	2.73	F	F
8	9.26	4.25	4.85	11.76	F	F
9	2.65	8.96	13.53	14.35	S	S
10	11.04	12.86	10.69	4.67	F	F
11	10.20	5.85	3.06	10.38	S	F
12	1.10	7.62	12.91	14.81	S	S
13	10.31	13.00	11.81	6.54	F	F
14	10.96	7.35	1.23	8.82	S	F
15	2.46	6.14	12.06	15.00	S	S
16	9.39	12.90	12.72	8.30	S	F
17	11.52	8.72	2.60	7.10	S	F
18	3.98	4.56	10.99	14.90	S	F
19	8.30	12.57	13.40	9.91	S	F
20	11.87	9.94	4.41	5.27	S	F

5-bar truss example

For this example, the results of the performed optimizations with 20 non-uniform initial designs are given in Table 9. With 20 randomly chosen initial designs except the one $A_1^0, A_2^0, A_3^0 = 1.64$, all of them converge to the global optima.

TABLE.9
RESULTS OF 5-BAR TRUSS WITH NON-UNIFORM INITIAL DESIGN

	A_1^0	A_2^0	A_3^0	A_4^0	A_5^0	$C-\varepsilon$	ε
1	8.91	6.85	1.09	8.30	12.90	F	F
2	4.30	3.59	9.46	11.87	8.72	F	F
3	5.35	9.65	10.06	5.44	4.56	S	F
4	9.00	7.76	2.32	7.07	12.57	S	F
5	5.29	2.35	8.63	12.00	9.94	F	F
6	4.36	9.21	10.56	6.82	2.90	F	F
7	8.92	8.53	3.71	5.71	12.00	S	F
8	6.20	1.08	7.64	11.91	10.98	F	F
9	3.30	8.62	10.88	8.08	1.21	F	F
10	8.69	9.15	5.04	4.26	11.21	S	F
11	7.01	2.19	6.51	11.60	11.82	F	F
12	2.20	7.86	11.00	9.20	2.48	F	F
13	8.30	9.60	6.29	2.74	10.22	S	S
14	7.69	3.44	5.28	11.08	12.45	F	F
15	1.07	6.97	10.92	10.15	4.15	S	F
16	7.77	9.89	7.44	1.19	9.04	S	S
17	8.24	4.64	3.96	10.36	12.84	F	F
18	2.06	5.96	10.64	10.92	5.75	S	F
19	7.10	10.00	8.45	2.36	7.71	S	S
20	8.65	5.76	2.59	9.45	13.00	S	F

With reference to the above results, the following observations are drawn:

ε-continuation approach has the high probability to locate the singular global optima starting from rather arbitrary *uniform initial design*. It is worth noting that starting the optimization process from uniform initial design is natural if we have no idea about the optimal topology in advance. Because of this feature, the method provides an ideal tool for singular topology optimization problems where the singular global optimum are usually very difficult to achieve by other methods.

For some non-uniform initial design, ε-continuation approach can lead to the singular optima, though the convergence to singular global optima cannot be guaranteed. However, it is well known that global optimum remains open for non-convex mathematical programming.

CONCLUSIONS

For making the most efficient use of resources, in engineering practice, the determination of global optima is always highly desirable. By this motivation, a ε-continuation approach which is a variant version of ε-relaxed approach is proposed in this paper. It is based on the solution of a sequence of problems constructed by relaxing the constraints to some extent through the introduction of a relaxation parameter ε. In the limit as ε tends to zero, the solution of the singular problem is approached. This approach works well for finding the global optimal solution of singular problems. By means of this approach, global optimal solution can be obtained from rather arbitrary choice of the initial design; thus the initial design-dependency problem of the ε-relaxed approach is alleviated. Though this approach cannot guarantee a global optimum from any initial design, numerical examples show that it does have the ability to avoid entrapment by local optima and locate the global optima with high probability. Although only truss topology optimization problems under stress constraints are discussed in this paper, the method presented can be applied equally to other discrete topology optimization problems with various behavior constraints.

REFERENCES

1. Sved G. and Gions Z.(1968). Structural optimization under multiple loading, Int. J. Sci., 10,803-805
2. Kirsch U.(1989) Optimal topologies of truss structures, Comput. Methods. Appl. Mech. Eng., 72(1),15-28
3. Cheng G. and Jiang Z.(1992), Study on topology optimization with stress constraint, Eng. Optim., 20, 129-148
4. Rozvany G.I.N. and Birker T.(1994), On singular topologies in exact layout optimization, Struct. Optim., 8, 228-235
5. Kirsch U.(1990), On singular topologies in optimum structural design, Struct. Optim., 2,39-45
6. Kirsch U.(1996), Integration of reduction and expansion process in layout optimization, Struct. Optim., 11, 13-18
7. Rozvany G.I.N.(1996), Difficulties in truss topology optimization with local buckling and system stability constraints, Struct. Optim., 11,13-18
8. Cheng G. and Guo X.(1997), ε-Relaxed approach in structural topology optimization, Struct. Optim., 13(4)
9. Hoback A.S.(1996), Optimization of singular problems, Struct. Optim., 12, 93-97
10. Hogan W.W.(1973), Point to set maps in mathematical programming, SIAM review, 15, 591-603

RECENT DEVELOPMENTS IN BASIC FINITE ELEMENT TECHNOLOGIES

Carlos A. Felippa

Department of Aerospace Engineering Sciences and Center for Aerospace Structures
University of Colorado, Boulder, Colorado 80309-0429, USA

ABSTRACT

High performance (HP) elements are simple finite elements constructed to deliver engineering accuracy with arbitrary coarse meshes. This paper overviews original developments based on parametrized variational principles, which provide a common foundation for various approaches to HP element construction. This work led to the template approach. Templates are parametrized algebraic forms of finite element stiffness equations. The application of templates to the construction of an optimal 3-node plate bending element is outlined. The template approach holds future promise in the unification of finite element methods and connection to arbitrary grid finite differences. Essential to this unification work is the availability of powerful computer algebra systems.

KEYWORDS

Finite element method, variational principles, templates, parametrization, morphing, high performance elements, optimal elements, plate bending, triangular elements, computer algebra systems.

INTRODUCTION

The Finite Element Method (FEM) was first described in its presently dominant form by Turner et al. (1956). It was baptized by Clough (1960) at the beginning of an explosive growth period. The first applications book, by Zienkiewicz and Cheung (1967), appeared seven years later. The first monograph on the mathematical foundations was written by Strang and Fix (1973). The opening sentence of this book already declared the FEM an "astonishing success." And indeed the method had by then revolutionized computational structural mechanics and was in its way to impact non-structural applications.

The FEM was indeed the right idea at the right time. The key reinforcing factor was the expanding availability of digital computers. Lack of this enabling tool meant that earlier related proposals,

notably that of Courant (1943), had been forgotten. A second benefit was the heritage of classical structural mechanics and its reformulation in matrix form, which culminated in the elegant unification of Argyris and Kelsey (1960). A third influence was the victory of the Direct Stiffness Method (DSM) developed by Turner (1959, 1964) over the venerable Force Method, a struggle recently chronicled by Felippa (1995). Victory was sealed by the adoption of the DSM in the earlier general-purpose FEM codes, notably NASTRAN, MARC and SAP. In the meantime the mathematical foundations were rapidly developed in the 1970s.

"Astonishing success", however, carries its own dangers. By the early 1980s the FEM began to be regarded as "mature technology" by US funding agencies. By now that feeling has hardened to the point that it is virtually impossible to get significant research support for fundamental work in FEM. This viewpoint has been reinforced by major software developers, which proclaim their products as solutions to all user needs.

Is this perception correct? It certainly applies to the *core FEM*, or orthodox FEM. This is the material taught in textbooks and which is implemented in major software products. Core FEM follows what may be called the Ritz-Galerkin and Direct Stiffness Method canon. Beyond the core there is an *evolving FEM*. This is strongly rooted on the core but goes beyond textbooks. Finally there is a *frontier FEM*, which makes only partial or spotty use of core knowledge.

By definition core FEM is mature. As time goes, it captures segments of the evolving FEM. For example, most of the topic of FEM mesh adaptivity can be classified as evolving, but will eventually become part of the core. Frontier FEM, on the other hand, can evolve unpredictably. Some components prosper, mature and eventually join the core, some survive but never become orthodox, while others wither and die.

Four brilliant contributions of Bruce Irons, all of which were certainly frontier material when first published, can be cited as examples of the three outcomes. *Isoparametric elements* and *frontal solvers* rapidly became integral part of the core technology. The *patch test* has not become part of the core, but survives as a useful if controversial tool for consistent element development and testing. The *semi-loof shell elements* quietly disappeared.

The words "basic FEM technologies" in the title of this article refers to construction of element-level models of physical problems. Frontier topics therein include interface, multiscale, and high performance elements. The material that follows deals with the last topic.

HIGH PERFORMANCE ELEMENTS

An important objective of frontier FEM is the construction of high performance (HP) finite elements. These have been defined by Felippa and Militello (1989) as "simple elements that deliver engineering accuracy with arbitrary coarse meshes." This definition requires further clarification.

Simple means the simplest geometry and freedom configuration that fits the problem and target accuracy consistent with human and computer resources. This can be summed up in one FEM modeling rule: *use the simplest element that will do the job.*

Engineering accuracy is that generally expected in most FEM applications in Aerospace, Civil and Mechanical Engineering. Typically this is 1% in displacements and 10% in strains, stresses and derived quantities. Some applications, notably in Aerospace, require higher precision in quantities such as natural frequencies, shape tolerances, or in long-time simulations.

Coarse mesh is one that suffices to capture the important physics in terms of geometry, material and load properties. It does not imply few elements. For example, a coarse mesh for a fighter aircraft undergoing maneuvers may require several million elements. For simple benchmark problems such as a uniformly loaded square plate, a mesh of 4 or 16 elements may be classified as coarse.

Finally, the term *arbitrary mesh* implies *low sensitivity to skewness and distortion.* This attribute is becoming important as push-button mesh generators gain importance, because generated meshes can be of low quality compared to those produced by an experienced analyst.

Tools for Construction of HP Elements

The origins of HP finite elements may be traced to several investigators in the late 1960s and early 1970s. Notable early contributions are those of Clough, Irons, Taylor, Wilson and their coworkers. The construction techniques made use of incompatible shape functions, the patch test, reduced, selective and directional integration. These can be collectively categorized as unorthodox, and in fact were labeled as "variational crimes" at that time by Strang and Fix (1973).

A more conventional development, pioneered by Pian, Tong and coworkers, made use of mixed and hybrid variational principles. They developed elements using stress or partial stress assumptions, but the end product were standard displacement elements. This approach was further refined in the 1980s. A good expository summary is provided in the book by Zienkiewicz and Taylor (1992).

New innovative approaches came into existence in the 1980s. The most notable have been the Free Formulation of Bergan and Nygård (1984), and the Assumed Strain method pioneered by MacNeal (1978). The latter was further developed along different paths by Bathe and Dvorkin (1985), Park and Stanley (1986), and Simo and Hughes (1986).

Unification by Parameterized Variational Principles

The approach taken by the author started from collaborative work with Bergan in Free Formulation (FF) high performance elements. The results of this collaboration were a membrane triangle with drilling freedoms described in Bergan and Felippa (1985) and a plate bending triangle described by Felippa and Bergan (1987). It continued with exploratory work using the Assumed Natural Strain (ANS) method of Park and Stanley (1986). Eventually FF and ANS coalesced in a variant of ANS called Assumed Natural Deviatoric Strain, or ANDES. Elements based on ANDES are described by Militello and Felippa (1991) and Felippa and Militello (1992).

This unification work led naturally to a formulation of elasticity functionals containing free parameters. These were called parametrized variational principles, or PVPs in short. Setting the parameters to specific numerical values produced the classical functionals of elasticity such as Total Potential Energy, Hellinger-Reissner and Hu-Washizu. For linear elasticity, 3 free parameters in a 3-field functional with independently varied displacements, strains and stresses are sufficient to embed all classical functionals. Two recent survey articles with references to the original papers have been written by Felippa (1994,1996).

One result from the PVP formulation is that, upon FEM discretization, free parameters appear at the element level. One thus naturally obtains *families* of elements. Setting the free parameters to numerical values produces specific elements. Although the PVP Euler-Lagrange differential equations are the same, the discrete solution produced by different elements are different. Thus an

obvious question arises: which free parameters produce the best elements? It turns out that there is no clear answer to the question because the best set of parameters depends on the element geometry.

The PVP formulation led to an unexpected discovery. The configurations of elements constructed according to PVPs and the usual assumptions on displacements, stresses and strains were observed to obey certain algebraic rules. Such configurations could be parametrized directly without going through the source PVP. This observation led to a general formulation of finite elements as *templates*.

FINITE ELEMENT TEMPLATES

A finite element template, or simply *template*, is an algebraic form that represents element-level stiffness equations, and which fulfills three conditions:

(C) Consistency: the Individual Element Test (IET) form of the patch test, introduced by Bergan and Hansen (1975), is passed for any element geometry.

(S) Stability: the element stiffness matrix satisfies correct rank and nonnegativity conditions.

(P) Parametrization: the element stiffness equations contain free parameters.

(I) Invariance: the element equations are observer invariant. In particular, they are independent of node numbering and choice of reference systems.

Setting the free parameters to numeric values yields specific element instances.

Constructing Optimal Elements

By making a template sufficiently general, all published finite elements for a specific configuration can be generated. This includes those derivable by orthodox assumptions and those that are not. Furthermore, an infinite number of new elements result. The same question posed above arises: Can one select the free parameters to produce an optimal element?

The answer to this question is not yet known for general elements. An unresolved difficulty is the definition of unique optimality conditions at the element level. But even invoking reasonable criteria, a major technical difficulty arises: the actual construction of optimal elements poses formidable problems in symbolic matrix manipulation, because one has to carry along arbitrary geometries, materials and free parameters. Until recently those manipulations were beyond the scope of computer algebra systems (CAS) for all but the simplest elements. As personal computers and workstations gain in CPU speed and storage, it is gradually becoming possible to construct optimal two-dimensional elements for plane stress and plate bending. Most three-dimensional and curved-shell elements, however, still lie beyond the power of present systems.

The mathematical theory behind templates is elaborate and will not be pursued in this article. Only a few basic results needed for the plate bending example presented in Section 4 are given in the next subsection. For further historical and technical details the reader is referred to a recent article by Felippa, Haugen and Militello (1995).

The Fundamental Decomposition

The stiffness matrix derived through a template approach has the fundamental decomposition

$$\mathbf{K} = \mathbf{K}_b(\alpha_i) + \mathbf{K}_h(\beta_j) \tag{1}$$

Here $\mathbf{K}_b$ and $\mathbf{K}_h$ are the basic and higher-order stiffness matrices, respectively. The basic stiffness matrix $\mathbf{K}_b$ is constructed for *consistency* and *mixability*, whereas the higher order stiffness $\mathbf{K}_h$ is constructed for *stability* (meaning rank sufficiency and nonnegativity) and *accuracy*. The higher order stiffness $\mathbf{K}_h$ must be orthogonal to all rigid-body and constant-strain (curvature) modes.

In general both matrices contain free parameters. The number of parameters α_i in the basic stiffness is typically small for simple elements. For example, in the 3-node KPT elements considered below there is only one basic parameter, called α. Its value *must be the same for all elements in a mesh* to ensure satisfaction of the IET.

On the other hand, the number of higher order parameters β_j can be in principle *infinite* if certain components of $\mathbf{K}_h$ can be represented as polynomial series of element geometrical invariants. In practice, however, such series are truncated, leading to a finite number of β_j parameters. Although the β_j may vary from element to element without impairing convergence, usually the same parameters are retained for all elements.

A 3-NODE KPT ELEMENT TEMPLATE

The application of the template approach is rendered specific using a particular configuration: a 3-corner-node flat triangular element to model bending of Kirchhoff (thin) plates. The element has the conventional 3 degrees of freedom: one transverse displacement and 2 rotations at each corner. For brevity this will be referred to as a Kirchhoff Plate Triangle, or KPT, in the sequel.

Stiffness Decomposition

For the KPT under study the configuration of the stiffness matrices in (1) can be shown in more detail. Assuming that the 3×3 moment-curvature plate constitutive matrix $\mathbf{D}$ is constant over the triangle, we have

$$\mathbf{K}_b = \frac{1}{A}\mathbf{L}\mathbf{D}\mathbf{L}^T, \quad \mathbf{K}_h = \frac{A}{3}\left[\mathbf{B}_{\chi 4}^T\mathbf{D}_\chi\mathbf{B}_{\chi 4} + \mathbf{B}_{\chi 5}^T\mathbf{D}_\chi\mathbf{B}_{\chi 5} + \mathbf{B}_{\chi 6}^T\mathbf{D}_\chi\mathbf{B}_{\chi 6}\right]. \tag{2}$$

Here A is the triangle area, $\mathbf{L}$ is the 9×3 force lumping matrix that transforms a constant internal moment field to node forces, $\mathbf{B}_{\chi m}$ are 3×9 matrices relating natural curvatures at triangle midpoints $m = 4, 5, 6$ to node displacements, and $\mathbf{D}\chi$ is the plate constitutive matrix transformed to relate natural curvatures to natural moments. Parameter α appears in $\mathbf{L}$ whereas parameters β_j appear in $\mathbf{B}_{\chi m}$. Expressions of these matrices are given in the Appendix.

The KPT-1-36 Template

A useful KPT template is based on a 36-parameter representation of $\mathbf{K}_h$ in which the series noted above retains up to the *linear* terms in three triangle geometric invariants λ_1, λ_2 and λ_3, defined in the Appendix. The template is said to be of *order one* in the λs. It has a total of 37 free parameters: one α and 36 βs. Collectively the template is identified as KPT-1-36. Instances are displayed using the following tabular arrangement:

element-acronym	α	β_{10}	β_{20}	β_{30}	β_{40}	β_{50}	β_{60}	β_{70}	β_{80}	β_{90}
		β_{11}	β_{21}	β_{31}	β_{41}	β_{51}	β_{61}	β_{71}	β_{81}	β_{92}
		β_{12}	β_{22}	β_{32}	β_{42}	β_{52}	β_{62}	β_{72}	β_{82}	β_{93}
		β_{13}	β_{23}	β_{33}	β_{43}	β_{53}	β_{63}	β_{73}	β_{83}	β_{93}

(3)

Table 1. Template Signatures of Some Existing KPT Elements

Acronym	α	β_{1j}	β_{2j}	β_{3j}	β_{4j}	β_{5j}	β_{6j}	β_{7j}	β_{8j}	β_{9j}
ALR	0	0	0	0	0	0	0	0	3	0
		−3	0	0	0	0	0	0	0	0
		0	0	0	0	0	0	0	0	0
		0	0	0	0	0	0	0	−3	0
AQR1	1	−1	0	0	0	0	1	0	2	0
		−1	0	0	0	0	0	0	0	0
		0	0	0	0	0	−2	0	0	0
		0	0	0	0	0	0	0	−1	0
AQR0	Same as AQR1 except $\alpha = 0$									
AQRBE	Same as AQR1 except $\alpha = 1/\sqrt{2}$									
AQRV	1	0	−1	0	−1	0	0	0	3	1
		−3	0	0	1	0	0	1	0	0
		0	0	−1	0	0	0	0	0	−1
		0	1	0	0	1	0	0	−3	0
AVG	0	−3/2	0	0	0	0	0	0	3/2	0
BCIZ0	0	−3/2	1/2	1/2	0	0	0	−1/2	3/2	−1/2
BCIZ1	1	−3/2	−1/2	1/2	−1	0	0	−1/2	3/2	1/2
		0	0	0	1	0	0	1	0	0
		0	0	−1	0	0	0	0	0	−1
		0	1	0	0	1	0	0	0	0
DKT	1	−3/2	1/2	0	−1	0	0	0	3/2	−1/2
		0	0	0	1	0	0	−1/2	0	0
		0	0	1/2	0	0	0	0	0	1/2
		0	−1/2	0	0	1	0	0	0	0
FF0	0	−3/2	1/6	1/6	−1/3	1/3	0	−1/6	3/2	−1/6
FF1	Same as FF0 except $\alpha = 1$									
HCT	1	−7/2	0	−5/2	−1	0	0	−5/2	2	−5/2
		3/2	0	0	1	0	0	5/2	0	0
		0	0	5	0	0	0	0	0	5
		0	5/2	0	0	1	0	0	3/2	0

Setting the 37 parameters to numeric values yields specific elements, identified by the acronym displayed on the left. Some instances that are interesting on account of practical or historical reasons are collected in Table 1. This represents a tiny subset of the number of published KPT elements, which ranges in the hundreds, and is admittedly biased in favor of elements developed by the author. Table 2 identifies the acronyms of Table 1, correlated with original publications.

A historically important subclass of (3) is that in which the bottom 3 rows vanish: $\beta_{11} = \beta_{12} = \ldots \beta_{39} = 0$. This 10-parameter template is said to be of *order zero* because the invariants λ_1, λ_2 and λ_3 do not appear in the higher order stiffness. It is identified as KPT-1-9. For brevity it is

Table 2. Element Identifiers Used in Table 1

Name	Description
ALR	Assumed Linear Rotation element of Militello and Felippa (1991).
AQR1	Assumed Quadratic Rotation element of Militello and Felippa (1991).
AQR0	α-variant of AQR1 with $\alpha = 0$
AQRBE	α-variant of AQR1 with $\alpha = 1/\sqrt{2}$; of interest because it is BME.
AQRV	Non-energy-orthogonal variant of AQR1.
AVG	Average curvature element of Militello and Felippa (1991).
BCIZ0	Nonconforming element of Bazeley, Cheung, Irons and Zienkiewicz (1966) "sanitized" with $\alpha = 0$ as described by Felippa, Haugen and Militello (1995) Historically the first polynomial-based, complete, nonconforming KPT and the motivation for the original (multielement) patch test of Irons.
BCIZ1	Variant of the above, in which BCIZ is sanitized with $\alpha = 1$.
DKT	Discrete Kirchhoff Triangle of Stricklin et al. (1969), streamlined by Batoz (1974)
FF0	Free-formulation element of Felippa and Bergan (1987)
FF1	Variant of FF0 with $\alpha = 1$.
HCT	Hsieh-Clough-Tocher element (1966) with corner-averaged curvature field. The original (unaveraged) form was the first successful C^1 conforming KPT.

written simply as

element-acronym	α	β_{10}	β_{20}	β_{30}	β_{40}	β_{50}	β_{60}	β_{70}	β_{80}	β_{90}

(4)

omitting the zero entries.

Template Genetics: Signatures and Clones

An examination of Table 1 should convince the reader that template coefficients uniquely define an element once and for all, although the use of acronyms has been prevalent in the FE literature. The parameter set can be likened to an "element genetic fingerprint" or "element DNA" that makes it a unique object. This set is called the element *signature*.

If signatures were randomly generated, the number of possible elements would be of course huge: more precisely ∞^{37} for 37 parameters. But in practice elements are not fabricated at random. Attractors emerge. Some element derivation methods, notably those based on displacement shape functions, tend to "hit" certain signature patterns. The consequence is that the same element may be discovered separately by different authors, often using dissimilar derivation techniques. Such elements will be called *clones*. Cloning seems to be more prevalent among instances of the order-zero KPT-1-9 template (2). Two examples discovered in the course of this study are reported.

The first successful nonconforming triangular plate bending element was the original BCIZ, published by Bazeley et al. (1966). This element, however, does not pass the IET, and in fact fails Irons' original patch test for arbitrary mesh patterns. The cause of the disease resides in the basic

stiffness. The element can be "sanitized" by removing the infected matrix as explained by Felippa, Haugen and Militello (1995). This is replaced by a healthy $\mathbf{K}_b$ with, for example, $\alpha = 0$ or $\alpha = 1$. This transplant operation yields the elements called BCIZ0 and BCIZ1, respectively, in Table 1. Note that BCIZ0 pertains to the KPT-1-9 template.

Hansen, Bergan and Syversten (1978) reported a nonconforming element which passed the IET and (for the time) was of competitive performance. Construction of its template signature revealed it to be a clone of BCIZ0. An energy orthogonal version of the HBS element was constructed by Nygård (1986) in his Ph.D. thesis. Its signature turned out to agree with that of the FF0 element, constructed by Felippa and Bergan (1987) with a different set of higher order shape functions. Thus four apparently different elements coalesce into two.

Clones seem rarer in the realm of the full KPT-1-36 template because of its greater richness. The DKT appears to be an exception. Although this popular element is usually constructed by assuming rotation fields, it coalesced with one of the ANDES elements derived by Militello and Felippa (1991). At that time the coalescence was first suspected from benchmarks, and later verified by direct examination of numerical stiffness matrices. Using the template formulation such numerical tests can be bypassed, as it is sufficient to compare signatures.

OPTIMAL ELEMENT DESIGN

Given a template with a large number of free parameters, such as (3), the first order of business is to reduce their number by imposing optimality constraints. There is as yet no established general theory for selecting such constraints at the element or mesh-unit level.

Several conditions that have produced satisfactory results are discussed below with reference to the KPT template. The reader should be cautioned, however, that these may not represent the final word inasmuch as templates are presently a frontier subject.

Observer Invariance Constraints

The easiest constraints to write down pertain to *observer invariance*. If the element geometry exhibits symmetries, those must be reflected in the stiffness equations. For example, if a triangle becomes equilateral or isoceles, certain equality conditions between entries of the curvature-displacement matrices must hold. The resulting constraints are *linear* in the βs. As these are quite easy to obtain, they will not be discussed further.

Skew and Aspect Ratio Insensitivity Constraints

In the case of KPT-1-36, 29 linear constraints can be found by requiring that the element be both *skew and aspect ratio insensitive*, or SARI for short. Mathematically this means that the ratio of element energy to exact energy remain *bounded* for all possible mesh units of the form depicted in Figure 1, for any possible combinations of length L, aspect ratio r and skewangle ψ. Lack of boundedness leads to undesirable behavior known as skew and aspect ratio *locking*.

It is not difficult to show that no instance of the KPT-1-9 template can satify all of the SARI constraints. Consequently any 3-node KPT element whose higher order stiffness does not depend on the invariants λ_1, λ_2 and λ_3 defined in Appendix A *cannot be insensitive to aspect ratio and distortion*. This property explains, once and for all, why certain elements, such as BCIZ0, are not

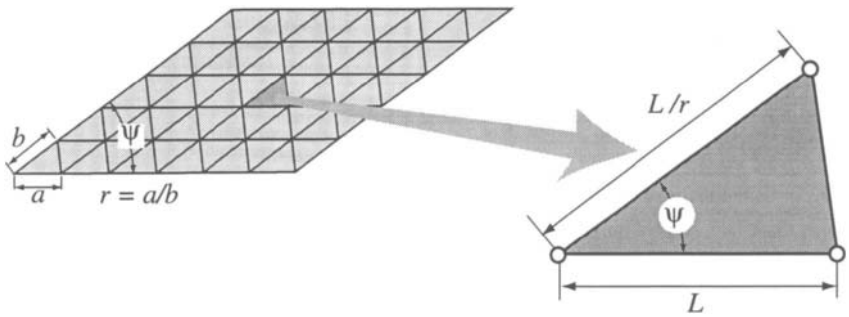

Figure 1. General triangle geometry used for establishing SARI constraints.

competitive in general mesh configurations. Thus a template signature of the form (4) is grounds for immediate KPT element rejection.

The technical derivation details of SARI conditions are quite elaborate and will not be given here. Suffices to say that it relies completely on symbolic algebra programs because the manipulations involved (even for this comparatively simple element) are way beyond human endurance. All SARI constraints are linear and *geometric* in nature, that is, independent of constitutive properties.

Morphing Constraints

This is a class of asymptotic optimality constraints that is presently being studied to ascertain whether enforcement would be generally beneficial to element performance.

Consider the 2-KPT-element rectangular mesh unit shown in the center of Figure 2. The aspect ratio r is the ratio of the longest rectangle dimension L to the width $b = L/r$. The plate is fabricated of a homogeneous isotropic material with zero Poisson's ratio and thickness t. Axis x is selected along the longitudinal direction. We study the two *morphing processes* depicted in Figure 2. In both cases the aspect ratio r is made to increase, but with two different objectives.

Plane Beam Limit. The width $b = L/r$ is decreased while keeping L and t fixed. The limit is the thin, Bernoulli-Euler plane beam member of rectangular cross section $t \times b$, $b << t$, shown on the right of Figure 2. This member can carry exactly a linearly-varying bending moment $M(x)$ and a constant transverse shear V, although shear deformations are not considered.

Twib Limit. Again the width $b = L/r$ is decreased by making r grow. The thickness t, however, is still considered small with respect to b. The limit is the twisted-ribbon member of narrow cross section $t \times b$, $t << b$, shown on the left of Figure 2. This member, called a "twib" for brevity, can carry a longitudinal torque $T(x)$. This torque may vary linearly in x.

Two conditions called *morphing constraints* are now posed as follows.

1. Does the mesh unit approach the exact behavior of a Hermitian (cubic) beam? If so, the plate element is said to be *beam-morphing-exact* or BME.
2. Does the mesh unit approach the exact behavior of a twib under linearly varying torque? If so, the plate element is said to be *twib-morphing-exact* or TME.

If the element satisfies both conditions, it is said to be beam-and-twib-morphing-exact, or BTME.

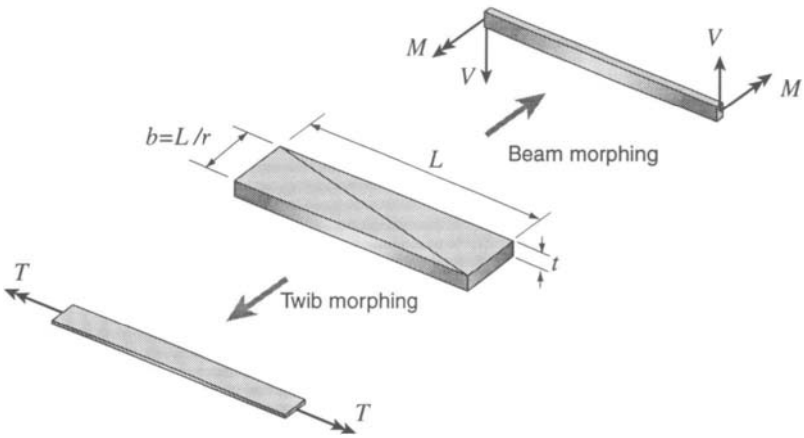

Figure 2. Morphing a rectangular plate mesh unit to beam and twib.

The BME and TME conditions can be derived by symbolically expanding transformed mesh-unit stiffness equations in Laurent series as $r \to \infty$. Unlike the invariance and SARI conditions, the morphing constraints are *nonlinear* (more precisely, quadratic) in the free parameters.

Energy Orthogonality and Energy Balance Constraints

These constraint types were extensively used in the construction of HP elements over the period 1984-1994. *Energy orthogonality* means that the average value of deviatoric strains over the element is zero. This condition was a key part of the early developments of the Free Formulation by Bergan (1980) and Bergan and Nygård (1984). Recent work has shown that it should not be imposed *a priori* but that it often emerges as a consequence of invariance and SARI constraints.

Energy balance conditions, introduced by Bergan and Felippa (1985), have been used in several HP elements. These impose the exactness of higher order energy for specific mesh unit geometries, and can be viewed as a form of higher order patch tests. Their replacement in favor of more physically transparent conditions, such as the morphing constraints discussed above, is under study.

Optimal KPT Element Family

Application of the invariance, SARI and morphing constraints reduces the 37 parameters of KPT-1-36 to one, which is taken to be α. Results obtained with members of this family on benchmark problems were presented at the Workshop. They are omitted from this article because of length restrictions.

CONCLUSIONS

The usual finite element construction process, which involves *a priori* selection of a variational principle and shape functions, hinders the exploration of a wide range of admissible finite element models. As such it is ineffectual for the design of finite elements with desirable physical behavior. The template approach attempts to implement the hope expressed two decades ago by Bergan and Hansen (1975) in the Introduction of their MAFELAP II paper:

"An important observation is that each element is, in fact, only represented by the numbers in its stiffness matrix during the analysis of the assembled system. The origin of these stiffness coefficients is unimportant to this part of the solution process ... The present approach is in a sense the opposite of that normally used in that the starting point is a generally formulated convergence condition and from there the stiffness matrix is derived ... The patch test is particularly attractive [as such a condition] for the present investigation in that it is a direct test on the element stiffness matrix and requires no prior knowledge of interpolation functions, variational principles, etc."

This statement sets out what may be called the *direct algebraic approach* to finite elements: the element stiffness is derived directly from consistency conditions — provided by the Individual Element Test — plus stability and accuracy considerations to determine algebraic redundancies if any. It has in fact many points in common with energy-based finite differences.

This ambitious goal has proven elusive because the direct algebraic construction of the stiffness matrix of most multidimensional elements becomes effectively a problem in constrained optimization. In the symbolic form necessitated by template design, that problem is much harder to tackle than the conventional element construction method based on shape functions. Only with the general availability of powerful computer algebra systems, plus the theoretical foundations provided by the parametrized variational principles, can the dream become a reality.

ACKNOWLEDGMENTS

Preparation of the present paper has been supported by the National Science Foundation under Grant ECS-9725504, and by Sandia National Laboratories under the Advanced Strategic Computational Initiative (ASCI) Contract AS-9991.

REFERENCES

Argyris, J. H. and Kelsey, S. (1960). *Energy Theorems and Structural Analysis*. London, Butterworth; reprinted from *Aircraft Engrg.* **26**, Oct-Nov 1954 and **27**, April-May 1955.

Bathe, K. J. and E. N. Dvorkin, E. N. (1985). A Four-Node Plate Bending Element Based on Mindlin-Reissner Plate Theory and a Mixed Interpolation. *Int. J. Numer. Meth. Engrg.*, **21**, 367–383.

Batoz, J. L. (1982). An Explicit Formulation for an Efficient Triangular Plate-Bending Element. *Int. J. Numer. Meth. Engrg.*, **18**, 1077–1089.

Bazeley, G. P., Cheung, Y. K., Irons, B. M. and Zienkiewicz, O. C. (1966). Triangular Elements in Plate Bending — Conforming and Nonconforming Solutions. In *Proceedings 1st Conference on Matrix Methods in Structural Mechanics*, AFFDL-TR-66-80, Air Force Institute of Technology, Dayton, Ohio, 547–584.

Bergan, P. G. and Hansen, L. (1975). A New Approach for Deriving 'Good' Finite Elements. MAFELAP II Conference, Brunel University, 1975. In *The Mathematics of Finite Elements and Applications – Volume II*, ed. by J. R. Whiteman, Academic Press, London, 483–497.

Bergan, P. G. (1980). Finite Elements Based on Energy Orthogonal functions. *Int. J. Numer. Meth. Engrg.*, **15**, 1141–1555.

Bergan, P. G. and Nygård, M. K. (1984). Finite Elements with Increased Freedom in Choosing Shape Functions. *Int. J. Numer. Meth. Engrg.*, **20**, 643–664.

Bergan, P. G. and Felippa, C. A. (1985). A Triangular Membrane Element with Rotational Degrees of Freedom. *Comp. Meths. Appl. Mech. Engrg.*, **50**, 25–69.

Clough, R. W. (1960). The Finite Element Method in Plane Stress Analysis. *Proc. 2nd ASCE Conference on Electronic Computation*, Pittsburgh, Pa.

Clough, R. W. and Tocher, J. L. (1966). Finite Element Stiffness Matrices for the Analysis of Plate Bending. In *Proceedings 1st Conference on Matrix Methods in Structural Mechanics*, AFFDL-TR-66-80, Air Force Institute of Technology, Dayton, Ohio, 515–547.

Courant, R. (1943). Variational Methods for the Solution of Problems in Equilibrium and Vibrations. *Bull. Amer. Math. Soc.*, **49**, 1–23.

Felippa, C. A. and Bergan, P. G. (1987). A Triangular Plate Bending Element Based on an Energy-Orthogonal Free Formulation. *Comp. Meths. Appl. Mech. Engrg.*, **61**, 129–160.

Felippa, C. A. and Militello, C. (1989). Developments in Variational Methods for High Performance Plate and Shell elements. In *Analytical and Computational Models for Shells*, CED Vol. 3, ed. by A. K. Noor, T. Belytschko and J. C. Simo, The American Society of Mechanical Engineers, ASME, New York, 191–216.

Felippa C. A. and Militello, C. (1992). Membrane Triangles with Corner Drilling Freedoms: II. The ANDES Element. *Finite Elem. Anal. Design*, **12**, 189–201.

Felippa, C. A. (1994). A Survey of Parametrized Variational Principles and Applications to Computational Mechanics, *Comp. Meths. Appl. Mech. Engrg.*, **113**, 109–139.

Felippa, C. A. (1995). Parametrized Unification of Matrix Structural Analysis: Classical Formulation and d-Connected Mixed Elements. *Finite Elem. Anal. Design*, **21**, 45–74.

Felippa, C. A., Haugen, B. and Militello, C. (1995). From the Individual Element Test to Finite Element Templates: Evolution of the Patch Test. *Int. J. Numer. Meth. Engrg.*, **38**, 199–229.

Felippa, C. A. (1996). Recent Developments in Parametrized Variational Principles for Mechanics. *Comput. Mech.*, **18**, 159–174.

Hansen, L., Bergan, P. G. and Syversten, T. J. (1979). Stiffness Derivation Based on Element Convergence Requirements. MAFELAP III Conference, Brunel University, 1978. In *The Mathematics of Finite Elements and Applications – Volume III*, ed. by J. R. Whiteman, Academic Press, London, 83–96.

MacNeal, R. H. (1978). Derivation of Element Stiffness Matrices by Assumed Strain Distribution. *Nuclear Engrg. Design*, **70**, 3–12.

Militello, C. and Felippa, C. A. (1991). The First ANDES Elements: 9-DOF Plate Bending Triangles. *Comp. Meths. Appl. Mech. Engrg.*, **93**, 217–246

Nygård, M. K. (1986). The Free Formulation for Nonlinear Finite Elements with Applications to Shells, *Ph. D. Dissertation*, Division of Structural Mechanics, NTH, Trondheim, Norway.

Park, K. C. and Stanley, G. M. (1986). A Curved C^0 Shell Element Based on Assumed Natural-Coordinate Strains. *J. Appl. Mech.*, **53**, 278–290.

Simo, J. C. and Hughes, T. J. R. (1986). On the Variational Foundations of Assumed Strain Methods. *J. Appl. Mech.*, **53**, 51–54.

Strang, G. and Fix, G. (1973). *An Analysis of the Finite Element Method.* Prentice-Hall, Englewood Cliffs.

Stricklin, J., Haisler, W., Tisdale, P. and Gunderson, R. (1969). A Rapidly Converging Triangular Plate Bending Element. *AIAA J.*, **7**, 180–181.

Turner, M. J., Clough, R. W., Martin, H. C. and Topp, L. J. (1956). Stiffness and Deflection Analysis of Complex Structures. *J. Aeron. Sci.*, **23**, 805–824.

Turner, M. J. (1959). The Direct Stiffness Method of Structural Analysis, Structural and Materials Panel Paper, AGARD Meeting, Aachen, Germany.

Turner, M. J., Martin, H. C. and Weikel, R. C. (1964). Further Development and Applications of the Stiffness Method. AGARD Meeting, Paris, 1962. In *AGARDograph 72: Matrix Methods of Structural Analysis*, ed. by B. M. Fraeijs de Veubeke, Pergamon Press, New York, 203–266.

Zienkiewicz, O. C. and Cheung, Y. K. (1967). *The Finite Element Method in Engineering Science*, McGraw-Hill, New York.

Zienkiewicz, O. C. and Taylor, R. E. (1989). *The Finite Element Method*, Vol. I, 4th ed. McGraw-Hill, New York.

APPENDIX A. FORMULATION OF KPT-1-36 TEMPLATE

This Appendix collects the formulas that define the 3-node KPT-1-36 element template.

Element Relations

The triangle geometry is defined by the corner coordinates in its (x, y) local system, which are $(x_i, y_i), i = 1, 2, 3$. Coordinate differences are abbreviated as $x_{ij} = x_i - x_j$ and $y_{ij} = y_i - y_j$. The signed triangle area A is given by $2A = x_{21}y_{31} - x_{31}y_{21} = x_{32}y_{12} - x_{12}y_{32} = x_{13}y_{23} - x_{23}y_{13}$ and requires that $A > 0$. The visible degrees of freedom of the element collected in $\mathbf{u}$ and the associated node forces collected in $\mathbf{f}$ are

$$\mathbf{u}^T = [\, u_{z1} \quad \theta_{x1} \quad \theta_{y1} \quad u_{z2} \quad \theta_{x2} \quad \theta_{y2} \quad u_{z3} \quad \theta_{x3} \quad \theta_{y3} \,]. \tag{5}$$

$$\mathbf{f}^T = [\, f_{z1} \quad \mathcal{M}_{x1} \quad \mathcal{M}_{y1} \quad f_{z2} \quad \mathcal{M}_{x2} \quad \mathcal{M}_{y2} \quad f_{z3} \quad \mathcal{M}_{x3} \quad \mathcal{M}_{y3} \,]. \tag{6}$$

The Cartesian components of the plate curvatures are κ_{xx}, κ_{yy} and $2\kappa_{xy} = \kappa_{xy} + \kappa_{yx}$, which are gathered in a 3-vector $\boldsymbol{\kappa}$. In the Kirchhoff model, curvatures and displacements are linked by

$$\kappa_{xx} = \frac{\partial^2 w}{\partial x^2}, \quad \kappa_{yy} = \frac{\partial^2 w}{\partial y^2}, \quad 2\kappa_{xy} = 2\frac{\partial^2 w}{\partial x \partial y}. \tag{7}$$

where $w = w(x, y) \equiv u_z$ is the plate transverse displacement. In the KPT elements considered here, however, the compatibility equations (7) must be understood in a weak sense because the assumed

curvature field is not usually integrable. The internal moment field is defined by the Cartesian components m_{xx}, m_{yy} and m_{xy}, which are placed in a 3-vector $\mathbf{m}$. Curvatures and moments are linked by the constitutive relation

$$\mathbf{m} = \begin{bmatrix} m_{xx} \\ m_{yy} \\ m_{xy} \end{bmatrix} = \begin{bmatrix} D_{11} & D_{12} & D_{13} \\ D_{12} & D_{22} & D_{23} \\ D_{13} & D_{23} & D_{33} \end{bmatrix} \begin{bmatrix} \kappa_{xx} \\ \kappa_{yy} \\ 2\kappa_{xy} \end{bmatrix} = \mathbf{D}\boldsymbol{\kappa}. \tag{8}$$

where $\mathbf{D}$ results from integration through the thickness in the usual way. Three dimensionless side direction coordinates π_{21}, π_{32} are π_{13} are defined as going from 0 to 1 by marching along sides 12, 23 and 31, respectively. The side coordinate π_{ji} of a point not on a side is that of its projection on side ij. The second derivatives of $w \equiv u_z$ with respect to the dimensionless side directions will be called the *natural curvatures* and are denoted by $\chi_{ji} = \partial^2 w/\partial \pi_{ji}^2$. These curvatures have dimensions of displacement. They are related to the Cartesian plate curvatures by the matrix relation

$$\boldsymbol{\chi} = \begin{bmatrix} \chi_{21} \\ \chi_{32} \\ \chi_{13} \end{bmatrix} = \begin{bmatrix} \dfrac{\partial^2 w}{\partial \pi_{21}^2} \\ \dfrac{\partial^2 w}{\partial \pi_{32}^2} \\ \dfrac{\partial^2 w}{\partial \pi_{13}^2} \end{bmatrix} = \begin{bmatrix} x_{21}^2 & y_{21}^2 & x_{21}y_{21} \\ x_{32}^2 & y_{32}^2 & x_{32}y_{32} \\ x_{13}^2 & y_{13}^2 & x_{13}y_{13} \end{bmatrix} \begin{bmatrix} \dfrac{\partial^2 w}{\partial x^2} \\ \dfrac{\partial^2 w}{\partial y^2} \\ 2\dfrac{\partial^2 w}{\partial x \partial y} \end{bmatrix} = \mathbf{T}^{-1}\boldsymbol{\kappa}, \tag{9}$$

the inverse of which is

$$\boldsymbol{\kappa} = \begin{bmatrix} \dfrac{\partial^2 w}{\partial x^2} \\ \dfrac{\partial^2 w}{\partial y^2} \\ 2\dfrac{\partial^2 w}{\partial x \partial y} \end{bmatrix} = \frac{1}{4A^2} \begin{bmatrix} y_{23}y_{13} & y_{31}y_{21} & y_{12}y_{32} \\ x_{23}x_{13} & x_{31}x_{21} & x_{12}x_{32} \\ y_{23}x_{31} + x_{32}y_{13} & y_{31}x_{12} + x_{13}y_{21} & y_{12}x_{23} + x_{21}y_{32} \end{bmatrix} \begin{bmatrix} \dfrac{\partial^2 w}{\partial \pi_{21}^2} \\ \dfrac{\partial^2 w}{\partial \pi_{32}^2} \\ \dfrac{\partial^2 w}{\partial \pi_{13}^2} \end{bmatrix} = \mathbf{T}\boldsymbol{\chi}. \tag{10}$$

The transformation equations (9) and (10) are assumed to hold even if $w(x, y)$ is only known in a weak sense

The Basic Stiffness Template

Following Militello and Felippa (1991), the α-parametrized basic stiffness is defined as the linear combination

$$\mathbf{K}_b = A^{-1}\mathbf{L}\mathbf{D}\mathbf{L}^T, \qquad \mathbf{L} = (1-\alpha)\mathbf{L}_l + \alpha\mathbf{L}_q \tag{11}$$

where $\mathbf{L}$ is a 9×3 force-lumping matrix that maps an internal constant moment field to node forces. $\mathbf{L}_l$ and $\mathbf{L}_q$ are called the linear and quadratic versions, respectively, of $\mathbf{L}$. Matrix $\mathbf{L}_l$ was introduced by Bergan and Nygård (1984) and $\mathbf{L}_q$ by Militello and Felippa (1991). Expressions for both matrices may be found in the latter paper.

The Higher Order Stiffness Template

For an element of constant $\mathbf{D}$, the higher order stiffness template is defined by

$$\mathbf{K}_h = \frac{A}{3}(\mathbf{B}_4^T\mathbf{D}_\chi\mathbf{B}_4 + \mathbf{B}_5^T\mathbf{D}_\chi\mathbf{B}_5 + \mathbf{B}_6^T\mathbf{D}_\chi\mathbf{B}_6) \tag{12}$$

where $\mathbf{D}_\chi = \mathbf{T}^T\mathbf{D}\mathbf{T}$ is the plate constitutive relation expressed in terms of natural curvatures and moments, and $\mathbf{B}_{\chi m}$ are the natural curvature-displacement matrices evaluated at the midpoints $m = 4, 5, 6$ opposing corners 3,1,2, respectively.

These matrices are parametrized as follows. Define the geometric invariants

$$\lambda_1 = \frac{x_{12}x_{13} + y_{12}y_{13}}{x_{21}^2 + y_{21}^2}, \quad \lambda_2 = \frac{x_{23}x_{21} + y_{23}y_{21}}{x_{32}^2 + y_{32}^2}, \quad \lambda_3 = \frac{x_{31}x_{32} + y_{31}y_{32}}{x_{13}^2 + y_{13}^2}. \tag{13}$$

which have a simple physical meaning as measures of triangle distortion (for an equilateral triangle, $\lambda_1 = \lambda_2 = \lambda_3 = 1/2$). In the following expressions, the β-derived coefficients γ_i and σ_i are selected so that the $\mathbf{B}_{\chi m}$ matrices are exactly orthogonal to all rigid body modes and constant curvature states. This is a requirement of the fundamental stiffness decomposition. Only the expression of $\mathbf{B}_{\chi 4}$ is given below. Those of $\mathbf{B}_{\chi 5}$ and $\mathbf{B}_{\chi 6}$ follow from appropriate cyclic permutations.

$$\begin{aligned}
&\beta_1 = \beta_{10}+\beta_{11}\lambda_3+\beta_{12}\lambda_1+\beta_{13}\lambda_2,\ \beta_2 = \beta_{20}+\beta_{21}\lambda_3+\beta_{22}\lambda_1+\beta_{23}\lambda_2,\ \beta_3 = \beta_{30}+\beta_{31}\lambda_3+\beta_{32}\lambda_1+\beta_{33}\lambda_2,\\
&\beta_4 = \beta_{40}+\beta_{41}\lambda_3+\beta_{42}\lambda_1+\beta_{43}\lambda_2,\ \beta_5 = \beta_{50}+\beta_{51}\lambda_3+\beta_{52}\lambda_1+\beta_{53}\lambda_2,\ \beta_6 = \beta_{60}+\beta_{61}\lambda_3+\beta_{62}\lambda_1+\beta_{63}\lambda_2,\\
&\beta_7 = \beta_{70}+\beta_{71}\lambda_3+\beta_{72}\lambda_1+\beta_{73}\lambda_2,\ \beta_8 = \beta_{80}+\beta_{81}\lambda_3+\beta_{82}\lambda_1+\beta_{83}\lambda_2,\ \beta_9 = \beta_{90}+\beta_{91}\lambda_3+\beta_{92}\lambda_1+\beta_{93}\lambda_2,\\
&\gamma_1 = \beta_1 + \beta_3,\ \gamma_2 = \beta_3,\ \gamma_3 = \beta_2 + \beta_3,\ \gamma_4 = \beta_4 + \beta_6,\ \gamma_5 = \beta_6,\ \gamma_6 = \beta_5 + \beta_6,\\
&\gamma_7 = \beta_7 + \beta_9,\ \gamma_8 = \beta_9,\ \gamma_9 = \beta_8 + \beta_9,\ \sigma_1 = -2\gamma_3,\ \sigma_2 = 2\gamma_3 - 2\gamma_1,\ \sigma_3 = 2\gamma_4,\\
&\sigma_4 = -2\gamma_6,\ \sigma_5 = 2\gamma_7,\ \sigma_6 = 2\gamma_9 - 2\gamma_7,\ \sigma_7 = 2\gamma_1,\ \sigma_8 = 2\gamma_6 - 2\gamma_4,\ \sigma_9 = -2\gamma_9
\end{aligned}$$

$$\mathbf{B}_{\chi 4} = \begin{bmatrix}
\sigma_3 & \gamma_4 y_{31} + \gamma_5 y_{23} & \gamma_4 x_{13} + \gamma_5 x_{32} & \sigma_4 & \beta_6 y_{31} + \gamma_6 y_{23} & \beta_6 x_{13} + \gamma_6 x_{32} \\
\sigma_5 & \gamma_7 y_{31} + \gamma_8 y_{23} & \gamma_7 x_{13} + \gamma_8 x_{32} & \sigma_9 & \beta_9 y_{31} + \gamma_9 y_{23} & \beta_9 x_{13} + \gamma_9 x_{32} \\
\sigma_7 & \gamma_1 y_{31} + \gamma_2 y_{23} & \gamma_1 x_{13} + \gamma_2 x_{32} & \sigma_1 & \beta_3 y_{31} + \gamma_3 y_{23} & \beta_3 x_{13} + \gamma_3 x_{32} \\
\sigma_8 & \beta_4 y_{31} + \beta_5 y_{23} & \beta_4 x_{13} + \beta_5 x_{32} & & & \\
\sigma_6 & \beta_7 y_{31} + \beta_8 y_{23} & \beta_7 x_{13} + \beta_8 x_{32} & & & \\
\sigma_2 & \beta_1 y_{31} + \beta_2 y_{23} & \beta_1 x_{13} + \beta_2 x_{32} & & &
\end{bmatrix} \tag{14}$$

This Page Intentionally Left Blank

STRUCTURAL OPTIMIZATION FOR PRACTICAL ENGINEERING: SOFTWARE DEVELOPMENT AND APPLICATIONS*

Yuanxian GU, Hongwu ZHANG, Zhan KANG, Zhenqun GUAN

State Key Laboratory of Structural Analysis of Industrial Equipment
Department of Engineering Mechanics
Dalian University of Technology, Dalian 116024, China

ABSTRACT

The design optimization software JIFEX, with its former version MCADS, is developed with the application-oriented concept. It is practically applicable to complex structures of general purposed engineering. The versatile structural modeling and simulation methods of JIFEX for the finite element analysis and design optimization are presented. The numerical approaches of structural sensitivity analysis for the problems of static stress, eigenvalue of vibration and buckling, dynamic frequency response, and transient dynamics and heat transfer are introduced. The software integration of the analysis, optimization, pre- and post-processing developed with advanced platform Windows 95/NT is implemented. The application examples of structural optimization has demonstrated the effectiveness of the optimization technology with application-oriented software.

KEYWORDS

Design Optimization, Sensitivity, Software

---

* Project supported by the Scientific Fund for National Outstanding Youth of China (19525206)

INTRODUCTION

With the development of modern computational technologies such as advanced computers and software techniques, finite element methods, computer-aided design and engineering, and etc., the technology of design optimization is becoming more and more significant in the structural engineering. On the basis of theories and algorithms of the optimization, the numerical methods and software implementation are particularly important to the practical application of the structural optimization technology. In the practical applications of the real life engineering, the numerical methods and software implementations of design optimization have to be composed of the following components:

- The numerical modeling and simulation of complex structures in the analysis and the optimization.
- The structural analysis with general purposed capabilities.
- The efficient sensitivity analysis, i.e. the sensitivity derivatives calculation for structural behavior functions.
- The efficient and robust solution algorithms of optimization problems.
- The reliable and applicable software with large-scale numerical computing capability and user friendly operations.

In the past three decades, there was much research on the numerical methods of structural optimization and some programs developed. However, most of these kinds existed programs are research oriented and insufficient in the capabilities such as the types of elements, loads, and variables, functions of analysis, constraints as well as sensitivity calculations, and computational scale. This has limited the applications of the structural design optimization technology in practical engineering. The problem is that the linkage between the theoretical research and the software development, and the requirement of software being application oriented. Due to the complexity of practical engineering, the above-mentioned facilities are necessary for structural optimization softwares.

This paper presents the development and applications of some numerical methods of structural design optimization implemented in the software system JIFEX[1] and its former version MCADS[2]. The development of JIFEX software is practical application oriented and based on the advanced computer techniques. First of all, the JIFEX and MCADS were developed on the basis of general purpose software for the finite element analysis of complex structures. Its general purpose analysis for the static, dynamic, and buckling problems is supported by the versatile modeling capability to complex structures with various elements, loads, and boundary conditions. On the basis of these structural analysis and modeling capabilities, the numerical methods of sensitivity analysis have been studied for the constraints of static stress and deformation, eigenvalues of vibration frequencies and

buckling loads, dynamic responses in the frequency domain and time domain, as well as the transient heat transfer in structures. This way, the design optimization model of JIFEX is implemented for various elements, loads, variables, constraints, and objectives.

The JIFEX system is developed on the platforms of Pentium PC and MS Windows 95/NT, with the 32bit C/C++ programming tool. The pre-processing of the finite element modeling is developed on the CAD package AutoCAD, and implemented the interactive geometric modeling and automatically generation of finite element model data. The computing visualization under the Windows 95/NT environment is available. The advanced technologies of computer software and numerical computing make JIFEX to be new generation software of structural analysis and design optimization.

STRUCTURAL MODELING OF ANALYSIS AND OPTIMIZATION

Firstly, JIFEX software is capable of simulating complex structures by means of various kinds of elements, loads, and boundary conditions. Particularly, it simulates boundary support and component connection conditions with displacement constraint on each freedom of node in arbitrary local co-ordinate system. And the displacement constraints include status of fixed, pre-assigned displacement value, and particularly, multi-level master-slave relation. The so-called master-slave relation means that the displacement status of a freedom of slave nodes can be controlled by (i.e. with the same value of) one master node and this control relation can be defined level by level. These methods make the simulation of complex structures convenient and easy.

The finite element analysis of JIFEX generally applicable to the design optimization of complex structures includes the following fundamental requirements:

- Structural static strength analysis,
- Free vibration frequency analysis,
- Dynamic response analysis both in frequency and time domains,
- Global buckling stability analysis,
- Transient heat transfer and thermal stress analysis,

In accordance to the versatile finite element modeling, the design optimization model of JIFEX has developed following three types of design variables:

- Size design variable. It includes the geometric sizes of cross section of various elements, such as bar, beam, membrane, plate, and shell elements.
- Shape design variable. It includes the co-ordinates of special nodes and geometric parameters of boundary shape interpolations. Then, the boundary shape of continuum structures, the configuration of frame structures, the locations of stiffeners and linkages can be optimized. The shape optimization modeling is cooperated with the parameterized design concept of the CAD.
- Composites design variable. It includes the design parameters of composite laminate and honeycomb sandwich plates, such as ply orientation, layer thickness, core height, and material parameters of special composite components.

The design constraint functions of JIFEX95 cover the following structural behaviors: structural weight, node displacement, stresses, vibration frequencies, dynamic displacement and stress responses, and buckling loads. The design objective function can be selected from any one constraint function or combined with several constraint functions. This way, the objective of design optimization can be

- Minimizing structural weight,
- Reducing structural stress and/or deformation,
- Improving structural stiffness,
- Increasing structural fundamental frequency or adjusting the distribution of a group of vibration frequencies,
- Minimizing structural dynamic responses,
- Increasing structural buckling loads,
- Multiple objectives optimization.

The basic feature of the modeling and simulation facilities of JIFEX is its general applicability to complex structures. This applicability is presented from the finite element model, analysis functions, design variables, design constraints, and optimization objectives. JIFEX is also capable of large-scale engineering computing. The finite element model with 100000 nodes can be computed with Pentium PC. Some analysis applications of practical structures with this scale have been completed.

STRUCTURAL SENSITIVITY ANALYSIS

The optimization solution algorithms of JIFEX are sequential linear programming and sequential quadratic programming. The solution efficiency and convergence stability of these algorithms are based on the sensitivity analysis on the constraint and objective functions. The difficulty of sensitivity analysis for the general purpose optimization software such as JIFEX is that it must be suitable to various elements, variables, and structural responses. The numerical methods of sensitivity analysis have been studied for (1) static stress and deformation, (2) eigenvalue problems of free vibration and buckling stability, (3) frequency response problem, and (4) transient problems of dynamic response in time domain and heat transfer in structures.

Static Strength Problem

The sensitivity derivatives of displacement vector $\boldsymbol{U}$ and stresses σ are calculated with Eq.(2) derived from Eq.(1), the finite element formulation. The $\boldsymbol{K}$ and $\boldsymbol{P}$ are structural stiffness matrix and load vector respectively, $\boldsymbol{S}$ is element stress matrix, subscript e denotes element.

$$KU = P, \quad \sigma = S_e U_e \tag{1}$$

$$KU' = P' - K'U, \quad \sigma' = S'_e U_e + S_e U'_e \tag{2}$$

Eigenvalue Problems

The eigenvalue problem can be expressed as below

$$K\phi - \lambda M\phi = 0 \tag{3}$$

Two kinds of eigenvalue problems have been considered: (a) The free-vibration, $\boldsymbol{M}$ is mass matrix, and λ is the square of vibration frequency; (b) The buckling problem, $\boldsymbol{M}$ is geometric stiffness matrix, λ is critical load factor. The derivatives of the eigenvalue are obtained by Eq.(4).

$$\begin{aligned} \lambda' &= \phi^T (K' - \lambda M')\phi \\ \phi^T M \phi &= 1 \end{aligned} \tag{4}$$

The following Rayleigh quotient can be used to improve the approximation accuracy of the eigenvalues.

$$\tilde{\lambda}_j(\mathbf{X}) = \tilde{U}_j(\mathbf{X}) / \tilde{T}_j(\mathbf{X}) \tag{5}$$

$$\tilde{U}_j(\mathbf{X}) = U_j(\mathbf{X}_0) + \sum_{i=1}^{n} \frac{\partial U_j}{\partial x_i}(x_i - x_{0i}),\ \tilde{T}_j(\mathbf{X}) = T_j(\mathbf{X}_0) + \sum_{i=1}^{n} \frac{\partial T_j}{\partial x_i}(x_i - x_{0i})$$

where U_j and T_j are modal strain energy and modal kinetic energy of the j-th eigenvector. For the buckling problem, Eq.(5) is approximate since $\boldsymbol{M}$ depends on pre-buckling stress field. The accurate derivatives are

$$\lambda' = \phi^T (K' - \lambda M')\phi + \lambda \Lambda^T K' U_B \tag{6}$$

where $\boldsymbol{U_B}$ is pre-buckling displacement, and the adjoint field Λ is obtained by

$$K\Lambda = -\{\frac{\partial(\phi^T M \phi)}{\partial U_B}\}^T \tag{7}$$

Dynamic Frequency Response Problem

The dynamic frequency response problem is formulated as below

$$M\ddot{u} + C\dot{u} + Ku = f \tag{8}$$

The $\boldsymbol{C}$ is damping matrix. The harmonic exciting is expressed as $\boldsymbol{f} = f_0 \mathrm{Cos}(\theta t)$ or $\boldsymbol{f} = f_0 \mathrm{Sin}(\theta t)$. Two kind of loads f_0 are dealt with: (a) the node-force load exciting is $f_0 = \boldsymbol{P}$, (b) the accelerate movement exciting is $f_0 = -\boldsymbol{M}\mathrm{A}\boldsymbol{u}_0$. $\boldsymbol{u}_0$ is the rigid displacement vector with unit

movement, A is accelerate scope. The displacement response of Eq.(8) is:

$$u = s\sin(\theta t) + c\cos(\theta t) \tag{9}$$

With the modal superposition method, the derivatives of eigenvectors are required. It is difficult in the case of repeated eigenvalues. Following subspace iteration method and direct eigenvector space method are implemented in JIFEX.

Subspace iteration method

Starting from trial vectors $\Psi^{(0)}$, compute eigenvector derivatives by following subspace iteration procedures with k=0,1,2,.....

(a) Inverse-iteration:

$$(K + \sigma M)V^{(k+1)} = \overline{F} + M\psi^{(k)} \tag{10}$$

$$\begin{aligned} \overline{F} &= M'\phi_p - (K' + \sigma M')W \\ W &= \phi_p P^{-1}, \quad P = \Lambda_P + \sigma I \end{aligned} \tag{11}$$

Λ_P and Φ_P are p eigenpairs, σ is shift value.

(b) Projecting into trial vector space for eigenvector derivatives:

$$\widetilde{K}D^{(k+1)} - \widetilde{M}D^{(k+1)}\Lambda_P = \widetilde{M}P\Lambda'_P + \widetilde{M}'^{(k+1)}P\Lambda_P - \widetilde{K}'^{(k+1)}P \tag{12}$$

$$\begin{aligned} \widetilde{K}'^{(k+1)} &= W^T K'W + W^T KV^{(k+1)} + (W^T KV^{(k+1)})^T \\ \widetilde{M}'^{(k+1)} &= W^T M'W + W^T MV^{(k+1)} + (W^T MV^{(k+1)})^T \\ \widetilde{K} &= W^T KW, \quad \widetilde{M} = W^T MW \end{aligned} \tag{13}$$

(d) Updating the trial vectors and convergence checking:

$$\begin{aligned} \Psi^{(k+1)} &= V^{(k+1)}P + WD^{(k+1)} \\ \Psi^{(k+1)} &\to \Phi'_P, \ (k \to \infty) \end{aligned} \tag{14}$$

The Nelson's method is used to solve Eq.(12) for repeated eigenvalues.

Eigenvector space method

Let C be independent to variable, exciting $f=f_O\mathrm{Cos}(\theta t)$. Differentiating Eq.(8) gives

$$\begin{aligned} M\ddot{u}' + C\dot{u}' + Ku' &= f_S\sin(\theta t) + f_C\cos(\theta t) \\ f_S &= M's\theta^2 - K's, \quad f_C = M'\theta^2 c - K'c + f'_O \end{aligned} \tag{15}$$

Solving Eq.(15) in eigenvector space twice with respect exciting $f_S\text{Sin}(\theta t)$ and $f_C\text{Cos}(\theta t)$ respectively, we have

$$\begin{aligned} u'_S &= s_S \sin(\theta t) + c_S \cos(\theta t) \\ u'_C &= s_C \sin(\theta t) + c_C \cos(\theta t) \end{aligned} \tag{16}$$

Then, the derivatives of $\boldsymbol{u}$ can be obtained

$$\{u\}' = \{u_s\}' + \{u_c\}' = (\{S_s\} + \{S_c\})Sin\theta t + (\{C_s\} + \{C_c\})Cos\theta t \tag{17}$$

Both of the methods have advantages of easy to be implemented on the basis of dynamic analysis, computational efficiency and accuracy, but without difficulty of eigenvector sensitivity calculation with repeated eigenvalues

Transient Problems

The motion equations and critical-point constraint of transient problems can be written in a general first-order form

$$A\dot{u} = f(u,\alpha,t), \quad u(\alpha,0) = u_0 \tag{18}$$

$$\bar{g}(u,\alpha) = \int_0^{t_f} p(u,\alpha,t)dt \le 0, \quad p(u,\alpha,t) = g(u,\alpha,t)\delta(t - t_{mi}) \tag{19}$$

where $\boldsymbol{u}$ is response vector, α is design variable, g is a general form constraint function, t denotes time. The sensitivity analysis with the direct method and the adjoint method are implemented with Eq.(20) and Eq.(21) respectively.

$$A\frac{d\dot{u}}{d\alpha} = J\frac{du}{d\alpha} - \frac{dA}{d\alpha}\dot{u} + \frac{\partial f}{\partial \alpha}, \quad \frac{du(\alpha,0)}{d\alpha} = 0, \quad J_{i,j} = \frac{\partial f_i}{\partial u_j} \tag{20}$$

$$A^{\mathrm{T}}\dot{\lambda} + (J^{\mathrm{T}} + \dot{A}^{\mathrm{T}})\lambda = 0, \quad A^{\mathrm{T}}\lambda(t_{mi}) = -\left(\frac{\partial g}{\partial u}(t_{mi})\right)^{\mathrm{T}} \tag{21}$$

For the transient heat transfer problem, the finite element formulation is

$$M\dot{T} + KT = Q = P + P_b \tag{22}$$

where $\boldsymbol{M}$ is the heat capacity matrix; $\boldsymbol{T}$ is the vector of node temperature; $\boldsymbol{P}_b$ is reduced by the given temperature on the boundary. With the implicit θ-difference method, the temperature $\boldsymbol{T}^{n+1}$ of time t_{n+1} is computed from $\boldsymbol{T}^n$ with

$$\begin{aligned} &(a_n M + K)T^{n+1} = (a_n M - bK)T^n + \frac{P}{\theta} - (a_n M + K)T_b \\ &a_n = 1/(\theta \Delta t_n), \quad b = (1-\theta)/\theta, \quad 0 < \theta < 1 \end{aligned} \tag{23}$$

With the direct method, the derivatives of temperature are computed by solving Eq.(24) simultaneously with the solving of Eq.(23) at each time point.

$$\begin{aligned}(a_n M+K)\frac{dT^{n+1}}{d\alpha} &= (a_n M-bK)\frac{dT^{n}}{d\alpha}+\left(a_n\frac{dM}{d\alpha}-b\frac{dK}{d\alpha}\right)T^{n}\\ &+\frac{dP}{\theta d\alpha}-\left(a_n\frac{dM}{d\alpha}+\frac{dK}{d\alpha}\right)\left(T_b+T^{n+1}\right)\end{aligned} \tag{24}$$

The derivatives of equivalent constraint are calculated at critical points as follows

$$\frac{d\bar{g}}{d\alpha}=\sum_i\left(\frac{\partial g}{\partial\alpha}(t_{mi})+\frac{\partial g}{\partial T}\frac{dT}{d\alpha}(t_{mi})\right) \tag{25}$$

With the adjoint method, the derivatives of the equivalent constraint are computed as below

$$\frac{d\bar{g}}{d\alpha}=\sum_i\left(\frac{\partial g}{\partial\alpha}(t_{mi})-\lambda^{\mathrm{T}}(t_{mi})\left(\frac{\partial Q}{\partial\alpha}-\frac{dK}{d\alpha}T(t_{mi})-\frac{dM}{d\alpha}\dot{T}(t_{mi})\right)\right),\ M^{\mathrm{T}}\lambda(t_{mi})=-\left(\frac{\partial g}{\partial T}(t_{mi})\right)^{\mathrm{T}} \tag{26}$$

For the generality of sensitivity analysis with respect to various design variables, elements, load and boundary conditions, the semi-analytic scheme simplified the programming implementation a great deal. The structural optimization is available for the design on the multiple behaviors of strength, stiffness, vibration frequency, buckling stability, and dynamic responses.

USER INTERFACE WITH ADVANCED PLATFORM

The development of JIFEX follows the strategies of:

- Using Pentium PC as the basic hardware environment and implement 32-bit computing for large-scale engineering applications.
- Using the MS Windows 95/NT as the standard platform, and implement unified graphics interface and computing visualization.
- Using the C/C++ programming tools for complete software system and make it compatible with MS Windows 95/NT and other CAD packages.
- Integrate the finite element modeling with popular CAD package AutoCAD, and employ it as the geometric modeling engine.

JIFEX has integrated the structural analysis, sensitivity analysis, design optimization, pre- and post-processing for practical application of general purpose engineering. Since the system is developed on the advanced software platform of MS Windows 95/NT, its interactive graphics interface is user-friendly and unify to the standard Windows 95/NT environment. And the multiple processing facility of Windows NT is employed to implement the distributed computing and visualization. The combination of the advanced software technologies and numerical computing methods make JIFEX to be new generation software of structural

analysis and design optimization.

The pre-processing of the finite element modeling is implemented on the basis of popular CAD package AutoCAD, with which as the geometric modeling platform. The interactive geometric modeling and automatical generation of finite element model data has been implemented, and the finite element modeling is linked with CAD directly. The geometric model of structures is constructed with AutoCAD easily, and then the finite element mesh is generated with a group algorithms developed in JIFEX. All of the attribute data of finite element model, such as load, material, element property, boundary condition, can be produced interactively. The Figure 1 is the finite element model of a complete containership generated by JIFEX.

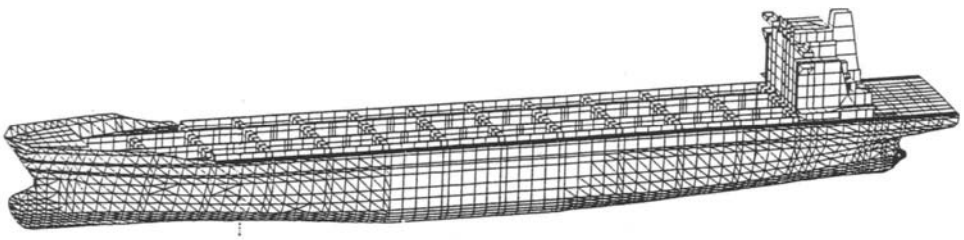

Figure 1: Finite element model of containership

The computer graphics and computing visualization under Windows 95/NT environment is available. Besides the conventional facilities of computer graphics, such as hidden line and surface removal, shading, contour, color filling, computer animation and etc., the advanced visualization technique of direct volume rendering and iso-surface have been developed in JIFEX for the 3D data field visualization. By means of the multiple processing and DDE support of the Windows 95/NT, the distributed computing and visualization has been implemented for structural analysis and optimization.

APPLICATION EXAMPLES

Example 1. The design optimization of a structural component of the launch rocket CZ-2E. The upper-stage component of the rocket is modeled with 580 nodes and 1460 elements, shown in Figure 2. The objective is to minimize the structural weight under the constraints of the structural fundamental frequency, the maximum stresses and deformations. There are a total of 20 master design variables to control all elements by means of the variable-link. These design variables are classified into three groups to represent: (1) the thickness of plate elements; (2) the size parameters of beam cross-sections such as the L-shaped, the I-shaped, and the complicated shape shown in Figure 3(a); and (3) the size parameters of milled regions of some plates shown in Figure 3(b). So the design model is rather complicated. The upper and lower bounds of the design variables are given by considering the design and manufacturing requirements. In the optimum design obtained, the structural weight has been reduced from the initial design by 12% and all of constraint conditions are satisfied. This optimization result indicates a great improvement over the initial design.

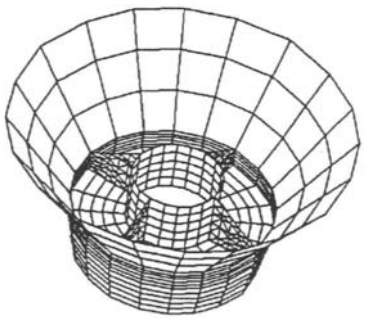

Figure 2: The rocket component

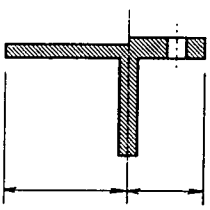

Figure 3(a)

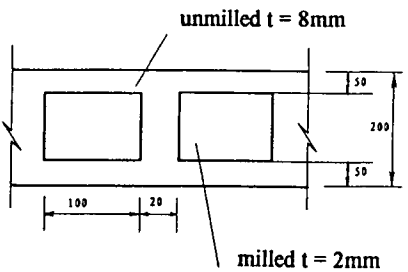

Figure 3(b)

Example 2. The dynamic synthesis of a spaceship orbit-module structure. The structural finite element model, shown in Figure 4, is composed of 369 shell and beam elements. The thickness of the shells and area of the beams are represented by 11 master design variables. Two problems are computed as follows.

(1) The optimum design of fundamental vibration frequency with weight constraint. Two group results of optimization have been obtained with different constraints of the structural weight. The first one is that the structural fundamental vibration frequency is increased by 9% without increasing weight, and the second one is that the structural fundamental vibration frequency is increased by 16% with the weight increasing by 9%.

(2) The design optimization with constraints on structural dynamic responses and free-vibration frequencies. The accelerated movement of the spaceship during the launch period is considered as the excitation source of structural dynamic response. The excitation frequency of accelerated movement changes from 42(HZ) to 55(HZ). The maximum value of displacement responses within this excitation frequency band is checked and put into constraints. The initial value of the maximum displacement response is 0.202, and its upper bound is limited by 0.22. The optimum design has reduced structural weight by 7% and satisfied all of the displacement response and vibration frequency constraints, shown in the Table 1. It is noticeable that the first two vibration frequencies are also repeated eigenvalues. Both of them are computed in optimization, and kept due to the symmetric variable-link.

Example 3. The design optimization of a spaceship orbit-module structure with the constraints on displacement, vibration frequency, and critical buckling load. The structural model is same as that of the example 2. The thickness of the shells and area of the beams are represented by 13 master design variables, six variables of cross-section area of beams and seven variables of thickness of shells. There are also 2000kg non-structural masses attached to cylinder nodes. The load is gravity due to the acceleration movement in z-direction. The optimization objective is to minimize structural weight W with the constraints on the maximum displacement in z-direction w_{max}, the fundamental vibration frequency ω_1, and the critical buckling load factor λ_{CR}. The constraint conditions are listed in Table 2. The optimum design is obtained after 6 iteration, and the structural weight is reduced by 9.5%. The design variables are listed in Table 3 with the initial, optimum, up- and low-bound values.

TABLE 1
SPACESHIP ORBIT-MODULE OPTIMIZATION

	Initial	Optimum
ω_1/ω_{min}	1.046	1.015
ω_2/ω_{min}	1.047	1.016
w_{max} (mm)	0.202	0.22
Weight/W_0	1.0	0.93

TABLE 2
SPACE ORBIT-MODULE OPTIMIZATION

	Constraints	Initial	Optimum
λ_{CR}	≥0.650	0.703	0.650
ω_1	≥10.00	10.28	10.01
w_{max}	≥-2.000	-1.809	-1.930
W/W_0		1.0	0.905

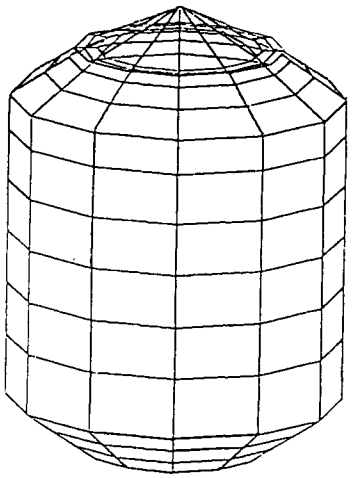

Figure 4: The Spaceship orbit-module

TABLE 3 DESIGN VARIABLES OF THE SPACE ORBIT-MODULE STRUCTURE

Design Variables	Initial	Optimum	Up-bound	Low-bound
Beam variable 1	477.00	441.20	500.00	420.00
Beam variable 2	477.00	441.20	500.00	420.00
Beam variable 3	158.00	140.30	170.00	130.00
Beam variable 4	158.00	140.30	170.00	130.00
Beam variable 5	158.00	140.30	170.00	130.00
Beam variable 6	158.00	140.30	170.00	130.00
Shell variable 1	10.00	9.16	10.00	8.50
Shell variable 2	3.00	3.20	3.50	2.50
Shell variable 3	2.00	1.64	2.50	1.50
Shell variable 4	2.00	1.64	2.50	1.50
Shell variable 5	2.00	1.64	2.50	1.50
Shell variable 6	5.00	4.64	5.50	4.50
Shell variable 7	6.00	5.60	6.50	5.50

REFERENCES

1. Gu Y.X., Zhang H.W., Guan, Z.Q., Kang Z. and Li, Y.P.(1997). New Development and Applications of Structural Analysis/Optimization Package JIFEX95, *Proc. 1st China-*

Australia Symp. Comput. Mech. (CASCM'97), 81-90.

2. Gu Y.X. and Cheng(1993). Structural Modeling and Sensitivity Analysis of Shape Optimization, *J. Struct. Opti.*, **6:1**, 29 –37.
3. Gu Y.X. and Cheng G.D.(1993). Research and Applications of Numerical Methods of Structural Shape Optimization, *J. Comput. Struct. Mech. and Appl.* (in Chinese), **10:3**, 321-335.
4. Gu Y.X., Kang Z., Guan Z.Q. and Jia Z.W.(1998). Dynamic Sensitivity Analysis and Optimum Design of Aerospace Structures, *Int. J. Struct. Eng. Mech.*, **6:1**, 31-40.
5. Nelson R.B.(1976), Simplified Calculation of Eigenvector Derivatives, *AIAA J*, **14:9**,1201-1205.

PARALLEL INTEGRATION ALGORITHMS FOR DYNAMIC ANALYSIS OF STRUCTURES IN THE CLUSTERED NETWORK SYSTEM*

[1]J.G. Cheng, [1]Z.H Yao [1]X.P. Zheng , [1]Y. Gao, [2]Z.J. Kou and [2]W.B Huang ,

[1]Department of Engineering Mechanics, Tsinghua University
Beijing 100084,China
[2]Applied Mechanics Institute, China Agricultural University
Beijing 100083, China

ABSTRACT

In this paper, parallel implementations of the explicit/implicit integration algorithms for dynamic analysis of structures are presented. The parallelism of the former is based on the domain decomposition method and the use of lumped mass matrix. That of the latter is on the block parallelization of the assembling, the triangular factorization of the equivalent stiffness matrices and the back/forward substitutions in each Newmark step. Implementations are carried out on the clustered network systems with PVM parallel environment. The developed parallel integration algorithms are incorporated into the PFEM, which is a general-purpose serial-parallel mixed system for structural analysis. Illustrative examples are presented and the parallel efficiencies are discussed.

KEYWORDS

Explicit/implicit integration method, parallel algorithm, clustered network system

INTRODUCTION

The parallel integration algorithms for dynamic analysis of large structures have been topics in the engineering analysis community for quite some time. Noor(1979) discussed the parallel explicit integration method on pipeline vector computer. On shared memory MIMD parallel

* Supported by the NNSF of China (19670232) and the Foundation of National Education Commission of China.

computer, Ou(1986) compared parallelization for explicit and implicit integration and concluded that the central difference method is favorable with diagonal mass matrix and damping matrix. Hajjar(1989) discussed the parallel efficiency of the central difference method for 3D nonlinear truss structure on distributed memory MIMD computer and presented a data structure to decrease communication. Chiang(1990) parallelized the central difference method on two kinds of MIMD environments and demonstrated that data communication is of key importance to improve parallel efficiency. Cheng et al. (1995, 1996) developed explicit integration algorithms on Transputer computer. The available literature on parallel explicit integration is mostly developed on vector computer or shared memory MIMD parallel computer.

In China the PCs usually serve as main hardware for structural analysis. The motivation of the current research of the authors is to enhance the capacity of PCs through network and parallel computing, aiming at solving more complicated dynamic problems of structures in available hardware. In this paper, explicit/implicit integration methods, namely, central difference method and Newmark method are parallelized on the clustered network system. The parallelized algorithms have also been incorporated into a general-purpose finite element system - PFEM.

THE PARALLEL CENTRAL DIFFERENCE METHOD

The dynamic equations of linear structures at time t can be generally expressed as

$$\boldsymbol{M}\ddot{\boldsymbol{U}}_t + \boldsymbol{C}\dot{\boldsymbol{U}}_t + \boldsymbol{K}\boldsymbol{U}_t = \boldsymbol{R}_t \tag{1}$$

where $\boldsymbol{M}$, $\boldsymbol{C}$ and $\boldsymbol{K}$ stand for the mass, damping and stiffness matrices respectively, and $\boldsymbol{U}, \dot{\boldsymbol{U}}, \ddot{\boldsymbol{U}}$ and $\boldsymbol{R}$ are, respectively, the displacement, velocity , acceleration and applied loading vectors.

The employed explicit central difference scheme for the damped structures is as follows, which requires no matrix factorization:

$$\boldsymbol{M}\ddot{\boldsymbol{U}}_t = \boldsymbol{R}_t - (\boldsymbol{C}\dot{\boldsymbol{U}}_t + \boldsymbol{K}\boldsymbol{U}_t) \tag{2a}$$

$$\boldsymbol{M}\ddot{\boldsymbol{U}}_t = \hat{\boldsymbol{R}}_t \tag{2b}$$

where $\hat{\boldsymbol{R}}_t = \boldsymbol{R}_t - (\boldsymbol{C}\dot{\boldsymbol{U}}_t + \boldsymbol{K}\boldsymbol{U}_t)$

$$\ddot{\boldsymbol{U}}_t = \frac{\dot{\boldsymbol{U}}_{t+\Delta t/2} - \dot{\boldsymbol{U}}_{t-\Delta t/2}}{\Delta t}, \qquad \dot{\boldsymbol{U}}_t = \frac{\boldsymbol{U}_{t+\Delta t} - \boldsymbol{U}_t}{\Delta t} \tag{3a, b}$$

Domain decomposition method is one of the most important and mature methods, the superiority of which is easy to implement on distributed memory MIMD environment. For the central difference method, it is very instructive to design the parallel programs and improve the parallel efficiency on the base of substructure.

Assuming that the parallel computer system consists of n_p processors, the engineering structure should be divided into n_p substructures. In the meanwhile, we must decide the elements of each substructure and the 'correlative elements' which relate directly to each substructure but belong to the neighboring one. Then at the time steps, each processor calculates the displacement, velocity, acceleration and stress for every element in the respective substructure independently. Only the displacement of the 'correlative element' at the last time step should be transferred between the related processors.

With diagonal M and the Rayleigh damping, the equations of motion can be reformulated:

$$\ddot{U}_t^{(i)} = \hat{R}_t^{(i)} / m_{ii} \tag{4}$$

$$\hat{R}_t = R_t - aM\dot{U} - \sum_t K_t^{(e)}(b\dot{U}_t^{(e)} + U_t^{(e)}) \tag{5}$$

Now, the detailed algorithm steps can be described as follows:

1) Preprocess: Decompose the structure and decide the elements belonging to each substructure and then construct the 'correlative elements' information table

2) Initial calculation (parallelized on the substructure level)
   a) form the element stiffness matrix K_i^e and the diagonal mass matrix $M^{(s)}$, where s=1, 2, ..., n_p
   b) initialize $U_0, \dot{U}_0$ and $\ddot{U}_0$
   c) calculate

$$\dot{U}_{\Delta t/2} = \frac{\Delta t}{2}\ddot{U}_0 + \dot{U}_0 \tag{6}$$

$$U_{\Delta t} = \dot{U}_{\Delta t/2}\Delta t + U_0 \tag{7}$$

$$\dot{U}_{\Delta t} = \ddot{U}_0\Delta t + \dot{U}_0 \tag{8}$$

3) For each time step(parallelized on the substructure level)
   a) communicate between processors, transfer the displacement and velocity of the 'correlative elements' of each substructure to each other
   b) calculate the effective load of each substructure at the time t

$$\hat{R}_t^{(s)} = R_t^{(s)} - aM^{(s)}\dot{U}^{(s)} - \sum K_t^{(e)}(b\dot{U}_{t(i)}^{(e)} + U_{t(i)}^{(e)}) \tag{9}$$

where $\sum \boldsymbol{K}_t^{(e)}(b\dot{\boldsymbol{U}}_{t(i)}^{(e)} + \boldsymbol{U}_{t(i)}^{(e)})$ is the contribution of the elements and the 'correlative elements' of the substructure to the effective load

c) calculate the acceleration at the time t

$$\ddot{\boldsymbol{U}}_t^{(s)} = \hat{\boldsymbol{R}}_t^{(s)} / \boldsymbol{m}_{ii}^{(s)} \tag{10}$$

where $\boldsymbol{m}_{ii}^{(s)}$ is the number I element of the effective mass matrix, and assume that

$$\boldsymbol{m}_{ii}^{(s)} > 0$$

d) calculate $\boldsymbol{U}_{t+\Delta t/2}$, $\dot{\boldsymbol{U}}_{t+\Delta t/2}$

4) Output the computational results if required, then turn to 3) for the next step, else stop at the last step.

It is noteworthy to point out that the parallel efficiency of this parallel algorithm on the substructure level is dependent on the structure decomposition. Thus, when decomposing and dispensing the substructures, we should pay attention to two points:

1) Balance load among different processors as possible as we can get. Otherwise, the parallel efficiency will be decreased because of the heaviest loading processor following the Amdahl principle.

2) Interfaces between the substructures (also the number of the correlative elements of each substructure) should be minimized to decrease the communication between processors and the computation repeatedly.

PARALLELIZATION OF NEWMARK INTEGRATION METHOD

For Eqn.1, Newmark integration method employs the following time-marching scheme:

$$\dot{\boldsymbol{U}}_{t+\Delta t} = \dot{\boldsymbol{U}}_t + \left[(1-\delta)\ddot{\boldsymbol{U}}_t + \delta\ddot{\boldsymbol{U}}_{t+\Delta t}\right]\Delta t \tag{11}$$

$$\boldsymbol{U}_{t+\Delta t} = \boldsymbol{U}_t + \dot{\boldsymbol{U}}_t\Delta t + \left[(\frac{1}{2}-\alpha)\ddot{\boldsymbol{U}}_t + \alpha\ddot{\boldsymbol{U}}_{t+\Delta t}\right]\Delta t^2 \tag{12}$$

By satisfying the Eqn.1 at time $t+\Delta t$, we obtain

$$\hat{\boldsymbol{K}}\ddot{\boldsymbol{U}}_{t+\Delta t} = \hat{\boldsymbol{R}}_{t+\Delta t} \tag{13}$$

Where

$$\hat{K} = M + \delta \Delta t C + \alpha \Delta t^2 K \tag{14}$$

$$\begin{aligned} \hat{R}_{t+\Delta t} = R_{t+\Delta t} - C\left(\dot{U}_t + (1-\delta)\Delta t \ddot{U}_t\right) \\ - K\left(U_t + \dot{U}_t \Delta t + (\frac{1}{2} - \alpha)\Delta t^2 \ddot{U}_t\right) \end{aligned} \tag{15}$$

Computing time for the Newmark integration is mostly spent on the assembling of global matrices, evaluating effective load vector $\hat{R}$, formation, factorization and back/forward substitutions of effective stiffness matrix $\hat{K}$ through the each time step.

Assembling

Since the effective stiffness matrix $\hat{K}$ is generally of large scale in the FEM analysis of engineering structures, the assembling, factorization and back/forward substitution, which have to be segmented into blocks even in the modern computers, and the incore - outcore swapping techniques have to be employed. A routine in the available PFEM provides the function of automatic segmentation of global matrices, which can be easily used for the parallelization of assembling. Suppose that m processors are available and $\hat{\mathbf{K}}$ has been separated into il blocks. Then the k-th processor cyclically processes block k, block m+k, etc., and store them in the local hard disk.

Computing effective load vector $\hat{R}$

After loading element stiffness matrices, the correlative nodes and the load vectors distributed on slave processors are updated simultaneously and are further transferred among the processors to fulfill the final load vector updating.

Triangular factorization

The global stiffness matrix can be factored:

$$\hat{K} = LDL^T \tag{16}$$

where L is the lower triangular matrix and D is the diagonal matrix. The global matrices are stored in one-dimensional array by employing the variable bandwidth technique. The largest bandwidth is denoted as d. Denote m_j as the row number of the first non-zero entry of column j, for which

$$S_{mj,j} = K_{mj,j} \tag{17}$$

For other elements of column j:

$$S_{ij} = K_{ij} - \sum_{r=mn}^{i-1} L_{ri}^T d_{rr} L_{rj}^T \qquad m_n = max\left(m_j, m_n\right) \tag{18}$$

where

$$L_{ij} = S_{ij} / d_{ii} \quad (j = 2,3,\cdots,d; i = 1,2,\cdots,n) \tag{19}$$

$$d_{ii} = K_{ii} - \sum_{r=mi}^{i-1} L_{ri}^T d_{rr} L_{ri}^T \qquad (i = 1,2,\cdots,n) \tag{20}$$

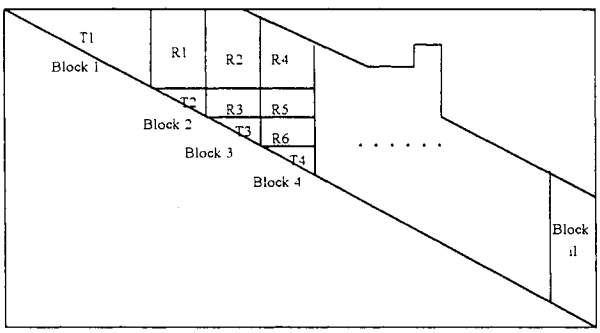

Figure 1: Blocking diagram of the variable bandwidth stiffness matrix

The block partition of $\hat{K}$ is illustrated in Figure 1. Triangular blocks and rectangular blocks are denoted as T1, T2, ..., etc. and R1, R2, ..., etc., respectively. The triangular factorization of T1 is the same as the original. The factorizations of T2 and R1 are affected by the factorization of T1. Generally the process of the following blocks is affected by its predecessors, and the blocks had to be swapped between the incore memory and the secondary memory.

Denote the triangular block size as n, and partition it into b=[n/m] sub-blocks. Thus processor Cn processes column Cn of each block:

(1) decompose the first sub-block in every processor

(2) processor 1 decomposes column 1 of sub-block 2 and transfers the decomposed element into the other processors.

(3) processor 2 decomposes column 2 of sub-block 2 and transfers the decomposed element into the follower processors.

(4) processors 3, 4, ..., m carry out the same processing as processors 1 and 2

(5) processor m transfers column m of block 2 into the former processors

(6) processor (m-1) transfers column m of block 2 into the former processors

(7) processors (m-2), (m-3), ..., 2 complete the message passing as processors m and (m-1)

Repeat the above procedures till current block is factorized.

Each rectangular block should be partitioned into jk=[n/2m] sub-blocks. Every sub-block is decomposed simultaneously as follows:

(1) processor 1 decomposes sub-blocks 1 and jk

(2) processor 2 decomposes sub-block 2 block jk-1

(3) processors 3, 4, ..., m complete the parallel work as processors 1 and 2

The results are transferred from each other after decomposing the last rectangular block in front of the triangular block.

Back substitution

Considering Eqn.1, Eqn.13 can be solved by the following two steps, i.e.

$$Ly = \hat{R} \tag{21}$$

$$DL^{T}\ddot{U}_{t+\Delta t} = y \tag{22}$$

The loading manipulations from outcore memory are intensive for large problems, so the parallelization of the loading manipulation is as important as that of algorithms. Here we take Eqn.21 to illustrate the procedure:

(1) processor 1 loads block 1, updates the corresponding part of **y** , and transfers results to the following processors.

(2) processors 2, 3, 4, ..., m load blocks 2, 3, 4, ..., m respectively and update the corresponding part of y with the triangular part of correlative blocks . Then these processors receive the results transferred from the former processors, update y, transfer the updated parts to other processors, and so on.

For blocks m+1, m+2, ..., the same solution procedures can be used.

NUMERICAL EXAMPLES

Examples of the parallel central difference integration algorithm

The computations are performed on three pyramid-shaped space frames, respectively, of DOFs 128, 288 and 512. The implementations are carried out in the PVM platform on high-speed hub-clustered PCs. The pre- and post-processing are finished with an available serial FEM package to which the parallel algorithms are incorporated. The results of parallel analysis are fully coincident with those of the serial analysis.

The effectiveness of a parallel algorithm can be assessed by the speed-up ratio $S_p(n)$ and the parallel efficiency $E_p(n)$, where $S_p(n)=t_s(n)/t_p(n)$, $E_p(n)=S_p(n)/n$. $t_s(n)$ and $t_p(n)$ are, respectively, the computer time used on the single processor with the best serial program and that on the n processor system with the parallel program .

The achieved parallel efficiencies are shown in Table 1. These parallel efficiencies increase with the number of time steps and the size of the problems.

TABLE 1
PARALLEL EFFICIENCY ON PVM

Examples	Time steps of load	Number of processors			
		2	3	4	5
1	500	0.92	0.86	0.76	0.72
	800	0.93	0.88	0.77	0.69
	1000	0.92	0.84	0.77	0.71
2	500	0.96	0.91	0.83	0.77
	800	0.94	0.89	0.84	0.76
	1000	0.95	0.89	0.82	0.75
3	500	0.95	0.90	0.84	0.76
	800	0.94	0.90	0.82	0.75
	1000	0.93	0.90	0.82	0.76

Examples of parallel Newmark algorithm

Computations are carried out on a plane stress problem and a 3D bending plate problem, shown in Figure 2.

The material and geometrical parameters are as follows:

$E = 2.1e+11N/m^2$, $\nu = 0.3$, $\rho = 7.84e+3kg/m^3$, $l = 100m$, $h = 20m$, $b = 0.1m$,

$\omega = 19.4224, a_1 = -1000N$, $\mathbf{a}_2 = (100 \quad 100 \quad 100)^T$ N, $\alpha = 0.25 \quad \delta = 0.50, \theta = 2.00, \Delta t = 0.04$.

Speedup S_p and parallel efficiency E_p under different DOFs n of the structure, bandwidth d, number of blocks il, and time steps are depicted in Table 2.

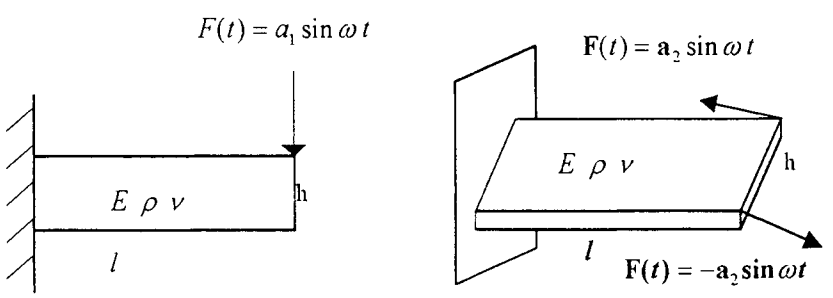

Figure 2: Structures and parameters

These results show that the parallel efficiency increases with the DOFs and the bandwidth of the problem, and with the time steps to be solved. For the available network system and the present examples, time spent on parallel computation is relatively smaller than that on communication, so the parallel efficiency of triangular factorization is lower comparatively. Since the stiffness matrix in Example 1 is partitioned into 6 blocks, the parallel efficiency is on the low side because of the load unbalance when the number of the processors is 4 and 5. The super linear speedups are observed in Example 2 due to the relatively larger buffers for swapping when the number of processors increased.

TABLE 2
PARALLEL EFFICIENCIES IN THE EXAMPLES

Number of Processors		Example 1			Example 2		
	N	3262			7579		
	D	318			726		
	Il	6			32		
	Steps	20	50	100	20	50	100
2	S_p	1.67	1.83	1.88	1.81	1.89	1.96
	E_p	0.84	0.92	0.94	0.91	0.95	0.98
3	S_p	2.30	2.62	2.65	2.61	2.75	2.91
	E_p	0.77	0.87	0.88	0.87	0.92	0.97
4	S_p	2.75	2.69	2.82	3.34	3.52	3.78
	E_p	0.69	0.68	0.71	0.84	0.88	0.95
5	S_p	2.79	2.75	2.88	3.56	4.04	4.49
	E_p	0.56	0.55	0.58	0.71	0.81	0.90

CONCLUSIONS

In this paper, the central difference method and the Newmark method are parallelized on a clustered network system and are also incorporated into a general-purpose finite element package - PFEM, which results in a serial-parallel mixed FEM package. Satisfactory parallel efficiencies are obtained for the examples presented. In both algorithms, the parallel efficiencies are found to increase with the size of the problems. In the Newmark algorithm, super linear speedups have also been observed, the reason for which can be ascribed to the increase of the swapping buffers with the number of processors and the swapping intensive nature of the devised algorithm.

Due to limitations of the hardware and software, the scale of the examples presented is rather small; it will be increased in further work.

REFERENCES

Cheng J.G. and Li M.R. (1995). A serial-parallel mixed finite element analysis software PFEM. *Computer and Mechanics Research*. Chengdu: Chengdu Science and Technology University Press, China.

Cheng J.G., Yao Z.H., Li M.R. and Huang W.B. (1996). Parallel algorithms for explicit integration of dynamics analysis of structures and their implementations. *Journal of Tsinghua University, Science and Technology*, 36:10, 80-85.

Chiang K.N. and Fulton R.E.(1990).Structural dynamics methods for concurrent processing computers. *Computer & Structure* 36:6, 1031-1037.

China Architecture Academy, Zhejiang University (1991), JGJ 7-91. *People's Republic of China jobs normal-frame structures design and described programs for implementation*. China Architecture Industry Press, China.

Hajjar J.F. and Abel J.F.(1989). Parallel processing of central difference transient analysis for three-dimensional nonlinear framed structures. *Communications in Applied Numerical Methods* 5:1, 39-46.

Noor A.K.(1979). Finite element dynamics analysis on CDC Star 100 computer. *Computer & Structure* 10:1, 7-19.

Ou R. and Fulton R.E.(1986). An investigation of parallel numerical integration methods for nonlinear dynamics. *Communications in Applied Numerical Methods* 30:1/2, 403-409.

Wang X.C., Shao M.(1988). The fundamental principle of the finite element method and numerical methods, Tsinghua University Press.

MAXIMUM ENTROPY PRINCIPLE AND TOPOLOGICAL OPTIMIZATION OF TRUSS STRUCTURES

B. Y. Duan, Y. Z. Zhao and H. Liu

School of Mechanical and Electronic Eng.
Xidian University, Xi'an 710071, China

ABSTRACT

This paper presents an entropy – based topological optimization method for truss structures. A group of variables meaning the density distribution of energy is defined first, so that a bridge between energy distribution and topological optimization is built. After the energy distribution is found, optimal cross – sectional areas are found . Then the above two steps are executed in turn till the convergence is reached. Next, the stiffness and strength reliability corresponding to the final topology are computed with reasonable results.

KEYWORDS

maximum entropy principle, topology optimization, structural reliability, linear programming

INTRODUCTION

Maximum entropy principle(MEP)[1] has been applied in most information systems. Since engineering analysis and optimum design can be viewed as an information system, MEP has been applied in this area too. Simoes and Templeman[2] applied MEP in a synthetic problem of pretensioned steel net; Li and Templeman[3]—[5] utilized MEP to solve structural optimum design; Erlander[6] used MEP in problems of distribution and assignment of traffic; Tiku and Templeman[8] applied MEP to the problem of analysis and optimum design of underground water net in a city. Recently, Abraham I. Beltzer [14] applied MEP to finite element with some interesting

results.

Study on topological optimization has continued several decades since the first paper[9] was published in 1964. So far, the two main methods are Ground Structural Approach(GSA) and Homogeneous Method(HM)[10]–[11]. Both methods view topological optimization from a viewpoint of either force transmitted or material distribution. Whether it is the force transmitted or material distribution, both can be classified as a problem of information treatment in engineering. That is to say, topological optimization is also information treatment which could be considered from an information entropy concept.

It can be anticipated that a new area of study might be opened if topological optimization can be studied from the angle of information treatment by MEP. This paper attempts to make such a study.

MATHEMATICAL MODEL OF ENTROPY – BASED METHOD FOR TOPOLOGICAL OPTIMIZATION OF TRUSS STRUCTURES

Introduction of Design Variables and Objective Functions

Considering a truss from the viewpoint of energy distribution reveals that different topological forms correspond to different energy distribution. Suppose the total structural energy is Q_0 and energy of the *ith* bar is q_i, both Q_0 and q_i will satisfy

$$Q_0 = \sum_{i=1}^{n} q_i \tag{1}$$

in which n is the total number of elements.

Now a set of variables $\{\lambda\}^T = (\lambda_1, \lambda_2, \cdots, \lambda_n)^T$ is defined as

$$\lambda_i = \frac{q_i}{Q_0} \quad , \quad (i = 1, 2, \cdots, n) \tag{2}$$

Variable λ_i is of obvious physical sense, its value stands for the percent of energy stored in the *ith* element. If λ_i equals zero, then the *ith* bar can be eliminated from the ground structure. As a result, all those elements with variable $\lambda_i (i = 1, 2, \cdots, n)$ being non – zero construct a topological form under consideration of a certain sense.

It is obvious that variables $\lambda_i (i = 1, 2, \cdots, n)$ satisfy equations

$$\sum_{i=1}^{n} \lambda_i = 1 \tag{3}$$

and

$$\lambda_i \geq 0, \ \forall \ i \in \Gamma \tag{4}$$

where Γ is a set consisting of all connectable elements for the given fixed points.

Because variables $\lambda_i (i = 1, 2, \cdots, n)$ satisfy non – negative and normality conditions required by entropy, the corresponding structural entropy can be described in the form of

$$S = -\Theta \sum_{i=1}^{n} \lambda_i \cdot \ln \lambda_i \tag{5}$$

where Θ is a large positive constant and S is structural entropy.

In addition, an energy - related function can be described in

$$f = \sum_{i=1}^{n} \Psi_i \cdot |F_i| \tag{6}$$

in which $\Psi_i = \dfrac{L_i[\sigma_i]}{2E}$; $[\sigma_i]$ is the permissible stress of the *ith* bar; L_i is the length of the *ith* bar; E is the modulus of material.

It can be noted from Eqn. 6 that volume of f is directly proportional to structural weight for the case of fully stressed design. In the general case (non - fully stressed design), this will not be valid. However, what we are interested in is if the *ith* bar exists and what is the concrete response in f. Actually, the situation whether the *ith* bar exists or not can be mathematically shown by if $|F_i| \to 0$. According to the sense of topological optimization, $|F_i| \to 0$ means that the *ith* bar will tend to be eliminated from ground structure. That is to say, the *ith* bar's weight will tend to be eliminated from the whole structural weight, which means the decrement of structural weight. Seen from this point of view, both problems of minimizing f and minimizing structural weight are equivalent.

Up to this point, two parameters have been defined. One is the structural entropy expressed in Eqn. 5 and the other is the function shown in Eqn. 6. It can be seen from the following discussion that both functions can be expressed as the functions of variables $\{\lambda\}^T = (\lambda_1, \lambda_2, \cdots, \lambda_n)^T$

Description of Behaviour Constraints

Substituting energy definition of the *ith* element into physical equation yields

$$q_i = \frac{1}{2} K_i \cdot \Delta_i^2 \tag{7}$$

where $K_i = EA_i/L_i$ is the *ith* bar's stiffness. A_i, Δ_i and F_i are cross - sectional area, elongation and member force respectively.

Solving Δ_i from Eqn. 7 and considering Eqn. 2 leads to

$$\Delta_i = \pm \sqrt{\frac{2Q_0\lambda_i}{K_i}} \quad , \quad (i = 1, 2, \cdots, n) \tag{8}$$

Similarly, the member force F_i can also be written as

$$F_i = \pm \sqrt{2K_iQ_0\lambda_i} \quad , \quad (i = 1, 2, \cdots, n) \tag{9}$$

Substituting Eqn. 9 into equilibrium equation

$$[N]\{F\} = \{P\} \tag{10}$$

results in

$$[N]\begin{Bmatrix} \pm\sqrt{2K_1Q_0\lambda_1} \\ \vdots \\ \pm\sqrt{2K_nQ_0\lambda_n} \end{Bmatrix} = \{P\} \tag{11}$$

in which $[N]$ is a projection - geometry matrix; $\{P\}$ is a loading vector to which structure is subjected.

From geometry equation

$$\{\Delta\} = [N]^T\{\delta\} \tag{12}$$

and considering boundary condition, we have

$$\{\delta\} = [D]\{\Delta\} \tag{13}$$

where $\{\Delta\}$ is a vector of elongations; $\{\delta\}$ is a vector of displacements; matrix $[D] = [[N][N]^T]^{-1}[N]$.

If the allowable values of m displacement constraints are given as $\{\bar{\delta}\} = (\bar{\delta}_1, \bar{\delta}_2, \cdots, \bar{\delta}_m)^T$, displacement constraints can be, by substituting Eqn. 8 into Eqn. 13, described as,

$$[D]\begin{Bmatrix} \pm\sqrt{\dfrac{2Q_0\lambda_1}{K_1}} \\ \vdots \\ \pm\sqrt{\dfrac{2Q_0\lambda_n}{K_n}} \end{Bmatrix} \leq \{\bar{\delta}\} \tag{14}$$

As for stress constraint, it can be written in the form of

$$\sqrt{2K_iQ_0\lambda_i} \leq A_i[\sigma_i], \quad (i = 1, 2, \cdots, n) \tag{15}$$

where $[\sigma_i]$ is the permissible stress of the *ith* element.

Up to this point, all constraints such as equilibrium equation, displacement and stress have been described as the functions of variables $\{\lambda\} = (\lambda_1, \lambda_2, \cdots, \lambda_n)^T$.

Mathematical Model of Topological Optimization

Synthesizing Eqns. 3, 6, 11, 14 and 15, and considering minimum weight and maximum entropy design simultaneously, yields the following mathematical model.

(P I) find variables $\{\lambda\} = (\lambda_1, \lambda_2, \cdots, \lambda_n)^T$ in space E^n

minimize $$f = \sum_{i=1}^{n} \Psi_i \cdot F_i = \sum_{i=1}^{n} \Psi_i \cdot \sqrt{2K_iQ_0\lambda_i} \tag{16}$$

maximize $$S = -\Theta \sum_{i=1}^{n} \lambda_i \cdot \ln\lambda_i \tag{5}$$

subject to
$$[N]\begin{Bmatrix} \pm\sqrt{2K_1Q_0\lambda_1} \\ \vdots \\ \pm\sqrt{2K_nQ_0\lambda_n} \end{Bmatrix} = \{P\} \tag{11}$$

$$[D]\begin{Bmatrix} \pm\sqrt{\frac{2Q_0\lambda_1}{K_1}} \\ \vdots \\ \pm\sqrt{\frac{2Q_0\lambda_n}{K_n}} \end{Bmatrix} \leq \{\bar{\delta}\} \tag{14}$$

$$\sqrt{2K_iQ_0\lambda_i} \leq A_i[\sigma_i], \quad (i = 1, 2, \cdots, n) \tag{15}$$

$$\sum_{i=1}^{n}\lambda_i = 1 \tag{3}$$

$$\lambda_i \geq 0 \quad , \quad \forall\, i \in \Gamma \tag{4}$$

Actually non - negative condition Eqn. 4 can be satisfied automatically due to the logarithmic form of entropy function.

In order to simplify problem (P I), to eliminate the absolute symbol and to have a standard LP model, let

$$\lambda_i = \frac{\alpha_i^2}{2Q_0} \quad , \quad (i = 1, 2, \cdots, n) \tag{17}$$

$$\begin{cases} \alpha_i = \bar{\alpha}_i - \tilde{\alpha}_i \\ |\alpha_i| = \bar{\alpha}_i + \tilde{\alpha}_i \end{cases} \quad , \quad (i = 1, 2, \cdots, n) \tag{18}$$

and adding slacking variables $\{Y\} = (y_1, y_2, \cdots, y_m)^T$ and $\{Z\} = (z_1, z_2, \cdots, z_n)^T$ to the left hand side of Eqns. 14 and 15, respectively, and introducing two weight coefficients γ_1 and γ_2, yields the following problem

(P Ⅱ)

find variables $(\{\bar{\alpha}\}^T, \{\tilde{\alpha}\}^T)^T = (\bar{\alpha}_1, \bar{\alpha}_2, \cdots, \bar{\alpha}_n, \tilde{\alpha}_1, \tilde{\alpha}_2, \cdots, \tilde{\alpha}_n)^T$ in space E^{2n}

minimize
$$\phi = \gamma_1\sum_{i=1}^{n}\Omega_i(\bar{\alpha}_i + \tilde{\alpha}_i) + \gamma_2\Theta\sum_{i=1}^{n}\frac{(\bar{\alpha}_i - \tilde{\alpha}_i)^2}{2Q_0}\cdot\ln\frac{(\bar{\alpha}_i - \tilde{\alpha}_i)^2}{2Q_0} \tag{19}$$

subject to
$$\begin{bmatrix} [NK] & -[NK] & [0_{nm}] & [0_{nn}] \\ [DK] & -[DK] & [I_{mm}] & [0_{mn}] \\ [I_{nn}] & [I_{nn}] & [0_{nm}] & [I_{nn}] \end{bmatrix}\begin{bmatrix} \{\bar{\alpha}\} \\ \{\tilde{\alpha}\} \\ \{Y\} \\ \{Z\} \end{bmatrix} = \begin{bmatrix} \{P\} \\ \{\bar{\delta}\} \\ \{\tilde{\sigma}\} \end{bmatrix} \tag{20}$$

$$\{\bar{\alpha}\}, \{\tilde{\alpha}\}, \{Y\}, \{Z\} \geq 0 \tag{21}$$

$$\sum_{i=1}^{n}(\bar{\alpha}_i - \tilde{\alpha}_i)^2 = 2Q_0 \tag{22}$$

in which
$$[NK] = [N]\begin{bmatrix} \sqrt{K_1} & & & 0 \\ & \sqrt{K_2} & & \\ & & \ddots & \\ 0 & & & \sqrt{K_n} \end{bmatrix} \tag{23}$$

$$[DK] = [D]\begin{bmatrix} \dfrac{1}{\sqrt{K_1}} & & & 0 \\ & \dfrac{1}{\sqrt{K_2}} & & \\ & & \ddots & \\ 0 & & & \dfrac{1}{\sqrt{K_n}} \end{bmatrix} \tag{24}$$

$$[\tilde{\sigma}_i] = \frac{A_i[\sigma_i]}{\sqrt{K_i}} \tag{25}$$

$$\Omega_i = \Psi_i \cdot \sqrt{K_i} \tag{26}$$

$[I_{mm}]$ is a unit matrix. $[0_{nm}]$, $[0_{nn}]$ and $[0_{mn}]$ are zero matrixes.

In problem (P Ⅱ), the expressions except for entropy and normality condition Eqn. 22 are all linear functions, provided cross - sectional areas are given. Considering the characteristics of problem (P Ⅱ), SLP is utilized to solve it without considering the normality condition first.

METHOD OF FINDING OUT ENERGY DISTRIBUTION

The normality condition of Eqn. 22 is dealt with in the following method.

For the known variables $(\{\bar{\alpha}^{(k)}\}^T, \{\tilde{\alpha}^{(k)}\}^T)^T$ after the *kth* iteration, let

$$\lambda_i^{(k)} = \frac{(\bar{\alpha}_i^{(k)} - \tilde{\alpha}_i^{(k)})^2}{2Q_0} \quad , \quad (i = 1, 2, \cdots, n) \tag{27}$$

Then parameters $\{\lambda^{(k)}\}$ are normalized by

$$\tilde{\lambda}_i^{(k)} = \frac{\lambda_i^{(k)}}{\tilde{\lambda}} \quad , \quad (i = 1, 2, \cdots, n) \tag{28}$$

where $\tilde{\lambda} = \sum_{i=1}^{n} \lambda_i^{(k)}$

Next, update variables $\alpha_i^{(k)} = \bar{\alpha}_i^{(k)} - \tilde{\alpha}_i^{(k)}$, $(i = 1, 2, \cdots, n)$ as,

$$\hat{\alpha}_i^{(k)} = \pm \sqrt{2Q_0\tilde{\lambda}_i^{(k)}} \quad , \quad (i = 1, 2, \cdots, n) \tag{29}$$

symbol $\pm$ of $\hat{\alpha}_i^{(k)}$ should be the same as that of $\alpha_i^{(k)}$.

Finally, $\hat{\alpha}_i^{(k)}$ is considered as the present design point ; go to the next iteration again.

METHOD OF FINDING OUT CROSS - SECTIONAL AREAS

The previous discussion is merely concerned with seeking $\{\lambda\} = (\lambda_1, \lambda_2, \cdots, \lambda_n)^T$ under the known area $\{A\} = (A_1, A_2, \cdots, A_n)^T$. As a matter of fact, topological form will be influenced by $\{A\}$. Meanwhile, what is necessary in engineering is to know the cross - sectional area. In order to find optimum topology and cross - sectional areas as well, both parameters of $\{\lambda\}$ and $\{A\}$ should be viewed as variables.

If the work of finding $\{\lambda\}$ under the given $\{A\}$ is called step (Ⅰ), process of seeking $\{A\}$ is called step (Ⅱ). The final result of $\{\lambda\}$ and $\{A\}$ can be obtained by carrying out two steps in turn.

Problem of seeking cross - sectional area under the given energy distribution can be described as follows.

(P Ⅲ) find variables $\{\xi\} = (\xi_1, \xi_2, \cdots, \xi_n)^T$ in space E^n

minimize
$$W = \sum_{i=1}^{n} \frac{\rho L_i}{\xi_i} \tag{30}$$

maximize
$$S = -\Theta \sum_{i=1}^{n} \beta_i \xi_i \cdot \ln \beta_i \xi_i \tag{31}$$

subject to
$$\sum_{i=1}^{n} \left(\frac{F_i U_{ji} L_i}{E} \right) \cdot \xi_i \leq \bar{\delta}_j \quad , \quad (j = 1, 2, \cdots, m) \tag{32}$$

$$\xi_i \leq \frac{[\sigma_i]}{|F_i|} \quad , \quad (i = 1, 2, \cdots, n) \tag{33}$$

in which parameter β_i is $\frac{L_i F_i^2}{2EQ_0}$ and $\lambda_i = \frac{\beta_i}{A_i}$; $\xi_i = \frac{1}{A_i}$; Eqn. 32 is from virtual work principle.

Similar to the previous method, two weights γ_1 and γ_2 are introduced so that both objective functions W and S can be integrated into a function $\omega = \gamma_1 W + \gamma_2 S$. Problem (P Ⅲ) is an NLP. To be in accordance with searching for $\{\lambda\}$, SLP is also utilized here to solve it.

RELIABILITY OF STRUCTURAL STIFFNESS AND STRENGTH OF FINAL TOPOLOGICAL FORM

Final topological form and cross - sectional areas corresponding to different combinations of γ_1 and γ_2 can be obtained by executing two steps in turn. In order to know if the obtained structure can be used in engineering and to attempt to see, perceptually, the relation between entropy level and reliability, it is necessary to make a reliability analysis of both stiffness and strength.

Suppose displacement and stress as well as their permissible values are all the normal random variables. For the sake of the discussion below, denoting the *ith* displacement or stress random variable by η_i, and corresponding allowable random variable by $[\eta_i]$, the following formulation holds

$$\begin{cases} \eta_i \sim \mathcal{N}(\mu_{\eta_i}, v_{\eta_i}) \\ [\eta_i] \sim \mathcal{N}(\mu_{[\eta_i]}, v_{[\eta_i]}) \end{cases} \tag{34}$$

where μ_{η_i} and v_{η_i} are the mean and variation of random variable η_i, respectively. $\mu_{[\eta_i]}$ and $v_{[\eta_i]}$ are the mean and variation of random variable $[\eta_i]$, respectively.

According to the mean of random variables η_i and $[\eta_i]$, stiffness and strength reliability can be generally stated as

$$R_{\eta_i} = P_{rob}\{\eta_i \leq [\eta_i]\} \tag{35}$$

The approximate expression of Eqn. 35 can be further described by second moment[13] as

$$R_{\eta_i} = \Phi\left[\frac{\mu_{[\eta_i]} - \mu_{\eta_i}}{\sqrt{v^2_{[\eta_i]} + v^2_{\eta_i}}}\right] \tag{36}$$

Considering the relationship between the mean and variance

$$\begin{cases} v_{[\eta_i]} = \zeta_{[\eta_i]} \cdot \mu_{[\eta_i]} \\ v_{\eta_i} = \zeta_{\eta_i} \cdot \mu_{\eta_i} \end{cases} \tag{37}$$

and taking variation factor $\zeta_{[\eta_i]} = \zeta_{\eta_i} = 0.1$ gives the formula of computing reliability

$$R_{\eta_i} = \Phi\left[\frac{\mu_{[\eta_i]} - \mu_{\eta_i}}{0.1\sqrt{\mu^2_{[\eta_i]} + \mu^2_{\eta_i}}}\right] \tag{38}$$

in which $\Phi(.)$ means the function with normal distribution.

NUMERICAL EXAMPLES AND DISCUSSION

Example 1: *five - bar truss* (*Figure* 1)

It is composed of four joints and five elements. Modulus of elasticity and density of material are $E=0.21\times10^7$ kg/cm^2 and $\rho=0.785\times10^{-2}$ kg/cm^3 respectively. Structural form and loading conditions are shown in Figure 1.

Constraints of displacement and stress are $\delta_{2y}\geq-0.25$ cm and $\sigma_e\leq\pm1600$ kg/cm^2, ($e=1, 2, \cdots, 5$).

Numerical computation is executed for four combinations of γ_1 and γ_2, (1.0, 0.0), (0.7, 0.3), (0.2, 0.8) and (0.0, 1.0). Optimum results are given in Tables 1, 2, 3 and 4, and corresponding topological forms are shown in Figures 2 (cases I and II) and 3 (cases III and IV). In each table, the second, third and fourth rows give the strain energy, cross - sectional area and strength reliability, respectively. Stiffness reliability with respect to displacement constraint for the four combinations is 0.7365, 1.0, 1.0, and 1.0 separately.

Table 1

Optimum Result I of Five - Bar Truss $\begin{pmatrix}\gamma_1=1.0\\ \gamma_2=0.0\end{pmatrix}$

Bar No.	1	2	3	4	5
λ_i	0.0	0.0	0.2612	0.0	0.7388
A_i	0.0	0.0	0.0625	0.0	0.08839
R_{η_i}	/	/	0.5000	/	0.5001

Table 2

Optimum Result II of Five - Bar Truss $\begin{pmatrix}\gamma_1=0.7\\ \gamma_2=0.3\end{pmatrix}$

Bar No.	1	2	3	4	5
λ_i	0.0	0.0	0.2612	0.0	0.7388
A_i	0.0	0.0	0.1556	0.0	0.2865
R_{η_i}	/	/	1.0000	/	1.0000

Table 3

Optimum Result III of Five - Bar Truss $\begin{pmatrix}\gamma_1=0.2\\ \gamma_2=0.8\end{pmatrix}$

Bar No.	1	2	3	4	5
λ_i	0.11461	0.11461	0.11666	0.32416	0.32997
A_i	0.06389	0.06389	0.06203	0.12096	0.28286
R_{η_i}	1.0000	1.0000	0.9955	1.0000	1.0000

Table 4

Optimum Result IV of Five - Bar Truss $\begin{pmatrix}\gamma_1=0.0\\ \gamma_2=1.0\end{pmatrix}$

Bar No.	1	2	3	4	5
λ_i	0.11461	0.11461	0.11666	0.32416	0.32997
A_i	0.048326	0.048326	0.08185	0.16080	0.28460
R_{η_i}	1.0000	1.0000	0.9999	1.0000	1.0000

It can be observed from the above results that when structural weight is the major one of two objectives, the same topological form (shown in Figure 2) is obtained for cases I and II, which is a static - determined structure consisting of elements 3 and 5. However, the distribution of

cross – sectional areas of the two cases is different (see Tables 1 and 2). The more interesting point is that both stiffness and strength reliability of case Ⅱ are higher than case Ⅰ. Stiffness reliability is increased from 0.7365 to 1.0, and strength reliability of bar 3 and 5 are enlarged from 0.5 and 0.5001 to 1.0, respectively.

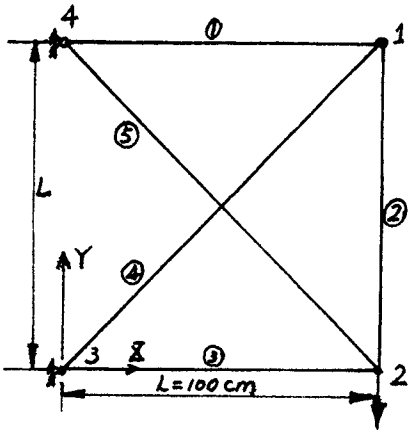

Figure 1 Five – bar truss

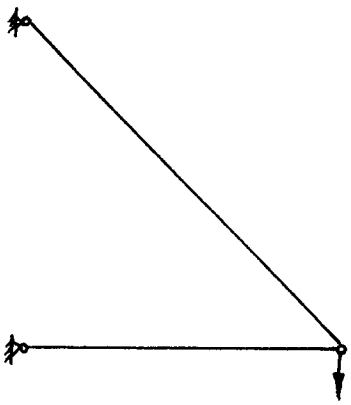

Figure 2 Optimum result of five – bar truss $(\gamma_1, \gamma_2) = (1.0, 0.0)$ and $(0.7, 0.3)$

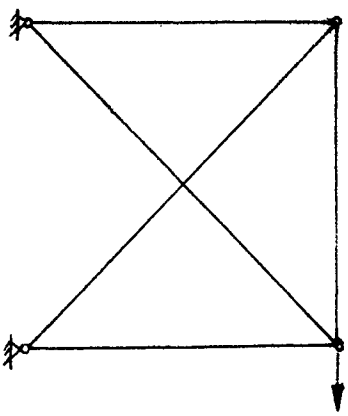

Figure 3 Optimum result of five – bar truss $(\gamma_1, \gamma_2) = (0.2, 0.8)$ and $(0.0, 1.0)$

When entropy is the major one of two objective functions, the final structure becomes a static undetermined structure (shown in Figure 3). Even though the topological form of cases Ⅲ and Ⅳ is the same, their cross – sectional area distribution is different (see Table 3 and 4). As for the corresponding situation of reliability, stiffness reliability of both cases is equal to 1.0. Strength reliability of element 3 is enhanced from 0.9955 of case Ⅲ to 0.9999 of case Ⅳ.

In short, stiffness and strength reliability of final topological form are increased, to some ex-

tent, with the increment of entropy's promotion within both objectives.

Example 2: ten - bar truss (Figure 4)

This familiar structure comprises six joints and ten elements. Modulus of elasticity and density of material are $E=0.1\times10^8$ psi and $\rho=0.1\text{lb/in}^3$, respectively. Structural form, geometrical size and loading condition are described in Figure 4.

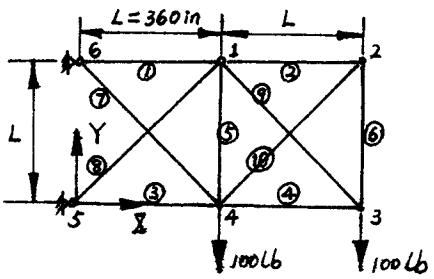

Figure 4 Ten - bar truss

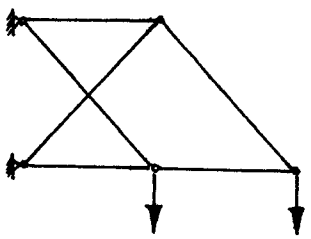

Figure 5 Optimum result of ten - bar truss $(\gamma_1,\gamma_2)=(1.0, 0.0)$ and $(0.7, 0.3)$

Constraints of displacement and stress are: $|\delta_{3y}|\leq2$ in and $\sigma_e\leq\pm25000$ psi, $(e=1, 2, \cdots)$.

Numerical computation is executed for four different combinations of γ_1 and γ_2, (1.0, 0.0), (0.7, 0.3), (0.2, 0.8) and (0.0, 1.0). Computation results are given in tables 5, 6, 7 and 8, respectively. In each table the second, third and fourth rows give the energy distribution, cross - sectional area and strength reliability respectively. The same structural form (Figure 5) is obtained for cases I and II. Topological forms of cases III and IV are described in Figures 6 and 7, respectively.

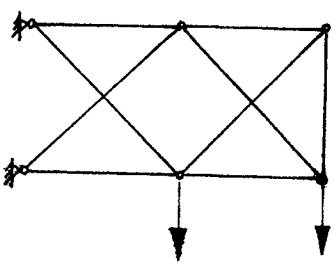

Figure 6 Optimum result of ten - bar truss $(\gamma_1,\gamma_2)=(0.2, 0.8)$

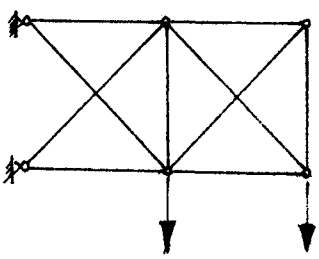

Figure 7 Optimum result of ten - bar truss $(\gamma_1,\gamma_2)=(0.0, 1.0)$

Stiffness reliability with respect to displacement constraint for the four cases is 0.3897, 0.9921, 0.9988 and 0.9985 , respectively.

Table 5

Optimum Result I of Ten - Bar Truss $\begin{pmatrix}\gamma_1=1.0\\ \gamma_2=0.0\end{pmatrix}$

Bar No.	1	2	3	4	5
λ_i	0.22876	0.0	0.22876	0.057191	0.0
A_i	0.02293	0.0	0.026912	0.01146	0.0
R_{η_i}	1.00000	/	1.0000	1.0000	/
Bar No.	6	7	8	9	10
λ_i	0.0	0.16176	0.16176	0.16176	0.0
A_i	0.0	0.00707	0.028507	0.0218	0.0
R_{η_i}	/	0.9407	1.0000	1.0000	/

Table 6

Optimum Result II of Ten - Bar Truss $\begin{pmatrix}\gamma_1=0.7\\ \gamma_2=0.3\end{pmatrix}$

Bar No.	1	2	3	4	5
λ_i	0.22876	0.0	0.22876	0.057191	0.0
A_i	0.033438	0.0	0.07312	0.01357	0.0
R_{η_i}	1.0000	/	1.0000	1.0000	/
Bar No.	6	7	8	9	10
λ_i	0.0	0.16176	0.16176	0.16176	0.0
A_i	0.0	0.05173	0.02884	0.03882	0.0
R_{η_i}	/	1.0000	1.0000	1.0000	/

Table 7

Optimum Result III of Ten - Bar Truss $\begin{pmatrix}\gamma_1=0.2\\ \gamma_2=0.8\end{pmatrix}$

Bar No.	1	2	3	4	5
λ_i	0.064418	0.060875	0.057432	0.062634	0.0
A_i	0.0538	0.00158	0.11603	0.01577	0.0
R_{η_i}	1.0000	1.0000	1.0000	1.0000	/
Bar No.	6	7	8	9	10
λ_i	0.060875	0.16728	0.17716	0.17716	0.17728
A_i	0.00148	0.05107	0.0392	0.0165	0.00468
R_{η_i}	1.0000	1.0000	1.0000	1.0000	1.0000

Table 8

Optimum Result Ⅳ of Ten - Bar Truss $\begin{pmatrix}\gamma_1=0.0\\ \gamma_2=1.0\end{pmatrix}$

Bar No.	1	2	3	4	5
λ_i	0.05733	0.062523	0.064304	0.060767	0.0000125
A_i	0.0771	0.00351	0.10519	0.0065	0.00309
R_{η_i}	1.0000	1.0000	1.0000	1.0000	1.0000
Bar No.	6	7	8	9	10
λ_i	0.062523	0.17684	0.16698	0.17188	0.17684
A_i	0.00351	0.05705	0.03688	0.01664	0.00984
R_{η_i}	1.0000	1.0000	1.0000	1.0000	1.0000

Investigating the result reveals that if structural weight is dominated within both objectives (case Ⅰ and Ⅱ), the optimal result will be a static determined structure (figure 5). The same topological form but different cross - sectional areas of elements is obtained for cases Ⅰ and Ⅱ. Moreover, both stiffness and strength reliability of case Ⅱ are all higher than that of case Ⅰ. The stiffness reliability is increased from 0.3897 to 0.9921 while strength reliability of element 7 is enhanced from 0.9047 to 1.0000. By contrast, if the entropy is dominated, the topological form becomes a static undetermined one. And more, the stiffness reliability is higher than that of cases Ⅰ and Ⅱ. The strength reliability of elements are all equal to 1.0000.

It should be noted that reliability target $\dfrac{\mu_{[\eta_i]}-\mu_{\eta_i}}{0.1\sqrt{\mu^2_{[\eta_i]}+\mu^2_{\eta_i}}}$ for four cases are different although strength reliability are all equal to 1.0000. Take the first element as an example, its reliability targets corresponding to cases Ⅰ, Ⅱ, Ⅲ and Ⅳ are 6.148, 7.399, 8.518, and 9.059 respectively. Obviously, its value is in the tendency of increment gradually. Since they are all greater than 6.0, the value of $\Phi(\,.\,)$ will be 1.0000. The reason why strength reliability are all equal to 1.0000, but the stiffness reliability is rather lower comparatively, is because displacement constraints are more tight than strength constraints.

CONCLUSIONS

The preceding discussion and results may lead us to conclude the following.

1) The introduced parameters $\lambda_i(i=1, 2, \cdots, n)$ from a viewpoint of energy distribution not only erect a bridge between information entropy and topological optimization, but also make a designer able to observe the distribution of energy among all elements, which is significant.

2) With increasing γ_2 and decreasing γ_1, energy distribution $\lambda_i(i=1, 2, \cdots, n)$ tends to be in agreement, in accordance with the principle of maximum entropy.

3) With the increment of entropy's promotion in both objectives (stiffness and strength), the cross - sectional area of each remaining bar is also increased. It is particularly obvious where distribution of $\lambda_i (i = 1, 2, \cdots, n)$ is the same but the combination of γ_1 and γ_2 is different. For instance, projects I and II of examples 1 and 2 show this characteristics.

4) Structural stiffness and strength reliability or reliability target (corresponding to displacement and stress constraints) tend to increase with the increment of entropy's promotion in the two objectives, which is an important point worthy of further study.

REFERENCES

[1] Jaynes E. T. (1957). Information theory and statistical mechanics. *The Physical Review* **106**, 620—630 and **108**, 171—190.

[2] Simoes M. C. and Templeman A. B. (1989). Entropy - based synthesis of pretensioned cable net structures, *Engineering Optimization*. **15**: **2**.

[3] Li X. S. and Templeman A. B. (1988). Entropy - based optimum sizing of truss. *Civil Engineering System* **5**: **3**.

[4] Li X. S. (1987). Entropy and Optimization, Ph. D. Dissertation, University of Liverpool.

[5] Templeman A. B. (1991). *Entropy - based Optimization Methods for Engineering Design*, Department of Civil Engineering, Liverpool University, United Kingdom.

[6] Erlander S. (1977). Accessibility, entropy and distribution and assignment of traffic, *Transportation Research* : **11**.

[7] Munro J. and Jowitt P. W. (1978). Decision analysis in the ready - mixed concrete industry, *Proc. Inct. Engrs.*, Part 2, **65**: 41 - 52.

[8] Devitt T. (1933). Ph. D. Dissertation, University of Liverpool.

[9] Dorn W. et al. (1964). Automatic design of optimal structures, *J. de Mechanique*, **3**. 25 - 52, March.

[10] Kikuchi N. (1994). Computational aspects on structural and material design optimization, *The Third World Conference on Computational Mechanics* (*WCCM* 3), Tokyo, Japan, August 1 - 5.

[11] Cheng G. (1994). New development of structural topology optimization, *WCCM* 3, Japan, August 1 - 5.

[12] Duan B. Y. et al. (1994). Entropy - based method for topological optimization of truss structures, *WCCM* 3, Tokyo, Japan, August 1 - 5.

[13] Thotf - Christensen P. and Murotsu Y. (1986). Application of structural systems reliability theory, Springer - Verlag.

[14] Beltzer Abraham I. (1996). Entropy characterization of finite elements, *Int. J. Solids Structures*, **33**: 24, 3459 - 3560.

PRACTICAL ISSUES IN THE APPLICATION OF STRUCTURAL IDENTIFICATION

Burcu Gunes[1], Doctoral Student; Behnam Arya[2], Doctoral Student,
Sara Wadia-Fascetti[1], Assistant Professor; Masoud Sanayei[2], Associate Professor

[1] Dept. of Civil and Environmental Engr., Northeastern University, Boston, MA 02115, USA

[2] Dept. of Civil and Environmental Engr., Tufts University, Medford, MA 02155, USA

ABSTRACT

The stiffness parameters of a structural system can be adjusted to match the analytical model's response in order to reproduce the measured test data. There are a number of practical issues that must be considered for the successful application of parameter estimation to full-scale structures. These include the design and implementation of the experiment; errors in the mathematical model used for parameter estimation; and errors in the parameter estimation procedure itself. Modeling error, the uncertainty in the parameters of a finite element model, can have a significant impact on the quality of the resulting parameter estimates. The impact of modeling error on the resulting parameter estimates is investigated with two scenarios: deterioration and damage. Deterioration error is modeled as uncertainty in a single parameter distributed across the structure. Damage error is modeled as localized undetected change in a single parameter and a single element. Three types of parameters are used in an existing parameter estimation procedure: (1) unknown parameters which are to be estimated, (2) known parameters assumed to be accurate, and (3) uncertain parameters that are assumed known and not to be estimated. The third group introduces the modeling error into the parameter estimation. Modeling error is investigated with respect to load and measurement locations, the type of error function used (stiffness-based or flexibility-based), and the selection of unknown parameters to be estimated. In the example presented, the stiffness-based error function performed much better than the flexibility-based error function. However, topology of the structure, load and measurement locations, and location of the uncertain parameters with respect to the unknown parameters can have a significant impact on the quality of the parameter estimates.

KEYWORDS

Modeling error, parameter estimation, model updating, structural identification, error function.

INTRODUCTION

Parameter estimation is the art of adjusting the parameters of an analytical model of a structure to reproduce measured data (static or dynamic). Parameter estimation also can be used to identify element parameters implicit in the stiffness or mass matrices describing a structural system at the component level and is a useful tool for finite element model updating. These implicit parameters include element properties such as EA, EI, GJ, and K_{spring}.

The theory behind parameter estimation is not new but advances in algorithm development have helped to make parameter estimation a useful tool for structural condition assessment. When successfully applied to a structure parameter estimation can be used for health monitoring and damage assessment as changes in particular parameters of a baseline model can be related to physical changes in a structural model. The application of parameter estimation to a physical model requires experiment design, controlled testing, data processing to evaluate data quality, parameter estimation, and finally, the interpretation of the results. The collection of objective inspection data obtained through nondestructive testing and parameter estimation can give a meaningful representation of the performance of a structure.

When applied to a small-scale structure with simulated data parameter estimation is a straightforward process. A number of challenges exist in the application of parameter estimation to a full-scale structure. For example, the quality of the testing procedures and the environment can be as important as the algorithm and error functions used in parameter estimation. Sanayei et al. (1998a) describes three primary challenges limiting the application of parameter estimation to full-scale structures. These challenges are summarized as:

- Design and implementation of the experiment, which consists of: the selection of excitation sources; excitation location and magnitude; sensor type and locations; selection of data acquisition systems; and testing economy.
- Errors in the mathematical modeling for parameter estimation including nonstructural members or members not accounted for in the a priori finite element model, nonlinear structural response not explicitly accounted for in the finite element model, inadequate knowledge or inability to accurately model the boundary conditions, damping, or environmental variability.
- Errors in parameter estimation consisting of the selection of the objective function and optimization techniques used, possible degree of freedom mismatch due to the inability to measure responses at sufficient and optimal locations, model order which can cause the problem to be over or under defined, and uncertainty in measured data (noise) and model parameters (modeling error).

Modeling error is defined as the uncertainty in the parameters in a finite element model. Although it is possible to quantify the effect of errors in a finite element model on the response of a structure (Wadia-Fascetti and Smith 1996), these errors complicate the solution of the inverse problem and can not be avoided in the practical application of parameter estimation (Wadia-Fascetti et al. 1998). The impact of modeling error on estimated parameters is

investigated with regard to location and magnitude. Two scenarios are considered. The first type of modeling error represents structural deterioration applied uniformly across all the elements of a finite element model. Inaccurate assumptions made during model calibration or even deterioration across a structure can lead to this type of error. The second type of modeling error is localized to one element and represents undetected damage.

PARAMETER ESTIMATION FOR STRUCTURAL IDENTIFICATION

Structural parameter estimation uses optimization to reconcile an analytical model of a structure with non-destructive test data. The theory behind parameter estimation and structural identification is not new and the reader is referred to the literature reviews prepared by Ghanem and Shinozuka (1995) and Doebling et al. (1996). Increased computational capability has resulted in significant progress in algorithm development and testing. As a result, structural identification and parameter estimation are objective tools for determining the actual state properties of a structure. Thus, it is possible to gain an improved understanding of a structure's properties leading to improved representation of the stiffness matrix describing a structure. The advantage of parameter estimation at the component level is that it can easily lend itself to condition assessment of structures as parameter estimation can detect changes in stiffness coefficients.

Parameter Estimation

Parameter estimation is used at the element level to identify the implicit parameters in the stiffness matrix of a structure. The analytical response used may be modal or static measurements (Sanayei et al. 1997; 1998b). Structural stiffness parameters (EA, EI, GJ, K_{spring}), and mass parameters (effective lumped masses) are estimated at the component level. The two types of parameters in the estimation procedure are those that are known and assumed to be accurate and those that are unknown and are to be estimated. Sanayei (1997) implements the following steps within the program PARIS (PARameter Identification System).

1. The assemblage of a finite element model with assumed accurate values for all known parameters and initial guesses for all unknown parameters.
2. The formulation of error functions as the difference in the response of the analytical model and the measured response. Error functions are based on static displacement and strains and modal responses.
3. The minimization of the error function with respect to the unknown structural stiffness parameters at the element level.

Parameter estimation using static responses is used in this study. The constrained stiffness matrix, $\boldsymbol{K}$, is assembled with known parameters and initial guesses for unknown parameters. The system equation is partitioned to distinguish between measured and not measured displacements ($\boldsymbol{U}$) and forces ($\boldsymbol{F}$) where the subscripts a and b denote degrees of freedom that are measured and not measured, respectively (Sanayei et al. 1997).

$$\begin{bmatrix} K_{aa} & K_{ab} \\ K_{ba} & K_{bb} \end{bmatrix} \begin{Bmatrix} U_a \\ U_b \end{Bmatrix} = \begin{Bmatrix} F_a \\ F_b \end{Bmatrix} \tag{1}$$

The substructured matrix in Eqn. 1 can be solved to relate measured forces or responses to those obtained from the analytical stiffness matrix updated through parameter estimation. Eqns. 2 and 3 are the stiffness-based (E_s) "equation error function" and the flexibility-based (E_f) "output error function" and are implicitly functions of all structural parameters, P that describe the stiffness of the structural system at the component level.

$$[E_s(p)] = \left([K_{aa}] - [K_{ab}][K_{bb}]^{-1}[K_{ba}]\right)[U_a]^m + [K_{ab}][K_{bb}]^{-1}[F_b]^m - [F_a]^m \tag{2}$$

$$[E_f(p)] = \left([K_{aa}] - [K_{ab}][K_{bb}]^{-1}[K_{ba}]\right)^{-1}\left([F_a]^m - [K_{ab}][K_{bb}]^{-1}[F_b]^m\right) - [U_a]^m \tag{3}$$

The superscript m denotes measured forces and responses. The error functions are minimized by updating stiffness parameters, P at the element level such that the scalar objective function, J, (shown in Eqn. 4) is minimized.

$$J(p) = \sqrt{\sum_i \sum_j E_{ij}^2} \tag{4}$$

J in Eqn. 4 is defined as the Eucledian norm of the error functions shown in Eqns. 2 and 3. When there is no modeling error or measurement noise, J will approach zero with an acceptable tolerance limit as the updated parameter estimates approach the true value of parameters.

PARIS uses the measured responses (modal and static) to obtain parameter estimates using Eqns. 1 through 4. Practical issues that need to be considered and can effect the quality of the final parameter estimates are the selection of load and measurement cases, the error function used, and the quality of the known parameters used to assemble the initial finite element model. Solution strategies such as the use of super elements and grouping can be used to reduce the number of unknown parameters sought (Sanayei et al. 1998b; McClain 1996) making parameter estimation adaptable to full-scale structures. However, these techniques do not account for modeling errors in the finite element model.

The change in the structural parameters to be estimated must be observable by the sensors and load cases. At a minimum, one independent measurement for each unknown parameter is required to avoid an underdefined problem. In most practical cases, the load and measurement cases available are dependent on accessibility and cost limiting the information available to the parameter estimation. Without measurement noise or modeling error additional load cases can improve the resulting parameter estimations. However, errors propagate in the presence of measurement noise and modeling error and can have a reverse effect on the quality of the final estimates. Sanayei et al. (1992; 1996) developed a heuristic method for design of NDTs to reduce the error in the geometric parameter estimates caused by noisy measurements.

Parameter Estimation Considering Modeling Error

When parameter estimation is performed in the presence of modeling errors there are three types of parameters considered in the analytical model:

- unknown parameters to be estimated,
- known parameters assumed to be accurate, and
- uncertain parameters that are assumed known and not to be estimated.

The impact of using uncertain parameters as known values on the unknown parameters is studied. Two scenarios are considered: 1) deterioration that effects a significant amount of the structure and 2) damage that effects a localized area of the structure are represented in the unknown parameters. In addition to these scenarios, the effect of load and measurement locations, error function selection, and magnitude of the uncertainty on the resulting parameter estimates are studied.

Influence of Modeling Error on J

As stated previously, the minimum value of the objective function, J, is zero when the true parameter values are used in the error functions E_s or E_f and when there is no measurement noise or modeling error in the system. Once modeling error is introduced into the parameter estimation as uncertain values in the stiffness matrix, J is no longer zero when error functions are evaluated with the true parameter values. Consider the frame shown in Figure 1. The columns and beams have I equal to 170 in^4 (7,076 cm^4) and 800 in^4 (33,299 cm^4), respectively. E is assumed to be 29,000 ksi (2.0x10^8 kPa) and constant for the whole structure. The measured response is obtained for degrees of freedom 1 and 3 and the loads are applied independently at degrees of freedom 16 and 18. The unknown parameters are I for members 1 and 3 and will be estimated due to the modeling error introduced to I of member 9. J is computed based on the stiffness (Eqn. 2) and flexibility (Eqn. 3) error functions.

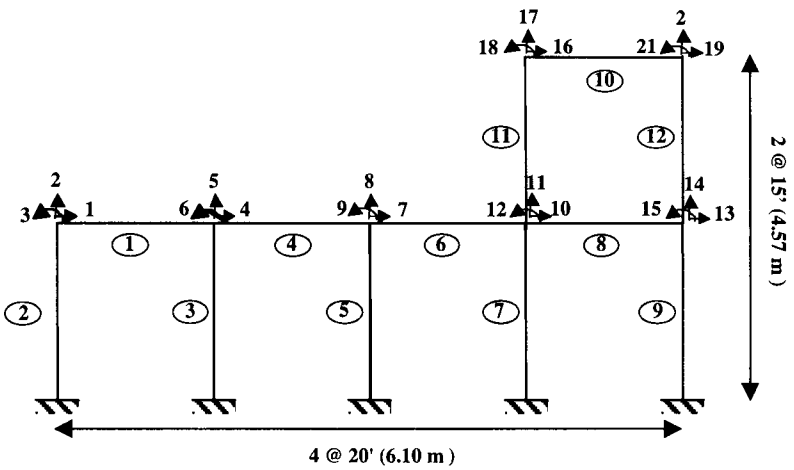

Figure 1: Two story frame

When the true values for members 1 and 3 are used and an uncertain value for I of member 9 is assumed to be 212.5 in^4 (8,449 cm^4) rather than the actual value, 170 in^4 (7,076 cm^4), J is equal to 5.96 (with force units) and 0.1217 (with displacement units) for the stiffness and flexibility error functions, respectively. The optimization procedure updates the unknown parameters until J reaches a minimum value. It is conceivable that a set of unknown parameters can be found that produces a value for J that is less than the values reported above. Thus, when modeling error exists and the parameter estimation converges, the parameters will never converge to the true values of the unknown parameters as the optimization blames the error in the uncertain parameters on the unknown parameters.

It is impossible to track the effect of modeling error through J as this scalar represents a complicated structural system. Although, the existence of modeling error is evident in J, the location and severity of the error can not be interpreted from a single scalar. The minimization of J causes the effect of modeling error to be distributed throughout the estimated parameters, effecting some unknown parameters more severely than others. Since the error function is partitioned based on the location of measured responses, a change in measured response will change the value of J. The effect of modeling error, which is illustrated in the next section is dependent on the location and magnitude of the modeling error, the load and measurement cases, and the error function used in the parameter estimation.

ILLUSTRATIVE EXAMPLE

Two possible types of modeling error are illustrated on the two-story frame shown in Figure 1. In each case for members with unknown stiffness, only I is estimated and E is assumed to be constant for the whole structure. Parameter estimates are obtained using the program PARIS. Modeling error is quantified on the estimated parameters to demonstrate the influence of deterioration or damage.

Influence of Deterioration on Estimated Parameters

All beam elements (1, 4, 6, 8, and 10) are assumed to be known with a high degree of certainty. Deterioration is simulated by assuming I for members 2, 3, 5, and 7 are known with some degree of uncertainty. Then, values for I of members 9, 11, and 12 are estimated. For the purposes of providing bounds on the final results each member is given the same amount of modeling error (i.e. +25% for all members). The four different load and measurement cases considered are shown in Table 1. Figure 2 shows the percent error in the estimated parameters I_9, I_{11}, and I_{12}. In this figure, "o" and "x" represent the stiffness-based and flexibility-based error functions, respectively. FDOF and MDOF denote the degrees of freedom at which loads are applied independently and measurements made.

TABLE 1
LOAD AND MEASUREMENT CASES USED IN FIGURES 2 AND 3

Case	FDOF	MDOF
a) All/All	1-21	1-21
b) Trans/All	1,4,7,10,13,16,19	1-21
c) Trans/Trans	1,4,7,10,13,16,19	1,4,7,10,13,16,19
d) Trans/Rot	1,4,7,10,13,16,19	3,6,9,12,15,18,21

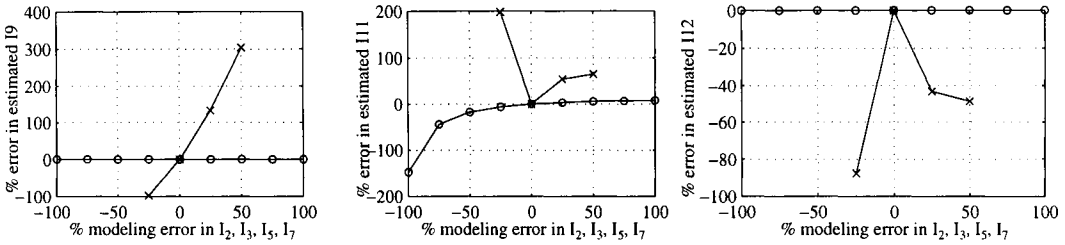

a) FDOF = 1-21; MDOF = 1-21

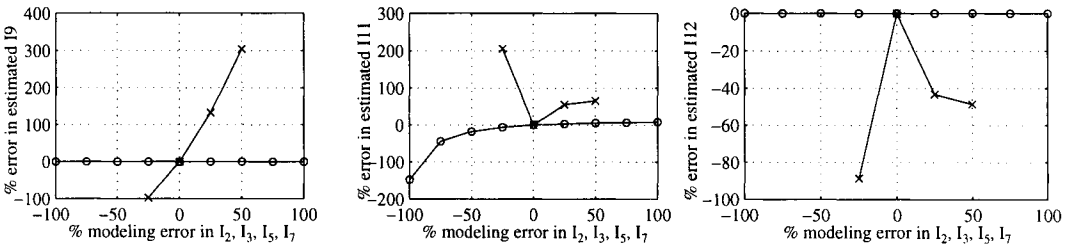

b) FDOF = 1, 4, 7, 10, 13, 16, 19; MDOF = 1-21

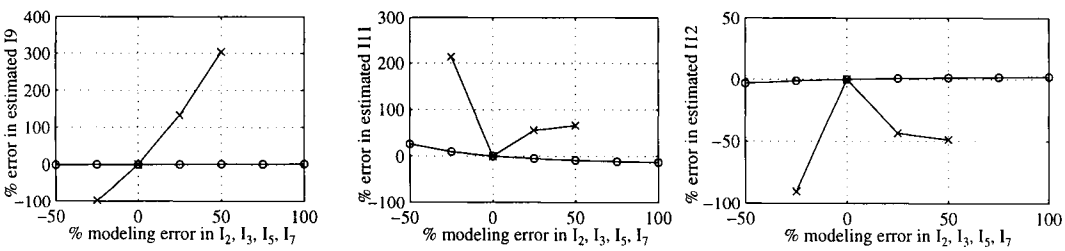

c) FDOF = 1, 4, 7, 10, 13, 16, 19; MDOF = 1, 4, 7, 10, 13, 16, 19

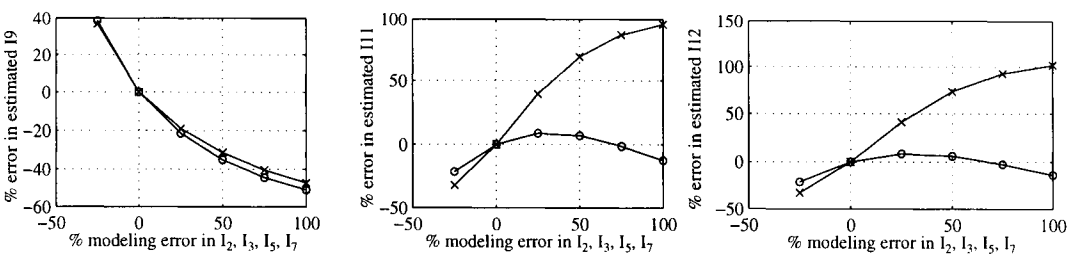

d) FDOF = 1, 4, 7, 10, 13, 16, 19; MDOF = 3, 6, 9, 12, 15, 18, 21

Figure 2. Parameter estimates for members 9, 11, and 12.
o = stiffness-based error function; x = flexibility-based function

In general, the stiffness-based error function yields more consistent results than the flexibility-based error function tolerating more modeling error and leading to parameter estimates with lower errors. All estimated parameters were checked for convergence. Parameters that converged to unreasonable values are reported, while divergent results are not. Both error functions are unbiased meaning that with no modeling error, they are capable of obtaining exact parameter estimates. The amount of modeling uncertainty that the error functions can tolerate is dependent on the load and measurement cases as well as the amount of error in the system. In three cases, the flexibility-based error function converged to unreasonable values yielding high errors in the estimated parameters (Figures 2a, 2b, and 2c). The stiffness error function, however, yielded excellent results in all estimated parameters (I_9, I_{11}, I_{12}) for three of the four cases (a, b, and c).

A similar analysis is performed with modeling error applied to members 7, 9, 11, and 12 to estimate moment of inertia for members 2, 3, and 5. Results for I_2, I_3, and I_5. are shown in Figure 3. In most cases, the flexibility error function didn't converge for cases with at least 25% modeling error (see Figures 3a, 3b, and 3c). Results that didn't tolerate at least 25% error are not reported. Again, the stiffness-based error function yields consistent and reliable results. It is interesting to note that the flexibility-based error function did not converge with more applied forces and measured displacements in cases a, b, and c. However, it converged and performed as well as the stiffness-based error function using less applied forces and measured rotations as shown in case (d) of Figure 3.

Figures 2 and 3 show that the resulting parameter estimates are sporadic and are highly dependent on the load cases, measurement locations, error functions, and location of the modeling errors. In general, the stiffness-based error function tolerates more modeling error and estimates more accurate parameter estimates compared to the flexibility-based error function.

Influence of Localized Damage on Estimated Parameters

Localized damage is simulated on the four bay frame by adding uncertainty to the stiffness of member 9, the column on the far right of the frame. The four different load and measurement cases used in this scenario are shown in Table 2.

TABLE 2
LOAD AND MEASUREMENT CASES USED IN FIGURES 4, 5 AND 6

Case	FDOF	MDOF
1	16, 18	1, 3
2	19, 21	4, 6
3	16, 18	19, 21
4	4, 6	1, 3

In each of these cases, two unknown parameters are estimated. All other parameters are assumed as known with a high degree of certainty. In addition to the amount of modeling error in the system, the value of the resulting parameter estimates also depends on the unknown parameters that are to be estimated together. For example if there are four unknowns, the effect of the modeling error may be distributed across all the unknowns rather than influencing an individual

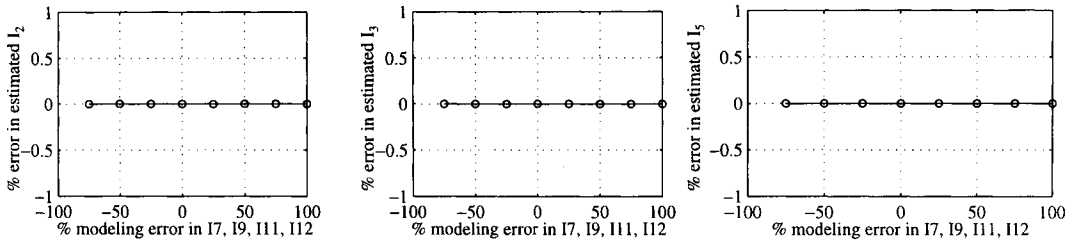

a) FDOF = 1-21; MDOF = 1-21

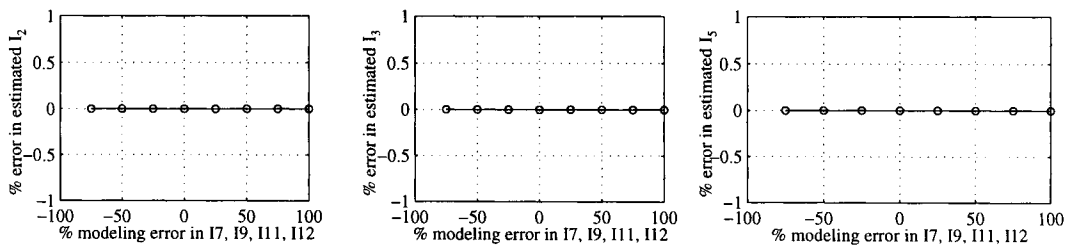

b) FDOF = 1, 4, 7, 10, 13, 16, 19; MDOF = 1-21

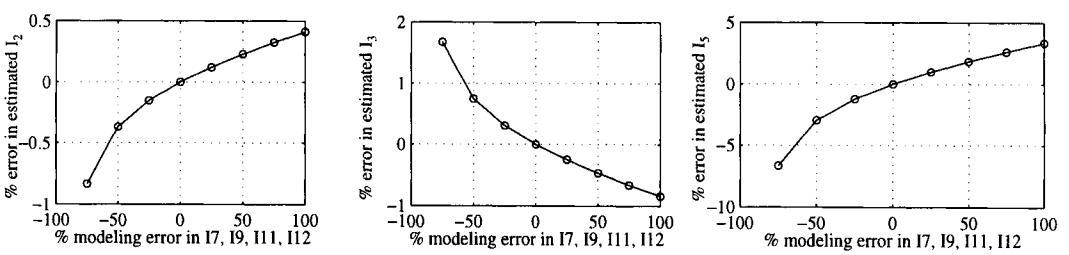

c) FDOF = 1, 4, 7, 10, 13, 16, 19; MDOF = 1, 4, 7, 10, 13, 16, 19

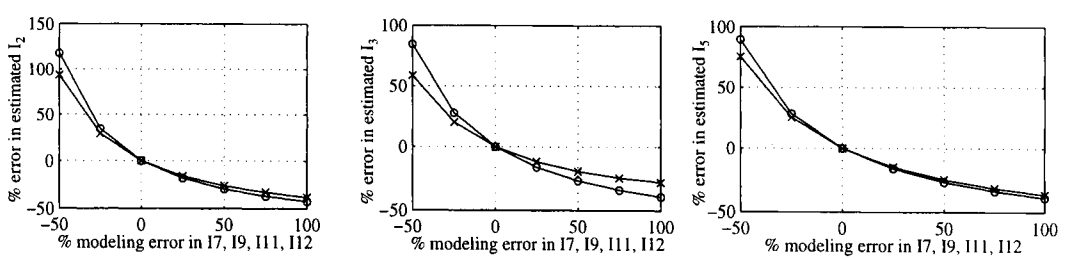

d) FDOF = 1, 4, 7, 10, 13, 16, 19; MDOF = 3, 6, 9, 12, 15, 18, 21

Figure 3. Parameter estimates for members 2, 3, and 5.
o = stiffness-based error function; x = flexibility-based function

parameter. Figure 4 shows that the final values for the parameter estimates depend on all unknown parameters estimated in a group. In this case, parameters I_6 and I_7 are estimated together (i), and parameters I_7 and I_8 are estimated together (ii).

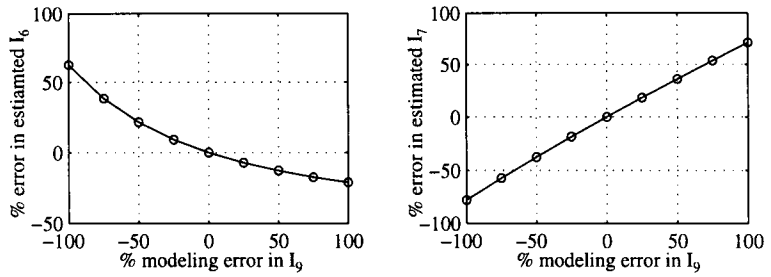

i) Parameters I_6 and I_7 are estimated together

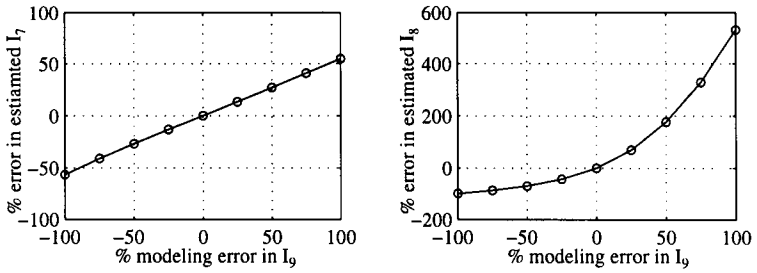

ii) Parameters I_7 and I_8 are estimated together

Figure 4. Parameter estimates for case (1) with modeling error applied to element 9. o = stiffness-based error function; x = flexibility-based function

Selection of load and measurement locations is important as the member in question must respond to the loads and the loads must be observable at the measurement locations. Often when an inappropriate load and measurement case is selected, the parameter estimation diverges. The selection of load cases also influences the quality of the parameter estimates as modeling error increases. Figure 5 shows the parameter estimates for I_1 and I_3 due to each load and measurement case. With +100% modeling error the parameter estimations of I_1 varies from 150% to -15% of the true values. In this example where localized damage was introduced, both error functions performed similarly. However, in case 2 of Figure 5, unlike the previous cases, the flexibility-based error function had a better convergence record while the stiffness-based error function did not tolerate large modeling errors with positive percentages.

A practical problem in the application of parameter estimation to in-service structures is that the modeling error may not be located near the area of the structure that is of interest in the identification. Thus, it is useful to understand the relationship or impact of modeling error in a localized region on parameter estimates at other locations of the structure. The relationship between the location of the parameters estimated and the location of the modeling error is an important consideration in experiment design. Figure 6 shows the effect of modeling error in element 9 for case 4 on the estimation of four different pairs of elements (1 & 3), (4 & 5), (6& 7), and (7 & 8).

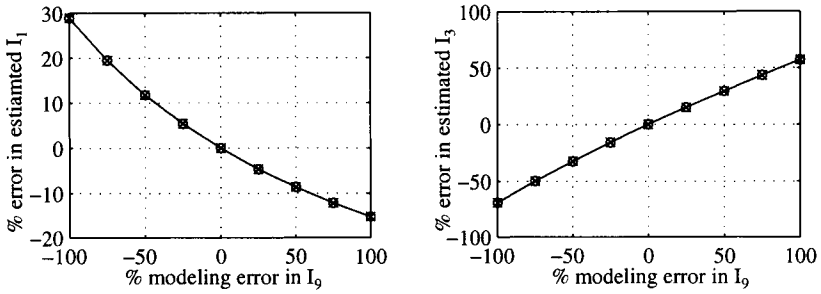

a) Case 1: FDOF= 16, 18; MDOF= 1, 3

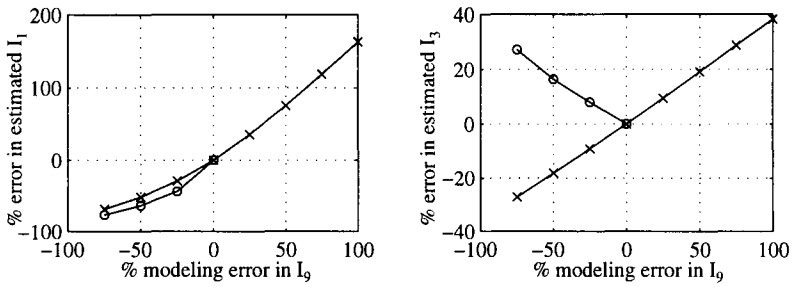

b) Case 2: FDOF = 19, 21; MDOF = 4, 6.

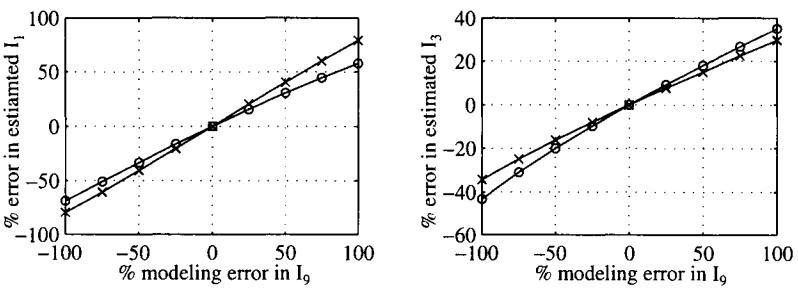

c) Case 3: FDOF = 16, 18; MDOF = 19, 21

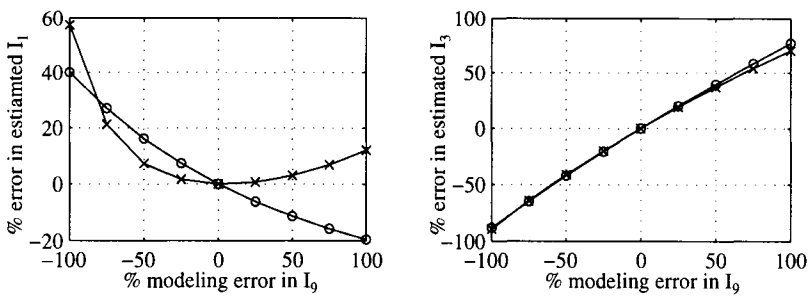

d) Case 4: FDOF = 4, 6; MDOF = 1, 3.

Figure 5. Parameter estimates for members 1 and 3.
o = stiffness-based error function; x = flexibility-based function

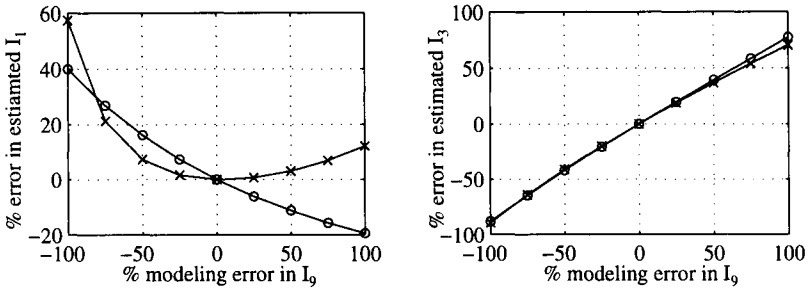

a) Case 4: Estimation of members 1 and 3.

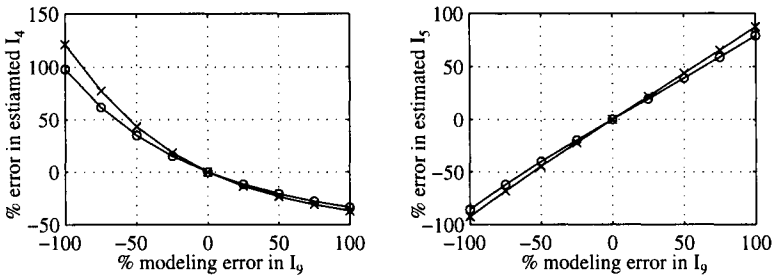

b) Case 4: Estimation of members 4 and 5.

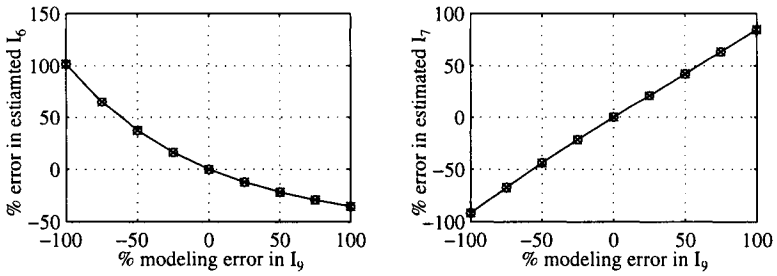

c) Case 4: Estimation of members 6 and 7.

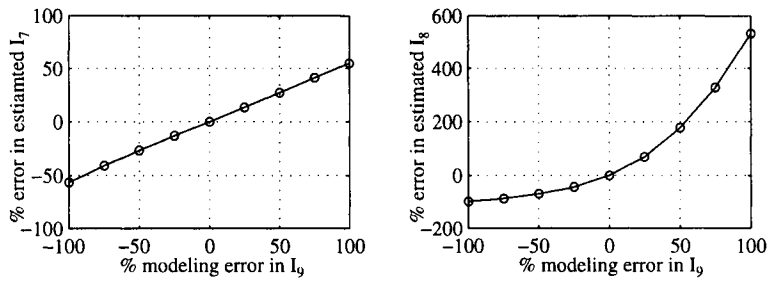

d) Case 4: Estimation of members 7 and 8.

Figure 6. Parameter estimates for different members estimated in case 4.
o = stiffness-based error function; x = flexibility-based function

The effect of the modeling error at element 9 has less of an impact on the location of the parameters to be estimated. In the case of the stiffness-based error function, the observability of the modeling error is higher in elements that are closer to the uncertain element The quality of the parameter estimates are similar for error functions as shown in Figures 6a, 6b, and 6c. However, in Figure 4d where I_7 and I_8 are unknown are very close to the uncertain parameter I_5 only the stiffness-based error function converged.

FINAL REMARKS

Parameter estimation can be a useful tool for condition assessment of in-service structures. However, before application to full-scale structures it is necessary to first understand the influence of modeling errors on the estimated parameters. The simulations presented in this paper give an overview of the impact of modeling error on a four-bay frame subjected to different types of modeling errors and load and measurement cases. The quality of the parameter estimates is highly dependent on the loading magnitude and locations; measurement type and locations; and error functions used for parameter estimation. Overall the stiffness-based error function yields more reliable results than the flexibility error function. Many parameter estimation cases diverged when the flexibility error function was used while the stiffness-based error function routinely converged and overall it tolerated more modeling error. Finally, it is important to stress that in addition to the type of error function used in the parameter estimation, the effect of modeling error is dependent on structure topology, load and measurement locations, and the location of the uncertain parameters with respect to the unknown parameters.

ACKNOWLEDGMENTS

The work presented in this paper is supported by NSF grant numbers: CMS-9622515 and CMS-9622067 with Drs. Shih-Chi Liu and Ken Chong as the NSF Program Directors. This support is gratefully appreciated.

REFERENCES

Doebling, S. W., Farrar C. R., Prime, M. B., and Shevitz, D. W. (1996). *Damage Identification and Health Monitoring of Structural and Mechanical systems from Changes in Their Vibration Characteristics: A Literature Review*, LA-13-70-MS, Los Alamos National Laboratory, Los Alamos, NM.

Ghanem, R., and Shinozuka, M. (1995) Structural-System Identification I: Theory. *Journal of Engineering Mechanics*, **121:2**, 255-264.

McClain, Jennifer A. S. (1996), *Parameter Estimation for Large Scale Structures*, M.S. Thesis, Tufts University, Medford, MA.

Sanayei, M. (1997) "PARIS"©, PARameter Identification System. Tufts University, Medford, MA.

Sanayei, M., Doebling, S., Farrar, C., Wadia-Fascetti, S., Arya, B. (1998a) Challenges in Parameter Estimation for Condition Assesment of Structures. *Proceedings of the Structural Engineers World Congress*. July 18-23, San Francisco, CA.

Sanayei, M., Imbaro, G., McClain, J. A. S., and Brown, L. C. (1997) Parameter Estimation of Structures Using NDT Data: Strains or Displacements. *Journal of Structural Engineering*, **123:6**, 792-798.

Sanayei, M., Onipede, O. and Babu, S. R. (1992) "Selection of Noisy Measurement Locations for Error Reduction in Static Parameter Identification", AIAA Journal, **30:9**, 2299-2309.

Sanayei, M. and Saletnik, M. J. (1996) Parameter Estimation of Structures from Static Strain Measurements II: Error Sensitivity Analysis, *Journal of Structural Engineering*, **122:5**, 563-572.

Sanayei, M., Wadia-Fascetti, S., McClain, J. A. S., Gornshteyn, I., and Santini, E. M. (1998b) Structural Parameter Estimation Using Modal Responses and Incorporating Boundary Conditions, *Proceedings of the Structural Engineers World Congress*, July 18-23, San Francisco, CA.

Wadia-Fascetti, S., Gunes, B., and Sanayei, M. (1998) Significance of Modeling Error in Structural Parameter Estimation, *Proceedings of the 12th Engineering Mechanics Conference: A Force for the 21st Century*, May 17 – 20, La Jolla, CA.

Wadia-Fascetti, S. and H. A. Smith (1996) "Calibration of Structural Models Using Fuzzy Mathematics." *Microcomputers in Civil Engineering.* **11:1**, 19-35.

ER DEVICES FOR CONTROL OF SEISMICALLY EXCITED STRUCTURES

Henri P. Gavin

Department of Civil and Environmental Engineering
Duke University, Durham NC 27708-0287, U.S.A.

ABSTRACT

This study illustrates the behavior of a closed-loop vibration control system making use of electrorheological electrorheological (ER) devices. ER fluids exhibit damping and stiffness properties which can be modulated by orders of magnitude when subjected to strong electric fields (kV/mm). An increase in yield stress (from 0 to 3 kPa) is characteristically observed when the field is applied. A Lyapunov-based controller results in control decisions which are independent of the structural model, and are therefore insensitive to modeling errors. Structures operated according to the control rule maintain an anti-resonant condition. In order to capitalize on the unique properties of ER materials in this application it is desirable that the material be configured in a device in such a way that when the device undergoes characteristic motions, the device forces can be modulated to a significant degree (a factor of 10 or more). Because the range of adjustable forces is closely linked to the ratio of finite field-controllable yield stresses to uncontrollable viscous stresses, it is desirable for controllable ER dampers to operate at low flow rates. In addition to the range of available forces, ER dampers should have a short characteristic time, low stored electrical energy, and forces high enough to be effective for the intended application. The ER damper described herein features multiple concentric electrodes which are electrically in parallel, but may be hydraulically interconnected through multiple paths.

KEYWORDS

vibration control, electrorheological materials, adaptive damping and stiffness, viscoelasticity

INTRODUCTION

Vibration suppression in civil engineering structures during strong earthquakes presents unique challenges [9]. Properly detailed structures behave non-linearly during earthquakes, large control forces must be applied rapidly to respond to impulsive ground motions, but control forces need not be accurately controlled. The control system should be able to operate in the absence of external power.

Because details regarding structural behavior and the earthquake characteristics can not be exactly foreseen, endowing a degree of adaptability to structural systems could satisfy safety and performance requirements for a broad range of earthquake characteristics.

While the required electric fields in ER materials are strong (kV/mm), the field's displacement currents are small (μamp/cm^2) [7] [4]. Thus, ER devices can be operated using low-power, battery-operated, energy sources [2, 11]. Therefore, ER devices designed to provide a wide range of adjustable forces must have small viscous stresses as compared to yield stresses. Instead of forcing a viscous material to flow at high velocity through a relatively narrow orifice, the proposed device develops large forces by forcing a dissipative fluid to flow at a relatively low velocity over a large surface area.

PRE-YIELD VISCOELASTICITY OF ER MATERIALS

Visco-elasticity in ER materials is strongly affected by the electric field at low strains (<0.1); at high strains a yield stress is quadratically related to the field [7]. At low shear rates, ER devices provide a large range of controllable forces. Based on extensive Couette shear measurements, Gamota and Filisko [7] elucidated the material behavior of ER materials with the mechanical analog illustrated in Figure 1.

Considering the mechanism of Figure 1, a balance of forces on the mass m_0 gives

$$m_0\ddot{x}_0 + c_0\dot{x}_0 + f_0(\dot{x}_0) = f(t), \tag{1}$$

where $f_0(\dot{x}_0)$ is the only non-linearity and represents the Coulomb friction element. This nonlinearity can be approximated by a hyperbolic tangent. The right hand side of Equation (1) is the applied stress. The total deformation of the element is the sum of x_0 and x_1, where x_1 is obtained from the equations of motion for the Zener element,

$$f(k_1 + k_2) + c_1\dot{f} = k_1k_2x_1 + c_1k_2\dot{x}_1. \tag{2}$$

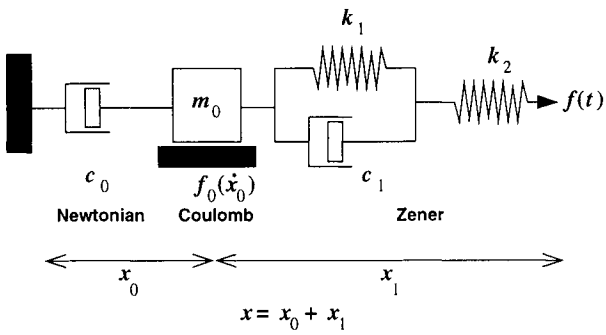

Figure 1: A mechanical analog for ER materials.

Equations(1) and (2) can be cast into a state-space form using a state vector of $[x_0\ \dot{x}_0\ f]^T$.

$$\frac{d}{dt}\begin{bmatrix} x_0 \\ \dot{x}_0 \\ f \end{bmatrix} = \begin{bmatrix} 0 & 1 & 0 \\ 0 & -c_0/m_0 & 1/m_0 \\ -k_1k_2/c_1 & -k_2 & -(k_1+k_2)/c_1 \end{bmatrix}\begin{bmatrix} x_0 \\ \dot{x}_0 \\ f \end{bmatrix} + \begin{bmatrix} 0 & 0 \\ 0 & 0 \\ k_1k_2/c_1 & k_2 \end{bmatrix}\begin{bmatrix} x \\ \dot{x} \end{bmatrix} + \begin{bmatrix} 0 \\ -1/m_0 \\ 0 \end{bmatrix} f_0(\dot{x}_0). \tag{3}$$

The dynamics are always asymptotically stable, provided that all parameters are positive; and the linear dynamics are explicitly separated from the sole dissipative nonlinearity, f_0. The equations are well conditioned and can be solved using a number of numerical techniques [8, 12].

The parameters in the state space models for the ER dampers (f_0, k_1, c_1, and k_2), increase monotonically as a function of an input voltage, u.

CONTROL SYNTHESIS

A control method, based on minimizing the kinetic energy content in a seismically-excited structure, leads to a bang-bang control rule, which can be physically implemented using a nonlinear analog feed-back loop. Consider the equations of motion for a base-excited structural system with unknown, and possibly highly non-linear, restoring forces $g(r, \dot{r})$, and a set of ER dampers described by the strictly proper Equation (3),

$$M\ddot{r} + g(r, \dot{r}) + B_f f(u) = -Mh\ddot{z}, \tag{4}$$

where M is an n by n positive definite symmetric mass matrix, $g(r, \dot{r})$ is the gradient of the non-negative definite potential energy function $W(r, \dot{r})$, B_f is a n by m matrix relating the m ER damper forces to the n structural coordinates, $f(u)$ is an m vector of

ER damper forces, given by Equation (3), and $\ddot{z}$ is the base acceleration. A new algebraic hysteresis model was developed to describe the restoring forces $g(r, \dot{r})$, and is represented by the closed-form expression

$$g(r, \dot{r}) = g_t + \bar{g} \tanh\left(\frac{k_{hi}(r - r_t)}{\bar{g}}\right) + k_{lo}(r - r_t), \tag{5}$$

in which the coordinate (g_t, r_t) is the coordinate at the most recent direction reversal, and

$$\bar{g} = F_y - (g_t - k_{lo} r_t)\mathrm{sgn}(\dot{r}) \tag{6}$$

This hysteresis model has three parameters corresponding to the pre-yield stiffness, k_{hi}, the post-yield stiffness, k_{lo}, and the yield strength F_y, is rate dependent, and enforces the Bauchinger effect.

The total energy in the system is

$$V = \frac{1}{2}(\dot{r} + h\dot{z})^T M(\dot{r} + h\dot{z}) + W(r, \dot{r}). \tag{7}$$

Following Lyapunov's direct method, the objective of the control is to minimize the internal energy by forcing the rate of change of internal energy to be as negative as possible. The rate of change of internal energy reduces to

$$\dot{V} = -\dot{z}^T g(r, \dot{r}) - (\dot{r} + h\dot{z})^T f(u). \tag{8}$$

The only term over which one has control in Equation (8) is f indirectly, through u. The "bang-bang" control rule reduces to making the last term in Equation (8) as positive as possible by varying u. The control is decentralized, robust to scaling errors of the sensors, robust to model errors, but is sensitive to phase and bias errors.

EXPERIMENTAL EXAMPLE

Experiments on a small 3 DOF shear building model illustrate the effects of the control rule. The mass of each floor was approximately 1.25 kg and inter-story stiffnesses were 5.5 N/mm. The identified natural frequencies of the bare frame were 4.3, 12.7, and 18.8 Hz. An ER shear wall was constructed of stainless steel and poly-carbonate, and was installed between the first DOF and the ground, The ER material was 30% (v/v) anhydrous Zeolite "3A" in paraffin oil [4]. The forces generated in the ER wall were on the order of the column shear. To perform the required control tasks, the device was charged and discharged up to 100 times per second.

The structure was excited on an electro-magnetic shaking table which made use of a proportional acceleration feedback control loop. This control was sufficient to obtain coherent transfer functions for the structure without the ER damper. Figure 2 illustrates the structure with the ER wall, the sensors and the control circuit.

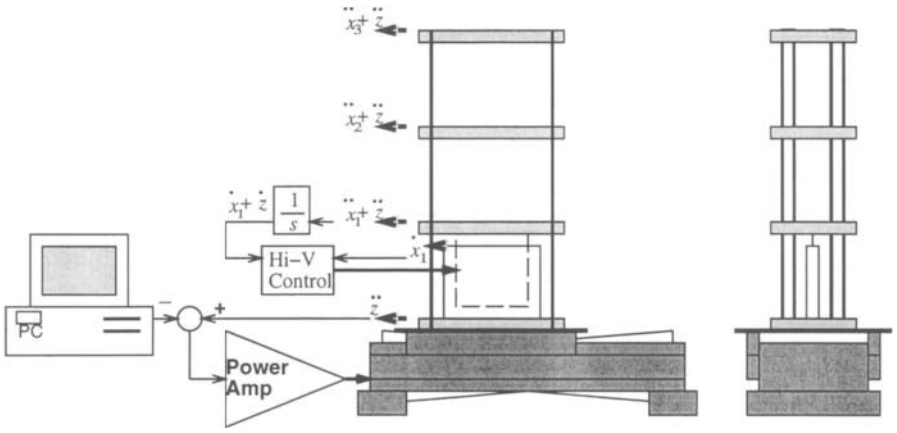

Figure 2: Structural model illustrating shaking table system with feed-back control loops.

Results of the vibration control experiments are given in Figures 3 and 4. Figure 3 shows transfer function data between the base acceleration and the second and third degrees of freedom. Three cases are shown in each figure. The two dashed lines correspond to the response with the device operating at constant low and high fields. The primary effect of the ER wall is to selectively increase or decrease the coupling between the support and the adjacent degree of freedom, and is exhibited by a shift of natural frequencies. The solid line corresponds to the controlled case, and follows the minimum of the two constant voltage transfer functions. The same wide-band random disturbance was used for all three cases.

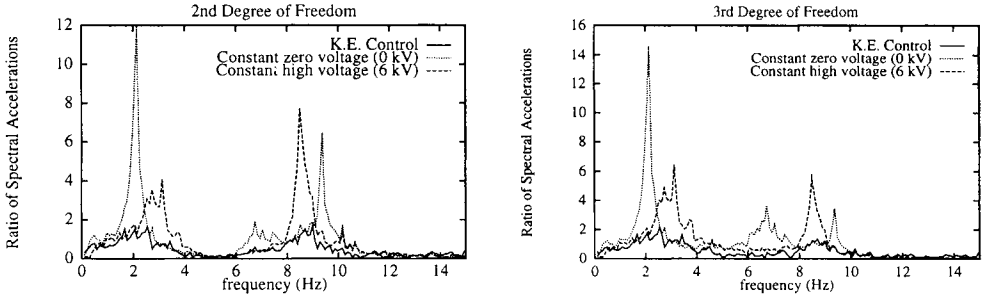

Figure 3: Frequency response data for second and third degrees of freedom. The controlled system follows the lower bound of the constant on and constant off cases.

A similar behavior is observed in the time-domain response to a sinusoidal excitation with slowly increasing frequencies: the controlled system follows the trajectory of lowest amplitude. Sections of the sine-sweep responses are shown in Figure 4. The fundamental resonance of the constant zero voltage and constant high voltage are shown by the dotted lines. In the left figure the solid line corresponds to the controlled case, and follows the

smallest signal. In the right figure the solid line corresponds to the "mis-controlled" case, (in which the polarity of the control decision is reversed) and follows the largest signal. This figure illustrates that the ER shear wall can be used to enhance resonance, should that ever be desired. Even in these narrow-band excitations, the control called for rapid periodic switching of the electric field.

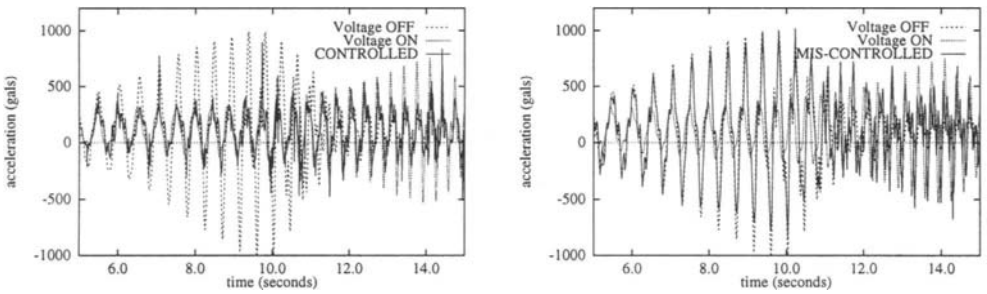

Figure 4: Time history data for the third degree of freedom. The control is applied correctly in the left plot. The polarity is reversed in the right plot.

NUMERICAL EXAMPLE

The above equations can be cast into a set of non-linearly coupled first order ordinary differential equations to model the dynamics of the closed loop system. Such a model incorporates the full interaction between the dampers and the structure.

$$\frac{d}{dt}\begin{bmatrix} r \\ \dot{r} \\ q \end{bmatrix} = \begin{bmatrix} \dot{r} \\ -M^{-1}B_g g(r,\dot{r}) - h\ddot{z} - M^{-1}B_f C_c q \\ A_c(u)q + B_c(u)[r_1\ \dot{r}_1]^T + [0\ \ -1/m_0]^T f_o(u)\tanh(\dot{r}_1) \end{bmatrix}, \tag{9}$$

where

$$B_g = \begin{bmatrix} 1 & -1 & 0 \\ 0 & 1 & -1 \\ 0 & 0 & 1 \end{bmatrix}, \tag{10}$$

q is the state vector in Equation (3), and $B_f = [1\ 0\ 0]^T$. A qualitative comparison of simulated responses of a system described by Equation (9) confirms the experimental results of the previous sections. To visually compare the time- and frequency- domain data, sine-sweep excitations were applied to a three degree of freedom building model. The typical hysteresis of the ER damping wall [1, 10, 13], as modeled by Equation (3) is shown in Figure 5. Simulation results of Equations (9) are shown in Figure 6. In each of these figures, absolute acceleration time histories, force-deflection hystereses of the structural elements, and frequency response functions of the absolute accelerations are plotted. The voltage "OFF" case is more flexible and passes through resonance first (at around 10 seconds), whereas the voltage "ON" case passes through resonance at around

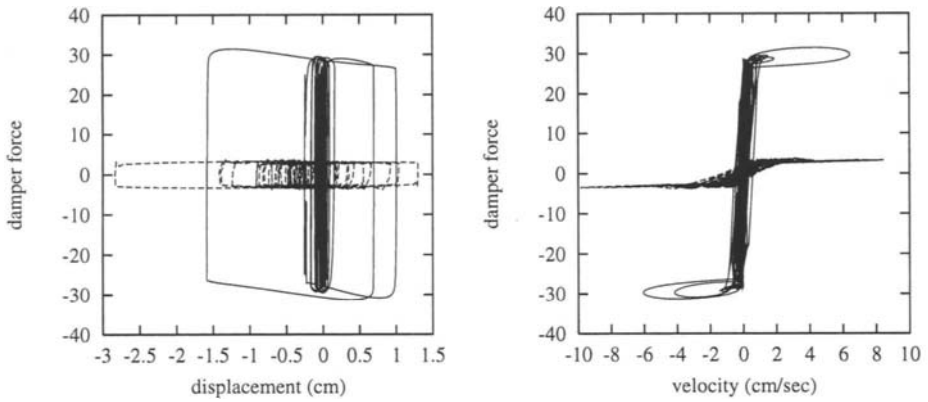

Figure 5: Typical hysteresis of ER devices, as modeled by Equation (3).

14 seconds. The "CONTROL" case does not demonstrate any resonance, and maintains amplitudes at or below the two constant voltage cases. This behavior is confirmed by the two frequency response functions at the bottom of the figure. The control also reduces relative deformations, as illustrated by hysteresis in the structural elements.

MULTI-DUCT ELECTRORHEOLOGICAL DEVICE DESIGN

The electrodes in a multi-duct ER device create a set of concentric annular ducts. These ducts can communicate hydraulically to form parallel ducts, ducts in series, or groups of parallel or series ducts. Apart from the nature of duct interconnections, design variables include the inter-electrode gap, h, the electrode (duct wall) thickness, w, the piston radius, R_p, the piston shaft radius, R_s, the device radius, R_b, and the device length, L, as illustrated in Figure 7. In this figure, the black electrodes are grounded and the white electrodes are at high voltage. Assuming incompressible flow, the total volumetric flow rate, Q_T, is proportional to the piston velocity, V_p,

$$Q_T = \pi({R_p}^2 - {R_s}^2)V_p. \tag{11}$$

In Figure 7 all ducts are hydraulically parallel.

The pressure gradient ($p' = -\partial p/\partial x$), in a homogeneous ER material following a Bingham constitutive law

$$\tau(\dot{\gamma}, E) = \tau_y(E)\mathrm{sgn}\dot{\gamma} + \eta\dot{\gamma} \tag{12}$$

along an annular gap of width h can be approximated by

$$p' \approx p'_N + 2.07\frac{\tau_y}{h} + \frac{\tau_y p'_N}{p'_N h + 0.4\tau_y} \tag{13}$$

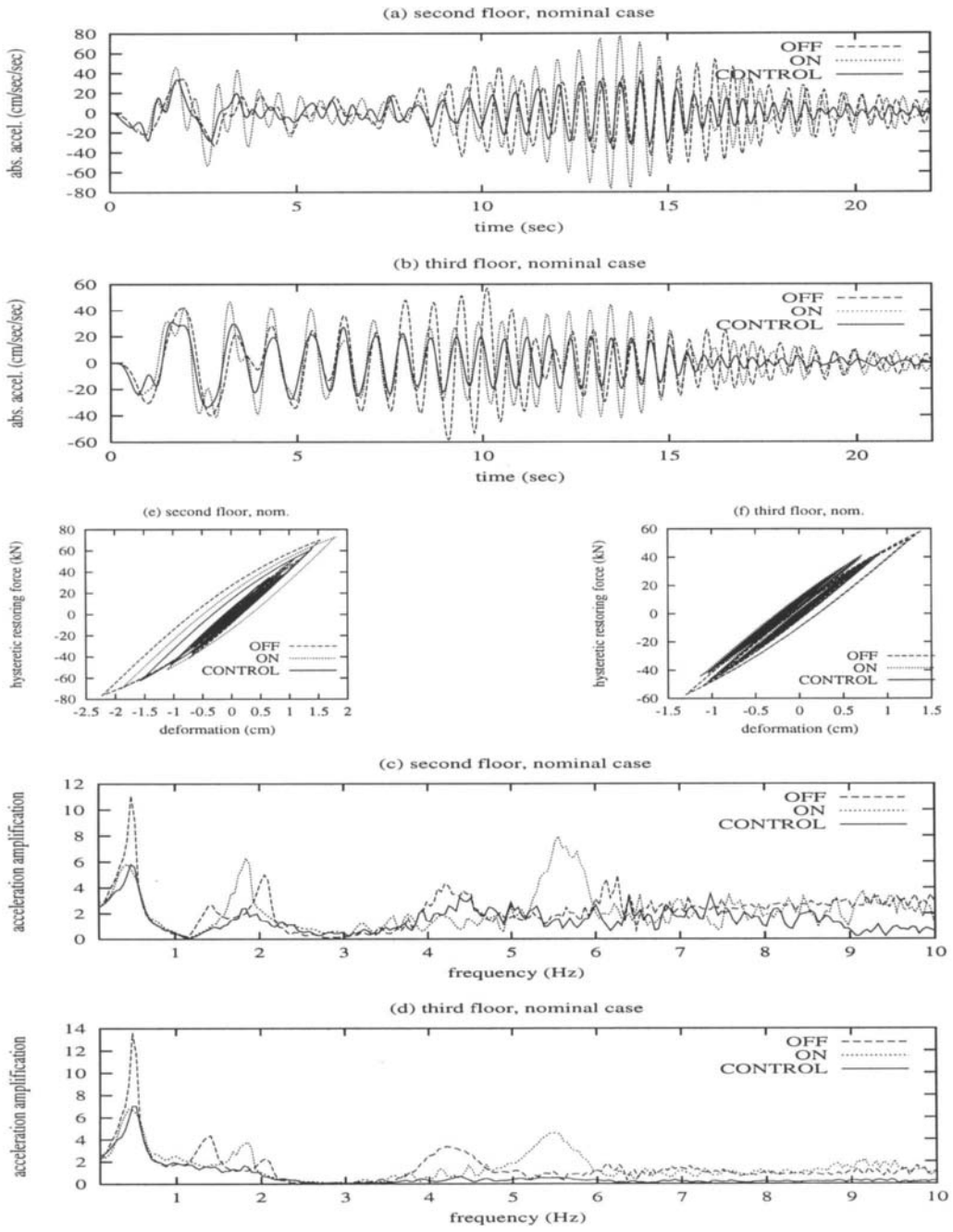

Figure 6: Acceleration response histories and hysteresis for second and third degrees of freedom for the nominal structure. The controlled system follows the lower bound of the constant on and constant off cases. Absolute accelerations and relative deformations are reduced.

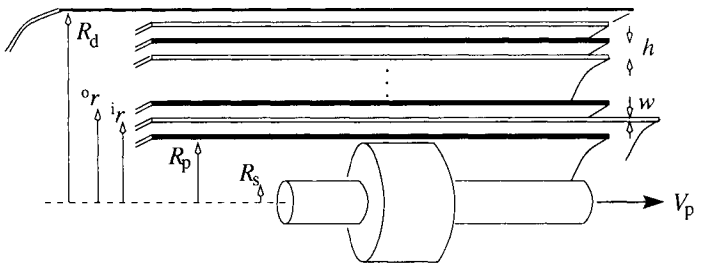

Figure 7: Arrangement of piston and ducts in the proposed ER damper design.

to within two percent of the true value of p'/p'_N [5]. The approximation

$$p' \approx p'_N + 2.1\frac{\tau_y}{h} \tag{14}$$

is linear in Q allows a closed form solution for the device forces. In the above expressions, τ_y is the field-dependent yield stress, p'_N is the pressure gradient of a Newtonian fluid of viscosity η flowing through a duct of width h at a volumetric flow rate, Q; and p' is the pressure gradient of a Bingham material with yield stress τ_y flowing through a duct of width h at a flow rate Q. Under steady flow conditions, the force in an ER device increases by a factor of p'/p'_N when the field is applied. The Newtonian pressure gradient is proportional to Q ($p'_N = Q\mathcal{R}$), where $\mathcal{R}$ depends only on geometry and viscosity,

$$\mathcal{R}_{gd}({}^ir_{gd}, {}^or_{gd}, \eta) = \frac{8\eta}{\pi}\left[{}^or_{gd}^4 - {}^ir_{gd}^4 - \frac{({}^or_{gd}^2 - {}^ir_{gd}^2)^2}{\log({}^or_{gd}/{}^ir_{gd})}\right]^{-1}. \tag{15}$$

The inner radius of the duct is ^ir and ^or is the outer radius. The across-flow dimension of the duct is $h = {}^or - {}^ir$. In the analyses that follow, flow ducts are separated into groups. Adjacent ducts within a group may be hydraulically connected in series, or in parallel. Adjacent groups may be connected in series or in parallel. The sub-scripts 'gd' indicate that the sub-scripted quantity pertains to duct d within group g, where $1 \le g \le G$ and $1 \le d \le D_g$. There are D_g ducts in group g. When the subscript g is omitted, $G = 1$. The values for the inner and outer radii can be derived from the geometry shown in Figure 7,

$${}^ir_{gd} = {}^or_{(g-1)D_{(g-1)}} + \sum_{\delta=1}^{d} w_{g\delta} + \sum_{\delta=1}^{d-1} h_{g\delta} \tag{16}$$

and

$${}^or_{gd} = {}^or_{(g-1)D_{(g-1)}} + \sum_{\delta=1}^{d} w_{g\delta} + \sum_{\delta=1}^{d} h_{g\delta} \tag{17}$$

where ${}^or_{0D_0} = R_p$.

The ER device designs are evaluated with four performance parameters: the maximum device force, F, at low piston velocities, the ratio of maximum to minimum device forces,

p'/p'_{N}, at high piston velocities, the electrical energy required to operate the damper, CE^2h^2, and the response time of the device due to fluid inertia, t. The optimal device has the design with the fastest response time, t, that meets or exceeds a required force level, and a required dynamic range within a given device size (R_{b}, L), and without exceeding a pre-specified energy requirement.

The total force developed by the device is proportional to the total pressure drop along the network of ducts, Δp. In the analyses which follow, p'_{T} is an effective total pressure gradient, such that $\Delta p = p'_{\mathrm{T}} L$. The time required for the Newtonian flow profile to develop from a nearly plugged flow profile is

$$t = 0.22\frac{\rho h^2}{\eta}, \tag{18}$$

where ρ is the mass density of the ER material ($\rho \approx 1$ g/cc) [5]. The capacitance of a multi-electrode device (as illustrated in Figure 7) in Farads is:

$$C = \kappa\epsilon_0\pi L \sum_{g=1}^{G}\sum_{d=1}^{D_g} \frac{{}^{\mathrm{o}}r_{gd} + {}^{\mathrm{i}}r_d}{{}^{\mathrm{o}}r_{gd} - {}^{\mathrm{i}}r_{gd}}. \tag{19}$$

where ϵ_0 is the permittivity of free space and κ is the dielectric constant of the material ($\kappa \approx 4$). The maximum field typically applied to an ER material is about 5kV/mm. The total capacitive energy at this field is about $25 \times 10^{12} Ch^2$ Joules.

Multiple-duct ER devices have more design variables (gap widths) than are easily managed. Because steel tubes are readily available in only discrete sizes of diameter and wall thickness, the following analysis will presume that the ducts in the ER device are annular gaps formed by tubes with a equal wall thicknesses, and that all of the ducts have the same across-flow dimension, h. Even within the constraint of limited tube availability and a fixed device size (diameter and length), the arrangement of the flow paths within the device leads to devices with a wide range of characteristics. While all of the ducts are electrically parallel, the flow paths can be arranged either in parallel, in series, or both. The number of possible hydraulic interconnections of N concentric ducts is $2^{(N-1)}$. Each configuration has distinctly different properties.

These configurations will be analyzed in the context of several parallel groups of ducts in series. In this configuration, the total pressure drop across the piston is equal to the the pressure drop along each group of ducts. Mass conservation and an incompressibility assumption require that the sum of the volumetric flow through each group equals the total volumetric flow rate, Q_{T}. Within each group, the sum of the individual duct pressure drops equals the total pressure drop and the volumetric flow through a duct equals the volumetric flow through that duct's group. These conditions give

$$Q_{\mathrm{T}} = \sum_{g=1}^{G} Q_{gd}, \tag{20}$$

and

$$p'_{\mathrm{T}} = \sum_{d=1}^{D_g} p'_{gd} \tag{21}$$

Assuming a conservative linear approximation for the ER pressure gradient (equation 14), the flow within group g of a set of parallel groups is

$$Q_g = \left[\sum_{d=1}^{D_g} \mathcal{R}_{gd}\right]^{-1} \left[p'_{\mathrm{T}} - 2.1\tau_{\mathrm{y}} \sum_{d=1}^{D_g} h_{gd}^{-1}\right]. \tag{22}$$

The total flow is then:

$$Q_{\mathrm{T}} = \sum_{g=1}^{G} \left[\left[\sum_{d=1}^{D_g} \mathcal{R}_{gd}\right]^{-1} \left[p'_{\mathrm{T}} - 2.1\tau_{\mathrm{y}} \sum_{d=1}^{D_g} h_{gd}^{-1}\right]\right]. \tag{23}$$

This equation can be solved for the total effective pressure gradient:

$$p'_{\mathrm{T}} = \left[\sum_{g=1}^{G} \left[\sum_{d=1}^{D_g} \mathcal{R}_{gd}\right]^{-1}\right]^{-1} \left[Q_{\mathrm{T}} + 2.1\tau_{\mathrm{y}} \sum_{g=1}^{G} \left[\sum_{d=1}^{D_g} h_{gd}^{-1} \left[\sum_{d=1}^{D_g} \mathcal{R}_{gd}\right]^{-1}\right]\right]. \tag{24}$$

The total effective pressure gradient due to a purely Newtonian flow is obtained by setting $\tau_{\mathrm{y}} = 0$ in the above equation,

$$p'_{\mathrm{NT}} = Q_{\mathrm{T}} \left[\sum_{g=1}^{G} \left[\sum_{d=1}^{D_g} \mathcal{R}_{gd}\right]^{-1}\right]^{-1}. \tag{25}$$

NUMERICAL EXAMPLE

To illustrate the analysis outlined above, a device with constrained geometry and material properties was investigated. The across flow dimension, h, and electrode thickness, w, were fixed at 1.59 mm (1/16 inch). The outer radius of the device was fixed at 3.81 cm (1.5 inches), and the length of the electrodes was fixed at 25.4 cm (10 inches). The maximum ER fluid yield stress, τ_{y}, is conservatively chosen to be 3 kPa, and the Newtonian viscosity, η, is set at 0.1 Pa-sec. Devices with five ducts and seven ducts were analyzed. The only design variables are the arrangement of the ducts in the device, and the total number of ducts. A device is determined to be "feasible" if the dynamic range, p'/p'_{N} is between 10 and 20, and if the force levels are above 1.5 kN.

The wide range of device performances, attributed to different hydraulic designs is illustrated in Figure 8. Each point in these figures corresponds to a different design duct configuration. These figures show three performance variables, p'/p'_{N}. The force,

F, increases with velocity due to the Newtonian stresses. Therefore F was conservatively evaluated at $V_p = 1$ cm/sec. Likewise, p'/p'_N decreases with velocity. So p'/p'_N was conservatively evaluated at $V_p = 50$ cm/sec. The other performance variables are velocity-independent, but depend on geometry, viscosity, and density. In each figure, the device with the greatest dynamic range corresponds to all ducts in parallel, and the device with the greatest force capacity corresponds to all ducts in series.

It is clear from Figure 8 that devices with seven ducts provides an outstanding dynamic range but sacrifices the force level. The effect of grouping the ducts enhances the trade-off between dynamic range and force level. Many designs with five ducts in groups have an adequate force level and dynamic range.

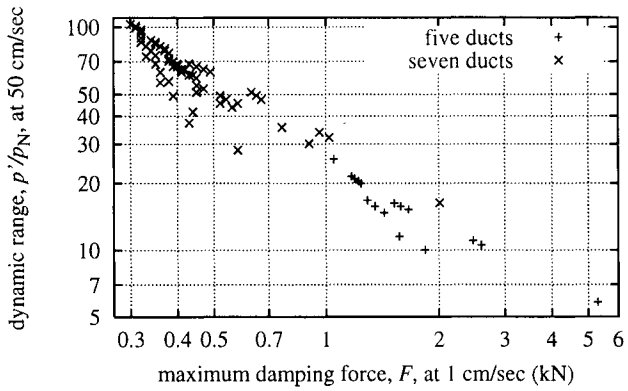

Figure 8: Dynamic range vs. force for a multi-electrode ER damper.

While there is a trade-off between dynamic range time and force level, dampers with higher force levels have shorter response times. Because the response time is assumed to vary only with h^2, the manner in which the ducts are interconnected does not effect the inertial response time. Because all devices in this analysis have the same h, the response time for every design is 5.5 milli-seconds.

Like the response time, the energy requirement is not dependent on flow rate. Therefore, all the designs require similar amounts of energy. The capacitive stored energy of the five duct devices is 0.35 Joules, and the capacitive stored energy of the seven duct devices is 0.44 Joules. These devices could be charged hundreds of times from a common 9-volt battery.

Devices made with more groups of ducts but the same total number of ducts have lower forces but greater dynamic range. Placing the groups with the greater number of ducts toward the outer perimeter of the device results in devices with slightly larger forces and slightly smaller dynamic ranges.

CONCLUSION

A linear approximation to exact solution of steady ER flow was used to obtain closed form design expressions for ER devices. Dampers in which the ER material flows through multiple concentric electrodes can demonstrate a wide range of behaviors within a fixed device size. The electrode gaps are electrically in parallel but hydraulically arranged in series, parallel, or combinations of series and parallel. Despite low yield stresses, high forces are generated in these dampers by virtue of the large surface area over which the ER material flows. Forces can be controlled by a factor of 10 or more, even at high velocities. By carefully separating and isolating the electrified metallic tubes, rugged devices with complicated flow paths can be easily assembled.

This study concludes that ER materials can be effective in reducing structural responses, when the electric field is switched according to a bang-bang control rule which minimizes kinetic energy. Although operating the ER devices in a bang-bang fashion requires much more electrical energy than the constant voltage case, the control system can be operated using a battery-operated high-voltage supply. The control rule described here requires only that the structure is base-excited, that the physical parameters of the ER material increase monotonically with electric field, and that the force- velocity relationship for the ER damper is always in the first and third quadrants. Because of the low, cyclic, shear rates of the material in ER devices, pre-yield, visco-elastic behavior is observed in experiments. This controllable pre-yield visco-elasticity is central to the behavior of the control system.

ACKNOWLEDGMENTS

This material is based on work supported by the National Science Foundation under Award No. CMS-9624949, and by the Oak Ridge Associated Universities. Any opinions, findings, and conclusions or recommendations expressed in this publication are those of the authors and do not necessarily reflect the views of the sponsors.

REFERENCES

[1] F. Arima, M. Miyazake, H. Tanaka, and Y. Yamazaki, "A Study on Buildings with Large Damping Using Viscous Damping Walls," *Proc. 9th World Conf. on Earthquake Engineering,* 1988 V-821 – V-826.

[2] H. Block, J.P. Kelly, A. Qin, and T. Watson, 'Materials and Mechanisms in Electrorheology,' *Langmuir,* vol. 6 (1990): 6–14.

[3] H. Block and J.P. Kelly, 'Review Article: Electro-rheology,' *J. Physics D: Applied Physics,* vol. 21 (1988): 1661–1677.

[4] F.E. Filisko and L.H. Radzilowski, "An intrinsic mechanism for the activity of alumino-silicate based electrorheological materials," *J. Rheology,* vol. 34, no. 4 (1990): 539–552.

[5] H.P. Gavin, R.D. Hanson, and F.E. Filisko, 'Electrorheological Dampers, Part I: Analysis and Design' *J. Appl. Mech, ASME* vol. 63 (1996): 669–675.

[6] H.P. Gavin, 'The effect of particle concentration inhomogeneities on the steady flow of electro and magneto-rheological materials,' *J. Non-Newtonian Fluid Mechanics* (Aug. 1997).

[7] D.R. Gamota and F.E. Filisko, 'Dynamic mechanical studies of electrorheological materials: Moderate frequencies,' *J. Rheology,* vol. 35, no. 3 (1991): 399–425.

[8] A.C. Hindmarsh, "ODEPACK, A systematized collection of ODE solvers," in *Scientific Computing,* R.S. Stepleman editor, (New York: Elsevier, 1983).

[9] G.W. Housner, T.T. Soong, and S.F. Masri (1994). Second Generation Of Active Structural Control In Civil Engineering. In: *Proc. 1st World Conf. on Structural Control,* (G.W. Housner, ed.), Vol. 1, 1–18. International Association for Structural Control, Los Angeles.

[10] M. Miyazaki and Y. Mitsusaka, "Design of a building with 20% or greater damping," *Proc. 10th World Conf. on Earthquake Engineering,* (Rotterdam: Balkema, 1992):4143–4148.

[11] M. Parthasarathy, and D.J. Klingenberg, "Electrorheology: mechanisms and models," *Materials Science and Engineering,* R17 No. 2 (15 October 1996):57–103.

[12] K. Radhakrishnan and A.C. Hindmarsh, "Description and use of LSODE, the Livermore solver for ordinary differential equations," *Lawrence Livermore National Laboratory Reports,* Report Number UCRL-ID-113853 (1993).

[13] A.M. Reinhorn and C. Li, *Experimental and Analytical Investigation of Seismic Retrofit of Structures with Supplemental Damping, Part III: Viscous Damping Walls,* (Buffalo, NY: National Center for Earthquake Engineering Research, Technical Report 95–0013, 1995).

PARALLEL PCG ALGORITHM ON DISTRIBUTED NETWORK BY PVM*

Z. C. Hou, J. G. Cheng, Z. H. Yao and Z. C. Zheng

Department of Engineering Mechanics, Tsinghua University,
Beijing 100084, China

ABSTRACT

Preconditioned conjugate gradient (PCG) method is an equation solver that is suitable for parallelism. Cluster technology leads parallel computation to a new stage and dramatically increases the transferability of parallel algorithms. This paper tries on a fast Ethernet to develop a parallel PCG algorithm as an independent solver of linear system of equations. After a brief review, a parallel PCG strategy is given through modification of an existing scheme. It is programmed on the parallel virtual machine (PVM) platform, and the local area network is composed of 5 Pentium PCs connected by 100BASE-TX Switching Hub. Considering load balance, two types of decomposition of the whole coefficient matrix are adopted, so as to implement the dominant and computation-exhausting processes, preconditioning and sparse-matrix vector product. As an initial approach, a Jacobian and block-Jacobian preconditioning are adopted respectively. Some simple examples show that the PCG converges very fast for those diagonal dominant matrices, but may fail for structural analyses.

KEYWORDS

Parallel PCG algorithm, Cluster technology, PVM, Equation solver, Sparse matrix vector product

INTRODUCTION

Using the Galerkin formulation on any continuum that is to be studied, structural analysis is

* Supported by NNSF of China, No. 19672032

reduced to solving the matrix equations

$$KX = F \tag{1}$$

where $K \in R^{n \cdot n}$ is the stiffness or equivalent stiffness matrix, $X, F \in R^n$ are the generalized displacement and force vectors, respectively. The solution of Eqn 1 may be obtained in one of two possible ways, direct or iterative approaches. In traditional FEM programs that are sequentially executed on one-processor computers, direct approaches have been almost exclusively used, see Zois (1988).

Iterative methods approach the real solution through successive approximation techniques. They not only require less storage and are easy for implementation, but also give users the possibility of controlling the accuracy of the solution. Along with time extension, CG/PCG families are attracting more and more attention. Although CG approach has poor reputation of low convergence in structural analysis, there have been some successes with PCG algorithms recently by preconditioning and special ordering techniques. The inherent characteristics of the family and these techniques imply better performance in parallel environment than in sequential one.

The most widely used pre-conditioners are derived either from the incomplete Cholesky factorization of the coefficient matrix or by SSOR characteristic matrix. Since CG/PCG can be easily executed without the factorization of the whole stiffness matrix, most of the implementation and preconditioning have been achieved in element or certain sub-domain levels. Hughes, Levit and Winget (1983a,1983b) may be the first people who introduced the idea of element-by-element process for the solution of linear systems of equations. Law (1986) developed a parallel CG algorithm by using the displacement (as well as force) vectors local to each processor and the corresponding global vectors. Carter, Sham and Law (1989) described a parallel implementation of the finite element method on a multiprocessor computer. A parallel element (or substructure) oriented CG procedure was employed to compute the displacements. Based on Law's work, Yalamanchili, Anand and Warner (1992) implemented a parallel PCG algorithm with a Jacobian preconditioning. Here the patterns of the matrix vector product were discussed. Chiang and Fulton (1992) put forward a PCG algorithm that was in a node-by-node pattern and executed on vector computers. The preconditioning was also Jacobian. Zhu and Qiao (1993) gave two PCG strategies in substructure level.

By means of Krylov subspace theory, Yang and Li (1993) depicted four solvers of linear algebraic equation with the large-scale coefficient matrix being sparsely inhabited. A PCG procedure was briefly described as an independent algorithm and pointed out to be executed in the YH-1 computer of China. The main contents of Chadha and Jr. Baugh (1996) are about a parallel PCG algorithm for structural analysis on a conventional Ethernet-connected workstation network. The performances on plane-elasticity problems are evaluated. The listed scheme should be executed after finite element modeling on each sub-domain. The local pre-conditioner assigned to each server was initially formed in another program, and was modified based on interface conditions during the starting steps of PCG. But there was no modification with stiffness matrix of each server.

It can be obviously found that most of PCG methods, whether being sequential or parallel, have been implemented with the combination of some domain decomposition technique(DDT). Of course, it is DDT that gives merits to PCG family. But there is difficulty for these schemes to directly solve those problems in which only the whole global stiffness matrix is given.

For real engineering problems, the users would rather give the global information, such as matrix of the whole structures, than show the design in detail. A lot of famous universal software for structural analysis already on hand is able to manage it. There are also some problems, such as the dynamic analysis on periodic or partially periodic structures, like large space flexible structures, the global stiffness matrix can be obtained easily (Hou and Zheng, 1997). In that situation, it is not necessary to modify the whole stiffness matrix. In the case of nonlinear structural analysis furthermore, the global matrix is the only object one has to confront. To solve these problems, parallel strategies of direct methods have been successfully implemented.

As a supplementary to mainstream research work on PCG approach, this paper develops a strategy. That strategy is implemented on fast Ethernet and is a real independent solver of linear system of equations. The rest content of this paper is arranged in four sections. The first describes the parallel environment and gives a strategy of PCG algorithm as an independent equation solver. The decomposition of matrix K is discussed in the second section, two partitions are demonstrated. The third section is on sparse matrix vector product. It is the extension of the previous section. Some opinions are put forward in the last section, based on our initial computational experiences.

IMPLEMENTATION OF PARALLEL PCG ALGORITHM

Parallel Environments

During parallel computing, the speedup and efficiency are two important indexes. They reflect the comprehensive performance of a parallel system and the corresponding algorithm. In order to have a good gain, one should attach importance to the performances of his node machines and local area network(LAN) before designing efficient algorithm.

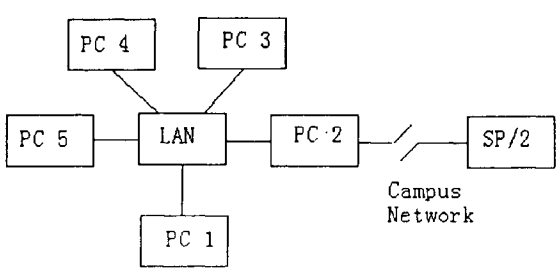

Fig 1 Parallel computer cluster

After careful survey on the development of parallel computing, we have set up a cluster system for research and application of parallel computation. The sketch is shown in Figure 1.

There are in the LAN 5 node machines, each of which is personal computer with CPU of Pentium 133. They are connected by SMC 100Mbps PCI network card and Intel Express 100BASE-TX switching Hub. This fast Ethernet adopts TCP/IP as network protocol. The Solaris 2.5 for X86 is chosen as operating system, and PVM (Parallel Virtual Machine) and MPI (Message passing Interface) as message transmitting platform. The programming language can be one of FORTRAN, C or C^{++}, which are all supported by Solaris for X86.

It is obvious that the distributed computing system has star-like topology and is homogeneous in architecture. By adding some workstations with high performance however, the architecture can be easily extended to be heterogeneous. In fact, our distributed system can be linked to the IBM SP/2 machine in the center of CERNET located in Tsinghua University through the campus network. More important, from the choice of the hardware, the operation systems and parallel computing platforms, one can find out the good flexibility of the system and so the transferability of the algorithms developed on it.

Scheme of PCG algorithm and Pre-conditioners

The algorithm in this paper is derived from that of Chadha and Jr. Baugh (1996). It is suitable for coarse-grained computing. A master-slave pattern is employed during the design of the principal computing process, although a pure node mode is also suitable. In fact, some processes have been programmed in the latter way.

Before listing the flow chart of our algorithm, a note on symbols is given at first. Subscripts e, m denote the code and total number of slave processes. The upper case and lower case symbols are used for global or local variables, which are respectively in the master and slave processes. Each process is executed on a personal computer. A guess for generalized displacement vector X_0 generates the initial values for the residual load vector R and residual displacement vector D. Their local counterparts, or their components, are respectively denoted as x, r, d. $\tilde{k}$ is the local pre-conditioner.

Now let's see the flow chart.

Step 0 : (a) *decompose K to k*
(b) *form* $\tilde{k}$
(c) *transfer f, k and* $\tilde{k}$

Step 1: (a) $x = x_0$
(b) $r = f - kx$
(c) $\tilde{k} = L \cdot L^{\mathrm{T}}$
(d) $d = (LL^{\mathrm{T}})^{-1} r$

Step 2: $\gamma_e = r^{\mathrm{T}} d$

Step 3: (a) **send** γ_e

if the first iteration

merge $\gamma = \sum_{e=1}^{m} \gamma_e$

else

merge $\gamma' = \sum_{e=1}^{m} \gamma_e$

if $\gamma' < tolerance$, *STOP*

$\beta = \gamma' / \gamma$

$\gamma = \gamma'$

(b) **receive** β

Step 4: if the first iteration

$p = d$

else

$p = d + \beta p$

Step 5: (a) **send** p

merge $P = \sum_{e=1}^{m} p$

(b) **receive** p

Step 6: $u = kp$

Step 7: (a) **send** u

merge $U = \sum_{e=1}^{m} u$

(b) **receive** u

Step 8: $\eta_e = p^{\mathrm{T}} u$

Step 9: (a) **send** η_e

merge $\eta = \sum_{e=1}^{m} \eta_e$

$\alpha = \gamma / \eta$

(b) **receive** α

Step 10: (a) $x = x + \alpha p$

(b) $r = r - \alpha u$

(c) $d = (LL^{\mathrm{T}})^{-1} r$

When $\tilde{k}^{-1} = I$, the above scheme degenerates to a parallel CG one. The focus of description is evidently put on slave process.

In this master-slave parallel pattern, a global quantity is evaluated on the client (executing the master process) by summing the components (*merge*) that each server (executing slave process) **sends**. The updated values are then returned to the respective servers. The client is thus involved only in operations between a **send** and a **receive,** all other tasks are performed on the servers. Step 0 is an exception and which will be discussed later in detail.

The computation flow is obvious. The vectors x, r, and d are initialized in step 1. Steps 2-10 are repeatedly performed until convergence is reached. While steps 1, 2, 4, 6, 8 and 10 consist only of computation on the servers, the times for steps 3, 5, 7 and 9 also include delays due to communication and synchronization that are required for server to **send** and **receive** components of the variables whose current values are to be computed on the client. All servers are synchronized at each *merge* since the client does summation only after it has received a message from each server.

As an initial edition, the pre-conditioner $\tilde{k}$ is chosen as unity matrix, the diagonal elements of a sub-matrix of $\tilde{k}$ noted as $\tilde{k}'$, and $\tilde{k}'$ itself, respectively. The latter two are also respectively called Jacobian or block-Jacobian preconditioning. No global pre-conditioner is to be formed or stored. Please refer to Figure 2(b).

MATRIX DECOMPOSITION

Because attached to domain decomposition process, most of the previous PCG strategies do not have step 0 as an independent module. Instead, some functions of the step are finished by the program of finite element analysis on sub-domain, and others are transacted in PCG module. For example, the modifications of $\tilde{k}$ and d have been done in steps 1 and 2 for each server according to the interface conditions (see Chadha and Jr. Baugh 1996). There is no necessary to divide stiffness matrix, and the load balance should be considered during domain decomposition.

When the finite element modeling has been constructed with the whole structure, the modifications are avoided. But one should have to divide the whole matrix and assign different parts to all the servers before computation. These are tasks of step 0. In order to develop an independent equation solver, step 0 can be either embraced by PCG algorithm as listed above, or treated in outside PCG algorithm. The former scheme will suffer in its efficiency, because the latter one can omit the time used by the independent program in computing speedup. The latter plan however, should not only execute the independent module in advance, but also pay attention to the alignment between two modules. In this paper, step 0 is embedded in the whole algorithm so as to enhance its independence and capability.

Let's see how many divisions may be confronted. The decomposition should be implemented on the base of load balance between different servers, therefore it should be designed with operations the matrix is experienced. For sparse matrix, there need at least two times of decomposition. One is done for matrix vector product, the other for preconditioning. From different divisions, we choose two natural forms as shown in Figure 2.

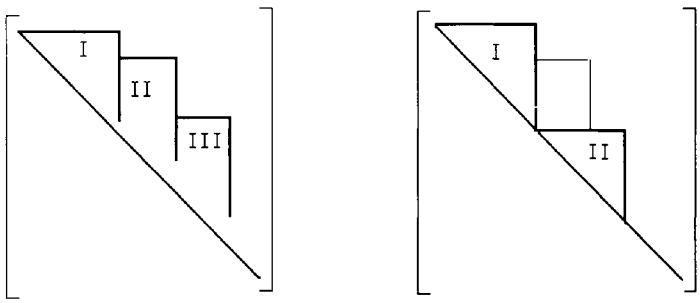

(a) For matrix-vector product (b) For preconditioning

Figure 2 Two types of matrix decomposition

In the first division, the numbers of elements assigned to each server are determined by

$$S = nwk / nhost\_1, \quad \text{or} \quad S = 1 + nwk / nhost\_1$$

where *nwk*, *nhost*_1 are the total element number of the global matrix and the number of servers, respectively. The numbers of elements assigned to servers are equal or almost equal to each other, but the corresponding column numbers are different. In fact some columns may be partitioned to different servers when a very large n appears.

The second partition constructs block-diagonal pre-conditioners for servers, and the dimensions of these pre-conditioners are almost the same. The number of columns of each local pre-conditioner is (n is the dimension of the matrix K as mentioned before)

$$T = n / nhost\_1, \quad \text{or} \quad T = 1 + n / nhost\_1$$

That can usually ensure good load balance among different servers when solving the following preconditioning equation

$$\tilde{k} d = r \tag{2}$$

SPARSE MATRIX VECTOR PRODUCT

Matrix vector product has many applications in dynamic analysis of engineering structures. It is one of the most dominant processes for PCG algorithm, and engrosses much of the time in executing the whole algorithm. Therefore it is very important for the success of PCG method to implement the procedure of matrix vector product satisfying load balance.

When a fully inhabited matrix is concerned, the load balance is relatively easy to reach and there are several mature schemes of matrix vector product, see Sun (1995). Unfortunately however, it is not so easy to satisfy load balance when a sparse matrix is confronted. In this paper, we decompose the coefficient matrix as in Figure 2(a) and compute the product accordingly. As mentioned above, the differences in the element numbers of the servers are in general not greater than 1, the load balance could then be considered achieved.

There is another matrix decomposition and so another strategy of matrix vector product. The product is evaluated along the direction parallel to the diagonal of the matrix. In other words, the diagonal elements are firstly multiplied by components of the right-hand vector, then the off-diagonal elements are dealt with and so on. It is complicated for programming, so is not adopted at this initial stage and will not be discussed here in detail.

DISCUSSION

Based on the above consideration, a PCG algorithm has been programmed with three preconditioning versions. One is no preconditioning, the other two are Jacobian and block Jacobian preconditioning, respectively. By the program, we have computed some simple examples. At first, the equations are solved with diagonal dominant coefficient matrices that are specially designed. Secondly, the deflection analysis on a type of truss structure is carried out.

From the examples, we can have some understanding on the time distribution and the speedup of the developed algorithm. It can also be deduced that:

1) the PCG converges very fast for those diagonal dominant matrices;
2) the condition number of the stiffness matrix of some trusses in large flexible space structures is very large, and PCG method may fail to accomplish static analysis, to say nothing of dynamic analysis.

Therefore, work in the future is to construct efficient preconditioning that is suitable for parallelism. The incomplete Cholesky factorization may give us better pre-conditioners.

We also find that from our other computing experiences that the LAN system does can be easily constructed with already computers and expanded with lower cost. Its performance is stable. We are confident in that cluster technology will bring about bright prospect for parallel computation.

REFERENCES

Carter W.T. Jr., Sham T.L. and Law K.H. (1989). A parallel finite element method and its prototype implementation on a hypercube. *Computers and Structures* **31:6,** 921-934.

Chadha H.S. and Jr. Baugh J.W. (1996). Network-distributed finite element analysis. *Advances in Engineering Software* **25,** 267-280.

Chiang K.N. and Fulton R.E. (1992). Parallel transient finite element analysis. *Computers and Structures* **42:5,** 733-739.

Hestenes M. R. and Stiefel E. (1952). Methods of conjugate gradients for solving linear systems. *J. Res. Nat. Bureau Stand.*, **Section B,** 409-436.

Hou Z.C. and Zheng Z.C. (1997). Partial assemblage FEM and Iterative algorithm for static and dynamic analysis of a type of structures. *Chinese Journal of Engineering Mechanics* **14:4**, 11-17.

Hughes T.J.R. Levit I. And Winget J. (1983a). Element-by-element implicit algorithm for heat conduction. *Journal of Engineering Mechanics* **109: 2,** 576-585.

Hughes T.J.R. Levit I. And Winget J. (1983b). An element-by-element solution algorithm for problems of structural and solid mechanics. *Comput. Meth. Appl.Mech. Engng* **36,** 241-254.

Law K. H. (1986). A parallel finite element solution method. *Computers and Structures* **23,** 845-858.

Sun J.C., Zhang L. B. and Chi X.B. et al (1996). Parallel computation on Network and distributed programming environment. Beijing: China Science Press.

Yalamanchili K. K., Anand S. C. and Warner D.D. (1992). Three-dimensional finite element analysis on a hypercube computer. *Computers and Structures* **42:1,** 11-20.

Yang Y.X. and Li X.M. (1993). The Krylov subspace methods to solve large sparse problems on supercomputers. *Journal of National University of Defense Technology* **15:3,** 51-55.

Zhu J.F. and Qiao X. (1993). Parallel iterative solutions for FEM on multi-transputer systems. *Chinese Journal of Numerical Computation and Computer Applications* **3**,192-199

Zois D. (1988). Parallel processing techniques for FE analysis: system solution. *Computers and Structures* **28:2**, 261-274

This Page Intentionally Left Blank

COMPUTER AIDED DESIGN FOR VIBRATION ISOLATION SYSTEMS WITH DAMPED ELASTIC STOPS

H. Y. Hu and F. X. Wang

Institute of Vibration Engineering, Nanjing University
of Aeronautics and Astronautics, Nanjing, 210016, China

ABSTRACT

From the viewpoint of nonlinear dynamics, a systematic design approach is proposed for the vibration isolation systems with a damped elastic stop. The approach consists of three steps. The first one is to design a slightly damped linear isolation system according to the linear theory of vibration isolation. Then, the optimal parameters for the damped elastic stop can be chosen in a region given according to the singularity analysis of the primary resonance. Finally, the continuation scheme for periodic motion and the interpolated cell-to-cell mapping for the global behavior of the system are used to test and evaluate the design. The approach enables one to make use of damping in the stop to attenuate the resonance transmissibility, while keeping very low transmissibility in the frequency range of vibration isolation.

KEYWORDS: vibration isolation, nonlinear vibration, elastic stop, design, primary resonance

INTRODUCTION

Elastic stops have been widely used to limit the excessive deformation of the elastic component of a vibration isolator in engineering. As reviewed in Hu (1996), no theoretical design approach for this kind of vibration isolators has been reported in archival publications, partially because the combined restoring force of the elastic component and the stop in the vibration isolator is no longer linear with respect to the large deformation. In the current

design of the vibration isolator with an elastic stop, the stiffness and damping of the main elastic component is determined first on the basis of linear theory of vibration isolation. Then, the elastic stop is empirically designed and modified through a series of tests. Such a design procedure is not only very expensive, but also dangerous in the test when the nonlinear dynamics of the vibration isolation system is totally unknown.

The primary aim of this paper is to present a theoretical design approach for the vibration isolation system with a damped elastic stop from the view point of nonlinear dynamics. As the system is piecewise linear, i.e., nonlinear by nature, it is not possible to gain insight into the complicated dynamics of the system by using any analytical approach. Thus, analytical approaches and computational approaches are combined to form a systematic and practical design approach.

MECHANICAL MODEL AND PRIMARY RESONANCE

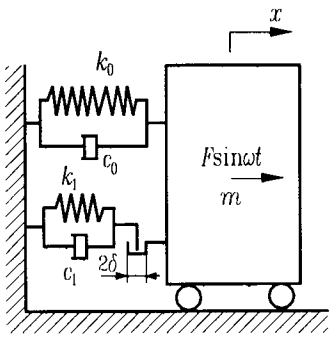

Figure 1: Mechanical model of the vibration isolation system

Consider the vibration isolation system shown in Figure 1, where a damped elastic stop with symmetric clearance is mounted so that the combined restoring force in the system is piecewise linear when $|x|$, the absolute value of the displacement, exceeds the clearance δ. Using the dimensionless time and displacement, as well as a set of dimensionless positive parameters

$$\begin{cases} \tau = \sqrt{\dfrac{k_0}{m}}t, & y = \dfrac{x}{\delta}, & \zeta_0 = \dfrac{c_0}{2\sqrt{mk_0}}, & \zeta_1 = \dfrac{c_1}{2\sqrt{mk_0}}, \\ \mu = \dfrac{k_1}{k_0}, & f = \dfrac{F}{k_0\delta}, & \lambda = \omega\sqrt{\dfrac{m}{k_0}}, \end{cases} \tag{1}$$

one can write out the differential equation of motion of the system

where the dot represents the derivative with respect to the dimensionless time τ and

$$g(y)=\begin{cases} y, & |y|\le 1, \\ (1+\mu)y-\mu\,\mathrm{sgn}(y), & |y|>1; \end{cases} \tag{3}$$

$$h(\dot{y})=\begin{cases} 2\zeta_0\dot{y}, & |y|\le 1, \\ 2(\zeta_0+\zeta_1)\dot{y}, & |y|>1; \end{cases} \tag{4}$$

are the piecewise linear forces of elastic components and damping, respectively.

To provide the theoretical background for the design, it is essential to study the nonlinear primary resonance of the system when $\max|y|>1$. If the parameters ζ_0,ζ_1,μ and f are small, the primary resonance can be approximated, through the use of average approach, as

$$y(\tau)=a(\tau)\cos[\lambda\tau+\varphi(\tau)], \tag{5}$$

where $a(\tau)$ and $\varphi(\tau)$ yield

$$\dot{a}=q(a)-\frac{f}{2\lambda}\cos\varphi, \qquad \dot{\varphi}=\frac{1-\lambda^2}{2\lambda}+\frac{p(a)}{\lambda a}+\frac{f}{2\lambda a}\sin\varphi, \tag{6}$$

$$\begin{cases} p(a)=\dfrac{\mu a}{2\pi}(2\varphi_0-\sin 2\varphi_0), \\ q(a)=\dfrac{a}{\pi}[\xi_0\pi+\xi_1(2\varphi_0-\sin 2\varphi_0)], \qquad \varphi_0=\arccos(\dfrac{1}{a}), \qquad a>1. \end{cases} \tag{7}$$

From Eqn.6, one has the relationship between the amplitude of the steady state resonance and the excitation frequency

$$[p(a)+\frac{a}{2}(1-\lambda^2)]^2+\lambda^2q^2(a)-(\frac{f}{2})^2=0. \tag{8}$$

To classify the types of the primary resonance, one can focus on the case of $a>>1$ and let $z=1/a<<1$. Using the Taylor expansion of order three with respect to z, one obtains the bifurcation equation of the primary resonance from Eqn.8 (see Wang and Hu, 1997)

$$G(z,\eta,\alpha_1,\alpha_2)\equiv[(z-z^3/6)+\eta]^2+\alpha_1^2-\rho\alpha_1^2z+\alpha_2z^2=0, \tag{9}$$

where

$$\alpha_1 = \frac{\pi\lambda\xi_1(1+\sigma)}{2\mu}, \qquad \alpha_2 = [\frac{4\alpha_1}{\pi(1+\sigma)}]^2 - (\frac{\pi f}{4\mu})^2, \tag{10}$$

$$\eta = \frac{\pi}{4}(\frac{\lambda^2 - 1}{\mu} - 1), \qquad \rho = \frac{8}{\pi(1+\sigma)}, \qquad \sigma = \frac{\zeta_0}{\zeta_1}. \tag{11}$$

According to the singularity theory, one can prove that Eqn.9 is a universal unfolding of the normal form $[(z - z^3/6) + \eta]^2$ with two unfolding parameters α_1 and α_2. The transition set of G consists of the following two subsets.

(1) Bifurcation set $B = B_1 \cup B_2 \cup B_3$:

$$B_1: \alpha_1 = 0, \qquad B_2: \alpha_2 = \frac{\rho^2}{4}\alpha_1^2, \qquad B_3: \alpha_2 = \frac{1}{8}[4\rho\alpha_1^2 - 1 \pm \sqrt{1 - 16\alpha_1^2 + 8\rho\alpha_1^2}]. \tag{12}$$

(2) Hysteresis set H:

$$H: \alpha_1 = \pm\sqrt{\frac{\alpha_2 z^4 + [\alpha_2 + (1 - z^2/2)^2]^2}{(\rho z - 1)z^2}}, \qquad \alpha_2 = \frac{1}{2}[-b \pm \sqrt{b^2 - 4c}], \tag{13}$$

where

$$\begin{cases} b = z^4 + 2(1 - \dfrac{z^2}{2})^2 + \dfrac{2(1-\rho z)z}{\rho}(1 + \dfrac{z^2}{2}), \\ c = (1 - \dfrac{z^2}{2})^3[(1 - \dfrac{z^2}{2}) + \dfrac{2(1-\rho z)z}{\rho}]. \end{cases} \tag{14}$$

It can be proved that the hysteresis set H intersects with the bifurcation set B only once at the subset B_3.

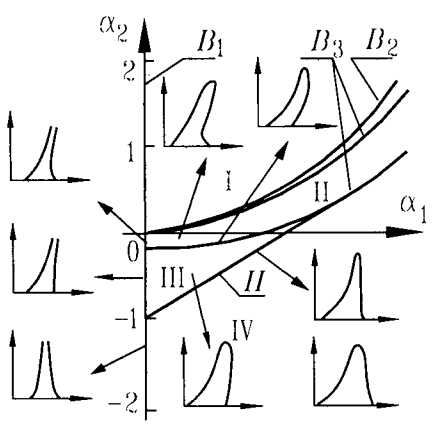

Figure 2: Transition set of G with respect to unfolding parameters α_1 and α_2

Now, one can check the possible types of the primary resonance for $\alpha_1 > 0$, which is the natural consequence of $\zeta_0 > 0$ and $\zeta_1 > 0$ in practice. Figure 2 shows a typical transition set of these two unfolding parameters. The transition set divides the right half plane of (α_1, α_2) into 4 regions as shown in Figure 2. In each region, the amplitude-frequency curve of the primary resonance looks the same qualitatively. This figure, thus, enables one to choose an appropriate combination of unfolding parameters so that the vibration isolation system possesses the desired qualitative behavior in primary resonance.

It should be emphasized at the end of this section that though the above analysis is made for a piecewise linear system on the assumption of weak nonlinearity, i.e., the parameters μ and ζ_1 are small, the numerical simulations in Wang and Hu (1997) showed that the results were valid even when μ and ζ_1 were not small.

DESIGN APPROACH

The basic idea of present approach is to design a linear vibration isolation system with very small damping first, and then an elastic stop with large damping. In the working frequency range, the slightly damped vibration isolation system has required vibration transmissibility. Once the vibration isolation system undergoes the primary resonance somehow, both the elastic stop and the large damping reduce the vibration amplitude and remove the jumping phenomenon that may occur for a harmonically forced nonlinear oscillator.

3.1 *Design of primary system*

The vibration isolation system without any stop is referred to as the primary system hereinafter for brevity. The vibration transmissibility of the primary system yields

$$T = \sqrt{\frac{1 + (2\xi_0\lambda)^2}{(1-\lambda^2)^2 + (2\xi_0\lambda)^2}}, \tag{15}$$

where only two dimensionless parameters λ and ζ_0 are to be designed. For a linear vibration isolation system in traditional sense, the vibration transmissibility in resonance can only be attenuated by increasing the damping ratio ζ_0. For the vibration isolation system with an elastic stop, however, the task of attenuating the vibration transmissibility in the case of resonance can be left to the damped stop. Hence, a very small damping ratio ζ_0 can be chosen in the design of primary system in order to avoid the system impacting the stop when the system starts running, see Hu (1996). In the case of $\zeta_0 < 0.1$ and $\lambda > 2$, the stiffness of the main elastic component can be determined by using the following approximation of Eqn.15

$$\lambda \geq \sqrt{1 + 1/T}\ . \tag{16}$$

3.2 *Design of Damped Elastic Stop*

3.2.1 *Preliminary Design*

Given the dimensionless excitation frequency λ, the damping ratios ζ_0 and ζ_1, the system parameters to be designed are only μ and f. These two parameters appear in the expressions of unfolding parameters α_1 and α_2, and hence, follow the selection of the two unfolding parameters. In principle, any parameter combination of α_1 and α_2 in region IV in Figure 2 makes sure that the frequency-amplitude curve of primary resonance does not have jumping. Thus, an arbitrary combination of (α_1, α_2) in region IV can be chosen to determine the corresponding parameters μ and f, provided that the vibration transmissibility is acceptable.

A great number of numerical simulations showed that the stiffness ratio μ should not be too large. As shown in Figure 3, the function of stop is very obvious in the lower frequency range. The response amplitude goes down very rapidly in the beginning of the increase of μ, and then changes not very much later until very complicated dynamics happens. For the sinusoidal excitation of high frequency, the response amplitude has a peak as shown in Figure 4. It is smaller than the initial value only when μ is very large. As a result, an excessive stiffness ratio μ is harmful.

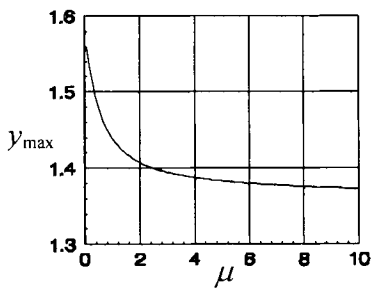

Figure 3: Maximal displacement versus stiffness ratio when $\lambda = 0.5$

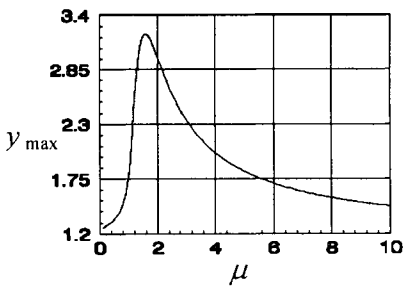

Figure 4: Maximal vibration amplitude versus stiffness ratio when $\lambda = 1.4$

Moreover, the dimensionless excitation amplitude f defined in Eqn.1 is inversely proportional to the clearance δ when the excitation amplitude F is fixed. So, the clearance δ can be determined from α_2. If the clearance is too large, the stop can not be in function. If too small, the vibration may become nonlinear and then undergoes a sub-harmonic resonance in working frequency range.

In summary, the stiffness of the stop should not be very large and the clearance should be appropriate. So, it is necessary to optimize these two parameters, or namely two unfolding parameters in region IV in Figure 2.

3.2.2 *Optimization for Parameters*

Now f, the dimensionless excitation amplitude, is taken as the design variable to look for the minimal stiffness ratio of an elastic stop such that the requirement for vibration transmissibility in the primary resonance is met. The constraint conditions for this problem are as follows:

(a) the parameter boundary where the forced vibration of the system is linear in the working frequency range;

(b) the minimal stiffness ratio of the stop for given resonance transmissibility at different excitation amplitudes (or clearances);

(c) the hysteresis set H that guarantees no jumping and no hysteresis in the primary resonance.

It is obvious that condition (c) has been given in Eqn.13. Hence, only the first two conditions are discussed hereafter.

By eliminating μ in the expressions of α_1 and α_2 in Eqn.10, one obtains

$$\alpha_2 = \frac{64\lambda^2\zeta_1^2 - \pi^2 f^2}{4\pi^2\lambda^2\zeta_1^2(1+\sigma)^2}\alpha_1^2. \tag{17}$$

The forced vibration of the system in the working frequency range is linear if the following inequality holds true

$$f < f_{\max} \equiv \sqrt{(1-\lambda_w{}^2)^2 + (2\xi_0\lambda_w)^2}, \tag{18}$$

where λ_w is the ratio of working frequency to the natural frequency of the primary system. Given $f_{\max}$, the critical value of Eqn.18, a parabola denoted by $f_{\max}$ in Figure 5(b) can be determined from Eqn.17. This is the parameter boundary of condition (a).

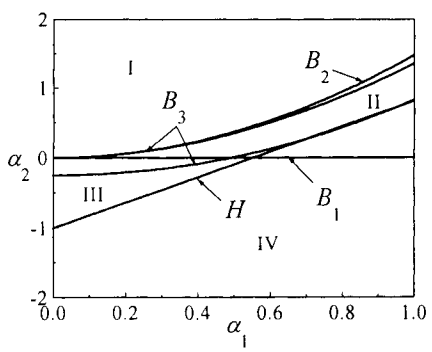

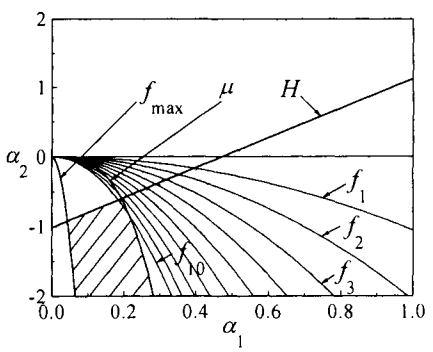

(a) Transition set of unfolding parameters (b) Optimal parameter region

Figure 5: Transition set and optimal parameter region in (α_1, α_2) plane when $\zeta_0 = 0.01$, $\zeta_1 = 0.2$, $\lambda_w = 2.75$ and $a_a = 1.2$ at $f = 0.52$

In the fourth quadrant of the (α_1, α_2) plane, i.e., $\alpha_1 > 0$ and $\alpha_2 < 0$, a contour chart shown in Figure 5(b) can be obtained from Eqn.17 if $f = f_i = \text{const.}$, $i = 1,2,...$ are taken respectively. It is easy to see from Eqn.10 that $(\alpha_1, \alpha_2) \to (0, 0)$ when $\mu \to +\infty$. Thus, the intersection of a contour curve with the hysteresis set H in Figure 5(b) gives the maximal stiffness ratio of stop, which guarantees no jumping and no hysteresis in the frequency-amplitude curve of the primary resonance. In addition, Eqn.10 implies that $\alpha_2 \to -\infty$ when $f \to +\infty$ or $\delta \to 0$ equivalently.

To derive condition (b), it is necessary consider the maximal amplitude of the primary resonance. By differentiating Eqn.8 with respect to λ and imposing $\frac{\mathrm{d}a}{\mathrm{d}\lambda} = 0$, one has

$$\lambda^2 = 1 + \frac{2}{a} p(a) - \frac{2}{a^2} q(a)^2 . \tag{19}$$

Substituting Eqn.19 into Eqn.8 yields

$$[1 + \frac{2}{a} p(a) - \frac{1}{a^2} q(a)^2] q(a)^2 - (\frac{f}{2})^2 = 0 . \tag{20}$$

Solving Eqn.20 for the stiffness ratio, one obtains

$$\mu = \frac{\pi}{2} \{[\frac{f}{2q(a)}]^2 + [\frac{q(a)}{a}]^2 - 1\} [\arccos(\frac{1}{a}) - \frac{\sqrt{1 - 1/a^2}}{a^2}]^{-1} . \tag{21}$$

If the acceptable dimensionless deformation of the vibration isolator is specified as a_a when $f = f_a$. Substituting the vibration amplitude a in Eqn.21 with a_a, one obtains the minimal stiffness ratio of the stop that guarantees the vibration transmissibility for given f_a. Let $\mu_{\min}$ be the stiffness ratio. Then, $\mu_{\min}$ results in a pair of (α_1, α_2) from Eqn.10. For other f, one can make use of the fact that the maximal amplitude of the primary resonance is approximate to the amplitude in Eqn.8 when $p(a) + a(1 - \lambda^2)/2 = 0$, and proportional to f approximately. Thus, one obtains the change of $\mu_{\min}$ with variation of f from Eqn.21 by substituting $a = a_a f / f_a$ into Eqn.21, and then has a curve denoted by $\mu_{\min}$ shown in Figure 5(b).

As shown in Figure 5b, the region of optimal design parameters is the shaded one surrounded by the boundary of linear vibration, the boundary of minimal stiffness ratio of stop and the hysteresis set *H*. In summary, the parameters f and μ should be chosen such that the system does not have the excessive vibration transmissibility and jumping in the resonance frequency range. Hence, the design of dynamic characteristics of the system is independent, and will not affect the vibration transmissibility of the primary system designed according to the linear theory of vibration isolation in the working frequency range.

3.3 *Numerical Verification*

The above design for the parameters of the damped elastic stop is based on the analysis of the primary resonance. Very often, a harmonically forced nonlinear system undergoes the sub-harmonic or superharmonic resonance, or vibrates chaotically when the system parameters are slightly perturbed or the initial state of the system does not fall into the basin of attraction of the designed state. Thus, it is necessary to verify the system design numerically from the viewpoint of both local and global nonlinear dynamics. The numerical verification includes the following steps.

3.3.1 *Accurate Computation of Primary Resonance*

At this step, the excitation frequency is taken as the control parameter and the periodic vibration designed is computed by using the continuation technique developed in Wang and Hu (1996). If the analytic result greatly deviates from the numerical one, a new parameter combination in the optimal parameter region should be taken to check the results. If the new result is still not good, the constraint damping ratio ζ_1 can be modified and the design in subsection 3.2 should be repeated.

3.3.2 *Analysis of Global Dynamics*

One of the most important features of a nonlinear dynamic system is the coexistence of multiple steady state motions evolving from different initial states, say, three coexisting periodic motions or two coexisting periodic motions and a chaotic motion of large amplitude. It is obvious that the continuation technique is not able to determine all these motions. So, it is necessary to examine the effect of the initial states on the system dynamics when the system parameters are fixed. This can be accomplished by using the technique of interpolated cell-to-cell mapping or the technique developed in Wang and Hu (1998). For the sake of reliability, it is better to make the analysis of cell-to-cell mapping in a large region of the Poincare section. The size of convergence criterion in the cell-to-cell mapping should not be too large in order that the results are reliable. If coexisting steady state vibrations are found in the cell-to-cell mapping, the amplitude of each vibration should be examined. Once the expected vibration is not tolerable, the design has to be modified. Otherwise, the possibility of jumping phenomenon should be examined in order that the isolated equipment will not undergo dangerous shock due to the jumping when the excitation frequency varies. If there is a wide frequency range wherein multiple steady state vibrations exist, the robustness of the expected vibration should be examined. The robustness includes the stability of expected vibration, the stability redundancy of the vibration against the perturbation of system parameters and initial states. For this purpose, the following concepts will be used in the evaluation of a design.

(a) The stability redundancy index is defined as the distance between the largest module of the eigenvalue of the linearized Poincare mapping and 1, i.e.,

$$R_s \equiv \left|\left|\nu\right| - 1\right| \times 100\%, \tag{22}$$

where ν is the eigenvalue with the largest module.

(b) The redundancy index against the perturbation of a system parameter p is defined as

$$R_p = (1 - \left|\frac{\left|\left|\nu_2\right| - \left|\nu_1\right|\right|}{\Delta p}\right|) \times 100\%, \tag{23}$$

where ν_1 and ν_2 are the eigenvalues with the largest modules before and after the variation of p.

(c) The redundancy index of a basin of attraction is defined as

$$R_a = \frac{\pi \left\| Y_F - Y_b \right\|_2^2}{A} \times 100\%, \tag{24}$$

where A is the area of the Poincare section of concern, Y_F is the fixed point, Y_b is the point which is on the boundary of basin of attraction and most close to the fixed point. The value of R_a reflects the robustness of a basin of attraction.

3.3.3 *Analysis of Bifurcated Periodic Motions*

The result of cell-to-cell mapping provides a set of initial fixed points for the continuation of periodic motions. At this step, larger meshes can be used so as to find the number and locations of the periodic motions efficiently. The technique developed in Wang and Hu (1998) is suggested to determine the fixed points of node-saddle type since they can hardly be determined by using cell-to-cell mapping. Once the initial fixed points are given, several kinds of continuation techniques can be used. Among them, the method suggested in Foal and Thompson (1991) is relatively simple.

The sub-harmonic number of the resonance of a piecewise linear system depends on μ, the stiffness ratio of the elastic stop, but the occurrence of a sub-harmonic resonance depends mainly on damping. In the traditional design, small damping is usually used to guarantee low vibration transmissibility in high frequency range, and no damping is artificially arranged in the elastic stop. Thus, the sub-harmonic resonance is likely to occur. In the present design, large damping will be arranged in the elastic stop to avoid the sub-harmonic resonance effectively.

A NUMERICAL EXAMPLE

For simplicity, an example is discussed here in the form of dimensionless parameters. The damping ratio of the primary system of concern is $\zeta_0 = 0.01$. It is required that the vibration

transmissibility at $\lambda_w = 2.75$ should be 0.2, the acceptable vibration amplitude should be 1.2 for $f = 0.52$, and the vibration transmissibility in primary resonance should be $T < 5.0$.

The region of the optimal parameters for this system is shown in Figure 5b when the damping ratio of stop was set to $\zeta_1 = 0.2$. If two unfolding parameters were chosen as $\alpha_1 = 0.16$ and $\alpha_2 = -1.05$, there followed $f = 2.73$ and $\mu = 2.06$. The corresponding frequency-amplitude curve of the primary resonance is shown in Figure 6. It is easy to verify from Figure 6 that $T \approx 2.81 < 5.0$. In the continuation of the periodic motion, two turning points were observed when $\lambda \in [0.5045, 0.5054]$. In this frequency range, there exist three periodic motions. As shown in Figures 7, two of these periodic motions are stable, while the other is unstable. The multiplicity of these periodic motions exists in a very narrow frequency range. Even though there is a jumping between the stable periodic motions, the variation of the vibration amplitude in jumping is very small.

The global dynamics of the system in the Poincare section of [-4,0] × [-2.4,2.4] was analyzed by using cell-to-cell mapping approach at $\lambda = 0.5053$. The result is shown in Figure 8, where two fixed points represent the above-mentioned stable periodic vibrations. The redundancy indexes of these two stable fixed points are as following. The first fixed point corresponds to $R_s = 72.5\%$, $R_\mu = 64.13\%$, $R_f = 53.56\%$ and $R_a = 0.32\%$, and so does the second fixed point to $R_s = 39.1\%$, $R_\mu = 95.31\%$, $R_f = 94.41\%$ and $R_a = 5.58\%$. It is easy to see that all the redundancy indexes of the second fixed point are relatively larger. Compared with the first fixed point, the second fixed point is more robust. This assertion was verified in the continuation of these periodic motions. Finally, the cell-to-cell mapping was made for the system when the excitation frequency was fixed at $\lambda = 0.5$, 0.75 , 1.0 , 1.25, respectively. As expected, the only periodic motion found is the motion of period 1. In addition, no sub-harmonic resonance was found when the excitation frequency was set as multiplication of natural frequency of the linearized system.

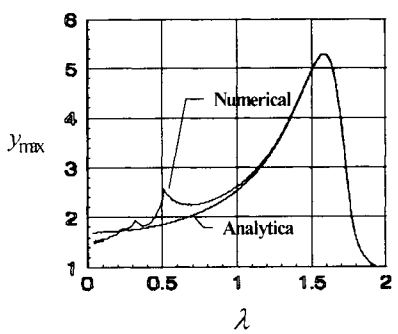

Figure 6: Frequency-amplitude curves of primary resonance when $\zeta_1 = 0.2$

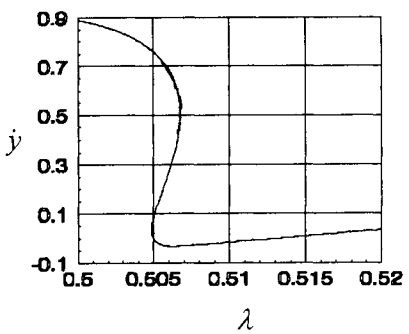

Figure 7: The Poincare velocity versus excitation frequency curve when $\zeta_1 = 0.2$

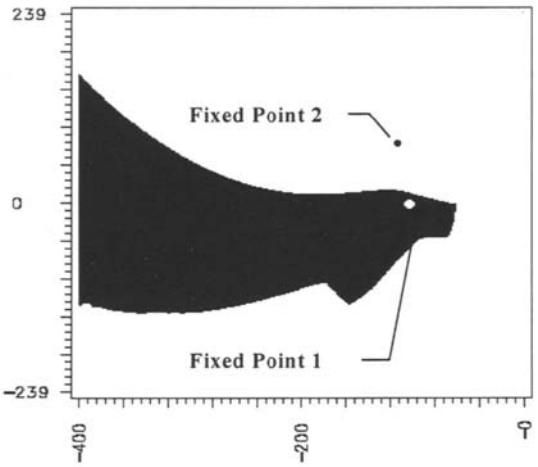

Figure 8: The Poincare section of basins of attraction of two periodic vibrations when $\lambda = 0.5053$

If a large stiffness ratio of the stop, say, $\mu = 15.0$ was chosen, a chaotic vibration was observed in the cell-to-cell mapping. The Poincare section of corresponding strange attractor is shown in Figure 9. In this case, the system lost the function of vibration isolation. Hence, it is very dangerous to increase the stiffness of the elastic stop intuitively in order to limit the vibration amplitude. However, the vibration amplitude can be greatly reduced if the damping in the elastic stop is increased. For instance, when the damping in the above system was increased to $\zeta_1 = 0.4$, the maximal amplitude was greatly reduced as shown in Figure 10. Moreover, only a period 1 motion was found in the cell-to-cell mapping.

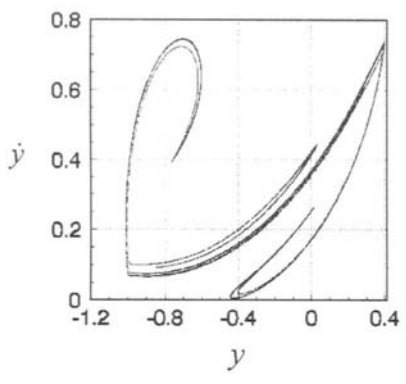

Figure 9: The Poincare section of a strange attractor when $\mu = 15.0$ and $\zeta_1 = 0.2$

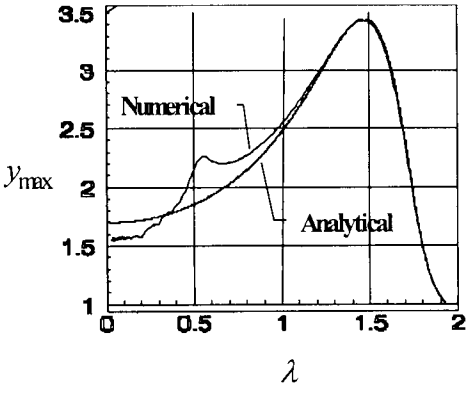

Figure 10: Frequency-amplitude curves when $\mu = 2.06$ and $\zeta_1 = 0.4$

CONCLUSIONS

A systematic design approach is suggested, by integrating several analytical and numerical approaches of nonlinear dynamics together, for the vibration isolation system with a damped elastic stop. This design approach has satisfied accuracy and reliability so that a great number of tests can be avoided. Both the numerical simulation and real test showed that the design of the vibration isolation system can greatly reduce the vibration transmissibility in the frequency range of resonance through the use of damping in the stop and keep very low vibration transmissibility in the working frequency range.

ACKNOWLEDGMENTS

This work was supported in part by the National Natural Science Foundation of China under Grant No. 59625511. The authors wish to thank Dr. Dongping Jin and Miss Wenfeng Zhang for their patient assistance during the research.

REFERENCES

1. Foal S. and Thompson J.M.T. (1991). Geometrical Concepts and Computational Techniques of Nonlinear Dynamics. *Computer Methods in Applied Mechanics and Engineering* **89**: 381-394.
2. Hu H.Y. (1995a). Simulation Complexities in the Dynamics of a Continuously Piecewise-Linear Oscillator. *Chaos, Solitons and Fractals* **5:11**, 2201-2212.
3. Hu H.Y. (1995b). Detection of Grazing Orbits and Incident Bifurcations of a Forced Continuous, Piecewise-Linear Oscillator. *Journal of Sound and Vibration* **187:3**, 485-493.
4. Hu H.Y. (1996). Design of Elastic Constraints from Viewpoint of Nonlinear Dynamics. *Chinese Journal of Mechanical Engineering* **9:2,** 135-142.
5. Wang F.X. and Hu H.Y. (1996). Calculating Accurate Periodic Solution of Piecewise-Linear Systems. *Transactions of Nanjing University of Aeronautics and Astronautics* **13:2**, 142-146.
6. Wang F.X. and Hu H.Y. (1997). Bifurcations of Primary Resonance of Harmonically Forced Symmetrically Piecewise-Linear Systems. *Journal of Nanjing University of Aeronautics and Astronautics* **29:3**, 283-288.
7. Wang F.X. and Hu H.Y. (1998). An Algorithm for Locating Coexisting Periodic Motions of Nonlinear Oscillators. *Chinese Journal of Applied Mechanics* **15:1**, 105-108.

This Page Intentionally Left Blank

CALCULATION OF THIN PLATES ON STATISTICAL NON－UNIFORM FOUNDATIONS

Yi Huang, Yuming Men and Guansheng Yin

Department of Basic Sciences, Xi'an University of Architecture and Technology, Xi'an 710055, P. R. China

ABSTRACT

In this paper, the calculation methods of reliability of structure (plate)－medium (soil) interaction are presented. Based on reliability theory, calculation methods of reliability of thin plates on statistical nonhomogeneous foundation are studied. Calculation formulas of reliability of elastic thin plates on Winkler, elastic half-space and two-parameter foundation are developed. The calculation procedure is further demonstrated by examples of plates with four free edges and the plates with four-simply supported edges.

KEYWORDS

Statistical nonhomogeneous foundation, thin plates, reliability calculation, Winkler foundation, elastic half-space, two-parameter foundation

INTRODUCTION

Thin plates on elastic foundations are widely employed in engineering. Many applications, such as raft foundation, road pavement, airport runway, etc. can be calculated by reducing them to thin plates on an elastic foundation; that is the typical problem of structure-medium (soil) interaction. Concerning the calculation of plate on an elastic foundation, the certainty analysis method has been used, i. e. the physical parameters, geometrical dimensions of plate and foundation properties are considered as determinate factors, and actual variabilities of them are considered through so-called "safety factor". Actually, each kind of parameter has a relatively large variability because the foundation (soil) is highly dispersed, so it should be considered as a statistical nonhomogeneous medium, that is a key to reliability calculation of structure－medium interation. On the other hand, there are also variabilities in varying degrees for material properties and

geometrical dimension of plates. This leads to uncertainty of the actual parameters that is difficult to represent by the classical "safety factor". Due to the lack of quantitative analysis of variability effect of all kinds of parameters on the deformation and strength of thin plates, unreasonable errors are caused in the design of foundation plate structures. Therefore, in order to reasonably design the foundation plates, it is very important to study the effects of all kinds of uncertain parameters on the deformation and internal force of the thin plates. So it is inevitable to introduce reliability calculation of structure — soil interaction.

Recently, the fast development of reliability theory provides a powerful method to study the variable effects of the parameters on the structural internal force and deformation, and the reliability theory has been used in structural design. But up till the present moment there are not many papers dealing with reliability calculation of structure—soil interaction at home and abroad. In this paper, the reliability theory of plate—soil interaction is discussed. Based on reliability theory, the reliability calculation of thin plates on elastic foundation is studied by considering the foundation as a statistical nonhomogeneous medium. The calculation procedure is further demonstrated by examples of a plate with four free edges and a plate with four simply supported edges. In fact , this paper presents reliability calculation method of structure-medium (soil) interaction.

RELIABILITY CALCULATION OF THIN PLATES ON STATISTICAL NON-HOMOGENOUS FOUNDATION

Reliability calculation of thin plates on Winkler foundation

Winkler model is one of the simplest linear elastic foundation models. Although it has some theoretical drawbacks , it is still used in current engineering because of its simplicity.

According to Winkler model, the deflection surface differential equation of elastic thin plates is

$$\Delta^4 W + \frac{k}{D} W = \frac{q}{D} \tag{1}$$

where $\Delta^4(\,;)$ is symbol of the double Laplacian, W is deflection of the thin plate, k is modulus of the foundation, q is load of the plates, $D = \dfrac{Et^3}{12(1-\mu^2)}$, h is thickness of the plate, μ is Poisson's ratio of the plate material, and E is modulus of elasticity of the plate material.

Once the deflection equation of plates is solved, the bending moment of plates can be obtained by the following equations:

$$\left.\begin{aligned} M_x &= -D\left(\frac{\partial^2 W}{\partial x^2} + \mu \frac{\partial^2 W}{\partial y^2}\right) \\ M_y &= -D\left(\frac{\partial^2 W}{\partial y^2} + \mu \frac{\partial^2 W}{\partial x^2}\right) \end{aligned}\right\} \tag{2}$$

In the strength design of elastic foundation plates, ultimate moment of resistance is considered as the critical point. Thus, the reliability of elastic foundation plates is the probability that the maximum moment is less than the ultimate moment of resistance. Under normal design, construction and usage, the probability of reliability p_s can be expressed as

$$p_s = p(M_j > M_{max}) \tag{3}$$

where M_j is ultimate moment of resistance M_{max} is actual maximum bending moment.

In the reliablity calculation of thin plates on Winkler foundation, the value of the modulus of subgrade is an important parameter, which is also the parameter of most variability. So, from a statistical nonhomogeneous viewpoint, it must be considered as a random variable in calculation. In addition, load p, modulus of elasticity E and plate thickness t, which should be considered as random variables, have a considerable effect on reliability. The ultimate moment of resistance, which depends on material properties and construction conditions, also has variability and should therefore be considered as a random variable. Poisson ratio of the plates has less variability and thus has less effect on calculation results. For this reason it can be considered as a constant in order to simplify the calculation. Other random variables can be regarded as independent of each other. Thus, the probability of reliability of thin plates on Winkler foundation can be approximately expressed in a function of the random variables, M_j, E, t, q and k; that is

$$p_f = f(M_j, E, t, q, k) \tag{4}$$

To simplify the expression, the above random variables can be written as X_i; that is, $X_1 = M_j$, $X_2 = E$, $X_3 = t$, $X_4 = q$, $X_5 = k$. The mean and standard deviation of each variable is μ_{X_i} and σ_{X_i} respectively. Hence the limit state equation of thin plates is

$$Z = g(X_1, X_2, X_3, X_4, X_5) = M_j - |M(X_2, X_3, X_4, X_5)|_{max} \tag{5}$$

where M_j is ultimate moment of resistance, which represent the resistance of the plates, and M is design bending moment, which represents the effects of actions of loads.

When every random variable is of normal distribution, the reliability index equation can be obtained by using checking points method of first-order second moment:

$$\beta = \frac{g(X_1^*, X_2^*, \cdots, X_5^*) - \sum_{i=1}^{5} \frac{\partial g}{\partial X_i}\Big|_{p^*} (X_i - \mu_{xi})}{\left[\sum_{i=1}^{5} \left(\frac{\partial g}{\partial X_i}\Big|_{p^*} \sigma_{X_i}\right)^2\right]^{1/2}} \tag{6}$$

where p^* is design checking points.

Substituting Eqns. 2 and 5 into Eqn. 6 and noting the expression

$$g(X_1^*, X_2^*, \cdots, X_5^*) = 0 \tag{7}$$

at the checking points, the formula of reliability index can be written in the following form

$$\beta = \{g(X_i^*) - \{(X_1^* - \mu_{x_1}) - \frac{Et^3}{12(1-\mu^2)}\{\overline{M}[\frac{1}{E}(X_2^* - \mu_{X_2}) + \\ + \frac{3}{t}(X_3^* - \mu_{X_3})] + \sum_{i=2}^{5}\frac{\partial \overline{M}}{\partial X_i}(X_i^* - \mu_{X_i})\}_{p^*}\}\}/A \tag{8}$$

where

$$\overline{M} = \left|\frac{\partial^2 W}{\partial x^2} + \mu\frac{\partial^2 W}{\partial y^2}\right| \quad (or \left|\frac{\partial^2 W}{\partial y^2} + \mu\frac{\partial^2 W}{\partial x^2}\right| \tag{8'}$$

$$A = \left\{\sigma_{X_1}^2 + \left[\frac{Et^3}{12(1-\mu^2)}\right]^2\left\{\left(\frac{\overline{M}^2}{E^2} + \frac{1}{E}\frac{\partial \overline{M}^2}{\partial X_2}\right)\sigma_{X_2}^2 \right.\right. \\ \left.\left. + \left(\frac{9\overline{M}^2}{t^2} + \frac{3}{t}\frac{\partial \overline{M}^2}{\partial X_3}\right)\sigma_{X_3}^2 + \sum_{i=2}^{5}\left[\frac{\partial \overline{M}}{\partial X_i}\sigma_{X_i}\right]^2\right\}_{p^*}\right\}^{1/2} \tag{8''}$$

Eqn. 8 is the reliability index equation of thin plates on Winkler foundation. The direction cosine of the normal op* to coordinate vector is:

$$\left.\begin{aligned} cos\theta_{X_1} &= -\frac{1}{A}\sigma_{X_1}, \quad cos\theta_{X_2} = -\frac{Et^3}{12(1-\mu^2)A}\left(\frac{\overline{M}}{E} + \frac{\partial \overline{M}}{\partial X_2}\right)\sigma_{X_2} \\ cos\theta_{X_3} &= \frac{Et^3}{12(1-\mu^2)A}\left(\frac{3}{t}\overline{M} + \frac{\partial \overline{M}}{\partial X_3}\right)\sigma_{X_3}, \quad cos\theta_{X_4} = \frac{Et^3}{12(1-\mu^2)A}\left(\frac{\partial \overline{M}}{\partial X_4}\right)\sigma_{X_4} \\ cos\theta_{X_5} &= \frac{Et^3}{12(1-\mu^2)A}\left(\frac{\partial \overline{M}}{\partial X_5}\right)\sigma_{X_5} \end{aligned}\right\} \tag{9}$$

Coordinates X_i^* of the checking points are

$$X_i^* = \mu_{X_i} + \beta\sigma_{X_i}cos\theta_{X_i} \tag{10}$$

Solving Eqns. 7, 9 and 10 simultaneously, the β value of plate on elastic foundation can be obtained. In actual calculation, β can be obtained only by iteration, of which the procedures are as, shown in Figure 1.

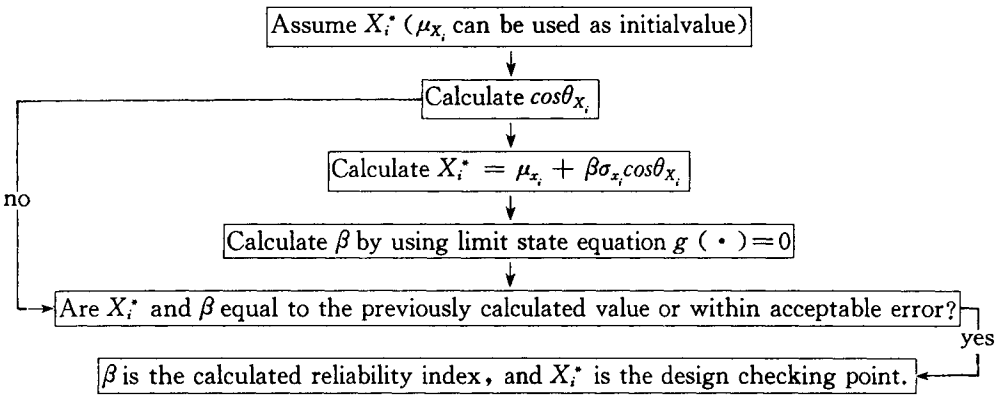

Figure 1 Procedures of iteration

In the above analysis, basic variables X_i are assumed of to be normal distribution. If X_i is not a normal random variable, it should be converted to an equivalent normal random variable before calculation. The calculation equations of mean μ_{X_i}' and standard diviation σ_{X_i}' can be found elsewhere [4].

Reliability calculation of thin plates on elastic half-space foundation

According to half-space foundation model, the foundation is assumed to be a continuous, homogeneous, isotropic, completely elastic half-space body. The mechanical properties of the foundation are functions of modulus of elasticity E_s and Poisson's ratio μ_s of soils. Although the solution of this model is much more complicated than that of Winkler foundation model, Eqn. 2 can still be used to describe the relationship between deflection and internal forces. Thus, the limit state equation of this model is similar to Eqn. 5. Among all parameters, M_j, E, t and q are still considered as random variables. Although both modulus of elasticity E_s and Poisson ratio μ_s of soil are actually random variables, only E_s is considered as a random variable during calculation in order to simplify calculation, and μ_s is regarded as a determinate variable because it has less variability. Neglecting the actual variability of μ_s does not very affect the results of reliability calculation. When each random variable X_i is of normal distribution, Eqns. 7, 8, 9 and 10 can still be used as reliability calculation for the plates on the elastic half-space foundation provided, replacing k in the above equations by E_s.

Reliability calculation of thin plates on two-parameter foundation

Two independent elastic constants are used to describe soil mechanical properties in the two-parameter model. According to the difference in the parameters used, this type of model can be further classified as Filoneko-Borodich model, Hetenyi model, Pasternak model, Vlazov model, etc.

In practice, the two parameters that characterize mechanical properties of soil are

always variable with the discreteness of soil properties, no matter which model is used. So they are all actually random variables. However, whether both parameters are used as random variables in calculation depends upon practical circumstances. If it is complicated or time-consuming to determine both parameters, only the parameter that represents the main soil properties is considered as a random variable, while the other one can be considered as a constant. For instance, subgrade coefficient k is considered as a random variable in Filonenko-Borodich model, while membrane tension T can be considered as a constant. The reliability calculation equations are thus exactly the same as those of Winkler model. However, It should to be noted that the subgrade coefficient here, k ,is different from that in Winkler model when T is introduced. If both parameters are relatively easy to determine, they can all be considered as random variables. For example, k and G in Pasternak model can be determined by means of ground testing,a relatively easy test and calculation. Both parameters are then considered as random variables. Let $X_5 = k, X_6 = G$. Then Eqn. 8, the reliability index equation, becomes

$$\beta = \{g(X_1) - \{(X_1^* - \mu_{X_1}) - \frac{Et^3}{12(1-\mu^2)}\{\overline{M}[\frac{1}{E}(X_2^* - \mu_{X_2}) + \\ + \frac{3}{t}(X_3^* - \mu_{X_3})] + \sum_{i=2}^{6}\frac{\partial \overline{M}}{\partial X_i}(X_i^* - \mu_{X_i})\}p^*\}\}/A \tag{11}$$

where

$$A = \left\{\sigma_{X_1}^2 + \left[\frac{Et^3}{12(1-\mu^2)}\right]^2\left\{\left(\frac{\overline{M}^2}{E^2} + \frac{1}{E}\frac{\partial \overline{M}^2}{\partial X_2}\right)\sigma_{X_2}^2 + \right.\right. \\ \left.\left. + \left(\frac{9\overline{M}^2}{t^2} + \frac{3}{t}\frac{\partial \overline{M}^2}{\partial X_3}\right)\sigma_{X_3}^2 + \sum_{i=2}^{6}\left[\frac{\partial \overline{M}}{\partial X_i}\sigma_{X_i}\right]^2\right\}p^*\right\}^{1/2} \tag{11'}$$

and the expression of $\overline{M}$ is the same as Eqn. 8′

A new item is added in the equation of $cos\theta_{X_i}$

$$cos\theta_{X_6} = \frac{Et^3}{12(1-\mu^2)A}\frac{\partial \overline{M}}{\partial X_6}\sigma_{X_6} \tag{12}$$

and

$$g(X_1^*, X_2^*, \cdots, X_6^*) = 0 \tag{13}$$

Calculation procedures are the same as above.

Obviously, the reliability index equations of thin plates on two-parameter foundation are almost the same as those on Winkler foundation except for the addition of the X_6 item. Thus, we conclude that for elastic thin plates on three-parameter foundation, the reliability index equations can be obtained only if items $\sum_{i=2}^{6}\left[\frac{\partial \overline{M}}{\partial X_i}(X_i^* - \mu_{X_i})\right]$ and $\sum_{i=2}^{6}\left[\frac{\partial \overline{M}}{\partial X_i}\sigma_{X_i}\right]^2$ in the

above expression are changed to $\sum_{i=2}^{7}\left[\frac{\partial \overline{M}}{\partial X_i}(X_i^* - \mu_{X_i})\right]$ and $\sum_{i=2}^{7}\left[\frac{\partial \overline{M}}{\partial X_i}\sigma_{X_i}\right]^2$, respectively, when three parameters are considered as random variables. Also, in the expression of $\cos\theta_{X_i}$, a new item $cos\theta_{X_7} = \frac{Et^3}{12(1-\mu^2)A}\frac{\partial \overline{M}}{\partial X_7}\sigma_{X_7}$ should be added .

When reliability index β is obtained, the probability of reliability p_s can be calculated by

$$p_s = \varphi(\beta) \tag{14}$$

where, p_s is the probability of reliability of the plate, and $\varphi(\beta)$ is the standard normal distribution function.

If there are complex limit state equations or many random variables in practical problems, this computation procedure is very complicated to solve reliability index by using checking point method of first-order second momnent. This can be avoid by using the iteration method of Fiesslur (1980). The principles can be found in reference [7] and the procedure is as follows:

(1) Determine an expression for $g(X)$

(2) Express the limit state equation $g(X)$ as a function of y_i by introducing standardization variable $y_i = \frac{X_i - \mu_{X_i}}{\sigma_{X_i}}$ $\quad (i = 1,2,\cdots\cdots,n)$

(3) Determine expressions for all first derivatives of $h(y)$, h_i'

(4) Set $y = 0$ and $\beta = 0$

(5) Evaluate all h_i' values

(6) Evaluate $h(y)$

(7) Evaluate standard deviation of Z from

$$\sigma_Z = \sqrt{\sum (h_i')^2}$$

(8) Evaluate new values for y from

$$y = -\frac{h_i'}{\sigma_Z}\left[\beta + \frac{h(y)}{\sigma_Z}\right]$$

(9) Evaluate $\beta = \sqrt{\sum y_i^2}$

(10) Repeat steps (5) to (9) until values converge.

Fiesslur's iterative procedure can be used together with variables. This method is very convenient for multi-variable problems or problems with complex relationships, because of its relative simplicity.

EXAMPLES

As an first example, we discuss a reliability calculation of a four-free-edge rectangular

plate on two—parameter foundation[8]. Length of the plate is $2l = 8$m and width of the plate is $2b = 4$m. The plate is acted upon by uniform load p. When soil thickness $H \to \infty$, the two parameters, K and G_p, of the foundation are

$$K = \frac{E_0 \gamma}{2(1 - \nu_0^2)} \qquad G_p = \frac{E_0 t}{4\gamma(1 + \nu_0)}$$

and

$$E_0 = \frac{E_s}{1 - \nu_s^2} \qquad \nu_0 = \frac{\nu_s}{1 - \nu_s}$$

where γ is a measurement of nonlinear variation of normal strain of foundation, and E_s, ν_s are elastic constants of soil material. Two parameters, K and G_p, can then be expressed by E_s and ν_s.

Let γ and ν_0 be equal to 1.5 and 0.4 respectively; the relative rigidity between foundation and plate system is $K_r = 1.0$. Solution of the deflection equation of plate is[8]

$$W(xy) = \frac{p_0 L(1 - \nu_0^2) \times 10^{-3}}{E_0}\left[408 + 2.37\cos\left(\frac{\pi x}{2b}\right) + 17.4\cos\left(\frac{\pi y}{2l}\right) + \right.$$
$$\left. + 0.4\cos\left(\frac{\pi x}{2b}\right)\cos\left(\frac{\pi y}{2l}\right)\right] \qquad (a)$$

The values of mean and standard deviation of each parameter are given in Table 1.

TABLE 1
VALUES OF MEAN AND STANDARD DEVIATION OF PARAMETERS

Variable	Symbol	Mean (μ_{x_i})	Standard deviation (σ_{X_i})	Unit
M_j	X_1	500	50	KN. m/m
E	X_2	2.25×10^7	3.6×10^6	KN/m^2
t	X_3	0.35	0	m
P_0	X_4	300	30	KN/m^2
E_s	X_5	635	190.5	KN/m^2

Poisson ratio of thin plates is $\mu = 1/6$, Poisson ratio of soil is $\nu_s = 0.2857$. Both of them are constants; then

$$\overline{M}_{max} = \left| \frac{\partial^2 W}{\partial y^2} + \mu \frac{\partial^2 W}{\partial x^2} \right|_{\substack{x=0 \\ y=0}} = 93.4913 \times 10^{-4} \frac{P_0}{E_s} = 93.4913 \times 10^{-4} \frac{X_4}{X_5}$$

Therefore, the limit state equation of the plate is

$$Z = g(X_i) = M_j - |D\overline{M}_{max}| = X_1 - 0.3436 \times 10^{-4} X_2 X_4 / X_5 \tag{b}$$

The reliability index equation can be expressed in the following form by using checking points method of first-order second moment as

$$\beta = \{g(X_i^*) - \{(X_1^* - \mu_{X_1}) - 0.3436 \times 10^{-4}[(\frac{X_4^*}{X_5^*})(X_2^* - \mu_{X_2}) -$$
$$- 0.3436 \times 10^{-4}(\frac{X_2^*}{X_5^*})(X_4^* - \mu_{X_4}) + 0.3436 \times 10^{-4}(\frac{X_2^* X_4^*}{X_5^{*2}})(X_5^* - \mu_{X_5})]\}\}/A$$

where

$$A = \{\sigma_{X_1}^2 + (0.3436 \times 10^{-4})^2 \left[\left(\frac{X_4^*}{X_5^*} \right)^2 \sigma_{X_2}^2 + \left(\frac{X_2^*}{X_5^*} \right)^2 \sigma_{X_4}^2 + \left(\frac{X_2^* X_4^*}{X_5^{*2}} \right)^2 \sigma_{X_5}^2 \right] \}^{1/2}$$

At the checking point

$$g(X_1^*, X_2^*, \cdots, X_5^*) = X_1^* - 0.3436 \times 10^{-4} \left(\frac{X_2^* X_4^*}{X_5^*} \right) = 0$$

that is

$$X_1^* X_5^* - 0.3436 \times 10^{-4} X_2^* X_4^* = 0 \tag{c}$$

Each direction cosine is

$$\left.\begin{aligned} \cos\theta_{X_1} &= -50/A \\ \cos\theta_{X_2} &= 123.696(X_4^*/X_5^*)/A \\ \cos\theta_{X_3} &= 0 \\ \cos\theta_{X_4} &= 10.308 \times 10^{-4}(X_2^*/X_5^*)/A \\ \cos\theta_{X_5} &= -65.4558(X_2^* X_4^*/X_5^{*2})/A \end{aligned}\right\} \tag{d}$$

Coordinate of each checking point is

$$\left.\begin{aligned} X_1^* &= 500 + 50\beta\cos\theta_{X_1} \\ X_2^* &= 2.25 \times 10^7 + 3.6 \times 10^6\beta\cos\theta_{X_2} \\ X_3^* &= 0.35 \\ X_4^* &= 300 + 30\beta\cos\theta_{X_4} \\ X_5^* &= 635 + 190.5\beta\cos\theta_{X_5} \end{aligned}\right\} \qquad (e)$$

Using the system of Eqns. (*d*) (*e*) and (*b*), the results can be obtained by iterations; the procedures are given in Table 2.

TABLE 2
PROCEDURES AND RESULTS OF ITERATIONS

Iteration order	X_1^*	X_2^*	X_3^*	X_4^*	X_5^*	β
1	500	2.25×10^7	0.35	300	635	0.8032
2	485.5304	2.3718×10^7	0.35	306.342	514.1684	0.7922
3	490.4025	2.3519×10^7	0.35	305.4781	503.3878	0.7922
4	490.6520	2.3510×10^7	0.35	305.4020	502.8143	0.7922
5	490.6679	2.3510×10^7	0.35	305.3973	502.7842	0.7922

Final result is $\beta=0.7922$; the probability of reliability of the plate can then be obtained

$$p_s = \varphi(\beta) = 78.58\%$$

and the probability of failure is

$$p_f = 1 - P_s = 21.42\%$$

It is evident that the probability of failure is larger. If we use the traditional safety factor method to calculate its safety factor, we obtain

$$K = \frac{500}{365.2441} = 1.37$$

It follows that the plate has enough safety capacity. That the variabilities of all kind of calculation parameters cannot be considered in safety factor is the main reason for different conclusions between the reliability and safety factor methods. Therefore unreasonable results arise.

If the standard deviation of E is decreased to $\sigma_{X_2}=2.25\times10^5\text{kN/m}^2$, and that of E, to $\sigma_{X_5}=76.2\text{kN/m}^2$, then probability of failure of the plate will be decreased to

$$p_f = 7.08\%$$

As our second example, we discuss reliability of a four-edge simply supported rectangular thin plate on Winkler foundation. This plate supports uniform load q and has length $a=6\text{m}$, width $b=4\text{m}$ and Poisson ratio $\mu=\frac{1}{6}$. Other variables are given in Table 3.

TABLE 3
VALUES OF MEAN AND STANDARD DEVIATION OF PARAMETERS

Variable	Symbol	Mean (μ_{x_i})	Standard deviation (σ_{x_i})	Unit
M_j	X_1	500	50	KN. m/m
E	X_2	2.304×10^7	2.88×10^6	KN/m^2
t	X_3	0.3	0.02	m
q_0	X_4	400	40	KN/m^2
k	X_5	30000	7500	KN/m^3

Thus, the solution of a four-edge simply supported rectangular thin plate under uniform load q_0 is [9]

$$W=\frac{16q_0}{\pi^2}\sum_{m=1,3,5,\cdots}^{\infty}\sum_{m=1,3,5,\cdots}^{\infty}\frac{\sin(\frac{m\pi}{a})x\ \sin(\frac{n\pi}{b})y}{mn[\pi^4D(\frac{m^2}{a^2}+\frac{n^2}{b^2})^2+k]} \qquad (f)$$

This series converges fast. Here, only the first item is taken to illustrate the calculation procedure.

Substituting Eqn. *f* into Eqn. 8, we find

$$\overline{M} = \left| \frac{\partial^2 W}{\partial y^2} + \mu \frac{\partial^2 W}{\partial x^2} \right| = \frac{16q_0}{\pi^2} \left\{ \frac{(\frac{\pi}{b})^2 + \mu \frac{\pi}{a})^2}{\pi^4 D(\frac{1}{a^2} + \frac{1}{b^2})^2 + k} \right\} sin \frac{\pi x}{a} sin \frac{\pi y}{b} \qquad (g)$$

Putting in known data into the formula and expressing it as a basic variable, the result is

$$\overline{M} = \frac{1074.1X_4}{68.05X_2X_3^3 + 1000X_5} sin \frac{\pi x}{6} sin \frac{\pi y}{4}$$

So, $Z = g(X_i) = M_j - |M|_{max} = M_j - |D\overline{M}|_{max} = X_1 - \dfrac{X_2X_3^3X_4}{0.7392X_2X_3^3 + 10.8618X_5}$

Introducing the standardization variable $y_i = \dfrac{X_i - \mu_{X_i}}{\sigma_{X_i}}$, $(i = 1, 2, \cdots, 5)$, the limit state equation can be expressed as

$$Z = h(y) = (y_1\sigma_{X_1} + \mu_{X_1}) - \frac{(y_2\sigma_{X_2} + \mu_{X_2})(y_3\sigma_{X_3} + \mu_{X_3})^3(y_4\sigma_{X_4} + \mu_{X_4})}{0.7392(y_2\sigma_{X_2} + \mu_{X_2})(y_3\sigma_{X_3} + \mu_{X_3})^3 + 10.8618(y_5\sigma_{X_5} + \mu_{X_5})}$$

Forming the derivative of this expression with respect to $y_i (i = 1 \sim 5)$, we obtain

$$\frac{\partial h(y)}{\partial y_1} = \sigma_{X_1}$$

$$\frac{\partial h(y)}{\partial y_2} = -\frac{10.8618(y_5\sigma_{X_5} + \mu_{X_5})(y_3\sigma_{X_3} + \mu_{X_3})^3(y_4\sigma_{X_4} + \mu_{X_4})\sigma_{X_2}}{[0.7392(y_2\sigma_{X_2} + \mu_{X_2})(y_3\sigma_{X_3} + \mu_{X_3})^3 + 10.8618(y_5\sigma_{X_5} + \mu_{X_5})]^2}$$

$$\frac{\partial h(y)}{\partial y_3} = -\frac{3 \times 10.8618(y_2\sigma_{X_2} + \mu_{X_2})(y_3\sigma_{X_3} + \mu_{X_3})^2(y_4\sigma_{X_4} + \mu_{X_4})(y_5\sigma_{X_5} + \mu_{X_5})\sigma_{X_3}}{[0.7392(y_2\sigma_{X_2} + \mu_{X_2})(y_3\sigma_{X_3} + \mu_{X_3})^3 + 10.8618(y_5\sigma_{X_5} + \mu_{X_5})]^2}$$

$$\frac{\partial h(y)}{\partial y_4} = -\frac{(y_2\sigma_{X_2} + \mu_{X_2})(y_3\sigma_{X_3} + \mu_{X_3})\sigma_{X_4}}{0.7392(y_2\sigma_{X_2} + \mu_{X_2})(y_3\sigma_{X_3} + \mu_{X_3})^3 + 10.8618(y_5\sigma_{X_5} + \mu_{X_5})}$$

$$\frac{\partial h(y)}{\partial y_5} = -\frac{10.8618(y_2\sigma_{X_2} + \mu_{X_2})(y_3\sigma_{X_3} + \mu_{X_3})(y_4\sigma_{X_4} + \mu_{X_4})\sigma_{X_5}}{[0.7392(y_2\sigma_{X_2} + \mu_{X_2})(y_3\sigma_{X_3} + \mu_{X_3})^3 + 10.8618(y_5\sigma_{X_5} + \mu_{X_5})]^2}$$

From Fiesslur's method, the iteration results are given in Table 4.

TABLE 4
PROCEDURES AND RESULTS OF ITERATIONS

Iteration order	y_1	y_2	y_3	y_4	y_5	β
1	0.0	0.0	0.0	0.0	0.0	0.0
2	−1.6540	0.5431	0.8690	1.0477	−1.0863	2.4624
3	−1.4704	0.4236	0.6841	1.1301	−1.2420	2.3726
4	−1.4207	0.4172	0.6721	1.0937	−1.2741	2.3375
5	−1.4250	0.4152	0.6700	1.1000	−1.2838	2.3474
6	−1.4242	0.4155	0.6693	1.1000	−1.2872	2.3486
7	−1.4237	0.4151	0.6688	1.1000	−1.2876	2.3483
8	−1.4236	0.4150	0.6687	1.0999	−1.2877	2.3482

where $y_i = \dfrac{X_i^* - \mu_{X_i}}{\sigma_{X_i}}$ is the conversion variable.

Reliability index is $\beta = 2.3482$; therefore, the probability of reliability of the thin plate is

$$p_s = \varphi(\beta) = 99.0567\%$$

According to the safety−factor method, safety factor $K = \dfrac{500}{316.70} = 1.58$

The above result is approximate because only the first item of the series is taken to demonstrate the calculation procedure.

CONCLUSIONS

The reliability calculation method of thin plates on Winkler, elastic half-space and two-parameter foundations is discussed in this paper. The equation of reliability calculation is established for three different models of foundation. In the reliability calculation, the ultimate moment of resistance M_j, modulus of elasticity E, thickness t and load q_0 are considered as random variables. Other random variables which represent soil properties should be selected according to the concrete model of the foundation.

Furthermore; the selection of random variables suggested in this paper is not unvaried; they depend on specific conditions of practical engineering. For instance, high construction quality of foundation plates leads to little variability of structure dimensions; the thickness t of the plate can then be treated as a constant. Otherwise, it should be treated as a random variable.

The reliability index equation in this paper is only suitable for the calculation of thin plate structure on elastic foundation. As to the probability of reliability for soil—foundation —structure interaction, this topic will be discussed in future papers.

REFERENCES

[1] Jinzhang Zai. (1994). *Foundation Analysis and Design of Tall Buildings, Soil-Structure Interaction Theory and Their Application*, China Construction Publishing House, Beijing.

[2]Selvadurai, A. P. S. (1979). *Elastic Analysis of Soil-Foundation Interaction*, Elsevier Scientific Publishing Co.

[3]Zhaohong Zhu, Binggang Wang and Dazhi Guo. (1985). *Mechanics Calculation for Pavement*, Peoples Traffic Publishing House, Beijing.

[4] The State Standard of the People's Republic of China. (1992). *Unified Design Standard for Reliability of Engineering Structures* (*GB*50153-92), China Planning Publishing House, Beijing.

[5] The State Standard of The People's Republic of China. (1994). *Unified Design Standard for Reliability of Railway Engineering Structures* (*GB*50216-94). China Planning Publishing House, Beijing.

[6] Tianyi Zou. (1991). *Reliability of Bridge Structures*, People's Traffic Publishing House, Beijing.

[7]G. N. Smith. (1986). *Probability and Statistics in Civil Engineering*. Nichols Publishing Company, New York.

[8]Yao Sheng and Yi Huang. (1987). *A Free Rectangular Plate on The Two — Parameter Elastic Foundation*, Applied Mathematics and Mechanics 8:4, 317—329.

[9]S. Timoshenko and S. Woinowsky—Krieger. (1959). *Theory of Plates and Shells*. McGraw—Hill Book Co.

[10]Zhiming Tan and Yao Zukang. (1991). *Reliability Analysis of Concrete Pavement*, Journal of Tongji University 19:2, 157—165.

[11]Dajun Ding and Zhongde Liu. (1986). *Calculation Theory and Method of Beam on Elastic Foundation*, Nanjing Technology Institute Publishing House, Nanjing.

[12]Zhilun Xu. (1979). *Mechanics of Elasticity, People's Education Publishing House*, Beijing.

[13]Shaozhong Xi, Shiying Zheng. (1981). *Applied Mechanics of Elasticity*. China Railway Publishing House, Beijing.

COMPUTER SIMULATION OF STRUCTURAL ANALYSIS IN CIVIL ENGINEERING

Jiang Jian-Jing, Guo Wen-Jun and Hua Bin

Department of Civil Engineering, Tsinghua University, Beijing

ABSTRACT

In this paper, structural analysis and failure process in civil engineering are discussed. The main contents are: (1) The philosophy of computer simulation in structural engineering; (2) The mathematical model for engineering problem; (3) The visualization of numerical results. Some simulation examples are presented.

KEYWORDS

Computer Simulation, Structure, Civil Engineering, Disaster Risk.

INTRODUCTION

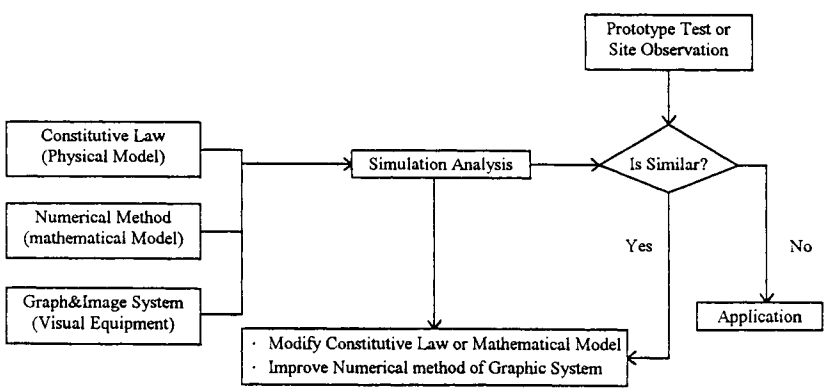

Figure 1: Philosophy of computer simulation in structural analysis

Computers are used widely to simulate the objective world, including natural phenomenon, system engineering, kinematics principles and even the human brain. Though civil engineering is a traditional trade, computer simulation has been applied successfully, especially in structural analysis. Three prerequisites are needed to perform structural analysis: (1) Constitutive law of specific material, which can be obtained by small-scale test; (2) Effective numerical method, such as finite element method (FEM), direct integration, etc.; (3) Graph display software and visual system. Figure 1 shows the philosophy of computer simulation in structural analysis. The following parts give a comprehensive explanation of several aspects.

SIMULATION OF STRUCTURAL FAILURE

Structural behavior under various loading conditions and environment is of great importance, especially its collapse procedure and ultimate loading capacity. When the structure form is very special, we usually resort to model experiment in order to determine the characteristic of the structure. Yet the model usually is small because of the constraints of space and equipment, thus can not reflect the behavior of real structure. If we want to study the influence of a parameter, series analogous experiments must be done, which is very time-consuming and expensive.

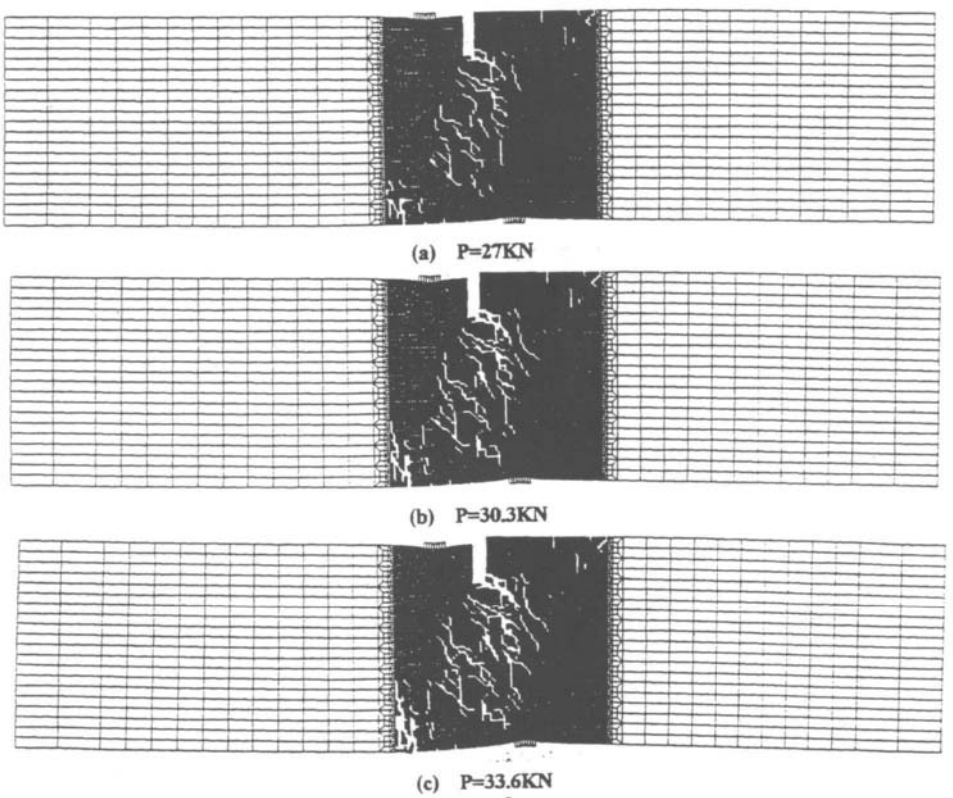

Figure 2: Development of micro fracture

Taking advantage of computer simulation, we can carry out "full-scale experiments" without worrying about time and budget. Simply changing several input parameters, we can obtain the influence of these parameters. Sometimes it is impossible to do real experiments, then computer simulation is of more significance. For example, it is obvious that we cannot repeat the procedure of accident of nuclear reactor safety shell. Using computer simulation, we can perform reversal analysis of the accidents to determine the cause and unfolding procedure of accidents. Other examples are high-speed collisions of car and structure collapse under earthquake, which can be performed only by computer. Under high speed loading, structural response is very quick, therefore what we get is the final result. An extremely contrary situation is the evolution of the earth's crust, which may take millions of years. Both can be simulated by computer by changing time rate according to request. Figures 2[4] and 3[1] show the development of micro-fracture and dynamic response of a frame, respectively.

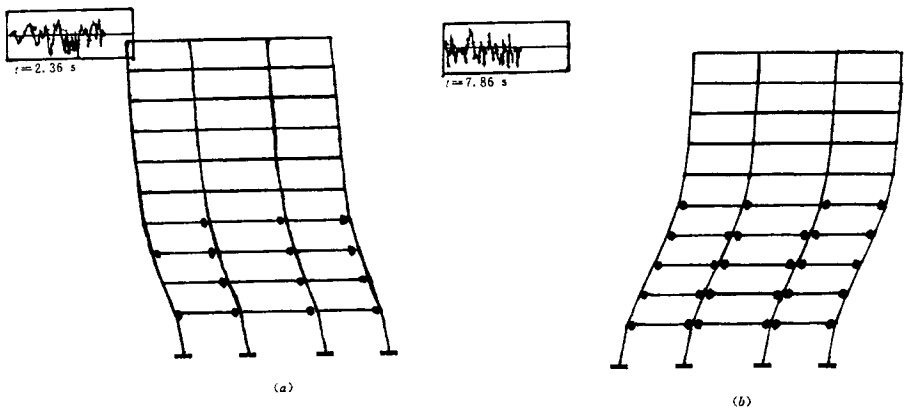

Figure 3: Dynamic response of frame

APPLICATION IN HAZARDS PREVENTION

The history of human being is a history of hard battle with various hazards, such as flood, fire, earthquake and so on. Because hazards are unreplicable for experiments, computer simulation has become more and more popular and of great value. Many simulation systems have been developed successfully. For instance, software has been developed and preloaded with landform, topography and surface features of a flood area. Given flood standard and specific location of burst, computers can demonstrate submerged areas at different time on screen, which are calculated according to water quantity, speed and area. People can view the gradual inundation process and, in turn, work out flood prevention and personnel dispersion programs. Fire prevention software is another successful example. Using this software, we could simulate spreading of fire in forest and building, which give guidelines to fire-fighting. Figure 4[3] shows

the distribution of debris after an earthquake.

Figure 4: Distribution of debris after earthquake

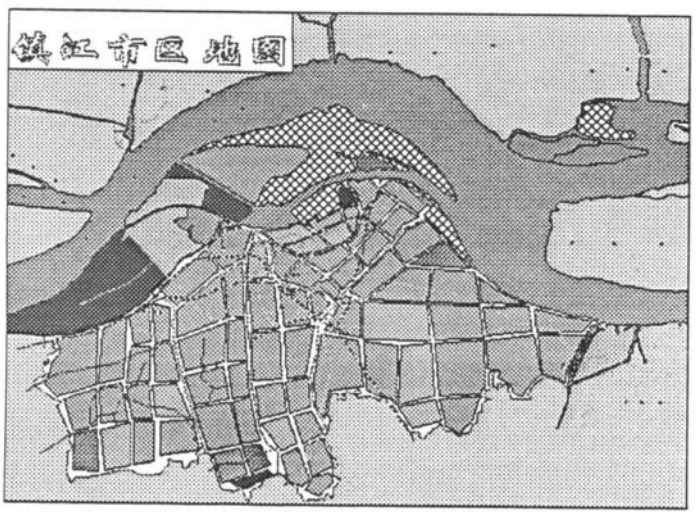

Figure 5: Submerged area

APPLICATION IN ROCK AND SOIL ENGINEERING

Construction in rock engineering is under-ground, hence it cannot be observed directly. Computer simulation which can reveal its inner procedure, is of great value. For example, during the excavation of underground construction, there is always collapse, which can be solved by thorough geological survey to find the strike of faults, crevices and joints. Through small-scale experiments we can determine the mechanics of rock body and joints, which can be stored in computer for later use.

Besides finite element method (FEM), there is discrete element method (DEM). The behavior of elements of DEM is similar to FEM ones in equilibrium, while elements of DEM will move under external force and gravity when equilibrium is lost until they get new equilibrium. In the analysis of underground rock structure and stability of slope, the structure is divided into elements along crevice and joint faults. In simulation of excavation, the upper and side part elements may lose equilibrium and fall down; this procedure can be shown on screen and thus we can obtain the cave-in area and provide reliable instruction to anchor design.

Computer simulation is also applied in research fields such as seepage of underground water, deposition of river silt, settlement of foundation and so on. For example, a simulation software of river-mouth deposition has been developed. When given the condition of river mouth, it can show the deposition rate of different size of silt and accumulating thickness, which give instruction to port design and river course dredging. Figure 5[2] shows a simulation of bridge pier collapse.

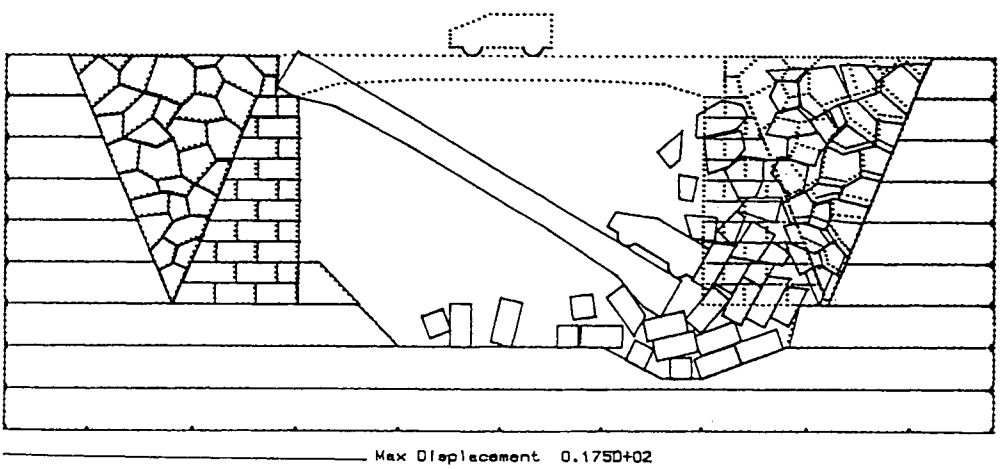

Figure 6: Collapse of bridge

SIMULATION SYSTEM OF TEACHING EXPERIMENTS

During the teaching of reinforced concrete element for students of civil engineering, demonstrating experiments is a key part, which can make the knowledge easier to understand and strengthen perceptual knowledge of students. Yet, the real element failure test is very tedious, time-consuming and expensive, not affordable by university teaching budget. With the aid of computer simulation method, we can build a graphic environment to simulate the experiment. After input geometric and physical data, the students can observe the procedure of element failure, details of the inner process, and other changes. Compared with teaching test, this method can initiate students' activity, giving them the opportunity to participate in the experiment as well as saving large quantity of work, material and time.

Three aims can be achieved through simulation teaching:
1)The student can get a clear and vivid knowledge of the phenomenon of element failure and its characteristics.

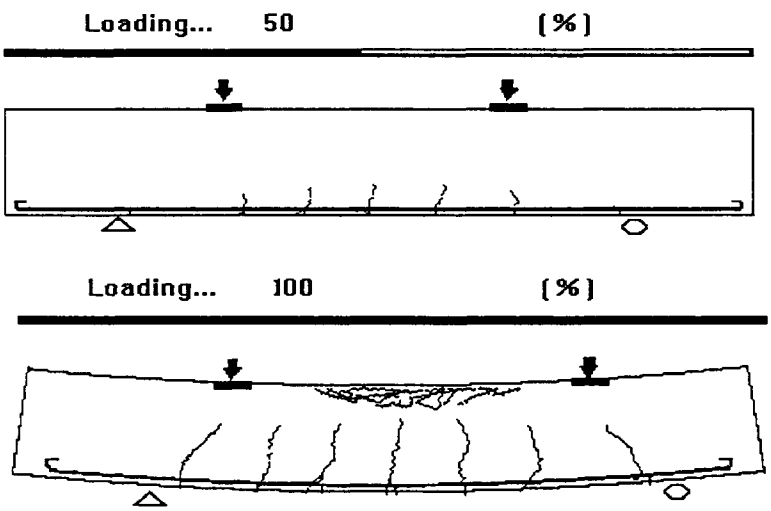

Figure 7: Demonstration of test

2)They can select different parameters of elements, such as section dimension, concrete strength, reinforced ratio, and the location of force and the influence of these parameters on failure shape, ultimate loading capacity.
3)When doing the simulation, there are instructions on the screen, as if there is a teacher.

In the simulation instruction system developed by the author, there are two types of experiment--the example experiment and free experiment. The former takes the role of a real instruction experiment usually used nowadays in teaching, and the students' job is to select what type of failure they want to see. Then everything is done by computer automatically.

With the self-experiment, students have an opportunity to experiment by themselves. They design their own elements; the system automatically analyses element failure and demonstrates the failure procedure. By selecting different values, the students can acquaint themselves with the influence of these parameters.

CONCLUSIONS

Computer simulation has achieved great success in many fields, including structural analysis. Through the above description, three conclusions can be reached:

(1) Along with the rapid improvement of CPU speed and update of hardware, the computer has been used not only as a tool of scientific calculation but also in structural analysis, hazard prevention, construction management and failure simulation.
(2) Much hard work, expense and time can be saved by using computer simulation. A combination of computer simulation and experiments will be the main tools of engineers.
(3) Computers can give miscellaneous dull data a vivid and lifelike form, they will play a more important role in teaching and management.
(4) Compared with the high level of hardware, simulation systems lag behind. More mature and businesslike simulation systems need to be developed.

REFERENCES

1 Jiang J.J. (1991). *The computer simulation system for R. C structure process.* Computational mechanics and application (in Chinese), (2), 32-38.
2 Wei Q.(1990). *The fundamental principle of distinct element method in geotechnics*, Ph.D. dissertation, Tsinghua University.
3 Jiang J.J. (1990). *Application of computer simulation to civil engineering.* Computational technique and computer application (in Chinese), (2),16-19.
4 Liu G.T. and Wang Z.M.(1996). *Numerical simulation study of fracture of concrete materials using random aggregate model.* Journal of Tsinghua University (Science and technology), (1),84-89.

This Page Intentionally Left Blank

A MIXED FINITE ELEMENT FOR LOCAL AND NONLOCAL PLASTICITY

Xikui Li

National Laboratory for Structural Analysis of Industrial Equipment,
Dalian University of Technology, 116023, P.R.China

ABSTRACT

This paper develops a mixed finite element with one point quadrature and hourglass control in local and non-local (gradient) plasticity for pressure dependent and independent materials at large strains, which allows for its application to the modelling of strain hardening and softening (strain localization) behaviors. The two yield strength parameters of strain hardening/softening materials not only depend on the internal state variable but also on its Laplacian. The evaluation of the Laplacian is based on a least square polynomial approximation of the internal state variable around each integration point. To derive the consistent element formulations in pressure dependent elasto-plasticity, a natural coordinate system in the stress space and a new definition of internal state variable are introduced. Numerical examples are given to demonstrate the performance of the mixed element, particularly in preserving ellipticity as strain softening behaviour is incorporated into the computational model.

KEYWORDS

mixed finite element, local plasticity, gradient plasticity, pressure dependent materials, natural coordinates, internal state variable, strain localization, consistent formulations

INTRODUCTION

Owing to the advantages of the one point quadrature mixed finite element with hourglass control in both accuracy and efficiency, it has been widely implemented in finite element codes and used to solve a variety of practical engineering problems with success. Many efforts have been devoted to develop and improve this type of mixed elements since it was first published

by Flanagan and Belytschko (1981). Jetteur and Cescotto (1991) developed their one point quadrature mixed element for the von-Mises elasto-plasticity with strain hardening at large strain and reported excellent results obtained with cheap cost in computation. Localization of deformation into narrow bands of intense strain caused by strain softening is a characteristic feature of plastic deformation and is a common occurrence in many pressure independent and dependent materials. Numerous attempts to simulate the localization behaviour by using classical (local) plastic continuum theories have been unsatisfactory. It has been realized that the effective and radical measure to remedy this situation is to introduce the regularization mechanism into the continuum to preserve ellipticity or hyperbolicity of the governing field equation for the quasi-static problems or the dynamic problems respectively . Among diverse approaches to introduce the regularization mechanism are: non-local continuum theory (Bazant et al.,1984, de Borst, 1992), Cosserat continuum theory (Muhlhaus et al., 1989) and rate dependent continua (Needleman, 1988). The basic idea of the non-local gradient plasticity is to include higher order spatial gradients of the effective plastic strain in the yield condition. de Borst et al.(1992) and Sluys et al.(1993) presented the formulations and algorithms for the gradient plastic continuum in a finite element context. A finite element method for gradient elasto-plastic continuum was presented by Xikui Li et al.(1996), in which the Laplacian of the effective plastic strain at a quadrature point is evaluated on the basis of a least square polynomial approximation by using the values of the effective plastic strains at neighbouring quadrature points. This non-local approach allows to satisfy exactly the non-local consistency condition of the yield function at each quadrature point, whereas the consistency condition is only enforced in a weak form and is not satisfied at each iteration but only at the end of a load step in de Borst et al.(1992) and Sluys et al.(1993).

The objective of the present work is to develop a nonlinear version of the element for both gradient and local plasticity of pressure dependent material models, such as the Drucker-Prager and the modified von-Mises models, at large strain. The element is formulated not only for the plane strain and the axisymmetric solid, but also for the plane stress state. To formulate the non-local consistent compliance matrix and the non-local consistent integration algorithm in a concise and numerically efficient manner for closed-form implementation, the so-called natural coordinate system in the stress (strain) space (Duxbury & Xikui Li et al.,1996) is introduced. The separation of the plastic strain into its deviatoric and hydrostatic components due to the introduction of the natural coordinates provides an opportunity to define a new internal state variable that is capable of capturing different post-yield curves in tension and compression simultaneously. To analyze the geometrically non-linear problem by utilizing the present mixed element, the co-rotational formulation (Jetteur and Cescotto, 1991) is adopted and the co-rotational Cauchy stress tensor and its energetically conjugated strain measure are employed.

THE MIXED FINITE ELEMENT

Let us start with the variation of the functional Π for the Hu-Washizu principle in the form

$$\delta\Pi = \int_{A_e} [\delta\varepsilon^T(\mathbf{C}\varepsilon - \sigma) + \delta\sigma^T(\varepsilon - \nabla\mathbf{u}) + \delta(\nabla\mathbf{u})^T\sigma]dA_e \tag{1}$$

where the stress , the strain ε, the displacement gradient $\nabla\mathbf{u}$ and the elastic modulus matrix $\mathbf{C}$ are referred to the original coordinates. For the two-dimensional case, we have

$$\sigma^T = [\sigma_x\ \sigma_y\ \sigma_z\ \tau_{xy}];\quad \varepsilon^T = [\varepsilon_x\ \varepsilon_y\ \varepsilon_z\ \varepsilon_{xy}];\quad \nabla\mathbf{u}^T = [u_{x,x}\ \ u_{y,y}\ \ u_{z,z}\ \ u_{x,y}+u_{y,x}] \tag{2}$$

The natural coordinate system in the stress (strain) space is introduced in such a way that the deviatoric and the hydrostatic components of the normal stress (strain) components are split and σ, ε and $\nabla\mathbf{u}$ are transformed into their counterparts $\hat{\sigma}, \hat{\varepsilon}$ and $\nabla\hat{\mathbf{u}}$ referred to the natural coordinates as follows

$$\hat{\sigma} = \mathbf{T}\sigma\ ;\ \hat{\varepsilon} = \mathbf{T}\varepsilon\ ;\ \nabla\hat{\mathbf{u}} = \mathbf{T}\nabla\mathbf{u}\ \text{ with } \hat{\sigma}^T = [\sigma_I\ \sigma_{II}\ \sigma_m\ \tau_{xy}];\ \hat{\varepsilon}^T = [\varepsilon_I\ \varepsilon_{II}\ \varepsilon_m\ \varepsilon_{xy}] \tag{3}$$

where the transformation matrix $\mathbf{T}$ is defined by

$$\mathbf{T} = \begin{bmatrix} 1/\sqrt{2} & 0 & -1/\sqrt{2} & 0 \\ -1/\sqrt{6} & \sqrt{2/3} & -1/\sqrt{6} & 0 \\ 1/\sqrt{3} & 1/\sqrt{3} & 1/\sqrt{3} & 0 \\ 0 & 0 & 0 & 1 \end{bmatrix} \tag{4}$$

According to the displacement field equivalent to the classical bilinear function of the isoparametric coordinates ξ and η

$$u_i = a_0^i + a_j^i x_i + a_3^i \frac{A_e}{4}\xi\eta \qquad (i=1, 2) \tag{5}$$

where A_e is the area of the element, the displacement gradient can be derived as

$$\nabla\hat{\mathbf{u}} = \mathbf{T}(\mathbf{B} + \mathbf{h}_b\Gamma)\mathbf{q} = \mathbf{T}\overline{\mathbf{B}}\,\mathbf{q} \tag{6}$$

where $\mathbf{q}^T = [\mathbf{u}^T\ \mathbf{v}^T]$ is the nodal displacement vector of the element and

$$\mathbf{B}^T = \begin{bmatrix} \mathbf{b}_{,x} & 0 & 0 & \mathbf{b}_{,y} \\ 0 & \mathbf{b}_{,y} & 0 & \mathbf{b}_{,x} \end{bmatrix};\quad \mathbf{h}_b^T = \begin{bmatrix} h_{,x} & 0 & 0 & h_{,y} \\ 0 & h_{,y} & 0 & h_{,x} \end{bmatrix};\quad \Gamma = \begin{bmatrix} \gamma^T & 0 \\ 0 & \gamma^T \end{bmatrix}$$

$$\mathbf{b}_{,x}^T = \frac{1}{2A_e}[y_{24}\ y_{31}\ y_{42}\ y_{13}];\quad \mathbf{b}_{,y}^T = \frac{1}{2A_e}[x_{42}\ x_{13}\ x_{24}\ x_{31}]$$

$$2A_e = x_{31}y_{42} + x_{24}y_{31};\quad x_{ij} = x_i - x_j;\quad y_{ij} = y_i - y_j$$

$$h = \frac{A_e}{4}\xi\eta;\quad h_{,x} = \frac{\partial h}{\partial x};\quad h_{,y} = \frac{\partial h}{\partial y};\quad \gamma = \frac{1}{A_e}[\mathbf{h} - (\mathbf{h}^T\mathbf{x}_j)\mathbf{b}_{,j}]$$

$$\mathbf{h}^T = [1\ -1\ \ 1\ -1];\quad \mathbf{x}_1^T = [x_1\ x_2\ x_3\ x_4];\quad \mathbf{x}_2^T = [y_1\ y_2\ y_3\ y_4] \tag{7}$$

The stress $\hat{}$ and the strain $\hat{\varepsilon}$ are chosen in the 'optimal incompressible' modes as

$$\hat{\sigma} = \hat{\bar{\sigma}} + \mathbf{h}_\alpha \hat{\sigma}^x \; ; \; \hat{\varepsilon} = \hat{\bar{\varepsilon}} + \mathbf{h}_\alpha \hat{\varepsilon}^x \; ; \text{ with } \mathbf{h}_\alpha^T = \begin{bmatrix} h_{,x} & -h_{,x} & 0 & 0 \\ -h_{,y} & h_{,y} & 0 & 0 \end{bmatrix} \tag{8}$$

where $\hat{\bar{\varepsilon}}^T = [\bar{\varepsilon}_I \; \bar{\varepsilon}_{II} \; \varepsilon_m \; \varepsilon_{xy}]$, $\hat{\varepsilon}^{xT} = [\varepsilon_1^x \; \varepsilon_2^x]$ and $\hat{\bar{\sigma}}^T = [\bar{\sigma}_I \; \bar{\sigma}_{II} \; \sigma_m \; \tau_{xy}]$, $\hat{\sigma}^{xT} = [\sigma_1^x \; \sigma_2^x]$. The constant field $(\hat{\bar{\sigma}}, \hat{\bar{\varepsilon}})$ is uncoupled with the anti-hourglass mode $(\hat{\sigma}^x, \hat{\varepsilon}^x)$. With substitution of expressions (6) and (9) into equation (1) we may integrate each term in the equation and obtain

$$\begin{aligned} \delta\Pi = A_e[&\delta\hat{\bar{\varepsilon}}^T(\hat{\mathbf{C}}\hat{\bar{\varepsilon}} - \hat{\bar{\sigma}}) + \delta\hat{\bar{\sigma}}^T(\hat{\bar{\varepsilon}} - \mathbf{T}\overline{\mathbf{B}}\mathbf{q}) + \delta\mathbf{q}^T\overline{\mathbf{B}}^T\mathbf{T}^T\hat{\bar{\sigma}}] + \delta\hat{\varepsilon}^{xT}[4G\mathbf{H}\hat{\varepsilon}^x - 2\mathbf{H}\hat{\sigma}^x] \\ &+ \delta\hat{\sigma}^{xT}[2\mathbf{H}\hat{\varepsilon}^x - \mathbf{H}^*\Gamma\mathbf{q}] + \delta\mathbf{q}^T\Gamma^T\mathbf{H}^{*T}\hat{\sigma}^x \end{aligned} \tag{9}$$

Here $\hat{\mathbf{C}} \in R^{4\times4}$ referred to the natural coordinates for isotropic elasticity can be given by

$$\hat{\mathbf{C}} = \mathbf{T}\mathbf{C}\mathbf{T}^T = diag(2G, \; 2G, \; 3K, \; G) \tag{10}$$

$$\mathbf{H} = \begin{bmatrix} H_{xx} & -H_{xy} \\ -H_{xy} & H_{yy} \end{bmatrix}; \quad H_{ij} = \int_{A_e} h_{,i} \, h_{,j} \, dA_e \; ; \; \mathbf{H}^* = \int_{A_e} \mathbf{h}_\alpha^T \mathbf{T} \mathbf{h}_b \, dA_e \tag{11}$$

where G and K are the elastic shear and bulk moduli. From the stationary condition of (9) and the arbitrariness of the variations $\delta\hat{\bar{\varepsilon}}, \delta\hat{\bar{\sigma}}, \delta\mathbf{q}, \delta\hat{\varepsilon}^x$ and $\delta\hat{\sigma}^x$, we obtain the constitutive laws, the element strain-displacement relations, the internal nodal forces $\mathbf{F}$ and the linear stiffness matrix of the element

$$\hat{\bar{\sigma}} = \hat{\mathbf{C}}\hat{\bar{\varepsilon}} \; ; \quad \hat{\sigma}^x = 2G\hat{\varepsilon}^x; \qquad \hat{\bar{\varepsilon}} = \mathbf{T}\overline{\mathbf{B}}\mathbf{q} \; ; \qquad 2\hat{\varepsilon}^x = \mathbf{H}^{-1}\mathbf{H}^*\Gamma\mathbf{q} \tag{12}$$

$$\mathbf{F} = A_e\overline{\mathbf{B}}^T\mathbf{T}^T\hat{\bar{\sigma}} + \Gamma^T\mathbf{H}^{*T}\hat{\sigma}^x \; ; \qquad \mathbf{K} = A_e \, \overline{\mathbf{B}}^T\mathbf{C}\overline{\mathbf{B}} + G\Gamma^T\mathbf{H}^{*T}\mathbf{H}^{-1}\mathbf{H}^*\Gamma \tag{13}$$

THE GRADIENT DEPENDENT PLASTICITY

Two pressure dependent elastoplastic models for the gradient plasticity are particularly considered. The yield functions for the gradient Drucker-Prager (GDP) and the modified von-Mises (GMVM) models can be given in the form (Duxbury and Li, 1996)

$$F = q + A(\bar{\varepsilon}^p, \nabla^2\bar{\varepsilon}^p)\sigma_m + B(\bar{\varepsilon}^p, \nabla^2\bar{\varepsilon}^p) \tag{14}$$

$$F = q^2 + A(\bar{\varepsilon}^p, \nabla^2\bar{\varepsilon}^p)\sigma_m + B(\bar{\varepsilon}^p, \nabla^2\bar{\varepsilon}^p) \tag{15}$$

where the effective deviatoric stress q and the hydrostatic stress σ_m are defined by

$$q = (\frac{1}{2}\hat{\sigma}^T\hat{\mathbf{P}}\hat{\sigma})^{1/2} \; ; \quad \sigma_m = \frac{1}{\sqrt{3}}(\sigma_x + \sigma_y + \sigma_z) \; ; \text{ with } \hat{\mathbf{P}} = diag(3, 3, 0, 6) \tag{16}$$

A and B are the current material parameters defined as

$$A = \frac{2Sin\phi(\bar{\varepsilon}^p, \nabla^2\bar{\varepsilon}^p)}{\sqrt{3}(3 - Sin\phi(\bar{\varepsilon}^p, \nabla^2\bar{\varepsilon}^p))} \; ; \quad B = \frac{-6c_h(\bar{\varepsilon}^p, \nabla^2\bar{\varepsilon}^p)Cos\phi(\bar{\varepsilon}^p, \nabla^2\bar{\varepsilon}^p)}{\sqrt{3}(3 - Sin\phi(\bar{\varepsilon}^p, \nabla^2\bar{\varepsilon}^p))} \tag{17}$$

for the Drucker-Prager criterion, where c_h is the cohesion and ϕ the internal frictional angle. For the modified von-Mises criterion,

$$A = \sqrt{3}(\sigma_y^c(\bar{\varepsilon}^p, \nabla^2\bar{\varepsilon}^p) - \sigma_y^t(\bar{\varepsilon}^p, \nabla^2\bar{\varepsilon}^p)); \quad B = -\sigma_y^c(\bar{\varepsilon}^p, \nabla^2\bar{\varepsilon}^p)\sigma_y^t(\bar{\varepsilon}^p, \nabla^2\bar{\varepsilon}^p) \tag{18}$$

where σ_y^t and σ_y^c are the current yield stresses in tension and compression respectively. For simplicity in the following discussion the associate plasticity rule is considered. The incremental plastic strain vector can be written

$$\Delta\hat{\varepsilon}^p = \lambda \frac{\partial F}{\partial \hat{\sigma}} = \lambda\,(\gamma_1 \hat{\mathbf{P}}\hat{\sigma} + A\mathbf{1}_m) \tag{19}$$

where $\gamma_1 = 1\,(GMVM)$ and $\gamma_1 = 1/2q\,(GDP)$, λ is the plastic multiplier, $\mathbf{1}_m = [0\ \ 0\ \ 1\ \ 0]$ and $\Delta\hat{\varepsilon}^p$ can also be decomposed into

$$\Delta\hat{\varepsilon}^p = \Delta\hat{\bar{\varepsilon}}^p + \mathbf{h}_\alpha \Delta\hat{\varepsilon}^{x,p} \quad \text{with} \quad \Delta\hat{\bar{\varepsilon}}^p = \lambda\,(\gamma_1 \hat{\mathbf{P}}\hat{\bar{\sigma}} + A\mathbf{1}_m); \quad \Delta\hat{\varepsilon}^{x,p} = 3\gamma_1\lambda\,\hat{\sigma}^x \tag{20}$$

The new definition of the internal state variable proposed by Duxbury and Li (1996) is given by

$$\Delta\psi = (\frac{2}{3} e_i\,(\Delta\hat{\varepsilon}_i^p)^2)^{1/2} + \frac{\sigma_m}{|\sigma_m|}\frac{\Delta\hat{\varepsilon}_m^p}{\sqrt{3}} \qquad (\text{no sum over m}) \tag{21}$$

where $|\sigma_m|$ is the absolute value of the hydrostatic stress σ_m, $\Delta\hat{\varepsilon}_i^p$ are the incremental plastic strain components referred to the natural coordinates and the coefficients e_i are given by $\mathbf{e}^T = [1\ \ 1\ \ 0\ \ 0.5]$. The effective plastic strain $\Delta\bar{\varepsilon}^p$ for the present element is defined as the average value of $\Delta\psi$ over the element and can be written in the forms

$$\bar{F}_2 = \Delta\bar{\varepsilon}^p - \lambda\,(2\bar{q} + \frac{\sigma_m}{|\sigma_m|}\frac{A}{\sqrt{3}}) = 0\ ; \qquad \bar{F}_2 = \Delta\bar{\varepsilon}^p - \lambda\,(1 + \frac{\sigma_m}{|\sigma_m|}\frac{A}{\sqrt{3}}) = 0 \tag{22}$$

for the modified von-Mises and the Drucker-Prager criteria, where

$$\bar{q} = (\frac{1}{A_e}\int_{A_e}(\frac{1}{2}\hat{\sigma}^T\hat{\mathbf{P}}\,\hat{\sigma})dA_e)^{1/2} = [\frac{1}{A_e}(\frac{1}{2}\hat{\bar{\sigma}}^T\hat{\mathbf{P}}\hat{\bar{\sigma}}\,A_e + 3\hat{\sigma}^{xT}\mathbf{H}\hat{\sigma}^x)]^{1/2} \tag{23}$$

As for the yield strengths to evaluate material parameters A and B in expressions (17) and (18) we assume the following non-local forms

$$c_h = c_{ho} + h_p^h\,\bar{\varepsilon}^p - c^h\,\nabla^2\bar{\varepsilon}^p\ ; \quad \phi = \phi_0 + h_p^\phi\,\bar{\varepsilon}^p - c^\phi\,\nabla^2\bar{\varepsilon}^p \tag{24}$$

for the Drucker-Prager criterion and

$$\sigma_y^t = \sigma_{y0}^t + h_p^t\,\bar{\varepsilon}^p - c^t\,\nabla^2\bar{\varepsilon}^p\ ; \quad \sigma_y^c = \sigma_{y0}^c + h_p^c\,\bar{\varepsilon}^p - c^c\,\nabla^2\bar{\varepsilon}^p \tag{25}$$

for the modified von-Mises criterion respectively. Here $c_h,\phi,\sigma_y^t,\sigma_y^c$ and $c_{h0},\phi_0,\sigma_{y0}^t,\sigma_{y0}^c$ are current and initial cohesions, the frictional angles, the tensile and the compressive yield strengths; $h_p^h,h_p^\phi,h_p^t,h_p^c$ are material softening/hardening parameters, c^h,c^ϕ,c^t,c^c are non-local material parameters. It is noted that the modified von-Mises model will degrade to the von-Mises model as the material tensile parameters σ_y^t, h_p^t, c^t are set to equal to the material compressive parameters σ_y^c, h_p^c, c^c respectively; in addition, the two gradient plasticity models will degrade to the local plasticity models as non-local parameters c^h,c^ϕ,c^t,c^c are set to zero.

To evaluate $\nabla^2\bar{\varepsilon}_i^p$ at an integration point i, we take account of the values of $\bar{\varepsilon}^p$ at the neighbouring integration points. Let L(i) and N(i) be the set of neighbouring integration points and the number of these points for integration point i. The Laplacian of $\bar{\varepsilon}^p$ at point i can be approximated in terms of $\bar{\varepsilon}_j^p$ (j ∈ L(i)) in the form

$$\nabla^2\bar{\varepsilon}_i^p = \sum_{j=1}^{N(i)} g_{ij}\bar{\varepsilon}_j^p \tag{26}$$

The coefficients g_{ij} are determined on the base of a least square polynomial approximation of the effective plastic strain around each integration point. For an integration point in an element on the boundary of the domain considered, we have to impose $\partial\bar{\varepsilon}^p/\partial n = \nabla\bar{\varepsilon}^p\,\mathbf{n} = 0$, where **n** is the normal to the boundary.

NON-LOCAL RETURN MAPPING ALGORITHM

Now we consider a typical time sub-interval [t, t + Δt] and an arbitrary integration point. The constitutive equation at time t + Δt can be given by

$$\hat{\bar{\sigma}}_{t+\Delta t} = \hat{\bar{\sigma}}_{t+\Delta t}^E - \hat{\mathbf{C}}\Delta\hat{\bar{\varepsilon}}^p \qquad \hat{\sigma}_{t+\Delta t}^x = \hat{\sigma}_{t+\Delta t}^{x,E} - 2G\,\Delta\hat{\varepsilon}^{x,p} \tag{27}$$

where the trial elastic stress vectors are

$$\hat{\bar{\sigma}}_{t+\Delta t}^E = \hat{\mathbf{C}}(\hat{\bar{\varepsilon}}_{t+\Delta t} - \hat{\bar{\varepsilon}}_t^p) \qquad \hat{\sigma}_{t+\Delta t}^{x,E} = 2G(\hat{\varepsilon}_{t+\Delta t}^x - \hat{\varepsilon}_t^{x,p}) \tag{28}$$

Substitution of equations (20) and (10) into (27) gives

$$\hat{\bar{\sigma}}_{t+\Delta t} = (\alpha\mathbf{1}_d + \beta\mathbf{1}_h)\hat{\bar{\sigma}}_{t+\Delta t}^E \;; \qquad \hat{\sigma}_{t+\Delta t}^x = \alpha\hat{\sigma}_{t+\Delta t}^{x,E} \tag{29}$$

where $\mathbf{1}_d = diag(1, 1, 0, 1)$ and $\mathbf{1}_h = diag(0, 0, 1, 0)$ and

$$\beta = 1 - \frac{3K\lambda A}{\sigma_m^E}\;; \quad \alpha = \begin{cases} 1/(1+6G\lambda) & \text{for the modified von-Mises criterion} \\ 1-(3G\lambda)/\bar{q}_{t+\Delta t}^E & \text{for the Drucker-Prager criterion} \end{cases} \tag{30}$$

$$\bar{q}^E = \bar{q}/\alpha = \left(\frac{1}{A_e}\int_{A_e}\left(\frac{1}{2}\hat{\sigma}^{E^T}\hat{\mathbf{P}}\,\hat{\sigma}^E\right)dA_e\right)^{1/2} = \left[\frac{1}{A_e}\left(\frac{1}{2}\hat{\bar{\sigma}}^{E^T}\hat{\mathbf{P}}\hat{\bar{\sigma}}^E A_e + 3\hat{\sigma}^{x,E^T}\mathbf{H}\hat{\sigma}^{x,E}\right)\right]^{1/2} \tag{31}$$

By using (30), (31) and $\sigma_m = \sigma_m^E - 3KA\lambda$ the yield functions are given in average form as

$$\bar{F} = \frac{1}{A_e}\int_{A_e} F dA_e = \bar{q}^E - 3\lambda(KA^2 + G) + A\sigma_m^E + B \tag{32}$$

$$\bar{F} = \frac{1}{A_e}\int_{A_e} F dA_e = (\bar{q}^E)^2/(1+6G\lambda)^2 - 3KA^2\lambda + A\sigma_m^E + B \tag{33}$$

for the Drucker-Prager and the modified von-Mises criteria and are written in a unified form as

$$\bar{F} = \bar{F}(\hat{\bar{\varepsilon}}, \hat{\varepsilon}^x, \lambda, \bar{\varepsilon}^p, \nabla^2\bar{\varepsilon}^p) = \bar{F}(\bar{q}^E, \sigma_m^E, \lambda, \bar{\varepsilon}^p, \nabla^2\bar{\varepsilon}^p) \tag{34}$$

In addition, a unified form for the consistency conditions in (22) can be given by

$$\dot{\bar{F}}_2 = (\frac{\partial \bar{F}_2}{\partial \lambda} + \frac{\partial \bar{F}_2}{\partial \bar{q}}\bar{q}^E \frac{d\alpha}{d\lambda})\dot{\lambda} + \frac{\partial \bar{F}_2}{\partial \bar{\varepsilon}^p}\dot{\bar{\varepsilon}}^p + \frac{\partial \bar{F}_2}{\partial \nabla^2\bar{\varepsilon}^p}\nabla^2\dot{\bar{\varepsilon}}^p + \frac{\partial \bar{F}_2}{\partial \bar{q}}\alpha\dot{\bar{q}}^E = 0 \tag{35}$$

It is noted that the strain vectors $\hat{\bar{\varepsilon}}$ and $\hat{\varepsilon}^x$ at each integration point are given in the return mapping algorithm to fulfill the yield condition. With the use of equations (34), (35) and (26) a non-local N-R iterative procedure at an integration point i for iteration k can be written as

$$[(\frac{d\bar{F}_i}{d\bar{\varepsilon}_i^p})^l_{k-1} + (\frac{d\bar{F}_i}{d\bar{\varepsilon}_i^p})^{nl}_{k-1}]\delta(\Delta\bar{\varepsilon}_i^p)_k = -\bar{F}_{i,k-1} - \sum_{\substack{j=1 \\ j\neq i}}^{N(i)} (\frac{d\bar{F}_i}{d\bar{\varepsilon}_j^p})^{nl}_{k-1}\delta(\Delta\bar{\varepsilon}_j^p)_k \tag{36}$$

where

$$(\frac{d\bar{F}_i}{d\bar{\varepsilon}_i^p})^l = \frac{\partial \bar{F}_i}{\partial \bar{\varepsilon}_i^p} - \frac{\partial \bar{F}_i}{\partial \lambda_i}\frac{\partial \bar{F}_{2,i}}{\partial \bar{\varepsilon}_i^p}\Big/(\frac{\partial \bar{F}_{2,i}}{\partial \lambda_i} + \bar{q}_i^E\frac{\partial \bar{F}_{2,i}}{\partial \bar{q}_i}\frac{\partial \alpha_i}{\partial \lambda_i}) \tag{37}$$

$$(\frac{d\bar{F}_i}{d\bar{\varepsilon}_j^p})^{nl} = (\frac{\partial \bar{F}_i}{\partial \nabla^2\bar{\varepsilon}_i^p} - \frac{\partial \bar{F}_i}{\partial \lambda_i}\frac{\partial \bar{F}_{2,i}}{\partial \nabla^2\bar{\varepsilon}_i^p}\Big/(\frac{\partial \bar{F}_{2,i}}{\partial \lambda_i} + \bar{q}_i^E\frac{\partial \bar{F}_{2,i}}{\partial \bar{q}_i}\frac{\partial \alpha_i}{\partial \lambda_i}))g_{ij} \tag{38}$$

It is noted that unlike in local computational plasticity, $\delta(\Delta\bar{\varepsilon}_i^p)_k$ cannot be determined at the local level. Nevertheless, the N-R iterative procedure is not a global one since only limited number of integration points within the localized plastic zone are involved and the non-local condition $\bar{F} = 0$ is still enforced in a pointwise fashion and at each iteration of a load step.

NON-LOCAL CONSISTENT TANGENT STIFFNESS MATRICES

Substitution of equations (26) and (35) into the consistency condition of equation (34) eliminates the terms relating to $\dot{\lambda}$ and $\nabla^2\dot{\bar{\varepsilon}}^p$ and gives the effective plastic strain rate $\dot{\bar{\varepsilon}}^p$ at each integration point with respect to the rate predictors $\dot{\bar{q}}^E$ and $\dot{\sigma}_m^E$ at its surrounding integration points , which are related to the rate strain vectors as

$$\dot{\bar{q}}^E = \frac{1}{2\bar{q}}[(\hat{\mathbf{P}}\hat{\bar{\sigma}})^T\hat{\mathbf{C}}\dot{\hat{\bar{\varepsilon}}} + \frac{12G}{A_e}(\mathbf{H}\hat{\sigma}^x)^T\dot{\hat{\varepsilon}}^x] \;\; ; \quad \dot{\sigma}_m^E = \mathbf{1}_m^T\hat{\mathbf{C}}\dot{\hat{\bar{\varepsilon}}} = 3K\mathbf{1}_m^T\dot{\hat{\bar{\varepsilon}}} \tag{39}$$

To derive the consistent tangent matrix we consider the variation of equations in (29)

$$\dot{\hat{\sigma}}_i = (\alpha_i \mathbf{1}_d + \beta_i \mathbf{1}_h)\dot{\hat{\sigma}}_i^E + \dot{\alpha}_i \mathbf{1}_d \hat{\sigma}_i^E + \dot{\beta}_i \mathbf{1}_h \hat{\sigma}_i^E; \qquad \dot{\hat{\sigma}}_i^x = \alpha_i \dot{\hat{\sigma}}_i^{x,E} + \dot{\alpha}_i \hat{\sigma}_i^{x,E} \tag{40}$$

Substituting $\dot{\bar{\varepsilon}}^p$ for each integration point as a function of $\dot{q}^E$ and $\dot{\sigma}_m^E$ at its surrounding points into equations (40) and using the definitions of α and β in (30) give local and non-local consistent tangent modulus matrices. With the use of strain-displacement relation (12) the integration of the virtual work done by the stress rate $\hat{\cdot}$ over the element i is given by

$$\int_{A_{e,i}} \delta\hat{\varepsilon}_i^T \dot{\hat{\sigma}}_i \, dA_{e,i} = \delta \mathbf{q}_i^T (\mathbf{K}_i^l \mathbf{q}_i + \sum_{j=1}^{N_i} (\mathbf{K}_{ij}^{nl} \mathbf{q}_j + \sum_{k=1}^{N_i} \mathbf{K}_{ijk}^{nl} \mathbf{q}_k)) \tag{41}$$

Here the local and the non-local element tangent stiffness matrices for the element i are

$$\begin{aligned}
\mathbf{K}_i^l &= \overline{\mathbf{B}}_i^T \mathbf{T}^T (\hat{\mathbf{D}}_{11}^l \mathbf{T} \overline{\mathbf{B}} + \frac{1}{2} \hat{\mathbf{D}}_{12}^l \mathbf{H}^{-1} \mathbf{H}^* \Gamma)_i + \frac{1}{2} \Gamma_i^T \mathbf{H}_i^{*T} \mathbf{H}_i^{-T} (\hat{\mathbf{D}}_{21}^l \mathbf{T} \overline{\mathbf{B}} + \frac{1}{2} \hat{\mathbf{D}}_{22}^l \mathbf{H}^{-1} \mathbf{H}^* \Gamma)_i \\
\mathbf{K}_{ij}^{nl} &= \overline{\mathbf{B}}_i^T \mathbf{T}^T (\hat{\mathbf{D}}_{11,ij}^{nl} \mathbf{T} \overline{\mathbf{B}}_j + \frac{1}{2} \hat{\mathbf{D}}_{12,ij}^{nl} \mathbf{H}_j^{-1} \mathbf{H}_j^* \Gamma_j) + \frac{1}{2} \Gamma_i^T \mathbf{H}_i^{*T} \mathbf{H}_i^{-T} (\hat{\mathbf{D}}_{21,ij}^{nl} \mathbf{T} \overline{\mathbf{B}}_j + \frac{1}{2} \hat{\mathbf{D}}_{22,ij}^{nl} \mathbf{H}_j^{-1} \mathbf{H}_j^* \Gamma_j) \\
\mathbf{K}_{ijk}^{nl} &= \overline{\mathbf{B}}_i^T \mathbf{T}^T (\hat{\mathbf{D}}_{11,ijk}^{nl} \mathbf{T} \overline{\mathbf{B}}_k + \frac{1}{2} \hat{\mathbf{D}}_{12,ijk}^{nl} \mathbf{H}_k^{-1} \mathbf{H}_k^* \Gamma_k) \\
&\quad + \frac{1}{2} \Gamma_i^T \mathbf{H}_i^{*T} \mathbf{H}_i^{-T} (\hat{\mathbf{D}}_{21,ijk}^{nl} \mathbf{T} \overline{\mathbf{B}}_k + \frac{1}{2} \hat{\mathbf{D}}_{22,ijk}^{nl} \mathbf{H}_k^{-1} \mathbf{H}_k^* \Gamma_k)
\end{aligned} \tag{42}$$

The local and the nonlocal compliance sub-matrices in (42) are

$$\begin{aligned}
&\mathbf{D}_{11,i}^l = A_{e,i}[(\alpha \mathbf{1}_d + \mathbf{1}_h)\hat{\mathbf{C}} + 6G(C_{\alpha 1} \mathbf{1}_d \hat{\bar{\sigma}} \hat{\bar{\sigma}}^T \mathbf{1}_d + C_{\beta 1} \mathbf{1}_m \hat{\bar{\sigma}}^T \mathbf{1}_d) + 3K(C_{\alpha 2} \mathbf{1}_d \hat{\bar{\sigma}} \mathbf{1}_m^T + C_{\beta 2} \mathbf{1}_h)]_i \\
&\mathbf{D}_{12,i}^l = 12G_i[C_{\alpha 1} \mathbf{1}_d \hat{\bar{\sigma}} + C_{\beta 1} \mathbf{1}_m]_i (\mathbf{H}\hat{\sigma}^x)_i^T; \quad \mathbf{D}_{21,i}^l = (\mathbf{H}\hat{\sigma}^x)_i [12GC_{\alpha 1} (\mathbf{1}_d \hat{\bar{\sigma}})^T + 6KC_{\alpha 2} \mathbf{1}_m^T]_i \\
&\mathbf{D}_{22,i}^l = [\frac{24G}{A_e} C_{\alpha 1} (\mathbf{H}\hat{\sigma}^x)(\mathbf{H}\hat{\sigma}^x)^T + 4G\alpha \mathbf{H}]_i
\end{aligned} \tag{43}$$

$$\begin{aligned}
&\mathbf{D}_{11,ij}^{nl} = A_{e,i}[\bar{f}_{ij}^1 (\mathbf{1}_d \hat{\bar{\sigma}})_i (\mathbf{1}_d \hat{\bar{\sigma}})_j^T + \bar{r}_{ij}^1 \mathbf{1}_m (\mathbf{1}_d \hat{\bar{\sigma}})_j^T + \bar{f}_{ij}^2 (\mathbf{1}_d \hat{\bar{\sigma}})_i \mathbf{1}_m^T + \bar{r}_{ij}^2 \mathbf{1}_h] \\
&\mathbf{D}_{12,ij}^{nl} = A_{e,i}[\bar{f}_{ij}^3 (\mathbf{1}_d \hat{\bar{\sigma}})_i (\mathbf{H}\hat{\sigma}^x)_j^T + \bar{r}_{ij}^3 \mathbf{1}_m (\mathbf{H}\hat{\sigma}^x)_j^T] \\
&\mathbf{D}_{21,ij}^{nl} = 2\bar{f}_{ij}^1 (\mathbf{H}\hat{\sigma}^x)_i (\mathbf{1}_d \hat{\bar{\sigma}})_j^T + 2\bar{f}_{ij}^2 (\mathbf{H}\hat{\sigma}^x)_i \mathbf{1}_m^T; \quad \mathbf{D}_{22,ij}^{nl} = 2\bar{f}_{ij}^3 (\mathbf{H}\hat{\sigma}^x)_i (\mathbf{H}\hat{\sigma})_j^T
\end{aligned} \tag{44}$$

$$\begin{aligned}
&\mathbf{D}_{11,ijk}^{nl} = A_{e,i}[\bar{f}_{ijk}^1 (\mathbf{1}_d \hat{\bar{\sigma}})_i (\mathbf{1}_d \hat{\bar{\sigma}})_k^T + \bar{r}_{ijk}^1 \mathbf{1}_m (\mathbf{1}_d \hat{\bar{\sigma}})_k^T + \bar{f}_{ijk}^2 (\mathbf{1}_d \hat{\bar{\sigma}})_i \mathbf{1}_m^T + \bar{r}_{ijk}^2 \mathbf{1}_h] \\
&\mathbf{D}_{12,ijk}^{nl} = A_{e,i}[\bar{f}_{ijk}^3 (\mathbf{1}_d \hat{\bar{\sigma}})_i (\mathbf{H}\hat{\sigma}^x)_k^T + \bar{r}_{ijk}^3 \mathbf{1}_m (\mathbf{H}\hat{\sigma}^x)_k^T] \\
&\mathbf{D}_{21,ijk}^{nl} = 2\bar{f}_{ijk}^1 (\mathbf{H}\hat{\sigma}^x)_i (\mathbf{1}_d \hat{\bar{\sigma}})_k^T + 2\bar{f}_{ijk}^2 (\mathbf{H}\hat{\sigma}^x)_i \mathbf{1}_m^T; \quad \mathbf{D}_{22,ijk}^{nl} = 2\bar{f}_{ijk}^3 (\mathbf{H}\hat{\sigma}^x)_i (\mathbf{H}\hat{\sigma})_k^T
\end{aligned} \tag{45}$$

The coefficients in sub-matrices (43) - (45) are given by Li and Cescotto (1997). It is noted that the second part of the non-local virtual work in equation (41) will disappear for the case without introduction of the non-local parameter c^ϕ into the second equation in (24), i.e. we will not need to calculate the sub-matrices in (45) under this condition.

THE PLANE STRESS

For the plane stress state, we have to enforce the constraint $\sigma_z \equiv 0$, (i.e. $\bar{\sigma}_z \equiv 0$) to the above formulations. Recalling equations (29) and (3) we have the constant component $\bar{\sigma}$

$$\bar{\sigma} = \mathbf{T}^T(\alpha \mathbf{1}_d + \beta \mathbf{1}_h)\mathbf{T}\bar{\sigma}^E \tag{46}$$

where the components $\bar{\sigma}_x^E, \bar{\sigma}_y^E$ and τ_{xy}^E in $\bar{\sigma}^E$ are the elastic trial stresses calculated from the given strains. The third component in equation (46) with the enforced constraint $\bar{\sigma}_z \equiv 0$ gives

$$\bar{\sigma}_z^E = \frac{\alpha - \beta}{2\alpha + \beta}(\bar{\sigma}_x^E + \bar{\sigma}_y^E) \tag{47}$$

It is seen that $\bar{\sigma}_z^E \equiv 0$ is only true at the integration points under the elastic state, for which $\alpha \equiv 1$ and $\beta \equiv$. Consequently the variation $\dot{\bar{q}}^E$ with respect to $\bar{\sigma}_z^E$ has to be involved in the calculation, which can be given by

$$\frac{\partial \bar{q}^E}{\partial \bar{\sigma}_z^E} = \frac{1}{2\bar{q}^E}(\hat{\mathbf{P}}\hat{\bar{\sigma}}^E)^T \mathbf{T}_z; \quad \mathbf{T}_z^T = [-\frac{1}{\sqrt{2}} \; -\frac{1}{\sqrt{6}} \; \frac{1}{\sqrt{3}}] \tag{48}$$

$\partial \bar{\sigma}_z^E / \partial \lambda$ can be calculated according to $\bar{\sigma}_z^E$ defined in (47). In order to form the consistent tangent stiffness matrices, the third column of the transformation matrix (4) is simply deleted in the calculation of the elasto-plastic stiffness matrices (42) to account for the effect of $\bar{\sigma}_z \equiv 0$. In addition, $\hat{\mathbf{C}}(3,3)$ in equation (10) should be replaced by the value of $E(1+2\upsilon)/(1-\upsilon^2)$.

NUMERICAL EXAMPLE

As the first example,the large deformation of the short cantilever beam with the ratio $l/h = 3$ is studied. The beam is subjected to a vertical prescribed displacement $u_y = 2$ at the right-hand side of the beam. We first check the performance of the present element in the case where the modified von-Mises criterion is degraded to the classical von-Mises one in the plane strain state. The material property data used are as same as those used for the example by Jetteur et al.(1991). The results and the convergence rates obtained by the present work exactly agree with those given by Jetteur et al.(1991). Then the beam is re-analysed with the use of the modified von-Mises criterion in the plane stress state. The material parameters used are: E = $10000\,N/mm^2$, $\upsilon = 0.15$, $\sigma_y^{t0} = 300\,N/mm^2$, $\sigma_y^{ct0} = 600\,N/mm^2$, $h_p^t = 1800 N/mm^2$, $h_p^c = 2200\,N/mm^2$. Three different meshes: (1) 4×12 element regular mesh; (2) 8×24 element regular mesh and (3) an irregular mesh with 174 elements and 201 nodes generated by a non-structured mesh generator are used. The deformed meshes and the three contours for the effective plastic strain are illustrated in Figure 1. The final values of the reaction at the specified value of the deflection equal to 2.0 are: $3.135 \times 10^2\,N$ for the mesh (1), $3.092 \times 10^2\,N$ for the mesh (2) and $3.095 \times 10^2\,N$ for the mesh (3). It is shown that the results obtained for three different meshes agree with each other well and, therefore, illustrate the excellent convergence of the element in the space domain.

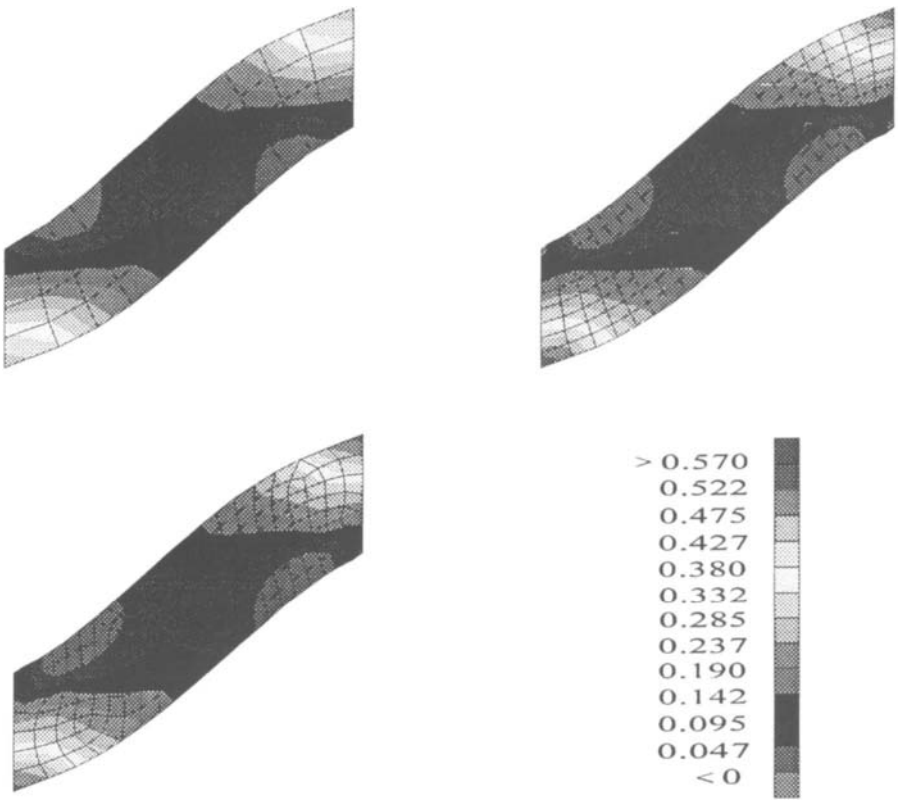

Figure 1 The contours' effective plastic strain on deformed meshes for the cantilever

The second example is to analyze a footing problem. Due to symmetry consideration, the calculation is carried out for half of the footing. The footing is simply supported at both the side ends and the bottom, and is subjected to uniformly prescribed vertical displacements, distributed on the range of 1.5 M at the left of the top edge of the footing. These increase until those corresponding to the collapse load. The material properties with the Drucker-Prager model are: E = $210\,N/mm^2$, $\upsilon = 0.3$, the internal frictional angle $\phi = 20^0$ and cohesion $c = 7\,N/mm^2$. The footing is modelled using two different discretizations with irregular meshes, generated by a non-structured mesh generator, which are: (1) 161 elements with 181 nodes; (2) 329 elements with 351 nodes. Figure 2 illustrates three sets of the contours for the effective plastic strain, the deviatoric effective stress and the mean stress respectively. It is shown that the results obtained for the both different meshes agree very well over most of the domain of the footing, except the values of the effective plastic strain at the local region, where high values of plastic strain gradient arise and which indicate that local mesh refinement in the region is necessary in order to ensure the accuracy of the analysis.

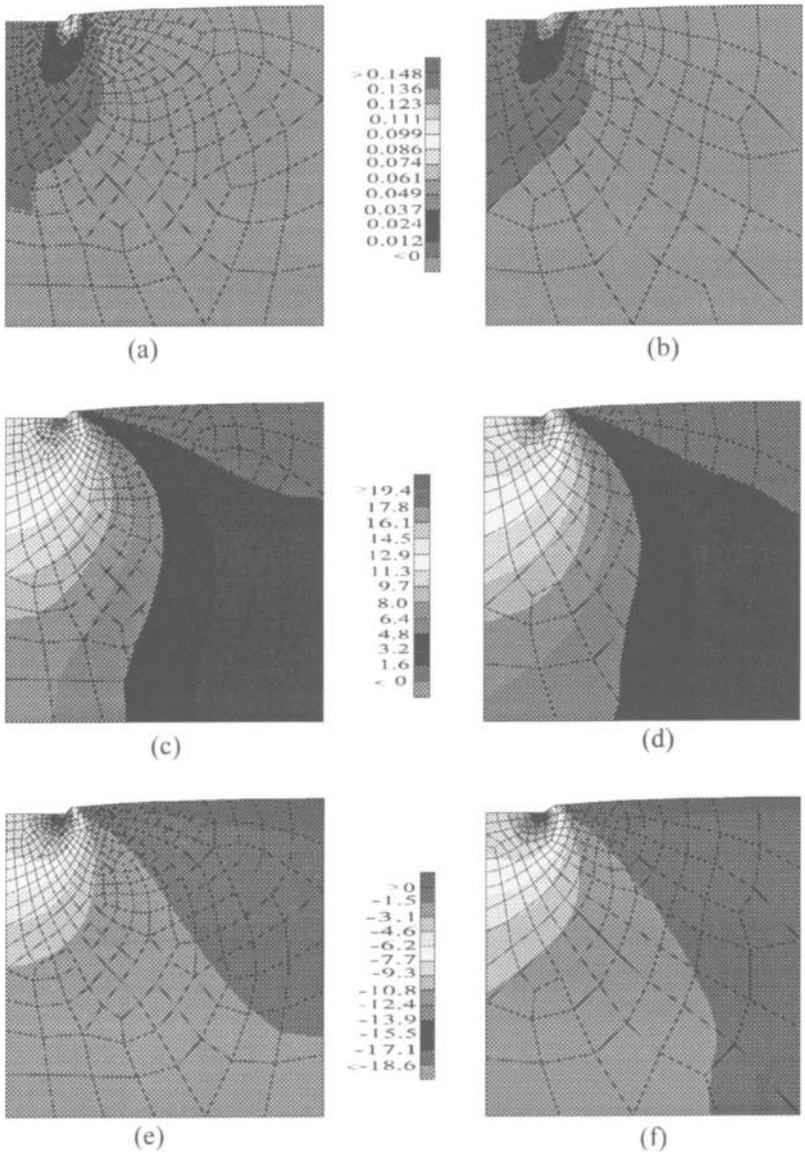

The footing problem

Effective plastic strain: (a) 323 element mesh; (b) 161 element mesh
Effective deviatoric stress: (c) 323 element mesh; (d) 161 element mesh
Mean stress: (e) 323 element mesh; (f) 161 element mesh

Figure 2 The contours on deformed meshes for the footing problem

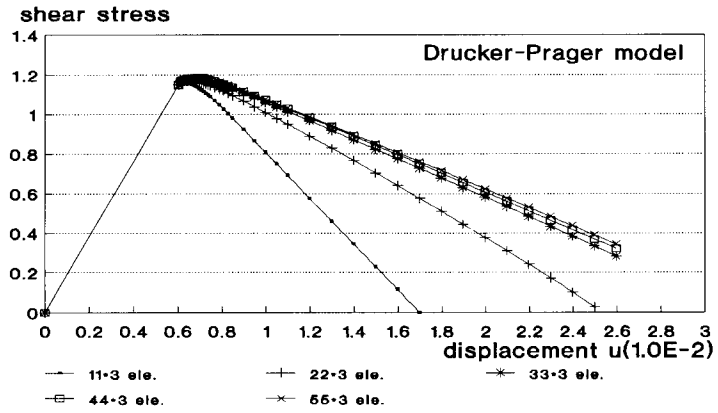

Figure 3 Shear stress curves with increasing displacement u of the top face with different meshes for the non-local Drucker-Prager model

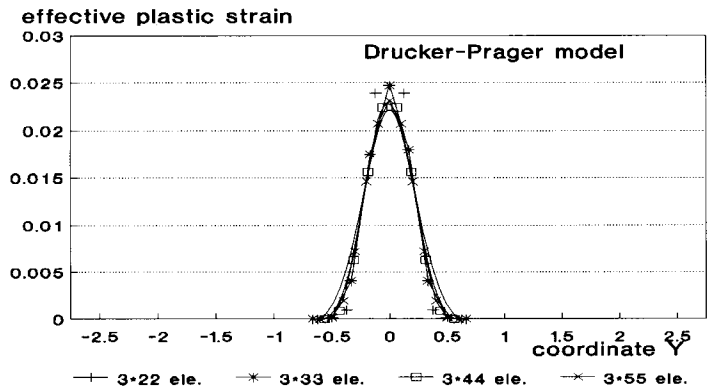

Figure 4 Distribution of effective plastic strain for u = 0.025 at the top of the plate

The third example considers a rectangular plate with initial length L_0 = 5.5 and initial width B_0=0.75, meshed by $N \times M$ elements. N and M are numbers of the elements in length(y axis) and width(x axis) respectively. The plate fixed at the bottom and loaded by an increasing prescribed horizontal (in x axis) displacement at the top, is analyzed as a plane strain problem by using the Drucker-Prager model. The vertical displacements of the nodes at the top are fixed. To manifest that pathological mesh dependence has been overcome by using the present element, we consider five test cases with different element meshes N×M: (1) 11×3; (2) 22×3; (3) 33×3; (4) 44×3; (5) 55×3 element meshes. The values of material elastic properties used for the entire plate are E = 2100 and μ=0. The constant frictional angle ϕ =

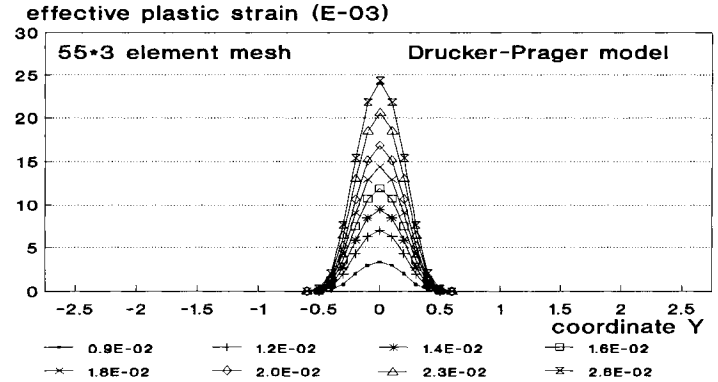

Figure 5 Evolution of effective plastic strain distribution with increasing displacement u of the top face

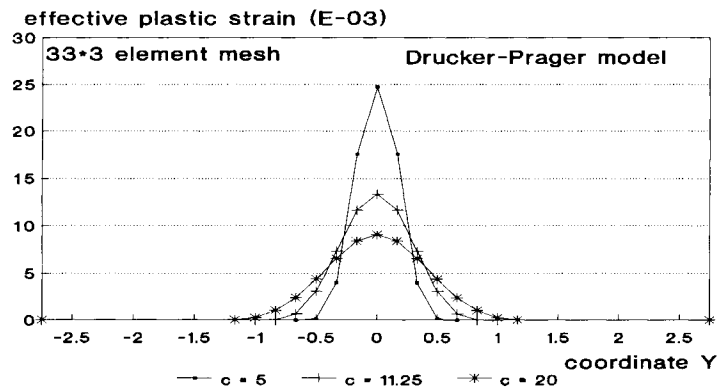

Figure 6 Distribution of effective plastic strains along Y axis of the plate subjected to a pure shear loading for different values of the non-local material plastic parameter for u = 0.025 at the top of the plate

40° is assumed. The initial cohesion c_{h0}=2.0 except for the elements which lie within the middle of the plate between y = -0.25 and y = 0.25. The initial cohesion for these elements has been weakened to the value of c_{h0}= 1.8. The softening modulus h_p^h = -200 and the non-local parameter c^h = 5 are used for all elements, including the weakened ones. Figure 3 illustrates the convergence of the shear stress - displacement (at the nodes on the top face) curves. Analytical solution of the width of the localization zone for a one-dimensional case for the Drucker-Prager criterion and the frictional angle ϕ = constant being assumed, can be given in the form $w = 2\pi\sqrt{-c^h/h_p^h}$. Numerical results shown in Figure 4 illustrate that the width of the

localization zone and the effective plastic strain distribution along y axis over the zone rapidly converge to a unique solution. It is observed that the width of the localization zone evaluated by the analytical solution gives a good approximation of the shear band thickness obtained in the present simulation. Figure 5 illustrates the evolution of effective plastic strain distribution. It is observed that the localization zone grows quickly to a certain width and then intense plastic strains are developed in the narrow band with the unchanged width. To show the dependence of the thickness of localization zone on the non-local material parameter c^h relating to the internal length, we consider the example again. All the data used for the example, except the value of c^h, are unchanged. The three test cases, with the different values of c^h, i.e. $c^h = 20, 11.25, 5$ are executed. Figure 6 illustrates the thicknesses of the localization zones and the effective plastic strain distributions within the zones for the three test cases. It is observed that using a large value for internal length results in the wider localization zone and the lower peak value of the effective plastic strain.

ACKNOWLEDGMENTS

The author is pleased to acknowledge the support of this work by the National Science Foundation of China (Project No. 19472016) and the State Scientific and Technological Commission of China through "China State Major Key Project for Basic Research": "The Theory and Methodology for Scientific and Engineering Computations with Large Scale".

REFERENCES

Bazant Z.P., Belytschko T. and Chang T.P. (1984). Continuum theory for strain softening. J. of Engng. Mech. ASCE, **110**, 1666-1692 .

de Borst R. and Muhlhaus H.B. (1992). Gradient- dependent plasticity: formulation and algorithmic aspects. Int. J. Numer. Methods Eng., **35**, 521-539.

Duxbury P.G. and Li Xikui (1996). Development of elasto-plastic material models in a natural coordinate system. Comp. Methods Appl. Mech. Eng., **135**, 283-306.

Flanagan,D.P. and Belytschko,T. (1981). A uniform strain hexahedron and quadrilateral with orthogonal hourglass control. Int.J.Numer. Methods Engng., **17**, 679-706.

Jetteur Ph.and Cescotto S. (1991). A mixed finite element for the analysis of large inelastic strain. Int. J. Numer. Methods Eng., **31**, 229-239.

Li Xikui and Cescotto S. (1996). Finite element method for gradient plasticity at large strains. Int. J. Numer. Methods Eng., **39**, 619-633.

Li Xikui and Cescotto S. (1997). A mixed element method in gradient plasticity for pressure dependent materials and modelling of strain localization. Computer Methods Appl. Mech. Eng., **144**, 287-305.

Muhlhaus H.B. (1989). Application of Cosserat theory in numerical solutions of limit load problems. Ingenieur Archiv, **59**, 124-137.

Needleman A. (1988). Material rate dependent and mesh sensitivity in localization problems. Comp. Method Appl. Mech. Eng., **67**, 69-86.

Sluys L.J., de Borst R. and Muhlhaus H.B. (1993). Wave propagation, localization and dispersion in a gradient- dependent medium. Int. J. Solids Struct., **30**, 1153-1171.

Zienkiewicz O.C. and R.L.Taylor (1991). The Finite Element Method, Vol.2, McGraw-Hill.

BEHAVIOR OF IN-FILLED STEEL PLATE PANELS SUBJECTED TO CYCLIC SHEAR

Ming Xue[1] and Le-Wu Lu[2]

[1] Becht Engineering Co. Liberty Corner, NJ 07938, USA.
[2] Department of Civil & Environmental Engineering, Lehigh University
Bethlehem, PA 18015, USA

ABSTRACT

A new seismic lateral load resisting system, consisting of steel frames and infilled plate panels, has been developed and extensive research has been conducted to study the overall response of the system as well as the behavior of the panels under cyclic shear. In this system, the thin-walled panels are connected only to girders of the frame. The research includes studies of the interaction between the frame and the panels, behavior of the girder-supported panels subjected to monotonic and cyclic in-plane shear and development of hysteretic models for use in seismic analysis.

A special finite element analysis package, ULSAS-GE, which is based on a program previously developed by Tetsuya Yao for analyzing plates under cyclic in-plane normal forces, has been prepared to perform the shear analysis. Included in the analysis are the effects of out-of-plane buckling and yielding. A special algorithm for circumventing the severe instability encountered at load reversals was implemented into the package. A detailed study of the cyclic behavior of four panels selected from a frame-panel system has been made. Simple formulas which can be used in design to predict the behavior and strength of the panels have been proposed. The paper presents a discussion of the problem, descriptions of the analysis procedure adopted, implementation of the algorithm and numerical results. A general discussion of the performance of thin-walled panels under cyclic shear is also given.

KEYWORDS

Plate panels, cyclic shear, post buckling, seismic resistance, plasticity, finite element.

INTRODUCTION

Cyclic behavior of thin plate panels under in-plane shear has recently been a subject of international studies because of the promising application of steel plates as shear walls in structural frames to resist wind and seismic loads. Owing to the tension field action, first revealed by Wagner in 1931 (Wagner, 1931), thin plates under in-plane shear possess substantial and stable post-buckling strength and deformation capacity. A recent study by the authors (Xue and Lu, 1994) suggests that a control on lateral stiffness can be exercised by selecting proper width-to-thickness ratios of the plates and the means to connect the plates to frame members. This control can be used in seismic design to contain structural deformations to certain limits under different magnitudes of loads. This control is also helpful for achieving a desirable balance between lateral strength and stiffness. The issues of deformation control and balanced design have been recognized as critical design measures for seismic-resistant structures, especially after the recent earthquake events in the U.S.A. and Japan. To effectively utilize these concepts, knowledge about the cyclic behavior of steel wall panels in the elasto-plastic, post-buckling range is necessary.

Similar to plate post-buckling behavior under uniaxial in-plane compression, a plate under in-plane shear has stable post-buckling behavior and substantial post-buckling strength because of the membrane stress restraints on the plate. Different from a plate under compression, a plate under shear experiences profile changes as well as magnitude changes of the out-of-plane deformations as load increases. The profile changes are due to the in-plane stresses, composed of in-plane shear and normal tension components. This feature of the plate post-buckling behavior under in-plane shear has been observed in laboratory tests and analytical studies by several researchers (Thorburn, Kulak and Montgomery, 1983; Elgaaly and Caccese, 1990; Kossira and Horst, 1991). In a numerical analysis, a profile change results in local instability and is responsible for severe convergence difficulties. For monotonic loading, these difficulties can be circumvented by using either advanced computational algorithms (Riks, 1972 and 1979) or initial imperfections which include all necessary profile modes. For cyclic loading, the severe instability and convergence at load reversals cannot be handled in the same manner, because a user control over loading is necessary and the tension field action can eliminate initial imperfections in some areas of the plate.

In this paper, an algorithm is presented to circumvent the instability at load reversals in analysis of the cyclic behavior of steel plates under in-plane shear. The algorithm was implemented in a finite element analysis package, ULSAS-GE. Four steel wall panels were analyzed and the results are presented.

BACKGROUND

Study on the post-buckling behavior of plates under in-plane shear was started in the early 1930s and is still going on now. Before the early 1980s, the focus was on prediction of plate ultimate strength under monotonic loading. Under in-plane shear, the stress state in a simply supported plate is initially described by a tension and a compression principal stress. The principal stress orientations can be parallel or inclined, with a small angle, to the two plate diagonals, depending on the plate aspect ratio. The diagonal along which the tension principal stress acts is called the tension diagonal.

The other diagonal is called the compression diagonal, because the stress in its direction is mainly compressive. As the applied shear increases, the plate buckles when its critical shear buckling load is reached. The buckling is produced by the compression principal stress, and the buckling profile along the compression diagonal usually has more waves than that along the tension diagonal. The profile difference along the two diagonals is an important feature of plate shear buckling. After buckling, the plate has both in-plane stresses and out-of-plane bending stresses. Despite the bending stress interference to the stress state in inner plate areas, the in-plane stresses are still dominant at the boundaries, but are very different from the state before buckling. Besides the in-plane shear stress, which is the only stress at boundaries before buckling, an in-plane normal tension stress emerges after buckling and keeps growing, due to the boundary restraints on the plate post-buckling deformations. The in-plane shear and normal tension stresses form an equivalent tension stress, at boundaries, leaning to the tension diagonal. The magnitude and orientation of the equivalent tension stress depend on the magnitudes of both the in-plane shear and normal tension stresses. While the in-plane shear stress acts as loading and continues to produce large buckling deformations, the in-plane normal tension stress acts as reaction and exerts restraints on the buckling deformations. Due to the effects of the two in-plane stresses on buckling deformations, the shear post-buckling behavior is distinguished from its compression counterpart by a unique character. That is, the plate experiences profile changes as well as magnitude changes of the out-of-plane deformations as the load increases. To avoid post-buckling behavior complexity, early studies focused on simple simulations of the equivalent tension stress, which has different magnitudes and orientations at different boundary locations. By approximating the actual stress by a tension stress uniformly distributed over a limited plate area, Wagner proposed the tension field theory (Wagner, 1931). To include rigidity effects of the boundary supports, Basler (Basler, 1960) and Rockey (Porter, Rockey and Evans, 1975) later modified and extended the tension field theory. In all versions of the tension field theory, the size and orientation of the tension field were formulated based on test data. By assuming material yield stress as the ultimate tension stress, the ultimate shear strength can be computed by the tension field theory.

The behavior under cyclic in-plane shear has been studied since the early 1980s when steel plates were used as shear wall panels in seismic-resistant structures. It is necessary to be able to predict the cyclic behavior of thin plates from elastic pre-buckling to elasto-plastic post-buckling range. Due to the difficulties encountered in the analytical studies, the early work had emphasized laboratory testing. A summary of the experimental studies and test observations has been provided by the first author (Xue, 1995).

Kossira and Horst (1991) studied the low cycle fatigue behavior of thirty-seven 50x50 mm aluminum plates under in-plane shear. The work involved both laboratory tests and finite element analyses. The analytical results were compared with the corresponding test data. They found that there were two different deformation paths for a plate to take at a load reversal (i.e., zero external loading). In one path, the unstable path, the plate experienced a sudden profile change of its out-of-plane deformations as it was reloaded in the opposite direction. The change involved sign switches as well as magnitude changes. In the other path, the stable path, only the magnitude of the out-of-plane deformations changed with reloading. The residual out-of-plane deformations were found to control the path that a plate would take at a load reversal. In the small square plates analyzed, the unstable path would be taken if the out-of-plane residual deformations were primarily anti-

symmetric. On the other hand, the stable path would be taken when the residual deformations were predominantly symmetric. However, the study showed that almost the same relationship of shear load versus shear deformation was obtained no matter which path was enforced in the analysis.

A sudden profile change with sign switches of the out-of-plane deformations signifies occurrence of a bifurcation or severe instability, and often leads to convergence difficulty in numerical analysis. Because the plate residual out-of-plane deformations depend primarily on the magnitude of the shear applied prior to unloading, the path that the plate would adopt is load-history dependent. Thus, the observed instability cannot be circumvented by using initial imperfections. To avoid the instability, Kossira and Horst artificially filtered out the anti-symmetric components of the residual out-of-plane deformations in their analyses. They found good agreement between the analytical results and test data.

BEHAVIOR OBSERVATIONS AND POSTULATES AT IN-PLANE SHEAR REVERSAL

Figure 1 illustrates the changes of the out-of-plane deformations of a plate at a shear reversal. The plate has elasto-plastic out-of-plane deformations under a shear in direction 1. Notice that in Fig.1(a) the out-of-plane deformation profiles are different along the two diagonals of the plate. The profile has more waves along one diagonal than the other. This profile difference along the plate diagonals can be described by profile orientation. The profile containing more waves is always orientated along the compression diagonal and the profile with less waves along the tension diagonal. The reason for this is that the tension field action tends to stretch out the out-of-plane deformations along the tension diagonal and to increase the constraints along the compression diagonal. On the other hand, the increase in the in-plane shear tends to increase the out-of-plane deformations. Because of this interaction, the plate must accommodate an increasing number of waves along the compression diagonal, as the shear load increases.

If the material yields, out-of-plane residual deformations will result when the load is completely removed, as shown in Fig.1(b). The residual deformations inherit many of the characteristics of the profile shown in Fig.1(a). As the shear load is applied in direction 2, opposite to direction 1, the equivalent tension stress at boundaries changes its direction. As a result, the previous tension diagonal is now subjected to compression and the previous compression diagonal to tension. As illustrated in Figs.1(c) and 1(d), the out-of-plane residual deformations will be reduced along one diagonal, the current tension diagonal (to be different from the previous tension diagonal), and increased along the other, the current compression diagonal. As the shear load increases, the out-of-plane deformations may take a profile different from that of the out-of-plane residual deformations when the current out-of-plane deformations are incompatible with the in-plane stresses produced by the reversed shear load.

It is reasonable to postulate that the new profile, which can stabilize the panel behavior during reloading, differs from that of the out-of-plane residual deformations in two aspects: orientation and component content. The new profile should orientate itself so that more waves would be present along the current compression diagonal and less along the current tension diagonal, which is just opposite to the profile orientation of the out-of-plane residual deformations. The component content

(a) Out-of-plane deformations under loading in direction 1

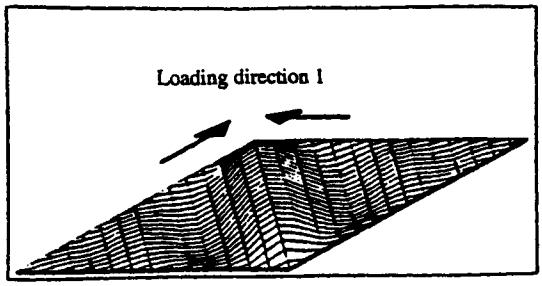

(b) Out-of-plane residual deformations

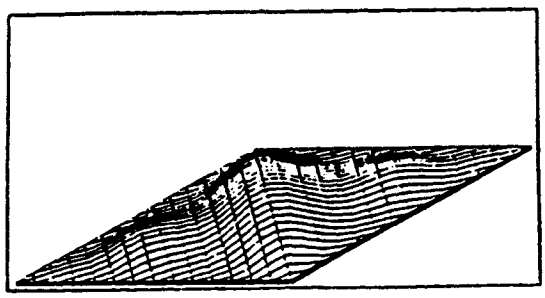

(c) Out-of-plane deformations at beginning of loading in direction 2

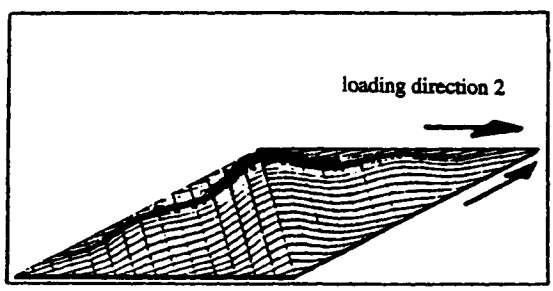

(d) Out-of-plane deformations under loading in direction 2

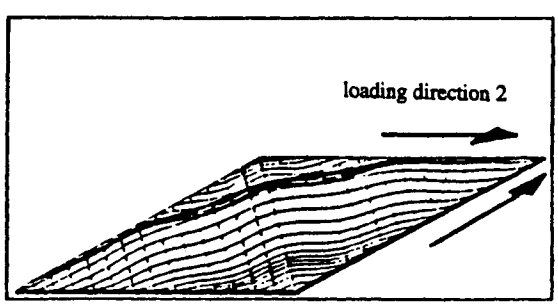

Figure 1 Changes of Out-of-Plane Deformations at Load Reversal

is defined by the number of modes included in a profile, if the profile is assumed to be composed of a series of linearly independent modes. The new profile should have more component content along the current compression diagonal and less along the current tension diagonal. Due to the nature of the interaction between the in-plane shear and normal tension stresses, the component content along the compression diagonal should monotonically increase, and that along the tension diagonal should monotonically decrease, as the load increases. This suggests that the profile of the out-of-plane deformations constructed with a mirror switch of the out-of-plane residual deformations about the plate central section would satisfy both the orientation and component content requirements, and can be used as the new profile.

With the stabilized out-of-plane deformations, tension field action can develop and again dominates the post-buckling behavior of the plate under the reversed shear loading. If the component content along current compression diagonal contains all the necessary modes, the stable behavior could continue till the next load reversal.

APPROACH TO BIFURCATION-LIKE INSTABILITY AT SHEAR LOAD REVERSAL

Based on the understanding of the plate post-buckling behavior at a shear load reversal, a general algorithm was proposed for shear panels to circumvent the instability problem discussed above. In the algorithm, small artificial out-of-plane deformations are introduced slightly before a load reversal. As illustrated in Fig. 2, the plate is divided into four rectangular areas by its horizonal and vertical center sections. T-I and T-II denote the areas linked by the current tension diagonal; C-I and C-II denote the areas linked by the current compression diagonal. The artificial out-of-plane deformations are formed by replacing the out-of-plane displacement of a node in area T-I (T-II) with the corresponding nodal displacement in area C-I (C-II), shown in Fig.2(b). The node correspondence is determined by symmetry about the plate vertical central section. As discussed in the previous section, the out-of-plane deformations formed in this way should be compatible with the in-plane stresses subsequently developed after the shear load is reversed. Therefore, the instability discussed before is prevented and consecutive analysis can be stabilized under reloading. Notice that the out-of-plane residual deformations in areas C-I and C-II are retained rather than replaced with the out-of-plane nodal displacements of areas T-I and T-II. There are two reasons to do this. One is that along the two diagonals the profile differences are insignificant in the small loading range. The other is that a significant reloading magnitude is required to stretch out the out-of-plane residual deformations for a moderate or large load. Thus, unrealistic stiffness will result at the beginning of reloading if the out-of-plane deformations of areas C-I and C-II are replaced by that of areas T-I and T-II, respectively.

The use of the artificial out-of-plane deformations in analysis causes behavior discontinuity of a plate and produces computation errors. However, because of the physical stability and insensitivity of the shear panel overall behavior to the out-of-plane deformations, the errors introduced can be quickly balanced out through consecutive iterations. The errors will be localized at load reversals, where external load magnitude is always small. By controlling load increment and number of iterations, analysis inaccuracy caused by using the artificial out-of-plane deformations can be limited to a tolerable range. This argument is based on the variational and computational principles which

(a) Out-of-plane deformation profile at end of unloading

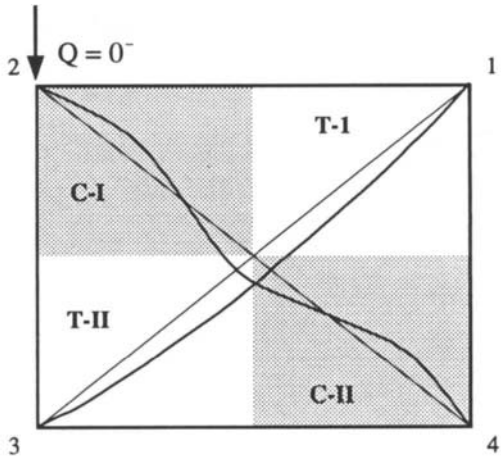

(b) Artificial out-of-plane deformation profile introduced at a load reversal

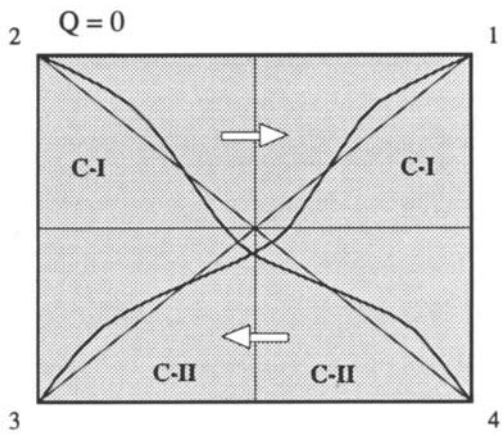

(c) Out-of-plane deformation profile at beginning of reloading

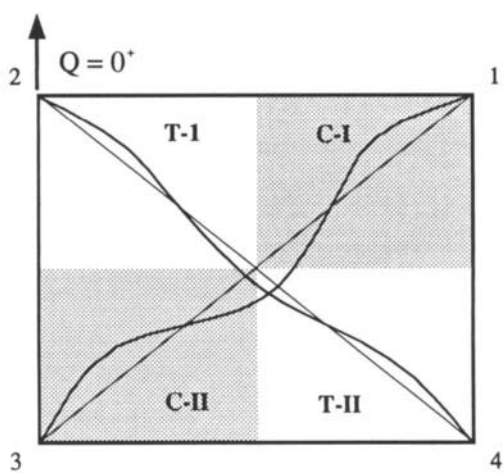

Figure 2 Artificial Out-of-Plane Deformation Formation

and Montgomery, 1983) was modeled and analyzed with ULSAS-GE under both monotonic and cyclic loading. Analytical results were compared in a large deformation range to the test data under monotonic loading. Due to the availability of the test data, however, the comparison under cyclic loading was made only in a small deformation range. The comparison showed that ULSAS-GE is capable of predicting both the monotonic and the cyclic behavior of the frame-wall panel assemblages. The ULSAS-GE program successfully circumvented the instability problem at load reversals. However, it is believed that the proposed algorithm should be verified with more test data, when available.

CYCLIC BEHAVIOR OF THIN PLATE UNDER IN-PLANE SHEAR

Four frame-wall panels assemblies were analyzed with ULSAS-GE. The assemblies were selected from a specially designed frame-wall system (Xue and Lu, 1994). As shown in Fig. 3, each assembly consists of a steel frame and a steel wall panel. The frame is composed of a top and bottom beam, a left and a right column. The beams, W18x35, are pin connected to the columns, varying from W14x233 to W14x74. The panel is filled in the frame with continuous connections to the beams only. Table 1 provides the width-to-thickness and aspect ratios, a/t and s/h, of the four panels in the selected assemblies.

Table 1 Shear Panels Selected for Cyclic Analysis

Shear Panel	PGS1	PGS2	PGS5	PGS9
s/h	0.8	1.0	1.0	1.0
a/t	1636	1309	1516	1694

Figure 4 shows the finite element model developed for the assemblies. Because of the large axial rigidity, the columns in the model are simulated by two rollers at top between the top beam and a rigid support. Found from studies by the authors, the beam bending deformations do not have significant effects on the panel behavior for the beam sizes commonly required by gravity load design. In the model, therefore, only the top beam is included and the panel is fixed at the bottom edge to a rigid support. The shear load to the panel is

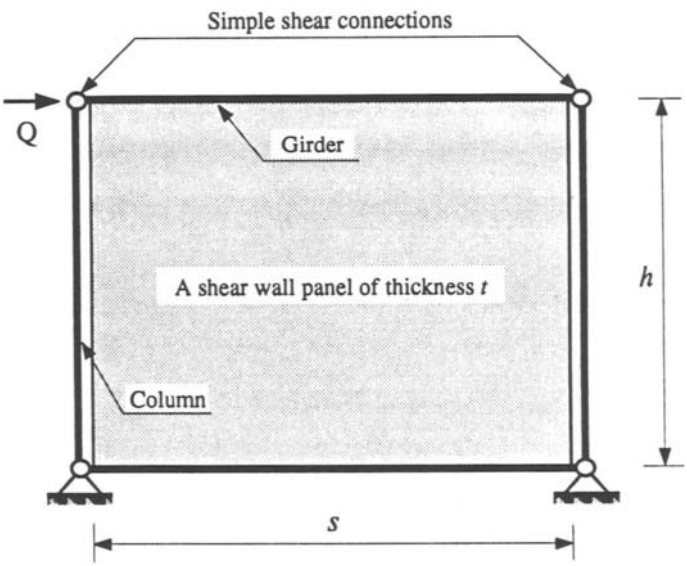

Figure 3 Frame-Wall Panel Assembly

are the mathematical basis for all the approximation methods.

In mechanics terms, the principles can be stated the following way, specifically for shear panels. If a set of continuous equations exists in a displacement domain to define deformations of thin plates subjected to in-plane shear, and the equations possess a stable and unique solution for a load condition in a given solution domain, the solution can be approached with an initial deformation approximation. For shear panels, the continuity requirement is guaranteed, at least in lower orders, by the satisfaction of basic mechanics principles: constitutive law, continuity and compatibility conditions. The existence of a stable and unique solution is enforced by the equilibrium conditions and yield criterion, and has been verified by test observations. In the finite element method, some of the conditions stated above may only be partially satisfied in the displacement domain. However, sufficient analysis cases have proved that such minor continuity violation does not significantly affect the solution accuracy in finite element analysis.

ALGORITHM IMPLEMENTATION

The procedure proposed above was implemented in ULSAS-GE, which is an enhanced plate version of ULSAS. Originally, ULSAS was a finite element package for the elastic-plastic post-buckling analysis of plates subjected to cyclic, uniaxial in-plane loading (Yao, 1991). The only element included in the package is a four-node isoparametric shell element. In the element formation, large deformation effects were included and were considered in the updated Lagrangian approach. To achieve computational efficiency, the element was further simplified to a bi-linear degenerate shell element so that integration points were reduced to one. In order to prevent the possible singularity due to the reduced integration scheme, hourglass control stiffness was used in the element stiffness calculation. The Kanok-Nukulchai method was employed to form the stiffness against the element in-plane rotation. The updated Green strains and the updated Kirchoff stresses were used to take into account the effects of large deformation on the equilibrium. To apply the flow theory of plasticity and hardening rules, the Kirchoff stress increments were transformed into the Jaumann stress increments at each load step. The Mises criterion was used to detect material yielding. To account for material hardening, options for isotropic hardening or kinematic hardening or a combination of both are available in ULSAS.

A number of limitations existed with the original plate version of ULSAS; for example, only one piece of plate in the XY plane can be analyzed and only uniaxial in-plane compressive loading can be applied. In order to analyze the cyclic behavior of frame-panel assemblages, significant modifications and enhancements were made in the enhanced version, ULSAS-GE. Different from its original, ULSAS-GE is capable of analyzing large plate assemblies under general load and support conditions. Certain auto-meshing capability and customized loading options are also available for modeling efficiency.

VERIFICATION

To verify the proposed algorithm, the frame-wall panel assembly tested by Kulak (Thorburn, Kulak

applied to the top beam.

Both the top beam and the panel were simulated with 4-node shell elements. Depending on the panel aspect ratio, 12x12 to 12x15 mesh densities were used in the analysis. Because of low stresses found in the beams from previous monotonic analyses by the authors, the beams were assumed to act elastically, and only the panels were modeled with the inclusion of material yielding. A bi-linear material model simulating A36 steel was used for the panels, with 0.4% tangent modulus in the strain hardening range. The material hardening effects was included by using the combined isotropic and kinematic hardening model available in ULSAS-GE.

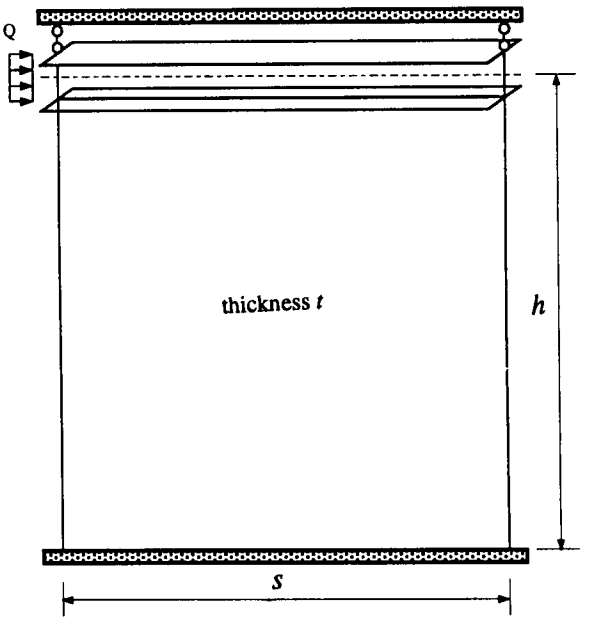

Figure 4 Model of Frame-Wall Panel Assembly

Initial imperfections with a maximum magnitude equal to 10% of the plate thickness were assigned to each wall panel during modeling. The initial imperfections were composed of the buckling modes proposed by Timoshenko for thin plate buckling under in-plane shear. The first 16 modes were used to form the initial imperfections. Shown in Figs. 5, 6 and 7 is the cyclic behavior obtained from the analyses with ULSAS-GE for panels PGS5, PGS1, and PGS2. In the figures, Q/Q_y and D/D_y are non-dimensionalized shear load and displacement of a panel, respectively. Q_y denotes the full shear yield capacity of a panel, so $Q_y = \tau_y st$ (τ_y is the shear yield stress of the panel material). D_y denotes the drift at the top of a panel when $Q = Q_y$; therefore, $D_y = (\tau_y/G)h$. Refer to Fig. 1 for definitions of h, s and t.

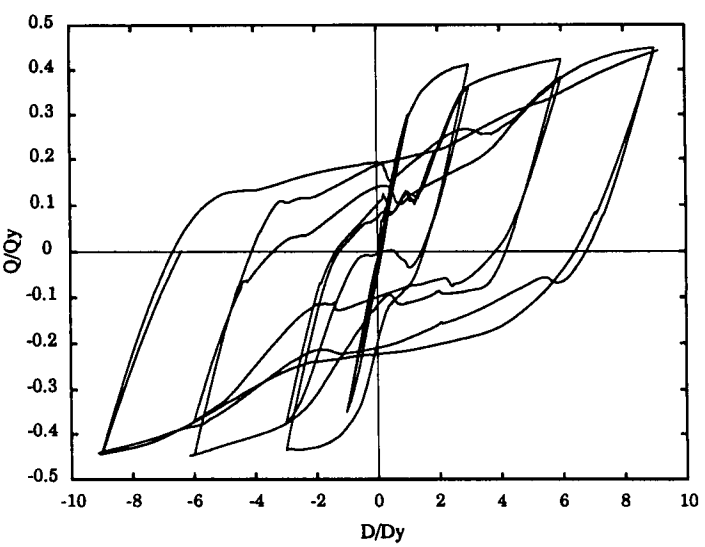

Figure 5 Cyclic Behavior of Panel PGS5

The following hysteretic characteristics of the plate

panels under cyclic in-plane shear may be observed from the results.

1) The linear behavior of a panel is not significantly affected by buckling and post-buckling deformations before the panel significantly yields due to in-plane stresses. Such behavior has been observed from both the previous tests and the analyses under monotonic loading performed by the authors.

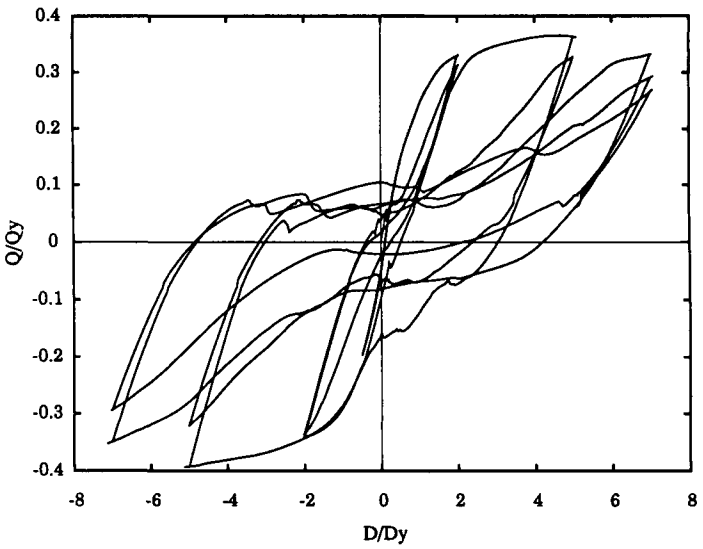

Figure 6 Cyclic Behavior of Panel PGS1

2) Shear panels exhibit pinching behavior after yielding caused by in-plane stresses has appeared. Both pinching and strength degradation were alleviated in the large deformation range. This behavior was observed in the tests conducted by Kulak and by Elgaaly.

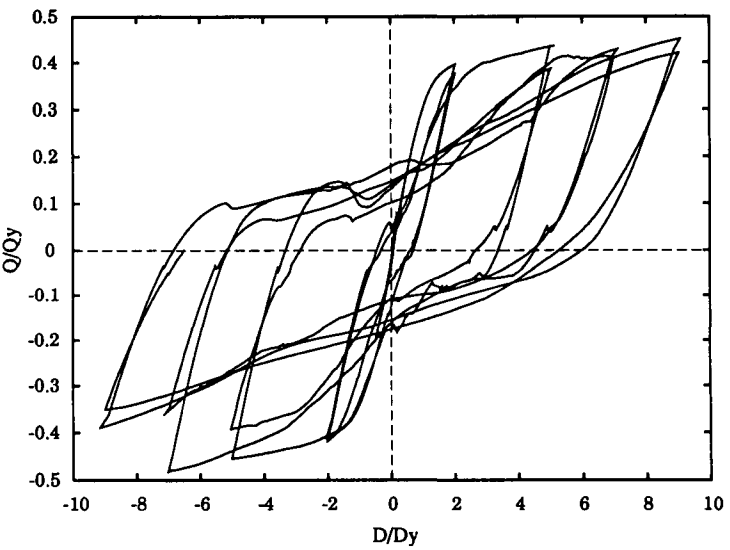

Figure 7 Cyclic Behavior of Panel PGS2

3) The ***a/t*** ratio has a strong effect on both pinching and strength degradation of the panels. Parameter a is the largest of h and s. As the ratio increases, the panels had more severe pinching and suffered more strength reduction. It should be noted that the effects of fracture or tearing have not been included in this study. It is anticipated that panels with very large ***a/t*** ratios may have a localized fracture or tearing failure. Flexible stiffeners can be used to prevent possible fracture or tearing of shear panels.

4) The hysteresis of the panels is rather sensitive to the change of the ***s/h*** ratio. When ***s/h*** ratio

is less than 1.0 (PGS1), the hysteresis loops have severe pinching, stiffness deterioration, and strength degradation. To achieve stable strength and good energy dissipation capacity, steel panels with $s/h \geq 1.0$ are preferred in the construction of frame-wall systems.

SUMMARY

An algorithm was proposed to circumvent instability at load reversals in cyclic analysis of thin plates under in-plane shear. The algorithm was implemented in a special finite element analysis package and used to analyze wall panels selected from a frame-wall system. The algorithm worked well in the analysis. Analytical results compared favorably with the available test data. The hysteretic behavior of steel plate panels subjected to in-plane shear can be closely predicted by ULSAS-GE program.

REFERENCES

Basler, K. (1960). Strength of plate girders in shear. *Fritz Engineering Laboratory Report No. 251-20*, Lehigh University.

Elgaaly, M. and Caccess, V. (1990). Steel plate shear walls. *Proceedings of National Steel Construction Conference*, Kansas City, 4-2--4-28.

Kossira, H. and Horst, P. (1991). Cyclic shear loading of aluminum panels with regard to buckling and plasticity. *Thin-Walled Structures* , **11**, 65-84 .

Porter, D.M., Rockey, K.C. and Evans, H.R. (1975). The collapse behavior of plate girders loaded in shear. *The Structural Engineer*, **53**, No.8, 313-325.

Riks, E. (1972). The application of Newton's method to the problem of elastic stability. *J. Applied Mechanics*, **39**, 1060-1066.

Riks, E. (1979). An incremental approach to the solution of snapping and buckling problems. *Int. J. Solids Struct.* **15**, 529-551.

Thorburn, L.J., Kulak,G.L. and Montgomery, C.J. (1983). Analysis of steel plate shear walls. *Structural Engineering Report No. 107*, University of Alberta, Canada.

Wagner, H. (1931). Flat sheet metal girders with very thin metal webs. *NACA Technical Memo. No.604.*

Xue, M. and Lu, L. (1994). Interaction of steel plate shear panels with surrounding frame members. *Proceedings of 50th Anniversary Conference of Structural Stability Research Council,* Bethlehem.

Xue, M. (1995). *Behavior of steel shear wall panels and frame-wall systems*. Ph.D. dissertation. Department of Civil & Environmental Engineering, Lehigh University.

Yao, T. (1991). *Introduction to plate version of ULSAS*. Department of Naval Architecture and Ocean Engineering, Hiroshima University, Japan.

This Page Intentionally Left Blank

A FINITE ELEMENT MODEL FOR GEOMETRICALLY NONLINEAR ANALYSIS OF MULTI-LAYERED COMPOSITE SHELLS

Arif Masud and Choon L. Tham

Department of Civil & Materials Engineering, (M/C 246)
The University of Illinois at Chicago
842 West Taylor Street
Chicago, Illinois 60607-7023, USA

ABSTRACT

This paper presents a multi-director and shear-deformable finite element formulation for geometrically nonlinear analysis of thick layered composite shells. The underlying variational formulation is based on an assumed strain method. The displacement field is continuous across the finite element layers through the composite thickness, whereas the rotation field is only layer-wise continuous and is assumed discontinuous across the discrete layers. From a kinematical viewpoint displacements and rotations are assumed finite while the strains are infinitesimal. The proposed model is then cast in a co-rotational framework which is derived consistently from the updated Lagrangian framework. The close relationship between the co-rotational procedure and its underlying updated Lagrangian procedure is presented to highlight the cost reduction for large and complicated geometric configurations. Numerical examples are presented to demonstrate the applicability of the proposed element.

KEY WORDS

Laminated composites, Multidirector shells, Finite deformations, Co-rotational framework, Nonlinear finite elements

INTRODUCTION

Laminated structures made of advanced filamentary composite materials continue to be of great interest for engineering applications. Their high strength to weight ratio, and the flexibility to tailor make various components with strength far exceeding that of the parent constituent materials are their main attributes. These engineered materials are generally orthotropic in nature and quite often show very unique response

even under simple loading and geometric configurations. For a detailed account on composite materials see Noor *et al.* [1989,1990], Reddy [1984,1996] Jones [1975] (and references therein). Most research efforts, as presented in the literature, can be grouped into three main categories. The first approach considers all material layers as one equivalent anisotropic layer and employs the classical plate theory with a non-deformable director and zero transverse shear. Limitations of this approach and the effect of ignoring transverse shear for advanced composites are well documented in the literature. Accordingly refined laminate theories, based on Reissner-Mindlin plate theory have been proposed. These theories provide an improved response as compared to the classical lamination theory. A third approach that claims to model the warping of the composite cross-section has gained considerable attention in literature. In this approach the through thickness component of the displacement field is expressed as a power series in terms of the plate thickness coordinate. Although this approach accounts for transverse shear as well as warping of the composite cross-section, it is kinematically homogenous. If a detailed response of individual laminates is required, this approach would necessitate high order expansion in terms of plate thickness coordinate, resulting in considerable increase in the number of unknowns in the system and also in the complexity of the theory.

In view of these issues, and because of the fact that these theories, although based on the concept of a two dimensional reference surface, are not much cheaper than a three dimensional analysis of laminated composites, has led some researchers to employ 3D elements to model the various material layers (Liao & Reddy [1990]).It is to be noted that 3D elements are not good for bending dominated response. The reason is that even under the application of a constant moment, these elements can only model a shear-type response (Hughes [1987]) which infact is exceedingly stiff than a bending response. The situation worsen when 3D elements are used to model a thin flat laminate with adverse aspect ratios.

In this paper we have endeavored to address these issues, and extend the linear model proposed by the first author to geometrically nonlinear anlysis. The underlying formulation is based on an assumed displacement field that results in an enhanced strain Hu-Washizu variational framework. A condition of orthogonality on the enhanced strains with respect to the 3D stress field results in a modified displacement based formulation which contains only translational and rotational degrees of freedom. Since the rotation field is only layerwise continuous and is assumed to be discontinuous across the different material layers through the thickness, it can be condensed out via static condensation. The resulting element thus contains the translational degrees of freedom as the nodal unknown at the global level. The multi-layered shell model is then cast in a co-rotational framework which is derived consistently from the updated Lagrangian formulation.

An outline of the paper is as follows. Section 2 presents the assumed displacement field. Section 3 presents the co-rotational framework for geometrically nonlinear analysis, evaluation of internal force vector, and a description of linear orthotropic constitutive relations in the co-rotational framework. In Section 4 we present the ensuing hybrid composite shell element. Numerical results are presented in Section 5 and conclusions are drawn in Section 6.

THE LAYER-WISE SHEAR DEFORMABLE FRAMEWORK

We start with the assumed displacement field

$$U_\alpha(x,y,z) = u_\alpha(x,y,z) + z^{(l)}\theta_\alpha(x,y) \qquad (\alpha = 1,2) \tag{1}$$

$$U_3(x,y,z) = u_3(x,y,z) \tag{2}$$

where the translational component of the displacement field is assumed continuous in the x, y and z directions while the rotation component is only layer-wise continuous, and is discontinuous from one layer to the other. Thus rotation is infact an internal field embeded in the 3D continuum displacement field, and is therefore defined on the reference surface alone. This layerwise rotation field results in enhancement of the transverse shear strains and bending strains, thereby improving the bending dominated response.

CO-ROTATIONAL FRAMEWORK FOR GEOMETRICALLY NONLINEAR ANALYSIS

This section presents the co-rotational procedure for geometrically nonlinear analysis, derived consistently from the updated Lagrangian framework. The updated Lagrangian framework involves the principle of virtual work being established for the equilibrium configuration at the previous load increment at time t_n.

$$\int_{\Omega_t} \frac{1}{J}\,\boldsymbol{\tau}_{n+1}\,\delta\boldsymbol{\varepsilon}_{n+1}\,d\Omega \;=\; \boldsymbol{f}^{\text{ext}}_{n+1} \tag{3}$$

where $\boldsymbol{\tau}_{n+1}$ and $\boldsymbol{\varepsilon}_{n+1}$ denote the second Piola-Kirchhoff stress tensor and the Green-Lagrange strain tensor measured in the updated configuration at time t_n, respectively. The equilibrium configuration at time t_n is then called the reference configuration for current load step. Neglecting the quadratic terms in the Green-Lagrange strain tensor, we obtain the linearized incremental constitutive relation $\boldsymbol{\sigma} = \frac{1}{J}\boldsymbol{\tau} = \boldsymbol{c}\colon\boldsymbol{e}$. Substituting the updated stresses and strains in (3), we obtain the linearized equation of motion

$$\int_{\Omega_t} \boldsymbol{e}\colon\boldsymbol{c}\colon\delta\boldsymbol{e}\,d\Omega + \int_{\Omega_t} \boldsymbol{\sigma}\cdot\delta\boldsymbol{\eta}\,d\Omega \;=\; \boldsymbol{f}^{\text{ext}} - \int_{\Omega_t} \boldsymbol{\sigma}\delta\boldsymbol{e}\,d\Omega \tag{4}$$

where the right hand side is the residual or the out-of-balance virtual work. In order to reduce the out-of-balance virtual work to within prescribed tolerance, we establish the incremental iterative form

$$\int_{\Omega_t} \boldsymbol{e}^{(i+1)}_{n+1}\colon\boldsymbol{c}\colon\delta\boldsymbol{e}_{n+1}\,d\Omega + \int_{\Omega_t} \boldsymbol{\sigma}_{n+1}\,\delta\boldsymbol{\eta}^{(i+1)}_{n+1}\,d\Omega \;=\; \boldsymbol{f}^{\text{ext}}_{n+1} - \int_{\Omega_t} \boldsymbol{\sigma}^{(i)}_{n+1}\,\delta\boldsymbol{e}^{(i)}_{n+1}d\Omega \tag{5}$$

Remark: After each iteration, displacements are accumulated and the incremental second Piola-Kirchhoff stress and Green-Lagrange strain tensors are evaluated which are then pushed forward to the current configuration.

Element Co-rotational Procedure

In the case of small strains, a series of approximations can be made to significantly simplify the updated Lagrangian formulation to the so-called element co-rotational

procedure. Theoretically, an arbitrary motion of a general continuous medium can be decomposed into a rigid body motion followed by a pure relative deformation. In finite element analysis, this decomposition can be accomplished by defining a local co-rotational coordinate system for each element which translates and rotates with the element, but does not deform with the element. If the finite element is sufficiently small, the pure deformation part of displacement obtained by subtracting the rigid-body motion components from the total displacement is normally small and is of same order of the magnitude as infinitesimal strains.

Coordinate system for co-rotational framework

In order to present the co-rotational procedure, we refer to the three sets of coordinate systems. They are:

(i) *The Global Coordinate System* which is the Cartesian coordinate system fixed in space.

(ii) *The Local Co-rotational Coordinate System,* $\boldsymbol{I} = [\boldsymbol{i}_1, \boldsymbol{i}_2, \boldsymbol{i}_3]$ which is associated with each element and undergoes rigid body rotations and translations with the element.

(iii) *The Surface Coordinate System,* $\boldsymbol{V}_a$, which is the nodal triad associated with a typical node a. During the equilibrium iteration, $\boldsymbol{V}_a$ experiences both the rigid body rotations and pure deformation.

Internal Force Vector

The internal force vector emanating from the second term on the right hand side in equation (5) can be expressed as

$$\boldsymbol{f}_{n+1}^{\mathrm{int}^{(i)}} = \int_{\Omega_{n+1}^{(i)}} \boldsymbol{B}^{(i)^T} \boldsymbol{\sigma}_{n+1}^{(i)} d\Omega \tag{6}$$

where $\boldsymbol{B}^{(i)^T}$ is form identical to the linear discrete strain-displacement matrix, but contains spatial derivatives with respect to the latest configuration $\Omega_{n+1}^{(i)}$, which may not necessarily be in an equilibrium state. $\boldsymbol{\sigma}_{n+1}^{(i)}$ is the Cauchy stress tensor and is also measured in the latest configuration. To satisfy the objectivity requirement and to obtain exact Cauchy stress tensor, we first have to calculate the incremental Green-Lagrange strain, from which, the incremental second Piola-Kirchhoff stress can be obtained. Secondly, we need to push-forward the result to the current configuration with the incremental deformation gradient $\bar{\boldsymbol{F}}_{n+1}$.

$$\boldsymbol{\sigma}_{n+1} = \frac{1}{J_{n+1}} \boldsymbol{\tau}_{n+1} = \frac{1}{J_n} \boldsymbol{\tau}_n + \frac{1}{J_{n+1}} (\bar{\boldsymbol{F}}_{n+1} \Delta \boldsymbol{S}_{n+1} \bar{\boldsymbol{F}}_{n+1}^T) \tag{7}$$

Note that $\boldsymbol{F}_{n+1} = \boldsymbol{F}_n + \mathrm{GRAD}\, \boldsymbol{u} = [\boldsymbol{1} + \nabla_n \boldsymbol{u}] \boldsymbol{F}_n = \bar{\boldsymbol{F}}_{n+1} \boldsymbol{F}_n$. Consequently $\bar{\boldsymbol{F}}_{n+1} = [\boldsymbol{1} + \nabla_n \boldsymbol{u}]$.

Remark: All variables in (6) are defined with respect to the global coordinate system.

To apply the co-rotational procedure, it is convenient to transform equation (6) into local co-rotational coordinate system as

$$\tilde{\boldsymbol{f}}_{n+1}^{\text{int}(i)} = \int_{\tilde{\Omega}_{n+1}^{(i)}} \tilde{\boldsymbol{B}}^{(i)^T} \tilde{\boldsymbol{\sigma}}_{n+1}^{(i)} d\Omega \tag{8}$$

where the tilde indicates quantities measured in the local co-rotational system. $\tilde{\boldsymbol{B}}^{(i)}$ = symm grad $\tilde{\boldsymbol{u}}$ represents the strain-displacement matrix in the local co-rotational coordinate system in configuration $\tilde{\Omega}_{n+1}^{(i)}$. The Cauchy stress tensor in the latest obtained configuration can be calculated through the stress transformation in local co-rotational coordinate system as follows

$$\tilde{\boldsymbol{\sigma}} = \frac{1}{J} \tilde{\boldsymbol{F}}\, \tilde{\boldsymbol{S}}\, \tilde{\boldsymbol{F}}^T \tag{9}$$

where $\tilde{\boldsymbol{F}} = \frac{\partial \tilde{\boldsymbol{\varphi}}(\boldsymbol{x},t)}{\partial \boldsymbol{x}}$ is the co-rotational deformation gradient that eliminates the rigid body rotation of the continuum. Consequently, the incrementally objective stress update in the current configuration can be expressed as

$$\tilde{\boldsymbol{\sigma}}_{n+1} = \tilde{\boldsymbol{\sigma}}_n + \frac{1}{J} \bar{\tilde{\boldsymbol{F}}}\, \Delta \tilde{\boldsymbol{S}}\, \bar{\tilde{\boldsymbol{F}}}^T \tag{10}$$

where $\bar{\tilde{\boldsymbol{F}}} = [\mathbf{1} + \nabla_n \tilde{\boldsymbol{u}}]$ is the incremental co-rotational deformation gradient that eliminates the incremental rigid body rotation of the continuum from configuration $\tilde{\Omega}_{n+1}^{(i)}$ to $\tilde{\Omega}_{n+1}^{(i+1)}$.

Because of the small strain assumption, the pure deformation part of the displacements is a small quantity as compared to the element dimensions in the local co-rotated coordinates. Consequently, it is reasonable for us to make the following two approximations:

1) The changes in element shapes are small in each individual local increment; and
2) The displacement derivatives of the pure deformation part of the displacement field with respect to the current configuration measured in the local co-rotated coordinate system are of the same order of magnitude as the small strains. Therefore, the quadratic terms in the Green-Lagrange strain components can be neglected. (See Belytschko *et al.* [1973]).

Based on the first assumption where the changes in element shapes are assumed to be negligible i.e., $\tilde{\boldsymbol{\varphi}}^{(i)}(\boldsymbol{x}, t_{n+1}) \approx \tilde{\boldsymbol{\varphi}}^{(i+1)}(\boldsymbol{x}, t_{n+1})$, the incremental deformation gradient matrix in the local co-rotated coordinate system is close to an identity matrix i.e.

$$\bar{\tilde{F}}_{jJ} = \frac{\partial \tilde{x_j}^{(i+1)}}{\partial \tilde{x_J}^{(i)}} = \begin{cases} 1 & j = J \\ 0 & j \neq J \end{cases} \tag{11}$$

where $\tilde{x}_j$ are coordinates of a point in the current co-rotational frame $\tilde{\Omega}_{n+1}^{(i+1)}$ and $\tilde{x}_J$ are the coordinates in the previous co-rotational frame $\tilde{\Omega}_{n+1}^{(i)}$. Furthermore, change

in mass density is also negligible, i.e., $\rho_o = \rho_t$ for $J = 1$. Substituting (11) into (10), we get further approximation

$$\begin{aligned} \tilde{\boldsymbol{\sigma}}_{n+1} &= \tilde{\boldsymbol{\sigma}}_n + \Delta\tilde{\boldsymbol{S}} \\ &= \tilde{\boldsymbol{\sigma}}_n + \tilde{\boldsymbol{C}}\colon\Delta\tilde{\boldsymbol{E}} \end{aligned} \tag{12}$$

where $\Delta\tilde{\boldsymbol{E}}$ is the Green Lagrange strain tensor in co-rotated coordinates. Based on the second assumption, the stress update in an iterative form can be expressed as

$$\begin{aligned} \tilde{\boldsymbol{\sigma}}_{n+1}^{(i+1)} &= \tilde{\boldsymbol{\sigma}}_n^{(i)} + \tilde{\boldsymbol{C}}\colon\Delta\tilde{\boldsymbol{E}}_{n+1}^{(i)} \\ &= \tilde{\boldsymbol{\sigma}}_n^{(i)} + \tilde{\boldsymbol{C}}\colon\frac{1}{2}(\nabla\tilde{\boldsymbol{u}} + \nabla\tilde{\boldsymbol{u}}^T)_{n+1}^{(i)} \\ &= \tilde{\boldsymbol{\sigma}}_n^{(i)} + \tilde{\boldsymbol{C}}\colon\tilde{\boldsymbol{B}}_{n+1}^{(i)}\tilde{\boldsymbol{d}}_{n+1}^{(i)} \\ &= \tilde{\boldsymbol{\sigma}}_n^{(i)} + \tilde{\boldsymbol{C}}\colon\tilde{\boldsymbol{B}}_{n+1}^{(i)}\boldsymbol{I}^T\boldsymbol{d}_{n+1}^{(i)} \end{aligned} \tag{13}$$

where we have used the transformation relation between the nodal degrees of freedom in the global and the local co-rotated coordinate systems. Once the internal force vector is obtained in local co-rotated coordinate system, a simple coordinate transformation can be performed to obtain the internal force vector in global coordinate system as:

$$\boldsymbol{f}_{n+1}^{\mathrm{int}(i)} = \boldsymbol{I}^T\,\tilde{\boldsymbol{f}}_{n+1}^{\mathrm{int}(i)} \tag{14}$$

where $\boldsymbol{I}$ is the transformation matrix.

Orthotropic Constitutive Relations in Co-rotational Frame

Most fibrous laminated composites are made of a repeated sequence of laminates that often have the same material properties but are oriented at $+\theta$ and $-\theta$ degrees with respect to one of the global axes. Let $\boldsymbol{C}^{'(l)}$ represent the linear orthotropic constitutive matrix for an individual laminate with regard to its mutually perpendicular planes of elastic symmetry. This constitutive matrix for a laminate can be projected onto the global composite coordinate system via a transformation matrix $\boldsymbol{Q}^{(l)}$ which is a function of the angle θ. The transformed constitutive matrix $\boldsymbol{C}^{(l)}$ is obtained as

$$\boldsymbol{C}^{(l)} = \boldsymbol{Q}^{T(l)}\,\boldsymbol{C}^{'(l)}\,\boldsymbol{Q}^{(l)} \tag{15}$$

These global orthotropic constitutive matrices defined layerwise, need to be mapped onto the co-rotational axes specific to each individual element to perform consistent numerical integeration of the element level quantities. Consequently, we need to develop an orthogonal transformation matrix from the global system on to the local element co-rotational system. The orthotropic constitutive relation in co-rotational frame can now be expressed as

$$\tilde{\boldsymbol{C}} = \boldsymbol{R}^{T(e)}\boldsymbol{C}^{(l)}\boldsymbol{R}^{(e)} \tag{16}$$

where $\boldsymbol{R}^{(e)}$ is the element specific orthogonal transformation matrix from the global frame to the local co-rotational coordinate frame. Equation (16) is then substituted into eqn. (13) to evaluate Cauchy stress in co-rotational system.

THE HYBRID ELEMENT

This section describes the hybrid element which is obtained via adding a 4-node shell type reference surface within the 8-noded 3D continuum element. The 4 noded reference surface is identified via a parameter $\tilde{\zeta}$ that places it with lower, middle or top surface of the element. The resulting hybrid element is also applicable to plate and shell type problems that can be modeled via single director Reissner-Mindlin type theories.

The three-dimensional element used in this work follows Liu *et al.* [1994a,b, 1998]. Emphasis is placed on avoiding locking and removal of spurious singular modes and stabilization via an hourglass control approach. We expand the strain rate $\dot{\boldsymbol{\varepsilon}}$ in Taylor series about the element center

$$\begin{aligned}\dot{\boldsymbol{\varepsilon}}(\xi,\eta,\zeta) &= \dot{\boldsymbol{\varepsilon}}(\mathbf{0}) + \dot{\boldsymbol{\varepsilon}}_{,\xi}(\mathbf{0})\,\xi + \dot{\boldsymbol{\varepsilon}}_{,\eta}(\mathbf{0})\,\eta + \dot{\boldsymbol{\varepsilon}}_{,\zeta}(\mathbf{0})\,\zeta \\ &\quad + \dot{\boldsymbol{\varepsilon}}_{,\xi\eta}(\mathbf{0})\,\xi\eta + \dot{\boldsymbol{\varepsilon}}_{,\eta\zeta}(\mathbf{0})\,\eta\zeta + \dot{\boldsymbol{\varepsilon}}_{,\zeta\xi}(\mathbf{0})\,\zeta\xi \\ &= \sum_{a=1}^{n_{en}} \bar{\boldsymbol{B}}_a(\xi,\eta,\zeta)\,\boldsymbol{v}_a \end{aligned} \tag{17}$$

where $\boldsymbol{v}_a$ are the nodal velocity degrees of freedom and

$$\begin{aligned}\bar{\boldsymbol{B}}_a(\xi,\eta,\zeta) &= \boldsymbol{B}_a(\mathbf{0}) + \boldsymbol{B}_{a,\xi}(\mathbf{0})\,\xi + \boldsymbol{B}_{a,\eta}(\mathbf{0})\,\eta + \boldsymbol{B}_{a,\zeta}(\mathbf{0})\,\zeta \\ &\quad + \boldsymbol{B}_{a,\xi\eta}(\mathbf{0})\,\xi\eta + \boldsymbol{B}_{a,\eta\zeta}(\mathbf{0})\,\eta\zeta + \boldsymbol{B}_{a,\zeta\xi}(\mathbf{0})\,\zeta\xi \end{aligned} \tag{18}$$

The first term on the right hand side of the equation (17) or (18) represents the constant strain rates evaluated at the quadrature point, $\mathbf{0}$, and the remaining terms are the linear and bilinear strain rate terms.

Treatment of Volumetric Locking

To treat volumetric locking, $\bar{\boldsymbol{B}}_a(\xi,\eta,\zeta)$ is decomposed into dilatational and the deviatoric parts.

$$\bar{\boldsymbol{B}}_a(\xi,\eta,\zeta) = \bar{\boldsymbol{B}}_a^{\mathrm{dil}}(\mathbf{0}) + \bar{\boldsymbol{B}}_a^{\mathrm{dev}}(\xi,\eta,\zeta) \tag{19}$$

The dilatational part of gradient matrices is underintegrated and evaluated at only one quadrature point, $\mathbf{0}$. We expand $\bar{\boldsymbol{B}}_a^{\mathrm{dev}}$ about the element center. Accordingly equation (19) can be written as

$$\begin{aligned}\bar{\boldsymbol{B}}_a(\xi,\eta,\zeta) &= \boldsymbol{B}_a(\mathbf{0}) + \boldsymbol{B}_{a,\xi}^{\mathrm{dev}}(\mathbf{0})\,\xi + \boldsymbol{B}_{a,\eta}^{\mathrm{dev}}(\mathbf{0})\,\eta + \boldsymbol{B}_{a,\zeta}^{\mathrm{dev}}(\mathbf{0})\,\zeta \\ &\quad + \boldsymbol{B}_{a,\xi\eta}^{\mathrm{dev}}(\mathbf{0})\,\xi\eta + \boldsymbol{B}_{a,\eta\zeta}^{\mathrm{dev}}(\mathbf{0})\,\eta\zeta + \boldsymbol{B}_{a,\zeta\xi}^{\mathrm{dev}}(\mathbf{0})\,\zeta\xi \end{aligned} \tag{20}$$

where $\boldsymbol{B}_a(\mathbf{0})$ are the one-point-quadrature gradient submatrices contributed from both the dilatational and deviatoric parts. The remaining terms on the right-hand-side of the above equation are the gradient submatrices corresponding to non-constant deviatoric strain rates.

Treatment of Shear Locking

In order to remove shear locking, the gradient submatrices corresponding to the assumed shear strain rates are written in an orthogonal co-rotational coordinate system rotating with the element. The gradient submatrices corresponding to strain rates $\dot{\epsilon}_{\alpha\alpha}$ and $\dot{\epsilon}_{\alpha\beta}$ (for $\alpha, \beta = 1, 3$) can be expressed as

$$\bar{\boldsymbol{B}}_{\alpha\alpha}(\xi,\eta,\zeta) = \boldsymbol{B}_{\alpha\alpha}(\mathbf{0}) + \boldsymbol{B}^{\text{dev}}_{\alpha\alpha,\xi}(\mathbf{0})\,\xi + \boldsymbol{B}^{\text{dev}}_{\alpha\alpha,\eta}(\mathbf{0})\,\eta + \boldsymbol{B}^{\text{dev}}_{\alpha\alpha,\zeta}(\mathbf{0})\,\zeta + \boldsymbol{B}^{\text{dev}}_{\alpha\alpha,\xi\eta}(\mathbf{0})\,\xi\eta + \boldsymbol{B}^{\text{dev}}_{\alpha\alpha,\eta\zeta}(\mathbf{0})\,\eta\zeta + \boldsymbol{B}^{\text{dev}}_{\alpha\alpha,\zeta\xi}(\mathbf{0})\,\zeta\xi \quad (\alpha = 1,2,3) \tag{21}$$

and

$$\bar{\boldsymbol{B}}_{\alpha\beta}(\xi,\eta,\zeta) = \boldsymbol{B}_{\alpha\beta}(\mathbf{0}) + \boldsymbol{B}^{\text{dev}}_{xy,\zeta}(\mathbf{0})\,\zeta \qquad (\alpha,\beta = 1,2,3) \tag{22}$$

NUMERICAL EXAMPLES

Composite Cantilever Beam. [45,-45]s

The first simulation is that of a laminated cantilever beam. Schematic diagram is shown in Fig. 1. The elastic moduli are $E_1 = 1.379E{+}08$, and $E_2 = E_3 = 1.448E{+}07$. The remaining material properties are given below. It is interesting to note that the coarse mesh also captures the nonlinear geometric response with a great degree of accuracy (see Fig. 2), thus confirming the robustnesss of the element for bending dominated cases.

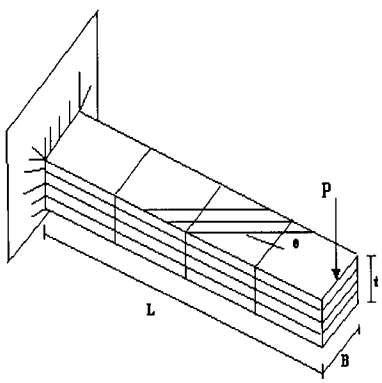

- **Material Properties**

$G_{23} = 586E{+}04$, $G_{31} = 586E{+}04$, $G_{12} = 586E{+}04$
$\nu_{23} = 0.21$, $\nu_{31} = 0.21$, $\nu_{12} = 0.21$

- **Geometric Properties**

L = 10.0
B = 1.0
t = 0.1478

- **Loading**

P = 270

Fig. 1. Schematic diagram of the composite beam problem.

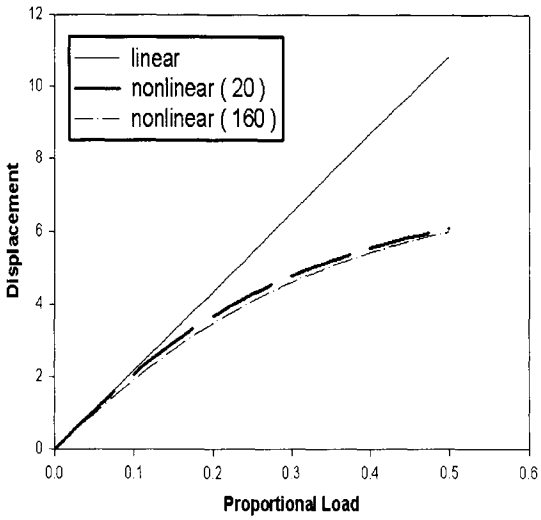

Fig. 2. Load-deflection diagram at load point.

Bending of a Narrow Cantilever Plate

The second simulation is that of a narrow cantilever isotropic plate subjected to a concentrated load. The superposed initial and final meshes are shown in Fig. 3a and surface stresses σ_{xx} are shown in Fig. 3b. The applied load versus the displacement path of the load point in our simulation shows a close agreement with that given by the shell element *SHEBA* of Argyris *et al.* [1994].One can clearly see that the plate is made of two layers of elements through the thickness.

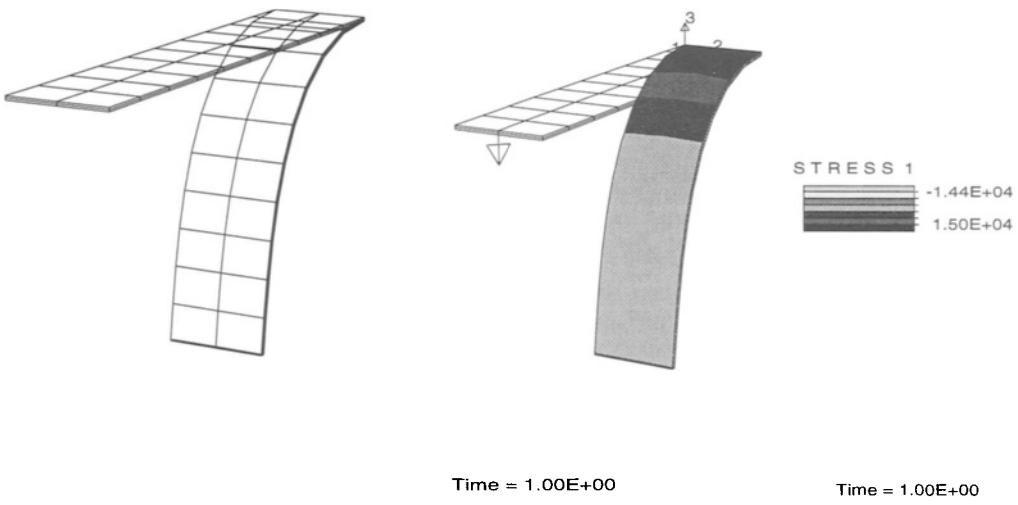

Fig. 3. Initial and Final deformed geometry and stress σ_{xx}.

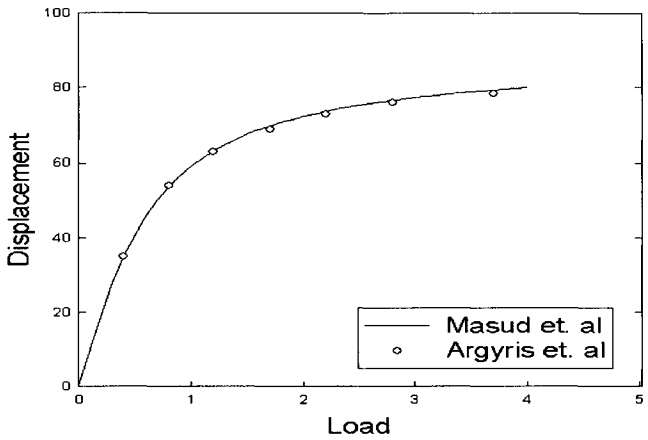

Fig. 4. Load-deflection diagram at load point.

Clamped Isotropic Plate under Uniform Pressure Load

The next numerical simulation is a large deformation analysis of a fully clamped isotropic plate. Again we have selected this isotropic problem to benchmark our element for geometrically nonlinear analysis. To solve this problem we generated a mesh of $8 \times 8 \times 2$ hybrid elements. The pseudo-time increment in the nonlinear solution strategy is $\Delta t = 0.01$. A total of 100 steps were required to apply the total load. Fig 6 presents the nonlinear load-deflection curve obtained at the center of the plate which compares very well with the experimental load-deflection curve reported in Kawai *et al.* [1969].

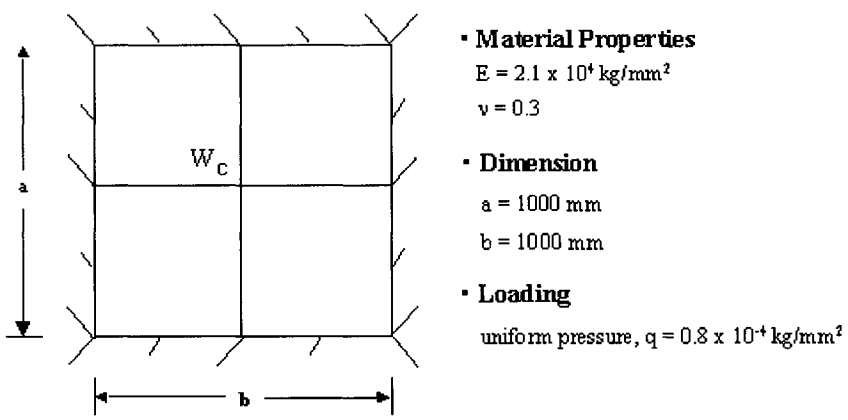

Fig. 5. Schematic diagram of the problem.

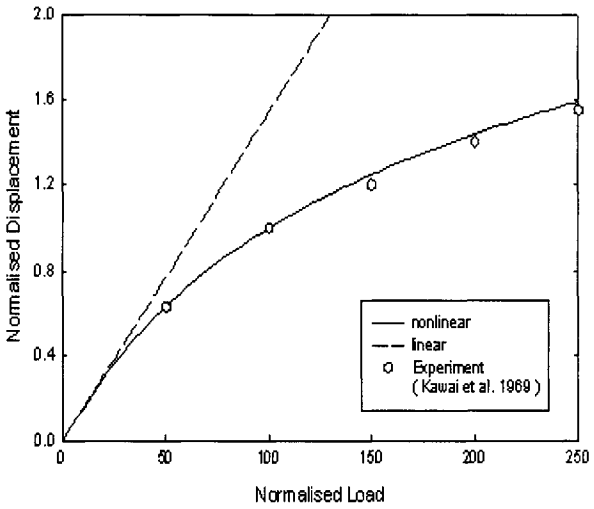

Fig. 6. Load-deflection diagram at the center of the plate.

CONCLUSIONS

In this paper we have presented a stabilized co-rotational formulation for geometrically nonlinear analysis of thick multi-layered composites with arbitrary ply lay-up sequences and orientations. The proposed approach is applicable to flat as well as curved geometric configurations. In the finite element context this formulation employs a eight-node hexahedral element with an embeded four-node reference surface to model the kinematics of composite laminates. The resulting hybrid element is free of volumetric and shear locking and possesses very good coarse mesh accuracy. In this element, stabilization is performed with respect to an orthogonal co-rotational framework attached to each individual element and the stabilization vectors are a function of element geometry alone. In the co-rotational framework the motion of element is conceived to be a finite rigid body motion followed by relatively small pure deformation. Elimination of the rigid body motion part from the total displacements leads to deformational displacement derivatives with respect to the co-rotated coordinates which are in the same order of magnitude as the small strains. A layerwise orthotropic constitutive model is incorporated in this co-rotational framework to accommodate the material directionality in each individual laminate. These individual material matrices are mapped onto the co-rotational framework to perform consistent numerical integration of the element level quantities. Numerical results show the good performance of the model.

REFERENCES

Argyris, J. and Tenek, L., (1994) "An efficient and locking-free flat anisotropic plate and shell triangular element", *Comput. Methods App. Mech. Engrg.*, **118**, 63-119.

Belytschko, T. and Hsieh, B.J., (1973), "Non-linear transient finite element analysis with convected coordinates", *Inter. J. Num. Meth. Engrg.*, **7**, 255-271.

Belytschko, T. and Leviathian, I., (1994) "Physical stabilization of the 4-node shell element with one point quadrature", *Comput. Methods App. Mech. Engrg.*, **113**, 321-350.

Burton, W.S. and Noor, A.K., (1995) "Assessment of computational models for sandwich panels and shells", *Comput. Methods App. Mech. Engrg.*, **124**, 125-151.

Flanagan, D.P. and Belytschko, T., (1981), "A uniform strain hexahedron and quadrilateral with orthogaonal hourglass control", *Inter. J. Num. Meth. Engrg.*, **17**, 679-706.

Hughes, T.J.R., (1987), *The Finite Element Method: Linear Static and Dynamic Finite Flement Analysis*, Prentice-Hall, Englewoods Cliffs, NJ.

Jones, R.M.,(1975), *Mechanics of Composite Materials*, McGraw-Hill Book Co., New York.

Kawai, T. and Yoshimura, N., (1969) "Analysis of large deflection of plates by the finite element method", *Inter. J. Num. Meth. Engrg.*, **1**, 123-133.

Liao, C.L. and Reddy, J.N., (1990), "Analysis of anisotropic, stiffened composite laminates using a continuum-based shell element", *Comp. Struct.*, **34**, No. 6, 805-815.

Liu, W.K., Guo, Y., Tang, S. and Belytschko, T., (1997) "A Multiple-Quadrature Eight-Node Hexahedral Finite Element for Large Deformation Elastoplastic Analysis", in press *Comput. Methods App. Mech. Engrg.*.

Liu, W.K., Hu, Y.K. and Belytschko, T., (1994a) "Multiple Quadrature Underintergrated Finite Elements", *Inter. J. Num. Meth. Engrg.*, **37**, 3263-3289.

Liu, W.K., Hu, Y. K. and Belytschko, T., (1994b) "Three-Dimensional Finite Elements with Multiple-Quadrature-Points, Transactions of the Eleventh Army Conference on Applied Mathematics and Computing", ARO Report 94-1, 229-246.

Liu, W.K., Ong, J.S. and Uras, R.A., (1985), "Finite element stabilization matriced - a unification approach", *Comput. Methods App. Mech. Engrg.*, **53**, 13-46.

Masud, A. and Panahandeh, M., "A Finite Element Formulation of Multi-layered shells for the analysis of laminated composites", *Computers and Structures*, To appear.

Moita, G.F. and Crisfield, M.A., (1996) "A finite element formulation for 3-D continua using the co-rotational technique", *Inter. J. Num. Meth. Engrg.*, **39**, 3775-3792.

Noor, A.K. and Burton, W.S., (1989) "Assessment of shear deformation theories for multi-layered composite plates", *Applied Mechanics Review*, **42**, No. 1, 1-13.

Noor, A.K. and Burton, W.S., (1990) "Assessment of computational models for multilayered composite shells", *Applied Mechanics Review*, **43**, No. 4, 67-97.

Pagano, N.J., (1989) *Interlaminar response of composite materials*, Composite Materials Series, Vol. 5., Elsevier, New York, NY, 1989

Pagano, N.J. and Pipes, R.B., (1973) "Some observations on the interlaminar strength of composite laminates", *Int. J. Mech. Sci.*, **15**, 679.

Palazotto, A.N., Tsai C.T. and Dennis S.T., (1991) "Large-rotation snap-through buckling in laminated cylindrical panels", *Finite Elements in Analysis and Design*, **9**, 65-75.

Reddy, J.N., (1996), *Mechanics of Laminated Composite Plates: Theory and Analysis*, CRC Press, Inc.

Reddy, J.N., (1984) "A simple higher-order theory for laminated composite plates", *Journal of Applied Mechanics*, **51**, 745-752.

Whitney, J.M. and Pagano, N.J., (1970) "Shear deformation in heterogeneous anisotropic plates," *J. App. Mech.*, **37**, 1031.

This Page Intentionally Left Blank

NONLINEAR AND BUCKLING ANALYSIS OF COMPLEX BRANCHED SHELLS OF REVOLUTION

J. G. Teng

Department of Civil and Structural Engineering
Hong Kong Polytechnic University
Hung Hom, Kowloon, Hong Kong, China

ABSTRACT

This paper introduces the NEPAS program which has been developed over a number of years for the nonlinear and buckling analysis of complex branched shells of revolution. Throughout its development, a strong emphasis has been placed on achieving robustness, efficiency, and accuracy. This has led to attempts to identify the best available numerical techniques and the development of new ones for implementation in the program. In this paper, the current capabilities of the NEPAS program are described and the numerical techniques implemented to achieve them are reviewed. A number of numerical examples are included to illustrate these capabilities. Further developments of the program to make it an attractive analysis tool for designers are also discussed.

KEYWORDS

Shells, Analysis, Finite Elements, Nonlinear Analysis, Buckling, Stability

INTRODUCTION

Axisymmetric shells are widely used in many engineering fields. Examples include aircraft, spacecraft, submarines, nuclear reactors, cooling towers, storage silos and tanks, roof domes, offshore platforms, tubular towers, chimneys, pressure vessels and pipelines. Shell structures, particularly civil engineering metal shell structures, have to be designed to avoid buckling or plastic collapse failures under combinations of load cases specified by design codes. Despite extensive research over many decades, existing knowledge of many shell buckling and collapse problems is still very limited (Teng, 1996). Consequently, shell stability/strength design criteria

given in codes of practice cover only simple geometries and loading conditions. For shells under non-ideal loads or having complicated geometries, there is little information either in the literature or in the design codes for the determination of their strength. For these complex shell structures, the use of numerical nonlinear and buckling analysis in design directly, or in the assessment of designs based on crude approximations has become an attractive alternative.

A fully nonlinear analysis considering geometric and material nonlinearities should be carried out for reliable strength predictions. A number of difficulties still exist in this approach, including the specification of appropriate geometric imperfections for a buckling strength assessment, as these imperfections are unknown at the design stage. These and other related issues are currently being studied by many researchers. Needless to say, for this approach to be widely used, designers require access to a robust, efficient, and accurate nonlinear and buckling analysis computer program which meets their design needs. Most existing computer programs for shells of revolution have been developed without designers' needs in mind, and consequently do not meet their requirements.

The aim of this paper is to introduce the NEPAS program developed over a number of years for the nonlinear and buckling analysis of complex branched shells of revolution and to review the numerical techniques implemented in this program. The initial development work (Teng and Rotter, 1989a; 1989b) took place with the aim of producing a program which can be used efficiently as a research tool in the study of shell buckling and collapse behaviour. It was envisaged that the program would be applied extensively to study many different problems. Consequently, a strong emphasis was placed on developing a robust, efficient and accurate program rather than one for the demonstration of a certain numerical procedure. It should be noted that the efficiency of a computer analysis does not rely only on a computationally less intensive numerical procedure, but also on the degree of automation of the analysis. As the computational power continues to advance rapidly, automation of analysis is becoming ever more important. The development of NEPAS has been carried out bearing this point in mind. The emphasis of recent and current work has been to further develop the program into an attractive analysis tool for designers. The strong emphasis placed on achieving robustness, efficiency, and accuracy of the analysis has led to attempts to identify the best available numerical techniques and the development of a number of new numerical techniques for implementation in the program.

The latest version of the NEPAS program is capable of performing linear elastic stress analysis of shells of revolution under unsymmetric loads and nonlinear and buckling analysis of geometrically nonlinear elastic-plastic shells under axisymmetric loads including torsional loads. Plastic limit loads, linear bifurcation buckling loads, non-linear collapse loads, nonlinear bifurcation buckling loads, post-collapse bifurcation loads can all be determined efficiently. More specialized versions of NEPAS exist (eg NEPAC, EPSAC) and are used in actual applications, but for the description of this paper, only the general NEPAS program will be referred to. The program was developed as part of the FELASH Suite of computer programs for analyzing axisymmetric shell structures (Rotter, 1989). The program is now being extended to analyze geometrically nonlinear elastic branched shells under unsymmetric loads.

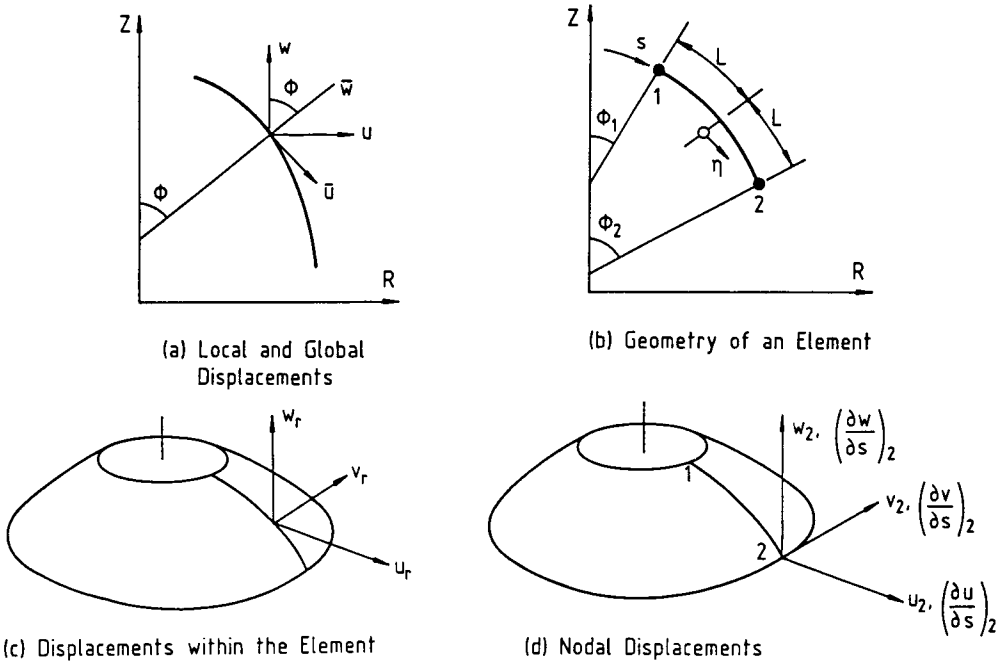

Figure 1: The doubly-curved axisymmetric shell element

THE DOUBLY-CURVED AXISYMMETRIC SHELL ELEMENT

The finite element formulation employs a doubly-curved isoparametric axisymmetric shell element with two ring nodes (Fig. 1). The element geometry is defined in cylindrical coordinates by the radius R, the axial coordinate Z and the element meridional curvature dφ/ds at the nodal points. The geometry is then interpolated between the nodes using cubic Hermitian functions (Teng and Rotter 1989a)

$$R = \sum_{i=1,2} \left\{ N_{0i} R_i + N_{1i} \left(\frac{dR}{ds} \right)_i \right\} = [N]\{R^e\} \tag{1a}$$

$$Z = \sum_{i=1,2} \left\{ N_{0i} Z_i + N_{1i} \left(\frac{dZ}{ds} \right)_i \right\} = [N]\{Z^e\} \tag{1b}$$

$$\left(\frac{d\phi}{ds} \right) = \sum_{i=1,2} \left\{ N_{0i} \left(\frac{d\phi}{ds} \right)_i + N_{1i} \left(\frac{d^2\phi}{ds^2} \right)_i \right\} = [N] \left\{ \left(\frac{d\phi}{ds} \right)^e \right\} \tag{1c}$$

in which

$$N_{01} = \frac{1}{4}\left(2 - 3\eta + \eta^3\right) \tag{2a}$$

$$N_{11} = \frac{L}{4}\left(1 - \eta - \eta^2 + \eta^3\right) \tag{2b}$$

$$N_{02} = \frac{1}{4}\left(2 + 3\eta - \eta^3\right) \tag{2c}$$

$$N_{12} = \frac{L}{4}\left(-1-\eta+\eta^2+\eta^3\right) \tag{2d}$$

$$[N] = [N_{01} N_{11} N_{02} N_{12}] \tag{3}$$

where η is a dimensionless curvilinear meridional coordinate related to the meridional coordinate s and the element half length L through (Fig. 1)

$$\eta = \frac{2s - s_1 - s_2}{2L} \tag{4}$$

$$L = \frac{s_2 - s_1}{2} \tag{5}$$

The nodal displacements are defined by u_i, $(du/ds)_i$, v_i, $(dv/ds)_i$, w_i and $(dw/ds)_i$ in the global coordinate system at each ring node at the end of the element. The displacements within the element, expressed in the global coordinate system, u, v and w (Figure 1) are interpolated between the nodal points in terms of the nodal values by the shape functions of Eqn. 2. The global displacements u, v and w at any point are related to the local displacements $\bar{u}$, $\bar{v}$ and $\bar{w}$ in the curvilinear coordinates by a transformation matrix [T] (Teng and Rotter,1989a).

The six nodal variables used at each node are satisfactory for shells with a smoothly curving meridian and without sudden changes of thickness. However, when an abrupt change of meridional slope or thickness occurs, excessive continuity is imposed between elements (Figure 2). To avoid this problem, a static condensation procedure was adopted (Teng and Rotter, 1989a). As a result, the element can be applied to analyze complex branched shells of revolution such as ring-stiffened cylinders, and elevated steel silos and tanks with a complex transition junction.

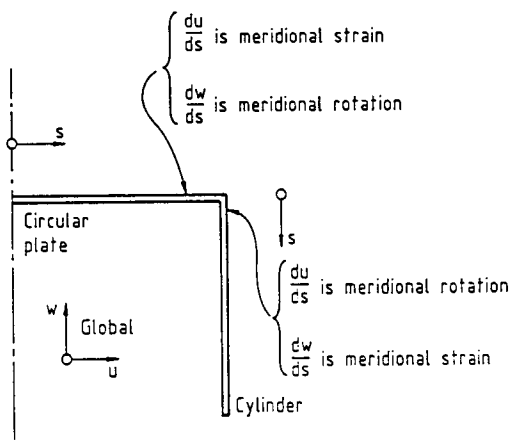

Figure 2: Compatibility at a Meridional Slope Discontinuity

NONLINEAR AXISYMMETRIC ANALYSIS

The total Lagrangian approach is adopted in which all the quantities are referred to the undeformed configuration. The vector of nodal displacement variables for each element, denoted as $\{\delta_a\}$, is given by

$$\{\delta_a\} = \left\{ u_1, \left(\frac{du}{ds}\right)_1, u_2, \left(\frac{du}{ds}\right)_2, v_1, \left(\frac{dv}{ds}\right)_1, v_2, \left(\frac{dv}{ds}\right)_2, w_1, \left(\frac{dw}{ds}\right)_1, w_2, \left(\frac{dw}{ds}\right)_2 \right\}^T \quad (6)$$

For a single element, the application of the principle of virtual displacements leads to the following nonlinear equations:

$$\{\Phi(\delta_a)\} = \{F\} - \int [B_a]^T \{\Sigma\}\, dV = 0 \quad (7)$$

in which $\{F\}$ is a vector of equivalent nodal forces due to body forces and surface tractions, $[B_a]$ is the incremental strain-displacement matrix, $\{F(\delta_a)\}$ represents a vector of nodal residual forces and $\{\Sigma\}$ is the vector of stress resultants. These relations constitute the basic equations for which a solution is sought. For each iteration, the displacement increments for the structure $\{\Delta\delta_a\}$ are obtained by solving the linearised system of equations

$$\{\Phi(\delta_a)\} = [K_T]\{\Delta\delta_a\} \quad (8)$$

where $[K_T]$ is termed the global tangent stiffness matrix. The tangent stiffness matrix for each element is given by

$$[K_T]_e = [K]_e + [K_\sigma]_e \quad (9)$$

where $[K]_e$ accounts for the change of geometry and $[K_\sigma]_e$ accounts for the effect of internal stresses. The element tangent stiffness matrices are condensed to reduce the inter-element continuity. The global tangent stiffness matrix $[K_T]$ may then be found by assembling the condensed element tangent stiffness matrices.

NON-SYMMETRIC BIFURCATION BUCKLING ANALYSIS

When the axisymmetric primary equilibrium path has been determined as described above, bifurcation into a secondary path may occur. The bifurcation displacements are assumed to be infinitesimal compared with the finite axisymmetric prebuckling deformations. The buckling displacements are expanded as symmetric and antisymmetric Fourier terms to allow non-symmetric buckling patterns with phase changes down the shell meridian to be described:

$$u_n = u_{ns}\cos n\theta + u_{na}\sin n\theta, \quad v_n = v_{ns}\sin n\theta + v_{na}\cos n\theta, \quad w_n = w_{ns}\cos n\theta + w_{na}\sin n\theta \quad (10)$$

where θ is the circumferential angular coordinate, n is an integer which specifies the number of circumferential waves in the buckling mode, and the subscripts s and a denote the symmetric and antisymmetric Fourier components respectively. There are 24 degrees of freedom per element in the buckling mode, and the vector of buckling displacements for each element is

$$\{\delta_n\} = \left\{ u_{s1}, \left(\frac{\partial u}{\partial s}\right)_{s1}, u_{s2}, \left(\frac{\partial u}{\partial s}\right)_{s2}, v_{s1}, \left(\frac{\partial v}{\partial s}\right)_{s1}, v_{s2}, \left(\frac{\partial v}{\partial s}\right)_{s2}, w_{s1}, \left(\frac{\partial w}{\partial s}\right)_{s1}, w_{s2}, \left(\frac{\partial w}{\partial s}\right)_{s2}, \right.$$

$$\left. u_{a1}, \left(\frac{\partial u}{\partial s}\right)_{a1}, u_{a2}, \left(\frac{\partial u}{\partial s}\right)_{a2}, v_{a1}, \left(\frac{\partial v}{\partial s}\right)_{a1}, v_{a2}, \left(\frac{\partial v}{\partial s}\right)_{a2}, w_{a1}, \left(\frac{\partial w}{\partial s}\right)_{a1}, w_{a2}, \left(\frac{\partial w}{\partial s}\right)_{a2} \right\}^T \quad (11)$$

in which the subscripts s and a denote symmetric and antisymmetric displacements with respect to the circumferential origin respectively. The buckling displacements in terms of global coordinates, u_n, v_n and w_n are related to the nodal global values of buckling displacements through element shape functions. Based on the principle of virtual displacements, the equilibrium of the buckled shell is governed by

$$\int_V [B_n]^T \frac{\partial\{\Sigma\}}{\partial\{\delta_n\}} dV + \int_V \frac{\partial[B_n]^T}{\partial\{\delta_n\}}\{\Sigma\} dV = 0 \tag{12}$$

where $\{\Sigma\}$ is the vector of stress resultants and $[B_n]$ is the strain-displacement matrix. The element stiffness matrix $[K_n]_e$ is defined by the first term of Eqn. 12, whilst the second term of Eqn. 12 leads to the stability matrix $[K_{sn}]_e$. After condensation, the global stiffness and stability matrices can be assembled. For a given buckling mode with n circumferential waves, Eqn. 12 may be written as an eigenvalue problem

$$\{[K_n]_c + \Lambda_n [K_{\sigma n}]_c\}\{\delta_n\} = 0 \tag{13}$$

in which Λ_n is the eigenvalue, $\{\delta_n\}$ is the eigenvector, and $[K_n]_c$ and $[K_{sn}]_c$ depend on the current state of the structure. This eigenvalue problem must be solved many times at different load levels and for different numbers of circumferential waves. The final solution is achieved only when the number of circumferential waves associated with the minimum eigenvalue is found and this minimum eigenvalue is unity.

NONLINEAR STRAIN-DISPLACEMENT RELATIONS

Different nonlinear shell theories may be used in numerical nonlinear and buckling analysis of thin shells. It should be noted that existing well-known nonlinear shell theories, including Donnell's (1934) theory as extended for general shells (often referred to as the Donnell-Mushtari-Vlasov theory) and Sanders' (1963) theory, were initially developed for analytical studies. In these theories, simplicity is an important consideration, and terms judged to be small in comparison with other terms are omitted. By contrast, in modern computer analysis, the extra complexity of a more accurate shell theory can be handled with little difficulty and only leads to a small increase in computing cost. As the NEPAS program is intended to analyze general complex shells of revolution with branches, it is necessary to ensure that the shell theory used yields correct results in all cases. The NEPAS program thus employs the nonlinear shell theory derived by Rotter and Jumikis (1988) for thin shells of revolution which is more complete than Sanders' (1963) theory.

For thin shell applications, three components of membrane strain together with three components of bending strain define the state of strain at any arbitrary distance z normal to the shell reference surface. The strain-displacement relations of Rotter and Jumikis (Jumikis, 1987; Rotter and Jumikis 1988; Teng and Hong, 1998) are given by

$$\varepsilon_\varphi = \frac{\partial\bar{u}}{\partial s} + \frac{\partial\varphi}{\partial s}\bar{w} + \frac{1}{2}\left[\left(\frac{\partial\bar{w}}{\partial s} - \bar{u}\frac{\partial\varphi}{\partial s}\right)^2 + \left(\frac{\partial\bar{v}}{\partial s}\right)^2 + \left(\frac{\partial\bar{u}}{\partial s} + \bar{w}\frac{\partial\varphi}{\partial s}\right)^2\right] \tag{14}$$

$$\varepsilon_\theta = \frac{\cos\varphi}{R}\bar{u} + \frac{1}{R}\frac{\partial\bar{v}}{\partial\theta} + \frac{\sin\varphi}{R}\bar{w} + \frac{1}{2R^2}\left[\left(\frac{\partial\bar{w}}{\partial\theta} - \bar{v}\sin\varphi\right)^2 + \left(\frac{\partial\bar{v}}{\partial\theta} + \bar{w}\sin\varphi + \bar{u}\cos\varphi\right) + \left(\frac{\partial\bar{u}}{\partial\theta} - \bar{v}\cos\varphi\right)^2\right] \tag{15}$$

$$\gamma_{\varphi\theta} = \frac{\partial \bar{u}}{R\partial\theta} - \frac{\bar{v}\cos\varphi}{R} + \frac{\partial \bar{v}}{\partial s} + \frac{1}{R}\left[\left(\frac{\partial \bar{w}}{\partial s} - \frac{\bar{u}\partial\varphi}{\partial s}\right)\left(\frac{\partial \bar{w}}{\partial\theta} - \bar{v}\sin\varphi\right)\right.$$
$$\left. + \frac{\partial \bar{v}}{\partial s}\left(\frac{\partial \bar{v}}{\partial\theta} + \bar{w}\sin\varphi + \bar{u}\cos\varphi\right) + \left(\frac{\partial \bar{u}}{\partial s} + \frac{\bar{w}\partial\varphi}{\partial s}\right)\left(\frac{\partial \bar{u}}{\partial\theta} - \bar{v}\cos\varphi\right)\right] \tag{16}$$

$$\kappa_\varphi = \frac{\partial^2\varphi}{\partial s^2}\bar{u} + \frac{\partial\varphi}{\partial s}\frac{\partial \bar{u}}{\partial s} - \frac{\partial^2 \bar{w}}{\partial s^2} \tag{17}$$

$$\kappa_\theta = \frac{\bar{u}}{R}\frac{\partial\varphi}{\partial s}\cos\varphi + \frac{1}{R^2}\sin\varphi\frac{\partial \bar{v}}{\partial\theta} - \frac{\cos\varphi}{R}\frac{\partial \bar{w}}{\partial s} - \frac{1}{R^2}\frac{\partial^2 \bar{w}}{\partial\theta^2} \tag{18}$$

$$\kappa_{\varphi\theta} = \frac{1}{R}\frac{\partial\varphi}{\partial s}\frac{\partial \bar{u}}{\partial\theta} + \left[\cos\varphi\frac{\partial\varphi}{\partial s} - \frac{2}{R}\sin\varphi\cos\varphi\right]\frac{\bar{v}}{R}$$
$$+ \frac{\sin\varphi}{R}\frac{\partial \bar{v}}{\partial s} + \frac{2}{R^2}\cos\varphi\frac{\partial \bar{w}}{\partial\theta} - \frac{2}{R}\frac{\partial^2 \bar{w}}{\partial s\partial\theta} \tag{19}$$

where ε_ϕ, ε_θ and $\varepsilon_{\phi\theta}$ are the meridional and circumferential membrane strains and membrane shear strain respectively, and κ_ϕ, κ_θ and $\kappa_{\phi\theta}$ are the meridional and circumferential curvatures and twisting curvature respectively. Rotter and Jumikis (1988) believed that even Sanders' theory, when applied in a conventional manner to complex branched axisymmetric shells, such as ring-stiffened shells of revolution, could lead to erroneous results. Teng and Hong (1998) recently developed a nonlinear theory for shells of general form which can be reduced to that of Rotter and Jumikis (1988) for shells of revolution. They also discovered that the same strain-displacement relations for shells of revolution were derived at about the same time by Su et al. (1987) and Yin et al. (1987).

Teng and Hong (1998) also presented a comprehensive comparative study of several nonlinear shell theories in nonlinear buckling analysis. The simply-supported ring-stiffened cylinder under uniform external pressure (Figure 3) is one of the two numerical examples considered by Teng and Hong (1998) for which the buckling loads obtained using different nonlinear shell theories are given in Table 1. The buckling loads in Table 1 are in terms of the dimensionless buckling pressure defined as $\lambda_{cr} = pa(1-\nu^2)/(Et)$, in which p is the external pressure, E is the elastic modulus, ν is the Poisson's ratio, a is the cylinder radius and t is the cylinder thickness. In the numerical analyses, the following values were used: $E = 2.0\times10^5$ MPa, $\nu = 0.3$, $a/t = 100$. The finite element model of the shell included only the ring-stiffened cylinder with one end allowed to have only meridional rotations and the other end allowed to have both meridional rotations and axial displacements. The circular plate covers at the ends of the cylinder were not included in the finite element model, but the pressure acting on the plate was included in the form of a circumferential line load on the cylinder end which was not restrained in the axial direction.

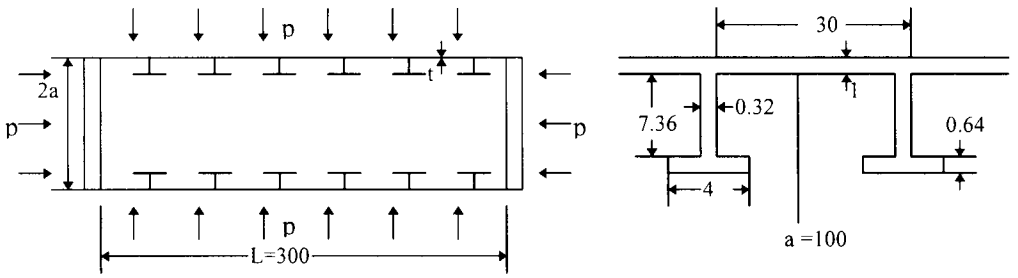

Figure 3: Ring-stiffened cylinders under external pressure

TABLE 1
BUCKLING PRESSURES OF RING-STIFFENED CYLINDERS

	General Instability					Interframe Buckling				
$\lambda_{cr} \times 10^3$	Donnell's Theory	Sanders' Theory β_n omitted	Sanders' Theory β_n retained	Subbiah & Natarajan (1982)	Rotter & Jumikis' Theory	Donnell's Theory	Sanders' Theory β_n omitted	Sanders' Theory β_n retained	Subbiah & Natarajan (1982)	Rotter & Jumikis' Theory
Linear Buckling	5.192 (3)*	6.403 (3)	6.000 (3)	6.451 (3)	5.967 (3)	3.745 (13)	3.755 (13)	3.749 (13)	3.755 (13)	3.749 (13)
Nonlinear Buckling	5.163 (3)	6.248 (3)	6.014 (3)	-	5.962 (3)	3.239 (12)	3.248 (12)	3.243 (12)	-	3.232 (12)

* Number of critical circumferential buckling waves

There are two possible buckling modes in such stiffened cylinders: global buckling and interframe buckling. These two modes correspond to two different numbers of circumferential waves. In the global mode of instability, the ring stiffeners' displacements are nearly all in the plane of the ring. On the other hand, these rings deform out-of-plane in the interframe mode of instability. Both linear buckling loads (prebuckling large deflection effect ignored) and nonlinear buckling loads (prebuckling large deflection effect included) are presented. The effect of prebuckling large deflections is seen to be small. It can be seen that for the interframe buckling mode, the results from the different shell theories are very close to each other as buckling displacements are out-of-plane in both the cylinder and the ring. For the general mode of instability, there are some significant differences. The predictions using the theory of Rotter and Jumikis are similar to those using Sanders' theory; however,the simplified Sanders' theory in which the rotation about the normal is ignored predicts buckling loads which are 7% higher than those of Rotter and Jumikis' theory. It is interesting to note that Subbiah and Natarajan's (1982) results are in very close agreement with those of the simplified Sanders' theory, but are different from those of Rotter and Jumikis' theory. Subbiah and Natarajan (1982) indicated that Sanders' theory was used in their analysis but did not elaborate whether the rotation about the normal was included. It seems very likely that the simplified Sanders theory was used by them. The unconservative predictions of the simplified Sanders' theory are due to its inability in modelling the in-plane buckling behaviour of the annular plate web of the T-section ring stiffeners as demonstrated by Teng and Hong (1998). Compared to the

theory of Rotter and Jumikis, the buckling loads predicted using Donnell's theory are lower by about 9%. The effect of Donnell approximations in the nonlinear strain terms leads to conservative predictions of the buckling load.

In their study, Teng and Hong (1998) recommended that Rotter and Jumikis' theory as a special case of their more general theory be used in computer analysis for complete peace of mind that no terms, however small, have been left out in the analysis, although for their two test cases Sanders' (1963) theory with the rotation about the normal to the shell reference surface retained is also accurate.

CONSTITUTIVE LAWS AND STATE DETERMINATION ALGORITHM

The vector of generalized stress resultants $\{\Sigma\}$ in the shell which consists of the three membrane forces N_φ, N_θ and $N_{\varphi\theta}$ and the three bending moments M_φ, M_θ and $M_{\varphi\theta}$ is related to the generalized strains $\{\varepsilon\}$ defined earlier in an incremental manner through the tangent modulus matrix $[D_T]$ as

$$d\{\Sigma\} = [D_T]d\{\varepsilon\} \quad \text{where} \quad [D_T] = \int_{-t/2}^{t/2} [Z]^T [D_{ep}][Z]dz \tag{20}$$

The matrix $[D_{ep}]$ relates the vector of stresses $\{\sigma\}$ and the vector of strains $\{\varepsilon^z\}$ at any point located at a distance z from the shell wall middle surface through

$$d\{\sigma\} = [D_{ep}]d\{\varepsilon^z\} \quad \text{where} \quad \{\varepsilon^z\} = [Z]\{\varepsilon\} \tag{21}$$

with $[Z]$ being a matrix relating the generalized strains to the strains at any point located at a distance z from the shell middle surface. The elastic-plastic modulus matrix $[D_{ep}]$ depends on the plasticity theory used. The J_2 flow theory is used in the axisymmetric nonlinear analysis of NEPAS to model metal plasticity, and the matrix $[D_{ep}]$ is given in Teng and Rotter (1989a). A carefully designed state determination algorithm was employed to minimize the effect of load step size on the predicted structural response. Figure 4 shows the load deflection response of the large deflection elastic-plastic bending of a circular plate (Teng and Rotter, 1889a) predicted using two large load steps compared with the load deflection curve predicted using 25 steps. Evidently the NEPAS results are rather insensitive to load step sizes. This is an important feature, particularly when the program is used by inexperienced users to do elastic-plastic analysis.

For plastic bifurcation buckling analysis of metal plates and shells, the paradox remains that the analytically less satisfactory deformation theory of plasticity gives results in closer agreement with experimental results than the more rigorous and well-accepted flow theory. The many available explanations are still inconclusive, and recent results once again confirm that the deformation theory predicts bifurcation loads in much better agreement with experimental results (Teng, 1996). As bifurcation analyses using the deformation theory usually also predict lower buckling loads than those with the flow theory, bifurcation analyses using the J_2 deformation theory of plasticity are allowed in the NEPAS program which can also carry out plastic bifurcation analyses using the J_2 flow theory and the modified J_2 flow theory. The modified J_2 flow theory is the J_2 flow theory with the shear modulus replaced by that from the J_2 deformation theory (Bushnell, 1976). The incremental stress-strain relations for the J_2 deformation theory of

plasticity under three-dimensional stress regimes have been given in tensor notation by Hutchinson (1974) as

$$d\sigma_{ij} = L_{ijkl}\, d\varepsilon_{kl} \tag{22}$$

with

$$L_{ijkl} = \frac{E}{1+\nu+h}\left[\frac{1}{2}\left(\delta_{ik}\delta_{jl}+\delta_{il}\delta_{jk}\right)+\frac{3\nu+h}{3(1-2\nu)}\delta_{ij}\delta_{kl}-\frac{dh/dJ_2}{1+\nu+h+2(dh/dJ_2)J_2}s_{ij}s_{kl}\right] \tag{23}$$

where

$$J_2=\frac{1}{3}\sigma_v^{\,2}\,,\quad h=\frac{3}{2}[E/E_s-1]\,,\quad dh/dJ_2 = \frac{9E}{4\sigma_v^{\,2}}[1/E-1/E_s] \tag{24}$$

in which s_{ij} are the stress deviators, σ_v is the von Mises equivalent stress, ν is the Poisson's ratio, E is the elastic modulus, E_s is the secant modulus, and δ_{ij} is the Kronecker delta. These relations, when specialized for the plane stress condition, give the required matrix $[D_{ep}]$. The deformation theory option has been usefully exploited in numerical studies of shell buckling problems to develop simple design methods (**e.g. Teng, 1975; 1977**).

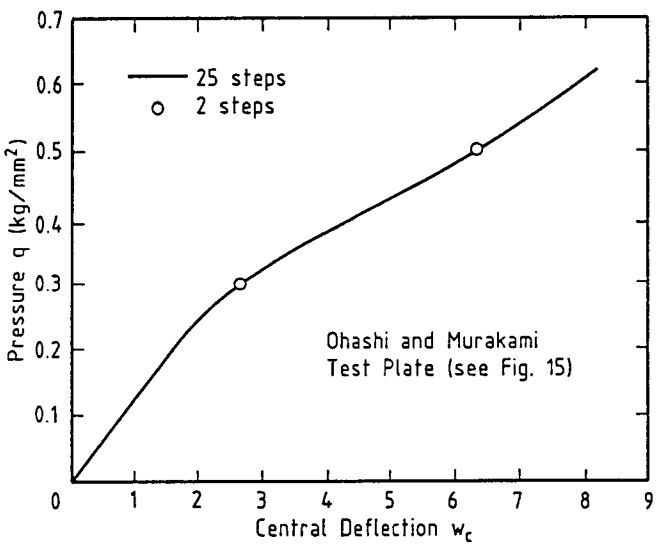

Figure 4: Effect of load step size on predicted load-deflection response

SOLUTION PROCEDURE FOR NONLINEAR ANALYSIS

Among the many existing incremental iterative nonlinear solution methods, the arc-length method still appears to be the most effective and popular. The arc-length method as given by Crisfield (1981) has thus been implemented in the NEPAS program together with the conventional load-controlled Newton-Raphson method. While the arc-length method (or other methods with similar capabilities) can handle complex load-deflection paths effectively, the analyst has no control over the load incrementation scheme to achieve convergence to specific locations along the load-deflection path. There are a number of situations in which such control is required. In particular, when nonlinear structural analysis programs are used in structural

design, both the ultimate load carrying capacity and the deformations under service loads may need to be found. The arc-length method is suitable for the former task, but not the latter. The analyst needs to conduct two separate analyses if he needs to know both the ultimate load and the state of the structure at a particular load level. This is inconvenient for both programming and program application. A user-controlled arc-length method has recently been developed and implemented in NEPAS so that it can converge to pre-defined load levels (Teng and Luo, 1998). This user control is achieved by coupling the conventional arc-length method with the accumulated arc-length control procedure of Teng and Luo (1997). The proposed approach is equally effective for convergence to a pre-defined value of any other parameter and to multiple values of a parameter. As an example, an elastic circular plate with a completely fixed edge was analyzed by Teng and Luo (1998) for convergence to multiple stress levels. The plate has the following properties: radius R = 100 mm, thickness t = 1 mm, elastic modulus E = 2.0 x 10^5 MPa and Poisson's ratio ν = 0.3. The reference load of the plate is 1 MPa. The NEPAS program was instructed to find the load levels at which the maximum von Mises equivalent stress is equal to 100 MPa, 200 MPa and 250 MPa, respectively (Figure 5). A pre-defined stress level was judged to have been reached if the difference between the converged and pre-defined stress level was less than 0.1%. This kind of analysis is useful in design application of nonlinear analysis where first yield constitutes a limit state as it can precisely determine the load level corresponding to first yield.

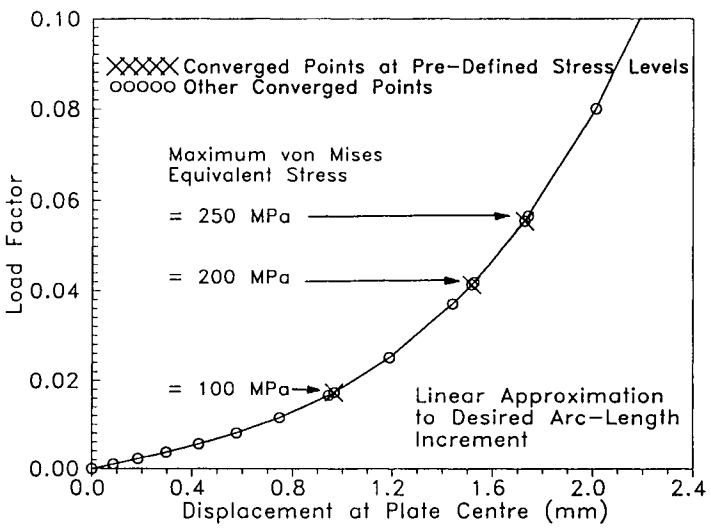

Figure 5: Load deflection path tracing with convergence to multiple pre-defined stress levels

AUTOMATED BIFURCATION SOLUTION PROCEDURE

To find the critical mode and load in a linear bifurcation analysis, one only needs to search through a range of circumferential buckling wave numbers. The critical wave number is the one associated with the lowest buckling load factor and the critical load is the applied load times this

buckling load factor. Finding the critical bifurcation mode and load following a nonlinear axisymmetric prebuckling path is much more difficult. The critical bifurcation mode is uncertain before the analysis is completed. A range of circumferential wave numbers must be tested to find the wave number corresponding to the minimum eigenvalue at each load level as this wave number varies with load level. A solution is reached when this minimum eigenvalue at a certain load level is unity. This load level is the buckling load level, and the circumferential wave number corresponding to the minimum eigenvalue is the critical mode. In all previous programs for shells of revolution, this search is done by trial and error and requires several repetitions of the analysis, which is often very tedious and time consuming. An automatic procedure was developed and implemented in NEPAS (Teng and Rotter, 1989b). This automatic procedure was made possible for plastic bifurcation analysis using the innovative idea of reversible plasticity (Figure 6) developed from the incrementally reversible plasticity assumption initially proposed by Nyssen (1981). With this reversible plasticity assumption, the search for a bifurcation point can be conducted forward and backward for many cycles. Otherwise, the search has to move forward only and there is no permission to move back.

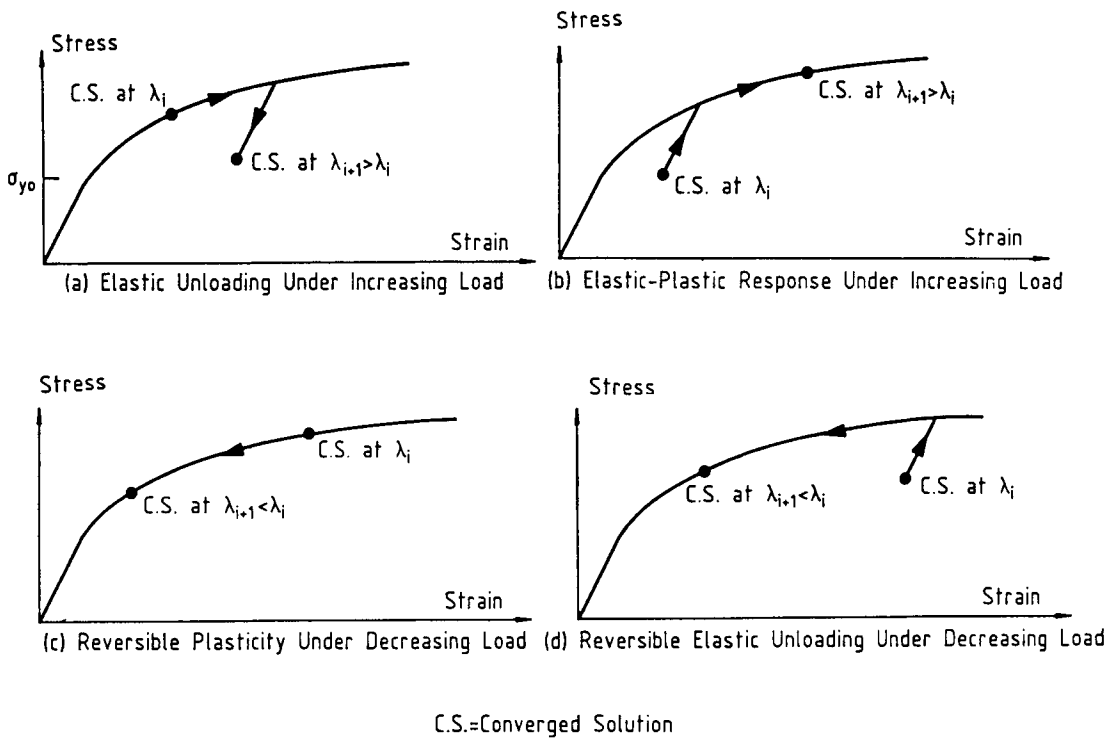

Figure 6: Stress-strain curves and reversible plasticity

Shells of revolution under axisymmetric loads may bifurcate into a non-symmetric mode after the axisymmetric failure load has been reached. The existence of a post-collapse bifurcation point indicates a mode change, and has a strong bearing on the ductility of structural behaviour in the post-collapse range. The accumulated arc-length method (Teng and Luo, 1997) is a new

technique recently developed for the determination of a post-collapse bifurcation point and implemented in NEPAS.

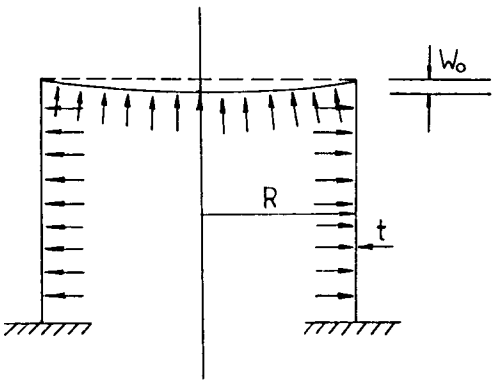

Figure 7: Plate-end pressure vessel

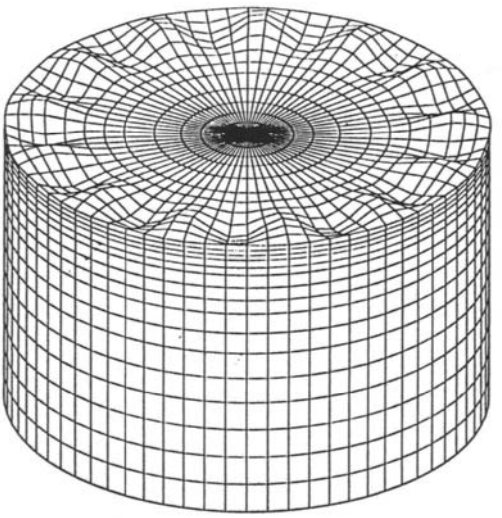

Figure 8: Non-symmetric bifurcation mode of a perfect plate-end pressure vessel

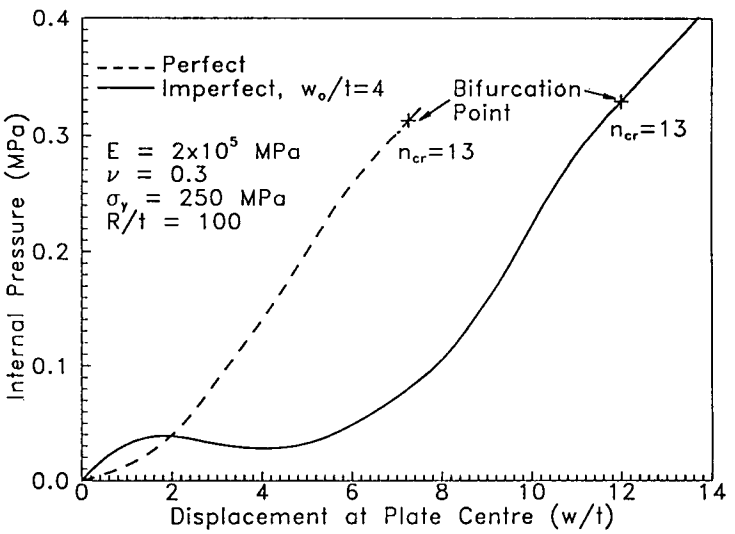

Figure 9: Load-deflection and bifurcation behaviour of plate-end pressure vessels

An interesting application of this method is to a structure with a shallow curved shape under compressive loading, for which snap-through buckling can occur under a very small load, but the real load carrying capacity may need to be taken as much higher at a bifurcation point on the second ascending branch in the post-snap-through range. The plate-end pressure vessel shown in Figure 7 serves as such an example. The buckling behaviour of internally pressurized perfect plate-end pressure vessels was investigated by Teng and Rotter (1989c). Due to inevitable

fabrication errors, the initial shape of the end plate may actually be that of a very shallow inverted dome. The effect of this kind of imperfection of significant amplitude can only be assessed if a post-collapse bifurcation analysis is carried out. In Teng and Luo (1997), a perfect and an imperfect vessel were analyzed. The imperfect plate is represented by an inverted spherical cap with a rise of w_0 equal to 4 times the shell wall thickness t. The vessels have an R/t ratio of 100 with the following material properties: elastic modulus $E = 2 \times 10^5$ MPa, Poisson's ratio $\nu = 0.3$, yield stress $\sigma_y = 250$ MPa with elastic perfectly-plastic behaviour. The material is modelled by the J_2 deformation theory in the bifurcation analysis. Figure 8 shows the bifurcation mode of the perfect vessel while the load deflection curves of both the perfect and the imperfect structure are shown in Figure 9. Substantial yielding has taken place before bifurcation buckling. For the imperfect vessel, bifurcation buckling occurs on the ascending branch of the load-deflection curve after snap-through (Figure 9). It is interesting to note that the initial shape imperfection increases the bifurcation buckling load slightly, contrary to conventional wisdom about the effect of imperfections. The number of circumferential buckling waves is not affected by this imperfection.

Another recent development of the NEPAS program is the implementation of a general nonlinear elastic foundation into the buckling analysis option (Luo and Teng, 1998), and this foundation may be a tensionless one if axisymmetric deformations only are being studied (Hong et al., 1997).

CONCLUSIONS AND FURTHER DEVELOPMENTS

This paper has introduced the current capabilities of the NEPAS program for nonlinear and buckling analysis of complex branched shells of revolution, and provided a review of the numerical techniques implemented in this program to achieve them. A number of numerical examples have also been included to illustrate these capabilities. The development of the program has been carried out with a strong emphasis on robustness, accuracy and efficiency. For axisymmetrically loaded metal shells of revolution, the NEPAS program is believed to be one of the most powerful programs available with a number of important features not present in other well-known programs (Bushnell, 1976; Cohen, 1982; Esslinger et al, 1984; Wunderlich et al, 1985; Combescure et al., 1987). The program has been applied to study many buckling and collapse problems in axisymmetric shell structures (eg Teng and Rotter, 1989c; Teng, 1995; 1997).

The NEPAS program is currently being extended to perform geometrically nonlinear analysis of elastic shells of revolution under non-symmetric loads. The programming work has been completed and the program is currently being tested. In the near future, the capability of including general non-symmetric initial imperfections in analysis will be added, and the nonlinear non-symmetric analysis will be further extended to elastic-plastic shells. In the longer term, the program shall be augmented with an automated procedure to realistically account for the effect of geometric imperfections, a user friendly post-processing facility, and a dynamic analysis capability. The ultimate aim of future development is to produce a program for the buckling and collapse strength prediction of complex branched shells of revolution under general

non-symmetric loads which will possess all the necessary features for direct applications in shell stability design and hence offer distinct advantages over other existing programs.

ACKNOWLEDGMENTS

The NEPAS program was first developed at the University of Sydney when the author was a PhD student under the supervision of Professor J.M. Rotter and is now being further developed at the Hong Kong Polytechnic University. In addition to Professor Rotter who led the development of the FELASH Suite of programs (Rotter, 1989), Dr. P.T. Jumikis, Dr. Y.F. Luo and Mr. T. Hong also contributed significantly to the development of the NEPAS program as described here, as may be seen from the cited references. The financial support from the University of Sydney and the Hong Kong Polytechnic University is also gratefully acknowledged.

REFERENCES

Bushnell, D. (1976). BOSOR5 - Programme for Buckling of Elastic-Plastic Complex Shells of Revolution Including Large Deflections and Creep. *Computers and Structures*, **6**, 221-239.

Cohen, G.A. (1982). FASOR-A Programme for Stress, Buckling and Vibration of Shells of Revolution. *Finite Element Systems*, edited by C.A. Brebbia, 2nd Edn, Springer-Verlag.

Combescure, A. Pernette, E. and Reynouard, J.-M. (1987). Linear and Nonlinear Buckling of a Discretely Supported Cooling Tower Using Special Axisymmetric Shell Elements. *Proc., Int. Colloq. on Stability of Plate and Shell Structures*, Ghent, Belgium, 6-8 April, 283-291.

Crisfield, M.A. (1981). A Fast Incremental/Iterative Solution Procedure That Handles Snap-Through. *Computers and Structures* **13**, 55-62.

Donnell, L. H. (1934). *Stability of Thin-Walled Tubes under Torsion*, NACA Report No.479.

Esslinger, M., Geier, B. and Wendt, U. (1984) Berechnung der Spannungen and Deformationen von Rotationsschalen im Elasto-Plastischen Bereich, *Stahlbau*, **1**, 17-25.

Hong, T., Teng, J.G. and Luo, Y.F. (1997). Large Deflection Analysis of Shells and Plates on Tensionless Elastic Foundations. *Proc., The Fourth International Kerensky Conference*, 3-5 September, Hong Kong, 473-479.

Hutchinson, J.W. (1974) Plastic Buckling, in *Advances in Applied Mechanics*, ed. C. S. Yih, Academic Press, Ontario, **14**, 85-197.

Jumikis, P.T. (1987). *Stability Problems in Silo Structures*, PhD Thesis, School of Civil and Mining Engineering, University of Sydney.

Luo, Y.F. and Teng, J.G. (1998). Stability Analysis of Shells of Revolution on Nonlinear Elastic Foundations. *Computers and Structures*. **accepted for publication.**

Nyssen, C. (1981). An Efficient and Accurate Iterative Method, Allowing Large Increment Steps, to Solve Elastic-Plastic Problems. *Computers and Structures* **13**, 63-71.

Rotter, J.M. (1989). The FELASH Suite of Computer Programs for the Analysis of Axisymmetric Shells. *Proc., 4th International Conference on Civil and Structural Engineering Computing*, London, **1**, 323-328.

Rotter, J. M. and Jumikis, P. T. (1988). Nonlinear strain-displacement relations for thin shells of revolution. *Res. Rep. R563*, School of Civil and Mining Engineering, University of Sydney.

Sanders, J.L.Jr. (1963). Nonlinear Theories for Thin Shells. *Quarterly J. of Applied Math.*, **21:1**, 21-36.

Su, X. Y., Wu, J. K. and Hu, H. C.(1987). A Large Displacement Analysis for Thin Shells of Revolution. *Science in China,* 400-410.

Subbiah, J. and Natarajan, R.(1982). Stability Analysis of Ring-Stiffened Shells of Revolution. *Journal of Ship Research,* **26:2**, 125-134.

Teng, J.G. (1995). Cone-Cylinder Intersection under Internal Pressure: Non-Symmetric Buckling. *Journal of Engineering Mechanics, ASCE* **121:12**, 1298-1305.

Teng, J.G. (1996). Buckling of Thin Shells: Recent Advances and Trends. *Applied Mechanics Reviews, ASME* **49:4**, 263-274.

Teng, J.G. (1997). Plastic Buckling Approximation for Transition Ringbeams in Steel Silos. *Journal of Structural Engineering, ASCE* **123:12**, 1622-1630.

Teng, J.G. and Hong, T. (1998). Nonlinear Thin Shell Theories for Numerical Buckling Predictions. *Thin-Walled Structures*, **accepted for publication.**

Teng, J.G. and Luo, Y.F. (1997). Post-Collapse Bifurcation Analysis of Shells of Revolution by the Accumulated Arc-Length Method. *International Journal for Numerical Methods in Engineering* **40:13**, 2369-2383.

Teng, J.G. and Luo, Y.F. (1998). A User-Controlled Arc-Length Method for Convergence to Pre-defined Deformation States. *Communications in Numerical Methods in Engineering* **14**, 51-58.

Teng, J.G. and Rotter, J.M. (1989a). Elastic-Plastic Large Deflection Analysis of Axisymmetric Shells. *Computers and Structures*, **31:2**, 211-235.

Teng, J. G. and Rotter, J. M. (1989b). Non-Symmetric Bifurcation Analysis of Geometrically Nonlinear Elastic-Plastic Axisymmetric Shells Subject to Combined Loads Including Torsion. *Computers and Structures*, **32:2**, 453-477.

Teng, J.G. and Rotter, J.M. (1989c). Non-Symmetric Buckling of Plate-End Pressure Vessels. Journal of Pressure Vessel Technology, ASME, **111:3**, 304-311.

Yin, J., Suo, X. Z. and Combescure, A. (1987). About Two New Efficient Nonlinear Shell Elements. *SMIRT Conference Proceedings,* Lausanne, Paper No. B12/1.

Wunderlich, W., Cramer, H. and Obrecht, H. (1985). Application of Ring Elements in the Non-Linear Analysis of Shells of Revolution under Non-Axisymmetric Loading. *Computer Methods in Applied Mechanics and Engineering*, **51**, 259-275.

Structural Optimization for Seismic Loads: Pseudo-Static, Response Spectra and Time History

Kevin Z. Truman[1]

[1] Department of Civil Engineering, Washington University
Campus Box 1130, St. Louis, MO 63122, USA

ABSTRACT

Optimal design of structures subject to seismic loads using an optimality criterion approach is presented. The fact that inertia related seismic loads are dependent upon the natural period of the structure provides a challenge in structural optimization as compared to statically loaded systems. The inertia loads, being dependent upon the natural frequency of the structure, become a function of the structural stiffness and mass which changes within each optimization iteration. Therefore, the loads also change within each iteration. The typical gradient calculations for static response assumes a constant load, whereas, the gradients of the dynamic structural responses are dependent upon the non-zero gradients associated with these seismic loads. The load gradients are directly affected by the type of seismic analysis performed. Descriptions of the required sensitivity analyses for equivalent lateral force, modal response spectra analysis and time history analysis procedures are presented. An example of how structural optimization can be used to benefit a structural designer is presented. This example clarifies how structural optimization can lead to better understanding of seismic resistant designs.

KEYWORDS

Equivalent lateral force, pseudo-static, response spectra, seismic loads, sensitivity analysis, structural optimization, time history.

INTRODUCTION

Structural optimization of dynamically excited structures has been ongoing for several decades. Many times the word "optimization" is taken literally as finding the global optimal design. Realistically, structural optimization for earthquake loads should be viewed as an automated design process. A major advantage of using structural optimization for seismically designed structures is the capability of simultaneously optimizing a structure for multiple deterministic earthquakes. Traditionally, seismic designers design for the anticipated earthquake and verify that the structure could survive other earthquakes within the given design constraints. If the structure violates any of these design constraints, an iterative process ensues until a viable structure for all the deterministic earthquakes can be designed. This process can be avoided by using structural optimization procedures that can simultaneously design for multiple earthquakes. The optimization procedure resizes members in a fashion providing the most efficient dynamic properties for all of the predetermined earthquake events, whereas, a traditional design focuses on only one event resulting in an over designed structure with respect to the other design earthquakes.

The research associated with structural optimization for earthquake loads is growing in volume, but is still limited. Cheng and Juang (1988, 1989), Truman and Cheng (1990, 1997) and Truman and Jan (1988) studied 2-D and 3-D building structures with respect to various code provisions and cost functions. Truman and Cheng (1983) have studied optimization of structures analyzed by modal response spectrum analyses. Truman and Petruska (1991) have applied optimality criteria techniques for optimization of 2-D structures using time history analysis procedures coupled with actual seismic accelerogram base excitations. Structural optimization of systems subjected to random seismic excitations and reliability theory is still in its developmental stage but has been studied by Cheng and Chang (1988), and Austin, Pister and Mahin (1978a, 1978b).

A major difference between optimizing for statically loaded and earthquake loaded structures is the inertia related seismic loads. The loads are heavily dependent upon the natural period, mass and stiffness of the structure. Therefore, both the structural stiffness, inertia (dead) loads, and dynamic responses change after each optimization iteration. This fact requires changes in the manner by which the gradients of the dynamic structural responses are determined. A statically loaded structure changes with each iteration, but the loading remains essentially constant allowing certain simplifications in the calculation of the response gradients that cannot be made for seismic optimization. Currently, seismic analyses are performed using one of three methods, pseudo-static (equivalent lateral force), modal response spectra, or time history. The changes required to find the gradients of the structural response are directly affected by the type of seismic analysis performed. Descriptions of the required changes for pseudo-static, modal response spectra analysis and time history analysis procedures are presented. The use of structural optimization can lead to better understanding of seismic resistant designs and the limitations of the current state of design code based analysis procedures.

SEISMIC DESIGN LOADS

Deterministic, seismically designed structures are typically loaded either through pseudo-static (equivalent lateral) forces based on design code formulae, a site specific design spectrum or a time dependent accelerogram, either actual or synthetic. Pseudo-static force procedures can be a single set of forces or multiple sets of modal forces used as a means of approximating a full modal response spectra analysis. The pseudo-static force method is a common approach for designers when actual earthquake data is scarce or its use is unwarranted (noncritical structures). Modal response spectrum and time history analysis procedures are very common when earthquake data for a specific site is known or when the structure is deemed a critical facility. Many times these procedures are used for structures located in a region of frequent seismic activity or a region of potentially high magnitude seismic events.

Pseudo-Static Forces

The Uniform Building Code (UBC) (1997) pseudo-static force procedures are based on finding a total base shear and then distributing this base shear to each floor according to the mass distribution and distance above the ground. The UBC equivalent static base shear equation is of the form:

$$V = \frac{C_v I}{RT} W \tag{1}$$

where I is an importance factor, C_v is a seismic coefficient, R is a structural over strength and related ductility factor, T is the fundamental period of the structure and W is the seismic dead load. Typically, the lateral forces are vertically distributed as a percentage of the base shear according to height and mass of a given level. The UBC lateral force distribution is of the form:

$$F_x = \frac{(V - F_t) w_x h_x}{\sum_{i=1}^{n} w_i h_i} = (V - F_t)\rho_x \tag{2}$$

where F_x is the xth level horizontal force, F_t=0.07TV and is the top story horizontal lateral force, w_x is the xth level portion of the weight W used in Eqn. 1, h_x is the height above the base to level x and ρ_x is the xth story distribution percentage. Note that the base shear and lateral forces are dependent upon the natural period of the structure, T, as well as the dead weight, W, which includes the structural weight.

Modal Response Spectra

The modal response spectrum procedure suggested by the NEHRP Provisions (1995) is also based on finding a set of pseudo-static forces based on modal base shear forces for a prescribed number of modes. The displacements, stresses and drifts resulting from individual modes are then combined through the use of a statistically based procedure such as the square-root-of-the-sum-of-the squares (SRSS) or complete-quadratic-combination (CQC). The jth modal base shear for a response spectrum analysis is of the form:

$$V_j = \frac{\overline{W_j}}{g} S_{Aj} \tag{3}$$

where the effective weight $\overline{W_j}$ is defined as:

$$\overline{W_j} = \frac{\left[\{\phi\}_j^T [M]\{I\}\right]^2}{\{\phi\}_j^T [M]\{\phi\}_j} g \tag{4}$$

where $\{\phi\}_j$ is the jth mode shape, [M] is the mass matrix, S_{Aj} is the jth mode spectral acceleration, g is the gravitational constant and {I} is a unity vector. Note that the mode shapes and the spectral acceleration are dependent upon the natural period of the structure. A classical response spectrum procedure with structural optimization procedures is presented in Cheng and Truman (1985).

Ground Motion Accelerogram

Time history analyses are based on the solution of the classic differential equation for seismic analysis using a ground motion accelerogram. The differential equation can be solved by numerous techniques. Truman and Petruska (1991) have successfully used Newmark integration procedures within the optimization algorithms. The classical differential equations are of the form:

$$[M]\{\ddot{u}\} + [C]\{\dot{u}\} + [K]\{u\} = [M]\{I\}\ddot{x} = \{R\} \tag{5}$$

where [C] is the damping matrix, [K] is the stiffness matrix, {u} is the relative displacement vector, {R} is the load vector, x is the ground displacement and each dot is one derivative with respect to time. Note that the inertia force on the right side of Eqn. 5 is mass and time dependent, therefore, the maximum response for each iterative design typically occurs at different times within a single earthquake loading. Using a Newmark integration scheme allows direct formulation of the gradients for the velocity and acceleration in terms of the displacement gradients (Truman and Petruska, 1991). Newmark's Integration scheme is based on a formulation that is similar to a static load calculation as shown in Eqn. 6:

$$\left[\hat{K}\right]\left\{U_{t+\Delta t}\right\} = \left\{\hat{R}_{t+\Delta t}\right\} \tag{6}$$

where the terms with "hats" are effective stiffness and loading terms:

$$\left[\hat{K}\right] = [K] + a_0[M] + a_1[C] \tag{7}$$

and

$$\left\{\hat{R}_{t+\Delta t}\right\} = \left\{R_{t+\Delta t}\right\} + [M]\left(a_0\left\{U_t\right\} + a_2\left\{\dot{U}_t\right\} + a_3\left\{\ddot{U}_t\right\}\right) + [C]\left(a_1\left\{U_t\right\} + a_4\left\{\dot{U}_t\right\} + a_5\left\{\ddot{U}_t\right\}\right) \tag{8}$$

The a_j terms are the Newmark integration constants. Eqn.6 is then solved for the incremental change in the displacements throughout the time history. These terms are greatly affected by the change in structural properties during the optimization of a system. The loading term is heavily dependent upon the stiffness and the mass (ultimately the period) of the structure.

OPTIMIZATION PROCEDURES

Any structural optimization algorithm that can account for the gradient of the loads with respect to the design variables can be used for structural optimization for earthquake loads. The gradients of these loads with respect to the design variables can be found explicitly or implicitly, but are typically necessary for stable convergence of the optimization algorithms. The need for the gradients of the loads can easily be seen by exploring the use of an optimality criteria approach which has been modified for earthquake loads.

Optimality Criteria

Truman *et al.* (1990, 1991 and 1997) have had much success using optimality criteria methods. Their major advantage is the significant reduction of iterations required for convergence to an optimum design. The optimality criteria used in the optimization algorithm is derived from the Kuhn-Tucker conditions of optimality and can be stated as:

$$\tau_i = -\sum_{j=1}^{l} \lambda_j \left(\frac{\partial g_j}{\partial X_i}\right) \div \left(\frac{\partial f}{\partial X_i}\right) = 1 \qquad i = 1, \ldots, n \tag{9}$$

where λ_j is the jth constraint Lagrange Multiplier, g_j is the jth constraint, X_i is the ith design variable (member size), f is the function being minimized (objective function), l is the number

of active constraints and n is the number of structural members. As the structure reaches its optimal design τ_i approaches unity. Therefore, a recurrence relationship using Eqn. 9 can be derived as shown in Truman and Cheng (1990). Prior to the use of Eqn. 9 in a recurrence function for resizing of the structural elements, an estimate of the optimal Lagrange multipliers must be determined as described in detail in Truman and Cheng (1983). The gradient of, g_j, requires the gradient of the different constraint responses such as displacements, stresses, natural frequencies and drifts be calculated.

Sensitivity Analyses

Eqn. 9 indicates that the gradients for the constraints are required which is where the major difference occurs between statically and dynamically loaded structural optimization algorithms. Using the simplest case of finding the gradients for the displacements of a statically loaded system, differentiating the equation [K]{u} = {P}, the general formulation becomes:

$$\frac{\partial\{u\}}{\partial X_i} = [K]^{-1}\left[\frac{\partial\{P\}}{\partial X_i} - \frac{\partial[K]}{\partial X_i}\{u\}\right] \qquad (10)$$

where {P} is the vector of applied forces. For a statically loaded system, each term of the gradient of {P} is zero. The first term in the brackets, the partial derivative of the load vector with respect to the design variable, is not zero for seismic loads.

Equivalent Static Forces

For the UBC equivalent static case the gradient of load vector {P} from Eqns. 1 and 2 becomes:

$$\frac{\partial\{P\}}{\partial X_i} = \frac{\partial\{F_x\}}{\partial X_i} = (1 - 0.07T)\frac{C_v I}{R}\left[T^{-1}\frac{\partial W}{\partial X_i} + W\frac{\partial T^{-1}}{\partial X_i}\right]\{\rho\} - 0.07V\frac{\partial T}{\partial X_i} \qquad (11)$$

where $\{\rho\}$ is the vector of story percentages for the distribution of the base shear according to story heights and mass. The gradient of the period can be found by using the chain rule and the well known natural frequency gradient (Cheng and Truman, 1983):

$$\frac{\partial\omega_j^2}{\partial X_i} = \frac{\{\phi\}_j^T\left[\frac{\partial[K]}{\partial X_i} - \omega_j^2\frac{\partial[M]}{\partial X_i}\right]\{\phi\}_j}{\{\phi\}_j^T[M]\{\phi\}_j} \qquad (12)$$

Modal Response Spectra

The gradients for the modal response spectra displacements, stresses, and drifts are also derived by direct differentiation and application of the chain rule (Truman and Cheng, 1990). Therefore, the gradient for the jth modal base shear from Eqn. 3 can be written as:

$$\frac{\partial V_j}{\partial X_i} = \frac{1}{g}\left[\frac{\partial \overline{W}_j}{\partial X_i} S_{Aj} + \overline{W}_j \frac{\partial S_{Aj}}{\partial X_i}\right] \tag{13}$$

where the partial derivative of the effective weight $\overline{W}_j$ from Eqn. 4 requires the partial derivatives of the mode shapes, the mass and the spectral acceleration as developed in Truman and Cheng (1990). The gradient of the load vector {P} is found by using the appropriate lateral force distribution equations which would be similar to Eqn. 2.

Ground Motion Accelerogram

The equilibrium equations of motion are approximately solved for by using Newmark's numerical integration method shown in Eqns. 6-8. Differentiating Eqn. 6 with respect to the design variable, X, and noting that the derivatives of the integration constants with respect to the design variables X are zero, gives the gradient of the dynamic displacement for each time step as:

$$\frac{\partial\{U_{t+\Delta t}\}}{\partial X_i} = [\hat{K}]^{-1}\left(\frac{\partial\{\hat{R}_{t+\Delta t}\}}{\partial X_i} - \left[\frac{\partial[K]}{\partial X_i} + a_0\frac{\partial[M]}{\partial X_i} + a_3\frac{\partial[C]}{\partial X_i}\right]\{U_{t+\Delta t}\}\right) \tag{14}$$

where

$$\begin{aligned}\frac{\partial\{\hat{R}_{t+\Delta t}\}}{\partial X_i} = {} & \frac{\partial\{R_{t+\Delta t}\}}{\partial X_i} + \frac{\partial[M]}{\partial X_i}\left(a_0\{U_t\} + a_2\{\dot{U}_t\} + a_3\{\ddot{U}_t\}\right) + \\ & [M]\left(a_0\frac{\partial\{U_t\}}{\partial X_i} + a_2\frac{\partial\{\dot{U}_t\}}{\partial X_i} + a_3\frac{\partial\{\ddot{U}_t\}}{\partial X_i}\right) + \\ & [C]\left(a_1\frac{\partial\{U_t\}}{\partial X_i} + a_4\frac{\partial\{\dot{U}_t\}}{\partial X_i} + a_5\frac{\partial\{\ddot{U}_t\}}{\partial X_i}\right) + \\ & \frac{\partial[C]}{\partial X_i}\left(a_1\{U_t\} + a_4\{\dot{U}_t\} + a_5\{\ddot{U}_t\}\right)\end{aligned} \tag{15}$$

and the derivatives of the acceleration and velocity can be found by direct differentiation of the Newmark equations for velocity and acceleration. With the displacement gradients for

each time step calculated, the story drift gradients can be obtained and so can the stress gradients (Truman and Cheng, 1985).

TYPICAL CONSTRAINTS

From a practical point of view, constraints are used to produce a feasible design. The constraints can be used to control drift, displacements, frequencies, stresses, stability, reliability and maximum and minimum member sizes. Note that each constraint must have quantifiable gradients to be used in Eqn. 9 as shown for displacements in Eqns. 10 and 14. Once these gradients are derived, the structural optimization, using the Kuhn-Tucker relationship, is able to control these responses while finding an optimal structural system. To be able to control these responses simultaneously for multiple earthquake loads is extremely useful for seismic resistant design.

OBJECTIVE FUNCTIONS

Deterministic seismic related objective functions are typically expressed in terms of structural weight or structural cost per geometric property such as volume or surface area. Structural weight is commonly used due to its importance as a major contributor to total construction cost. More importantly, design variables can be clearly defined vis-a-vis structural weight. Other objective functions can be and have been formulated to include any combination of the expense of structural members, nonstructural elements, painting, connections, and maintenance (Cheng and Juang, 1988).

EXAMPLE: TIME HISTORY OPTIMIZATION

The three-story, two bay frame shown in Figure 1, Truman and Cheng (1997), was analyzed to show the capability of a time history optimization algorithm. The constraints for this design problem are displacement and minimum and maximum member sizes. The absolute value of the horizontal displacement at each floor was limited to 2.54, 4.19 and 5.97 cm (1.00, 1.65, and 2.35 in.) for the first, second and third floors, respectively. The lower limit on the moment of inertia is 12,070 cm^4 (290 $in.^4$). Initial values for the member sizes were 62,400 cm^4 (1500 $in.^4$). Material constants are E = 200,100 MPa (29000 ksi) and ρ = 7820 kg/m^3 (490 $lb/ft.^3$). A uniformly distributed non-structural weight totaling 148.3 kN (33.33 kips) was applied to each beam member of the frame. Damping of the structure was neglected. Three different loadings were examined. At time t = 0, the structure is at rest and the base undergoes a transient acceleration. The first base acceleration is defined as:

$$\ddot{a}_g(t) = 343\sin(2\pi t)\ cminches/\sec^2, \quad 0 \le t \le 1.0 \text{ sec} \tag{16}$$

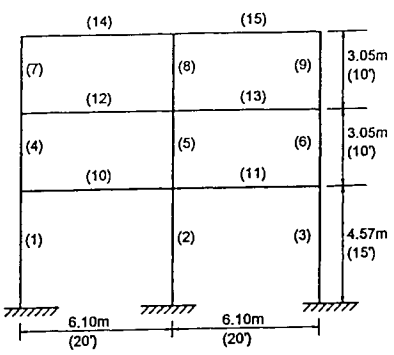

Figure 1: Three story, two bay frame

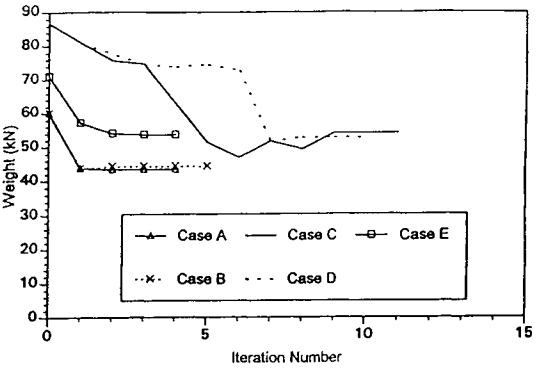

Figure 2: Optimization History

and is zero for t greater than 1.0 seconds. The second base acceleration is defined by the accelerogram for the north-south component of the El-Centro, California earthquake on May 18, 1940. The third base acceleration is for the north-south component of the San Fernando, California earthquake on February 9, 1971 taken at the Caltech Seismological Lab. The constant of 343 used in the sine function was chosen to match the peak acceleration of the El-Centro earthquake record. The San Fernando earthquake was also multiplied by a constant of 1.81 so that both earthquakes would have the same peak acceleration. The time step selected was 0.01 seconds. For the sine load, the time frame examined was 2.0 seconds and for the El-Centro and San Fernando earthquake, the time frame was 10.0 seconds. Table 1, Truman and Cheng (1997), shows the optimum designs and Figure 2, Truman and Cheng (1997), shows optimization history.

In this example, linking refers to forcing each column on a given level to be of one size and each beam on a given level to be of one size. Therefore, for this example a linked system has six design variables; the size of the columns on levels 1, 2 and 3 and the size of the beams on levels 1, 2, and 3. Comparing Case A to Case B and Case C to Case D (defined below Table 1) shows that the linking examples produce heavier structures since each member is not able to take on its optimum size. The El-Centro Earthquake results in a slightly lighter structure than the structures simultaneously optimized for the San Fernando and El-Centro earthquakes. It is worth noting that both earthquakes in Case E, simultaneous earthquakes, produce active constraints. This indicates that a design based on only one earthquake would most likely violate the constraints when loaded by the other earthquake. Figure 2 shows for Case C a zig-zag pattern between iteration 5 through 9 because at iteration 4, the process violates the displacement constraint, and the optimization process is returning to the constraint in iterations 5 through 9. Case D shows a large decrease in weight at iteration 6 due a change in the active constraints thus allowing the optimization process to use a new path to produce a better solution.

TABLE 1
OPTIMAL SOLUTION FOR THE THREE STORY, TWO BAY STRUCTURE

MEMBER	MOMENT OF INERTIA (cm^4)				
	CASE A	CASE B	CASE C	CASE D	CASE E
1	50867	67921	115504	62559	44798
2	94655	67921	115504	237015	404007
3	50867	67921	115504	62485	54473
4	15883	26630	39292	25868	41823
5	44620	26630	39292	76058	71550
6	15883	26630	39292	25960	41952
7	12071	14639	27367	14776	16529
8	22631	14639	27367	43733	52104
9	12071	14639	27367	14918	16204
10	52062	53577	71338	78543	99683
11	52062	53577	71454	78547	109585
12	30834	32566	44820	43080	73631
13	30834	32566	44037	43375	72666
14	12071	12071	16811	12670	14826
15	1207	12071	16358	12799	14859
W^*_{Total}(kN)	43.35	44.26	54.03	52.81	60.15
ITERATION	4	5	11	10	12
	ACTIVE CONSTRAINTS				
DOF TIME (sec) VALUE (cm)	X_3 t=0.69 5.98	X_3 t=0.69 5.97	X_2 t=8.00 4.23	X_2 t=3.58 4.14	X_3(El-C) t=4.74 -5.99
DOF TIME VALUE (cm)			X_3 t=8.02 6.09	X_3 t=3.59 6.04	X_3(SF) t=6.81 5.98
DOF TIME VALUE (cm)				X_3 t=4.22 -5.91	

Case A Sine Function (No linking of members)
Case B Sine Function (Linking of members)
Case C El-Centro Earthquake (Linking of columns)
Case D El-Centro Earthquake (No linking of members)
Case E El-Centro and San Fernando as separate load cases (No linking)

CONCLUSIONS

Several observations can be made with regards to the use of optimization procedures for earthquake loads. Structural optimization is a viable means of producing seismic resistant designs. The optimization procedures can produce a series of feasible designs which can be used for the final seismic resistant design. This series of feasible structures can be extremely useful in enhancing the designers understanding of the interaction between the structure and the seismic loads. The use of structural optimization procedures for full modal response spectra and time history analyses provides an opportunity to design structures for multiple earthquakes simultaneously. Being able to design a structure for a family of varied seismic accelerograms is of tremendous benefit. Objective functions can be related to cost, weight, damage, energy absorption or any other quantity that can be related to the actual design of the structure. Nondeterministic procedures are available in order to explore seismic resistant design from a probabilistic point of view. These techniques are useful in exploring potential structural costs associated with probable events and failures. The use of structural optimization for earthquake loads is not as easily applied as that for static loads, but it is possible. Structural optimization can be an extremely useful and beneficial tool for seismic resistant system designers.

REFERENCES

Austin M.A., Pister K.S., and Mahin S.A. (1987a). Probabilistic design of moment-resistant structures. *Journal of Structural Engineering* **118:8,** 1642-1659.

Austin M.A., Pister K.S., and Mahin S.A. (1987b). Probabilistic design of moment-resistant frames under seismic loading. *Journal of Structural Engineering* **118:8,** 1660-1677.

Cheng F.Y. and Chang C.C. (1988). Safety-based optimum design of nondeterministic structures subjected to various types of seismic loads, NTIS No. PB90-133489/AS, U.S. Department of Commerce, Washington, D.C., USA.

Cheng F.Y. and Juang D.S. (1988). Assessment of various code provisions based on optimum design of steel structures. *Journal of Earthquake Engineering and Structural Dynamics* **16:1,** 46-61.

Cheng, F.Y. and Juang, D.S. (1989). Recursive optimization for seismic steel frames. *Journal of Structural Engineering* **115:2,** 445-466.

Cheng F.Y. and Truman K. Z. (1983). Optimization of 3-D building systems for static and seismic loadings. *Modeling and Simulation in Engineering*, North-Holland Publishing Co., New York, N.Y., 315-326.

Cheng F.Y. and Truman K. Z. (1985), Optimal design of 3-D reinforced concrete and steel buildings subjected to static and dynamic loads including code provisions, NTIS Access No. PB87-168564/AS, U.S. Dept. of Commerce,, Washington, D.C., USA.

NEHRP (1995), Recommended provisions for the development of seismic regulations for new buildings (FEMA 222A), Building Seismic Safety Council, Washington, D.C., USA.

Truman K.Z. and Cheng F.Y. (1990). Optimum assessment of irregular 3-D buildings. *Journal of Structural Engineering* **116:12,** 3324-3337.

Truman K.Z. and Cheng F.Y. (1997). Chapter 12 - How to optimize for seismic loads. *Guide to Structural Optimization.* ASCE, Manuals and Reports, No. 90, 237-262.

Truman K.Z. and Jan C.T. (1988). Optimal bracing schemes for structural systems subject to the ATC 3-06, UBC, and BOCA seismic provisions. *Proc. of the 9th World Conference on Earthquake Engineering*, **V**, 1149-1155.

Truman K.Z. and Petruska D.J. (1991). Optimum design of dynamically excited structural systems using time history analysis. *Optimization of Structural Systems and Industrial Applications*, Elsevier Applied Science, London, 197-207.

UBC (1997). *Uniform Building Code*, International Conference of Building Officials, Whittier, CA, USA.

MONITORING OF CABLE FORCES USING MAGNETO-ELASTIC SENSORS

M. L. Wang [1], D. Satpathi [1], S. Koontz [1], A. Jarosevic [2], and M. Chandoga [3]

[1] Bridge Research Center, University of Illinois at Chicago, IL-60607, USA.
[2] Department of Radio Physics, Cormenius University, Bratislava, Slovak Republic.
[3] Department of Civil Engineering, University of Bratislava, Slovak Republic.

ABSTRACT

While a lot of research work has been done in the area of disaster prevention of large structural systems, very few methods have really been applied at field. The primary reason for this is the inherent complexity of most systems and the associated cost of instrumentation. The authors in this article have introduced the concept of utilizing a novel sensor technology for monitoring bridges. The technology is based on the principle of magnetostriction and work in this area is currently being carried out by the authors under a National Science Foundation International Cooperation grant involving researchers from both the United States and the Slovak Republic.
KEYWORDS: Magneto-elastic, stress measurement, sensor, bridge monitoring.

INTRODUCTION

Instrumenting the critical locations of the structure with different types of strain sensors is definitely one way to evaluate the stress levels material has been subjected to. This has been implemented in quite a few monitoring schemes (Bartolli, et al. 1996; Shahawy, 1996). The world's infrastructural needs are growing at a rapid pace, and to keep up with these needs a large number of new bridges have been commissioned or are in various stages of design and construction. A number of these bridges have very long spans, and use cable- stayed, cable-suspended or various forms of pretensioning and post-tensioning systems. Service properties of prestressed concrete structures depend on the real value of the prestressing forces. Similarly, the performance of both cable-stayed and cable-suspended bridges are dependent on the cable forces in the stays. While these forces are measured during the construction phase of a structure via built in load cells and strain gauges, what happens in the post-construction service life of the structure is usually guessed based on rules of thumb and laboratory simulations.

Measurement of forces during the service live of a structure is typically very difficult, and can be carried out only if the structure was instrumented to begin with. In the vast majority of existing structures, this was not the case, and in a number of situations

structures were instrumented as an afterthought to carry out diagnostic and forensic investigation into the health of an ailing structure. Strain measurements at select distressed locations are carried out to measure the stress levels in the structure. The primary problem of such a measurement is that such measurements completely ignore the dead load component. However, in very large span structures, the dead load component is the most significant component of the actual loads. For the most part, the measurement of the total stress level in a member is virtually an impossible task. Research has shown that the magnetic properties of ferromagnetic materials are strongly dependent on the stress history of the material (Bozorth, 1951). Sensors for monitoring the prestressing force in rock bolts and post-tensioning operations can be designed on the basis of this principle (Kwun and Teller, 1994).

The magneto-elastic method of force measurement that the authors have presented provides an innovative way of measuring forces, stresses and corrosion in cables and strands. The measurements can be carried out even when the cables and strands are enclosed in sheathing and ducts, which are grouted. The technique is relatively inexpensive and is one of the most commercially viable non-destructive evaluation tools available for bridge monitoring.

THEORY OF OPERATION

The magnetic properties of most ferromagnetic materials change with the application of stress to such an extent that stress may be ranked with field strength and temperature as one of the primary factors affecting magnetic properties. Depending on the material, magnetic properties can increase or decrease with the application of stress, The extent of the change being a function of the material itself. This forms the basis of magneto-elasticity. Therefore, it is possible to measure the stress level in ferromagnetic materials based on their measured magnetic characteristics.

The magnetic field strength, H, and the flux density, B, for any material can be expressed by the constitutive law

$$B = \mu H \tag{1}$$

where, μ is called the magnetic permeability. Fig. 1 shows the partial magnetization curve for cast iron, and it serves as a representative example of most ferromagnetic materials. It is evident that the permeability, μ, is not constant, but is dependent on the field strength, H. This results in the magnetization curve being nonlinear. It should be noted that μ is not the slope of the magnetization curve, but simply represents the ratio B/H. The maximum permeability μ_{max} is at the point on the magnetization curve with the largest B/H ratio.

If we now apply an alternating current to a coil that is wrapped around a ferromagnetic core, the magnetization curve of the core moves around a hysteresis loop (Fig. 2). The slope (dB/dH) varies over a very wide range and the average permeability or ordinary permeability is defined as the permeability at the maximum value of B attained in the cycle. However, if a small alternating current is added to a relatively large DC component, then the magnetization curve follows a minor hysteresis loop as shown in Fig. 3 (Krauss 1992). In this case, the average value of (dB/dH) is given by the line passing through the tips of the minor hysteresis loop and is called incremental permeability μ_{inc}.

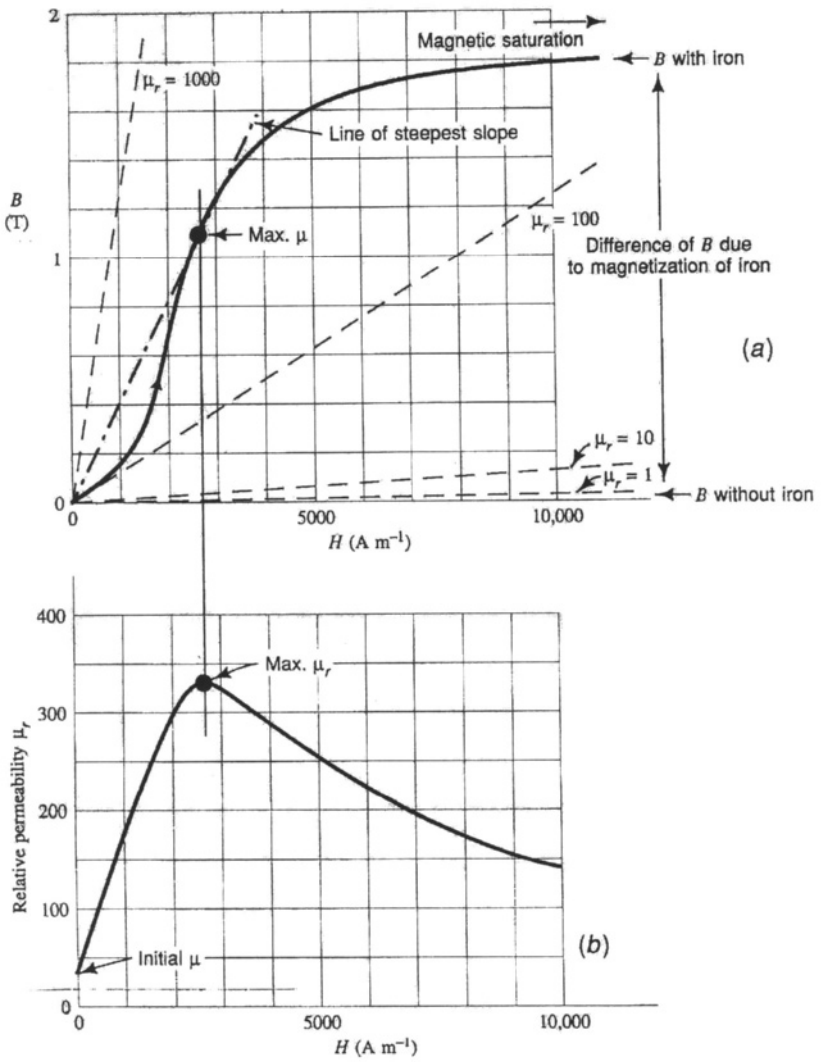

Figure 1. Relationship between magnetic flux density (B) and magnetic field (H)

Referring to Fig 3., μ_{inc} can be defined as

$$\mu_{inc} = \left(\frac{dB}{dH} \right) = \frac{\Delta B}{\Delta H} \tag{2}$$

The effect of stress on the magnetic properties introduced above are large. Stress severely alters magnetization behavior. The magnetic properties of ferromagnetic materials may be described by the magnetic domain theory. This theory postulates that material is

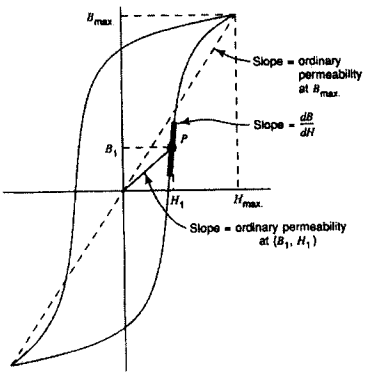

Figure 2. Magnetic hysteresis curve

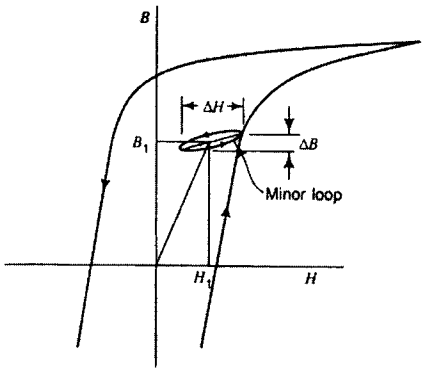

Figure 3. Concept of incremental permeability

made up of local regions called ferromagnetic domains, each magnetized to saturation but aligned according to the state of local magnetization. Adjacent domains are separated by a highly localized magnetic transition region called the domain wall. Even in the demagnetized state, all domains are still magnetized to saturation, but the orientation of the individual domain magnetization vector is random; which results in a net magnetization of zero for a specimen. The application of a magnetic field or a mechanical stress can change the configuration of the domains, principally by wall movement (Sablik and Jones, 1993). In some materials, a tensile stress increases the permeability and these materials are said to exhibit positive magnetostriction. In other materials called negative magnetostrictive materials, application of a tensile stress decreases permeability. Within the elastic limit, the effect of stress on magnetic properties is usually described by magnetization curves obtained by first applying a constant stress and then applying a varying magnetic field (σ, H). If this is reversed (H, σ) such that, the field is applied before the stress, the magnetization curve differs from the one obtained earlier.

MEASUREMENT PRINCIPLE

Using the phenomena of magnetoelasticity described in the previous section, stresses in a test structure (steel prestressing strands and cables) can be evaluated through a measurement of the magnetization characteristics. Measuring its permeability at various bias conditions would allow us to determine the stress of the structure in a non-destructive way. The measurement of permeability is based on the principle of electromagnetic induction. The schematic diagram of the proposed sensor is shown in Fig 4. The stress transducer is essentially a coil wound around the test specimen. A long cylindrical cable with N turns of coil winding around it is used as an example (Fig 5.). A DC current is applied to the coil to produce a magnetic field (H) and the magnetic flux density (B) within the specimen. If we are able to determine the (B/H) ratio within the coils, the permeability at that bias condition can be determined. The direct measurement of magnetic flux or flux density is difficult. An easier way is to measure the induced terminal voltage across a pickup or secondary coil wrapped around the specimen also. This voltage is produced due

to rate of change of flux linkage through the pickup coil. According to Faraday's law:

$$V_{ind}(t) = -N\frac{d\phi}{dt} \tag{3}$$

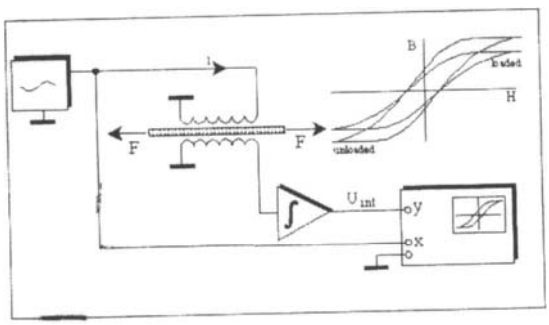

Figure 4. Schematic of magnetoelastic stress measurement

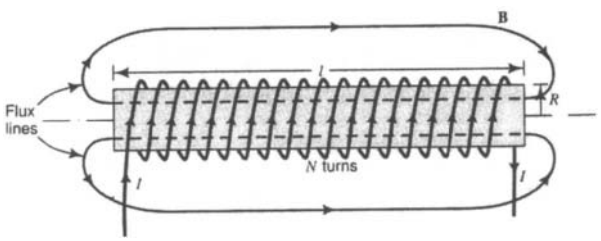

Figure 5. A steel core inside a cylindrical solenoid

The flux through the coil is along the direction of the test specimen. In the testing procedure, the specimen may not completely fill the surface enclosure of the coils. Therefore, the total flux consists of flux through air and through the specimen. The induced voltage can be written as (Kvasnica and Fabo, 1996):

$$V_{ind}(t) = -N\frac{d}{dt}\left[\mu_0 \int_{S\mu 0} H(\rho,\varphi,t)ds + \int_{S\mu} B(\rho,\varphi,t)ds\right] \tag{4}$$

where $S\mu_0$ and $S\mu$, are the surface areas of the coils occupied by air and the specimen, respectively, $\mu_0$is the permeability of air.

Based on (4), a number of measurement schemes can be devised. The first approach is to measure the total permeability *B/H.* The second approach is to measure the incremental permeability *(dB/dH).* It is also possible to obtain the entire magnetization curve (hysterisis curve) on the basis of those measurements.

In the first approach, the induced voltage is integrated with respect to time, the resultant time average output voltage is

$$V_{out} = -\frac{1}{T}\int_{t_1}^{t_2} V(t)_{ind}dt$$

$$= \frac{N}{T}\left[\mu_0 \int_{S\mu 0} \Delta H(\rho,\varphi,t)ds + \int_{S\mu} \Delta B(\rho,\varphi,t)ds\right] \tag{5}$$

where ΔH and ΔB are the change of the magnetic field intensity and magnetic flux density in the time interval (t_2 - t_1), respectively, where the current is increased from 0 to I_a. I_a corresponds to the magnetic field strength, H_a, at which the permeability is to be found. According to the theory of electromagnetism, if the number of turns are large and the spacing between each turn is very small, the magnetic field within the coil is almost uniform, even with the presence of the specimen. As a result (5) may be simplified to

$$V_{out} = \frac{N}{T}\left[\mu_0 (S_0 - S_f)\Delta H + S_f \Delta B\right] \tag{6}$$

where S_0 is the area of the entire cross-section of the coils, and S_f is the cross-section area of the specimen. The integration of the time-varying output voltage from the coils may be carried out by a RC analog integrator. T, which appeared in (6) is the time constant of the RC circuit and is given as *RC.* In order to find the total permeability, the integration of the time varying output voltage *(V_0)* is first performed without the specimen. It can be easily shown that

$$V_0 = \frac{N}{T}\mu_0 S_0 \Delta H \tag{7}$$

By taking the ratio of (6) and (7), we may find the permeability from the following equation:

$$\mu = \frac{\Delta B}{\Delta H} = \mu_0\left[1 + \frac{S_0}{S_f}\left(\frac{V_{out}}{V_o} - 1\right)\right] \tag{8}$$

The permeability in (8) is the total permeability which is proportional to the output voltage.

From this measurement, it is possible to obtain calibrated curves of the type shown in Figs. 6 and 7 by varying ΔH.

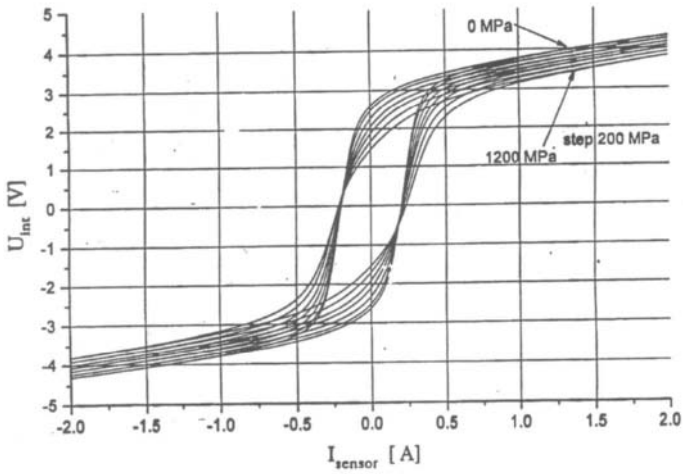

Figure 6. Complete hysteresis loop for different stress levels in a strand

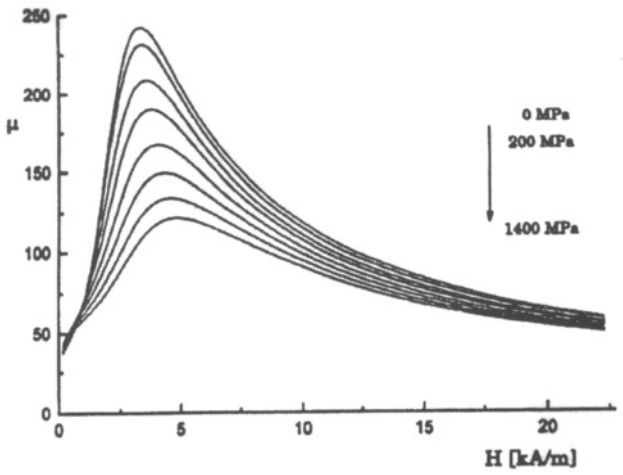

Figure 7. Plot of permeabilty versus field strength (H) for a strand for different stress levels

The second approach is to measure the incremental (or differential) permeability, which is the slope of the *B-H* curve. In this approach, a DC current is applied to the coil and, subsequently, a small AC modulation signal is added to the DC signal to produce a minor hysteresis loop. It has been shown by Jarosevic et al. (1994) that the incremental permeability obtained from the minor loop is essentially a linear function of stress (Figure 8). This material property is particularly useful in developing the magnetic-stress sensor. Experiments have also shown that as the material reaches saturation (due to a large DC current), the minor hysteresis loop becomes essentially a straight line. The μ_{inc} can be expressed in terms of the measured quantities $dH = \alpha\, dI$ and V_{out} according to

$$\mu_{inc} = \frac{dB}{dH} = \frac{RC V_{out}}{NSdI} - \mu_0 \left(\frac{S_0}{S_f} - 1 \right) \tag{9}$$

Note that dI in (9) is the incremental current due to the small modulating AC current.

While the principle is rather simple, a number of issues must be addressed before a reliable sensor can be designed. These are related to removal of EMI, isolating the temperature effect, optimizing the sensor dimensions, power requirements, etc. The first step in the process is essentially the magneto-elastic characterization of the material itself. Since the metallurgical processes for manufacturing steel vary slightly across the globe, it is necessary to characterize the magnetic properties of the local material.

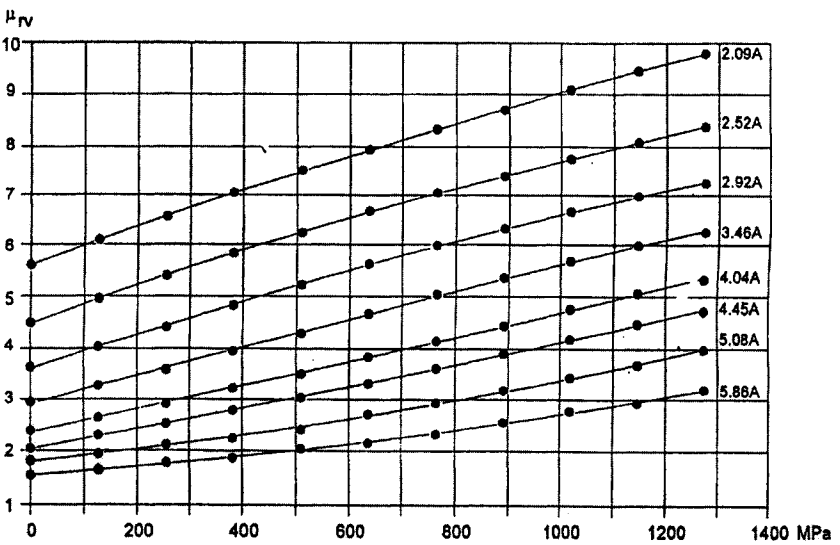

Figure 8. Incremental permeability versus stress for different field strength (I)

EXPERIMENTAL DATA

As a first step it is necessary to carry out the magnetic characterization of the material to be encountered at site. With this in mind, the authors have initiated the process of measuring the measuring the magnetic properties as a function of applied stress and magnetic field strength. The dependence of the magnetic hysteresis curve for low carbon steel (σ_u = 1400 Mpa, dia= 15.5 mm) have been investigated by the authors using a cylindrical sensor design, which is essentially a primary and a secondary coil wrapped around the strand. The complete hysteresis curves have been obtained in this case for stress steps of 200 MPa and is as shown in Fig 6. The data from the same experiment has been plotted in the form of μ versus H in Fig 7. In order to make these measurements, the specimen of the prestressing strand was prestressing bed in the laboratory, with the sensor attached. The prestressing force was measured using a load cell. While the prestressing load was kept constant, the sensor output voltage was measured for different input current values (H). Once the complete hysteresis curve for a given stress level was measured, the strand would be unloaded and then stressed to a different level, and the process repeated.

As can be seen, this is a rather cumbersome process and can be carried out inside a laboratory environment only. Also it can be seen that the relationship between stress and permeability isn't necessarily linear. However, as the material is carried into it's saturation zone, the relationship gets more linear. Fig. 8 shows a plot of the μ_{inc} as a function of stress for different values of excitation current. It can be seen that as the current changes, the slope of the curve increases, which means that as the field strength increases, the sensitivity of the method increases. However, increasing the current, increases the power requirement as well as generates heat, which affects the performance. Thus the input current needs to be optimized and in order to do so it is necessary to have access to data of the type shown in Fig. 8. The magnitude of the necessary excitation current is dependent on the cross-sectional area of the coil, which is in turn dependent on the size of the cable or strand being monitored. Finally, at the end of the calibration process, a calibration curve of the type shown in Fig 9 will be developed for each combination of material and size for an optimized excitation current. Once that is achieved, the stress level can be measured from a single measurement of μ.

Utilizing this technique, the authors have successfully implemented a scheme for monitoring the cable forces in the stays of the Tabor cable stayed bridge in Slovak Republic. Data from the experiment is shown in Fig 10. Based on this experience, the authors are confident that stresses can be measured with an accuracy of +/- 1 % if the sensors have been calibrated for a given material type and strand diameter.

CONCLUSIONS

In this article the authors have introduced the concept of stress monitoring in structural systems using magneto-elasticity. They have provided a brief outline of the underlying principle and have enumerated the steps that are necessary for carrying out such a task. Typical experimental data that has been obtained in the calibration process has been presented. Data obtained from a monitoring program implemented by the European members of the group has been presented. The technique offers an unique ability to monitor prestressing forces in cables and tendons of existing structures, without the need

for cutting open the sheathing. Measurements can be made for cases where the strands are enclosed in pressure grouted ducts.

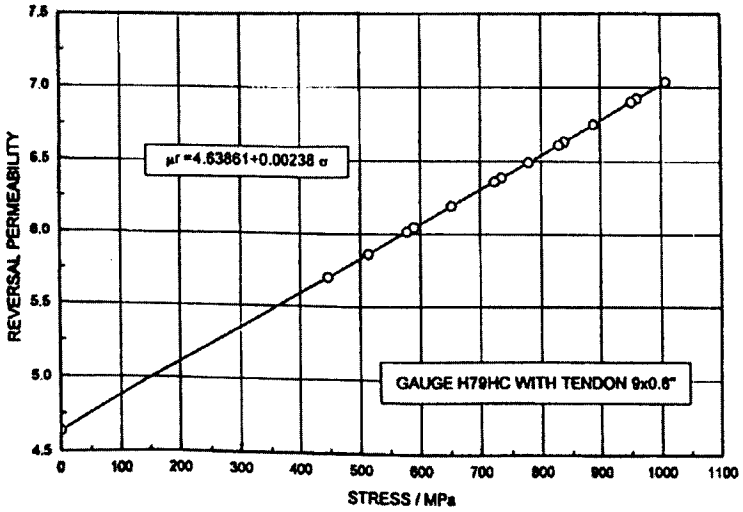

Figure 9. Typical optimized calibration curve for sensor

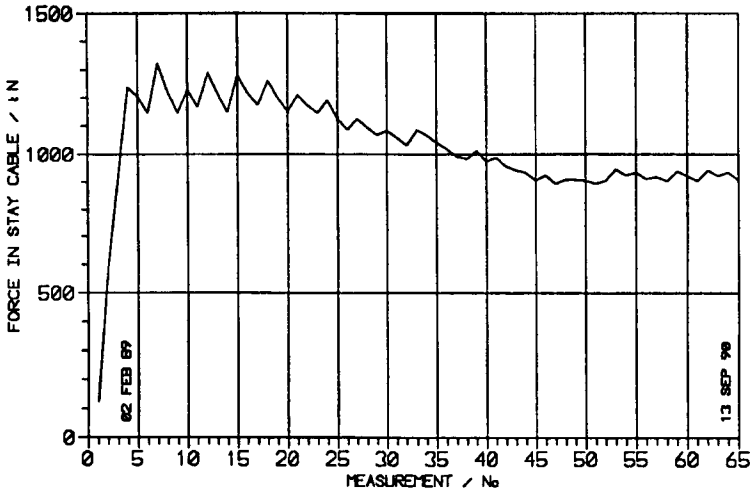

Figure 10. Monitoring data for a cable stay from the Tabor Bridge in Slovak Republic

REFERENCES

1. Bartolli, G., Chiarugi, A. and Gusella, V., "Monitoring Systems on Historic Buildings: The Brunelleschi Dome", *ASCE J. Struct. Engrg.*, pp. 663-673, June (1996).
2. Bozorth, R. M., Ferromagnetism, D. Van Nostrand Co., NY, USA, (1951).
3. Jarosevic, A., Fabo, P., Chandoga, M., and Begg, D. W., "Elastomagnetic method of force measurement in prestressing steel", *Inzinerske Is Stavby*, v. 7., pp. 262-267, Bratisala, Slovakia, (1996).
4. Krauss, J. D., Electromagnetics, McGraw Hill Inc., (1992).
5. Kvasnica, B., and Fabo, P., "Highly precise non-contact instrumentation for measurement of mechanical stress in low carbon steel wires", *Meas. Sci. & Tech.*, pp. 763-767, (1996).
6. Kwun, H., and Teller, C. M., " Detection of fractured wires in steel cables using magnetostrictive sensors", *Materials Eval.*, pp. 503-507, April (1994).
7. McCurie, R., Ferromagnetic materials: Structure and Properties, Academic Press, (1994).
8. Moon, F., Magneto-solid Mechanics, Wiley InterScience, (1984).
9. Sablik, M., and Jiles, D., "Coupled magnetoelastic theory of magnetic and magnetostrictive hysteresis", *IEEE Trans. On Magnetics*, v. 29, no. 3, pp. 2113-2122, (1993).
10. Shahawy M., and Arockiasamy, M., "Field Instrumentation to study the Time Dependent Behavior in Sunshine Skyway Bridge. I", *ASCE J. Bridge Engrg.*, pp. 76-86, (1996).
11. Shahawy M., and Arockiasamy, M., "Field Instrumentation to study the Time Dependent Behavior in Sunshine Skyway Bridge. II", *ASCE J. Bridge Engrg.*, pp. 87-97, (1996).
12. Stanley, R. K., "Simple explanation of the theory of total magnetic flux method for the measurement of ferromagnetic coss sections", *Materials Eval.*, Jan (1995).

This Page Intentionally Left Blank

FRACTURE ESTIMATION: BOUND THEOREM AND NUMERICAL STRATEGY

Chang-Chun Wu Qi-Zhi Xiao Zi-Ran Li

Dept. of Modern Mechanics, Univ. of Science and Technology of China
Hefei 230026 China

ABSTRACT

A bound analysis of fracture parameters is proposed. It is found that the lower bound for *J*-integral can be obtained by a compatible displacement finite element method. On the other hand, the upper bound of the *I**-integral, as the dual of the *J*-integral can be obtained by an equilibrium finite element method. To avoid the difficulty of designing equilibrium finite element models, a hybrid stress model is modified by incorporating a penalty equilibrium constraint. Moreover, a relative error measure formula for J and I* is suggested. Numerical examples on different crack and loading configurations are presented to verify the validity of the bound theorems.

KEYWORDS

Fracture, Path-independent integral, Upper/lower bound, Hybrid finite element

INTRODUCTION

The *J*-integral had been proven to be equivalent to the release rate of the strain energy $\Pi(u_i)$ with respect to the crack area (Rice,1968). Hence, the bound of the numerical solutions for the *J*-integral, if it exists, may possibly be established using the assumed displacement finite element method which is founded on $\Pi(u_i)$. On the other hand, the *I**-integral proposed as the dual counterpart of *J*-integral (by Wu et al.) has also been shown to be the release rate of the

complementary energy $\Pi_c(\sigma_{ij})$ with respect to the crack area. A natural conjecture is that the bound of the numerical solutions for the I^*-integral, if it exists, may possibly be established using the assumed stress finite element method which is founded on $\Pi_c(\sigma_{ij})$.

In computational fracture mechanics, the estimation of upper/lower bounds for fracture parameters becomes a matter of great significance as one cannot obtain an accurate or reliable solution no matter what experimental or numerical method is used due to the complexity of fracture problems. The bound problem consists of two aspects: (1) theoretically, the existence of an approximate upper/lower bound for a certain path integral, and (2) if it exists, numerically, the evaluation approach. In addition, the error measure should be considered once the bound solutions are obtained.

DUAL PATH-INDEPENDENT INTEGRAL

For a given plane crack system with actual states of stress, strains and displacement $(\sigma_{ij}, \varepsilon_{ij}, u_i)$, the J-integral (Rice,1968) can be defined as:

$$J = -\frac{d\Pi}{da} = \int_\Gamma [W(\varepsilon_{ij})dx_2 - \sigma_{ij} n_j (\frac{\partial u_i}{\partial x_1})ds] \tag{1}$$

To find a dual integral of J, we introduce the Legendre transformation

$$W(u_i) + B(\sigma_{ij}) = \sigma_{ij}\varepsilon_{ij} \tag{2}$$

into (1); then an alternative path integral can be derived:

$$\begin{aligned} I^*(=J) &= \int_\Gamma \{[\sigma_{ij}\varepsilon_{ij} - B(\sigma_{ij})]dx_2 - \sigma_{ij} n_j \frac{\partial u_i}{\partial x_1} ds\} \\ &= \int_\Gamma [-B(\sigma_{ij})dx_2 + \sigma_{ij}\varepsilon_{ij}dx_2 - \sigma_{i1}\frac{\partial u_i}{\partial x_1}dx_2 + \sigma_{i2}\frac{\partial u_i}{\partial x_1}dx_1] \\ &= \int_\Gamma [-B(\sigma_{ij})dx_2 + \sigma_{i2}\frac{\partial u_i}{\partial x_j}dx_j] \end{aligned} \tag{3}$$

It is easy to verify that the present I^* is a path-independent integral. The I*-integral can also be defined as a complementary energy release rate(Xiao,1996):

$$I^* = \frac{d\Pi_c}{da} = \int_\Gamma [-B(\sigma_{ij})dx_2 + u_i \frac{\partial \sigma_{ij}}{\partial x_1} n_j ds + \frac{\partial}{\partial x_j}(u_i \sigma_{i2})dx_j] \tag{4}$$

For an equilibrium stress field, $\sigma_{ij,j} = 0$, then it can be verified that (3) is equivalent to (4). In numerical calculations, the expression (3) is especially recommended due to its simplicity and the absence of derivative of stresses.

BOUND THEOREMS

Corresponding to the dual integrals J and I*, the following bound theorems can be established for a certain linear or nonlinear elasticity crack system with homogeneous displacement boundary constraint, i.e.

Lower Bound Theorem for J: For the given cracked system, if u_i *and* $\tilde{u}_i$ *are respectively the exact displacement and the approximate one based on the minimum potential energy principle, the approximate J-integral will take a lower bound of its exact one, i.e.*

$$J(\tilde{u}_i) \le J(u_i) \tag{5}$$

Therefore, the lower bound of J can be obtained by displacement compatible elements.

Upper Bound Theorem for I: For the given cracked system, if* σ_{ij} *and* $\tilde{\sigma}_{ij}$ *are, respectively, the exact stresses and the approximate one based on the minimum complementary energy principle, the approximate I*-integral will take the upper bound of its exact one:*

$$I^*(\tilde{\sigma}_{ij}) \ge I^*(\sigma_{ij}) \tag{6}$$

Therefore, the upper bound of I can be obtained by stress equilibrium elements.*

In the case of linear elasticity, a proof for above theorems was presented by Wu, Xiao and Yagawa(1998). Furthermore, in the case of nonlinear elasticity, including deformation theory-based plasticity, the theorems still hold. As an illustrating example, the lower bound theorem for J is proved here.

For the given nonlinear crack system with homogenous displacement boundary constraints, it can be verified that for the actual solutions (u_i, σ_{ij}):

$$\Pi_c(\sigma_{ij}) = V(\sigma_{ij}) \tag{7}$$

$$\Pi(u_i) = -kU(u_i) \tag{8}$$

where $V(\sigma_{ij})$ and $U(u_i)$ are the complementary energy and the strain energy, and the finite constant

$$k = V(\sigma_{ij}) / U(u_i) > 0 \tag{9}$$

For linear elasticity, $k = 1$. Let $\tilde{u}_i = u_i + \delta u_i$, then we have

$$\Pi(\tilde{u}_i) = \Pi(u_i) + \delta\Pi + \delta^2\Pi(\delta u_i) \tag{10}$$

As the displacement finite element method is an implementation of the potential energy principle, the first and second variations are respectively

$$\delta\Pi = 0$$

and

$$\delta^2\Pi(\delta u_i) = \int_V A(\delta u_i)dV$$

Hence, Eqn.(10) becomes

$$\Pi(\tilde{u}_i) - \Pi(u_i) = \int_V A(\delta u_i)dV$$

In accordance with the definition of J,

$$J(\tilde{u}_i) - J(u_i) = -\frac{d}{da}\left(\Pi(\tilde{u}_i) - \Pi(u_i)\right) = -\frac{d}{da}\int_V A(\delta u_i)dV \tag{a}$$

Considering an actual status of the given system, the J-integral must be positive, i.e. $J(u_i) \geq 0$, and
Eqs.(8) and (9) must be satisfied. Thus we have

$$J(u_i) = -\frac{d}{da}\Pi(u_i) = -\frac{d}{da}\left[-kU(u_i)\right] = k\frac{d}{da}\int_V A(u_i)dV \geq 0 \tag{b}$$

Observing that the employed compatible displacement elements can keep the strain energy to be positive definite, the comparison of (a) and (b) results in

$$-\frac{d}{da}\int_V A(\delta u_i)dV \leq 0 \tag{11}$$

Thus the inequality(5) holds.

NUMERICAL STRATEGY

As for J, its lower bound can easily be obtained by using conventional isoparametric elements. For I^*, however, its upper bound should be estimated by stress equilibrium elements. Unfortunately it is hard to get a reliable equilibrium model for 2D and 3D problems because of numerical difficulties, such as rank deficiency, displacement indeterminacy, etc. cannot be avoided .We face the problem of how to implement the upper bound theorem for I^*.

It is observed that the stress equilibrium element is based on the complementary energy formulation $\Pi_c(\sigma)$, while the stress hybrid element based on the Reissner formulation $\Pi_R(\sigma,u)$. However, $\Pi_R(\sigma,u)$ is identical to $\Pi_c(\sigma)$. Thus a hybrid model may degenerate into equilibrium model when the stress equilibrium equations are enforced to the hybrid element.

For an individual element, let

$$\Pi^e_{RG} = \int_{V^e}\left[\sigma^T(\mathbf{Du}) - \frac{1}{2}\sigma^T \mathbf{S}\sigma\right]dV \tag{12}$$

A generalized functional can be created in the manner of (Wu and Cheung,1995).

$$\Pi^e_{RG} = \Pi^e_R - \frac{\alpha}{2}\int_{V^e}(\mathbf{D}^T\sigma)^T(\mathbf{D}^T\sigma)dV \tag{13}$$

In Eqn.(13) the penalty factor $\alpha > 0$ is taken to be a large constant such that the homogeneous equilibrium condition $\mathbf{D}^T\sigma = \mathbf{0}$ is enforced to the element in a least-squares sense.

Recalling the 4-node plane hybrid stress element, termed as P-S, proposed by Pian and Sumihara(1984), the assumed element stress trial functions can be expressed, in terms of the element coordinates (ξ , η), as

$$\sigma = \begin{Bmatrix}\sigma_{11}\\ \sigma_{22}\\ \sigma_{12}\end{Bmatrix} = \begin{bmatrix}1 & 0 & 0 & a_1^2\eta & a_3^2\xi\\ 0 & 1 & 0 & b_1^2\eta & b_3^2\xi\\ 0 & 0 & 1 & a_1b_1\eta & a_3b_3\xi\end{bmatrix}\begin{Bmatrix}\beta_1\\ \vdots\\ \beta_5\end{Bmatrix} = \Phi\beta \tag{14}$$

where the coefficients a_i and b_i are related to the element nodal coordinates (x_i , y_i) in the manner:

$$\begin{bmatrix} a_1 & b_1 \\ a_2 & b_2 \\ a_3 & b_3 \end{bmatrix} = \frac{1}{4}\begin{bmatrix} -1 & 1 & 1 & -1 \\ 1 & -1 & 1 & -1 \\ -1 & -1 & 1 & 1 \end{bmatrix}\begin{bmatrix} x_1 & y_1 \\ x_2 & y_2 \\ x_3 & y_3 \\ x_4 & y_4 \end{bmatrix} \tag{15}$$

By substituting the stress (13) and the bilinear displacements $\mathbf{u}_q = \mathbf{N}(\xi, \eta)\mathbf{q}$ into the functional (12), we have

$$\Pi_{RG}^{e}(\beta, \mathbf{q}) = \beta^T \mathbf{G}\mathbf{q} - \frac{1}{2}\beta^T \left(\mathbf{H} + \frac{\alpha}{E}\mathbf{H}_p \right)\beta \tag{16}$$

After condensing β, the element stiffness matrix is now

$$\mathbf{K}^e = \mathbf{G}^T \left(\mathbf{H} + \frac{\alpha}{E}\mathbf{H}_p \right)^{-1}\mathbf{G} \tag{17}$$

In Eqn.(17) the matrices G and H are identical to those of P-S element, while the penalty matrix

$$\mathbf{H}_p = \int_{V^e} (\mathbf{D}^T \Phi)^{\mathrm{T}} (\mathbf{D}^T \Phi)\, dV \tag{18}$$

In such a way, P-S hybrid element, is developed into a penalty-equilibrating model, termed as P-S(α), in which the stress equilibrium equation is imposed by the penalty function method.

ERROR MEASURE

Let $\delta u_i = \tilde{u}_i - u_i$ be the displacement error induced by using the assumed displacement finite elements. Then, in accordance with the lower bound theorem (5), the relative error for the J-integral must be

$$J(\delta u_i) = J(\tilde{u}_i) - J(u_i) \leq 0 \tag{19}$$

and the absolute error

$$\left| J(\delta u_i) \right| = J(u_i) - J(\tilde{u}_i) \tag{20}$$

Let $\delta\sigma_{ij} = \tilde{\sigma}_{ij} - \sigma_{ij}$ be the stress error induced by using the assumed stress finite elements; in accordance with the upper bound theorem (6), the relative error for I*-integral must be

$$I^*(\delta\sigma_{ij}) = I^*(\tilde{\sigma}_{ij}) - I^*(\sigma_{ij}) \geq 0 \tag{21}$$

and

$$\left|I^*(\delta\sigma_{ij})\right| = I^*(\tilde{\sigma}_{ij}) - I^*(\sigma_{ij}) \tag{22}$$

Corresponding to (20) and (22), the relative errors can respectively be expressed as

$$\left|J(\delta u_i)\right| / J(u_i) \quad \text{and} \quad \left|I^*(\delta\sigma_{ij})\right| / I^*(\sigma_{ij}) \tag{23}$$

The strength estimation for a certain structure can be carried out once the upper and lower bounds are obtained, and the approximate strength is usually taken to be a combination of the bound solutions. In order to measure the error of the fracture parameters given by finite element methods, a relative dual error for J and I* is defined as:

$$\Delta_{J-I^*} = \frac{\left|J(\delta u_i)\right| + \left|I^*(\delta\sigma_{ij})\right|}{J(u_i) + I^*(\sigma_{ij})} \tag{24}$$

In Eqn.(24), the sum of reference solutions is

$$J(u_i) + I^*(\sigma_{ij}) = J(\tilde{u}_i) + I^*(\tilde{\sigma}_{ij}) - \left[J(\delta u_i) + I^*(\delta\sigma_{ij})\right] \tag{25}$$

Observing the small quantities $J(\delta u_i) \leq 0$, whereas $I^*(\delta\sigma_{ij}) \geq 0$, the last term in (24) can be ignored. we then have

$$J(u_i) + I^*(\sigma_{ij}) \approx J(\tilde{u}_i) + I^*(\tilde{\sigma}_{ij}) \tag{26}$$

Substitute (20), (22) and (26) into (23), and note that the actual J and I* are identical in value; we finally obtain

$$\tilde{\Delta}_{J-I^*} = \frac{I^*(\tilde{\sigma}_{ij}) - J(\tilde{u}_i)}{I^*(\tilde{\sigma}_{ij}) + J(\tilde{u}_i)} \tag{27}$$

The above relative dual error formula only depends on the approximate solutions of J and I*, so as to be easily used in nonlinear fracture estimations. Obviously, the error will vanish when the adopted finite element meshes become more and more fine.

NUMERICAL TESTS

In numerical calculations, the well known 4-node isoparametric element Q4 and the present penalty-equilibrium element P-S(α) are employed to estimate J and I* respectively.

The center cracked panel CCP with uniform stretching load σ_∞(Fig.1-a) and the single edge cracked panel SECP with uniform stretching load σ_∞(Fig.2-b) are calculated. Only a quarter or half of a specimen needs to be considered due to the symmetry. Three finite element meshes and two integral paths are shown in Fig.2-a,b,c. The specimen material consists of Young's modulus E =1.0 and Poisson ratio ν =0.3. The distributed stretching load $\sigma_\infty = 1.0$. For linear elastic crack problems, all the solutions of J or I* will be transferred to the stress intensity factor K_I for convenient comparisons. The reference solutions of K_I are offered by H.L. Ewalds and R.J.H. Wanhill (1984).

To inspect the convergence behavior of the solutions of J and I^*, three meshes with different densities and two independent integral paths are simultaneously considered for each specimen. From the results shown in Fig.3-a,b and Fig.4-a,b , it can be seen that the solutions of J by Q4 always converge to the exact one from a certain lower bound. On the contrary, the solutions of I* by P-S(α) always converge to the exact one from a certain upper bound. All the numerical solutions demonstrate the bound theorems presented in the paper.

The error formula $\tilde{\Delta}_{J-I}$. in (27) is implemented to measure the relative error of the bound solutions for CCP. The results are listed in Table 1~2. The results given by the formula Δ_{J-I}. in (24) are also shown in parentheses in the tables for comparisons. It is found that, independent of the selection of meshes and paths, both $\tilde{\Delta}_{J-I}$. and Δ_{J-I}. always offered almost the same results. These numerical tests exhibit the efficiency of the present approximate error formula (27).

CONCLUSIONS

- Lower and upper bound theorems have been established for J and I* respectively such that the estimation of fracture parameters can be carried out by means of

$$J(\tilde{u}_i) \le J(u_i) = I^*(\sigma_{ij}) \le I^*(\tilde{\sigma}_{ij})$$

- As an effective numerical strategy, the penalty equilibrium hybrid element is developed and implemented to estimate the upper bound of I*-integral.

- A practical error measure for dual integrals is presented to predict the relative error for the approximate bound solutions obtained.

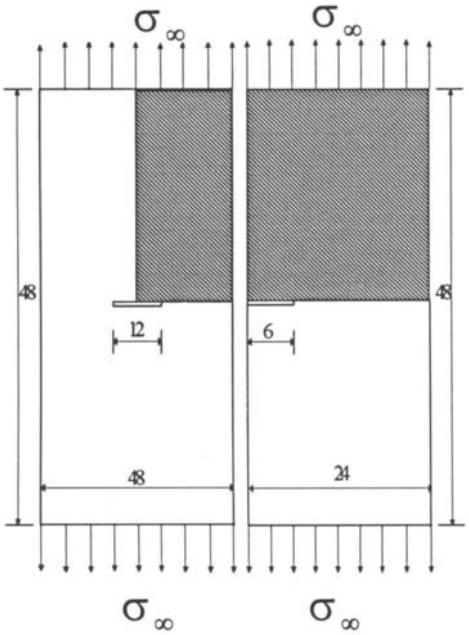

Fig.1-a

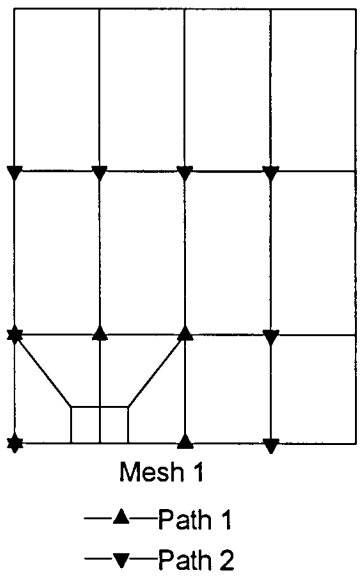

Fig.1-b Fig.2-a

Figure 1:Specimen (a) CCP and (b) SECP

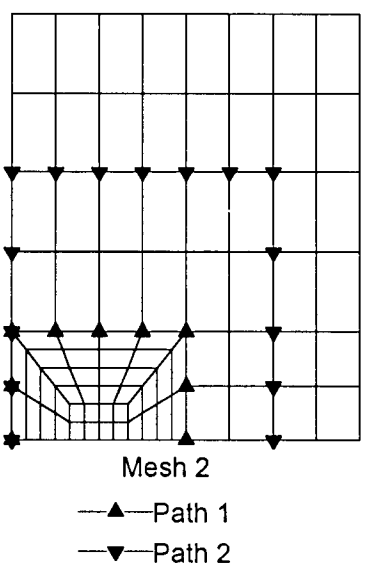

Fig.2-b

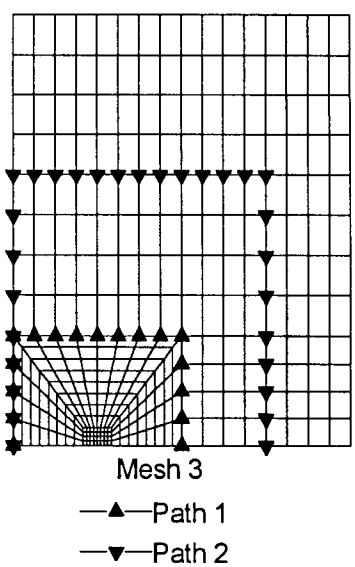

Fig.2-c

Figure 2:The employed finite element meshes and the selected integral paths

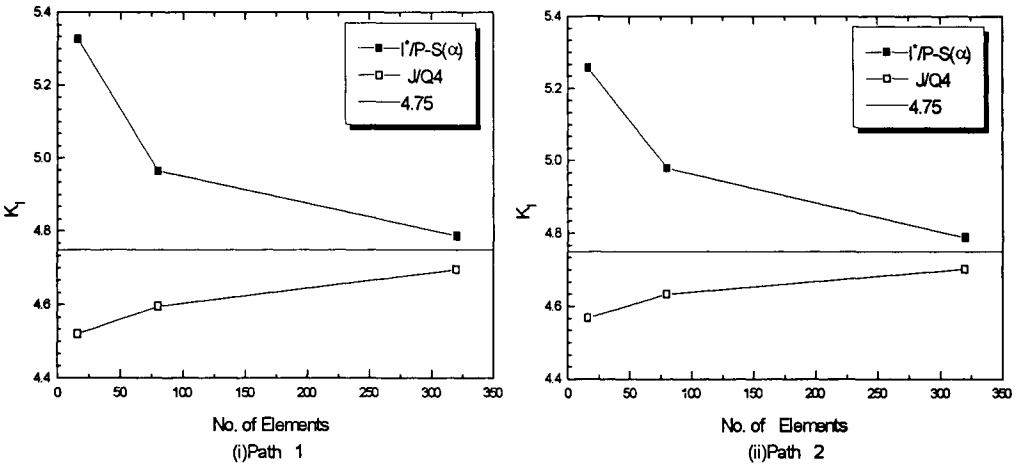

Fig.3-a

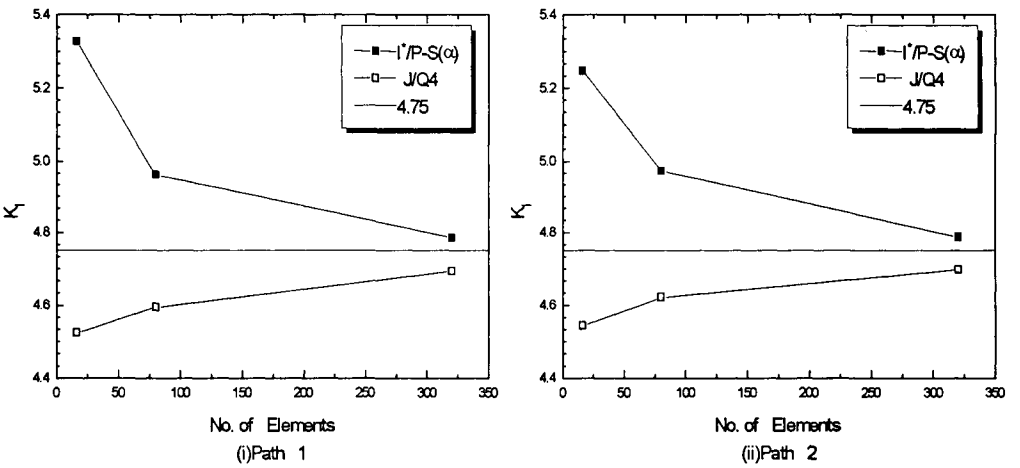

Fig.3-b

Figure 3: The bound behavior of the solutions of J and I^* (transferred to K_I)in three meshes with different densities and two independent integral paths of CCP

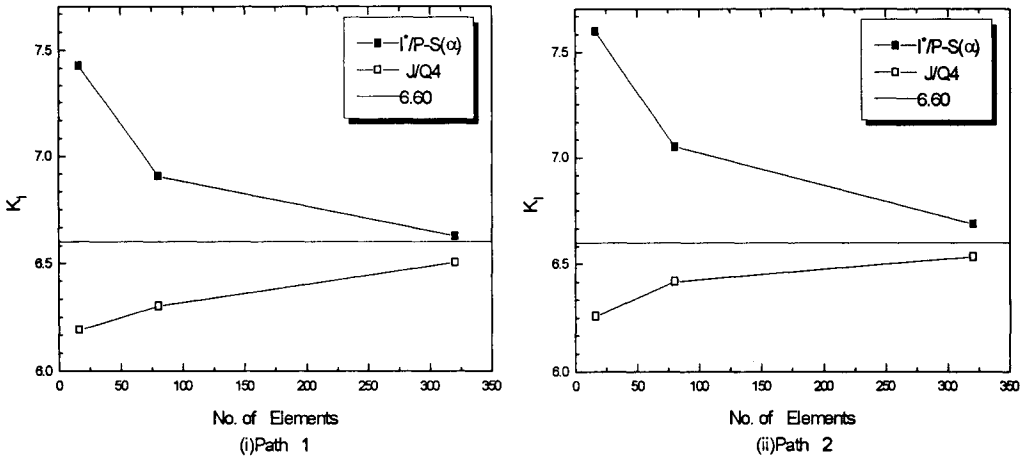

PLANE STRAIN

Fig.4-a

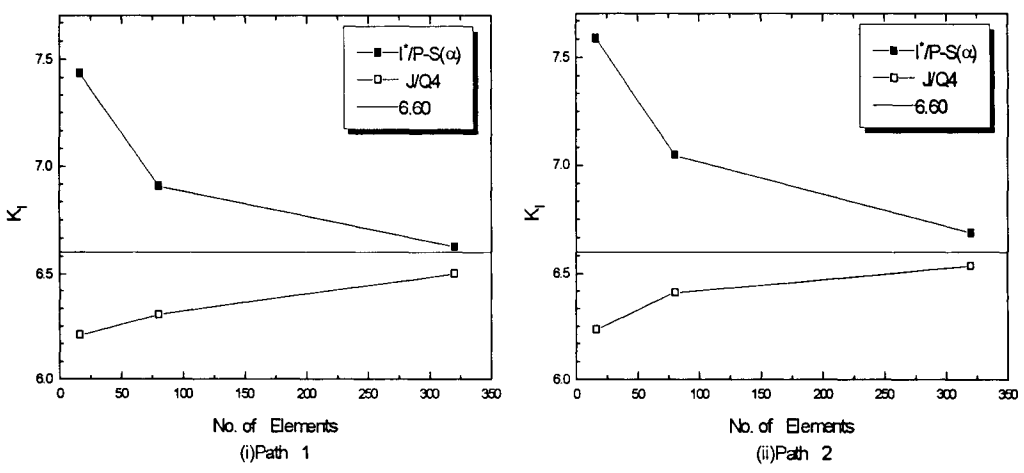

PLANE STRESS

Fig.4-b

Figure 4: The bound behavior of the solutions of J and I^* (transferred to K_I)in three meshes with different densities and two independent integral paths of SECP

TABLE 1

THE RELATED ERROR $\tilde{\Delta}_{J-I}$. & Δ_{J-I}. (%) FOR CCP (PLANE STRAIN)

Mesh	1	2	3
Path 1	8.187 (8.487)	3.855 (3.880)	0.965 (0.963)
Path 2	7.015 (7.225)	3.597 (3.639)	0.922 (0.921)

TABLE 2

THE RELATED ERROR $\tilde{\Delta}_{J-I}$. & Δ_{J-I}. (%) FOR CCP (PLANE STRESS)

Mesh	1	2	3
Path 1	8.157 (8.459)	3.828 (3.851)	0.971 (0.969)
Path 2	7.815 (7.405)	3.661 (3.698)	0.942 (0.941)

ACKNOWLEDGMENTS

Financial support from the National Natural Science Foundation of China (under grant no. 19772-51) is gratefully acknowledged.

REFERENCES

Ewalds H.L. and Wanhill R.J.H.(1984). *Fracture Mechanics.*

Pian T.H.H. and Sumihara K.(1984). Rational approach for assumed stress finite elements, *Int.J.Num.Meth.Engng.* 20,1685-1695.

Rice J.R., (1968), Mathematical analysis in the mechanics of fracture, *Fracture-An Advanced Treatise*, Vol. II, H. Liebowitz(ed.), Academic, New York, 191-308.

Wu C.C., Xiao Q.Z. and Yagawa G.(1998). Dual analysis for path integrals and bounds for crack parameter, *Int.J. Solids & Structures* 35, 1635-1652.

Wu C.C. and Cheung Y.K.(1995). On optimization approaches of hybrid stress element, *Finite Elements in Analysis & Design*, 21, 111-128.

Xiao, Q.Z.(1996), Path integrals in nonlinear fracture mechanics and related numerical methodology, *Ph.D. Thesis*, University of Science and Technology of China, Hefei, 1996.

FINITE ELEMENT-BASED BUFFETING ANALYSIS OF LONG SPAN BRIDGES

Y.L. Xu [1], D.K. Sun[2], J.M. Ko[1] and J.H. Lin[2]

[1]Department of Civil & Structural Engineering, The Hong Kong Polytechnic University, Hung Hum, Kowloon, Hong Kong, People's Republic of China
[2]Research Institute of Engineering Mechanics, Dalian University of Technology, Dalian, People's Republic of China

ABSTRACT

A formulation for fully-coupled buffeting analysis of long span bridges is presented, in which dynamic coupling between modes of vibration, interaction between bridge deck and towers and cables, and varying wind speed and structural properties along bridge deck and towers and cables can be taken into consideration. This formulation is featured mainly by a complete finite element approach and a pseudo-excitation method. The Tsing Ma long suspension bridge in Hong Kong is taken as a case study, in which the new formulation is validated through a comparison with Scanlan's method, and aeroelastic effects, multi-mode effects, inter-mode effects, interaction between bridge components are investigated.

KEYWORDS

Buffeting analysis, long span bridge, finite element approach, pseudo-excitation method, case study, aeroelastic effects, multi-modes, inter-modes, bridge component interaction

INTRODUCTION

Wind-induced vibrations of bridge deck of a long span cable-supported bridge are classified mainly as buffeting due to wind turbulence and self-excited vibration, such as flutter, vortex shedding and galloping. Many efforts have been made in last two decades so as to successfully prevent bridge deck from flutter instability and to significantly reduce vortex shedding

response through the optimisation of deck cross section and/or the installation of aeroelastic devices. Attention to the deck buffeting response was relatively less, probably because the buffeting response does not generally lead to catastrophic failure. However, with the record-breaking span lengths of modern long span bridges, the buffeting response is significantly increased, which may lead to serious fatigue damage to structural components and connections, instability of vehicles travelling on the deck, and discomfort to pedestrian.

The buffeting analysis of modern long span bridges is basically performed using either Davenport's theory (1962a) or Scanlan's theory (1977), which is actually a combination of numerical, experimental, and analytical approaches. Finite element technique is used to determine the natural frequencies and mode shapes of a modern long span bridge. The wind tunnel tests of bridge section models provide flutter derivatives and aerodynamic coefficients. A continuous beam is then used to model the bridge deck and analysed to determine the buffeting response in each mode of vibration and then to superimpose the modal responses using the SRSS method (the square root of the sum of squares of modal responses). Obviously, such a buffeting analysis ignores the coupling between the modes of vibration.

Modern long-span cable-supported bridges tend to have very closely-spaced natural frequencies and significant coupling of flexural and torsional modes of vibration due to the separation of mass centre and stiffness centre of the deck (Xu et al. 1997). The contributions from multi-modes of vibration and inter-modes of vibration to the total buffeting response of the bridge deck, therefore, may have to be included. To consider multi-mode buffeting responses of a bridge deck, Lin and Yang (1983) proposed a general linear theory for the computation of cross-spectra of the deck response to turbulent wind. Jain et al.(1996) considered both multi-mode and inter-mode buffeting responses using a continuous beam model and a random vibration-based mode superposition approach. They demonstrated the significance of the inter-mode responses and multi-mode responses of bridge deck.

For all the aforementioned research work, the interaction between bridge deck, towers and cables during wind-induced vibration are completely disregarded. The wind-induced dynamic responses of bridge deck, towers and cables are traditionally determined separately to simplify the problem. Recently, with respect to flutter instability of cable-stayed bridges, Ogawa et al. (1992) pointed out that the ignorance of interactions between bridge deck, towers and cables may positively or negatively affect the prediction of flutter instability. Davenport (1994) also mentioned several possible mechanisms of interactions between bridge deck and cables.

With the rapid development of modern computer technology, it is now possible for the writers to propose a fully-coupled three-dimensional buffeting analysis of a long span bridge, including not only the dynamic coupling between modes of vibration but also the interaction between bridge deck and towers and cables. The formulation is featured mainly by a complete finite element approach and a pseudo-excitation method. Aeroelastic forces on the bridge deck are changed into nodal forces to form aeroelastic damping and stiffness matrices while aerodynamic forces on bridge deck, towers and cables are converted into nodal forces to obtain a loading vector. After the system equation of motion is assembled and the loading spectral density function matrix is constituted, the pseudo-excitation method in conjunction with the mode reduction technique are applied to determine the bridge buffeting response with reasonable computation effort.

The formulation derived for fully-coupled buffeting analysis is then applied to the Tsing Ma suspension bridge in Hong Kong. The features of the bridge, its natural frequencies and mode shapes from the finite element analysis, and its flutter derivatives and aerodynamic force coefficients from wind tunnel tests are presented. The buffeting response of bridge deck is computed and compared with that from Scanlan's method. After a satisfactory comparison, the effects from aeroelastic forces and multi-modes and inter-modes of vibration on deck response are examined. Finally, the fully-coupled buffeting of bridge deck, towers and main cables is investigated.

AEROELASTIC STIFFNESS AND DAMPING MATRICES

Aeroelastic or self-excited forces on a bridge deck come from the interaction between the wind flow and the motion of the deck (Scanlan and Gade, 1977; Scanlan and Jones, 1990; Jain, et al. 1996). They can be expressed as:

$$\mathbf{F}^{ae} = \mathbf{S}^{ae}\mathbf{d} + \mathbf{D}^{ae}\dot{\mathbf{d}} \tag{1}$$

where

$$\mathbf{F}^{ae} = \begin{Bmatrix} D^{ae} \\ L^{ae} \\ M^{ae} \end{Bmatrix};\ \mathbf{d} = \begin{Bmatrix} p \\ h \\ \alpha \end{Bmatrix};\ \dot{\mathbf{d}} = \begin{Bmatrix} \dot{p} \\ \dot{h} \\ \dot{\alpha} \end{Bmatrix} \tag{2}$$

$$\mathbf{S}^{ae} = \begin{bmatrix} C_{1,d}K^2P_4^*\dfrac{1}{B_d} & C_{1,d}K^2P_6^*\dfrac{1}{B_d} & C_{1,d}K^2P_3^* \\ C_{1,d}K^2H_6^*\dfrac{1}{B_d} & C_{1,d}K^2H_4^*\dfrac{1}{B_d} & C_{1,d}K^2H_3^* \\ C_{2,d}K^2A_6^*\dfrac{1}{B_d} & C_{2,d}K^2A_4^*\dfrac{1}{B_d} & C_{2,d}K^2A_3^* \end{bmatrix} \tag{3}$$

$$\mathbf{D}^{ae} = \begin{bmatrix} C_{1,d}KP_1^*\dfrac{1}{U} & C_{1,d}KP_5^*\dfrac{1}{U} & C_{1,d}KP_2^*\dfrac{B_d}{U} \\ C_{1,d}KH_5^*\dfrac{1}{U} & C_{1,d}KH_1^*\dfrac{1}{U} & C_{1,d}KH_2^*\dfrac{B_d}{U} \\ C_{2,d}KA_5^*\dfrac{1}{U} & C_{2,d}KA_1^*\dfrac{1}{U} & C_{2,d}KA_2^*\dfrac{B_d}{U} \end{bmatrix} \tag{4}$$

in which $C_{1,d} = \frac{1}{2}\rho U^2 B_d$, and $C_{2,d} = \frac{1}{2}\rho U^2 B_d^2$; D^{ae}, L^{ae}, and M^{ae} are the self-excited drag, lift, and torsional moment, respectively, on the deck segment of unit length; ρ is the air density; U is the mean velocity of the incident wind at the deck segment; if the deck segment is located at height z above the ground level, the mean velocity U(z) at the segment is equal to $U_r(z/z_r)^{\beta}$, in which U_r is the mean velocity at the reference height z_r and β is an

exponent constant; x, y, and z are the system coordinates with the z-axis being the vertical axis starting from the ground level and the x-axis being the horizontal axis along the longitudinal axis of the bridge deck and the y-axis being determined according to the right-hand rule; B_d is the width of the bridge deck segment; K is equal to $B_d\omega/U$ (called the reduced frequency); P_i^*, H_i^*, and A_i^* (i=1-6) are the functions of $2\pi/K$ (called the flutter derivatives); p(t), h(t), and $\alpha(t)$ are the lateral, vertical, and angular dynamic displacements of the deck segment, respectively; and each over-dot denotes one partial differentiation with respect to time.

Assume that the bridge deck is modelled by three-dimensional beam elements, and the relation between the internal displacements of the ith element and its nodal displacements can be expressed as

$$\mathbf{d}_i = \mathbf{B}_i \mathbf{d}_i^e \tag{5}$$

where the vector $\mathbf{d}_i$ is the 3x1 internal displacement vector of the ith deck element, corresponding to the vector **d,** in the local coordinate system denoted by $\bar{x}$, $\bar{y}$, $\bar{z}$; the vector $\mathbf{d}_i^e$ is the 12 x 1 local nodal displacement vector of the ith deck element; and the matrix $\mathbf{B}_i$ is the 3 x12 interpolation function matrix of the beam element. By using the principle of virtual work the aeroelastic stiffness and damping matrices of the ith element can be then, respectively, expressed as

$$\mathbf{K}_i^{ae} = \int_{L_i} \mathbf{B}_i^T \mathbf{S}_i^{ae} \mathbf{B}_i \, d\bar{x} \tag{6}$$

$$\mathbf{C}_i^{ae} = \int_{L_i} \mathbf{B}_i^T \mathbf{D}_i^{ae} \mathbf{B}_i \, d\bar{x} \tag{7}$$

where the integrals are definite integrals over the element length. The system aeroelastic stiffness matrix $\mathbf{K}_s^{ae}$ and aeroelastic damping matrix $\mathbf{C}_s^{ae}$ can be then assembled from the element aeroelastic stiffness and damping matrices in the same way as the system structural stiffness matrix $\mathbf{K}_s^s$ and structural damping matrix $\mathbf{C}_s^s$ are assembled from the element structural stiffness and damping matrices.

AERODYNAMIC FORCES DUE TO TURBULENCE

By assuming no interaction between the aeroelastic and aerodynamic forces and by using quasi-steady aerodynamic force coefficients, the aerodynamic forces (buffeting forces) on the deck segment of unit length are expressed by Scanlan and his co-workers (Scanlan and Jones 1990; Jain et al. 1996; Simiu and Scanlan, 1996) as:

$$\mathbf{F}_d^b = \mathbf{A}_d^b \mathbf{q} \tag{8}$$

in which

$$\mathbf{F}_d^b = \begin{Bmatrix} D_d^b \\ L_d^b \\ M_d^b \end{Bmatrix}; \quad \mathbf{q} = \begin{Bmatrix} u \\ w \end{Bmatrix}; \quad \mathbf{A}_d^b = \begin{bmatrix} C_{1,d}\left(\frac{2C_{D,d}}{U}\right) & C_{1,d}\left(\frac{C'_{D,d}}{U}\right) \\ C_{1,d}\left(\frac{2C_{L,d}}{U}\right) & C_{1,d}\left(\frac{C'_{L,d}+C_{D,d}}{U}\right) \\ C_{2,d}\left(\frac{2C_{M,d}}{U}\right) & C_{2,d}\left(\frac{C'_{M,d}}{U}\right) \end{bmatrix} \tag{9}$$

where D_d^b, L_d^b, and M_d^b are the buffeting drag, lift, and moment, respectively, on the deck segment of unit length; $C_{D,d}$, $C_{L,d}$, and $C_{M,d}$ are the drag, lift, and moment coefficients, respectively; $C'_{D,d} = dC_{D,d} / d\alpha$; $C'_{L,d} = dC_{L,d} / d\alpha$; $C'_{M,d} = dC_{M,d} / d\alpha$; α is the angle of attack of normal incident wind referring to the horizontal plane of the deck segment; and u(t) and w(t) are the horizontal and vertical components of fluctuating wind, respectively. The consistent buffeting forces at the nodal points of the ith deck element in the local co-ordinate system can be obtained by the following definite integral.

$$\mathbf{P}_{i,d}^b = \int_{L_i} \mathbf{B}_i^T \mathbf{A}_{i,d}^b \mathbf{q}_i d\bar{x} \tag{10}$$

If the length of the element is sufficiently small, the aerodynamic coefficients and their derivatives, the wind velocities for the element, and the width of the element can be regarded as constant along the element. Consequently, the buffeting forces at the nodal points of the ith deck element can be expressed as

$$\mathbf{P}_{i,d}^b = \mathbf{E}_{i,d}^b \mathbf{q}_i \tag{11}$$

The aerodynamic forces on a bridge tower caused by along-wind and cross-wind turbulence can be derived based on the quasi-steady assumption in a similar way to the aerodynamic forces on the bridge deck (Davenport,1962b; Solari, 1985). The bridge tower is usually modelled as a series of three-dimensional beam elements. The consistent buffeting forces at the nodal points of the ith element in the local co-ordinate system for the bridge tower can be obtained by the following definite integral.

$$\mathbf{P}_{i,t}^b = \int_{L_i} \mathbf{B}_i^T \mathbf{A}_{i,t}^b \mathbf{r}_i d\bar{x} \tag{12}$$

where $$\mathbf{r} = \begin{Bmatrix} u \\ v \end{Bmatrix}; \quad \mathbf{A}_t^b = \begin{bmatrix} C_{1,t}\left(\frac{2C_{D,t}}{U}\right) & C_{1,t}\left(\frac{C'_{D,t}}{U}\right) \\ C_{1,t}\left(\frac{2C_{L,t}}{U}\right) & C_{1,t}\left(\frac{C'_{L,t}}{U}\right) \\ C_{2,t}\left(\frac{2C_{M,t}}{U}\right) & C_{2,t}\left(\frac{C'_{M,t}}{U}\right) \end{bmatrix} \tag{13}$$

in which D_t^b, L_t^b, and M_t^b are the buffeting drag, lift, and moment, respectively, on the tower segment of unit height; $C_{D,t}$, $C_{L,t}$, and $C_{M,t}$ are the drag, lift, and moment coefficients referring to the width B_t of the tower segment; $C'_{D,t} = dC_{D,t} / d\phi$; $C'_{L,t} = dC_{L,t} / d\phi$; $C'_{M,t} = dC_{M,t} / d\phi$; ϕ is the angle of attack of normal incident wind referring to the vertical plane of the tower segment; u(t) and v(t) are the horizontal and lateral components of fluctuating wind,

respectively; and $C_{1,t} = \frac{1}{2}\rho U^2 B_t$, and $C_{2,t} = \frac{1}{2}\rho U^2 B_t^2$. If the length of the tower element is sufficiently small, the aerodynamic coefficients and their derivatives, the wind velocities for the element, and the width of the element can be regarded as constant along the element. Consequently, the buffeting forces at the nodal points of the ith tower element can be expressed as

$$\mathbf{P}_{i,t}^b = \mathbf{E}_{i,t}^b \mathbf{r}_i \tag{14}$$

In the eigenvalue analysis of the bridge, the cable is usually modelled as a series of two-nodes cable elements. In accordance with this arrangement and the quasi-steady assumption, the consistent buffeting forces at the nodal points of the ith cable element in the local co-ordinate system for the bridge cable can be obtained by the following definite integral.

$$\mathbf{P}_{i,c}^b = \int_{L_i} \mathbf{B}_{i,c}^T \mathbf{A}_{i,c}^b u_i d\bar{x} \tag{15}$$

in which $\mathbf{B}_{i,c}$ is the 2 x 6 interpolation function matrix for the cable element and

$$\mathbf{A}_c^b = \begin{Bmatrix} C_{1,c}\left(\frac{2C_{D,c}}{U}\right) \\ C_{1,c}\left(\frac{2C_{L,c}}{U}\right) \end{Bmatrix} \tag{16}$$

where D_c^b and L_c^b are the buffeting drag and lift, respectively, on the bridge cable segment of unit height; $C_{D,c}$ and $C_{L,c}$ are the drag and lift coefficients referring to the dominant dimension B_c of the cable segment, and if the cable has a circular section, the lift coefficient is regarded as zero; and $C_{1,c} = \frac{1}{2}\rho U^2 B_c$. Assuming that the structural properties and wind properties are constant with respect to the element, the buffeting forces at the nodal points of the ith cable element can be expressed as

$$\mathbf{P}_{i,c}^b = \mathbf{E}_{i,c}^b u_i \tag{17}$$

LOADING SPECTRAL DENSITY FUNCTION MATRIX

The nodal forces obtained by Eqs. 11, 14 and 17 are in the local coordinate systems. They should be converted to those in the global coordinate system through the coordinate transformation matrix $\mathbf{T}_i$ which is used in the eigenvalue analysis of the bridge.

$$\mathbf{P}_{i,s}^b = \mathbf{T}_i \mathbf{P}_{i,e}^b \tag{18}$$

where $\mathbf{P}_{i,e}^b$ can be either the aerodynamic forces on the deck element $\mathbf{P}_{i,d}^b$ or the aerodynamic forces on the tower element $\mathbf{P}_{i,t}^b$ or on the cable element $\mathbf{P}_{i,c}^b$; $\mathbf{P}_{i,s}^b$ is the nodal force vector of the ith element in the global coordinate system with the same dimension as the system nodal force vector; and $\mathbf{T}_i$ is the coordinate transformation matrix with the dimensions equal to the

dimension of the system nodal force vector times 12 for a beam element or 6 for a cable element. As a result, the global (system) aerodynamic force vector, including the bridge deck and towers and cables, can be obtained by

$$\mathbf{P}_s^b = \sum_i^n \mathbf{P}_{i,s}^b = \sum_i^n \mathbf{T}_i \mathbf{P}_{i,e}^b = \mathbf{T}\mathbf{P}^g \tag{19}$$

where

$$\mathbf{T} = \left[\mathbf{T}_1, \mathbf{T}_2, \cdots \mathbf{T}_i, \cdots \mathbf{T}_n\right] \tag{20}$$

$$\mathbf{P}^{g\,T} = \left\{\mathbf{P}_{1,e}^{b\,T}, \mathbf{P}_{2,e}^{b\,T}, \cdots \mathbf{P}_{i,e}^{b\,T}, \cdots \mathbf{P}_{n,e}^{b\,T}\right\}^T \tag{21}$$

where the superscript T means the transposition of a matrix; n is the total number of the elements subject to wind loading. Notice that the coordinate transformation matrix **T** is not a function of t. Therefore, if assuming that the fluctuating wind components u (t), v(t), and w(t) acting on the elements can be represented by stationary random process, the spectral density function matrix of the nodal buffeting forces acting on the whole bridge in the global coordinate system is thus

$$\mathbf{S}_{pp}^b(\omega) = \mathbf{T}\begin{bmatrix} \mathbf{S}_{P_1P_1}^e(\omega) & \mathbf{S}_{P_1P_2}^e(\omega) & \cdots & \mathbf{S}_{P_1P_n}^e(\omega) \\ \mathbf{S}_{P_2P_1}^e(\omega) & \mathbf{S}_{P_2P_2}^e(\omega) & \cdots & \mathbf{S}_{P_2P_n}^e(\omega) \\ \vdots & \vdots & \cdots & \vdots \\ \mathbf{S}_{P_nP_1}^e(\omega) & \mathbf{S}_{P_nP_2}^e(\omega) & \cdots & \mathbf{S}_{P_nP_n}^e(\omega) \end{bmatrix}\mathbf{T}^T \tag{22}$$

The cross-spectral density function matrix of the nodal buffeting forces acting on the ith and jth elements can be expressed in a general form as

$$\mathbf{S}_{P_iP_j}^e\left(x_i, x_j, z_i, z_j, \omega\right) = \mathbf{E}_i(z_i)\mathbf{S}_{ij}\left(x_i, x_j, z_i, z_j, \omega\right)[\mathbf{E}_j(z_j)]^T \tag{23}$$

If both the ith and jth elements are deck elements, $\mathbf{S}_{P_iP_j}^e\left(x_i, x_j, z_i, z_j, \omega\right)$ is the 12x12 cross-spectral density function matrix; $\mathbf{E}_k(z_k) = \mathbf{E}_{k,d}^b(z_k)$, k = i, j ; and

$$\mathbf{S}_{ij}\left(x_i, x_j, z_i, z_j, \omega\right) = \begin{bmatrix} S_{uu}\left(x_i, x_j, z_i, z_j, \omega\right) & S_{uw}\left(x_i, x_j, z_i, z_j, \omega\right) \\ S_{wu}\left(x_i, x_j, z_i, z_j, \omega\right) & S_{ww}\left(x_i, x_j, z_i, z_j, \omega\right) \end{bmatrix} \tag{24}$$

in which x_i and z_i, and x_j and z_j can be selected as the global coordinates of the midpoint of the ith and the jth bridge deck element, respectively. Similar explanation can be given to the two tower elements, the two cable elements, and the two elements of which one is a tower element and other is cable element or to the two elements of which one is a tower element and other is a deck element, and so on. The cross-spectral density functions of the wind components on the elements used by Scanlan (Simiu and Scanlan, 1996) are adopted in this study.

PSEUDO-EXCITATION METHOD

The equation of motion of the whole bridge for the buffeting analysis can be expressed as

$$\mathbf{M}\ddot{\mathbf{Y}}(t) + \mathbf{C}\dot{\mathbf{Y}}(t) + \mathbf{K}\mathbf{Y}(t) = \mathbf{R}\mathbf{P}(t) \tag{25}$$

in which $\mathbf{Y}(t)$ is the total nodal displacement vector of N dimensions including the bridge deck, towers, cables, and other components; $\mathbf{M}$ is the NxN total mass matrix; $\mathbf{C}$ is the NxN total damping matrix which consists of both aeroelastic damping matrix $\mathbf{C}_s^{ae}$ and structural damping matrix $\mathbf{C}_s^s$; $\mathbf{K}$ is the NxN total stiffness matrix containing the aeroelastic stiffness matrix $\mathbf{K}_s^{ae}$ and the structural stiffness matrix $\mathbf{K}_s^s$; $\mathbf{P}$ is the total loading vector of m dimensions (in general, m << N), and it is equal to $\mathbf{P}_s^b$; $\mathbf{R}$ is the N x m matrix consisting of 0 and 1, which expands the m dimensional loading vector into the N dimensional loading vector. The Fourier transformation of Eq. 25 gives the frequency-domain transfer function between loading and displacement response as

$$\mathbf{H}(i\omega) = \left[-\omega^2\mathbf{M} + i\omega\mathbf{C} + \mathbf{K}\right]^{-1} \tag{26}$$

in which the superscript -1 means the matrix inversion. The pseudo-excitation algorithm is suggested here to determine the spectral density function matrix for the buffeting response. This algorithm actually converts the random response calculation to the deterministic response calculation. The principle of the algorithm (Lin et al. 1994) and its application to wind-excited structures are introduced as follows:

Notice that the spectral density function matrix $\mathbf{S}_{PP}(\omega)$ or $\mathbf{S}_{PP}^b(\omega)$ is a symmetric matrix. Therefore, this excitation spectral matrix can be decomposed as

$$\mathbf{S}_{PP}(\omega) = \mathbf{L}^*\mathbf{D}\mathbf{L}^T \tag{27}$$

in which $\mathbf{L}$ = the lower triangular matrix ; $\mathbf{D}$ is the diagonal matrix. With the k-th column of $\mathbf{L}$ denoted as $\mathbf{L}_k$ and the k-th diagonal element of $\mathbf{D}$ denoted as d_{kk}, $\mathbf{S}_{PP}(\omega)$ can be further expressed as

$$\mathbf{S}_{PP}(\omega) = \sum_{k=1}^{m} d_{kk}\mathbf{L}_k^*\mathbf{L}_k^T \tag{28}$$

Then, the pseudo excitations are constituted as follows:

$$\mathbf{f}_k = \mathbf{L}_k \exp(i\omega\ t) \qquad (k = 1,2,\ldots,m) \tag{29}$$

For each pseudo-excitation vector, a pseudo displacement response vector, $\mathbf{Y}_k(\omega)$, can be determined by

$$\mathbf{Y}_k = \mathbf{H}(\omega)\mathbf{R}\mathbf{f}_k \tag{30}$$

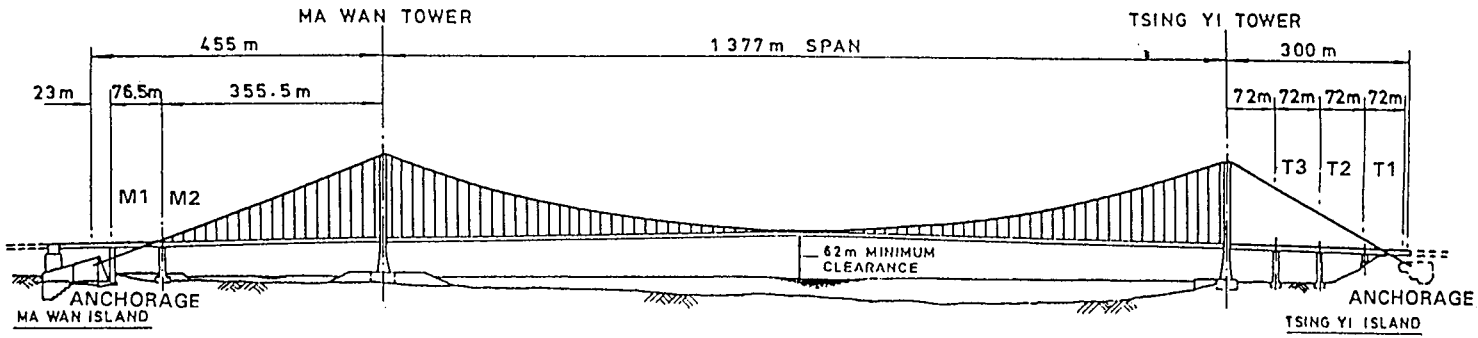

Fig.1 Configuration of Tsing Ma Bridge

It can be readily proved that the spectral density function matrix of the displacement response of the bridge can be obtained by

$$\mathbf{S}_{YY}(\omega) = \sum_{k=1}^{m} d_{kk} \mathbf{Y}_k^* \mathbf{Y}_k^T \tag{31}$$

Much less computation effort is needed to calculate the response spectral density matrix by the pseudo-excitation method, in particular if the internal force response spectral density matrix is required. Further reduction of computation time can also be achieved if the buffeting response of a long span bridge is dominated by the first few modes of vibration. In this case, the equation of motion (Eq. 25) can be first reduced from N dimensions to r dimensions in terms of the mode shapes found in the eigenvalue analysis, where r is the number of modes of vibration interested. After that, the pseudo-excitation method is applied in the same way as the aforementioned. Different from the SRSS method, the pseudo-excitation method retains the cross-correlation terms between the first r normal modes. The modal coupling effects can be thus included. The standard deviations of the displacement, velocity, and acceleration of the node can be readily computed according to the random vibration theory after the auto spectral density functions for each node are determined.

TSING MA LONG SUSPENSION BRIDGE

Hong Kong's new airport and port development are located on Lantau Island. The key section of the transportation between the new facilities and the existing commercial centres of Hong Kong Island and Kowloon is the Lantau Fixed Crossing, in which the Tsing Ma long suspension bridge (Fig.1) is the central structure carrying a dual three-lane highway on the upper level of the bridge deck and two railway tracks and two carriageways on the lower level within the deck (Beard and Young, 1995).

The Tsing Ma Bridge, stretching from Tsing Yi Island to Ma Wan Island, has a main span of 1,377 m between the Tsing Yi tower in the east and the Ma Wan tower in the west. The height of the towers is 206 m, measured from the base level to the tower saddle. The two main cables of 36 m apart in the north and south are accommodated by the four saddles located at the top of the tower legs in the main span. A three-dimensional dynamic finite element model has been established for the Tsing Ma Bridge (Xu, et al. 1997). The modal analysis of the Tsing Ma Bridge shows that the natural frequencies of the bridge are spaced very closely. The first 20 natural frequencies include the first 12 lateral modes, the first 6 vertical modes, and the first 2 torsional modes. They range from 0.068 Hz to 0.380 Hz only. The computed natural frequencies and mode shapes have been verified by the field measurements. Among the first 20 natural frequencies, the lowest frequency of the bridge is 0.068 Hz, corresponding to the first lateral mode of a half wave with the bridge deck and cables moving in phase in the main span. The first vertical mode of the bridge is almost antisymmetric in the main span at a natural frequency of 0.117 Hz in one wave and the second vertical mode is almost symmetric in the main span at a natural frequency of 0.137 Hz in a half wave approximately. The first torsional vibrational mode occurs at a natural frequency of 0.271 Hz in a half wave in the main span. This mode is structurally coupled with the seventh lateral vibrational mode, i.e, the first torsional mode contains the lateral component which is similar to the seventh lateral mode and

in turn the seventh lateral mode contains the torsional component which is similar to the first torsional mode. The more information on the structural properties, the finite element modelling, the dynamic characteristics of the bridge can be found in Xu et al. (1997).

AEROELASTIC AND AERODYNAMIC PARAMETERS

The flutter derivatives of the bridge deck section were measured for a range of wind incidence for the deck alone and for an incidence of 0° for the deck with traffic and trains in a laminar flow (Coleman et al. 1994). Only those derivatives corresponding to the 0° wind incidence without traffic and trains are considered in the present study. All H_i^*(i=1,2,..,4) curves are basically negative within the reduced wind speed range concerned. Among the A_i^*(i=1,2..,4) curves, the A_1^* curve exhibits the positive values in the reduced velocity ranging from 6 and 12, indicating the possibility of negative aerodynamic damping in the torsional motion. The positive A_3^* and negative A_4^* curves, on the other hand, indicate respectively that the aeroelastic forces from torsional motion may generate negative torsional stiffness, and that the aeroelastic forces from vertical motion may generate positive torsional stiffness.

The aerodynamic force coefficients of the bridge deck with angle of wind incidence were also obtained from the wind tunnel tests. (Lau and Wong, 1997). The drag, lift, and moment coefficients are 0.135, 0.090 and 0.063, respectively, at the wind incidence of 0° with respect to the deck width of 41 m. The first derivatives of the drag, lift, and moment coefficients with respect to wind incidence (in degree) at the wind incidence of 0° are -0.253, 1.324, and 0.278, respectively. For the two bridge towers, the drag coefficient is taken as 1.5 with respect to the tower width of 9.25 m (Flint and Neill, 1991). For the main cables, force coefficients critically depend on the Reynold's number and cable surface roughness. Conservatively, the drag coefficient of 1.0 is chosen with reference to the cable diameter of 1.1 m.

SOME SELECTED RESULTS

Comparison of Deck Response

The displacement and acceleration responses of the bridge deck along the span are computed using the new formulation and compared with those from Scanlan's method (Jain et al. 1996). Only the bridge deck is subjected to buffeting loading and no buffeting loading is applied to the towers and cables. The first 20 modes of vibration are included in the computation. Each mode of vibration contains three components, but for most of vibrational modes only one component is dominant. The results from both methods encompass multi-modes and inter-modes contributions as well as aeroelastic effects. The results from the new formulation are very compatible with those from Scanlan's method, but the varying wind speed and turbulence considered in the new method have some effects on displacement responses around the midspan. The satisfactory comparison verifies the accuracy of the new formulation and the new computer program and also highlights the advantages of the proposed method.

Aeroelastic Effects

It is a common belief that self-excited forces (aeroelastic forces) would affect buffeting response of long span bridges (Davenport, 1962a; Scanlan and Gade, 1977). To understand such effects on the Tsing Ma Bridge, the response spectra of the bridge deck with and without aeroelastic effects (i.e., with and without flutter derivatives) are computed using the new formulation. The results show that the aeroelastic damping considerably reduces the vertical response of the bridge deck. The aeroelastic coupling between the second vertical and the first torsional modes of vibration significantly affects the torsional vibration of the bridge deck. The multi-mode approach should be taken into consideration of determining buffeting response of the bridge, in particular, the acceleration response.

Multi-Mode Effects

The spectral analysis of the deck response has demonstrated that the vertical and torsional displacement responses may not be dominated by a single mode of vibration. To further discuss this matter, the lateral displacement response attributed to the first lateral mode only, the vertical displacement response due to the second vertical mode only, and the angular displacement response arising from the first torsional mode only are computed and compared with the same quantities from the first 20 modes of vibration. From the results obtained, it can be concluded that for the Tsing Ma Bridge, multi-mode effects are significant for the vertical and torsional displacement responses but not for the lateral displacement response.

Inter-Mode Effects

To investigate effects of inter-modes, a number of pairs of vibrational modes are selected from lateral, vertical, and torsional motions respectively as well as their combination. For each pair of vibrational modes, the deck response along the span from each single mode is computed first and then the deck response from the two modes are computed using both the SRSS method (the square root of the sum of the squares of the model response) and the CQC method (the Complete Quadratic Combination). The CQC method used here is actually the pseudo-excitation method as introduced before. By comparing the responses from both the methods, inter-mode effects can be estimated. The results obtained show that for the Tsing Ma Bridge, inter-mode effects are negligible for the two modes from either lateral motion or vertical motion or torsional motion but inter-mode effects are considerable for the structurally-coupled torsional and lateral modes and also for the aeroelastically-coupled vertical and torsional modes of similar mode shapes.

Interaction between Bridge Components

The buffeting forces on the towers and the cables are now included in the computation in addition to the aeroelastic forces and aerodynamic forces on the bridge deck. This result is denoted by the term "full bridge". The full bridge results are then compared with those from the forces on the bridge deck only, the bridge tower only, and the main cable only. In this way, the interaction between the bridge deck, towers, and main cables can be examined. From the results obtained , one can conclude that the lateral displacement response of the bridge deck should include interactive effects from the main cables and towers. The buffeting responses of both towers and main cables should include interactive effects from the bridge deck.

CONCLUSIONS

A new formulation has been presented for fully-coupled three dimensional buffeting analysis of long span cable-supported bridges. The formulation is featured by a complete finite element approach and a pseudo-excitation method. The advantages of the suggested formulation are: (1) to readily handle the bridge deck with significantly varying structural properties and mean wind speed along the deck; (2) to make good use of the ready-made finite element models of the bridge for both static and eigenvalue analyses as well as the relevant results; (3) to naturally include inter-mode and multi-mode responses; (4) to determine wind-induced responses of the bridge deck, towers, and cables simultaneously; (5) to examine the dynamic interactions between bridge deck, bridge towers and cables; and (6) to lay down a solid foundation for investigation of vibration mitigation or control of cable-supported bridges.

The proposed formulation has been applied to the Tsing Ma suspension Bridge in Hong Kong. The buffeting response of the bridge deck from the new formulation is in good agreement with that computed using the latest Scanlan's method which includes multi and inter-mode effects. The aeroelastic damping was found to reduce the vertical response of the bridge deck, but the aeroelastic effects on the torsional vibration of the Tsing Ma Bridge are significant. The multi-mode effects are considerable on the vertical motion and torsional motion but not on the lateral motion of the bridge deck. Inter-mode effects can be neglected for the two modes in either lateral motion or vertical motion or torsional motion but inter-mode effects should be considered for the aeroelastically-coupled vertical and torsional modes of similar mode shapes. Finally, the buffeting of bridge deck considerably impacts the buffeting of towers and main cables whereas the buffeting of towers and main cables only moderately affects the lateral vibration of bridge deck.

ACKNOWLEDGEMENTS

The writers are grateful for the financial support from both the Hong Kong Research Grant Council through a UGC grant and from the Hong Kong Polytechnic University through its Area of Excellence Program. The support from the Lantau Fixed Crossing Project Management Office, Highways Department of Hong Kong , to allow the writers to access the relevant materials is particularly appreciated.

REFERENCES

Beard, A.S. and Young, J.S. (1995). Aspect of the design of the Tsing Ma Bridge. *Proc., Int. Conf. on Bridge into 21st Century*, Impressions Design & Print Ltd., Hong Kong, 93-100.

Coleman, S.A., Elliott, A.M. and Johnson, R. (1994). Tsing Ma Bridge: wind tunnel tests to determine aerodynamic derivatives. *BMT Project Report No.* 43001/00 for Mott MacDonald Hong Kong Limited.

Davenport, A.G.(1962a). Buffeting of a suspension bridge by storm winds. *Journal of Structural Division,* ASCE, Vol.88, No.ST3, 233-268.

Davenport, A.G. (1962b). The response of slender line like structures to a gusty wind. *Proceedings of Institution of Civil Engineers,* Vol.23, 389-408.

Davenport, A.G.(1994). A simple representation of the dynamics of a massive stay cable in wind. *AFPC Conference*, Deauville, France, 427-437.

Flint and Neill Partnership (1991). Independent appraisal of the design of Tsing Ma Bridge. *Report No.*113, for Highways Department, Hong Kong Government.

Jain, A., Jones, N.P., and Scanlan, R.H.(1996). Coupled flutter and buffeting analysis of long-span bridges. *Journal of Structural Engineering*, ASCE, Vol.122, No.7, 716-725.

Lau, C.K. and Wong K.Y. (1997). Aerodynamic stability of Tsing Ma Bridge. *Proc. of the Fourth Int. Kerensky Conf.*, Hong Kong, Sept., 131-138.

Lin, J.H., Zhang, W.S. and Li, J.J.(1994). Structural responses to arbitrarily coherent stationary random excitations. *Computers & Structures*, Vol.50, No.5, 629-633.

Lin, Y.K. and Yang, J.N.(1983). Multimode bridge response to wind excitations. *Journal of Engineering Mechanics*, ASCE, Vol. 109, No.2, 586-603.

Ogawa, K., Shimodoi, H. and Ishizaki, H. (1992). Aeroelastic stability of a cable-stayed bridge with girder, tower and cables. *Journal of Wind Engineering and Industrial Aerodynamics*, 41-44, 1227-1238.

Scanlan, R.H. (1997). Amplitude and turbulence effects on bridge flutter derivatives. *Journal of Structural Engineering*, ASCE, Vol. 123, No.2, 232-236.

Scanlan, R.H. and Gade, R.H.(1977). Motion of suspended bridge spans under gusty wind. *Journal of Structural Division*, ASCE, Vol.103, No.ST9, 1867-1883.

Scanlan, R.H. and Jones, N.P. (1990). Aeroelastic analysis of cable-stayed bridges. *Journal of Structural Engineering,* ASCE, Vol. 116, No. 2, 279-297.

Simiu,E. and Scanlan, R.H.(1996). *Wind Effects on Structures.* John Wiley & Sons, Inc., New York.

Solari, G. (1985). Mathematical model to predict 3-D wind loading on buildings. *Journal of Engineering Mechanics,* ASCE, Vol. 111, No.2, 254-276.

Xu, Y.L., Ko, J.M. and Zhang, W.S.(1997). Vibration studies of Tsing Ma suspension bridge *Journal of Bridge Engineering*, ASCE, Vol.2, No.4.,149-156.

ODE-ORIENTED SEMI-ANALYTICAL METHODS

Si Yuan

Department of Civil Engineering, Tsinghua University, Beijing, 100084, P. R. China

ABSTRACT

With the rapid advances of modern computational technology, a number of high-quality, general-purpose ordinary differential equation (ODE) solvers have emerged. As a result, a new class of ODE-oriented semi-analytical methods have been developed rapidly. The present paper reviews several classical ODE-oriented methods such as the Kantorovich method and the method of lines (MOL), and presents a series of new methods that are developed or developing by the research group in Tsinghua University in recent years. The potential superiority of ODE-oriented methods is emphasized and discussed.

KEYWORDS

ODE, solver, adaptivity, semi-analytical, Kantorovich method, method of lines, finite element method of lines, extended Kantorovich method

INTRODUCTION

Many engineering problems are originally cast into partial differential equations (PDEs), the solution of which, if no discretization is made, calls for analytical methods. However, the common strategy in most existing numerical methods is to convert a PDE problem, by various means such as finite element (FE), finite difference (FD), finite strip, weighted residual, boundary element, etc. into a set of algebraic equations (AE). These fully discretized methods can be termed as AE-oriented methods. The dominance of AE-oriented methods is a natural

result of the appearance of the computer that makes solution of algebraic equations much easier than before.

However, between the analytical approach to continuous PDE problems and the fully discretized approach to AE problems, there exists an intermediate semi-analytical approach which solves ordinary differential equations (ODEs) to approximate the original PDE problems. This class of methods might as well be termed as ODE-oriented methods. Due to the limitation of solution means for ODE problems, this class of methods did not gain their due development.

With the rapid advances of modern computational technology, a number of high-quality, general-purpose ODE solvers have emerged. Taking advantage of these ODE solvers, ODE-oriented methods come alive and have gained substantial development rapidly. Similar to AE-oriented methods, the strategy in ODE-oriented methods is that the original PDEs in engineering problems are semi-discretized, by various means such as FD, FE, etc. into ODE problems which are then efficiently and accurately solved by using a standard ODE solver. Owing to the self-adaptive capability built in the modern ODE solver, the accuracy of the ODE solution satisfies the user-specified error tolerances, which ensures the semi-analytical property inherent in this class of methods. The purpose of this paper is to give a state-of-the-art review of both developed and developing ODE-oriented methods.

ODE SOLVERS

ODE-oriented methods depend heavily on ODE solvers for boundary value problems (BVP). Without ODE solvers, there will be no ODE-oriented methods. As early as in 1976, Keller predicted in his significant monograph: "Indeed, the signs are rather clear that over the next five to ten years (or less), standard computer codes will be available to 'solve' most such problems". This turned out to be very true, and the following ten years saw ODE codes for BVP become fruitful.

Among many existing ODE codes for BVP, we have chosen the collocation code COLSYS (Ascher, Christiansen & Russell (1981)) to serve us as the ODE solver. COLSYS solves mixed order, linear and nonlinear ODE systems by spline collocation at Gaussian points. In COLSYS, approximate solutions are computed on a sequence of automatically selected meshes until a user-specified set of tolerances is satisfied. For nonlinear problems, the damped and modified Newton methods are used for nonlinear iteration. The code was written using FORTRAN with about 3000 statements and is freely downloadable from TOMS web site. There are several reasons for us to make our choice, e.g. see Yuan (1993).

ODE-SOLVER METHOD

Most ODE codes, although very powerful, are designed for certain standard forms of ODE problems which can hardly cover the variety of special forms in practical applications, and hence their direct applications are, to various degree, limited. However, there exist some feasible ODE conversion techniques to transform "special" forms into "standard" forms (Ascher & Russell (1981)). Using these ODE techniques, a large number of ODE problems of special forms can be transformed into "standard forms", and hence standard ODE solvers can be used for direct and efficient solution. Among the existing techniques, the following three appear to be most basic and useful (Yuan (1991)).

1) *Trivial ODE.* For problems containing certain unknown constants, say α (e.g. an eigenvalue, an interface point, a Lagrange multiplier, etc.), we can establish a trivial ODE $\alpha' = 0$ for the unknown constant. This guarantees α to be a constant while incorporating the unknown α into the ODE system for a solution.
2) *Interval Mapping.* This technique maps special intervals (e.g. irregular intervals, intervals with moving end-points, infinite intervals, etc.) to a standard and definite interval. For instance, $\eta = (x-a)/(\xi - a)$ maps the moving interval $[a, \xi]$ with ξ unknown in advance to a unit interval $[0,1]$, making the definition interval of the problem definite.
3) *Equivalent ODE.* This technique is used to transform an integral such as

$$\overline{W} = \int_a^b F(t; \{y(t)\}) dt \tag{1}$$

to the following equivalent ODE problem

$$\begin{aligned} R'(x) &= F(x; \{y(x)\}) \qquad a < x < b \\ R(a) &= 0, \qquad R(b) = \overline{W} \end{aligned} \tag{2}$$

This technique can be used for normalization of eigenfunctions in eigenvalue problems.

Equipped with these ODE techniques, a much larger range of practical problems can be solved by using standard ODE solvers. This has naturally produced a new computational tool, the ODE-solver method. This method turns out to be a convenient, powerful and efficient method for most one-dimensional problems. There have been many serious applications of the ODE-solver-method, e.g. see Yuan (1993).

METHOD OF LINES (MOL)

This is a classical ODE-oriented method. The basic idea of the method is to semi-discretize a

PDE into a system of ODEs defined on discrete mesh lines by means of replacement of derivatives with respect to all but one independent variables with finite differences (FD). For example, consider the Poisson equation (elastic torsion problem) on a rectangular domain:

$$\frac{\partial^2 u}{\partial x^2}+\frac{\partial^2 u}{\partial y^2}=-2 \tag{3}$$

Replacing the derivative $\partial^2 u/\partial x^2$ by three-point central difference (with $O(h^2)$ accuracy) leads to a set of ODEs defined on discrete lines of $x=x_i$ as follows

$$u_i''=-\frac{u_{i+1}-2u_i+u_{i-1}}{h^2}-2 \qquad i=0,1,\ldots,N \tag{4}$$

where $u_i=u_i(y)=u(x_i,y)$. Introducing proper boundary conditions (BC) the ODE system is well-established and solvable. MOL is very simple, but there are two major difficulties that prevent it from being well-developed: one is how to solve the derived ODE systems which can easily be overcome by using an ODE solver, and the other one is that the method with usual FD strategy can only be applied to problems defined on regular domains. To overcome the second difficulty, the parametric FD strategy is proposed by Yuan (1993), which will be briefly discussed in next section.

PARAMETRIC FINITE DIFFERENCE METHOD OF LINES

By using parametric mesh line mapping, the classical method of lines can be extended to solve problems defined on irregular domains (Yuan (1993)). Figure 1 shows an irregular domain partitioned by vertical mesh lines of different lengths, each of which is mapped, by introducing a local parametric coordinate t, to a standard interval $t\in[-1,\ 1]$. Then a three-point central difference formula of second-order accuracy $O(h^2)$ can be constructed, e.g.

$$\begin{aligned}\left.\frac{\partial^2 u}{\partial x^2}\right|_{x_i}&=\frac{u_j-2u_i+u_k}{h^2}-\frac{u'_{yj}b_j+u'_{yk}b_k}{h^2}\\&+\frac{(2b_j-b_k)(b_j+b_k)u''_{yj}+2(b_j^2-b_jb_k+b_k^2)u''_{yi}+(2b_k-b_j)(b_j+b_k)u''_{yk}}{6h^2}+O(h^2)\end{aligned} \tag{5}$$

where $u'_{yi}=du_i/dy$, $b_j=y_j-y_i$ and $b_k=y_k-y_i$. It can be seen that when all lines are the same length, i.e. $b_j=b_k=0$, the above formula degenerates to the regular one used in Eqn. (4).

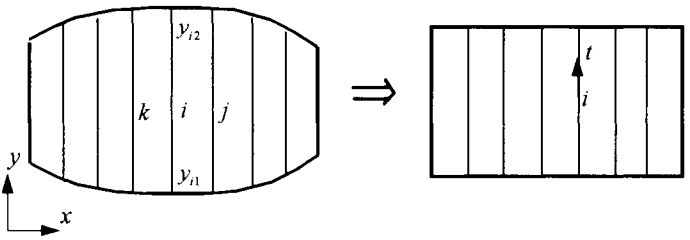

Figure 1: Parametric line mapping

Parametric finite difference formulae approximating upto fourth order derivatives on irregular mesh lines have been successfully constructed and allow a wide range of engineering problems to be solved in a semi-analytical fashion by directly discretizing a PDE into ODEs.

KANTOROVICH METHOD

Another class of ODE-oriented methods derives ODE systems by using variational principles or energy theorems. The most well-known classical method of this category is the Kantorovich method, in which a typical two-dimensional trial function is assumed to be of the form

$$u(x,y)=\sum_{i=1}^{n}\bar{X}_i(x)Y(y) \tag{6}$$

where the variation in x direction $\bar{X}_i(x)$ is *a priori* specified (e.g. series of polynomials, trigonometric functions, etc.) whereas the variation in y direction $Y_i(y)$ is left completely unknown and is to be determined by solving ODEs derived from certain variational principles. The classical Kantorovich method is superior to its fully-discrete counterpart, the Ritz method, in terms of accuracy. For many years, however, solving ODE systems had been a prohibitive difficulty and the method stopped further development. Nowadays, the situation has tremendously been changed as a number of ODE solvers appeared. Equipped with modern ODE solvers, not only can the Kantorovich method continue its due development but also a series of new ODE-oriented methods are emerging. Among those newly-developed ODE-oriented-methods, the finite element method of lines turns out to be the most well-established and developed one.

FINITE ELEMENT METHOD OF LINES (FEMOL)

The finite element method of lines (FEMOL) (Yuan, (1990, 1992, 1993)) was formally established at Tsinghua University in 1989 under the support of the National Natural Science

Foundation of China. In this method, a PDE problem defined on an arbitrary domain is semi-discretized, by FE techniques via variational principles, into a system of ODEs defined on discrete mesh lines (straight or curved), and then the resulting ODE system is solved directly by using a standard state-of-the-art ODE solver, such as COLSYS.

Using finite elements in semi-discretization allows this method to be almost as flexible and convenient as finite element methods and the use of robust ODE solvers makes the solution of the resulting ODE systems highly reliable, accurate and efficient. As a result of the combination of the FE technique and ODE solvers, the semi-analytical characteristic inherent in this method is well-preserved without introducing additional analytical work.

For the last several years, FEMOL has experienced both intensive and extensive study in the author's research group and gained remarkable advances in various directions and areas. The method tends to be mature in linear elastic fields and has shown potential power for nonlinear problems. "The Finite Element Method of Lines" (Yuan (1993)) is the first monograph about this method, which summarizes most important work in this method. Since this method is the most well-established and developed one in the ODE-oriented methods, we shall give a more extended description of the method in the following part of this section.

Standard FEMOL Elements with Curved Lines and End-sides

For general C^0 problems, FEMOL elements with curved nodal lines and end-sides can easily be established. Figure 2 shows a typical quadratic FEMOL element mapping. In general, an element mapping of degree p is

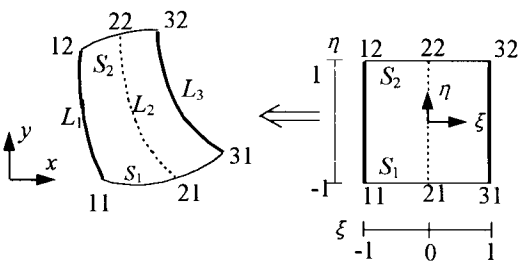

Figure 2: Typical quadratic FEMOL element mapping

$$x = \sum_{i=1}^{p+1} N_i(\xi) x_i(\eta), \quad y = \sum_{i=1}^{p+1} N_i(\xi) y_i(\eta) \tag{7}$$

where N_i's are Lagrange shape functions. The element nodal line displacement vector $\{d\}^e$ is left to be unknown, and the displacement vector $\{u\}$ on the element can be expressed by shape function interpolation to nodal line displacements, i.e.

$$\{u\} = [N(\xi)]\{d(\eta)\}^e = [N]\{d\}^e \tag{8}$$

where $[N]$ is element shape function matrix, $\{d\}^e$ is element nodal line displacement vector that contains different degrees of freedom for different problems under consideration. From the minimum potential energy principle or virtual work theorem, the following set of second order ODEs can be derived

$$[A]\{d''\}+[G]\{d'\}+[H]\{d\}+\{F\}=\{0\} \qquad -1<\eta<1 \tag{9a}$$

with three standard types of BCs:

1) Fixed end-node DOF : $d_m = \bar{d}_m$
2) Loaded end-node DOF : $Q_{jm} = \eta_j P_{jm}$ (9b)
3) Interface end-node DOF : $d_m = d_n$, $Q_{jm}+Q_{jn} = \eta_j(P_{jm}+P_{jn})$

where $\{d\}$ is global nodal line displacement vector, d_m is the m-th component in $\{d\}$, $(\ )'$ represents $d(\ )/d\eta$. Eqns. (9a) and (9b) form a standard two-point BVP in ODEs and can be solved directly by a standard ODE solver.

Error Estimates

As a semi-analytical method, FEMOL is most suitable for problems that, in the two-dimensional case, exhibit "wild" behavior in one direction (mesh-line direction) while being rather "mild" in the other. This is justified theoretically by an error analysis made by Pang (1993). An important conclusion in this error estimate is that, for standard line meshes, the errors in FEMOL solutions are independent of the true solution variations in the mesh-line direction.

"Triangular" Elements —— Degenerate Lines and End-sides

The reasonable and efficient application of FEMOL requires flexibility and arbitrariness in mesh design, which can be greatly facilitated if element end-sides and nodal lines are allowed to degenerate to points. Through careful study of the FEMOL formulation, it was found that the artificial singularity at degenerated points could be completely removed without losing accuracy and compatibility to regular elements. The detailed formulation is given in Yuan (1993). The success of degenerate elements equips FEMOL with a class of "triangular" elements that greatly enhance the flexibility and versatility of the method.

Other Special Elements

There are a number of other special elements available:

- Three-dimensional solid FEMOL element with curved lines and end-sides.
- Thin plate bending rectangular element of C^1-type. This element only requires two DOF (deflection and normal rotation) on each nodal line and is found to be highly accurate. Arbitrary shaped plate bending elements of C^1-type are not available now to the author's best knowledge.
- Singular element for singularity problems. This element can be used for crack/notch problems in fracture mechanics. Mesh lines are given radial direction and mesh-line mapping is given the following singularity mapping : $\eta = -1 + 2(r/L)^{\lambda}$, which converts a polynomial of r^{λ} to a polynomial of the local independent variable η and hence makes the solution very easy. This type of element is applicable to V-notches with any opening angles and hence is more general and accurate than the quarter-node technique frequently used in the finite element method.
- Infinite element for infinite domain problems. The idea is to introduce infinite line mapping, which, on the one hand, maps an infinite line onto a standard interval $[-1, 1]$ and, on the other hand, converts a polynomial of $1/(r+a)$ to a polynomial of the local independent variable η and hence makes the solution very easy. Unlike infinite elements in FE methods, the position of the interior node on an infinite line only modestly affects the computation time but not the final results since the ODE solver adaptively solves the solutions along the mapped infinite lines.

Software Package FML98

A general-purpose software package was developed as early as in 1992 and its newest version, FML98 for Windows (3.x, 95/NT), can solve a wide range of engineering problems of linear elasticity and free vibration, including infinite domain and singularity problems. The core computation module is written with Fortran 90 and is highly dynamic, encapsulated and modularized. A user-friendly interface written with MS Visual Basic provides an integrated environment for all preprocessing, solving and post-processing phases. The problems the package FML98 can solve are listed in Table 1.

Many practical applications have shown that FML 98 is a convenient and powerful software and is especially good for certain tough problems such as stress concentration, stress singularity, almost incompressible material, narrow and long domain problem, infinite domain problem, etc.

TABLE 1
PROBLEMS COVERED IN FML 98 FOR WINDOWS

	Problem type	Rectangular coordinates	Polar coordinates	Displacement DOF
1	Poisson's equation	(x,y)	(r,θ)	u
2	Plane stress	(x,y)	(r,θ)	u, v
3	Plane strain	(x,y)	(r,θ)	u, v
4	Axisymmetric stress	(r,z)	(R,ϕ)	w, u
5	Mindlin plate bending	(x,y)	(r,θ)	w, ψ_x, ψ_y
6	Mindlin shallow shell	(x,y)	(r,θ)	u, v, w, ψ_x, ψ_y
7	3D elasticity	(x,y,z)	(r,θ,z)	u, v, w
8	3D Poisson's equation	(x,y,z)	(r,θ,z)	u
9	Thin shells of revolution (mixed method)		(r,θ,z)	$u, v, w, \psi_\phi, \psi_\theta,$ $N_\phi, N_\theta, Q_\phi, M_\phi, M_\theta$
10	Thick shells of revolution (mixed method)		(r,θ,z)	$u, v, w, \psi_\phi, \psi_\theta,$ $N_\phi, N_\theta, Q_\phi, M_\phi, M_\theta$
11	Thick shells of revolution (displacement method)		(r,θ,z)	$u, v, w, \psi_\phi, \psi_\theta$
12	Elasticity solid of revolution		(r,θ,z)	u, v, w
13	Poisson's equation in 3D domains of revolution		(r,θ,z)	u

EXTENDED KANTOROVICH METHOD

All the methods discussed so far are characterized by solving ODEs in one coordinate direction and the other direction is left to be discretized by various means. This semi-analytical property is both good and bad. The good side is that at least it eliminates our concern in one direction (better than none), and the bad side is that the other directions still depends on us. Since the variation of a trial function is left completely unknown only in one direction (the analytical direction) and is *a priori* specified in other directions (specified direction), the quality of the solution in terms of accuracy and reliability is higher in one direction than in others.

This situation, however, can be tremendously changed by assuming a trial function that is completely unknown in both directions. Then the solution can be sought in a natural and efficient iterative manner. Since the final solution obtained from this approach is analytical in two directions (not in all directions!), we term it a bi-analytical method.

The extended Kantorovich method is a typical bi-analytical method. This method was originally proposed by Kerr (1968, 1969) and has experienced substantial development recently due to the introduction of ODE solvers. In this method, an n term trial function for a 2D problem is assumed to be of the following form

$$u(x,y)=\sum_{i=1}^{n} X_i(x)\,Y_i(y)=\{X(x)\}^T\{Y(y)\} \tag{10}$$

Compared with the classical Kantorovich method, none of the two sets $\{X(x)\}$ and $\{Y(y)\}$ is *a priori* specified, i.e. the trial function in Eqn. (10) represents a broader class of functions by removing all assumptions on both sets, and hence considerably improves the solution accuracy with the same number of terms. Applying the trial function in a variational process, we can derive two coupled sets of ODEs of the following form

$$\left[L_1(\{X\})\right]\{Y\}=\left\{F_1(\{X\})\right\},\quad \left[L_2(\{Y\})\right]\{X\}=\left\{F_2(\{Y\})\right\} \tag{11}$$

Taking the first equation as an example, $\left[L_1(\{X\})\right]$ is a differential operator matrix, $\left\{F_1(\{X\})\right\}$ is a load vector, in which each coefficient is of the form of an energy integral of $\{X\}$. The solution procedure is as follows: first a usual Kantorovich method is applied with $\{X\}$ being given, and solving the first set of equations in Eqn. (11) gives $\{Y\}$; then the obtained $\{Y\}$ is used to establish the second set of equations in Eqn. (11), the solution of which provides an improved solution $\{X\}$; these iterative steps are repeated until satisfactory results are obtained.

Due to the difficulty of the solution of ODE systems, this method did not achieve its due development. Recently, Yuan *et al.* (1992, 1998) first introduced the use of multi-term trial functions with the aid of ODE solvers and have also extended the applications of this method to a variety of problems. Theoretical study and practical applications have clearly shown the following advantages of the method.

1) *Bi-analytical:* The two dimensions are equally treated and the solution in both directions are optimally obtained by solving ODEs, and hence the accuracy is equally good in both directions.
2) *Fast convergence:* The iteration procedure converges very fast, and usually two to three iterations are sufficient.

3) *Arbitrary initial choice:* The convergence is independent of the initial function choice and it is not necessary for the initial trial functions to satisfy any boundary conditions.
4) *High accuracy:* Highly accurate results can be obtained by using very few terms of the trial functions. In most cases, however, three terms are sufficient to produce nearly exact solutions.
5) *Multi-term necessary:* In certain cases, a single-term trial function is not adequate although in many cases one term is sufficient.
6) *Solver essential:* The use of ODE solvers plays an essential role in the new implementation of the method, especially in the cases of multi-term functions.

OPTIMIZATION OF SHAPE FUNCTIONS

The above discussed bi-analytical idea can easily be extended to the existing semi-analytical method FEMOL. A typical FEMOL element trial function of degree p is usually assumed, in the local coordinate system, to be of the following form:

$$u(\xi,\eta)=\sum_{i=1}^{p+1}N_i(\xi)d_i(\eta)=[N(\xi)]\{d(\eta)\}^e \tag{12}$$

where $[N(\xi)]$ is the shape function matrix which is *a priori* assumed and $\{d(\eta)\}^e$ is the nodal line displacement vector which is to be solved from the FEMOL ODE system. The similarity of the two trial functions given in Eqn. (10) and (12) leads to a similar approach based on the same bi-analytical idea: after a standard FEMOL solution with nodal line displacement functions is obtained, the roles of the shape functions and nodal line displacement functions are exchanged, i.e. $\{d(\eta)\}^e$ is now given and known whereas $[N(\xi)]$ is in turn considered to be unknown and to be computed by another variational process. In this way, we obtain the first optimization of the shape functions for the particular problem under consideration and if needed, the above iterative procedure can be repeated as in the extended Kantorovich method.

In fact, if only one element is used for a problem, then this approach is the same as the extended Kantorovich method except for a domain mapping. If more elements are used, however, the FEMOL-based approach gains several additional advantages:

1) *Flexibility:* Problems defined on irregular domains can easily be tackled.

2) *Sparse system:* The ODEs for $[N(\xi)]$ are not coupled and only linked by BCs.

3) *Numerical stability:* The decoupled systems of ODEs tremendously enhance the numerical procedure.

Although this is a developing method that is currently undergoing intensive study, the potential advantages of this approach over the extended Kantorovich method are promising.

FINITE ELEMENT METHOD OF NETWORK LINES

FEMOL has turned out to be a general and versatile semi-analytical method. In FEMOL, element edges are distinguished by nodal lines and end-sides. The nodal lines can exactly model arbitrary domain boundary shape and the nodal line displacement function is solved from ODEs. In contrast, the element end-sides can, in general, only model boundary shape approximately and the displacement is obtained by interpolation to the nodal line values. Even with the shape function optimization presented in the previous section, the rough modeling on end-sides remains unchanged. To overcome this drawback in FEMOL, we proposed the so-called Finite Element Method of Network Lines (Yuan & Jin (1996)). In this method, we no longer distinguish lines and sides, i.e. all edges are lines and the displacements on the four edges (lines) of an element are all computed by solving ODEs. Taking a linear element as the example, the element trial function is of the following form which is basically Coon's surface interpolation (also called blending function interpolation):

$$u(\xi,\eta)=\sum_{i=1}^{2}N_i(\xi)d_i(\eta)+\sum_{j=1}^{2}N_j(\eta)d_j(\xi)-\sum_{i=1}^{2}\sum_{j=1}^{2}N_i(\xi)N_j(\eta)d_{ij} \tag{13}$$

where $N_i(\xi)$ and $N_j(\eta)$ are assumed shape functions, $d_i(\eta)$ and $d_j(\xi)$ are displacements on lines and d_{ij} is the corner displacement. In implementation, $d_i(\eta)$ and $d_j(\xi)$ are solved in an iterative manner (usually two steps) similar to the previously discussed method. Practical computation also shows that the iteration converges very fast, usually two to three steps are sufficient.

This method is a major improvement over FEMOL in that it greatly increases solution accuracy by equalizing two dimensions without increasing problem sizes.

HILBERT CONJECTURES

The common strategy in ODE-oriented methods is to approximate "PDE" by using "ODEs". Essentially, using "ODEs" to approximate "PDE" is of the same nature as using "single variable functions" to approximate "multiple variable functions". Although very little can be found about this topic in the literature, one of the twenty-three conjectures proposed by the great mathematician Hilbert is very encouraging.

The Hilbert thirteenth conjecture states roughly as follows: an arbitrary function of multiple variables on a regular domain can be represented in terms of finite number of functions of single variables. Later, Kolmogorov proved that for an arbitrary function of two variables $f(x,y)$, there exist five pair of functions of single variables $h_i(x)$ and $g_i(y)$ such that

$$f(x,y)=\sum_{i=1}^{5} F_i(h_i(x)+g_i(y)) \tag{14}$$

However, Kolmogorov only proved the existence but did not provide the construction method.

Suppose the Hilbert conjecture holds true. Then this implies that instead of solving a PDE problem directly, one can equivalently solve a set of finite number of ODEs. In other words, a PDE can be converted into a system of ODEs in which the number of the unknown components is finite. Then, an ODE-oriented method can, if appropriately configured, serve as an exact method for a PDE problem. This is especially attractive nowadays when a number of powerful ODE solvers are available.

Perhaps this is only a dream. But it is a nice dream. It is such a nice dream that we do not want to wake up and lose it. We wish one day this dream would come true.

ACKNOWLEDGMENTS

This project is supported by the National Natural Science Foundation of China.

REFERENCES

Ascher U., Christiansen J. and Russell R.D. (1981). Collocation Software for Boundary-Value ODEs. *ACM Trans. Math. Software* **7:2**, 209-222.

Ascher U., Christiansen J. and Russell R.D. (1981). Algorithm 569, COLSYS: Collocation Software for Boundary-Value ODEs [D2]. *ACM Trans. Math. Software* **7:2**, 223-229.

Ascher U. and Russell R.D. (1981). Reformulation of Boundary Value Problems into 'Standard' Form. *SIAM Rev.* 23, 238-254.

Keller H.B. (1976). *Numerical Solution of Two Point Boundary Value Problems*, Philadelphia.

Kerr A.D. (1968). An Extension of the Kantorovich Method. *Quarterly Journal of Applied Math.* **26**, 219-229.

Kerr A.D. and Alexander H. (1968). An Application of the Extended Kantorovich Method to the Stress Analysis of A Clamped Rectangular Plate. *Acta Mech.* **6**, 180-196.

Kerr A.D. (1969). An Extended Kantorovich Method for the Solution of Eigenvalue Problems. *Int. J. Solids Structures* **5**, 559-572.

Pang Z. (1993). An Error Estimate of the Finite Element Method of Lines. *Computational Mathematics,* **15:5,** 552-560 (in Chinese).

Yuan S. (1991). ODE Conversion Techniques and Their Applications in Computational Mechanics. *Acta Mechanica Sinica* **7:3,** 283-288.

Yuan S. (1990). A New Semidiscrete Method: The Finite Element Method of Lines. *Proc. of 1st National Conference on Anaytical and Numerical Combined Methods, Hunan, China,* 132-136 (in Chinese).

Yuan S. (1993). The Finite Element Method of Lines. *Chinese J. Num. Math. & Appl.* **15:1,** 45-59.

Yuan S. (1993). *The Finite Element Method of Lines: Theory and Applications*, Science Press, Beijing-New York.

Yuan S. and Zhang Y. (1992). Further Extension of the Extended Kantorovich Method. *Computational methods in engineering — advances and applications, eds. Tay, A. A. O. and Lam, K. Y., World Scientific*, **2**, 1240-1245.

Yuan S. and Jin Y. (1996). A Class of Bi-analytical Methods in Structural Analysis. *New Developments in Structural Engineering —— Theories and Practices (eds. Si Yuan and Zhiliang Ma, China Architecture and Building Press, Beijing*, 243-248.

Yuan S., Jin Y. and Williams F.W. (1998). Bending Analysis of Mindlin Plates by the Extended Kantorovich Method. *ASCE Engineering Mechanics*, accepted for publication.

Yuan S. and Jin Y. (1998). Computation of elastic buckling loads of rectangular thin plates using the extended Kantorovich method. *Computers and Structures*, **66:6,** 861-867.

INDEX OF CONTRIBUTORS

KEYWORD INDEX